Échanges de CO_2 atmosphérique dans les marais Charentais : processus, dynamique et facteurs de contrôle associés.

Jérémy Mayen

COLLEGE DOCTORAL PAYS DE LA LOIRE
VEGETAL ANIMAL, ALIMENT MER, ENVIRONNEMENT

Nantes Université

THESE DE DOCTORAT

NANTES UNIVERSITE

ECOLE DOCTORALE N° 642
Ecole doctorale Végétal, Animal, Aliment, Mer, Environnement
Spécialité : *Biologie et écologie marine*

Par

Jérémy MAYEN

Échanges de CO_2 atmosphérique dans les marais Charentais : processus, dynamique et facteurs de contrôle associés

Thèse présentée et soutenue à Nantes, le 29 février 2024
Unité de recherche : Ifremer, Unité Littoral, Laboratoire Environnement Ressources des Pertuis Charentais (LER-PC) et Morbihan Pays de Loire (LER-MPL)

Rapporteurs avant soutenance :

Gwenaël ABRIL	Directeur de recherche, CNRS, Paris
Philippe PONDAVEN	Professeur, Université de Bretagne Occidentale, Plouzané

Composition du Jury :

Président :	Vona MELEDER	Professeure, Nantes Université
Examinateurs :	Gwenaël ABRIL	Directeur de recherche, CNRS, Paris
	Philippe PONDAVEN	Professeur, Université de Bretagne Occidentale, Plouzané
	Christine DUPUY	Professeure, La Rochelle Université
	Vona MELEDER	Professeure, Nantes Université
	Vanina PASQUALINI	Professeure, Université de Corse
Directeur de thèse :	Philippe SOUCHU	Cadre de recherche HDR, Ifremer, Nantes
Co-encadrants de thèse :	Pierre POLSENAERE	Cadre de recherche, Ifremer, La Tremblade
	Aurore REGAUDIE DE GIOUX	Cadre de recherche, Ifremer, Plouzané

Invité
Philippe GOULLETQUER Directeur scientifique HDR, Ifremer, Nantes

Cette thèse est dédiée à ma maman

Résumé

Les marais littoraux sont des écosystèmes productifs permettant la captation de CO_2 atmosphérique par une forte production primaire. Leur métabolisme entraine également une exportation latérale importante de carbone (C) organique et inorganique via le compartiment aquatique. Au regard de l'importance des marais dans le cycle du C, l'objectif général de la thèse a été de comprendre les processus biologiques et physico-chimiques contrôlant les flux de C aux interfaces terrestre-aquatique-atmosphérique des marais Charentais. Les mesures des pCO_2 de l'eau ont montré un fort contrôle de la typologie des écosystèmes côtiers sur la dynamique du C inorganique avec des variations spatiales significatives le long d'un continuum plateau continental – estuaire – marais. Dans les marais salés rétro-littoraux, les pratiques de gestion (naturelle ou anthropique) et les types de producteur primaire (macroalgues ou herbiers) influencent le statut métabolique (source ou puits de C). Au sein d'un marais tidal, les échanges nets de CO_2 à l'échelle de l'écosystème (NEE) ont été mesurés pour quantifier le statut métabolique et évaluer l'influence des facteurs biotiques et abiotiques. Un fort puits de CO_2 atmosphérique a été mesuré par la photosynthèse des plantes émergées. Cependant, l'immersion a fortement influencé les flux métaboliques en diminuant la captation de CO_2 le jour et les émissions de CO_2 la nuit. Au sein d'une troisième partie, les formes organiques et inorganiques du C, les nutriments et le métabolisme planctonique ont été mesurés sur des cycles de 24-h en simultané avec la NEE pour évaluer la contribution du métabolisme aquatique dans les flux horizontaux et verticaux de C des marais.

Mots clés : marais littoraux, pCO_2 de l'eau, flux de CO_2 atmosphérique, producteur primaire, métabolisme aquatique, variations temporelles.

Abstract

Coastal marshes are shallow productive ecosystems allowing atmospheric CO_2 uptake through strong primary production of plants and algae. The metabolism of these dynamics systems also exports significant and variable amounts of organic and inorganic carbon (C) to coastal waters through the aquatic compartment. Due to the importance of marshes in the C cycle, the general objective of this PhD thesis was to measure and understand the biological, physical and chemical processes controlling C fluxes at the terrestrial – aquatic – atmospheric interfaces of the Charentais marshes. High-frequency measurements of water pCO_2 showed a strong control of the coastal ecosystem typology on inorganic C dynamics, with significant spatial variations along a continental shelf – estuary – marsh continuum. In artificial salt marshes, management practices (natural or anthropogenic) and the types of primary producer (macroalgae or seagrass) influence the metabolic status (source or sink of CO_2). Within a tidal salt marsh, net ecosystem CO_2 exchange (NEE) were measured to quantify the marsh metabolic fluxes and evaluate the relevant environmental factors that control NEE fluxes. The results showed a strong annual atmospheric CO_2 sink through the photosynthesis of emerged halophyte plants. However, tidal immersion significantly disrupted the marsh metabolic fluxes, reducing net CO_2 uptake during the day and net CO_2 emissions during the night. In the third part, organic and inorganic forms of C, nutrients and planktonic metabolism were measured over 24-h cycles simultaneously with the NEE fluxes to assess the contribution of aquatic metabolism to horizontal and vertical fluxes of C in marshes.

Keywords: coastal marshes, water pCO_2, atmospheric CO_2 flux, primary producers, aquatic metabolism, temporal variations.

Remerciements

Je remercie tout d'abord la Direction Scientifique de l'Ifremer pour avoir financé ces travaux de thèse en biogéochimie au sein de l'Unité Littoral. Je remercie également les membres du jury pour avoir rapporté et examiné mes travaux : Gwenaël Abril et Philippe Pondaven en tant que rapporteurs ; Christine Dupuy, Vona Méléder et Vanina Pasqualini en tant qu'examinatrices ; Philippe Souchu, Pierre Polsenaere et Aurore Regaudie De Gioux en tant qu'encadrants ; Philippe Goulletquer en tant qu'invité. Vos différentes remarques, vos précieux conseils et nos discussions scientifiques lors de la soutenance m'auront énormément apporté pour finaliser ce manuscrit et pour que ma thèse soit une aide à la gestion du littoral face aux changements climatiques. Je suis très honoré que vous ayez accepté d'évaluer mes travaux de thèse.

Cette thèse n'aurait jamais pu être possible sans l'aide précieuse, les conseils et les encouragements de mes encadrants Pierre, Philippe et Aurore. Je souhaite à tous les doctorants d'être aussi bien accompagné durant leur parcours de thèse !

Tout d'abord, je souhaite remercier très chaleureusement Pierre pour m'avoir fait confiance dans cette belle aventure scientifique sur le carbone qui a débuté à la station de L'Houmeau en 2019 ! Tu auras contribué de manière très forte dans ma formation à la recherche depuis mon stage de Master 1 jusqu'à la rédaction de cette thèse. Je t'adresse un immense MERCI pour ta grande disponibilité pendant ces cinq dernières années, pour toutes les connaissances scientifiques que tu m'as transmises et surtout pour ton aide précieuse dans la relecture des manuscrits. Je te remercie de m'avoir soutenu dans les moments intenses. Je garderai en mémoire des moments incroyables sur le terrain pendant nos cycles de 24 heures, les échantillonnages et les filtrations entre minuit et 6 heures auront toujours été les plus durs et surtout les plus froids (même en été) mais nous avons tenus sans n'avoir quasiment jamais dormis ! C'était formidable ! Je n'oublie pas non plus notre semaine de congrès à l'AGU de San Francisco en décembre 2023 qui fut une très belle découverte pour moi, même si j'étais déjà en panique pour la rédaction de cette thèse. Merci encore pour tout !

Je souhaite également remercier tout particulièrement Philippe, mon directeur de thèse, qui m'a accueilli les bras ouverts dans son bureau à l'été 2022. Tu auras été un véritable guide et soutien pendant la deuxième partie de ma thèse, merci pour ton implication si précieuse. Tu m'auras beaucoup appris en écologie et en biogéochimie, sur la rédaction des articles et sur la recherche scientifique, je garderai une trace très forte de mon travail à tes côtés et de toutes

tes connaissances que tu m'as transmises. Ta passion de la recherche m'aura vraiment donné l'envie de continuer mon projet vers un post-doc, je t'en remercie énormément. J'ai l'impression d'avoir progressé rapidement suite à nos nombreuses discussions et à tous les « caviardages » à l'encre rouge. Mais heureusement, nous n'avons pas discuté que de science, nous avons aussi partagé nos belles analyses rugby pendant cette coupe du monde 2023 ! C'est avec beaucoup d'amitiés que je te souhaite une très bonne retraite et que je te remercie pour tout ce que tu m'as apporté.

Pour finir, je tiens également à remercier très chaleureusement Aurore pour ton soutien tout au long de ma thèse, pour la grande disponibilité que tu m'as accordé malgré notre éloignement géographique, pour la relecture des manuscrits et pour toutes les connaissances que tu m'as apporté sur le métabolisme planctonique. Merci également pour les moments partagés sur le cycle de 24 h et pour toute ta gentillesse. Je te remercie également d'avoir facilité ma venue à PELAGOS à la fin de l'année 2020 et à l'été 2022.

Je remercie Éric Lamaud (INRAE) et Laurent André (BRGM) pour avoir fait partie de mon comité de suivi de thèse et bien plus ! Éric, ton investissement précieux et ta rigueur tout au long de ma thèse m'auront énormément aidé dans le traitement et l'analyse des données d'eddy et dans la relecture de l'article Biogeosciences, merci beaucoup encore pour ton accompagnement. Laurent, je te remercie sincèrement pour tout ce que tu m'as apporté dans en géochimie, pour ton soutien, ta gentillesse et ta disponibilité ! Je suis très heureux d'avoir pu suivre le stage en modélisation au BRGM à Orléans avec toi.

Je remercie l'équipe du LER/PC (L'Houmeau et La Tremblade) pour m'avoir accueilli et accompagné pendant mes stages de master 1 (2019) et master 2 (2020) et pendant la première moitié de ma thèse. Merci beaucoup à tous pour cette expérience scientifique au sein de ce laboratoire et pour votre aide au cours de ma thèse. Je remercie tout particulièrement Jonathan pour être venu faire l'ensemble des cycles de 24 h avec Pierre et moi, merci pour ton investissement précieux sur le terrain et pour le déploiement des sondes. Je remercie sincèrement Philippe pour ton aide sur le terrain, dans la réalisation des cartes et pour la construction du MNT. Merci pour tous les moments passés ensemble ! Merci également à Aude pour les lectures de flore dans les échantillons de Brouage. Je remercie Audrey (responsable du LER/PC) et Bénédicte (responsable de la station de La Tremblade) pour leur aide et leur accueil chaleureux. Pour finir, je remercie Marie Arnaud et Pierre Kostyrka qui sont passés par le LER/PC et qui m'auront accompagné et aidé durant une partie de ma thèse. Merci également pour vos contributions dans les cycles de 24 h !

Je tiens à remercier vraiment très sincèrement toute l'équipe du LER/MPL à Nantes pour leur accueil chaleureux pendant la deuxième partie de ma thèse et pour l'ensemble des analyses laboratoire réalisées (le carbone avec Karine, les nutriments avec Yoann et les lectures de flore avec Anne). Vous avez été d'un soutien immense et d'une aide précieuse pendant ma période de rédaction, je garderai un souvenir très fort de mon passage au sein de l'équipe et des sorties en mer. Merci tout particulièrement à Olivier, Karine, Lucie, Mathilde, Yoann et Anne pour tous ces très bons moments passés ensemble ! Je n'oublie pas non plus Victor qui vient d'arriver au labo, merci pour ton soutien et je te souhaite le meilleur pour ta thèse ! Je remercie aussi Cathy (responsable du LER/MPL) pour ton aide, ta disponibilité et pour avoir fait en sorte que tout se passe le mieux possible dans ma thèse. Merci également aux jeunes retraités Mirelle et Françoise pour votre gentillesse et votre bonne humeur au quotidien. Je remercie également Alice pour les mêmes raisons et également pour ton aide dans ma mission à San Francisco et dans l'organisation de ma soutenance de thèse. Merci à tous pour cette très belle expérience scientifique et humaine au sein du labo, j'espère que l'on retravaillera ensemble ! Vous m'avez énormément apporté en biogéochimie des nutriments, j'espère vous avoir apporté en biogéochimie du carbone 😉

Merci beaucoup à tous les autres collègues à l'Ifremer qui ont réalisé des analyses laboratoires au cours de ma thèse : Élodie Foucault pour l'alcalinité à Sète (LER/LR), Marie Latimier pour la cytométrie en flux à Plouzané (PELAGOS) et Clarisse Hubert pour la matière organique particulaire à Nantes (PHYTOX). Un grand merci en particulier à Élodie pour son investissement à me former aux analyses alcalinité. Je remercie également Vincent Ouisse pour sa participation en permettant ces analyses d'alcalinité au LER/LR mais aussi dans sa relecture de l'article. Merci beaucoup Vincent et Élodie pour les moments très sympas passés ensemble à Sète. Je remercie le laboratoire LER/LR ainsi que le laboratoire PELAGOS pour m'avoir accueilli quelques jours à deux reprises au cours de ma thèse et de m'avoir donné l'opportunité de présenter mes travaux.

Pour terminer les remerciements professionnels, je tiens à remercier les doctorants et ex-doctorants que j'ai croisé pendant ma thèse à La Tremblade, à La Rochelle et à Nantes pour tous les bons moments passés ensemble (Raphael, Lauriane, Mireia, Camille, Antoine, Nicolas, Pauline, Thomas, Océane, Loïc, Victor et tous les autres). Mention spéciale à Loïc et Océane qui m'auront énormément soutenu pendant la période de rédaction et pour tous les moments de détente et de partage.

Je tiens également à remercier sincèrement Landry, Vincent et Mickael qui sont, depuis longtemps, bien plus que des amis ! Déjà 17 ans d'amitié et énormément de chemins parcourus depuis l'entrée au collège et au lycée, Vincent tu es déjà docteur, Landry tu le seras bientôt et Micka, tu es déjà papa, félicitions à vous ! Merci pour votre soutien immense et permanent tout au long de cette thèse et en particulier pendant les moments les plus intenses.

Je remercie très sincèrement ma famille pour son aide et son soutien immense tout au long de mes études et jusqu'à l'aboutissement de cette thèse ! Je remercie Isabelle et Laurent ainsi que les cousines pour m'avoir accueilli pendant mes stages de master et pour tous les moments passés ensemble ! Une grosse pensée aussi pour ma grand-mère « mamou » qui est très fière. Merci beaucoup à mes deux frangines Céline et Cynthia d'avoir toujours été présentes. Pour finir, je remercie tout particulièrement ma maman qui m'a apporté toute la force, le courage et la persévérance pour en arriver jusqu'ici. Merci pour tout ce que tu m'as apporté dans la vie !

Je tiens à garder ces dernières phrases de remerciement pour une personne très importante dans ma vie qui m'aura soutenu au quotidien tout au long de cette thèse. Chloé, je te remercie mille fois pour toute ta patience, ta fierté et ton amour ! Je ne te remercierai jamais assez pour tous les encouragements que tu m'as apporté, notamment lors de ces 6 derniers mois. Nous avons traversé cette expérience à deux, MERCI POUR TOUT !

Table des matières

THESE DE DOCTORAT 1
NANTES UNIVERSITE 1
Liste des publications 14
Liste des communications orales 15
Encadrement et enseignements 17
Vulgarisation scientifique 18
Abréviations 19
Listes des figures 21
Listes des tableaux 30
Introduction générale de la thèse 33
Chapitre I 38
1. Cycle du carbone 39
1.1. Le cycle global du carbone 39
1.2. Le cycle du carbone dans les océans 41
1.3. Le système des carbonates de l'océan ouvert à l'océan côtier 43
1.4. La zone côtière, une interface dynamique et hétérogène d'un point de vue du C 46
1.4.1. Rôle de la zone côtière dans les processus et flux de carbone 47
1.4.2. Biogéochimie du carbone en zone côtière 49
2. Les marais, écosystèmes complexes à l'interface entre la terre et la mer 53
2.1. Les marais naturels peu anthropisés 54
2.1.1. Les marais tidaux 54
2.1.2. Les marais non tidaux 57
2.2. Les marais anthropisés 57
2.2.1. Les marais salés rétro-littoraux 58
2.2.2. Les marais doux rétro-littoraux 59
2.3. Fonctions et services écosystémiques des marais littoraux 60
2.3.1. Fonctions écologiques 60
2.3.2. Services écosystémiques 60
2.3.3. Altérations des marais salés 61
3. Métabolisme et dynamique du carbone dans les marais 62
3.1. Métabolisme : photosynthèse versus respiration 62
3.2. Les facteurs physico-chimiques influençant le métabolisme phytoplanctonique 63
3.3. Dynamique et flux de carbone dans les marais salés 67
3.4. Relations entre métabolisme et échanges de CO_2 atmosphérique dans les marais tidaux. 71
4. Approches méthodologiques aux mesures des pCO_2 et des flux de CO_2 atmosphérique 73
4.1. Mesures des pCO_2 de l'eau et estimation des flux de CO_2 eau-air 73
4.2. Eddy Covariance atmosphérique 75
5. Présentation des sites d'études 78
6. Objectifs et organisation de la thèse 84
6.1. Les objectifs scientifiques de la thèse et travail de terrain 84
6.2. Organisation du mémoire de thèse 86
Chapitre II 89
1. Introduction 93
2. Materials and methods 95
2.1. Study sites 95
2.1.1. Tidal estuary (station *a*) and channel (station *b*) 95
2.1.2. Rewilded artificial salt marsh (station *c*) 97

2.1.3. Working artificial salt marsh (station *d*) 97
2.1.4. Additional station: continental shelf (station *F*) 98
2.2. Measurement strategy and biogeochemical measurements 98
2.3. Temperature and non-temperature effects on pCO_2 variations 100
2.4. Calculations of air-water CO_2 fluxes 100
2.5. Chl a concentrations and fluorometer data calibration 101
2.6. Statistical tools and analysis 102
3. Results 103
3.1. Biogeochemical overview of the aquatic continuums 103
3.2. Seasonal variations and controls along the aquatic continuums 106
3.3. Diurnal/tidal variations and controls along the aquatic continuums 112
3.4. Air-water CO_2 flux variations 115
4. Discussion 119
4.1. Biogeochemical parameter relationships and pCO_2 controls along the shelf - estuary - marsh continuums 119
4.2. Continuum typologies revealed from measured biogeochemical parameters 120
4.3. Temporal carbon modulation by management practices 122
4.4. Metabolism assessment of the sea-land continuums 125
5. Conclusion 126
Chapitre III 134
1. Introduction 137
2. Materials and methods 139
2.1. Study site 139
2.2. Eddy covariance and micrometeorological measurements 143
2.3. Footprint estimation and immersion/emersion marsh heterogeneity 145
2.4. EC data processing and quality control 146
2.5. Flux gap filling and statistic tools 147
2.6. Temporal analysis of NEE fluxes and partitioning 148
3. Results 150
3.1. Habitat covering of the footprint 150
3.2. Seasonal variations of environmental conditions and NEE fluxes 151
3.3. Environmental parameter and NEE flux variations at diurnal and tidal scales 154
3.4. Influence of environmental drivers on temporal NEE variations 156
3.5. Annual Carbon budgets 161
4. Discussion 164
4.1. Marsh CO_2 uptake and influence of management practice 164
4.2. Metabolism processes and controlling factors at multiple timescales 166
4.2.1. Seasonal scale 166
4.2.2. Diurnal and tidal scale influences 167
4.3. Salt marsh carbon budgets for future research perspectives 170
5. Conclusion 171
Chapitre IV 180
1. Introduction 184
2. Materials and methods 186
2.1. Study site 186
2.2. Sampling strategy and field techniques 188
2.3. Online parameters 192
2.3.1. Water pCO_2 measurements and associated physicochemical parameters 192
2.3.2. Atmospheric eddy covariance measurements 192
2.4. Analytical procedures 193

2.4.1. Discrete parameters 193
2.4.2. Planktonic metabolism parameters 195
2.5. Calculations 196
2.5.1. Air-water CO_2 fluxes 196
2.5.2. Net ecosystem production of water column ($NEP_{aquatic}$) 197
2.6. Data analysis and statistical analysis 197
3. Results 198
3.1. Meteorological and environmental settings 198
3.2. Temporal variations of water pCO_2 and atmospheric CO_2 exchanges 199
3.3. Planktonic biomass, abundance and metabolism 201
3.4. Analytical biogeochemical measurements from water samples 206
3.5. Statistical analysis 211
3.6. Net ecosystem CO_2 exchanges and daily C balances 211
4. Discussion 217
4.1. Temporal variations of water pCO_2 and controlling factors 217
4.2. Marsh primary producer influence on water pCO_2 and DOC 219
4.3. Aquatic marsh respiration processes as source of DIC 221
4.4. Influence of aquatic and benthic metabolism on marsh ecosystem CO_2 exchanges 223
Chapitre V 232
1. Synthèse des pCO_2 de l'eau dans les marais Charentais 233
1.1. Influence de la typologie des marais littoraux sur la dynamique des pCO_2 de l'eau…. 233
1.2. Influence du mode de gestion des marais littoraux sur la dynamique pCO_2 de l'eau…. 236
1.3. Influence de la renaturation des marais littoraux sur le statut métabolique du CO_2 de l'eau (source/puits) : cas du marais de Tasdon 241
2. Variations des échanges nets de CO_2 atmosphérique au sein d'un marais tidal 245
2.1. Aspects methodologies 245
2.2. Variations temporelles de la NEE d'un marais tidal 247
2.3. Variations spatiales de la NEE au sein d'un marais tidal 249
3. Influence du métabolisme aquatique sur les flux horizontaux et verticaux de carbone. 251
Conclusions de la thèse 256
Perspectives de thèse 259
Annexes chapitre V 263
Bibliographie chapitres I et V 265

Liste des publications

Articles acceptés et publiés

- **Mayen, J.**, Polsenaere, P., Regaudie De Gioux, A., Dupuy, C., Vagner, M., Lemesle, J.-C., Poitevin, B., and Souchu, P.: Influence of typology and management practices on water pCO_2 and atmospheric CO_2 fluxes over two temperate shelf–estuary–marsh water continuums, Regional Studies in Marine Science, 67, 103209, https://doi.org/10.1016/j.rsma.2023.103209, 2023.

- **Mayen, J.**, Polsenaere, P., Lamaud, É., Arnaud, M., Kostyrka, P., Bonnefond, J.-M., Geairon, P., Gernigon, J., Chassagne, R., Lacoue-Labarthe, T., Regaudie De Gioux, A. and Souchu, P.: Atmospheric CO_2 exchanges measured by eddy covariance over a temperate salt marsh and influence of environmental controlling factors, Biogeosciences, 21(4), 993-1016. Publisher's official version: https://doi.org/10.5194/bg-21-993-2024, Open Access version: https://archimer.ifremer.fr/doc/00882/99396/, 2024.

Articles en cours de préparation

- **Mayen, J.**, Polsenaere, P., Regaudie de Gioux, A., Deborde, J., Collin, K., Le Merrer, Y., Foucault, E., Ouisse, V., André, L., Lamaud, É. and Souchu, P.: Influence of aquatic metabolism on temporal marsh carbon dynamics and associated atmospheric CO_2 fluxes, Limnology and Oceanography. In preparation.

- Bergeon, L., **Mayen, J.**, Azémar, F., Polsenaere, P., Carré, C., Bouvy, M., Dubillot, B., Emery, C., Pineau, P., Agogué, H., Paoletti, M., Vagner, M., Tackx, M., Dupuy, C.: Impact of changing the management of an urban wetland on its ecological functions through the study of planktonic communities: the case of the Tasdon marsh (Charente-Maritime, France). In preparation.

Liste des communications orales

Conférences internationales

- **Mayen J.**, Polsenaere P., Geairon P., Chabirand J.-M., Deborde J., Grizon J., Lemesle J.-C., Poitevin B., Dupuy C., Vagner M.: Spatial and temporal variations in water pCO_2 and atmospheric CO_2 exchanges over a temperate salt marsh system. ASLO 2021– Aquatic Sciences Meeting "Aquatic Sciences for a Sustainable Future: Nurturing Cooperation". 22–27 June 2021, Virtual Meeting.

- Polsenaere P., Lamaud E., Bonnefond J.-M., Garrigou D., Gernigon J., Deborde J., Geairon P., Kostyrka P., **Mayen J.**, Arnaud M., Chassagne R., Lacoue-Labarthe T.: Water inputs influences on atmospheric CO_2 exchanges on a temperate salty meadow revealed through Eddy Covariance flux measurements. ASLO 2021 - Aquatic Sciences Meeting "Aquatic Sciences for a Sustainable Future: Nurturing Cooperation". 22–27 June 2021, Virtual Meeting.

- **Mayen J.**, Polsenaere P., Regaudie de Gioux A., Deborde J., Collin K., Le Merrer Y., Foucault É., Ouisse V., André L., Arnaud M., Kostyrka P., Lemesle J.-C., Lelong V., Vagner M., Souchu P.: Influence of aquatic metabolism on marsh carbon dynamics and associated atmospheric CO_2 fluxes. AGU23 – WIDE. OPEN. SCIENCE. 11–15 December 2023, San Francisco, USA.

- Polsenaere P., Afonso M., Amann B., Arnaud M., Bonnefond J.-M., Chassagne R., Chaumillon E., Costes L., Coutantin M., Deborde J., Dubillot E., Dupuy C., Geairon P., Gernigon J., Gueret J.-P., Kostyrka P., Lachaussée N., Lacoue-Labarthe T., Lamaud E., Long N., **Mayen J.**, Méléder V., Paschal M., Pery C., Philippine O., Rouquette H., Soudant D., Volto N. , Zhang M.: Atmospheric Eddy Covariance CO_2 exchanges over temperate mudflat, salt and freshwater marsh continuums: from ecological functioning understanding to future perspectives and collaborations. AGU23 – WIDE. OPEN. SCIENCE. 11–15 December 2023, San Francisco, USA.

Conférences nationales

- **Mayen J.** et Polsenaere P. : Le marais de Tasdon, émetteur ou puits de carbone ? Conférence Le carbone bleu au sein du projet La Rochelle Territoire Zéro Carbone (LRTZC). 3 juillet 2023, La Rochelle, France.

- **Mayen J.**, Polsenaere P., Regaudie de Gioux A., Deborde J., Arnaud M., Kostyrka P., Collin K., Le Merrer Y., Foucault É., Ouisse V., André L., Lemesle J.-C., Lelong V., Vagner M., Souchu P. : Influence du métabolisme planctonique sur la dynamique du carbone des marais. Colloque de restitution du projet de l'ANR-PAMPAS « Le patrimoine des marais littoraux face aux changements globaux ». 9-10 novembre 2023, La Rochelle, France.

Encadrement et enseignements

Encadrement de stage

- Delmer Stacy (2022). Dynamique temporelle du carbone au sein d'un marais tidal tempéré. Rapport de stage de L3 Université Paris Est Creteil.

Enseignements à l'université

- Gestion intégrée des zones humides côtières (6 h en 2022), Master 2 sciences pour l'environnement, parcours gestion de l'environnements et écologie littorale, La Rochelle Université. Enseignements en TD et TP.

- Océanographie côtière et dynamique trophique (22 h en 2023), Master 1 sciences pour l'environnement, parcours gestion de l'environnements et écologie littorale, La Rochelle Université. Enseignements en CM, TD et TP.

Vulgarisation scientifique

- Objectif Zéro carbone à La Rochelle (5) : le marais de Tasdon

https://www.youtube.com/watch?v=UIwgXallKbg

- Le marais de Tasdon à La Rochelle : puits de carbone ou source de carbone ?

https://www.sudouest.fr/charente-maritime/le-marais-de-tasdon-a-la-rochelle-puits-de-carbone-ou-source-de-carbone-7381503.php

- Un marais peut-il devenir un "puits de carbone" : l'expérience est lancée à La Rochelle

https://www.francebleu.fr/infos/sante-sciences/un-marais-peut-il-devenir-un-puits-de-carbone-l-experience-est-lancee-a-la-rochelle-1639653545

Abréviations

C	Carbon	Carbone
N	Nitrogen	Azote
P	Phosphorus	Phosphore
CO_2	Carbon dioxide	Dioxyde de carbone
pCO_2	Partial pressure of CO_2	Pression partielle de CO_2
FCO_2	Estimated water-air CO_2 fluxes	Flux de CO_2 eau-air estimé
k	Gas transfer velocity	Coefficient de transfert du CO_2 entre l'eau et l'air
α	CO_2 solubility coefficient	Coefficient de solubilité du CO_2 dans l'eau
EC	Eddy Covariance	Eddy Covariance
NEE	Net Ecosystem CO_2 Exchange measured by EC	Échanges nets de CO_2 de l'écosystème mesuré par EC
NEE_{marsh}	Net Ecosystem CO_2 Exchange estimated at the marsh-atmosphere interface without tidal immersion	Échanges nets de CO_2 de l'écosystème estimé à l'interface marais-atmosphère sans immersion tidale
NEP	Net Ecosystem Production	Production nette de l'écosystème
NPP	Net Primary Production	Production primaire nette
R_{eco}	Ecosystem Respiration	Respiration de l'écosystème
GPP	Gross Primary Production	Production primaire brute
NCP	Net Community Production	Production nette de la communauté
CR	Community Respiration	Respiration de la communauté
DO	Dissolved oxygen	Oxygène dissous
DO-sat.	Dissolved oxygen saturation level	Pourcentage de saturation en oxygène dissous
TC	Total Carbon	Carbone total
OC	Organic Carbon	Carbone organique
OM	Organic Matter	Matière organique
DOC	Dissolved Organic Carbon	Carbone organique dissous

POC	Particulate Organic Carbon	Carbone organique particulaire
DIC	Dissolved Inorganic Carbon	Carbone inorganique dissous
HCO_3^-	Bicarbonate ions	Ions bicarbonates
CO_3^{2-}	Carbonate ions	Ions carbonates
$CaCO_3$	Calcium carbonate	Carbonate de calcium
TA	Total Alkalinity	Alcalinité totale
TN	Total Nitrogen	Azote total
DON	Dissolved Organic Nitrogen	Azote organique dissous
PON	Particulate Organic Nitrogen	Azote organique particulaire
NH_4^+	Ammonium	Ammonium
NO_3^-_NO_2^-	Nitrate + Nitrite	Nitrate + Nitrite
DIN	Dissolved Inorganic Nitrogen	Azote inorganique dissous
$Si(OH)_4$	Silicate	Silicate
PO_4^{3-}	Phosphate	Phosphate
DIP	Dissolved Inorganic Phosphorus	Phosphore inorganique dissous
Chl *a*	Chlorophyll *a*	Chlorophylle *a*
PAR	Photosynthetically Active Radiation	Radiation active photosynthétique
VPD	Vapor Pressure Deficit	Déficit de pression de vapeur d'eau
RH	Relative Humidity	Humidité relative
Ta	Air temperature	Température de l'air
Tw	Water temperature	Température de l'eau
Hw	Water height	Hauteur d'eau

Listes des figures

• Chapitre I

Figure 1.1 : Budget global du carbone (CO_2) pour la période 2010-2019. Les flèches orange représentent les flux annuels de carbone (en Pg C an^{-1}) associés au cycle naturel, estimés pour la période précédant l'ère industrielle, vers 1750. Les flèches roses représentent les flux anthropiques de carbone moyennés sur la période 2010-2019. Le taux d'accumulation de carbone dans l'atmosphère est égal à la somme des émissions nettes liées aux changements d'occupation des sols et aux combustions fossiles auxquelles sont déduits les puits nets des terres et des océans. Les cercles avec les nombres en jaune correspondent aux stocks de carbone préindustriel (en Pg C an^{-1}) et les cercles avec des nombres en rose correspondent aux changements anthropiques (flux anthropiques cumulés) de ces stocks depuis 1750. Le carbone dans les eaux océaniques existe sous plusieurs formes : carbone inorganique dissous (37 100 Pg DIC), carbone organique dissous (700 Pg DOC) et carbone organique particulaire (13-23 Pg POC) dans un rapport proche de DIC:DOC:POC = 2000:38:1. 1 Pg = 1 Gt = 10^{15} g. Schéma issu du sixième rapport d'évaluation de l'IPCC (Intergovernmental Panel on Climated Change ; Canadell et al., 2021).

Figure 1.2 : Tendances historiques des émissions de CO_2 atmosphérique (en Pg C an^{-1} = 10^{15} g C an^{-1}) par les activités anthropiques (combustion fossiles et changements d'occupation des sols) pour la période entre 1880 et 2019. Le terme « others » dans la légende représente principalement les émissions de carbonates lors de la fabrication de ciment. Schéma issu du sixième rapport d'évaluation de l'IPCC (Canadell et al., 2021).

Figure 1.3 : Les trois pompes océaniques à carbone permettant la régulation des fluctuations naturelles de CO_2 atmosphérique : la pompe de solubilité, la pompe à carbone organique et la contre pompe de carbonate de calcium ($CaCO_3$). Schéma issu du quatrième rapport d'évaluation de l'IPCC (Denman et al., 2007).

Figure 1.4 : Processus de dissolution et de dissociation du CO_2 dans les eaux océaniques et côtières (Plymouth Marine Laboratory).

Figure 1.5 : Effets de différents processus biologiques et des échanges de CO_2 atmosphérique sur les paramètres chimiques des carbonates : carbone inorganique dissous (DIC, mmol kg^{-1}), alcalinité totale (TA, mmol kg^{-1}) et dioxyde de carbone (CO_2, µmol kg^{-1}) à une température T = 15°C, salinité S = 35 et pression P = 1 atm (Zeebe, 2012).

Figure 1.6 : Flux verticaux et horizontaux de carbone organique (OC) et inorganique (IC) au sein de la zone côtière (estuaires, zones humides tidales, plateaux continentaux). Le carbone (C) peut circuler à l'intérieur (valeurs en noir) et à l'extérieur (valeurs en rouge) des limites de l'océan côtier. Tous les flux de OC et IC sont présentés comme des valeurs positives, les flèches indiquent la direction des flux. Les flux de POC et DOC sont présentés comme des valeurs de OC total. L'équilibre entre la production primaire brute (GPP) et la respiration totale du système (autotrophe, A, et hétérotrophe, H ; R_{AH}) est la production nette de l'écosystème (NEP), les valeurs négatives indiquant la conversion du OC en IC. Incertitudes typiques pour les flux de carbone : *95% de certitude que l'estimation se situe dans les 50%

de la valeur rapportée ; †95% de certitude que l'estimation se situe dans les 100% de la valeur rapportée ; ‡incertitude supérieure à 100%. Les unités sont les Pg C an^{-1} (1 Pg = 10^{15} g) arrondies à ± 0,05 Pg C an^{-1} (Bauer et al., 2013).

Figure 1.7 : (A) Distribution en profondeur dans les sédiments côtiers des accepteurs d'électrons disponibles pour les réactions aérobie et anaérobie de minéralisation de la matière organique. **(B)** Représentation des zones chimiques associés aux réactions de respiration. Du haut (surface) vers le bas (profondeur), les réactions diagénétiques sont classées dans l'ordre de la chaîne d'oxydo-réduction de la réaction la moins énergivore (respiration aérobie) vers la plus énergivore (méthanogénèse) (Canfield et Thamdrup, 2009).

Figure 1.8 : Classification des marais tidaux en trois types selon le gradient de salinité le long d'un estuaire (marais salés, marais saumâtres et marais doux) (Luo et al., 2017 d'après Mitsch et Gosselink, 2015).

Figure 1.9 : Répartition mondiale des marais salés tidaux le long des côtes océaniques à l'échelle de la Terre (Pétillon et al., 2023).

Figure 1.10 : Schéma d'un marais salé et répartition des espèces végétales selon la fréquence d'inondation et de la tolérance à la salinité. L. Anras, Forum des Marais Atlantique.

Figure 1.11 : Exemples de marais non tidaux (tourbières et prairies humides) et leurs flux hydriques (www.zones-humides.org, septembre 2023).

Figure 1.12 : Schéma d'un système de marais salés rétro-littoraux (modifié de www.zones-humides.org, septembre 2023).

Figure 1.13 : Schéma d'un système de marais doux rétro-littoral (modifié de www.zones-humides.org, septembre 2023).

Figure 1.14 : Modèle conceptuel de la production primaire phytoplanctonique et des facteurs de contrôle biotiques et abiotiques dans les écosystèmes côtiers estuariens (Cloern et al., 2014).

Figure 1.15 : Les processus biologiques et physico-chimiques contrôlant la dynamique du CO_2 dissous ($CO_{2(d)}$) dans le compartiment aquatique des marais salés. NEP : production nette de l'écosystème ; $CO_{2(d)}$: CO_2 dissous dans l'eau ; $CaCO_3$: carbonates de calcium ; HCO_3^- : ions bicarbonates ; CO_3^{2-} : ions carbonates ; C : Carbone (Polsenaere, 2018).

Figure 1.16 : Budget de carbone d'un marais tidal (États-Unis, 12300 km^2) avec **(a)** les flux horizontaux et verticaux de carbone aux différentes interfaces d'échanges et **(b)** leurs pourcentages sur la production primaire brute (GPP). La GPP correspond à la captation de CO_2 atmosphérique par l'ensemble des organismes autotrophes du marais. La somme des flux correspond à la GPP (1361 ± 246 g C m^{-2} an^{-1}) : GPP = $(FCO_{2\text{-inmarsh}})_{mc}$ + OC burial + DIC export + DOC export + POC export + $R_{un\text{-}inundated}$. Les flux de carbone sont donnés en g C m^{-2} an^{-1}. GPP : production primaire brute ; P : photosynthèse dans l'eau ; $R_{un\text{-}inundated}$: respiration du compartiment terrestre lors de l'émersion du marais ; $(FCO_{2\text{-}inmarsh})_{mc}$) : flux de CO_2 atmosphérique influencés du compartiment aquatique du marais lors de l'immersion ; $(FCO_{2\text{-}inmarsh})_{ec}$) : flux de CO_2 atmosphérique influencés par les eaux estuariennes lors de l'immersion ; $(FCO_{2\text{-}inmarsh})_P$) : impact de la photosynthèse sur les flux de CO_2 atmosphérique ; OC : carbone organique ; DIC : carbone organique dissous ; DOC : carbone organique dissous ; POC : carbone organique particulaire (Song et al., 2023).

Figure 1.17 : Concentrations en alcalinité totale (TA, **a**) et en carbone inorganique dissous (DIC, **b**) dans les eaux porales (PW) et les eaux de surfaces (SW) au sein des marais salés et les mangroves. Les chiffres indiquent les médianes. Les diagrammes en boîte indiquent la

médiane (ligne centrale), les 25e et 75e percentiles (boîte) et les 5e et 95e percentiles (moustaches) (Reithmaier et al., 2023).

Figure 1.18 : Relation entre la NEE, la NEP et les échanges horizontaux de carbone au sein d'un système de marais salé tidal. **A.** marais émergé. NEE majoritairement à l'interface sédiment-atmosphère (NEP benthique). **B**. marais immergé, NEE à l'interface eau-atmosphère (NEP totale = NEP benthique + NEP planctonique) mais avec une influence des eaux côtières prédominante. BMA : microalgues benthiques. PMA : pélagique benthiques (modifié d'après Polsenaere, 2011).

Figure 1.19 : (A) Flux d'air horizontal composé de nombreux tourbillons rotatifs. **(B)** Composante verticale de deux tourbillons turbulents au même point mais à deux temps différents. C_1 : concentration de CO_2 atmosphérique transporté par le tourbillon 1 (eddy 1) lors du temps 1 (time 1) à une vitesse W_1 ; C_2 : concentration de CO_2 atmosphérique transporté par le tourbillon 2 (eddy 2) lors du temps 2 (time 2) à une vitesse W_2. Le tourbillon 1 est descendant (captation de CO_2 atmosphérique par l'écosystème) et le tourbillon 2 est ascendant (émission de CO_2 atmosphérique par l'écosystème) (Burba, 2021).

Figure 1.20 : Localisation des réserves naturelles nationales (RNN) en Charente Maritime (France). Un premier site d'étude concerne les marais salés du Fier d'Ars au sein de la réserve de Lilleau des Niges (Ile de Ré), un deuxième site d'étude concerne les marais de Brouage au sein de la réserve de Moëze-Oléron et un troisième site d'étude concernant les marais périurbains de Tasdon (La Rochelle). Modifié de LPO.

Figure 1.21 : L'estuaire tidal du Fier d'Ars (Ile de Ré) et localisation des points de mesures et d'échantillonnage au sein des marais tidaux (en aval de la digue), des marais rétro-littoraux (en amont de la digue) et des chenaux. La zone bleue correspond à la zone intertidale de l'estuaire et la ligne orange correspond à la digue permettant de délimiter les zones terrestres et maritimes. Les croix bleues (partie A ; voir 6.1.) correspondent aux mesures *in situ* des pCO_2 de l'eau sur des cycles de 24 heures au sein de deux continuums aquatiques estuaire – chenal – marais. Les flèches verticales rouges (partie B ; voir 6.1.) correspondent aux mesures des échanges nets de CO_2 atmosphérique (NEE) sur une année entière au sein du marais tidal des Bossys perdus. L'étoile verte (partie C ; voir 6.1.) correspond aux cycles de 24 heures d'échantillonnages de la colonne d'eau pour l'étude du métabolisme aquatique du marais tidal en lien avec les mesures de flux de NEE. Figure modifiée de Mayen et al. (2023).

Figure 1.22 : Localisation du marais urbanisé de Tasdon (agglomération de La Rochelle) et des différentes stations étudiées (T2, T6 et T7) après les travaux de renaturation. Carte issu de la Ville de La Rochelle.

• Chapitre II

Figure 2.1: The Fier d'Ars estuary (Ré Island, French Atlantic coast) and locations of the four studied stations along aquatic continuums: tidal estuary at station *a*, channel at station *b*, rewilded artificial salt marsh at station *c* (in green) and working artificial salt marsh at station *d* (in blue). The dyke (in red) delimits terrestrial and maritime areas. The locks in the two studied artificial marshes are represented within the two map expansions. An atmospheric Eddy Covariance station was deployed at station *e* on the tidal salt marsh downstream from the dyke. Station *F* is located in the centre of the Breton Sound continental shelf; station *a* is

located at the entry of the estuary; stations *b*, *c* and *e* are within the National Natural Reserve to the west of the estuary; station *d* to the east of the estuary is within a salt-farm.

Figure 2.2: Principal Component Analysis (PCA) of the biogeochemical parameters measured at each season along the studied aquatic continuums (stations *a*, *b*, *c* and *d*). The PCA is based on temperature (Temp), salinity, turbidity, dissolved oxygen concentration (DO), dissolved oxygen saturation level (DO-sat.) and pCO_2 mean values for each 24-h cycle. Stations *a*, *b*, *c* and *d* are represented in red, brown, green and blue, respectively. The additional station *F* is represented in light blue. Win: Winter; Spr: Spring; Sum: Summer; Aut: Autumn.

Figure 2.3: Temporal variations at station *a* (tidal estuary) of water temperature (°C), salinity, DO saturation level (DO-sat., %), turbidity (NTU), pCO_2, $NpCO_2$ (pCO_2 variations related to non-temperature effects, ppmv) and $TpCO_2$ (pCO_2 variations related to temperature physical effects, ppmv) during each 24-h cycle from winter 2018 to autumn 2018. Parameters were autonomously measured once per minute by *in situ* probes. Water heights (H, m) were retrieved from the SHOM station (9 km away; Fig. 2.1). Grey areas correspond to night-time periods. Vertical dotted lines correspond to high tides. Horizontal dotted lines correspond to the CO_2 atmospheric concentration (411 ppm; NOAA 2018). Each graduation of the x-axis corresponds to one hour.

Figure 2.4: Temporal variations at station *b* (channel) of water temperature (°C), salinity, DO saturation level (DO-sat., %), turbidity (NTU), pCO_2, $NpCO_2$ and $TpCO_2$ (ppmv) during each 24-h cycle from winter 2018 to autumn 2018. See the Fig. 2.3 caption for more details.

Figure 2.5: Temporal variations at station *c* (rewilded artificial salt marsh) of water temperature (°C), salinity, DO saturation level (DO-sat., %), turbidity (NTU), pCO_2, $NpCO_2$ and $TpCO_2$ (ppmv) and *in situ* Chl *a* (µg L^{-1}) during each 24-h cycle from spring 2019 to winter 2020. Vertical dotted lines correspond to coastal water inflows to the marsh during incoming tide. Horizontal dotted lines correspond to the atmospheric CO_2 concentration simultaneously measured (i) by the Eddy Covariance (station *e*) during the summer and winter cycles and (ii) by NOAA during the spring and autumn cycles. *In situ* Chl *a* values are represented by black crosses (Chl $a_{measured}$); no water samples could be taken in spring 2019. See the Fig. 2.3 caption for more details.

Figure 2.6: Temporal variations at station d (working artificial salt marsh) of water temperature (°C), salinity, DO saturation level (DO-sat., %), turbidity (NTU), pCO_2, $NpCO_2$ and $TpCO_2$ (ppmv) and in situ Chl *a* (µg L^{-1}) during each 24-h cycle from summer 2019 to winter 2020. Chl *a* values in green were derived from the C3-fluorometer every 10 min. (Chl $a_{estimated}$). See the Fig. 2.3 caption for more details.

Figure 2.7: Derived temperature-normalized pCO_2 (seasonal $NpCO_2$, blue curves with empty blue dots) and thermally forced pCO_2 (seasonal $TpCO_2$, pink curves with empty pink dots) at the seasonal scale at stations *F*, *a*, *b*, *c* and *d*. Seasonal means of water temperature (in red dotted lines) and pCO_2 (red curves with filled red dots) are also represented. Horizontal dotted lines correspond to CO_2 atmospheric concentration (411 ppm; NOAA 2018).

Figure 2.8: Diurnal/tidal correlation plots of temperature *vs.* salinity and water pCO_2 *vs.* salinity at stations *b* and *c* for each season. Only significant R^2 (slopes significantly different from zero; $n = 1441$; $p < 0.05$) are showed. HT/D: high tide day; LT/D: low tide day; HT/N: high tide night; LT/N: low tide night. At station *c*, HT periods correspond to coastal water

inflows to the marsh. Note that the temperature and salinity ranges across the seasons are not the same. Horizontal dotted lines correspond to the atmospheric CO_2 concentration.

Figure 2.9: Seasonal and spatial variations in estimated CO_2 fluxes (FCO_2, in mmol m^{-2} h^{-1}) at the water-atmosphere interface at stations *F*, *a*, *b*, *c* and *d*. The means and associated standard deviations over each 24-h cycle are shown. k_{660} and FCO_2 estimations were calculated according to the R22 parametrization. FCO_2 values at stations *a* and *b* are only given for high tide periods.

Figure 2.10: CO_2 budget over the two aquatic sea - land continuums: (1) continental shelf - estuary - channel - rewilded artificial salt marsh and (2) continental shelf - estuary - working artificial salt marsh. Annual means (± SD) and ranges (min - max) of water pCO_2 (ppmv) and air-water FCO_2 (mmol m^{-2} h^{-1}) are showed. The picture of station *c* in spring 2019 (© P. Polsenaere) allows to visualize the macroalgae bloom.

• Chapitre III

Figure 3.1: The studied Bossys perdus salt marsh located on the French Atlantic coast within the National Natural Reserve (blue line delimitation) on Ré Island. The salt marsh is connected to the Fier d'Ars tidal estuary (light blue). The dyke separates terrestrial and maritime marsh areas (orange line). The eddy covariance system and associated estimated footprint are indicated (black cross and red line; see Fig. 3.2). From geo-referenced IGN orthogonal images (IGN 2019).

Figure 3.2: Location and set-up of the eddy covariance (EC) system within the Bossys perdus salt marsh and its associated footprint estimated from Kljun et al. 2015 and averaged over the year 2020 (70% contour line, i.e. 13042 m^2). Wind sectors (45°) and marsh habitats (see Table 3.1) are represented. The canopy height of the studied marsh is short and constant (from 0.15 m for *H. portulacoides* to 0.30 m for *S. maritima*). The STPS sensor (in yellow), measuring water heights (Hw) and temperatures (Tw), was located in the SSW sector. The EC system includes (1) the ultrasonic anemometer (CSAT3), (2) the open-path infrared gas analyser (EC150), (3) the temperature probe (100K6A1A), (4) the temperature/relative humidity sensor (HMP155A), (5) the silicon quantum sensor (SKP215) and (6) the central acquisition system (CR6) and the electronics module (EC100). A rainfall sensor (TE525MM) simultaneously measured the cumulative precipitation. From geo-referenced IGN orthogonal images (IGN 2019). Photographs of four wind sectors within the studied footprint area (NNW, ENE, WSW and SSE) were taken from the EC system during an emersion period in summer 2021 when all the marsh habitats were emerged into the atmosphere: (a) *Spartina maritima*, (b) *Halimione portulacoides*, (c) *Suaeda vera* and (d) mudflat. © S.-C. Zech.

Figure 3.3: Net ecosystem exchanges and associated environmental parameters measured every 10 min throughout the year 2020. The measured environmental parameters include (A) the photosynthetically active radiation (PAR, µmol m^{-2} s^{-1}), (B) air temperature (Ta, °C), vapour pressure deficit (VPD, Pa), (C) wind speed (m s^{-1}), (D) water height (Hw, m), water temperature (Tw, °C) and (E) the net ecosystem exchanges (NEE, µmol CO_2 m^{-2} s^{-1}) computed from the 20 Hz atmospheric CO_2 and wind speed measurements with the EddyPro

software. The red line in E is the moving average of NEE (daily mean). Seasons are delimited by vertical lines.

Figure 3.4: Seasonal variations (means ± SD) of the measured NEE, estimated NEE_{marsh}, estimated GPP and estimated R_{eco} (µmol CO_2 m^{-2} s^{-1}) recorded throughout the year 2020. NEE: net ecosystem exchange, NEE_{marsh}: net ecosystem exchange at the marsh-atmosphere interface without coastal water, GPP: gross primary production, R_{eco}: ecosystem respiration. The NEE fluxes were partitioned into GPP and R_{eco} according to Kowalski et al. (2003) and Wei et al. (2020b) (see section 2.6).

Figure 3.5: Hourly plots of the measured NEE, estimated NEE_{marsh}, estimated GPP and estimated R_{eco} diurnal variations obtained every 10 minutes in winter (A), spring (B), summer (C) and fall (D) for the year 2020. NEE averages are represented by solid blue lines and standard deviations are represented by blue areas. The NEE_{marsh}, GPP and R_{eco} averages are represented by dotted red, green and black lines, respectively. The measured NEE fluxes were partitioned into GPP and R_{eco} according to Kowalski et al. (2003) using monthly coefficients (see the "Materials and methods" section). Night-time periods correspond to GPP = 0 µmol m^{-2} s^{-1} and $NEE_{marsh} = R_{eco}$. All values are in µmol CO_2 m^{-2} s^{-1}.

Figure 3.6: Diurnal variations of NEE fluxes (µmol CO_2 m^{-2} s^{-1}) measured every 10 min according to different variables within five PAR groups: 0-10 (night-time), 10-500, 500-1000, 1000-1500 and 1500-2000 µmol m^{-2} s^{-1}. Panel (A) shows PAR (µmol m^{-2} s^{-1}), (B) VPD (Pa), (C) air temperature (°C), (D) water temperature (°C), (E) wind speed (m s^{-1}) and (F) wind direction (°). NEE fluxes are averaged after separating each variable into five classes and the coloured area is the standard error at the mean.

Figure 3.7: Spatial split of NEE fluxes (µmol CO_2 m^{-2} s^{-1}) within each 45° wind sector (Fig. 3.2) during emersion periods (Hw = 0 m) at the seasonal and diurnal scales. During daytime, the brightest emersion periods (PAR ≥ 500 µmol m^{-2} s^{-1}) were chosen to reduce NEE fluctuations due to PAR influence (see Fig. 3.6-a).

Figure 3.8: Diurnal variations of NEE fluxes (µmol CO_2 m^{-2} s^{-1}) measured every 10 minutes according to water height (Hw, m) within five PAR groups (see caption of Fig. 3.6) in winter (A), spring (B), summer (C) and fall (D). NEE values were averaged every 0.1 m. The coloured areas represent the standard error of the mean.

Figure 3.9: Cumulative carbon fluxes (g C m^{-2}) of the measured NEE (in blue) and estimated NEE_{marsh} (in green) throughout the year 2020. Vertical lines are used to delimit the four seasons. NEE fluxes correspond to net vertical CO_2 exchanges measured by EC whereas NEE_{marsh} fluxes correspond to net vertical CO_2 exchanges estimated from NEE partitioning at the benthic interface only, without any tidal influence.

- **Chapitre IV**

Figure 4.1: (A) The Bossys perdus salt marsh located on the French Atlantic coast within the National Natural Reserve on Ré Island. This intertidal salt marsh is connected to the downstream Fier d'Ars estuary (light blue under tidal immersion) and the upsteam artificial salt marshes (salt ponds). The dyke (orange line) separates terrestrial and maritime marsh areas. Blue arrows represents coastal water inputs from the estuary and the continental shelf at high tides (tidal marsh flooding and artificial marsh supplying) and green arrows represents exported waters from artificial salt marshes to the estuary through the Bossys perdus channel at low tides. The studied footprint area (80% countour line) of the Bossys perdus marsh is indicated (red line). **(B)** Location and set-up of the eddy covariance (EC) system within the Bossys perdus salt marsh at low tide (marsh emersion) and its associated footprints averaged over the year 2021 (Kljun et al., 2015). The red arrows corresponds to the studied 80% footprint countour line encompassing the water sampling location (blue cross).

Figure 4.2: Temporal variations of biogeochemical parameters measured during each 24-h cycle from winter to fall: water salinity, water height (Hw, m), water temperature (Tw; °C), DO saturation level (DO-sat.; %), pCO_2 (ppmv), $NpCO_2$ (pCO_2 variations related to non-temperature effects; ppmv), $TpCO_2$ (pCO_2 variations related to temperature effects; ppmv), air CO_2 concentration (ppm) and NEE fluxes (µmol CO_2 m^{-2} s^{-1}). Estimated NEE_{marsh}, GPP_{marsh} and R_{marsh} fluxes (µmol CO_2 m^{-2} s^{-1}) are presented simultanesouly with NEE fluxes measured by EC. All parameters were measured or estimated every 10 min. during each 24-h cycle. White and grey areas correspond to daytime and night-time, respectively. No variation of Hw (Hw = 0.50 m) corresponds to low tides and increase/decrease of Hw (Hw > 0.50 m) correspond to high tides. Vertical dotted lines distinguish low tide day (LT/Day, 1), high tide day (HT/Day, 2), low tide night (LT/Night, 3) and high tide night (HT/Night, 4) (see M&M section for further information). Each graduation of the x-axis corresponds to two hours.

Figure 4.3: Boxplot distribution of water pCO_2 variations measured every 10-min. at the diurnal/tidal scales within each seasonal 24-h cycles. Horizontal dotted line corresponds to the CO_2 atmospheric concentration measured by the EC station and averaged over the four seasonal 24-h cycles (416 ppm). LT/Day: low tide day; HT/Day: high tide day; LT/Night: low tide night; HT/Night: high tide night. Daytime and night-time periods were separated into PAR > 10 and PAR ≤ 10 µmol m^{-2} s^{-1}, respectively, whereas low tide (LT) and high tide (HT) periods were separated into Hw = 0.50 m and Hw > 0.50 m, respectively (see Fig. 2 and M&M section for further information on these temporal periods).

Figure 4.4: Abundance of microphytoplankton (10^5 cell L^{-1}), pico-nanophytoplankton (10^8 cell L^{-1}) and bacteria (10^{10} cell L^{-1}) sampled at the diurnal/tidal scales during each 24-h cycle simultaneously with NCP measurements. Contrary to the biogeochemical parameters sampled every hour or two hours over 24-h cycles, planktonic communities were sampled every 6 h once of each period of LT/Day, HT/Day, LT/Night and HT/Night (n = 4). The Chl*a* concentration associated to each sampled planktonic community was added in green. Microphytoplankton was separated into centric diatoms, pennate diatoms and dinoflagellates. LT/Day: low tide day; HT/Day: high tide day; LT/Night: low tide night; HT/Night: high tide night (see Fig. 2 for further information on these temporal periods).

Figure 4.5: Planktonic metabolism and associated standard errors at diurnal/tidal scale over the four seasonal 24-h cycles: net community production (NCP, µmol CO_2 L^{-1} h^{-1}), community respiration (CR, µmol CO_2 L^{-1} h^{-1}) and gross primary production (GPP, µmol CO_2 L^{-1} h^{-1}). Specific rates of NCP **(D)**, CR **(E)** and GPP **(F)** were standardized per unit of Chl*a* (µmol CO_2 µg Chl*a* h^{-1}). Specific CR rates standardized per abundance of bacteria **(G)** were also indicated (µmol CO_2 cell h^{-1}). Planktonic metabolism rates were measured by the Winkler method with *in situ* water incubation in transparent and dark bottles. LT/Day: low

tide day; HT/Day: high tide day; LT/Night: low tide night; HT/Night: high tide night (see M&M section for further information on these temporal periods).

Figure 4.6: Linear regressions between normalized DIC (nDIC) *versus* normalized TA (nTA) for each 24-h cycle at the seasonal scale. For each cycle, nTA and nDIC data were calculated from Friis et al. (2003) with a mean salinity value from all samples (25.0, 36.7, 36.0 and 33.2 at C1-winter, C2-spring, C3-summer and C4-fall, respectively; see section 2.6.).

Figure 4.7: Boxplot distribution (median, minimum and maximum) of inorganic nutrients (µM) at the diurnal/tidal scales within each seasonal 24-h cycle: NO_3^-_NO_2^- **(A)**, NH_4^+ **(B)**, DSi **(C)** and DIP **(D)**. LT/Day: low tide day; HT/Day: high tide day; LT/Night: low tide night; HT/Night: high tide night.

Figure 4.8: Median concentrations of total carbon (TC; in µM) and total nitrogen (TN; in µM) at high tides and low tides over the four 24-h cycle from winter to fall 2021. The sum of DOC, POC, HCO_3^-, CO_3^{2-} and CO_2 correspond to total carbon (TC) and the sum of DON, PON, NO_3^-_NO_2^- and NH_4^+ correspond to total nitrogen (TN). The DIC partitioning into CO_2, HCO_3^- and CO_3^{2-} was described in the M&M section.

Figure 4.9: Boxplot distribution (median, minimum and maximum) of POC:PON molar ratio (**A**) and POC:Chl*a* mass ratio (**B**; in mg mg^{-1}) at the diurnal/tidal scales within each seasonal 24-h cycle. The horizontal dotted line in **(A)** corresponds to the Redfield ratio (i.e. theorical molar ratio for plankton; POC:PON = 6.6) (Redfield, 1958). The horizontal dotted line in **(B)** allows characterizing particulate organic matter either as autotrophic (POC:Chl*a* < 200 mg mg^{-1}, dominance of "fresh" living phytoplankton) or heterotrophic (POC:Chl*a* > 200 mg mg^{-1}, dominance of detrital organic material; Savoye et al., 2003). LT/Day: low tide day; HT/Day: high tide day; LT/Night: low tide night; HT/Night: high tide night.

Figure 4.10: Non-metric multidimensional scaling (NMDS) using Euclidean distance of the biogeochemical parameters measured from hourly water samples (n = 59) at the seasonal **(A)**, tidal **(B)** and diurnal **(C)** scales (stress of 0.08). Each NMDS is based on pCO_2, DIC, DOC, POC, PON, DON, TA, Chl*a*, NO_3^-_NO_2^-, NH_4^+, DSi and DIP values. Biogeochemical data were reported in table 3. Seasonal factor assesses variability between 24-h cycles (C1-winter, C2-spring, C3-summer and C4-fall); tidal factor assesses variability between high tides (Hw > 0.50 m) and low tides (Hw = 0.50 m); diurnal factor assesses variability between daytime (PAR > 10 µmol m^{-2} s^{-1}) and night-time (PAR < 10 µmol m^{-2} s^{-1}).

• Chapitre V

Figure 5.1 : Analyse en Composante Principale (ACP) des paramètres biogéochimiques de l'eau échantillonnés à l'échelle diurne au cours de trois cycles de 24 heures (C1-hiver, C2-printemps et C3-automne) au marais saumâtre MAD à Brouage. Les plus petits points représentent les échantillons horaires au sein de chaque cycle de 24 h (n = 12) et les plus gros points représentent les barycentres. L'ACP est basée sur les valeurs de température (T, °C), turbidité (TU, FNU), oxygène dissous (DO, µM), pression partielle de CO_2 (pCO_2, ppmv), carbone inorganique dissous (DIC, µmol kg^{-1}), carbone organique dissous (DOC, µM), carbone organique particulaire (POC, µM), azote organique particulaire (PON, µM), alcalinité totale (TA, µmol kg^{-1}), chlorophylle-*a* (Chl*a* ; µg L^{-1}), nitrate_nitrite (NO_3^-_NO_2^- ; µM), ammonium (NH_4^+ ; µM), silicates (DSi, µM) et phosphate (DIP, µM). Les trois cycles de 24 h ont été réalisés en hiver (février 2021), au printemps (mai 2021) et en automne (novembre 2021) ; l'été a été associé uniquement à des mesures biogéochimiques *in situ* des pCO_2 de l'eau (voir Tableau 5.1). Pour chaque cycle de 24 h, la stratégie d'échantillonnage et les différentes méthodes analytiques ont été entièrement décrites au sein du chapitre IV (Mayen

et al., in prep.). Le logiciel R-studio et le package "FactoMineR" (Lê et al., 2008) ont été utilisés pour réaliser l'ACP.

Figure 5.2 : Influence de la typologie (marais rétro-littoraux vs marais tidaux) et du mode de gestion (stade mature vs stade de développement) des marais littoraux sur leur statut comme puits ou source de CO_2 atmosphérique. Les flèches noires correspondent à la typologie, les flèches marrons correspondent au mode de gestion et les flèches vertes correspondent aux producteurs primaires dominants. Les flèches rouges correspondent au changement de typologie ou de mode de gestion selon les activités humaines ou les évènements extrêmes.

Figure 5.3 : Variations spatiales et saisonnières des pCO_2 de l'eau (moyenne ± écart-type, en ppmv) et des flux de carbone atmosphérique (g C m^{-2} j^{-1}) aux stations T7, T6 et T2 avant (2019) et après (2021 et 2022) la renaturation du marais de Tasdon. Les valeurs de salinité sont indiquées en bleu. Les lignes horizontales en pointillé correspondent à la pCO_2 de l'air pour chaque période (NOAA). Les pCO_2 de l'eau inférieures à la pCO_2 de l'air indiquent une sous-saturation en CO_2 de l'eau par rapport à l'atmosphère et les pCO_2 de l'eau supérieures à la pCO_2 de l'air indiquent une sursaturation en CO_2 de l'eau par rapport à l'atmosphère. Les flux de CO_2 à l'interface eau-air (mmol CO_2 m^{-2} h^{-1}), estimés avec la paramétrisation de Raymond et Cole (2001), ont été cumulés sur 24 h et convertis en flux de carbone atmosphérique (g C m^{-2} j^{-1}). Des flux de C cumulés négatifs à l'interface eau-air indiquent un puits net de C atmosphérique sur 24 h et des flux de C cumulés positifs à l'interface eau-air indiquent une source nette de C atmosphérique sur 24 h. La stratégie de mesure des pCO_2 de l'eau et la méthode d'estimation des flux de CO_2 atmosphérique ont été décrites au sein du chapitre II (Mayen et al., 2023).

Figure 5.4 : Schéma de la dynamique du carbone entre la marée haute (immersion du marais par les eaux côtières) et la marée basse (émersion du marais et exportation des eaux vers le chenal) au cours de nos cycles de 24 h au marais tidal des Bossys perdus. Les eaux des marais rétro-littoraux en amont sont évacuées dans le chenal uniquement lors des périodes de marée basse. Les bilans de carbone en hiver, au printemps et en été pour la NEE (échanges de CO_2 atmosphérique mesurés par EC), la NEE_{marsh} (flux métabolique du marais sans immersion) et la NCP (métabolisme planctonique) sont donnés en g C m^{-2} j^{-1}. Pour les taux journaliers de NCP, les bilans négatifs correspondent à une autotrophie (puits net de C pour les eaux) et les bilans positifs correspondent à une hétérotrophie (source nette de C pour les eaux). Pour le métabolisme net du marais avec immersion (NEE) et sans immersion (NEE_{marsh}), les bilans négatifs correspondent à une captation de C atmosphérique par le marais. Les valeurs en DIC, DOC et POC sont les concentrations moyennes à marée basse et à marée haute (en µM) pour chaque cycle de 24 h.

Listes des tableaux

• Chapitre I

Tableau 1.1 : Réactions diagenétiques influençant les paramètres des systèmes des carbonates (DIC, TA et CO_2) (Krumins et al., 2013 ; Rasssmann et al., 2020).

• Chapitre II

Table 2.1: Meteorological conditions (air temperature in °C and cumulative precipitation in mm) obtained from the "Infoclimat" station on Ré Island (Fig. 1; https://www.infoclimat.fr) at the monthly and annual scales over our measurement periods in 2018, 2019 and 2020 in bold compared to the reference period (1990-2020).
Table 2.2: Seasonal means (± SD) and ranges (min - max) of temperature (°C), salinity, DO (µmol L^{-1}), pH (NBS scale) and pCO_2 (ppmv) values measured (i) once every two weeks in 2018 at station *F* (Coignot et al., 2020) and (ii) during each 24-h cycle from 2018 to 2020 at stations *a*, *b*, *c* and *d* in this study.
Table 2.3: Seasonal means (± SD) and ranges (min - max) of wind speed (km h^{-1}), gas transfer velocity (k_{660}, cm h^{-1}) and estimated water-atmosphere CO_2 flux (FCO_2, mmol m^{-2} h^{-1}) values measured (i) once every two weeks in 2018 at station *F* (Coignot et al., 2020) and (ii) during each 24-h cycle from 2018 to 2020 at stations *a*, *b*, *c* and *d* in the present study. Air CO_2 concentrations used for FCO_2 calculations are: 408 ppm (stations *a*, *b* and *F* in 2018), 411 ppm (station *c* in spring 2019), 413 ppm (stations *c* and *d* in autumn 2019), 400 ppm (stations *c* and *d* in summer 2019) and 403 ppm (stations *c* and *d* in winter 2020; see M&M sections).
Table 2.4: Stepwise multilinear regression analyses to test the contribution of physicochemical variables on water pCO_2 variations through the percentage of explained variance (adjusted R^2). Each selected multilinear model ($p < 0.001$, $n = 1441$) had the highest adjusted R^2 value with all variables explaining at least 5% of the pCO_2 variation. In bold is indicated the parameter explaining at least 50% of the pCO_2 variation. Input variables: DO-sat. (dissolved oxygen saturation level), T (water temperature), S (salinity) and TU (turbidity). The statistic (F) and adjusted R^2 (adj. R^2) are given.

• Chapitre III

Table 3.1: Bossys perdus marsh habitat (percentages are in bold and associated surface area, in square metres, are in brackets) within each 45° wind sector in the corresponding footprint areas (Fig. 3.2) and the whole averaged footprint for the year 2020 (13042 m^2, 70% contour line). *Negligible surfaces on the total area of the sector.
Table 3.2: Emersion and immersion periods (percentage in bold) at the studied salt marsh for four water height ranges of 0.5 m during the year 2020 and at the seasonal scale. The emersion and immersion durations in hours per day (h d^{-1}) were calculated (shown in brackets).

Table 3.3: Diurnal/tidal variations (means ± SD in bold) of NEE fluxes (µmol CO_2 m^{-2} s^{-1}) during each season in 2020. The associated ranges (min/max) are indicated in brackets. Daytime and night-time periods were separated into PAR > 10 and PAR ≤ 10 µmol m^{-2} s^{-1}, respectively, whereas emersion and immersion periods were separated into Hw = 0 m and Hw > 0 m, respectively.

Table 3.4: Net seasonal carbon balances for the measured NEE and estimated NEE_{marsh} values (g C m^{-2}). Corresponding seasonal percentages (%) of marsh immersion and daytime marsh immersion are indicated. NEE corresponds to net vertical CO_2 exchanges measured by EC whereas NEE_{marsh} corresponds to net vertical CO_2 exchanges estimated at the benthic interface without any tidal influence.

Table 3.5: Comparison of the annual NEE budget (g C m^{-2} yr^{-1}) using EC measurements across the salt, brackish and freshwater marshes of the coastal zone.

- # Chapitre IV

Table 4.1: *In situ* 24-h cycles and associated meteorological parameters measured by the EC station (means and standard deviations in bold and ranges in brackets) across the seasons of the year 2021 at the Bossys perdus salt marsh. Dates and times of start and end of each 24-hour cycles were indicated (times in universal time). Cumulated rain over 7 days before cycles were done. Meteorological parameter averages over each 24-h cycle were compared to a longer seasonal reference period (Table A.1). NA: wind data could not be measured over the C4-fall. Ta: air temperature; RH: relative humidity.

Table 4.2: *In situ* 24-h cycles and associated tidal rhythm parameters corresponding to each sampling period across the seasons of the year 2021. The same diurnal/tidal synchronism (low and high tides at the same period of the day) during each 24-h cycle was adopted. Hw ranges (m) correspond to the water height amplitudes measured for each tidal cycle in the sampling channel (Fig. 1-B). The daytime and night-time marsh immersion duration corresponded to hours per day (h d^{-1}) where coastal waters completely fill the channel and flood the habitats of the Bossys perdus salt marsh. See the Table 1 caption for more information.

Table 4.3: Medians (in bold) and associated ranges (in brackets) of biogeochemical parameters measured during our 24-h cycles (n = 13 over C1-winter, n = 15 over C2-spring and C3-summer and n = 16 over C4-fall; see Fig. A.1).

Table 4.4: Multiple factor variance analysis of biogeochemical parameters measured from hourly water samples during all 24-h cycles (n = 59). Seasonal factor assesses variability between 24-h cycles (C1-winter, C2-spring, C3-summer and C4-fall); tidal factor assesses variability between high tides (Hw > 0.50 m) and low tides (Hw = 0.50 m); diurnal factor assesses variability between daytime (PAR > 10 µmol m^{-2} s^{-1}) and night-time (PAR < 10 µmol m^{-2} s^{-1}). Parameters that did not respect a normal distribution were transformed into $\log_{10}(x)$ or $\log_{10}(x+1)$ for variance analysis. The F values of the Fisher test were added. The higher the value of F, the greater the influence of the factor on the parameter.

Table 4.5: Spearman's rank correlations of biogeochemical parameters and phytoplankton biomass recorded from hourly water samples during the four 24-h cycles at the Bossys perdus salt marsh (n = 59). Asterisks designate significant correlations (*** $p < 0.001$, ** $p < 0.01$, * $p < 0.05$, NA $p > 0.05$).

Table 4.6: Diurnal comparison (day *vs* night) of planktonic metabolism (NCP) and overall aquatic metabolism ($NEP_{aquatic}$) during marsh immersion over each 24-h cycle at the Bossys perdus salt marsh. Simultaneously, water-air CO_2 fluxes (FCO_2) estimated from water pCO_2 measurements and net ecosystem CO_2 exchanges (NEE) measured by EC were simultaneously recorded (means and SD in bold, ranges in brackets) and related to planktonic and aquatic metabolism. Wind direction (wind dir.) measured by the EC station was added for each immersion period. NA: EC data could not be measured for C4-fall.

Table 4.7: Daily net C balances (g C m^{-2} d^{-1}) of measured NCP rates (planktonic metabolism), measured NEE fluxes (atmospheric CO_2 exchanges) and estimated NEE_{marsh}, GPP_{marsh} and R_{marsh} fluxes (marsh metabolic fluxes) during the four seasonal 24-h cycles at the Bossys perdus salt marsh. For daily NCP rates, negative balances correspond to an autotrophy (net C sink for waters) and positive balances correspond to a heterotrophy (net C source for waters). For net marsh metabolism with immersion (NEE) and without immersion (NEE_{marsh}), negative balances correspond to an atmospheric C uptake by the marsh. NA: EC data could not be measured for C4-fall.

- # Chapitre V

Tableau 5.1 : Moyennes saisonnières (± écart-type et min-max entre parenthèses) des pressions partielles de CO_2 de l'eau (pCO_2 en ppmv) mesurées sur des cycles de 24 heures dans les marais littoraux Charentais (Fier d'Ars, Brouage et Tasdon **;** Fig. 1.20). Les pCO_2 de l'eau ont été mesurées toutes les minutes par une sonde autonome *in situ* (C-sense™, PME/Turner Designs) sauf en automne à MAD, les pCO_2 ont été estimées à partir du système des carbonates en utilisant les mesures de DIC et de TA. En rouge, les eaux de marais en moyenne sursaturés en CO_2 sur 24 heures et en bleu, les eaux de marais en moyenne sous-saturés en CO_2 sur 24 heures. Au sein de chaque cycle de 24 heures, les amplitudes (min-max) des pCO_2 de l'eau correspondent aux variations diurne (jour/nuit) et tidale (marée haute/marée basse). Aux stations *c* et *d* (Fier d'Ars), les mesures ont été réalisées entre 2019 et 2020 tandis qu'aux autres stations, les mesures ont été réalisées au cours de l'année 2021 (après la renaturation pour le marais de Tasdon). A MAS et MAD, les mesures ont été réalisées en simultané.

Tableau 5.2 : Bilans nets de carbone journaliers (g C m^{-2} j^{-1}) à l'échelle tidale (marée haute/marée basse) des taux de NCP mesurés par la méthode Winkler (métabolisme planctonique), des flux de NEE mesurés par EC (échanges de CO_2 atmosphérique) et des flux de NEE_{marsh}, GPP_{marsh} et R_{marsh} estimés à partir du partitionnement de Kowalski et al. (2003) (flux métabolique du marais sans immersion) au cours des quatre cycles de 24 heures au marais salé de Bossys perdus. Pour les taux journaliers de NCP, les bilans négatifs correspondent à une autotrophie (puits net de C pour l'eau) et les bilans positifs correspondent à une hétérotrophie (source nette de C pour l'eau). Pour le métabolisme net du marais avec immersion (NEE) et sans immersion (NEE_{marsh}), les bilans négatifs correspondent à une captation de C atmosphérique par le marais. NA : les données EC n'ont pas pu être mesurées pour C4-fall (chapitre IV).

Introduction générale de la thèse

Sur Terre, les activités anthropiques croissantes depuis le XIXème siècle ont fortement modifié l'équilibre naturel du cycle du carbone en libérant des grandes quantités de gaz à effet de serre dans l'atmosphère sous forme de CO_2, principalement par combustion des matières fossiles, provoquant des bouleversements climatiques majeurs tels que le réchauffement de la planète et l'augmentation du niveau des mers (IPCC 2022).

Les environnements côtiers sont des systèmes clés dans les flux de carbone entre les continents, les océans et l'atmosphère. Ces écosystèmes dynamiques et hétérogènes (i.e. zones humides, baies, estuaires) permettent le transport de grandes quantités de carbone entre (i) le bassin versant et l'océan côtier (flux horizontaux) et (ii) entre la colonne d'eau et l'atmosphère ou les sédiments (flux verticaux). Parmi les systèmes côtiers, les zones humides correspondent « à des étendues de marais, de fagnes, de tourbières ou d'eaux naturelles ou artificielles, permanentes ou temporaires, où l'eau est stagnante ou courante, douce, saumâtre ou salée, y compris les étendues d'eau marine dont la profondeur à marée basse n'excède pas six mètres » (convention de Ramsar, 1971). Au sein des zones humides, les marais sont des écosystèmes d'intérêt majeur d'un point de vue écologique, biogéochimique et économique (Gedan et al., 2009 ; AcclimaTerra, 2018). Tout d'abord, ils abritent une forte biodiversité de végétaux terrestres et aquatiques, d'oiseaux migrateurs et des poissons d'eau douce et d'eau salée (fonctions de nurserie et de nourricerie). De plus, les marais assurent d'autres fonctions écosystémiques majeures comme la fonction hydrologique permettant la régulation du cycle de l'eau et la fonction biogéochimique permettant la filtration naturelle des eaux (nutriments) et la séquestration de carbone (Duarte et al., 2008 ; McLeod et al., 2011 ; EPA, 2023). Depuis plusieurs siècles, les marais littoraux sont aussi le support de nombreuses activités anthropiques telles que la pisciculture, l'ostréiculture et la saliculture qui ont fortement façonné la typologie de ces écosystèmes (poldérisation, endiguement ; Paticat, 2007 ; Tortajada, 2011). Ces activités économiques nécessitent des usages différents de l'eau selon leurs besoins (contrôle du temps de résidence par des écluses, quantité et qualité spécifiques) pouvant affecter la dynamique du carbone et les échanges de CO_2 atmosphérique (puits/source) des marais. Les marais littoraux possèdent également une forte identité patrimoniale en raison de leur site, de leur paysage remarquable, de leur histoire et de leur rôle de refuge pour la biodiversité (Champion et al., 2012). Cependant depuis quelques décennies, les marais littoraux sont de plus en plus exposés à aux submersions marines, aux

changements climatiques et aux pressions anthropiques nécessitant une meilleure protection et gestion de ces zones humides côtières afin de restaurer et favoriser notamment la fonction de puits de carbone (Gedan et al., 2009 ; AcclimaTerra, 2018 ; Pétillon et al., 2023).

Les marais salés sont le siège de flux significatifs d'éléments nutritionnels et de processus métaboliques complexes aux différentes interfaces d'échanges (eau-air, sédiments-air, sédiments-eau). Malgré leur faible superficie à l'échelle mondiale, ces environnements côtiers hautement productifs captent du carbone depuis l'atmosphère (CO_2) au travers de la production primaire de la végétation. Une partie significative du carbone atmosphérique capté par la photosynthèse est séquestrée dans les sédiments des marais et représente une composante majeure du stockage de carbone biologique sur Terre. De plus, l'immersion des marais par les eaux côtières peut modifier les échanges de CO_2 à l'interface entre l'écosystème et l'atmosphère (et notamment la fonction puits de CO_2) mais aussi générer un export important de carbone rendant les eaux côtières adjacentes sources de CO_2 pour l'atmosphère.

En Charente-Maritime, les marais couvrent environ 15% de la superficie du territoire, avec un degré d'anthropisation important, principalement lié aux fortes activités salicoles au cours des siècles passés (Paticat, 2007). Face aux modifications majeures du climat, les marais sont devenus des territoires stratégiques d'un point de vue écologique, notamment dans les Pertuis Charentais, pour la captation et la séquestration de carbone (projets PAMPAS 2019-2024, HypEddy 2019-2021 ; DYCIDEMAIM 2021-2022 et LRTZC 2019-2027). Cependant, peu d'études se sont intéressées au fonctionnement du cycle du carbone dans les marais littoraux gérés par l'Homme. Ainsi, au cours de mon parcours universitaire à l'UPPA (Université de Pau et des Pays de l'Adour), ma rencontre avec Pierre Polsenaere m'a permis de réaliser mes stages de Master 1 (Mayen, 2019) à la station Ifremer de l'Houmeau et de Master 2 (Mayen, 2020) à la station Ifremer de La Tremblade afin de mieux comprendre l'influence de la typologie et du mode de gestion des marais salés sur les variations des pressions partielles de CO_2 de l'eau (pCO_2) et des flux de CO_2 atmosphérique associés. Curieux et déterminé de poursuivre les recherches en biogéochimie sur les facteurs contrôlant les flux de carbone aux interfaces d'échange des marais, j'ai eu l'occasion de continuer en thèse (station Ifremer de La Tremblade et Centre Ifremer Atlantique de Nantes) dans un sujet qui s'intègre pleinement dans le contexte environnemental actuel. Je remercie la Direction Scientifique de l'Ifremer pour le financement de cette thèse qui s'est déroulé sous la direction de Philippe Souchu (LER/MPL) et sous le co-encadrement de Pierre Polsenaere (LER/PC) et

d'Aurore Regaudie De Gioux (PELAGOS). D'une part, ces travaux de thèse ont permis de s'intéresser aux différentes variations spatio-temporelles des échanges de CO_2 atmosphérique à l'échelle de l'écosystème sur une année de mesures en continu au sein d'un marais salé tidal. Ensuite, afin d'étudier la contribution du métabolisme aquatique des marais sur les échanges de CO_2 atmosphérique, des cycles de 24 h de mesures (pCO_2, pH, etc.) et d'échantillonnages de la colonne d'eau (carbone organique et inorganique, nutriments et métabolisme planctonique) ont été réalisés à chaque saison de l'année 2021 au sein de deux stations hétérogènes (un marais salé tidal et un marais saumâtre endigué).

Ces travaux de thèse ont également été marquée par plusieurs analyses au LER/PC, principalement associées aux mesures de la balance métabolique des communautés planctoniques (production et respiration) et aux dosages de la chlorophylle-*a* au sein des échantillons horaires au cours des cycles de 24 h. Les différentes collaborations au sein de l'Ifremer m'ont permis de me déplacer (i) au laboratoire PELAGOS à Plouzané (23-27/11/2020 et 27-30/06/2022) pour me former aux analyses sur le métabolisme planctonique et aux traitements de données associés, (ii) au LER/MPL à Nantes (15-19/03/2021) pour participer aux mesures biogéochimiques associées au carbone et aux nutriments et (iii) au LER/LR à Sète (23-27/08/2021 et 08-14/03/2022) pour participer aux analyses d'alcalinité totale.

Plusieurs stages, notamment à l'Ifremer, ont permis d'environner et d'enrichir mon travail de thèse : Kostyrka (2021) concernant le traitement des données Eddy Covariance, Coutantin (2023) concernant l'étude de la variabilité interannuel des échanges de CO_2 atmosphérique par Eddy Covariance et Xaus (2023) concernant les liens entre les pCO_2 de l'eau et les réseaux trophiques planctoniques. De plus, j'ai pu co-encadrer le stage de licence 3 de Stacy Delmer au LER/PC (2022) sur la dynamique temporelle des pCO_2 de l'eau d'un marais tidal au cours de nos cycles de 24 h de 2021 ; ceci m'a permis d'acquérir une première expérience d'encadrement sur un sujet qui s'intègre dans ma thèse. Aussi, les heures de vacations réalisées au sein de La Rochelle Université avec les étudiants du Master 1 et 2 Sciences pour l'Environnement parcours Gestion de l'Environnement et Écologie Littoral m'ont également permis de découvrir l'enseignement et la pédagogie. Enfin, la formation effectuée au BRGM m'a permis d'acquérir des notions sur la modélisation en hydrogéochimie pour l'analyse des données liées au système des carbonates.

Une partie importante de ma thèse a aussi été consacrée à l'analyse des données et à la valorisation de mon travail qui a abouti la publication de deux articles (Mayen et al., 2023,

2024) tandis qu'un troisième est en cours de finalisation (Mayen et al., in prep.). Concernant les communications orales, j'ai eu l'occasion de présenter mes travaux de thèse lors de deux congrès internationaux (ASLO 2021 Aquatic Sciences Meeting en visioconférence et AGU 2023 Wide Open Science à San Francisco), ce qui m'a permis d'enrichir mes connaissances scientifiques.

Dans le cadre de mon parcours, cette thèse en écologie et biogéochimie côtière aura été une véritable expérience scientifique me permettant d'acquérir une forte expérience en recherche sur le fonctionnement du cycle du carbone dans les écosystèmes littoraux (processus et flux associés) en intégrant l'influence du métabolisme planctonique et des nutriments. Le déroulement de cette thèse m'aura donné l'opportunité de prendre part activement à toutes les étapes du projet de recherche et d'acquérir de l'autonomie dans l'organisation et la mise en place des campagnes d'échantillonnages sur 24 h, dans l'analyse de paramètres biogéochimiques en laboratoire, dans le traitement des résultats et dans la rédaction des articles (+ processus de publication). Ce travail de thèse m'a également donné l'occasion d'interagir avec plusieurs laboratoires au sein de l'Ifremer (LER/PC, LER/MPL, LER/LR, PELAGOS) mais également avec d'autres instituts de recherche (l'UMR LIENSs à La Rochelle, l'INRAE de Bordeaux et le BRGM d'Orléans) lors de travaux menés en étroite collaboration. Pour terminer, je remercie mon encadrement de thèse qui aura permis cette formation scientifique très riche me permettant de poursuivre mon projet professionnel en recherche vers un post-doctorat au sein de l'UMR EPOC (Bordeaux) afin de continuer à contribuer aux connaissances sur le fonctionnement biogéochimique des écosystèmes littoraux dans le contexte du changement climatique.

Chapitre I

État de l'Art

L'île de Ré et les marais salés du Fier d'Ars. © Les vols de Max (2017).

1. Cycle du carbone

1.1. Le cycle global du carbone

Sur Terre, le cycle global du carbone (C) peut être décrit comme un ensemble de réservoirs (continents, océans, atmosphère) en équilibre et interconnectés par des flux naturels de C (flèches oranges ; Fig. 1.1) permettant le fonctionnement biogéochimique des écosystèmes terrestres et aquatiques (Canadell et al., 2021 ; IPCC 2021).

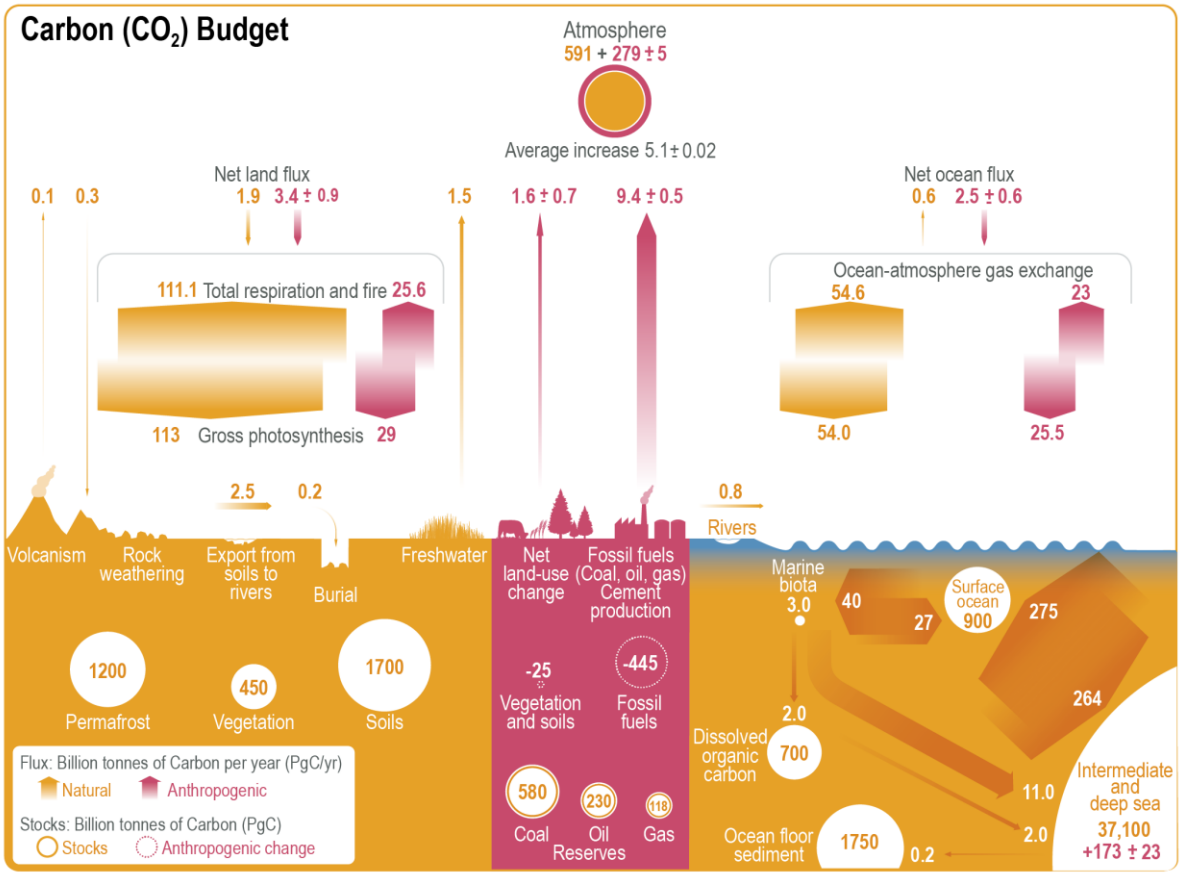

Figure 1.1 : Budget global du carbone (CO_2) pour la période 2010-2019. Les flèches orange représentent les flux annuels de carbone (en Pg C an^{-1}) associés au cycle naturel, estimés pour la période précédant l'ère industrielle, vers 1750. Les flèches roses représentent les flux anthropiques de carbone moyennés sur la période 2010-2019. Le taux d'accumulation de carbone dans l'atmosphère est égal à la somme des émissions nettes liées aux changements d'occupation des sols et aux combustions fossiles auxquelles sont déduits les puits nets des terres et des océans. Les cercles avec les nombres en jaune correspondent aux stocks de carbone préindustriel (en Pg C an^{-1}) et les cercles avec des nombres en rose correspondent aux changements anthropiques (flux anthropiques cumulés) de ces stocks depuis 1750. Le carbone dans les eaux océaniques existe sous plusieurs formes : carbone inorganique dissous (37 100 Pg DIC), carbone organique dissous (700 Pg DOC) et carbone organique particulaire (13-23 Pg POC) dans un rapport proche de DIC:DOC:POC = 2000:38:1. 1 Pg = 1 Gt = 10^{15} g. Schéma issu du sixième rapport d'évaluation de l'IPCC (Intergovernmental Panel on Climated Change ; Canadell et al., 2021).

Le cycle global du carbone est composé d'un cycle court et d'un cycle long (Canadell et al., 2021). Le cycle court, controlé uniquement par les processus de photosynthèse, de respiration, de dégradation et de transfert gazeux, permet des échanges importants de C et un renouvellement rapide des réservoirs (atmosphère, océans, sédiments océaniques et terrestres de surface, soils et eaux douces). Le temps de renouvellement des réservoirs varie de quelques années pour l'atmosphère à quelques décénnies ou siècles pour les principaux réservoirs de C de la végétation terrestre et océanique. Le cycle lent s'adresse à de grandes réserves de C dans les roches et les sédiments qui échangent avec le cycle court par le biais des émissions volcaniques de dioxide de carbone (CO_2), de l'altération (processus chimiques en partie entranant la désagrégation des roches situés à la surface suite à une oxydation, hydratation et décarbonation des roches calcaires) et l'érosion des roches et de la formation de sédiments au fond de l'océan. Le temps de renouvellement des réservoirs du cycle lent est de plusieurs millénaires.

Au début de l'Holocène (il y a 11 700 ans), les flux de C au sein du cycle court étaient proche d'un état stable (Fig. 1.1) comme mis en évidence par de faibles variations de CO_2 atmosphérique dans les carottes glaciaires (Canadell et al., 2021). Cependant depuis le XVII^{e} siècle, les activités anthropiques ont modifié l'équilibre des échanges biogéochimiques de la biosphère en libérant des quantités de plus en plus importantes de CO_2 vers l'atmosphère pour atteindre 11,0 ± 0,9 Pg C an^{-1} (Fig. 1.1 ; flèches rose) principalement par la combustion des matières fossilles (86%) et par le changement d'occupation des sols tels que la déforestration et l'agriculture intensive (14%) (Fig. 1.2 ; Canadell et al., 2021). Les échanges verticaux de CO_2 atmophérique avec les continents et les océans ont donc été fortement modifiés avec des augmentations jusqu'à 142 et 80 Pg C an^{-1}, respectivement, permettant ainsi à 5,9 Pg C an^{-1} d'émissions anthropiques d'être re-captés principalement par la photosynthèse de la végétation terrestre et océanique, le reste étant accumulé dans l'atmosphère (Fig. 1.1 ; Canadell et al., 2021). Ainsi, la concentration en CO_2 atmosphérique est passé de 290 ppm en 1750 à 367 ppm en 1999 pour atteindre 422 ppm en décembre 2023 (National Oceanic and Atmospheric Administration (NOAA), 2023). Le CO_2 est un gaz à effet de serre (GES) qui absorbe les rayonnements infrarouges émit à la surface de la Terre. Ainsi, les augmentations des concentrations en GES anthropiques sont à l'origine du changement climatique tels que le réchauffement terrestre et océanique, l'augmentation du niveau des mers, l'augmentation des évènements extremes et l'acidification des océans (Lee et al., 2021). D'après le rapport IPCC 2021, le scénario le plus optimiste pour 2081-2100 (par rapport à 1986-2005) estime des

augmentations de la température de l'air et du niveau moyen des océans entre 0,3 et 1,7°C et entre 0,26 et 0,55 m, respectivement, tandis que le scénario le plus pessimiste estime des augmentations entre 2,6 et 4,8°C et entre 0,45 et 0,82 m, respectivement (Lee et al., 2021). Face à ces prédictions, il est important d'étudier et de mieux comprendre les processus et facteurs qui contrôlent les flux de C entre les différents compartiments et en particulier, au sein de la zone côtière qui abrite des écosystèmes d'interfaces majeurs entre l'océan, le continent et l'atmosphère.

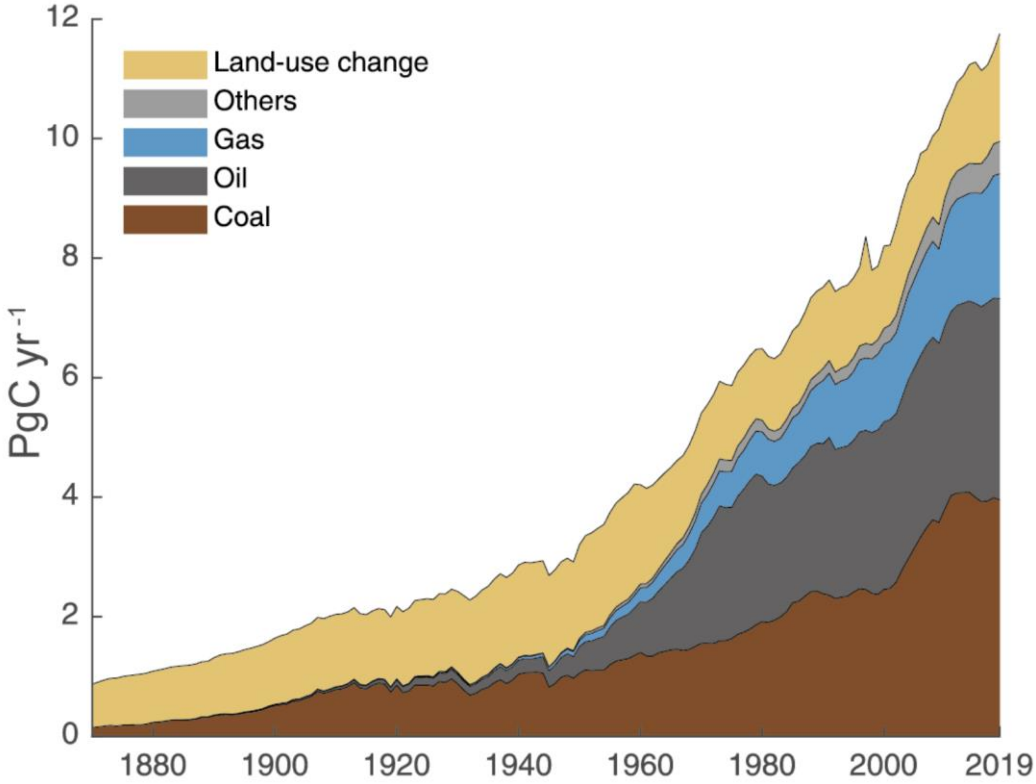

Figure 1.2 : Tendances historiques des émissions de CO_2 atmosphérique (en Pg C an^{-1} = 10^{15} g C an^{-1}) par les activités anthropiques (combustion fossiles et changements d'occupation des sols) pour la période entre 1880 et 2019. Le terme « others » dans la légende représente principalement les émissions de carbonates lors de la fabrication de ciment. Schéma issu du sixième rapport d'évaluation de l'IPCC (Canadell et al., 2021).

1.2. Le cycle du carbone dans les océans

Les océans jouent un rôle majeur dans la régulation du cycle global du C (Fig. 1.1). Chaque année, ils permettent la captation d'environ 25% des émissions de CO_2 anthropique (i.e. 2,5 ± 0,6 Pg C an^{-1} ; Fig. 1.1) car l'altération des roches a créé un océan légèrement

alcalin (pH de surface de 8.1 en moyenne) permettant la diffusion du CO_2 atmosphérique dans l'eau (Canadell et al., 2021). À l'interface air-eau, la diffusion du CO_2 gazeux à la surface des océans est déterminée par la difference entre la pression partielle de CO_2 de l'air (pCO_{2air}) et la pression partielle de CO_2 dissous dans l'eau (pCO_{2eau}). La sous-saturation de l'eau de mer en CO_2 par rapport à l'atmosphère ($pCO_{2eau} < pCO_{2air}$) entraîne un flux de diffusion de CO_2 atmosphérique dans les eaux océaniques (captation). Les variations des pCO_{2eau} à la surface des océans sont contrôlées par trois principales pompes liées aux échanges atmosphériques, à l'activité biologique et à la circulation des masses d'eau (Fig. 1.3) :

- La pompe de solubilité du CO_2 dans l'eau : elle contrôle la captation ou l'émission de CO_2 gazeux en fonction de la température de l'eau (McGillis et Wanninkhof, 2006 ; Fig. 1.3). En hiver, les eaux de surface des hautes latitudes, denses, froides et chargés en CO_2 à cause de leur forte solubilité, coulent vers l'océan profond où elles permettent le transport d'une forte concentration de carbone inorganique dissous et sont à l'origine de la circulation thermohaline à grande échelle (Denman et al., 2007). De plus, la capacité tampon du système des carbonates (voir 1.3) dans l'océan maintien élevé le gratien océan-atmosphère de pCO_2 et donc des flux de CO_2 à l'interface.

- La pompe du carbone organique (pompe biologique) : elle est principalement liée à la photosynthèse du phytoplancton qui convertit le CO_2 dissous en carbone organique en utilisant la lumière et les nutriments inorganique dissous (nitrates, phosphates). Cette pompe permet d'alimenter le flux de carbone organique particulaire (POC) vers l'océan profond après la mort du phytoplancton ou par son intégration dans le réseau trophique (Fig. 1.3). Alors que la majorité du carbone organique produit en surface est recyclée en CO_2 par le broutage du zooplancton, 30% s'enfonce dans les eaux profondes avant d'être reconverti en CO_2 lors de la reminéralisation bactérienne (Fig. 1.3). Sur l'ensemble du carbone organique produit en surface, seulement 0,1% atteint le fond des océans (11 Gt C yr^{-1} ; Fig. 1.1) où il est stocké dans les sédiments marins (Feely et al., 2001).

- La contre-pompe des carbonates (pompe biologique) : elle est liée aux processus de dissolution et calcification du carbonate de calcium ($CaCO_3$). Le processus de calcification biogénique par les bivalves (huitres), les coraux durs (scléractiniaires) et

les espèces calcifiantes du plancton (coccolithophores) produit du CO_2 lors de la formation de la coquille calcaire dans les eaux de surface. À la mort de ces organismes, la dissolution du $CaCO_3$ en profondeur induit un puits de CO_2 (sous-saturation de l'eau), qui peut être ramené vers la surface par les processus de remontées d'eau profonde appelés upwelling (Fig. 1.3 ; Denman et al., 2007).

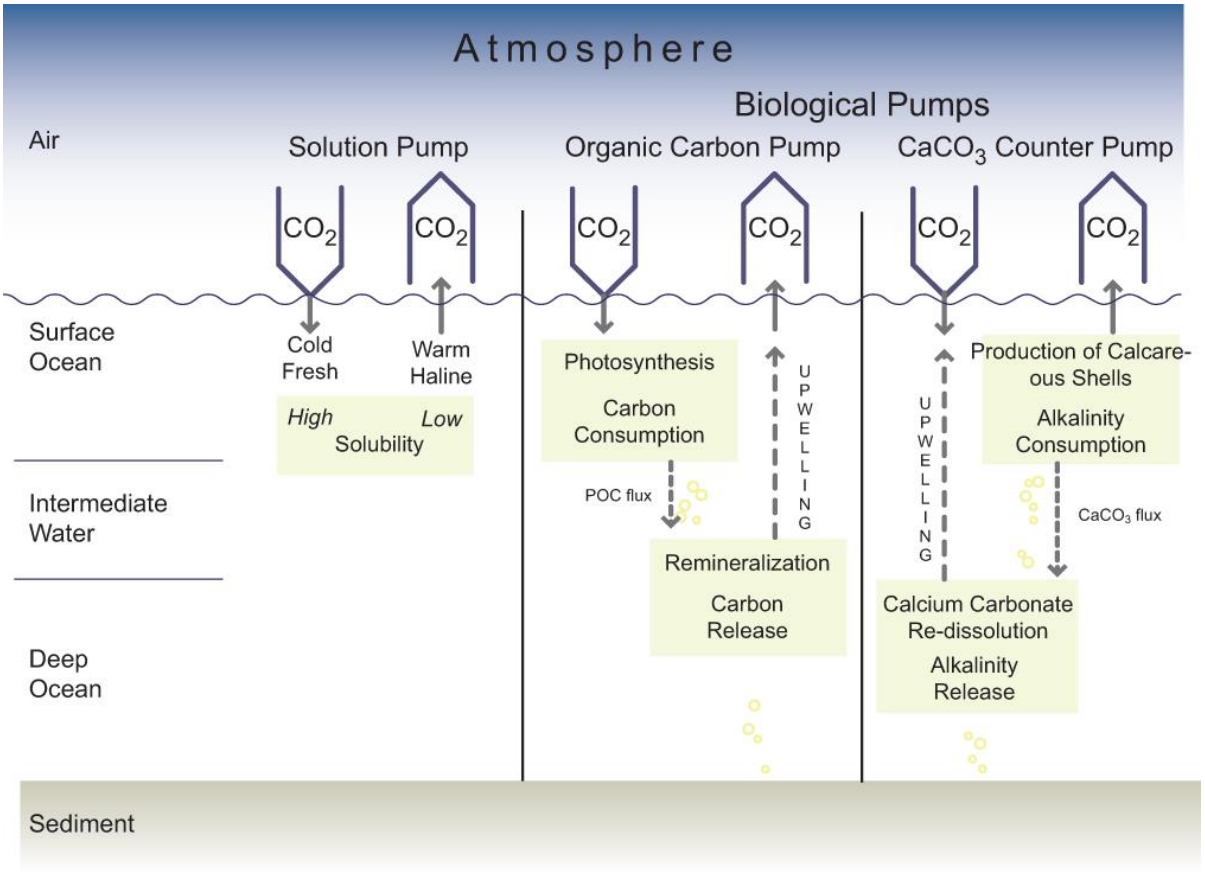

Figure 1.3 : Les trois pompes océaniques à carbone permettant la régulation des fluctuations naturelles de CO_2 atmosphérique : la pompe de solubilité, la pompe à carbone organique et la contre pompe de carbonate de calcium ($CaCO_3$). Schéma issu du quatrième rapport d'évaluation de l'IPCC (Denman et al., 2007).

1.3. Le système des carbonates de l'océan ouvert à l'océan côtier

Dans les eaux océaniques et côtières, le carbone inorganique dissous (DIC ou ΣCO_2 ou TCO_2 ; Eq. 1) est formé par le dioxyde de carbone dissous (CO_2 (aq)) et par les ions bicarbonates (HCO_3^-) et carbonates (CO_3^{2-}) dont la spéciation des différentes formes est contrôlée par le pH (Wolf-Galdrow et al., 2007). Dans les conditions actuelles de pH en surface de l'océan (8.1 en moyenne), la majorité du DIC est formé par les ions HCO_3^- (91%)

et CO_3^{2-} (8%) tandis que la forme CO_2 (aq) est très peu représentée (1% ; Canadell et al., 2021) mais cette spéciation peut être modifiée en zone côtière en raison des fortes variations de pH dans l'eau (Petton et al., 2023).

$$DIC = \Sigma CO_2 = TCO_2 = [CO_2] + [HCO_3^-] + [CO_3^{2-}] \quad (1)$$

Une quatrième forme existe (l'acide carbonique, H_2CO_3) mais sa concentration est négligeable par rapport à celle du CO_2 (aq) (< 0,3%). Ainsi, dans les équations 1 et 2, on peut définir le terme $[CO_2]$ par la somme de ces deux formes (les crochets indiquent la concentration).

$$[CO_2] = [CO_2\ (aq)] + [H_2CO_3] \quad (2)$$

Les échanges de CO_2 atmosphérique avec le compartiment aquatique sont contrôlés par le coefficient de solubilité du CO_2 dans l'eau permettant un équilibre thermodynamique entre le CO_2 atmosphérique et le CO_2 dissous (CO_2 (g) ↔ $[CO_2]$; Zeebe, 2012). La concentration en CO_2 dissous est décrite par la loi de Henry (Eq. 3) :

$$[CO_2] = K_0(T, S)pCO_2 \quad (3)$$

K_0 (mol kg^{-1} atm^{-1}) est le coefficient de solubilité du CO_2 dans l'eau dépendant des conditions de température (T) et de salinité (S) (Weiss, 1974) et pCO_2 (ppmv) est la pression partielle de CO_2 dans l'eau.

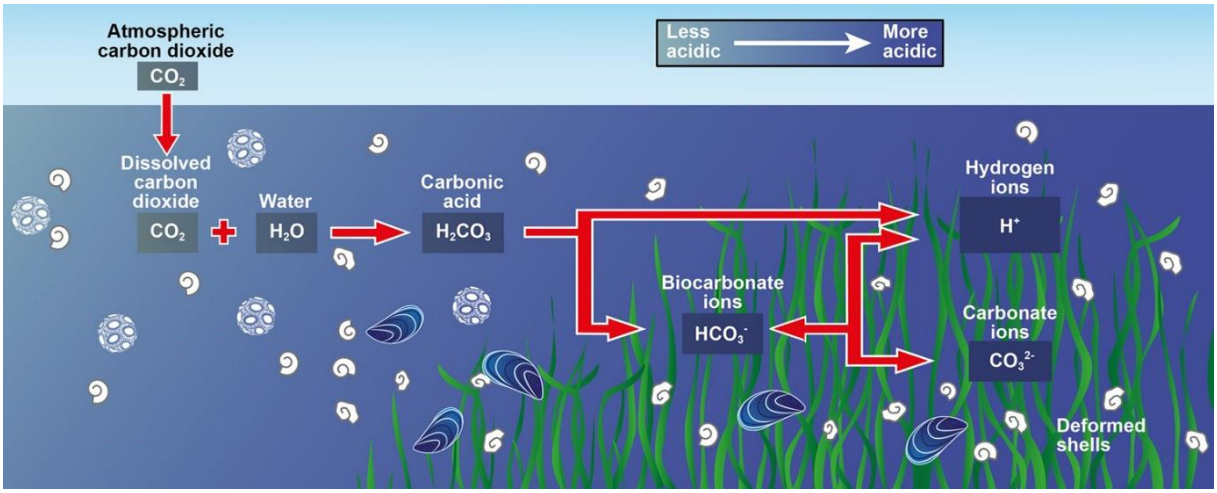

Figure 1.4 : Processus de dissolution et de dissociation du CO_2 dans les eaux océaniques et côtières (Plymouth Marine Laboratory).

Lors de la diffusion du CO_2 atmosphérique dans l'eau, le CO_2 (g) se dissout en CO_2 (aq) pour former l'acide carbonique (H_2CO_3) (Fig. 1.4). L'apport d'acide carbonique entraine une baisse du pH dans l'eau par sa dissociation en ions HCO_3^- et H^+ (Fig. 1.4). Les ions HCO_3^- peuvent à leur tour se dissocier en ions CO_3^{2-} et H^+ (Fig. 1.4). Dans les eaux océaniques et côtières, cette acidification (augmentation des ions H^+) est limitée en fonction de l'alcalinité totale (TA). Cette dernière est définie comme la somme de toutes les bases faibles libres dans un kilo d'eau qui sont titrables par un acide fort (Dickson et al., 2007). Dans l'eau de mer, la majorité de la TA est formée d'ions carbonates et bicarbonates comme l'équation suivante :

$$TA = [HCO_3^-] + 2[CO_3^{2-}] + [OH^-] + [B(OH)_4^-] + [HPO_4^{2-}] + 2[PO_4^{3-}] + [H_3SiO_4^-] + [NH_3] + [HS^-] - [H^+] - [HSO_4^-] - [HF] - [H_3PO_4] \quad (4)$$

Les ions H^+ libérés lors de la dissociation du CO_2 dans l'eau peuvent être neutralisés par la transformation des ions CO_3^{2-} en HCO_3^-, c'est le pouvoir tampon de l'eau de mer (Fig. 1.4). Ainsi, lorsque la concentration en ions CO_3^{2-} devient limitante, les ions H^+ s'accumule et le pH de l'eau diminue favorisant l'acidification (Zeebe, 2012). Aussi, la diminution des concentrations en ions CO_3^{2-} abaisse l'état de saturation des minéraux biogéniques des carbonates de calcium (calcite et l'aragonite) et peut réduire la capacité des organismes à se calcifier (par exemple, les coraux qui construisent les récifs et les mollusques à coquille) (Zeebe, 2012 ; Canadell et al., 2021).

Le cycle du carbone en milieu marin est donc lié au système des carbonates où la dissolution (R1 ; Tableau 1.1) et la précipitation (R2 ; Tableau 1.1) des carbonates de calcium ($CaCO_3$) consomme et produit du CO_2 dissous, respectivement (Fig. 1.5). Ces processus liés à la chimie des carbonates peuvent être d'origine chimique (équilibre calco-carbonique) ou biologique (phytoplancton et mollusques calcifiants). Ils contrôlent la contre-pompe des carbonates et impactent à la fois le DIC et la TA dans l'eau (Fig. 1.5). Par exemple, la dissolution du $CaCO_3$ augmente les concentrations en DIC et en TA avec un ratio de 1:2 tandis que la précipitation du $CaCO_3$ diminue les concentrations en DIC et en TA avec un ratio 1:2 (Fig. 1.5). Par comparaison, la captation ou la libération de CO_2 par la photosynthèse et la respiration aérobie influencent fortement le DIC mais très peu la TA (légère modification de la concentration en TA liée à la production ou à la captation de nitrates et phosphates ; Gattuso et al., 1999 ; Zeebe, 2012). Ces processus liés à la chimie des carbonates dans l'eau sont également présents au sein de la zone côtière, située à l'interface entre le domaine océanique et le domaine terrestre.

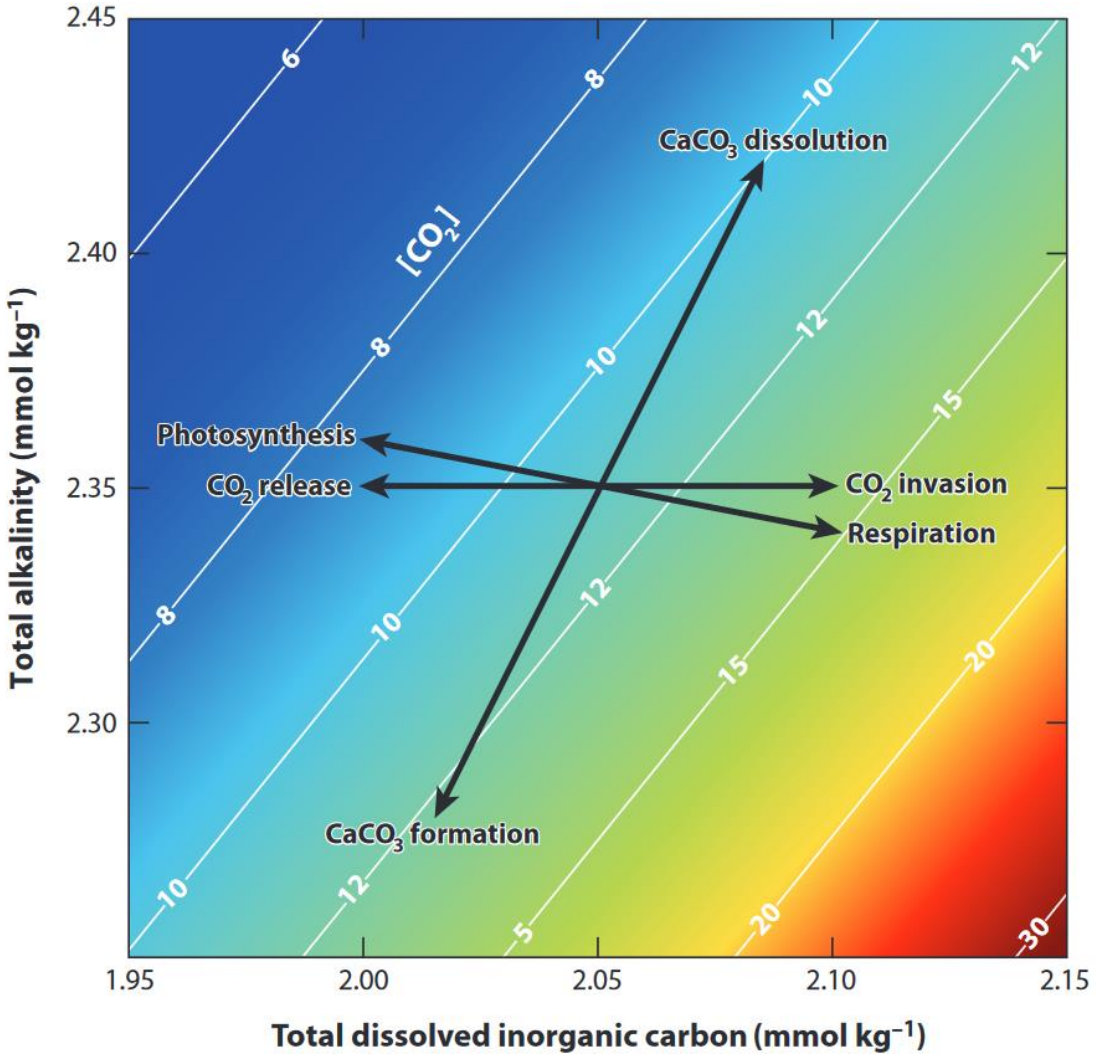

Figure 1.5 : Effets de différents processus biologiques et des échanges de CO_2 atmosphérique sur les paramètres chimiques des carbonates : carbone inorganique dissous (DIC, mmol kg^{-1}), alcalinité totale (TA, mmol kg^{-1}) et dioxyde de carbone (CO_2, µmol kg^{-1}) à une température T = 15°C, salinité S = 35 et pression P = 1 atm (Zeebe, 2012).

1.4. La zone côtière, une interface dynamique et hétérogène d'un point de vue du C

La zone côtière est définie comme la zone océanique localisée sur le plateau continental incluant toute la surface d'influence des marées jusqu'à une profondeur de 200 mètres (Polsenaere, 2011 ; Fig. 1.6). Malgré sa faible surface (7% de l'océan global), la zone côtière assure de grandes fonctions écologiques telles que la production primaire (14 à 30% de la production primaire océanique totale), la calcification, la minéralisation de la matière organique et le recyclage des nutriments (Pernetta et Milliman, 1995 ; Gattuso et al., 1998).

1.4.1. Rôle de la zone côtière dans les processus et flux de carbone

Constituée d'un mélange d'eau douce et d'eau salé, les environnements côtiers présentent une large diversité de types géomorphologiques et d'écosystèmes (plateaux continentaux, estuaires, vasières, baies, zones humides) permettant l'interaction des cycles biogéochimiques (C, N, P) entre les continents, les océans et l'atmosphère (Aufdenkampe et al., 2011 ; Bauer et al., 2013). D'une part, ces écosystèmes dynamiques et hétérogènes reçoivent horizontalement des quantités importantes de carbone organique et inorganique (~0,85 Pg C an^{-1} ; Fig. 1.6) et d'azote inorganique dissous (~0,02 Pg N an^{-1} ; Cai, 2011) depuis le bassin versant et échangent de grandes quantités de matières et d'énergies avec l'océan ouvert (Gattuso et al., 1998 ; Borges et al., 2005). D'autre part, les environnements côtiers échangent verticalement des quantités importantes et variables de carbone avec les sédiments et l'atmosphère (Cole et al., 2007 ; Cai, 2011). A l'échelle globale, les plateaux continentaux se comportent comme des puits de CO_2 atmosphérique permettant la captation de 0,25 ± 0,05 Pg C an^{-1} au travers de la production primaire phytoplanctonique (Bauer et al., 2013 ; Dai et al., 2022). Au contraire, les eaux estuariennes, généralement sursaturées en CO_2 par rapport à l'atmosphère, émettent environ 0,25 ± 0,05 Pg C an^{-1} (Bauer et al., 2013 ; Dai et al., 2022) (Fig. 1.6). Dans ces systèmes aquatiques très turbides où la lumière pénètre peu, la captation de CO_2 par la production primaire est généralement plus faible que les émissions de CO_2 liées à la reminéralisation de la matière organique et aux apports de DIC provenant des rivières et les zones humides adjacentes (Frankignoulle et al., 1998 ; Borges et Abril, 2011). Les zones humides côtières incluant les marais absorbent 0,55 ± 0,05 Pg C an^{-1} de l'atmosphère grâce à une forte production primaire de la végétation terrestre et aquatique (Bauer et al., 2013 ; Forbrich et al., 2018 ; Tobias et Neubauer, 2019). Ainsi, ces zones d'interfaces situées le long du continuum terre-mer peuvent jouer un rôle majeur dans la captation et la séquestration de carbone sur Terre (Cai, 2011 ; Mcleod et al., 2011). Les échanges verticaux de carbone atmosphérique au sein de la zone côtière sont donc hétérogènes (Borges et al., 2005) et doivent être mesurés sur une échelle de temps relativement courte pour prendre en compte leur variabilité temporelle et réduire les incertitudes quant à leur contribution dans le cycle globale du carbone (Cai, 2011 ; Bauer et al., 2013 ; Najjar et al., 2018).

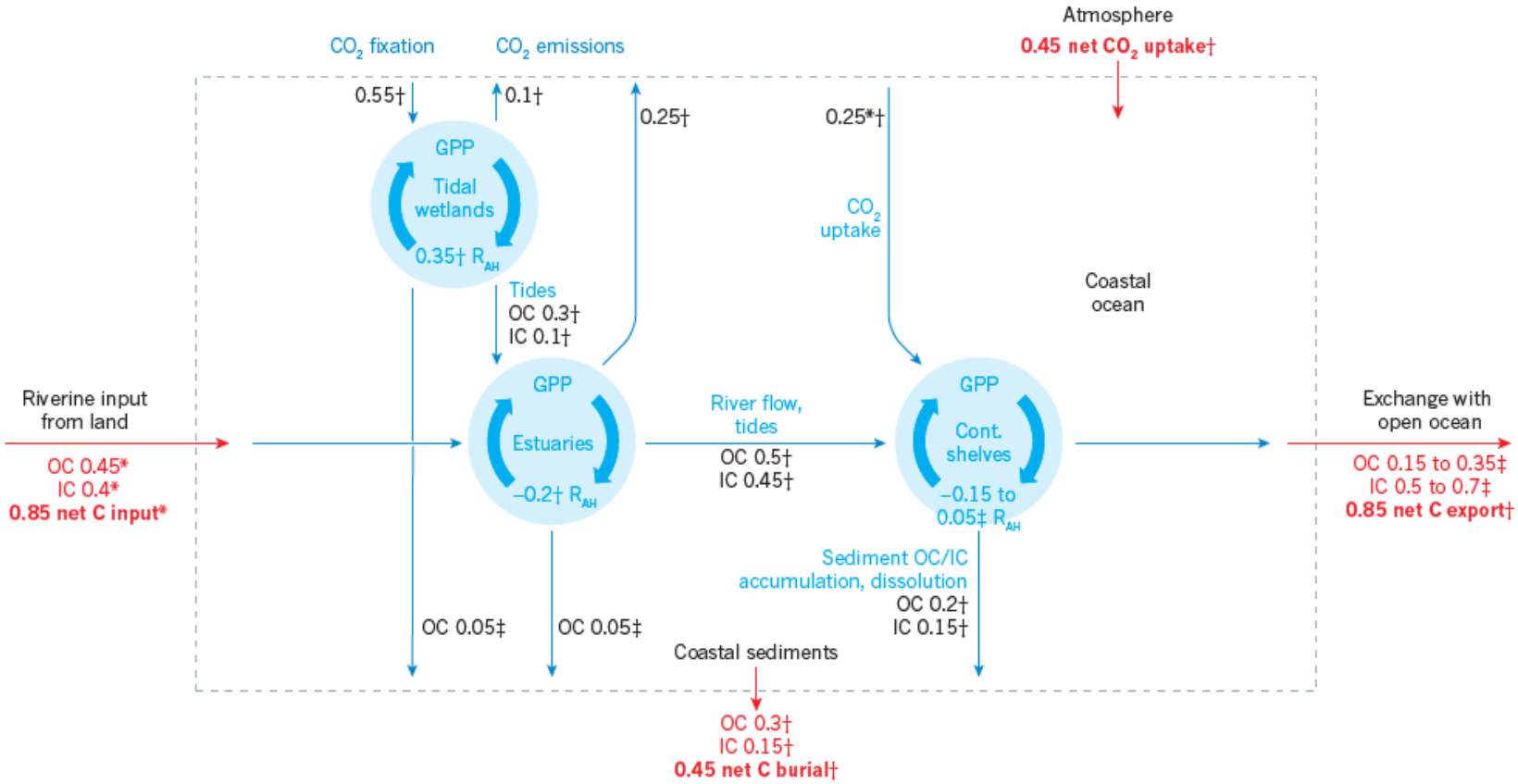

Figure 1.6 : Flux verticaux et horizontaux de carbone organique (OC) et inorganique (IC) au sein de la zone côtière (estuaires, zones humides tidales, plateaux continentaux). Le carbone (C) peut circuler à l'intérieur (valeurs en noir) et à l'extérieur (valeurs en rouge) des limites de l'océan côtier. Tous les flux de OC et IC sont présentés comme des valeurs positives, les flèches indiquent la direction des flux. Les flux de POC et DOC sont présentés comme des valeurs de OC total. L'équilibre entre la production primaire brute (GPP) et la respiration totale du système (autotrophe, A, et hétérotrophe, H ; R_{AH}) est la production nette de l'écosystème (NEP), les valeurs négatives indiquant la conversion du OC en IC. Incertitudes typiques pour les flux de carbone : *95% de certitude que l'estimation se situe dans les 50% de la valeur rapportée ; †95% de certitude que l'estimation se situe dans les 100% de la valeur rapportée ; ‡incertitude supérieure à 100%. Les unités sont les Pg C an^{-1} (1 Pg = 10^{15} g) arrondies à ± 0,05 Pg C an^{-1} (Bauer et al., 2013).

1.4.2. Biogéochimie du carbone en zone côtière

Le carbone dans les eaux côtières alimentant les marais salés par l'advection horizontale est présent sous forme inorganique ou organique, particulaire (> 0,45 μm) ou dissoute (< 0,45 μm) (Aminot et Kérouel, 2004 ; Cai, 2011). Le carbone inorganique particulaire (PIC) provient principalement de l'érosion des roches sédimentaires (origine allochtone) et de la précipitation du $CaCO_3$ (origine autochtone) (Meybeck, 1992 ; Cai, 2011). Le carbone inorganique dissous (DIC) dans les eaux côtières peut provenir de la respiration du réseau trophique, de la minéralisation de la matière organique, des échanges eau-sédiment, mais aussi être apporté par les eaux continentales provenant du bassin versant (Wang et Cai, 2004 ; Cai, 2011). Le carbone organique particulaire (POC) est soit apporté par les rivières lors de l'érosion des bassins versants (origine allochtone), soit produit à l'intérieur des écosystèmes côtiers (origine autochtone) par la production primaire végétale (plantes et algues) (Cai, 2011). Dans l'océan, le POC est principalement d'origine phytoplanctonique, alors que dans les environnements côtiers et en particulier dans les estuaires, la contribution terrestre provenant des rivières prédomine lorsque les débits sont élevés en hiver (Abril et al., 2002). Au contraire, en été, lors de l'étiage des fleuves, le POC peut être produit par une forte activité phytoplanctonique d'eau douce et, ensuite, dégradée dans les eaux estuariennes (Abril et al., 2002 ; Aminot et Kérouel, 2004). Le carbone organique dissous (DOC) dans les eaux côtières peut avoir plusieurs sources (autochtones ou allochtones) avec différents niveaux de labilité (d'un renouvellement rapide des formes les biodisponibles jusqu'à un renouvellement long des formes réfractaires dans l'océan profond ; Hansell, 2013). Le DOC autochtone est produit dans l'écosystème principalement par les organismes planctoniques, les microalgues benthiques et les macrophytes tandis que le DOC allochtone est principalement d'origine terrestre avec du matériel humique dérivé du sol (Lønborg et al., 2020).

Dans les environnements côtiers, les producteurs primaires (plantes, algues) produisent de nombreux composés organiques labiles (sucres simples, acides gras, acides aminés) au travers de la photosynthèse (section 3.1). Ce DOC peut être facilement dégradé par les microorganismes lors de la minéralisation aérobie de la matière organique dans l'eau et les sédiments. Ce processus produit du DIC mais peu de TA contribuant ainsi à l'acidification du milieu en augmentant les pCO_2 de l'eau (Tableau 1.1). Dans les écosystèmes côtiers peu profonds et très productifs comme les marais littoraux, le carbone organique labile se dépose à l'interface eau-sédiment favorisant des taux élevés de minéralisation aérobie. Ainsi, les

sédiments côtiers des marais salés sont typiquement anaérobies à partir des premiers millimètres de profondeur (Wiebe et al., 1981 ; Hulot et al., 2023) car la consommation d'oxygène excède les apports atmosphériques et la production biologique. Les microorganismes décomposeurs doivent donc utiliser d'autres accepteurs terminaux d'électrons ou oxydants (nitrate, sulfate, fer, manganèse, méthane ; Fig. 1.7) dont la dépense énergétique est de plus en plus importante pour assurer le recyclage de la matière organique (Canfield et Thamdrup, 2009). Cette minéralisation anaérobie produit de grandes quantités de DIC et de TA permettant d'augmenter la capacité tampon des eaux côtières lors des augmentations de CO_2 dissous (Krumins et al., 2013 ; Rassmann et al., 2020). Dans les sédiments estuariens et des marais salés, la respiration anaérobie est dominée principalement par la dénitrification (R6 ; Tableau 1.1) et la sulfato-réduction (R7 ; Tableau 1.1 et Fig. 1.7) en raison des apports terrestres importants en nitrate et des fortes concentrations en sulfate dans les eaux marines et côtières (Wang et al., 2018).

Potentiellement, cette pompe anaérobie lors de la minéralisation de la matière organique labile impacte fortement le cycle du carbone de l'océan côtier et ses marais salés en limitant l'acidification de l'eau lié aux flux de DIC et de TA sortant des sédiments (Reithmaier et al., 2023). De plus, de la matière organique réfractaire (lignine et la cellulose) sont également produit au sein de la zone côtière, spécifiquement par les végétaux supérieurs des marais salés comme les macrophytes terrestres ou aquatiques (Moran et Hodson, 1990 ; Wang et al., 2014). Ces macromolécules complexes sont plus ou moins résistantes à l'activité bactérienne et peu assimilé par le réseau trophique entrainant une dégradation lente et une accumulation dans les sédiments ou dans les eaux côtières (Marchand et al., 2005 ; Jiao et al., 2010 ; Hansell, 2013 ; Wang et al., 2014).

Tableau 1.1 : Réactions diagenétiques influençant les paramètres des systèmes des carbonates (DIC, TA et CO_2) (Krumins et al., 2013 ; Rassmann et al., 2020).

	Réactions		**DIC**	**TA**
		Réactions de la chimie des carbonates		
R1	Dissolution des carbonates	$CaCO_3 + CO_2 + H_2O \rightarrow Ca^{2+} + 2HCO_3^-$	+1	+2
R2	Précipitation des carbonates	$Ca^{2+} + 2HCO_3^- \rightarrow CaCO_3 + CO_2 + H_2O$	-1	-2
		Hydrolyse et minéralisation aérobie de la matière organique		
R4	Hydrolyse de la matière organique	$\frac{1}{106}(CH_2O)_{106}(NH_3)_{16}(H_3PO_4) + \frac{15}{106}H^+ \rightarrow CH_2O + \frac{16}{106}NH_4^+ + \frac{1}{106}H_2PO_4^-$	0	+0,14
R5	Minéralisation aérobie	$CH_2O + O_2 \rightarrow CO_2 + H_2O$	+1	0
		Minéralisation anaérobie de la matière organique		
R6	Dénitrification	$CH_2O + 0{,}8\ NO_3^- + 0{,}8\ H^+ \rightarrow CO_2 + 0{,}4\ N_2 + 1{,}4\ H_2O$	+1	0,8
R7	Sulfato-réduction	$CH_2O + 0{,}5\ SO_4^{2-} \rightarrow CO_2 + 0{,}5\ H^+ + H_2O$	+1	+1
R8	Réduction du fer-III	$CH_2O + 4\ Fe(OH)_3 + 8\ H^+ \rightarrow CO_2 + 4\ Fe^{2+} + 11\ H_2O$	+1	+8
R9	Réduction du manganèse-IV	$CH_2O + 2\ MnO_2 + 4H^+ \rightarrow CO_2 + 2\ Mn^{2+} + 3\ H_2O$	+1	+4
R10	Méthanogenèse	$CH_2O \rightarrow 0{,}5\ CH_4 + 0{,}5\ CO_2$	+0,5	0

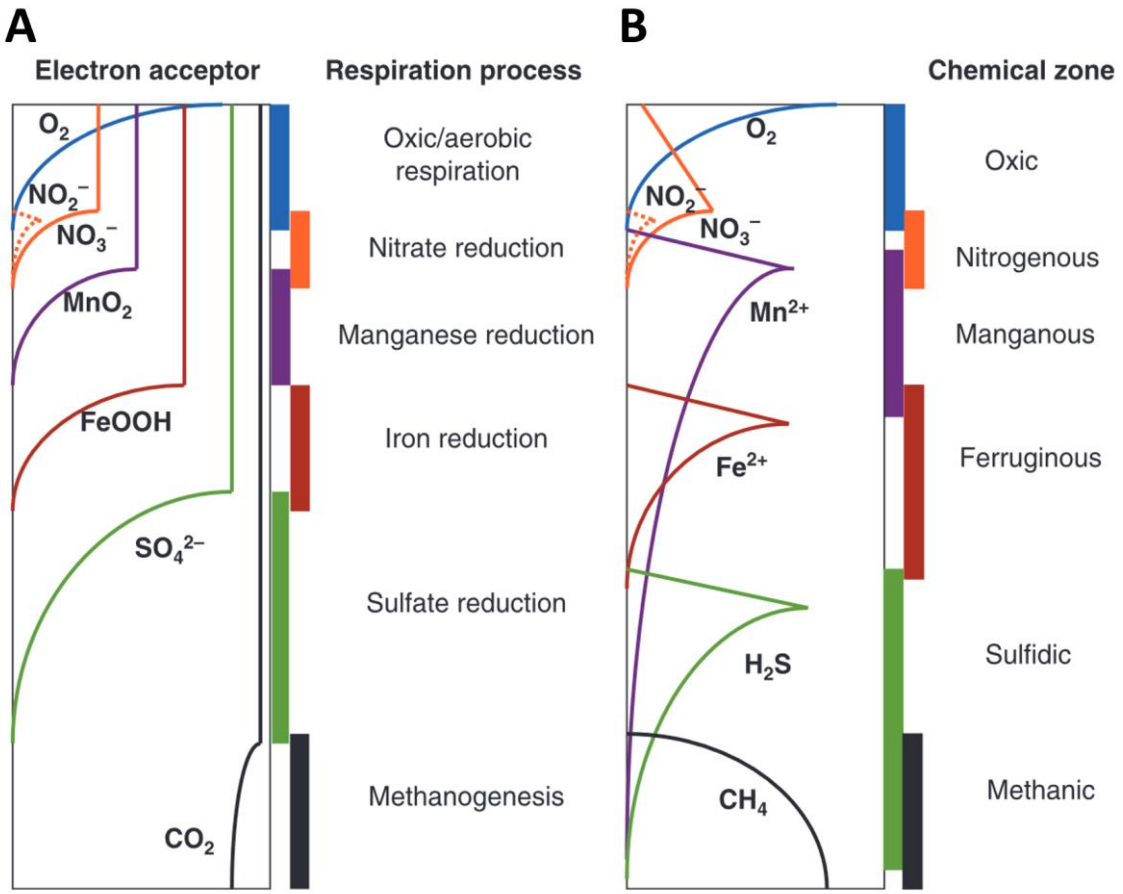

Figure 1.7 : (A) Distribution en profondeur dans les sédiments côtiers des accepteurs d'électrons disponibles pour les réactions aérobie et anaérobie de minéralisation de la matière organique. **(B)** Représentation des zones chimiques associés aux réactions de respiration. Du haut (surface) vers le bas (profondeur), les réactions diagénétiques sont classées dans l'ordre de la chaîne d'oxydo-réduction de la réaction la moins énergivore (respiration aérobie) vers la plus énergivore (méthanogénèse) (Canfield et Thamdrup, 2009).

2. Les marais, écosystèmes complexes à l'interface entre la terre et la mer

Les marais sont définis comme des zones humides peu profondes, fréquemment ou continuellement inondées par l'eau, et caractérisées par une végétation herbacée adaptée à des conditions saturées en eau (Environmental Protection Agency (EPA), 2023). Tous les types de marais sont alimentés par des eaux de surface (eau douce des rivières, eau salée des océans, estuaires ou lagunes et eau de pluie) et certains d'entre eux sont également alimentés par des eaux souterraines. Ces apports d'eau dépendent de la localisation des marais sur le bassin versant et du réseau hydrographique local. Ils sont principalement situés à proximité des cours d'eau et/ou du littoral où les eaux de surface peuvent s'écouler vers la mer. Les nutriments sont présents en abondance favorisant la vie végétale et animale (EPA, 2023). Les marais peuvent être classés selon l'influence de la marée (marais tidaux et marais non-tidaux ; Fig. 1.8) ou selon le niveau de salinité (marais salés, saumâtres et doux ; Fig. 1.8).

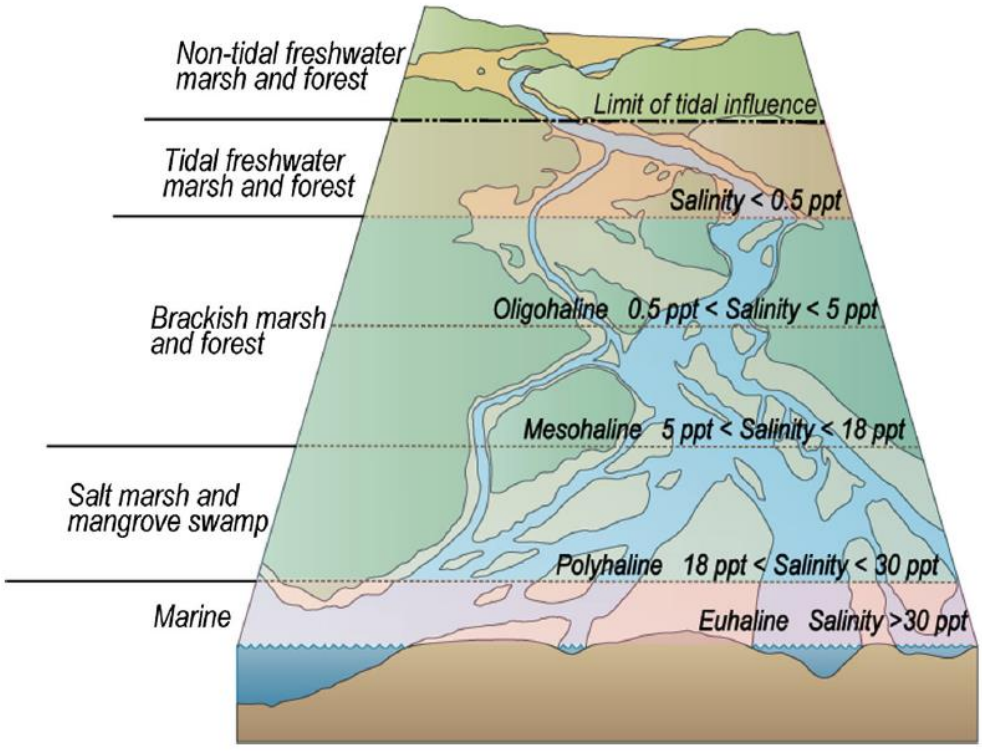

Figure 1.8 : Classification des marais tidaux en trois types selon le gradient de salinité le long d'un estuaire (marais salés, marais saumâtres et marais doux) (Luo et al., 2017 d'après Mitsch et Gosselink, 2015).

2.1. Les marais naturels peu anthropisés

2.1.1. Les marais tidaux

Les marais tidaux correspondent aux marais littoraux sous l'influence directe de l'hydrodynamisme des marées situés le long des côtes océaniques et des estuaires (EPA, 2023). Selon la classification de Odum (1988), les marais tidaux peuvent être classés en trois types en fonction d'un gradient de salinité le long d'un estuaire (Fig. 1.8) : les marais salés situés en aval de l'estuaire et directement connectés à l'océan côtier (18 < salinité < 30), les marais saumâtres qui peuvent être mesohaline (5 < salinité < 18) ou oligohaline (0,5 < salinité < 5) en fonction de leur distance à la mer et enfin les marais doux tidaux (salinité < 0,5) situés en amont de l'estuaire juste avant la limite de l'influence des marées (Luo et al., 2017). Comme les marais salés et saumâtres, les marais doux tidaux sont inondés par la marée mais la forte dilution par les eaux douces provenant des fleuves et des rivières entraine des salinités proches de 0 (Luo et al., 2017 ; Fig. 1.8).

Figure 1.9 : Répartition mondiale des marais salés tidaux le long des côtes océaniques à l'échelle de la Terre (Pétillon et al., 2023).

Les marais salés tidaux sont des zones humides côtières inondées et drainées par l'eau salée apportée par la marée (NOAA, 2023). Situés à l'interface entre le domaine terrestre et le domaine océanique, ces écosystèmes dynamiques sont dominés par des plantes terrestres tolérantes au sel (halophyte) qui s'étendent sur les zones intertidales de tous les continents (54 650 km^2), en particulier aux latitudes moyennes et élevées (Mcowen et al., 2017 ; Fig. 1.9).

Au sein de la zone intertidale, les marais salés peuvent former deux entités morpho-sédimentaires (la slikke et le schorre) qui sont caractérisées par des fréquences de submersion et des communautés végétales différentes (Fig. 1.10). Tout d'abord, la slikke est la partie inférieure et moyenne de la zone intertidale, immergée à chaque marée haute (marées de mortes-eaux et de vives-eaux), et constituée de sédiments vaseux à la granulométrie très fine. La topographie de la slikke est caractérisée par de vastes étendues subhorizontales plates, incisées par de grands chenaux (Verger, 2005). La végétation y est réduite, à l'exception des parties supérieures où des herbiers de phanérogames marines (*Zostera*) peuvent se développer. Les hautes-slikkes sont également associées à une végétation telle que les salicornes (*Salicornia*) et les spartines (*Spartina*) (Fig. 1.10). Ensuite, le schorre (i.e. le pré-salé) occupe la partie supérieure de la zone intertidale dont la limite continentale est souvent représentée par une digue (Verger, 2005). Contrairement à la slikke, le schorre est inondé par les eaux côtières uniquement pendant les marées de vives-eaux (Fig. 1.10). La végétation halophile dense et continue de type macrophytes appartient à des espèces ligneuses (*Puccinellia maritima*, *Halimione portulacoides*, *Aster tripolium*, *Suaeda maritima* ; Fig. 1.10) permettant de ralentir la force des marées et à contribuer à la sédimentation des matières en suspension présentes dans l'eau (Oustin, 2003). D'après Verger (2005), la digue est une frontière entre le domaine anthropique conquis sur la mer et l'espace soumis à l'hydrodynamisme de la marée tandis que, la transition entre l'estran nu et le pré-salé constitue la frontière entre le paysage marin (slikke) et le paysage terrestre des prairies halophiles (schorre).

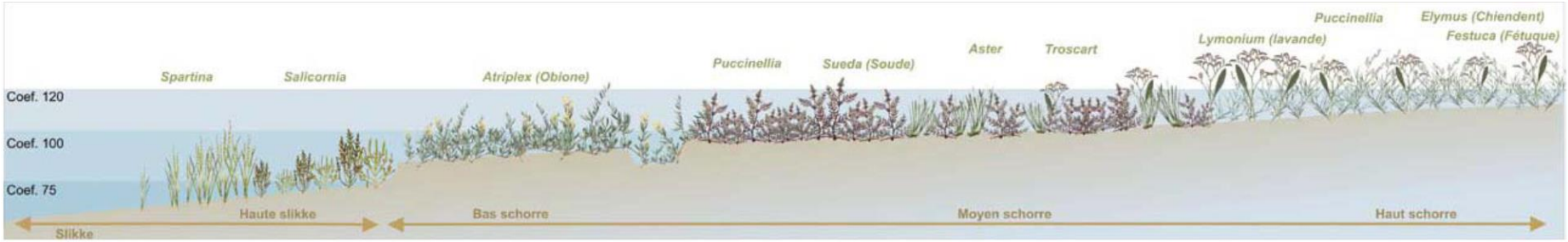

Figure 1.10 : Schéma d'un marais salé et répartition des espèces végétales selon la fréquence d'inondation et de la tolérance à la salinité. L. Anras, Forum des Marais Atlantique.

2.1.2. Les marais non tidaux

Contrairement aux marais tidaux, les marais non tidaux ne sont pas influencés par l'inondation de la marée. Il s'agit principalement de marais doux, bien que certains soient saumâtres ou salés (EPA, 2023). Selon leur localisation sur le bassin versant et de leur éloignement à la mer, deux principaux types de marais sont retrouvés dont les apports d'eau douce proviennent principalement des ruissellements, des précipitations et des nappes : en amont, les haut-marais correspondent à des tourbières généralement pauvre en nutriments et en aval, les bas-marais correspondent à des prairies humides riche en nutriments (Fig. 1.11).

Figure 1.11 : Exemples de marais non tidaux (tourbières et prairies humides) et leurs flux hydriques (www.zones-humides.org, septembre 2023).

2.2. Les marais anthropisés

Depuis plusieurs siècles, les marais littoraux ont subi des aménagements importants par l'Homme (poldérisation, endiguement, etc.) dans le but de gagner des étendues artificielles de terre sur la mer et d'y développer des productions économiques par le contrôle des flux hydrauliques (Tortajada et al., 2011). Au sein de ces marais rétro-littoraux (marais en arrière des digues), l'eau circule dans des canaux ou des chenaux dans lesquels les niveaux d'eau et le sens de circulation sont contrôlés par des écluses pour les activités humaines. Nous retrouvons les marais rétro-littoraux d'eau douce ou d'eau salée (Paticat, 2007 ; Tortajada, 2011). Dans le département de la Charente-Maritime (France), les marais rétro-littoraux sont répartis sur 110 000 ha (i.e. 15% de la superficie du département) représentant un intérêt écologique majeur pour le territoire.

2.2.1. Les marais salés rétro-littoraux

Les marais salés rétro-littoraux sont d'anciens marais tidaux isolés de l'influence de la marée par des digues et divisés en plusieurs bassins reliés entre eux par un réseau hydraulique complexe dans lesquels le temps de résidence de l'eau salée est contrôlé selon les besoins de l'Homme (Tortajada et al., 2011 ; Fig. 1.12). En Charente-Maritime, les marais salés rétro-littoraux (ou marais salés endigués) sont principalement localisés sur l'île de Ré, l'île d'Oléron et le long de l'estuaire de la Seudre représentant une superficie de 15 000 ha (i.e. 20% des marais Charentais anthropisés).

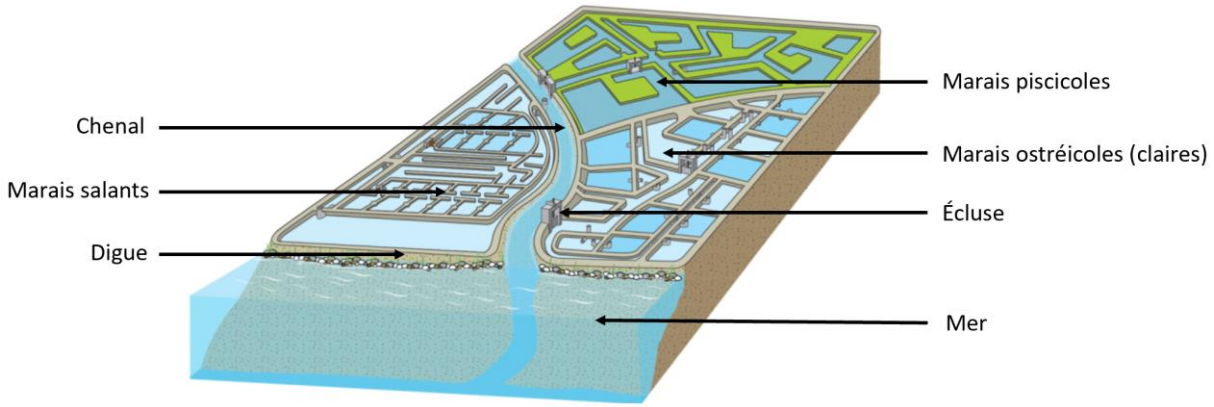

Figure 1.12 : Schéma d'un système de marais salés rétro-littoraux (modifié de www.zones-humides.org, septembre 2023).

Ces mosaïques de marais salés rétro-littoraux sont le siège de plusieurs activités anthropiques (ostréiculture, saliculture et pisciculture ; Fig. 1.12). Lors des périodes de marées montantes, les chenaux servent à alimenter en eau les marais rétro-littoraux avec un temps de résidence de l'eau dans les marais qui peut varier de quelques heures à deux semaines selon le mode de gestion (Paticat, 2007). Lors des périodes de marées descendantes, les marais sont vidangés dans les chenaux (Fig. 1.12) pouvant influencer la qualité de l'eau (Tortajada, 2011). Par exemple, la pisciculture semi-intensive entraîne une pollution nutritive dans les marais (Hussenot, 1998) et nécessite un renouvellement rapide de l'eau (quelques heures seulement). La décharge des marais salés piscicoles dans les chenaux libère de fortes concentrations en azote inorganique dissous (nitrates, nitrites, ammonium) et en phosphore inorganique dissous (phosphate) provenant des aliments donnés aux poissons (Hussenot, 1998). Au contraire, dans les marais ostréicoles, le temps de résidence de l'eau est plus long

(deux semaines). Ainsi, dans ces bassins, le phytoplancton se développe et assimile les composés azotés et phosphatés contrairement aux marais piscicoles. Lors des vidanges, ces bassins enrichissent donc les chenaux de matière organique phytoplanctonique (Tortajada, 2011). Au sein des marais salicoles (ou marais salants ; Fig. 1.12), les eaux stagnent jusqu'à complète évaporation pour récupérer le sel, ainsi cette activité n'influence pas la qualité de l'eau dans les chenaux.

2.2.2. Les marais doux rétro-littoraux

Les marais doux rétro-littoraux sont séparés en marais mouillés (marais inondables) et marais desséchés (marais non inondables ; Fig. 1.13). Les marais mouillés sont inondés régulièrement lors des périodes de crues et sont utilisés comme des réservoirs d'eau douce pendant la période estivale. En aval, les marais doux desséchés sont localisés entre les marais mouillés et la mer, ils sont associés à des digues et des ouvrages hydrauliques permettant (i) la régulation des entrées d'eau douce provenant du marais mouillé en amont et (ii) la protection du marais desséché contre les arrivées d'eaux marines en aval. Ce territoire poldérisé forme un ensemble de parcelles de prairies ou cultures rectilignes délimités par un réseau de canaux secondaires. L'eau est évacuée au moyen de portes à flot (ou portes à la mer) qui s'ouvrent à marée basse (Fig. 1.13). À marée haute, les portes à flot se ferment et empêchent l'eau salée d'inonder les parcelles agricoles du marais desséché. Durant la saison sèche, les portes à flot sont fermées, afin de garder l'eau au sein des canaux nécessaire à l'alimentation des cultures (Fig. 1.13). En Charente-Maritime, les marais desséchés sont principalement localisés dans le marais Poitevin, le marais de Brouage et le marais de Rochefort représentant la grande majorité des marais doux, soit une superficie de 80 000 ha (i.e. 80% des marais Charentais anthropisés).

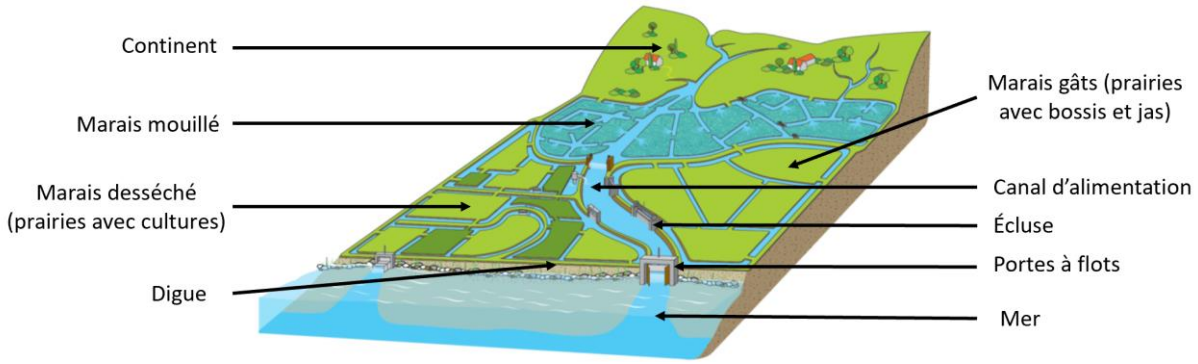

Figure 1.13 : Schéma d'un système de marais doux rétro-littoral (modifié de www.zones-humides.org, septembre 2023).

2.3. Fonctions et services écosystémiques des marais littoraux

2.3.1. Fonctions écologiques

Les marais assurent d'importantes fonctions écologiques qui sont définies comme des actions naturelles dans les zones humides résultant de l'interaction entre la structure de l'écosystème et les processus physiques, chimiques et biologiques (Maltby et al., 1996). Les fonctions des marais peuvent être réparties en fonctions biogéochimiques, hydrologiques et d'habitats (AcclimaTerra, 2018) :

- La fonction biogéochimique va transformer et dégrader la matière dissoute et particulaire arrivant dans le milieu et permettent l'assimilation des nutriments (Bel Hassen, 2001 ; Masclaux et al., 2015) et la reminéralisation du carbone organique au travers de l'activité des végétaux et des microorganismes.
- La fonction hydrologique permet la régulation du cycle de l'eau. Ces écosystèmes assurent le stockage de l'eau en périodes d'excédent hydraulique et la restitution aux milieux adjacents en périodes de déficit hydraulique (AcclimaTerra, 2018).
- Les fonctions d'habitat, de nourricerie et de nurserie permettent la conservation et le développement d'une forte biodiversité (Philippe et al., 2017).

2.3.2. Services écosystémiques

Les services écosystémiques sont les avantages que les Hommes tirent des écosystèmes et sont générés directement par les processus qui soutiennent les écosystèmes, ou fonctions écosystémiques, tels que la productivité primaire et secondaire, la décomposition et la transformation des nutriments (UNEP, 2006). Dans l'ensemble, ces différents services sont souvent évalués en fonction de leur valeur économique (Gedan et al., 2009). Nous pouvons définir trois grandes catégories de services écosystémiques (AcclimaTerra, 2018) :

- Les services de régulation permettent l'épuration naturelle des eaux et la séquestration de carbone dans les sédiments au travers de la production primaire des végétaux (fonction biogéochimique). Les marais littoraux forment également des zones tampon et assurent ainsi une protection contre les inondations liées à l'élévation du niveau de la mer et aux tempêtes. De plus, ces écosystèmes minimisent l'érosion du littoral grâce à leur capacité à absorber l'énergie des courants océaniques et des vagues (fonction hydrologique) (King et Lester, 1995 ; Moeller et al. 1996).

- Les services de production permettent aux marais de fournir de l'eau aux populations notamment grâce à leur fonctions hydrologiques et biogéochimiques. De plus, les services de production les plus courants sont directement liés des ressources alimentaires comme la saliculture, la conchyliculture et la pêche (Gedan et al., 2009).
- Les services culturels permettent aux marais de fournir des espaces récréatifs pour la population humaine (Ghermandi et Nunes, 2013) et de constituer des zones de refuge pour les oiseaux migrateurs (Bradshaw et al., 2020).

2.3.3. Altérations des marais salés

Les marais salés assurent les services écosystémiques les plus importants parmi les écosystèmes naturels sur Terre (les marais représentent 50% de la surface globale des zones humides et fournissent 75% des services ; Costenza et al., 1997). Aujourd'hui, la préservation et l'augmentation de la qualité et de la quantité de ces services sont les principaux arguments pour la protection des marais salés (Gedan et al., 2009).

Malgré leurs potentiels écologiques majeurs, ces zones d'interfaces sont les écosystèmes les plus menacés sur Terre par les changements globaux tels que les activités anthropiques, l'augmentation des émissions de CO_2 atmosphérique et l'élévation du niveau des océans (Cai, 2011 ; Mcleod et al., 2011). À l'échelle globale, 25% de la surface des marais salés a disparu depuis le début du XIX^{e} siècle (perte de 1 à 2% an^{-1} ; Bridgham et al., 2006 ; Duarte et al., 2008 ; Mcleod et al., 2011). Par exemple, le delta du Mississippi a perdu environ 5 000 km^2 de ses marais salés entre 1932 et 2010 (Couvillion et al., 2011). Ces écosystèmes littoraux ont souvent été anthropisés au travers de la poldérisation et l'endiguement pour soutenir le développement économique comme l'agriculture, l'aquaculture et la saliculture (McCurdy, 1988 ; Gedan et al., 2009) mais aucune étude n'a montré l'impact de cette anthropisation sur leur capacité de captation de CO_2 atmosphérique. De plus, l'eutrophisation côtière, au travers de l'enrichissement en nutriments (nitrate en particulier), favorise la décomposition microbienne anaérobie de la biomasse souterraine des plantes provoquant une diminution de la géomorphologie des marais (Deegan et al., 2012). Ces altérations entraînent une diminution importante de la superficie des marées salés à l'échelle mondiale (Duarte et al., 2008). Ces pertes de superficie contribuent mécaniquement à la réduction de la captation de CO_2 atmosphérique mais également à l'augmentation des émissions de CO_2 atmosphérique due à la décomposition du carbone organique stocké dans leur sol en présence d'oxygène (Altor et Mitsch, 2008). Les marais salés sont reconnus comme des écosystèmes exceptionnels dont

leur conservation et leur restauration peuvent être des stratégies efficaces d'atténuation et d'adaptation au changement climatique (McLeod et al., 2011 ; Duarte et al., 2013). En effet, les marais salés ont la plus vaste répartition spatiale sur Terre parmi les principaux écosystèmes littoraux stockeurs de carbone biologique (marais salés, mangroves et herbiers marins) avec les taux de séquestration du carbone par unité de surface parmi les plus élevés (McLeod et al., 2011 ; Duarte et al., 2013). Leur importance en tant que réservoirs de services écosystémiques (puits de carbone, protection contre l'érosion côtière) a permis la mise en place de politiques de protection et de conservation au sein de réserves naturelles qui contribuent à leur meilleure gestion mais aussi au maintien et au développement de leurs potentiels écologiques et économiques (AcclimaTerra, 2018). De plus, dix priorités de recherche mondiale sur les marais salés ont été identifiés par un consortium international et multidisciplinaire d'experts. Les priorités ont été regroupées en quatre domaines de recherche thématiques : (1) agrandissement des zones de marais salés et potentiel de restauration, (2) services écosystémiques des marais salés (influence du contexte environnemental et du changement climatique sur les services), (3) modèles et processus du fonctionnement des marais salés (comprendre les facteurs de contrôle des fonctions associées aux marais et intégration des processus biologiques dans les modèles physiques) et (4) besoins en matière de gestion et de politique (comment la gestion peut-elle avoir un impact sur la protection des côtes) (Pétillon et al., 2023).

3. Métabolisme et dynamique du carbone dans les marais

3.1. Métabolisme : photosynthèse versus respiration

Le métabolisme est un concept important dans l'étude du cycle du carbone dans les écosystèmes terrestres et aquatiques permettant de décrire leur capacité à transformer le carbone au travers des processus de la production primaire et de la respiration (Chapin et al., 2006). La production nette de l'écosystème (NEP), développée par Woodwell et Whittaker (1968), peut être définie comme la différence entre la captation de CO_2 par les organismes photosynthétiques (plantes, algues) au niveau de l'écosystème (production primaire brute, ou GPP) et les émissions de CO_2 par la respiration de l'ensemble des organismes vivants (microorganismes, plantes, algues, animaux) au niveau de l'écosystème (respiration de l'écosystème, ou R_{eco}) :

$$NEP = GPP - R_{eco} \quad (5)$$

La NEP permet ainsi de décrire le statut métabolique des écosystèmes. Un écosystème est autotrophe lorsque la GPP excède la R_{eco} (NEP > 0 ; accumulation de carbone dans l'écosystème) ou hétérotrophe lorsque la R_{eco} excède la GPP (NEP < 0 ; perte de carbone dans l'écosystème). Au sein de la zone côtière, les écosystèmes autotrophes tels que les marais importent du DIC et des nutriments et exportent ou séquestrent du carbone organique dans les sédiments alors que les écosystèmes hétérotrophes tels que les estuaires importent du carbone organique et exportent du DIC et des nutriments (Nixon et al., 1995 ; Crosswell et al., 2017).

La photosynthèse est le principal processus de la production primaire de la biomasse dans les marais littoraux permettant la captation de CO_2 par l'activité des microalgues (benthiques et pélagiques) et des macrophytes (Tobias et Neubauer, 2019). Le processus nécessite l'assimilation d'azote inorganique dissous (DIN) soit sous forme réduite (ammonium, NH_4^+ ; Eq. 6) soit sous forme oxydé (nitrate, NO_3^- ; Eq. 7) mais la dépense énergétique de la cellule photosynthétique sera d'autant plus importante que le composé sera oxydé (Aminot et Kérouel, 2004) :

$$106CO_2 + 16NH_4^+ + HPO_4^{2-} + 106H_2O \rightarrow (CH_2O)_{106}(NH_3)_{16}H_3PO_4 + 106O_2 + 14H^+ \quad (6)$$

$$106CO_2 + 16NO_3^- + HPO_4^{2-} + 122H_2O + 18H^+ \rightarrow (CH_2O)_{106}(NH_3)_{16}H_3PO_4 + 138O_2 \quad (7)$$

La respiration est la réaction inverse à la photosynthèse permettant l'oxydation du carbone organique en CO_2 (minéralisation) (Eq. 8). Plus précisément, ce processus permet la conversion de la matière organique dissoute (secrétées par les cellules ou libérées à leur mort) et de la matière particulaire détritique (excrétées par les organismes supérieurs ou constituées de débris de cellules mortes) en nutriments minéraux et en carbone inorganique (Aminot et Kérouel, 2004 ; Tobias et Neubauer, 2019).

$$(CH_2O)_{106}(NH_3)_{16}H_3PO_4 + 106O_2 + 14H^+ \rightarrow 106CO_2 + 16NH_4^+ + HPO_4^{2-} + 106H_2O \quad (8)$$

3.2. Les facteurs physico-chimiques influençant le métabolisme phytoplanctonique

Dans les écosystèmes côtiers comme les marais salés, les baies et les estuaires, la production nette de la communauté phytoplanctonique (NCP) est contrôlée par de nombreux facteurs environnementaux, physiques et biologiques au niveau de l'écosystème. Dans les écosystèmes côtiers en milieu estuarien, un modèle conceptuel a mis en évidence que la

production primaire phytoplanctonique correspond au produit de la production de la biomasse et du taux de croissance du phytoplancton (Fig. 1.14 ; Cloern et al., 2014).

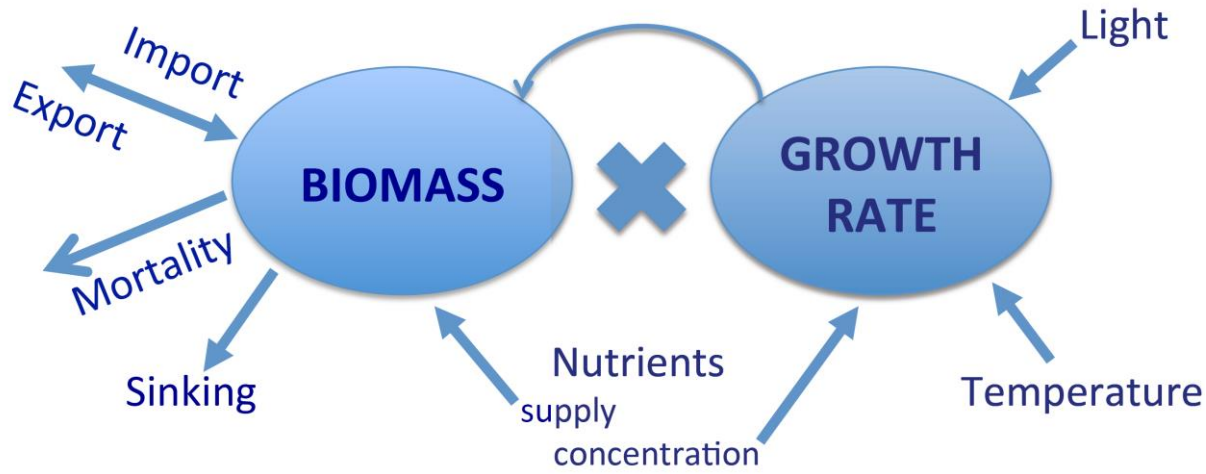

Figure 1.14 : Modèle conceptuel de la production primaire phytoplanctonique et des facteurs de contrôle biotiques et abiotiques dans les écosystèmes côtiers estuariens (Cloern et al., 2014).

La température

La température influence les processus métaboliques des communautés planctoniques (taux de croissance ; Fig. 1.14) avec une dépendance à la température plus importante concernant la respiration des communautés (CR) que la photosynthèse (GPP) (Regaudie de Gioux et Duarte, 2012). Dans un marais tidal (USA), Wang et al. (2004) a montré une corrélation positive entre la température et le métabolisme hétérotrophe du compartiment aquatique entraînant une augmentation des émissions de CO_2 atmosphérique. De plus, les températures plus élevées favorisent les niveaux trophiques supérieurs, en augmentant le rapport entre les hétérotrophes et les autotrophes (Archibald et al., 2022).

La lumière

La lumière est indispensable à la photosynthèse permettant la croissance du phytoplancton dans les milieux aquatiques côtiers (Fig. 1.14 ; Cloern et al., 2014). Elle contrôle l'équilibre métabolique des communautés phytoplanctoniques à l'échelle diurne avec, généralement, une autotrophie le jour (GPP:CR > 1) et une hétérotrophie la nuit

(GPP:CR < 1) et à l'échelle saisonnière avec des ratio GPP:CR plus élevés au printemps-été au cours des journées les plus lumineuses de l'année qu'en hiver-automne au cours des journées les moins lumineuses de l'année. Le taux de croissance du phytoplancton dans les estuaires riches en nutriments est déterminé en grande partie par la disponibilité de la lumière dans l'eau, mesurée par le PAR aquatique (Alpine et Cloern, 1988) et dont la variation dépend de l'irradiation solaire incidente, de la turbidité et de la profondeur de la couche euphotique (Wofsy, 1983). Ces trois composantes jouent un rôle majeur dans la régulation de la production primaire phytoplanctonique (Fig. 1.14).

Disponibilité en nutriments

Les nutriments sont également un facteur de contrôle important de la croissance du phytoplancton (Fig. 1.14) car ils sont intégrés dans la biomasse vivante lors de la photosynthèse (Eqs. 6 et 7 ; Aminot et Kérouel, 2004) selon les rapports molaires théoriques N:P:Si de 16:1:16 (Redfield, 1958 ; Brzezinski, 1985). En milieu marin, certaines cellules du nanophytoplancton comme les coccolithophoridés peuvent utiliser l'azote et le phosphore sous forme organique dissoute pour se développer pendant que la forme inorganique dissoute est limitante pour l'ensemble des communautés planctoniques. En milieu intertidal comme dans les marais salés, le microphytobenthos (MPB) essentiellement formé de microalgues benthiques (diatomées pennées) peut dissocier l'assimilation et l'utilisation des nutriments entre la période d'immersion (assimilation à l'interface eau-sédiment) et d'émersion (utilisation pour la photosynthèse en surface des sédiments), respectivement (Guarini, 1998 ; Savelli et al., 2019). Dans les milieux estuariens, la synthèse de Cloern et al. (2014) a montré l'importance des apports en nutriments provenant des bassins versants agricoles et/ou urbains sur la production primaire phytoplanctonique avec de fortes concentrations en chlorophylle-*a* dans les systèmes eutrophes (Chl-*a* > 100 µg L^{-1}) et de faibles concentrations dans les systèmes oligotrophes (Chl-*a* ≈ 0.1 µg L^{-1}).

De plus, dans des environnements côtiers peu profonds (marais salés, lagunes), le niveau d'eutrophisation peut influencer la contribution des producteurs primaires aquatiques. Par exemple, les algues à croissance lente et des herbiers sont dominants dans des conditions oligotrophes alors que les macroalgues opportunistes et du phytoplancton sont plutôt dominants dans des conditions eutrophes (Schramn et Nienhuis, 1996 ; Schraman, 1999 ; Le

Fur et al., 2017). Cependant, très peu d'études ont étudié la relation entre l'eutrophisation des écosystèmes littoraux et leur capacité de captation de CO_2 atmosphérique.

Interactions trophiques et mortalités

Alors que le taux de croissance du phytoplancton est déterminé par la lumière, la température et les concentrations en nutriments, la biomasse est contrôlée par l'équilibre entre les taux de croissance et de mortalité incluant la consommation par les brouteurs (Fig. 1.14 ; Cloern et al., 2014). Les taux de croissance et de consommation du phytoplancton sont souvent à l'équilibre, à l'exception d'événements comme l'augmentation de la photopériode au printemps (Riley, 1967), de l'apports de nutriments (Ara et al., 2011) ou de la mise en place d'une stratification (Pennock, 1985) où les taux de croissance du phytoplancton dépassent temporairement le taux de broutage permettant une augmentation de la biomasse en Chl-*a*. Généralement, les cellules phytoplanctoniques sont consommées par les brouteurs qui peuvent être du microzooplancton à croissance rapide (flagellés, ciliés), du phytoplancton mixotrophe (dinoflagellés et haptophytes) et du mésozooplancton (copépodes). À l'échelle annuelle, la perte liée au broutage par le mésozooplancton ne représente qu'une faible fraction (10%) de la production primaire phytoplanctonique (PPP) dans les estuaires productifs (Calbet, 2001) mais la variabilité interannuelle des copépodes peut être également un régulateur important de la PPP. Par exemple, une PPP annuelle anormalement faible a été observée dans la baie du Massachusetts (USA) en 1998, année marquée par un hiver exceptionnellement chaud et une croissance rapide des copépodes, dont le broutage a supprimé l'efflorescence hiver-printemps qui contribue normalement à plus de 40% de la PPP annuelle (Keller et al., 2001). Le broutage par les bivalves peut être un puissant régulateur de la biomasse et de la production de phytoplancton.

Échanges horizontaux

Dans les systèmes macrotidaux, les apports allochtones importants de matière organique labile en provenance des fleuves favorisent la respiration des communautés planctoniques alors que la photosynthèse est limitée par la faible disponibilité en lumière (Gattuso et al., 1998). Au contraire, dans les systèmes stratifiés microtidaux, la production primaire phytoplanctonique est favorisée (Koné et al., 2009).

3.3. Dynamique et flux de carbone dans les marais salés

Dans les marais salés, la dynamique du CO_2 dissous ($CO_{2(d)}$) ou de la pression partielle de CO_2 (pCO_2) de l'eau est contrôlée par de nombreux processus physico-chimiques et biologiques (Fig. 1.15) : (1) les échanges verticaux de carbone à l'interface eau-atmosphère soit comme source ou puits de CO_2 atmosphérique ; (2) les échanges horizontaux de carbone avec d'une part, les apports d'eaux continentales par les rivières et d'autre part, les échanges d'eaux marines par l'advection horizontale des marées ; (3) le métabolisme des communautés planctoniques et des végétaux terrestres et aquatiques avec une captation de $CO_{2(d)}$ par la production primaire et une libération de $CO_{2(d)}$ par la respiration ; (4) le système des carbonates ($CaCO_3$) permettant soit une captation de $CO_{2(d)}$ par la dissolution du $CaCO_3$, soit une libération de $CO_{2(d)}$ par la précipitation du $CaCO_3$; (5) le couplage benthique-pélagique qui peut libérer des quantités importantes de $CO_{2(d)}$ issus de la minéralisation de la matière organique dans les sédiments (Fig. 1.15).

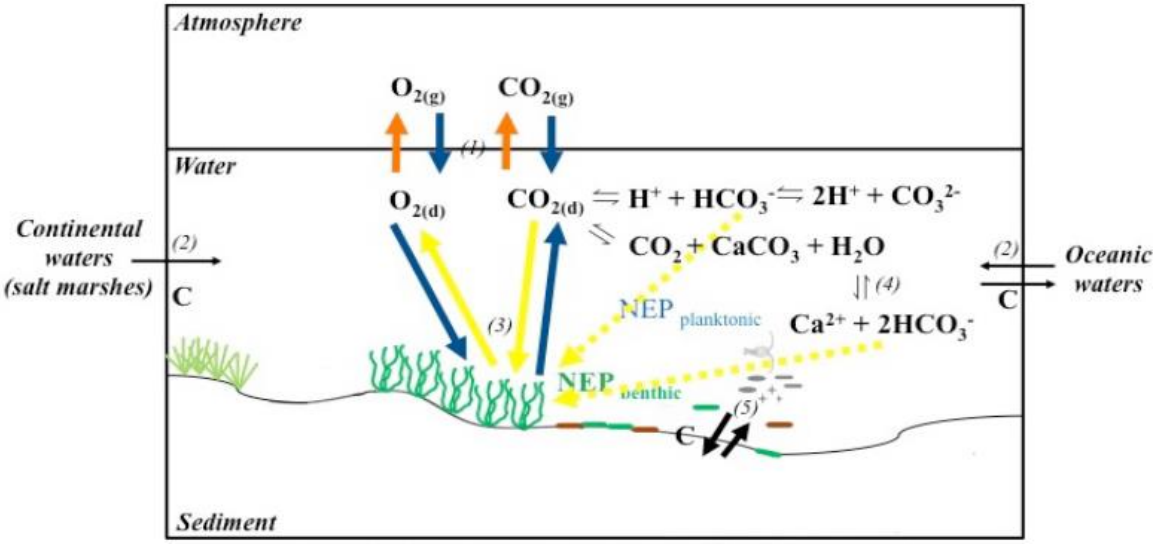

Figure 1.15 : Les processus biologiques et physico-chimiques contrôlant la dynamique du CO_2 dissous ($CO_{2(d)}$) dans le compartiment aquatique des marais salés. NEP : production nette de l'écosystème ; $CO_{2(d)}$: CO_2 dissous dans l'eau ; $CaCO_3$: carbonates de calcium ; HCO_3^- : ions bicarbonates ; CO_3^{2-} : ions carbonates ; C : Carbone (Polsenaere, 2018). Les équations de la photosynthèse et de la respiration sont données dans la partie 3.1.

Les processus de production primaire dans les marais salés sont parmi les plus intenses sur Terre avec des taux de GPP variant de 1900 à 3600 g C m^{-2} an^{-1} et de NEP variant de 150 à 1600 g C m^{-2} an^{-1} (Hopkinson, 1998 ; Duarte et al., 2005 ; Hopkinson et Smith, 2005 ; Gedan et al., 2009). Ces écosystèmes hautement productifs se comportent donc comme des puits de CO_2 atmosphérique (Cai, 2011) principalement par l'activité photosynthétique des plantes vasculaires et des microalgues benthiques (Tobias et Neubauer, 2019). Généralement dans l'océan, les communautés planctoniques sont en équilibre métabolique (GPP:CR ≈ 1 ; Duarte et al., 1999, 2001 ; Del Giorgio et Duarte, 2002) alors que dans les environnements côtiers, les apports allochtones de matière organique peuvent générer une forte hétérotrophie planctonique (GPP:CR < 1 ; Navarro et al., 2004 ; Gazeau et al., 2005 ; Borges et Abril, 2011 ; Wang et al., 2018). Cependant, dans les marais salés, le métabolisme des communautés planctoniques est systématiquement inférieur à celui de l'ensemble du compartiment aquatique (Ragotzkie, 1959 ; Wang et al., 2018). Ainsi, une partie significative du carbone organique issu de la production primaire est séquestrée et stockée sous forme de « carbone bleu » dans les sédiments des marais salés et/ou dans la biomasse vivante des végétaux (Chmura et al., 2003 ; Macreadie et al., 2017 ; Mcleod et al., 2011). Les taux de séquestration de C par unité de surface dans les écosystèmes côtiers végétalisés (écosystèmes « carbone bleu ») tels les marais salés (218 ± 24 g C m^{-2} an^{-1}), les mangroves (226 ± 39 g C m^{-2} an^{-1}) et les herbiers (138 ± 38 g C m^{-2} an^{-1}) sont parmi les plus élevés sur Terre contribuant ainsi fortement au cycle global du C malgré leur faible superficie mondiale par comparaison aux écosystèmes terrestres (Mcleod et al., 2011). Cette différence avec les écosystèmes terrestres est principalement liée à la forte saturation en eau dans les systèmes aquatiques littoraux qui limite la diffusion de l'oxygène dans les sédiments et provoque une anoxie à partir des premières couches de surface (quelques millimètres ; Wiebe et al., 1981 ; Kristensen et al., 2008). La matière organique produite par photosynthèse est ainsi principalement dégradée par des processus de minéralisation anaérobie (Tableau 1.1) plus lents et moins efficaces que la minéralisation aérobie (Aller, 1994 ; Sun et al., 1993) permettant une meilleure séquestration du C. Les marais salés exportent également des quantités importantes et variables de carbone inorganique issu de la reminéralisation de la matière organique autochtone dans les marais (Wang et Cai, 2004 ; Wang et al., 2016) et pourraient ainsi fortement influencer le bilan de carbone des systèmes côtiers en aval (Cai, 2011). L'hypothèse de la "pompe CO_2 des marais" propose que la captation du CO_2 atmosphérique principalement par les plantes des marais et l'export d'une partie de ce carbone sous forme inorganique par l'advection tidale seraient l'un

des principaux mécanismes rendant des eaux côtières adjacentes sources de CO_2 pour l'atmosphère (Wang et Cai, 2004 ; Jiang et al., 2008).

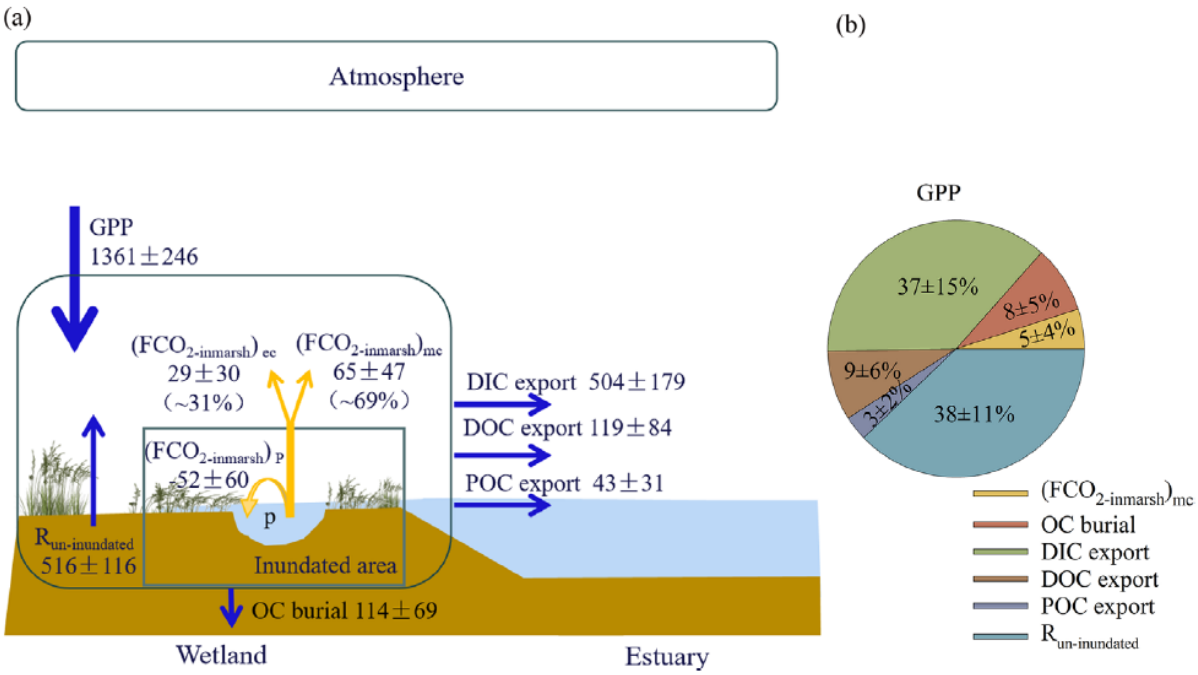

Figure 1.16 : Budget de carbone d'un marais tidal (États-Unis, 12300 km^2) avec **(a)** les flux horizontaux et verticaux de carbone aux différentes interfaces d'échanges et **(b)** leurs pourcentages sur la production primaire brute (GPP). La GPP correspond à la captation de CO_2 atmosphérique par l'ensemble des organismes autotrophes du marais. La somme des flux correspond à la GPP (1361 ± 246 g C m^{-2} an^{-1}) : GPP = $(FCO_{2\text{-inmarsh}})_{mc}$ + OC burial + DIC export + DOC export + POC export + $R_{un\text{-}inundated}$. Les flux de carbone sont donnés en g C m^{-2} an^{-1}. GPP : production primaire brute ; P : photosynthèse dans l'eau ; $R_{un\text{-}inundated}$: respiration du compartiment terrestre lors de l'émersion du marais ; $(FCO_{2\text{-}inmarsh})_{mc}$) : flux de CO_2 atmosphérique influencés du compartiment aquatique du marais lors de l'immersion ; $(FCO_{2\text{-}inmarsh})_{ec}$) : flux de CO_2 atmosphérique influencés par les eaux estuariennes lors de l'immersion ; $(FCO_{2\text{-}inmarsh})_{P}$) : impact de la photosynthèse sur les flux de CO_2 atmosphérique ; OC : carbone organique ; DIC : carbone organique dissous ; DOC : carbone organique dissous ; POC : carbone organique particulaire (Song et al., 2023).

Par exemple, au sein d'un marais salé (côte est des États-Unis ; 12300 km^2), Song et al. (2023) estime une GPP de 1361 ± 246 g C m^{-2} an^{-1}. La majorité de cette GPP est respirée au sein du marais (> 80%) et les produits de cette respiration (autotrophe et hétérotrophe) sont (i) dégazés vers l'atmosphère sous forme de CO_2 par le compartiment terrestre (38 ± 11% ; $R_{un\text{-}inundated}$) et le compartiment aquatique (5 ± 4% ; $(FCO_{2\text{-}inmarsh})_{mc}$) et (ii) exportés vers l'océan côtier sous forme de DIC (37 ± 15% ; Fig. 1.16). Ces résultats illustrent que l'exportation de carbone inorganique dissous (DIC) par les marais tidaux, calculée par des

mesures simultanées des concentrations en DIC et des flux d'eau lors de la marée descendante, représente une quantité majeure (504 ± 179 g C m^{-2} an^{-1}) dans le budget global du C des marais littoraux (Wang et al., 2016 ; Song et al., 2023). Dans la plupart des marais salés et les mangroves, cette production importante de DIC proviennent principalement des processus métaboliques anaérobiques dans les sédiments et de l'exportation d'eau porale par la pompe tidale pendant la marée descendante (Koné et Borges, 2008 ; Reithmaier et al., 2023). Ce résultat est confirmé par des concentrations en DIC et en TA deux à trois plus élevées dans les eaux porales que dans les eaux de surface (Fig. 1.17). Ensuite, une faible proportion de la GPP des marais est exportée sous forme de carbone organique dissous (DOC ; 9 ± 6%) et particulaire (POC ; 3 ± 2%) tandis que, la partie restante de la GPP est séquestrée dans les sédiments (8 ± 5%) sous forme de "carbone bleu" (Song et al., 2023 ; Fig. 1.16). Les marais tidaux jouent donc un rôle majeur dans le cycle global du carbone permettant une séquestration de carbone bleu dans les sédiments (Mcleod et al., 2011) et de matière organique dissoute dans l'océan concernant les parties les plus réfractaires (Shen et al., 2018). Cependant, la forte hétérogénéité spatio-temporelle de ces flux horizontaux et verticaux de carbone dans les marais salés nécessite des mesures intégratives en continu des échanges nets de CO_2 atmosphérique à l'échelle de l'écosystème (NEE) simultanément avec des mesures de carbone inorganique (pCO_2, DIC) et organique (DOC, POC) pour mieux comprendre la contribution respective métabolisme benthique et aquatique sur les échanges de CO_2 atmosphérique.

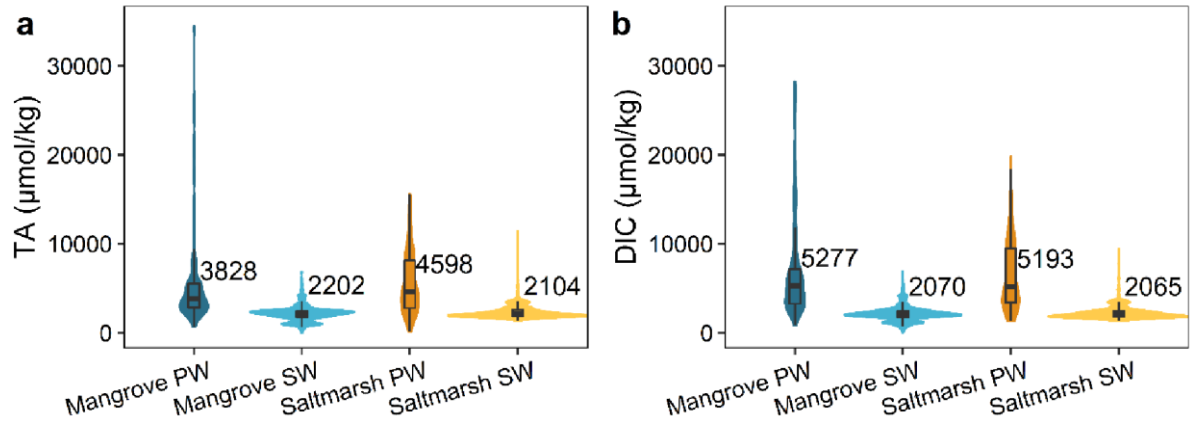

Figure 1.17 : Concentrations en alcalinité totale (TA, **a**) et en carbone inorganique dissous (DIC, **b**) dans les eaux porales (PW) et les eaux de surfaces (SW) au sein des marais salés et les mangroves. Les chiffres indiquent les médianes. Les diagrammes en boîte indiquent la médiane (ligne centrale), les 25e et 75e percentiles (boîte) et les 5e et 95e percentiles (moustaches) (Reithmaier et al., 2023).

3.4. Relations entre métabolisme et échanges de CO_2 atmosphérique dans les marais tidaux

Situés à l'interface entre le domaine terrestre et le domaine océanique, les marais tidaux sont soumis au rythme semi-diurne de la marée permettant une immersion variable en durée et en fréquence par les eaux côtières selon les cycles de marée (marées de mortes-eaux ou de vives-eaux). Lors des périodes de marée haute, les eaux côtières advectées peuvent remplir complètement les chenaux adjacents et immerger les marais tidaux avec des hauteurs d'eau variables selon les coefficients de marée et les conditions météorologiques (pression atmosphérique, direction et vitesse du vent ; Fig. 1.18). Au contraire, lors des périodes de marée basse, la végétation terrestre des marais à l'interface benthique est émergée dans l'atmosphère et l'eau est restreinte au fond des chenaux (Fig. 1.18). Ainsi, le temps de résidences des eaux côtières au sein des marais tidaux est relativement court variant de quelques minutes pendant les marées de mortes-eaux à quelques heures pendant les marées de vives-eaux. Contrairement aux écosystèmes terrestres où une relation directe existe entre le métabolisme (NEP) et les échanges nets de CO_2 atmosphérique (NEE) (Kowalski et al., 2003 ; Chapin et al., 2006), l'immersion tidale des marais salés rend cette relation complexe et indirecte (Gattuso et al., 1998 ; Borges et al., 2006).

Lors de l'émersion des marais (marée basse), la NEE se produit principalement à l'interface sédiment-atmosphère impliquant une forte contribution de la NEP benthique (plantes, sédiments) sur les échanges de CO_2 atmosphérique (Fig. 1.18-A). En effet, la végétation terrestre des marais salés peut assurer une forte production primaire pendant la journée favorisant une captation de CO_2 atmosphérique (Kathilankal et al., 2008 ; Schäfer et al., 2014 ; Forbrich et al., 2015). De plus, le MPB, composé d'un assemblage de microalgues benthiques (diatomées, cyanobactéries, euglènophytes, chlorophytes) et présent dans les sédiments vaseux, peut migrer vers la surface lors des périodes d'émersion de jour pour capter la lumière nécessaire à la photosynthèse (Consalvey et al., 2011) et ainsi contribuer à la NEP benthique (Hubas et al., 2006 ; Migné et al., 2007). Au sein de la lagune d'Arcachon, Polsenaere et al. (2012) ont montré un fort contrôle d'une vasière non végétalisée sur la NEP benthique indiquant une activité biologique importante du MPB. Aussi, lors de l'émersion des marais, la surface d'échange entre l'eau et l'atmosphère est restreinte au niveau des chenaux réduisant probablement la contribution de la NEP planctonique sur la NEE (Fig. 1.18-A) ; cependant, des mesures simultanées du métabolisme aquatique et de la NEE lors de ces périodes d'émersion sont nécessaire afin de lever cette incertitude.

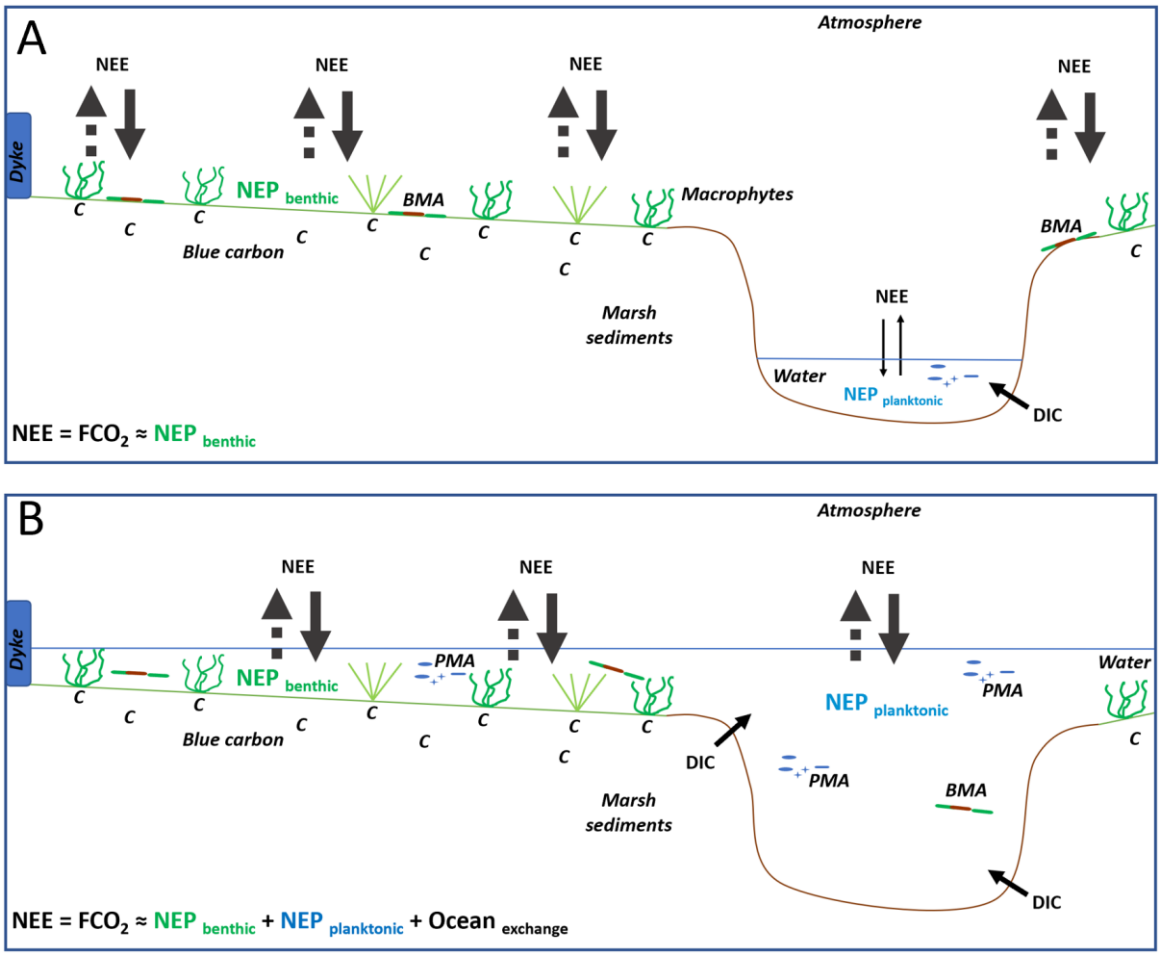

Figure 1.18 : Relation entre la NEE, la NEP et les échanges horizontaux de carbone au sein d'un système de marais salé tidal. **A.** marais émergé. NEE majoritairement à l'interface sédiment-atmosphère (NEP benthique). **B**. marais immergé, NEE à l'interface eau-atmosphère (NEP totale = NEP benthique + NEP planctonique) mais avec une influence des eaux côtières prédominante. BMA : microalgues benthiques. PMA : microalgues pélagiques (modifié d'après Polsenaere, 2011).

Lors de l'immersion des marais (marée haute), les eaux côtières advectées forment une barrière physique entre le compartiment benthique et l'atmosphère pouvant fortement influencer la NEE à l'échelle de l'écosystème (Fig. 1.18-B). Ainsi, la NEE se produit principalement à l'interface eau-atmosphère impliquant une contribution simultanée de la NEP benthique, de la NEP planctonique et des échanges horizontaux de carbone par l'advection tidale (Polsenaere et al., 2012). La photosynthèse des producteurs primaires (phytoplancton, algues et macrophytes) pendant l'immersion des marais salés peut encore fortement contribuer sur les flux atmosphériques en réduisant significativement les émissions de CO_2 provenant des eaux côtières hétérotrophes (Song et al., 2023). En milieux intertidales, Ouisse et al. (2011) ont montré que les taux de production primaire brute de deux herbiers

marins (*Zostera marina* et *Zostera noltii*) étaient 3 à 5 fois plus élevés pendant immersion que pendant l'émersion en partie liée à l'ombre des feuilles à l'émersion qui limite la photosynthèse. La faible immersion des systèmes intertidaux comme les marais salés peut favoriser un fort métabolisme planctonique au travers d'une pénétration significative de la lumière dans la colonne d'eau (Gazeau et al., 2004) et aussi un fort couplage eau-sédiment (Wang et Cai, 2004 ; Wang et al., 2016). En effet, de fortes libérations de DIC provenant de la minéralisation de la matière organique dans les sédiments (Fig. 1.17) induisent des augmentations la pCO_2 de l'eau (Wang et al., 2018 ; Song et al., 2023) pouvant augmenter la NEE en retour (Fig. 1.18-B). De plus, la matière organique produite lors de l'émersion peut être transférée à la colonne d'eau et alimentée la NEP planctonique. Par exemple, sur la vasière intertidale de Brouage (Charente Maritime), 43% de la production primaire microphytobenthique annuelle a été remis en suspension dans la colonne d'eau par l'immersion (60,8 g C m^{-2} an^{-1}) influençant le cycle du carbone des eaux côtières (Savelli et al., 2019). Ces producteurs à croissance rapide et à forte teneur en carbone organique labile (Brouwer et Stal, 2001 ; Morelle et al., 2022) peuvent être rapidement dégradés localement par reminéralisation et contribuer à des augmentations des pCO_2 de l'eau.

4. Approches méthodologiques aux mesures des pCO_2 et des flux de CO_2 atmosphérique

4.1. Mesures des pCO_2 de l'eau et estimation des flux de CO_2 eau-air

La forte hétérogénéité des processus biogéochimiques du carbone dans les écosystèmes côtiers végétalisées comme les marais littoraux aux différentes échelles spatio-temporelles nécessite davantage de mesures intégratives concernant les échanges de CO_2 aux interfaces d'échanges terrestre – aquatique – atmosphère afin de mieux comprendre leur fonctionnement écologique face aux changements globaux. La mesure de la pression partielle de CO_2 de l'eau (pCO_2 en ppmv, partie par million en volume, i.e. 1 m^3 de CO_2 pour 1 million de m^3 d'eau) est un indicateur simple pour étudier les processus biogéochimiques du carbone et le statut métabolique du compartiment aquatique (puits ou source de CO_2 atmosphérique). La mesure des pCO_2 de l'eau de surface peut être réalisée à partir (1) de la technique de l'équilibrateur (Frankignoulle et al., 2003 ; Polsenaere et al., 2022), (2) des constantes d'équilibre du système des carbonates et des mesures de température, de pH et de concentrations en DIC (Cai et Wang, 1998) et (3) de sondes *in situ* aquatiques, autonomes et hautes fréquences (Berg et al., 2019 ; Song et al., 2023). Certaines études dans les zones humides côtières telles que les

mangroves, les herbiers et les marais salés ont réalisé des mesures de pCO_2 de l'eau sur 24 heures permettant d'étudier la dynamique du CO_2 en relation avec d'autres processus biotiques et abiotiques. Par exemple, Borges et al. (2003) a montré que les pCO_2 de l'eau dans une mangrove intertidal (Gaderu, Inde) ont varié entre 1380 et 4770 ppmv en été (juin) avec un fort contrôle de ces fluctuations par la marée (hauteur d'eau) et l'activité biologique (production primaire et respiration). Au sein d'une lagune côtière tempérée (Arcachon, France), constituée à 67% d'herbiers de Zostère (*Zostera noltei*), les effets biologiques induisant une hétérotrophie de l'eau en hiver et une autotrophie de l'eau en été ont été combinés avec les effets thermiques (température) résultant d'une faible variation des pCO_2 à l'échelle saisonnière (entre 405 et 601 ppmv ; Polsenaere et al., 2022). Dans un marais salé tempéré en milieu estuarien (île de Sapelo, États-Unis), les pCO_2 de l'eau ont montré de plus fortes variations saisonnières et tidales avec des valeurs variant de 500 à 4000 ppmv entre la marée haute et la marée basse en hiver (février) et de 1600 à 12000 ppmv entre la marée haute et la marée basse en été (août) (Wang et al., 2018). Ces fortes sursaturations en CO_2 de l'eau des marais par rapport à l'atmosphère, en particulier sur les périodes de marée basse, ont été favorisées par un métabolisme hétérotrophe intense produisant de grandes quantités de DIC dans les chenaux (Wang et Cai, 2004 ; Wang et al., 2018). Cependant, encore trop peu d'études ont effectué des mesures à haute fréquence des pCO_2 de l'eau dans les marais pour mieux prendre en compte toutes les variabilités temporelles (diurne, tidal, saisonnière, annuelle) et spatiales (marais salés ou doux, marais tidaux ou non-tidaux) de ces écosystèmes littoraux, et *in fine*, les intégrer dans les budgets régionaux et globaux de carbone.

Les variations temporelles des pCO_2 de l'eau affectent fortement les flux verticaux de CO_2 qui peuvent être estimés entre le compartiment aquatique et l'atmosphère (Cotovicz et al., 2015 ; Burgos et al., 2018 ; Polsenaere et al., 2022). Dans les marais salés, Song et al. (2023) a mis en évidence l'importance de réaliser des mesures de pCO_2 de l'eau à haute fréquence sur toutes les échelles de temps (diurne, tidal, saisonnier) afin de réduite les incertitudes dans l'estimation des flux de CO_2 atmosphérique (Eq. 9).

$$FCO_2 = \alpha\, k\, (pCO_{2eau} - pCO_{2air}) \quad (9)$$

Où FCO_2 (mmol CO_2 m^{-2} h^{-1}) est le flux de CO_2 à l'interface eau-air, α (mol kg^{-1} atm^{-1}) est le coefficient de solubilité du CO_2 dans l'eau dépendant des conditions de température et de salinité (Weiss, 1974), k (cm h^{-1}) est le coefficient d'échange ou la vitesse de transfert du CO_2 à l'interface eau-air (Raymond et Cole, 2001 ; Abril et al., 2009 ; Wanninkhof et al., 2022), pCO_{2eau} et pCO_{2air} (ppm) sont les pressions partielles dans l'eau et l'air, respectivement. Les

paramétrisations du coefficient d'échange *k* selon Raymond et Cole (2001) et Abril et al. (2009) sont spécifiques aux eaux estuariennes plutôt confinées tandis que la paramétrisation selon Wanninkhof et al. (2022) est spécifique aux eaux océaniques ouvertes. L'équation de Raymond and Cole (2001) est basée sur la compilation des vitesses de transfert de gaz dérivées de traceurs appliqués à des rivières et des estuaires en utilisant uniquement la vitesse du vent comme variable. L'équation d'Abril et al. (2009) est basée sur 159 mesures en simultanées de flux CO_2 par chambres flottantes et de pCO_2 de l'eau dans l'estuaire macrotidal de la Gironde (France) et utilise la vitesse du vent, la surface de l'estuaire, la vitesse du courant d'eau et la concentration du matériel en suspension comme variables. L'estimation du coefficient d'échange *k* avec ces méthodes peut ajouter de grandes incertitudes dans les calculs de flux de CO_2 à l'interface eau-air (Frankignoulle et al., 1998 ; Wanninkhof et Mcgillis, 1999 ; Upstill-Goddard, 2006). Actuellement, il n'y a pas de consensus clair sur la paramétrisation du coefficient d'échange *k* dans les systèmes côtiers comme les marais littoraux et les estuaires (Borges et al., 2004 ; Ho et al., 2018). Cependant, une paramétrisation précise du coefficient d'échange *k* est possible dans des écosystèmes côtiers peu profonds à partir de mesures directes et simultanées de flux de CO_2 atmosphérique par Eddy Covariance et de pCO_2 de l'eau (Polsenaere et al., 2013 ; Van Dam et al., 2019). Une étude réalisée dans un estuaire microtidal (USA) a montré que la relation entre la vitesse de transfert de gaz et la vitesse du vent pendant la journée était différente de celle de la nuit, probablement en raison de la différence de convection thermique à la surface de l'eau entre la nuit et le jour (Van Dam et al., 2019).

La méthode d'estimation des flux de CO_2 atmosphérique, à partir des mesures in situ de pCO_2 de l'eau (Eq. 9), a été utilisée au sein de ce travail de thèse et décrite précisément au sein du chapitre II (Mayen et al., 2023).

4.2. Eddy Covariance atmosphérique

Des mesures en continu des flux verticaux de CO_2 atmosphérique à l'échelle de l'écosystème peuvent être réalisées par la technique de l'Eddy Covariance (EC) atmosphérique, basée sur le principe de covariance entre les fluctuations turbulentes de la vitesse verticale du vent et celles de la concentration de CO_2 de l'air (Baldocchi et al., 1988 ; Aubinet et al., 2012 ; Baldocchi, 2003 ; Burba, 2021). L'atmosphère est caractérisée par des

flux d'air horizontaux formés par de nombreux tourbillons rotatifs de tailles et de fréquences différentes causés par la flottabilité et le cisaillement de l'air ascendant et descendant (Fig. 1.19-A) permettant le transport du CO_2 atmosphérique (Burba, 2021). Chaque tourbillon présente ses propres composantes tridimensionnelles incluant le mouvement vertical du vent et chaque parcelle d'air transportée par les tourbillons possède ses propres caractéristiques micrométéorologiques (concentration en gaz, température, humidité, etc.). Par exemple, à un moment donné (temps 1), le tourbillon numéro 1 descendant déplace la parcelle d'air C_1 vers le bas à la vitesse W_1. Au moment suivant (temps 2), au même point, le tourbillon numéro 2 ascendant déplace la parcelle d'air C_2 vers le haut à la vitesse W_2 (Fig. 1.19-B). La technique EC peut être utilisée pour mesurer les caractéristiques micrométéorologiques et la vitesse verticale de ces tourbillons turbulents pour quantifier les flux nets de CO_2 à l'interface entre l'écosystème et l'atmosphère (Burba, 2021).

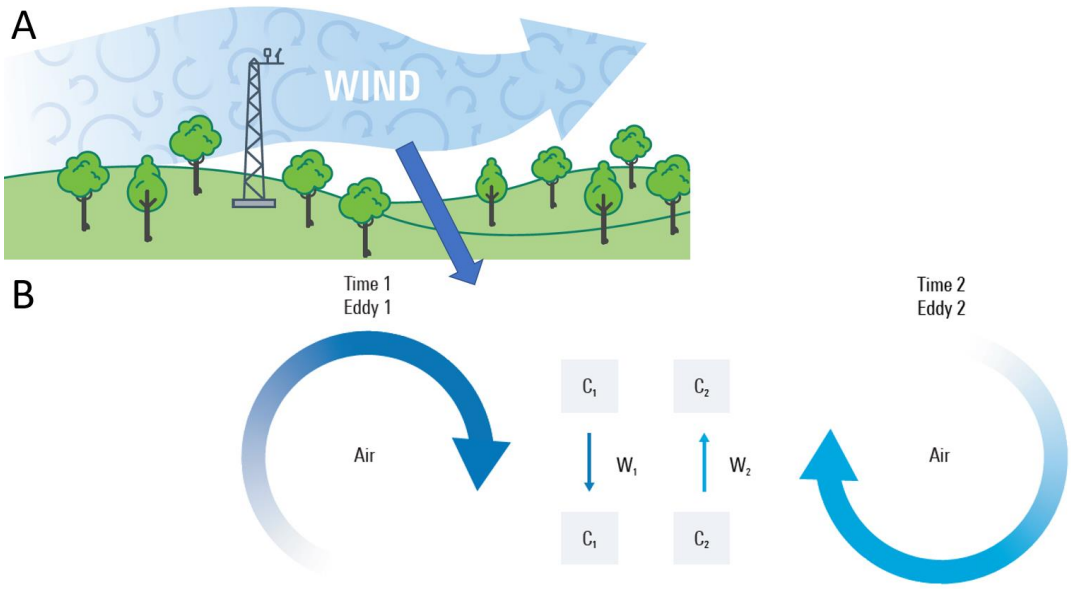

Figure 1.19 : (A) Flux d'air horizontal composé de nombreux tourbillons rotatifs. **(B)** Composante verticale de deux tourbillons turbulents au même point mais à deux temps différents. C_1 : concentration de CO_2 atmosphérique transporté par le tourbillon 1 (eddy 1) lors du temps 1 (time 1) à une vitesse W_1 ; C_2 : concentration de CO_2 atmosphérique transporté par le tourbillon 2 (eddy 2) lors du temps 2 (time 2) à une vitesse W_2. Le tourbillon 1 est descendant (captation de CO_2 atmosphérique par l'écosystème) et le tourbillon 2 est ascendant (émission de CO_2 atmosphérique par l'écosystème) (Burba, 2021).

Le flux vertical moyen d'un gaz comme le CO_2 (F, µmol m^{-2} s^{-1}) peut être exprimé comme le produit de la densité de l'air moyenne (ρ, Kg m^{-3}) et de la covariance moyenne entre les fluctuations turbulentes instantanées de la vitesse verticale du vent (w', m s^{-1}) et de la fraction molaire sèche (s') du gaz selon l'équation 10 :

$$F = \overline{\rho\, w\, s} \approx \bar{p}\ \overline{w's'} \qquad (10)$$

La barre supérieure représente la moyenne temporelle du paramètre et l'apostrophe indique les fluctuations turbulentes instantanées de ces paramètres par rapport à leur moyenne temporelle (Reynolds, 1883). La décomposition de Reynold a été utilisée pour décomposer le terme instantané en sa moyenne et son écart (e.g. w = $\bar{w}$ + w') (Reynolds, 1883 ; Burba, 2021). De plus, cette équation est obtenue en supposant, sur une surface plane et homogène, que (1) la variation de la densité de l'air est négligeable, (2) qu'il n'y a pas de divergence ou de convergence des mouvements verticaux de l'air à grande échelle et (3) que les conditions atmosphériques sont stables et stationnaires (Aubinet et al., 2012). Un flux négatif de CO_2 atmosphérique est dirigé vers l'écosystème et est donc caractérisé comme un puits, et inversement pour les flux positifs qualifiés de sources de CO_2 vers l'atmosphère.

Cette technique micrométéorologique directe et non invasive présente un intérêt croissant dans les systèmes intertidaux hétérogènes et variables comme les marais salés pour évaluer les échanges nets de CO_2 à l'échelle de l'écosystème (NEE, µmol m^{-2} s^{-1}) (Schäfer et al., 2014 ; Artigas et al., 2015 ; Forbrich et Giblin, 2015 ; Forbrich et al., 2018). L'avantage majeur de l'EC est de mesurer les flux de CO_2 provenant de tous les habitats au sein de l'empreinte (footprint) de manière intégrative sur des échelles de temps allant de quelques heures à plusieurs années, à la fois à l'interface sédiment/air à marée basse et à l'interface eau/air à marée haute (Kathilankal et al., 2008 ; Polsenaere et al., 2012). Cependant, l'utilisation de la méthode EC nécessite d'importants traitements qualitatifs et quantitatifs et une correction de données en raison de son contexte physique et théorique (Baldocchi et al., 1988 ; Burba, 2021).

Cette méthode de mesure des échanges nets de CO_2 à l'échelle de l'écosystème (NEE) par Eddy Covariance atmosphérique (Eq. 10) a été utilisée au sein de ce travail de thèse et décrite précisément au sein du chapitre III (Mayen et al., 2024).

La technique EC a confirmé les estimations du puits de CO_2 atmosphérique dans les marais salés (Wang et al., 2016 ; Alongi, 2020 ; Song et al., 2023) mais a également révélé de fortes hétérogénéités dans les flux de NEE en fonction des conditions climatiques et des influences anthropiques (Herbst et al., 2013 ; Schäfer et al., 2019). Par exemple, la NEE mesurée dans un marais salé peu anthropisé (USA) a montré une captation nette de CO_2 atmosphérique avec une variation interannuelle dans les bilans de carbone liée aux précipitations lors de la saison de croissance des plantes des marais (Forbrich et al., 2018). En comparaison, dans un marais intertidal urbain (USA), Schäfer et al. (2014) ont montré une plus grande variabilité interannuelle en raison des pratiques de gestion et des espèces végétales majoritaires. Cependant, les bilans nets de carbone mesurés avec la technique de l'EC sont encore trop rares pour prendre en compte toutes les variabilités annuelles et spatiales des marais salés. De plus, les marais salés représentent une zone d'interface biogéochimiquement active au sein de la zone côtière mais ils sont également menacés par l'élévation du niveau de la mer, l'érosion et le réchauffement climatique (Gu et al., 2018), ce qui pourrait altérer de manière significative leur capacité à absorber et à stocker le carbone (Campbell et al., 2022). Ainsi, les échanges de CO_2 atmosphérique doivent être mesurés avec précision et mieux compris, en particulier l'influence des facteurs de contrôle biotiques et abiotiques, afin d'être inclus dans les bilans régionaux et mondiaux de carbone (Borges et al., 2005 ; Cai, 2011) et de prédire les futurs puits de carbone dans le contexte du changement climatique.

5. Présentation des sites d'études

Dans le cadre de cette thèse, l'étude de la dynamique du carbone et des échanges de CO_2 atmosphérique dans les marais Charentais a été réalisée au sein de trois zones d'études choisies selon leur typologie et leur mode de gestion associés : (1) les marais du Fier d'Ars (île de Ré), (2) les marais de Brouage (sud de l'estuaire de la Charente) et (3) les marais de Tasdon (La Rochelle ; Fig. 1.20).

Au sein de l'océan Atlantique, le Fier d'Ars représente une zone maritime Françaises de 750 ha au nord de l'île de Ré qui communique avec les eaux côtières du Pertuis Breton (plateau continental) par une ouverture de 700 m de large (Fig. 1.20). Il correspond à un estuaire tidal tempéré de type II selon la typologie des systèmes côtiers de Dürr et al. (2011). Avec une hauteur d'eau maximal de 6,5 m, cet estuaire tidal échange entre 2,4 et 10,2 millions

de m^3 d'eaux côtières avec le plateau continental adjacent en fonction des coefficients de marée (Bel Hassen 2001). À marée basse, sa zone intertidale est composée de vasières (slikke) et de marais tidaux végétalisés (schorre) traversés par de nombreux chenaux de différentes tailles (Fig. 1.21). À marée haute, la zone intertidale est inondée par les eaux côtières jusqu'aux digues (Fig. 1.21), gérées pour contrôler les échanges d'eau entre l'estuaire et les marais salés artificiels (marais rétro-littoraux en amont de la digue). Ces marais endigués sont en partie utilisés pour des activités de saliculture, de pisciculture et d'ostréiculture avec différents modes de gestion de l'eau selon leurs usages (Bel Hassen, 2000 ; Paticat, 2007). Depuis 1981, une partie de ces marais salés (1200 ha) est protégée au sein de la Réserve Naturelle Nationale (RNN) de Lilleau des Niges (Figs. 1.20 et 1.21) abritant une grande biodiversité d'oiseaux migrateurs et de végétaux terrestres et aquatiques (Champion et al., 2012).

Figure 1.20 : Localisation des réserves naturelles nationales (RNN) en Charente Maritime (France). Un premier site d'étude concerne les marais salés du Fier d'Ars au sein de la réserve de Lilleau des Niges (Ile de Ré), un deuxième site d'étude concerne les marais de Brouage au sein de la réserve de Moëze-Oléron et un troisième site d'étude concernant les marais périurbains de Tasdon (La Rochelle). Modifié de LPO.

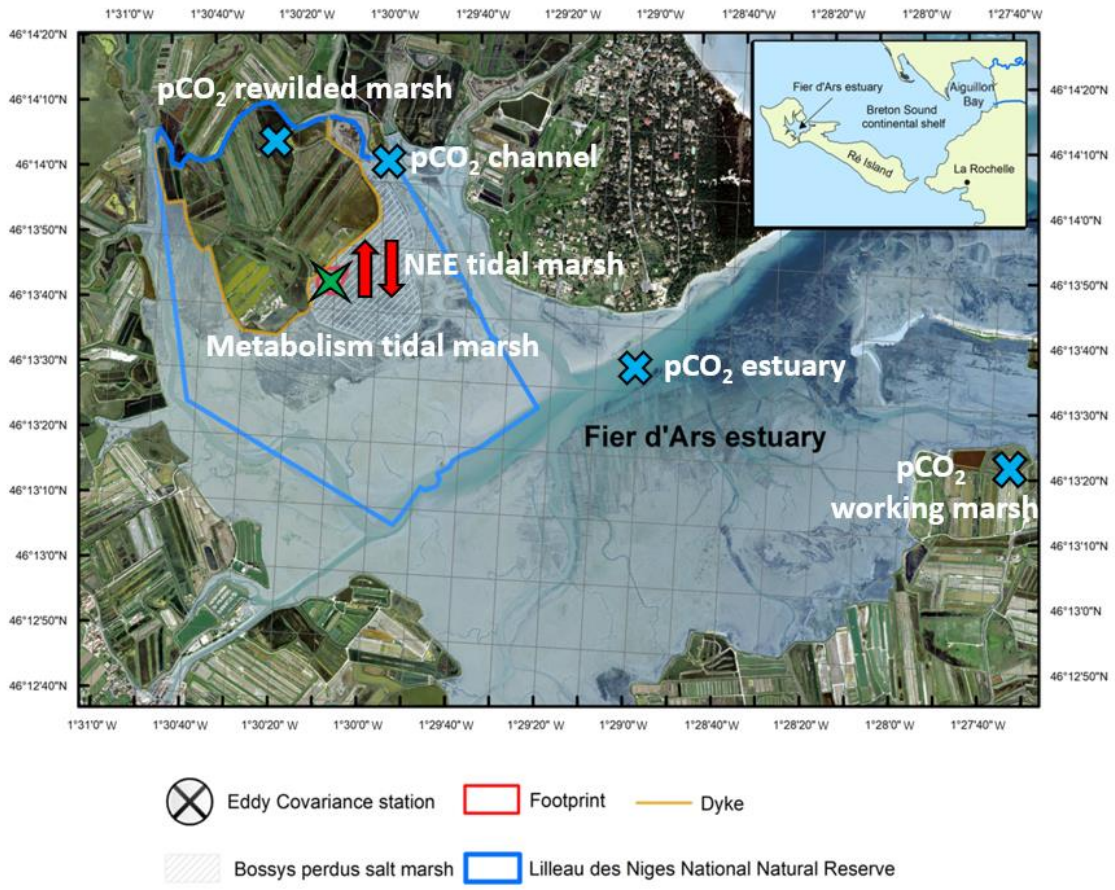

Figure 1.21 : L'estuaire tidal du Fier d'Ars (Ile de Ré) et localisation des points de mesures et d'échantillonnage au sein des marais tidaux (en aval de la digue), des marais rétro-littoraux (en amont de la digue) et des chenaux. La zone bleue correspond à la zone intertidale de l'estuaire et la ligne orange correspond à la digue permettant de délimiter les zones terrestres et maritimes. Les croix bleues (partie A ; voir 6.1.) correspondent aux mesures *in situ* des pCO_2 de l'eau sur des cycles de 24 heures au sein de deux continuums aquatiques estuaire – chenal – marais. Les flèches verticales rouges (partie B ; voir 6.1.) correspondent aux mesures des échanges nets de CO_2 atmosphérique (NEE) sur une année entière au sein du marais tidal des Bossys perdus. L'étoile verte (partie C ; voir 6.1.) correspond aux cycles de 24 heures d'échantillonnages de la colonne d'eau pour l'étude du métabolisme aquatique du marais tidal en lien avec les mesures de flux de NEE. Figure modifiée de Mayen et al. (2023).

Au sein de la partie maritime de la RNN de Lilleau des Niges (en aval de la digue), le marais tidal des Bossys perdus a été suivi pour étudier les échanges de CO_2 atmosphérique (Fig. 1.21). C'est un pré-salé formé d'habitats caractéristiques du schorre avec des plantes terrestres (spartines, obiones, soudes, salicornes) et des zones de vases nues (microphytobenthos). L'ensemble étant traversé par un réseau de petits chenaux et immergé par les eaux côtières du Fier d'Ars et du Pertuis Breton de façon différentielle dans le temps et l'espace suivant les coefficients de marée. À marée basse, le pré-salé et la végétation terrestre associée sont émergés dans l'atmosphère ; au cours de cette période, le chenal principal des Bossys perdus permet de drainer les eaux des marais endigués vers l'estuaire en aval. À marée montante et haute, les eaux côtières advectées par la marée remplissent progressivement le chenal et, à partir d'un coefficient de marée supérieur à 50, peuvent inonder le pré-salé avec des hauteurs d'eau variables. Une hauteur maximale de 2 m peut immerger l'ensemble de la végétation terrestre pendant deux heures à haute mer par forts coefficients de marée. Ainsi, le choix du marais tidal des Bossys perdus est parfaitement justifié par les connaissances acquises sur la dynamique temporelle des pCO_2 et paramètres biogéochimiques associés dans les masses d'eau adjacentes sur le continuum Pertuis Breton – estuaire du Fier d'Ars – marais salé (Fig. 1.21).

L'estuaire tidal du Fier d'Ars et ses marais salés associés (île de Ré) sont également détaillés dans la section Matériels et Méthodes des chapitres II, III et IV au sein de ce manuscrit. Les photos des marais salés rétro-littoraux sont présentées dans les annexes du chapitre II (Mayen et al., 2023) tandis que les photos du marais tidal des Bossys perdus sont présentées dans les annexes du chapitre III (Mayen et al., 2024).

Sur la côte Atlantique de Charente Maritime, le marais de Brouage correspond à une zone basse poldérisée associée à un endiguement important depuis plusieurs siècles pour protéger l'ensemble des terres et des marais conquis sur la mer pour les activités anthropiques (élevage et saliculture ; Fig. 1.20). Cependant, les digues construites par l'Homme ont été fortement endommagées par les aléas climatiques récurrents tels que les tempêtes Martin (1999), Xynthia (2010) et Ciarán (2023) entraînant des submersions marines des marais. Plusieurs scénarios sont envisagés pour le devenir de cette zone humide protégée par le conservatoire du littoral : poursuivre la lutte contre les assauts de la mer en reconstruisant les digues à chaque fois qu'elles sont détruites par les tempêtes ou envisager l'acceptation d'un

recul du trait de côte et modifier les pratiques agricoles pour favoriser celles qui s'acclimatent le mieux aux élévations ponctuelles du niveau de la mer. Dans le cadre de cette thèse, nous avons étudiés deux marais rétro-littoraux au sein de la RNN de Moëze-Oléron, initialement utilisés pour la saliculture mais aujourd'hui gérés afin de conserver et protéger l'identité patrimoniale des marais (Fig. 1.20). La station MAD est un marais saumâtre (surface de 17 640 m^2, profondeur de 25 cm) avec une végétation aquatique peu développée. Ce marais a été éloigné de la mer, il est désormais connecté au canal de Brouage permettant d'être alimenté en eaux douces provenant du bassin versant agricole (influencées par le fleuve Charente). La station MAS est un marais salé (surface de 81 552 m^2, profondeur de 65 cm), situé juste derrière la digue et alimenté périodiquement en eaux salées au travers d'une écluse à la mer. Cette station MAS abrite de la végétation aquatique associée à une densité important d'herbiers.

Le marais de Tasdon est un marais périurbain (124 ha) localisé à proximité de la ville de La Rochelle et alimenté en eaux douces par la Moulinette (Fig. 1.22). Depuis le Moyen Age et jusqu'en 1935, le marais de Tasdon a été relié aux Pertuis Charentais, il a ainsi été utilisé pour les activités de saliculture pendant plusieurs siècles. Néanmoins, l'urbanisation a bouleversé l'équilibre naturel du marais de Tasdon en l'éloignant du rivage océanique, le site est ainsi devenu progressivement un marais d'eau douce. Depuis 2020, le marais de Tasdon a subi un projet important de renaturation permettant un réaménagement des bassins, l'implantation de végétation terrestre et aquatique mais aussi une reconnexion progressive de certains bassins à l'océan afin de préserver la biodiversité et de restaurer les fonctions écologiques du site. Ainsi, trois stations contrastées ont été étudiées au sein du marais de Tasdon (Fig. 1.22). La station T2 est un lac d'eau douce (profondeur maximale de 1,3 m) où les travaux de restauration ont permis l'implantation de végétation pour aider à maintenir la structure des rives. La station T6 était un étang d'eau douce stagnant (profondeur maximale de 0,8 m) mais les travaux ont permis un remodelage du paysage et une rectification du cours d'eau (La Moulinette ; Fig. 1.22). La station T7 était également un étang d'eau douce stagnant (profondeur maximale de 1,0 m) qui est maintenant reconnecté aux eaux côtières par une vanne qui laisse circuler l'eau salée selon les marées. Depuis le premier printemps 2021, cette station reçoit de l'eau salée toutes les deux semaines : la vanne reste ouverte 2-3 jours en fonction du niveau d'eau initial du marais afin d'éviter tout débordement. Pendant les saisons de fortes pluies (du milieu de l'automne à la fin de l'hiver), il n'y a pas d'apport d'eau salée.

Figure 1.22 : Localisation du marais urbanisé de Tasdon (agglomération de La Rochelle) et des différentes stations étudiées (T2, T6 et T7) après les travaux de renaturation. Carte issue de la Ville de La Rochelle.

6. Objectifs et organisation de la thèse

6.1. Les objectifs scientifiques de la thèse et travail de terrain

Dans le cadre des projets de l'ANR-PAMPAS (2019-2023) et de LEFE-DYCIDEMAIN (2021-2022), ce travail de recherche en écologie et biogéochimie côtière porte principalement sur les facteurs biotiques et abiotiques contrôlant les flux de carbone au sein des différentes interface d'échanges des marais littoraux qui sont ces écosystèmes côtiers dynamiques et hétérogènes. Le projet PAMPAS est un projet de recherche collaborative qui vise à comprendre le fonctionnement des zones humides côtières face à l'aléa submersion marine afin de questionner l'évolution de leur identité patrimoniale en fonction de leur mode de gestion. Ce projet interdisciplinaire a permis de répondre aux enjeux sociétaux actuels d'adaptation au changement climatique et de transmission, appliqué à une échelle locale, mais transposable à l'échelle plus large des zones humides littorales. Le projet DYCIDEMAIN a permis d'étudier la dynamique du carbone organique et inorganique aux interfaces d'échange des marais tidaux tempérés et aux différentes échelles temporelles.

L'objectif général de la thèse est de comprendre les processus biologiques, physiques et chimiques contrôlant les flux de carbone aux interfaces terrestre-aquatique-atmosphérique des marais Charentais, au travers de mesures *in situ* et d'échantillonnages dans la colonne d'eau aux différentes échelles spatiales et temporelles caractéristiques de ces environnements côtiers. Pour cela, plusieurs problématiques ont été abordées :

- Comment la typologie et le mode de gestion anthropique des marais littoraux influencent la dynamique des pCO_2 de l'eau et la fonction puits de CO_2 atmosphérique ?
- Quelles sont les variations temporelles (diurne, tidale et saisonnière) des échanges nets de CO_2 atmosphérique à l'échelle d'un marais tidal selon les conditions environnementales et l'immersion tidale ?
- Comment le métabolisme aquatique des marais littoraux influence les processus et les flux de carbone (flux verticaux et horizontaux) ?

Afin de répondre aux problématiques ci-dessus liées au cycle du carbone dans les marais, un important travail de mesures biogéochimiques et de prélèvements d'eau a eu lieu dans les marais du Fier d'Ars, les marais de Brouage et les marais de Tasdon :

Dans une première partie (partie A), des mesures *in situ* à hautes fréquences des pCO_2 de l'eau et des estimations de flux de CO_2 eau-air ont été réalisées sur plusieurs cycles de 24 heures entre 2018 et 2020 au sein de deux continuums aquatiques entre l'estuaire tidal du Fier d'Ars et les marais rétro-littoraux (croix bleues ; Fig. 1.21). Aussi, entre 2019 et 2021, nous avons déployé la même stratégie de mesure au marais de Tasdon (Fig. 1.22) afin de comprendre le fonctionnement biogéochimique du CO_2 au sein cette zone humide périurbaine et *in fine,* son rôle dans les cycles régionaux et globaux du C après les travaux de renaturation du marais et de reconnexion de certaines stations à la mer. Cette première partie de thèse fait suite à mes travaux de stages de Master 1 (2019) et Master 2 (2020) et s'inscrit dans le projet de l'ANR-PAMPAS.

Dans une deuxième partie (partie B), un système d'Eddy Covariance atmosphérique a été déployé au sein du marais tidal des Bossys perdus (île de Ré) pour mesurer en continu et à hautes fréquences les échanges nets de CO_2 atmosphérique de l'écosystème (NEE) de juin 2019 à décembre 2022 (flèches rouges ; Fig. 1.21). Cette deuxième partie de thèse est associée aux travaux de stages de Master 2 de Pierre Kostyrka (2021) et Maxime Coutantin (2023) et s'inscrit dans le projet de l'ANR-PAMPAS.

Dans une troisième partie (partie C), des cycles de 24 heures de mesures *in situ* et d'échantillonnages de la colonne d'eau ont été réalisés au sein du marais tidal des Bossys perdus (île de Ré) et du marais saumâtre MAD (Brouage) à chaque saison de l'année 2021 (étoile verte ; Fig. 1.21). Ainsi, nous avons mesuré simultanément les pCO_2 de l'eau ainsi que (i) les autres formes biogéochimiques du carbone (carbone inorganique dissous, carbone organique dissous et particulaire, alcalinité totale) et (ii) les paramètres écologiques associés (nutriments, matière organique particulaire, chlorophylle-*a*). Des échantillonnages ont également permis d'étudier la balance métabolique des communautés planctoniques. Au marais des Bossys perdus, ces différentes mesures ont permis de suivre la dynamique tidale, diurne et saisonnière des paramètres biogéochimiques (carbone, nutriments) en subsurface en lien avec les mesures de NEE par Eddy Covariance. De plus, un suivi annuel avec des prélèvements mensuels a été réalisé en 2021 au marais MAD afin de repositionner nos données des cycles de 24 heures sur une année de mesures. Pour finir, l'originalité a été de réaliser des mesures *in situ* des pCO_2 de l'eau en simultané au marais saumâtre MAD et au marais salé MAS afin de les comparer d'un point de vue du carbone (Fig. 1.20). Cette troisième partie de thèse est associée aux travaux de stages de Licence 3 de Stacy Delmer (2021) et s'inscrit dans le projet LEFE-DYCIDEMAIN.

6.2. Organisation du mémoire de thèse

Ce manuscrit de thèse s'organise en quatre chapitres (II, III, IV et V), principalement centrés sur les marais salés du Fier d'Ars (île de Ré, France), permettant de répondre de manière chronologique aux problématiques en lien avec le cycle du carbone dans les marais littoraux (voir 5.1). L'ensemble des éléments concernant le matériel et méthode au sein de ces travaux de thèse sont directement présentés au sein des chapitres II, III et IV (articles publiés

ou en préparation) ; il n'y a pas de chapitre matériels et méthodes au sein de ce manuscrit de thèse.

Le chapitre II se focalise sur les variations spatiales et temporelles des pressions partielles de CO_2 (pCO_2) de l'eau et des flux de CO_2 calculés à l'interface eau-atmosphère au niveau du compartiment aquatique des marais salés rétro-littoraux qui restent peu étudiées du point de vue de la dynamique du carbone. En effet, si les parties terrestres végétalisées des marais sont généralement associées à une fonction puits de CO_2, le milieu aquatique, suivant la typologie et la gestion associée, peut être totalement différent en termes de processus physiques, chimiques et biologiques, d'échanges atmosphériques (puits ou source) et de facteurs de contrôle biotiques impliqués. Ce chapitre fait l'objet d'un article publié au journal *Regional Studies in Marine Science* (Mayen et al., 2023). Cette publication de thèse concerne les variations spatio-temporelles des pCO_2 de l'eau au sein de deux continuums aquatiques estuaire – marais rétro-littoraux et l'influence de la gestion anthropique des marais (protégé *vs.* exploité) sur les flux de CO_2 atmosphérique et les budgets de carbone associés.

Le chapitre III s'intéresse aux échanges nets de CO_2 entre un marais tidal végétalisé et l'atmosphère par des mesures en continu et à l'échelle de l'écosystème (milieux terrestres et aquatiques). Pour cela, la technique d'Eddy Covariance atmosphérique a permis d'obtenir des séries annuelles de flux de CO_2 à hautes fréquences aux interfaces sédiment-air (marée basse) et eau-air (marée haute) sur le marais tidal des Bossys perdus permettant de qualifier et quantifier son statut métabolique en fonction des paramètres environnementaux (rythme diurne, tidal, saisonnier, habitats aquatique et terrestre). Ce chapitre fait l'objet d'un article publié au journal *Biogeosciences* (Mayen et al., 2024). Les objectifs ont été de décrire les variations temporelles des flux de CO_2 mesurés au cours de l'année 2020, d'évaluer l'importance des différents facteurs biotiques et abiotiques contrôlant les échanges de CO_2 atmosphérique et de quantifier précisément les effets de l'immersion tidale sur la captation de CO_2 atmosphérique. Le rythme tidal au sein des marais tidaux entraîne de fortes incertitudes quant à la contribution précise du métabolisme benthique et du métabolisme aquatique sur la NEE lors des différentes périodes de la journée nécessitant des mesures simultanées du métabolisme planctonique et des échanges de CO_2 atmosphérique aux différentes échelles temporelles.

Le chapitre IV s'intéresse plus spécifiquement à l'influence du métabolisme aquatique des marais littoraux sur la dynamique du carbone. Ce chapitre permet d'apporter des informations dans la littérature sur l'influence des communautés planctoniques dans le cycle du carbone des marais, et plus particulièrement, sur leur statut métabolique comme source ou puits de CO_2. Ainsi, la production primaire et la respiration des communautés planctoniques ont été mesurées pour mieux comprendre leur contribution sur les variations des pCO_2 de l'eau et les flux de CO_2 atmosphérique associés. Ce chapitre intègre les données acquises au cours des cycles d'échantillonnage de 24 heures (voir 6.1.) au marais tidal des Bossys perdus à la fois à marée basse et à marée haute en simultanée avec des mesures hautes fréquences des pCO_2 de l'eau et des flux de NEE. Ce chapitre fait l'objet d'une publication en préparation pour une soumission au journal *Limnology and Oceanography* (Mayen et al., en préparation).

Le chapitre V correspond à la synthèse générale de la thèse qui vise à replacer l'ensemble de ces mesures liées au cycle du carbone dans les marais littoraux par rapport au rôle joué par ces écosystèmes côtiers au sein des budgets régionaux et globaux de carbone, en prenant en compte la variabilité spatiale, temporelle, méthodologique associées. Au sein de ce chapitre, nous discuterons également de l'influence des activités anthropiques en termes d'aménagement (endiguement), de gestion de l'eau (temps de résidence) et de pollution par les nutriments (eutrophisation) sur leur capacité de captation de CO_2 atmosphérique.

Chapitre II

Variations spatiales et temporelles des pressions partielles de CO_2 de l'eau et des flux de CO_2 estimés à l'interface eau-atmosphère des marais salés.

Marais salé rétro-littoraux (île de Ré, Fier d'Ars). © Polsenaere

Influence of typology and management practices on water pCO_2 and atmospheric CO_2 fluxes over two temperate shelf – estuary – marsh water continuums

Jérémy Mayen[1,2*], Pierre Polsenaere[1], Aurore Regaudie De Gioux[3], Christine Dupuy[4], Marie Vagner[5], Jean-Christophe Lemesle[6], Benoit Poitevin[7], Philippe Souchu[2]

*Corresponding author: jeremy.mayen@ifremer.fr

[1] IFREMER, Littoral, Laboratoire Environnement Ressources des Pertuis Charentais (LER/PC), BP 133, 17390, La Tremblade, France

[2] IFREMER, Littoral, Laboratoire Environnement Ressources Morbihan Pays de Loire (LER/MPL), BP 21105, 44311, Nantes, France

[3] IFREMER, Dyneco, Pelagos, ZI de la Pointe du Diable - CS 10070 - 29280 Plouzané, France

[4] UMR 7266 Littoral Environnement et Société (LIENSs), CNRS – La Rochelle Université, France

[5] LEMAR, UMR 6539 CNRS/Univ Brest/IRD/Ifremer, ZI pointe du diable, 29 280, Plouzané, France

[6] LPO, Réserve Naturelle de Lilleau des Niges, 17880, Les Portes en Ré, France

[7] Pôle-Nature de l'Ecomusée du Marais Salant, route de Loix, 17111, Loix en Ré, France

A research article published to Regional Studies in Marine Science (Mayen et al. 2023).

https://doi.org/10.1016/j.rsma.2023.103209

Abstract

Within the coastal zone, salt marshes often behave as atmospheric CO_2 sinks, allowing for blue carbon (C) sequestration associated with intense autotrophic metabolism. However, C dynamics over salt marshes are complex since various biogeochemical processes and fluxes occur at different terrestrial – aquatic – atmospheric exchange interfaces and spatiotemporal scales. This study focuses on seasonal, tidal and diurnal variations of water pCO_2, estimated water-air CO_2 fluxes and controlling factors along two temperate shelf – estuary – marsh continuums. The latter include typical coastal systems with artificial salt marshes that have contrasting water management practices and primary producer types. Our high-frequency biogeochemical measurements (seasonal 24-hour cycles) highlighted a strong control of ecosystem typology on inorganic C dynamics with lower water pCO_2 values in the artificial salt marshes, due to stronger biological activity and longer water residence times, than in the tidal estuary. In the marine-dominated estuary, water pCO_2 variations (267 - 569 ppmv) were strongly controlled by tidal effects and phytoplankton activity particularly in spring/summer. On the contrary, the greatest amplitudes in water pCO_2 were recorded in the artificial salt marshes (6 - 721 ppmv) due to intense macrophyte activity. In the rewilded marsh, eutrophication favoured spring/summer fast-growing macroalgae produced, in turn, strong fall atmospheric CO_2 outgassing from degraded algae waters and thus a net annual source of CO_2 to the atmosphere (17.5 g C m^{-2} yr^{-1}). Conversely, specific management practices at the working marsh for salt-farming activity favoured rather slow-growing macrophytes (i.e. seagrasses) which greatly contribute to the yearly observed atmospheric CO_2 sink (-97.7 g C m^{-2} yr^{-1}). In this work, we suggest that salt marsh management can be used to control the contribution of primary producers to marsh C budget as atmospheric CO_2 (sink and/or source).

Key words

Shelf – estuary – marsh continuums; water pCO_2; air-water CO_2 fluxes; diurnal, tidal, seasonal scales; marsh management practices; macrophytes.

Graphical Abstract

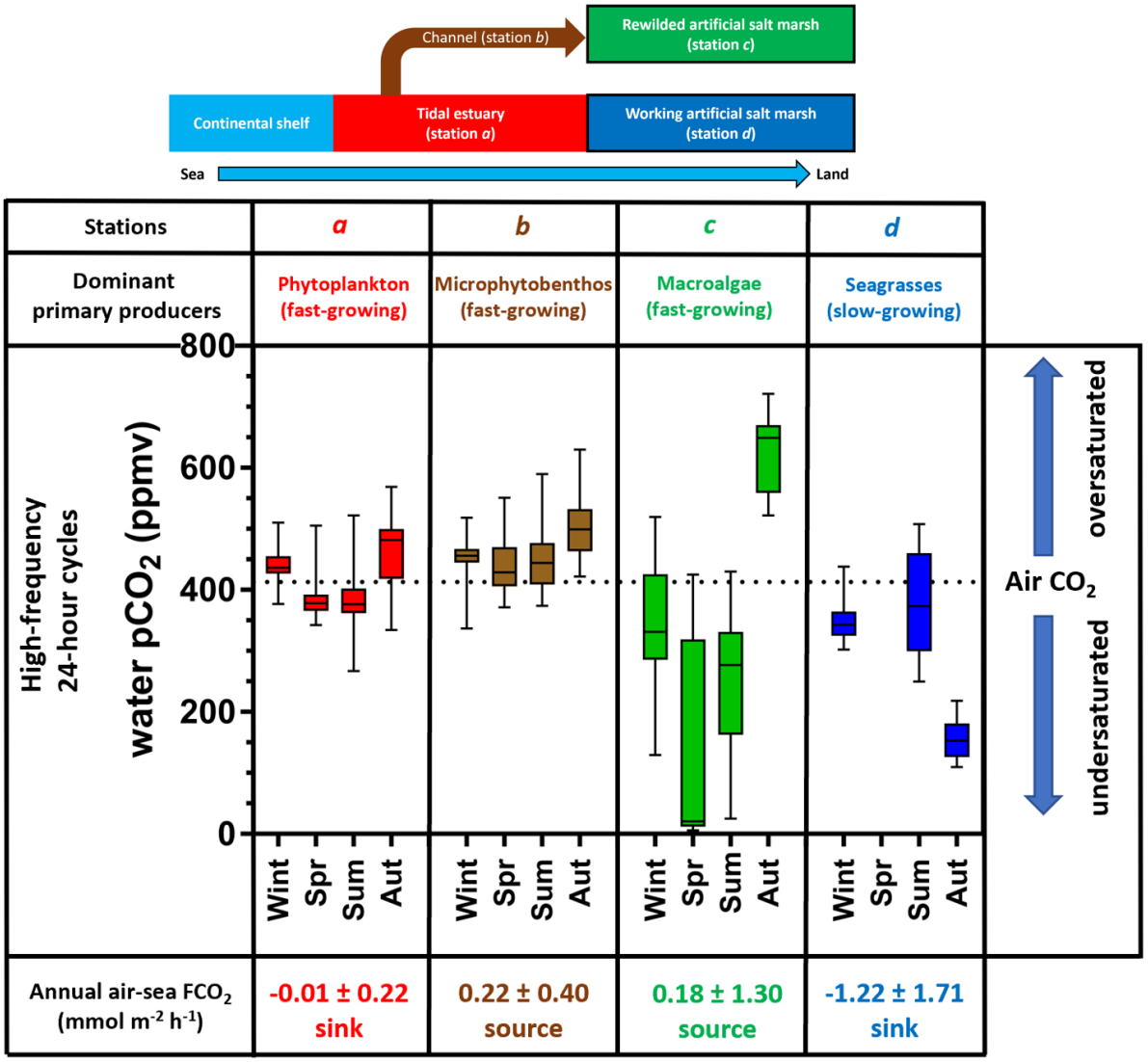

Water management practices and primary producer types influence the marsh CO_2 behaviour (sink/source)

1. Introduction

Marine coastal environments, which only account for 7% of the global ocean, perform major ecological functions such as primary production, bacterial mineralization and organic matter burial (Gattuso et al., 1998). The coastal zone presents a wide diversity of geomorphological types and ecosystems (shelves, estuaries, bays, wetlands) shaping the biogeochemical cycle coupling between land, ocean and atmosphere (Aufdenkampe et al., 2011; Bauer et al., 2013). These dynamics and heterogeneous ecosystems vertically exchanges large and variable quantities of carbon (C) with the atmosphere (Cole et al., 2007; Polsenaere et al., 2012). At the global scale, continental shelves behave as atmospheric CO_2 sinks and absorb 0.25 ± 0.05 Pg C yr^{-1} due to phytoplankton primary production (Bauer et al., 2013; Dai et al., 2022). On the contrary, CO_2 supersaturated estuarine waters emit 0.25 ± 0.05 Pg C yr^{-1} to the atmosphere (Bauer et al., 2013) due to a strong mineralization of organic matter from the land (Frankignoulle et al., 1998; Borges and Abril, 2011). These atmospheric C exchanges within the coastal zone are heterogeneous (Borges et al., 2005) and need to be better taken into account in regional and global C budgets (Najjar et al., 2018). For instance, coastal wetlands, including salt marshes located along inner shelf – estuary – marsh continuums, absorb 0.55 ± 0.05 Pg C yr^{-1} from the atmosphere (Bauer et al., 2013) and may play a major role in atmospheric CO_2 uptake and associated organic C burial on Earth (Cai, 2011; Mcleod et al., 2011).

In salt marshes, inorganic C dynamics and water pCO_2 are influenced by several physicochemical and biological processes within and between each ecosystem compartment such as tidal exchanges, calcium carbonate precipitation/dissolution, benthic-pelagic coupling, air-water exchanges and photosynthesis/respiration balance (Cai, 2011; Bauer et al., 2013; Macreadie et al., 2017). Due to high photoautotrophy rates of both aquatic (phytoplankton and seagrasses) and terrestrial (vascular plants) primary producers (Tobias and Neubauer, 2019), these highly productive ecosystems mostly behave as net atmospheric C sinks (Schäfer et al., 2014; Artigas et al., 2015; Forbrich and Giblin, 2015). A refractory part of organic C produced through photosynthesis in these vegetated coastal ecosystems can then be sequestered in sediments and/or plant biomass (Chmura et al., 2003) and stored as blue C, and greatly contribute to the regional/global C cycle in comparison with terrestrial ecosystems (Mcleod et al., 2011). Salt marshes also produce and horizontally export significant quantities of C through tidal water advection (Najjar et al., 2018) which could, in turn, strongly influence the C balance of the system itself as well as the estuary and shelf systems (Cai,

2011). The "marsh CO_2 pump" hypothesis proposes that atmospheric CO_2 uptake by marsh primary producers and the export of a part of the associated C may be one of the major mechanisms making adjacent coastal waters sources of CO_2 to the atmosphere (Wang and Cai, 2004). For instance, in a tidal marsh area (USA; 12300 km^2), Wang et al. (2016) estimated that 56% of the atmospheric C uptake by the marsh net primary production (NPP) was exported to the coastal ocean by tides (39% inorganic and 17% organic C forms). Nevertheless, despite these major ecological potentials (storm protection, nursery areas, long-term C storage), these interface areas are the most threatened in the world by land-use changes, climate changes and sea level rise (Gu et al., 2018). Moreover, coastal eutrophication causes the loss of salt marshes by decreasing the below-ground biomass of plant roots through microbial degradation processes thereby producing a decrease in the geomorphic stability of marshes (Deegan et al., 2012). Since the 1800s, salt marshes have lost about 25% of their global area with negative effects on the atmospheric CO_2 sink and the associated C sequestration (Mcleod et al., 2011). Their importance as ecosystem service reservoirs has made it possible to implement protection and restoration policies that contribute to their better management and to the development of their ecological and economic potentials (Gu et al., 2018; Adam, 2019).

The high heterogeneity in biogeochemical processes within coastal systems at spatial and temporal scales (Cai, 2011; Bauer et al., 2013) requires more integrative C process and exchange measurements at the various terrestrial – aquatic – atmospheric interfaces over different timescales (tidal, diurnal and seasonal) to better understand the ecological functioning of these ecosystems facing global changes. Some studies in coastal wetlands such as salt marshes or seagrasses have taken water pCO_2 measurements at different temporal scales allowing the study of in situ CO_2 dynamics in relation to other biotic and abiotic processes (Burgos et al., 2018; Wang et al., 2018; Berg et al., 2019; Polsenaere et al., 2022). For instance, in an intertidal mangrove (Gaderu Creek, India), Borges et al. (2003) showed a strong control of diurnal pCO_2 variations by tides and biological activity (primary production and respiration). However, still too few studies have taken high-frequency water pCO_2 measurements in salt marshes at the diurnal and tidal scales to better understand the biogeochemical status of marsh waters which are still little studied from a C point of view (Song et al., 2023). These temporal variations in water pCO_2 strongly affect associated air-water CO_2 fluxes that can, in turn, be estimated from the CO_2 gas transfer velocity, CO_2 solubility in the water and air-water CO_2 gradient (Borges et al., 2003; Crosswell et al., 2017).

The atmospheric Eddy Covariance technique represents an alternative way to directly measure atmospheric CO_2 fluxes at the ecosystem scale (Baldocchi et al., 1988; Schäfer et al., 2014). This non-intrusive micrometeorological technique allows to study the metabolism of coastal ecosystems (sink or source) under real field conditions and to integrate them into regional C budgets (Polsenaere et al., 2012; Van Dam et al., 2021).

The purpose of this study was to better understand CO_2 dynamics at different temporal scales and locations over two aquatic sea – land continuums along the Atlantic French coast on Ré Island. These continuums include coastal systems (shelf, estuary, marsh) such as those studied elsewhere by Cai (2011) and Bauer et al. (2013) with regards to horizontal and vertical C exchanges in the coastal ocean. Unlike tidal salt marshes, which are more generally discussed in the literature (Cai, 2011; Wang et al., 2016), here we studied two artificial salt marshes (i.e. salt ponds) in which water exchanges are controlled by dykes and locks for human uses (biodiversity protection or anthropogenic activities; Tortajada et al., 2011). Through in situ high-frequency measurements of biogeochemical parameters in waters and estimations of atmospheric CO_2 fluxes from 2018 to 2020, we sought to (1) identify biophysical controlling factors of water pCO_2 by establishing biogeochemical relationships both at the seasonal and diurnal/tidal scales, (2) highlight the influence of continuum typologies on measured biogeochemical parameters and (3) identify role of station typologies and salt marsh management practices on temporal pCO_2 dynamics and associated CO_2 budgets. The results allowed us to contextualize the associated continuum metabolism among other studied systems from a C dynamics and budget point of view.

2. Materials and methods

2.1. Study sites

2.1.1. Tidal estuary (station *a*) and channel (station *b*)

The Fier d'Ars estuary is a semi-closed maritime area of 750 ha on Ré Island within the French Atlantic Ocean and connected to the Breton Sound continental shelf (Fig. 2.1). It corresponds to a type II temperate tidal estuary according to Dürr et al.'s (2011) coastal system typology. At low tide (LT), its subtidal zone (in light blue; Fig. 2.1) is composed of mudflats (slikke) and tidal salt marshes (schorre) traversed by numerous channels of different sizes. At high tide (HT), the subtidal zone is flooded by coastal waters from the shelf up to the

dykes (Fig. 2.1), managed to control water exchanges between the estuary and upstream artificial salt marshes. Station *a*, with a maximum water height of 6.5 m, is located within the subtidal zone of the estuary along the main channel connected to the slikke (Fig. 2.1). Station *b* is a secondary tidal channel associated to the schorre and located at the back of the estuary before the dyke. With a maximum water height of 5.3 m, it is connected to station *a* (distance of 1.6 km) enabling the supply of coastal waters to artificial salt marshes upstream from the dyke (Fig. 2.1).

Artificial salt marshes are old tidal salt marshes divided into multiple ponds by dykes mainly located along European coasts for which water residence times (from a few hours to fifteen days according to the management practices; Bel Hassen, 2001) were originally controlled for salt-farming through locks (Tortajada et al., 2011).

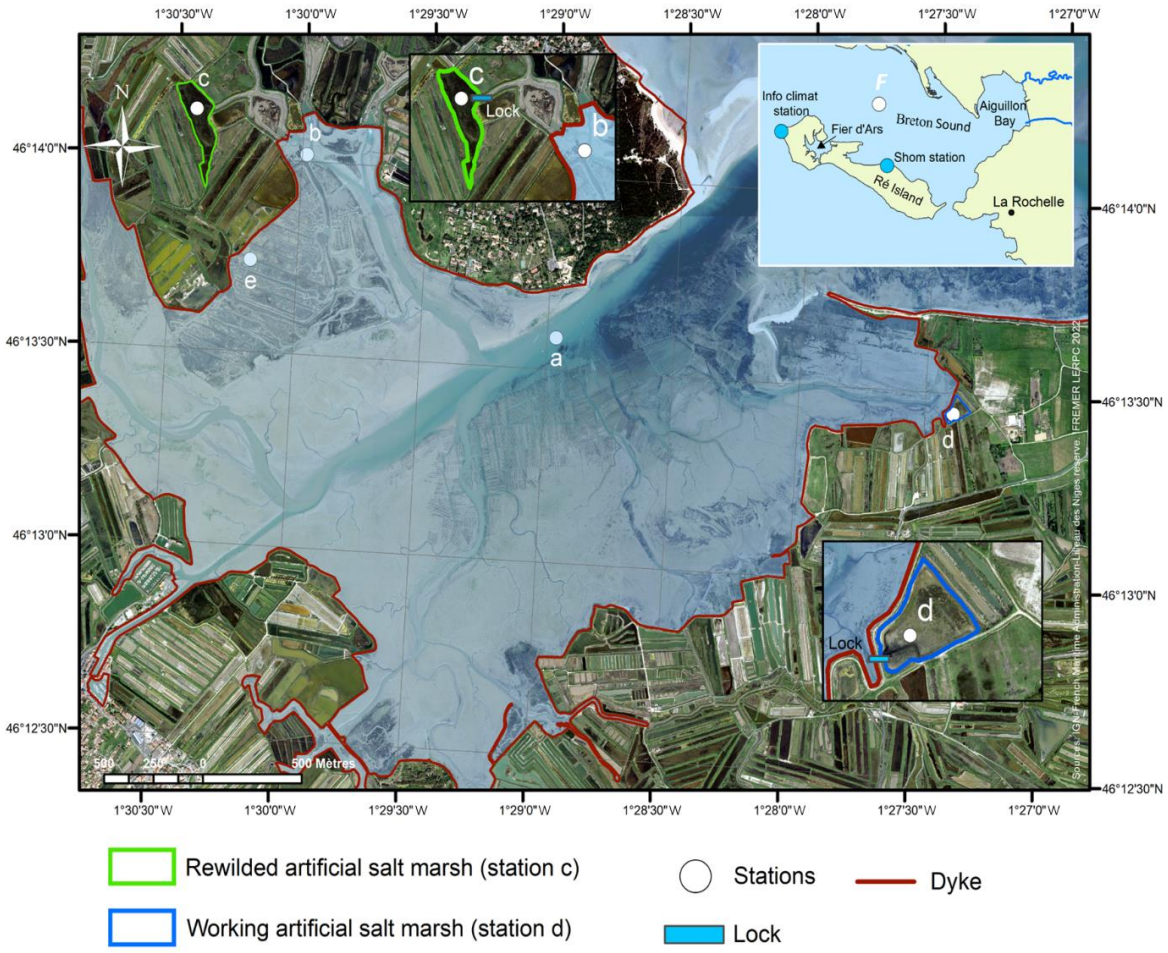

Figure 2.1: The Fier d'Ars estuary (Ré Island, French Atlantic coast) and locations of the four studied stations along aquatic continuums: tidal estuary at station *a*, channel at station *b*, rewilded artificial salt marsh at station *c* (in green) and working artificial salt marsh at station *d* (in blue). The dyke (in red) delimits terrestrial and maritime areas. The locks in the two studied artificial marshes are represented within the two map expansions. An atmospheric Eddy Covariance station was deployed at station *e* on the tidal salt marsh downstream from the dyke. Station *F* is located in the centre of the Breton Sound continental shelf; station *a* is located at the entry of the estuary; stations *b*, *c* and *e* are within the National Natural Reserve to the west of the estuary; station *d* to the east of the estuary is within a salt-farm.

2.1.2. Rewilded artificial salt marsh (station *c*)

Station *c* is a rewilded artificial salt marsh upstream from the dyke (surface area of 40100 m^2, depth of 60 cm), protected and managed inside a National Natural Reserve (NNR). During HT periods, this rewilded marsh is supplied indirectly with coastal waters from the estuary by the station *b* channel (distance of 500 m between stations *b* and *c*; Fig. 2.1) through a lock management practice to promote biodiversity protection (former salt farm that has been rewilded; Fig. S1). From November to March (winter period), the lock is open only during the highest tidal amplitudes in order to have the best compromise between salt- and fresh-mixing waters (salinity around 30) to allow aquatic fauna passing from the continental shelf to the marsh. From April to October (summer period) with lower tidal amplitudes, the lock is permanently open to avoid large salinity fluctuations in marsh waters and favour the development of *Ruppia spp.* seagrass beds in the marsh (salinity between 30 and 45). Lately, this rewilded marsh is characterized by significant macroalgae development from early spring to late summer each year thereby preventing seagrass development (Champion et al., 2012).

2.1.3. Working artificial salt marsh (station *d*)

Station *d* is a working artificial salt marsh upstream from the dyke (surface area of 8500 m^2, depth of 75 cm) directly communicating (no channel in between) with coastal waters at HT from the estuary through a lock (distance of 2 km between stations *a* and *d*; Fig. 2.1). This working marsh was chosen for its specific management practice of the lock related to a salt-farming activity. In spring and summer, the lock is regularly open to store salt waters and then allow to supply a succession of upstream ponds during neap tides for the salt production through the evaporation process (Fig. S1). Moreover, the use of this working marsh requires a drying up and a cleaning once a year in early spring before the start of the salt production

period to remove seagrass, macroalgae and organic matter in the marsh (Poitevin, personal communication).

2.1.4. Additional station: continental shelf (station *F*)

The Breton Sound corresponds to a coastal maritime area located on the French continental shelf, characterized by a surface area of 425 km^2 (Fig. 2.1). The Breton Sound continental shelf exchanges salt waters with the Atlantic Ocean to the west at each semi-diurnal tidal cycle and receives continental inputs through the Aiguillon Bay discharges to the east depending on hydrodynamic and meteorological conditions (Stanisiere et al., 2006; Soletchnik et al., 2015). The highest and lowest river water flows were recorded in winter and summer, respectively, influencing salinity of the shelf waters differently. Station *F* in the centre of the Breton Sound (Fig. 2.1) is located in a predominantly marine environment with a low freshwater contribution (Stanisiere et al., 2006; Soletchnik et al., 2015). At each HT, the continental shelf supplies our studied stations (*a*, *b*, *c* and *d*) with various water masses based on the tidal amplitudes and seasonal periods along two aquatic sea – land continuums: (1) continental shelf (station *F*) – estuary (station *a*) – channel (station *b*) – rewilded salt marsh (station *c*) and (2) continental shelf (station *F*) – estuary (station *a*) – working salt marsh (station *d*). Conversely, at each LT, different water masses from salt marshes are exported (indirectly through the station *b* channel for station *c* or directly for station *d*) to the estuary and then to continental shelf (Fig. 2.1).

In this study, meteorological parameters (air temperature, rain, wind speed) corresponding to our measurement cycles were used from the Eddy Covariance station (Campbell Scientific) deployed on a nearby tidal salt marsh (station *e*; Fig. 2.1).

2.2. Measurement strategy and biogeochemical measurements

In the sub-surface waters (~30 cm depth), partial pressure of CO_2 (pCO_2), temperature, salinity, turbidity, dissolved oxygen concentration (DO) and pH were autonomously measured with in situ probes at a frequency of 1 min. during fifteen 24-h cycles at stations *a*, *b*, *c* and *d* during each season (Table S1). These high frequency measurements allowed to record relevant temporal (diurnal, tidal and seasonal) and spatial (continuums) variations of water pCO_2 and associated physicochemical parameters. The diurnal scale corresponds to fluctuations occurring between daytime and night-time whereas, the tidal scale corresponds to

fluctuations between LT and HT. The seasonal measurement cycles were performed in 2018 at stations *a* and *b* and in 2019/2020 at stations *c* and *d*. Measurements could not be taken at station *d* in spring 2020 due to the Covid pandemic. At station *F*, the same biogeochemical measurements were taken biweekly over the year 2018 (Table S1) by Coignot et al. (2020).

A pCO_2 underwater probe (C-Sense^{TM}; PME/Turner Designs), a multiparameter probe (EXO2; YSI) and a submersible fluorometer (C3^{TM}; Turner Designs) were deployed to measure water pCO_2, physicochemical parameters and fluorescence, respectively. The measurement range of the C-Sense probe is 0-2000 ppmv with an absolute accuracy of 60 ppmv (3% of the full scale; Turner Designs). The C-Sense probe was calibrated by the manufacturer before the study. The EXO2 probe was used to measure temperature (± 0.1 °C), salinity (± 0.5 salinity unit), turbidity (± 0.3 NTU), DO concentration (± 3.1 µmol L^{-1}), DO saturation level (± 1%) and pH (± 0.01 pH unit). The pH was calibrated before and after each 24-h cycle using three YSI buffer solutions (pH 4.01, pH 7.00 and pH 10.01) as outlined by Aminot and Kérouel (2004). It was not possible to measure pH at stations *a* and *b*. The C3-fluorometer was used to estimate the sub-surface Chl *a* values from the 10-min. fluorescence data. This latter was deployed only at station *c* and *d* in summer 2019 and winter 2020.

Water pCO_2 measured by the C-Sense probe are influenced by the total dissolved gas pressure (TDGP) which corresponds to the total pressure exhibited by all gases within the water column. When this pressure greatly exceeded the pressure at which the C-Sense probe was calibrated, the output needed to be corrected. Then, a pCO_2 correction was applied taking both TDGP, atmospheric pressure during sensor calibration (1009 hPa) and the measured pCO_2 by the C-Sense probe into account, as per equation ($pCO_{2measured}$ × 1009) / TDGP (Turner Designs). Over all 24-h cycles, the corrected pCO_2 values with TDGP were 2.6 ± 0.9% lower than the measured pCO_2 values. Total alkalinity (TA) and dissolved inorganic carbon (DIC) were estimated from salinity, temperature, pH and water pCO_2 using the carbonic acid constant from Mehrbach et al. (1973) as modified by Dickson and Millero (1987), the K_{HSO4} constant from Dickson (1990) and the borate acidity constant from Lee et al. (2010). The CO_2 system calculation program (version 2.1.) performed these calculations (Lewis and Wallace, 1998).

2.3. Temperature and non-temperature effects on pCO_2 variations

To distinguish between the temperature and non-temperature effects on in situ pCO_2 variations at the seasonal and diurnal scales, $TpCO_2$ (pCO_2 variations related to temperature physical effects, in ppmv) and $NpCO_2$ (pCO_2 variations related to non-temperature effects, in ppmv) were calculated respectively, following Eq. (1) and Eq. (2) from Takahashi et al. (2002):

$$TpCO_2 = pCO_{2mean} \times \exp[0.0423 \times (T_{obs} - T_{mean})] \quad (1)$$

$$NpCO_2 = pCO_{2obs} \times \exp[0.0423 \times (T_{mean} - T_{obs})] \quad (2)$$

where T_{obs} and pCO_{2obs} are the temperature and pCO_2 values measured by the probes at each time step (1 min.), respectively. T_{mean} and pCO_{2mean} are the temperature and pCO_2 averaged either at the seasonal (annual mean) or diurnal scale (means per 24-h cycle). $TpCO_2$ is only associated with the physical pump whereas, $NpCO_2$ is associated with biological processes, tidal advection and benthic-pelagic coupling (Cotovicz Jr. et al., 2015; Polsenaere et al., 2022).

2.4. Calculations of air-water CO_2 fluxes

For all 24-h measurement cycles, the gas transfer velocity (k_{600}) and hourly CO_2 fluxes (FCO_2) at the air-water interface were estimated following Ribas-Ribas et al. (2011) and Polsenaere et al. (2022) in coastal environments. At stations *a* and *b*, only air-water FCO_2 during HT periods (four hours around each HT) were calculated whereas at stations *c* and *d*, all hourly FCO_2 were calculated using the following Eq. (3):

$$FCO_2 = \alpha \times k \times \Delta pCO_2 \quad (3)$$

where FCO_2 (mmol m^{-2} h^{-1}) is the estimated air-water CO_2 fluxes, α (mol kg^{-1} atm^{-1}) is the CO_2 solubility coefficient in saltwater, k (cm h^{-1}) is the gas transfer velocity of CO_2 and ΔpCO_2 (ppmv) is the gradient between mean water and air pCO_2. Water pCO_2 were measured by the C-Sense probe. Atmospheric CO_2 concentrations were measured by (1) the Eddy Covariance (station *e*; Fig. 2.1) for summer 2019 and winter 2020 and (2) the National Oceanic and Atmospheric Administration (NOAA) at the Mauna Loa Observatory for all other periods (see values caption Table 2.3). The α coefficient depends on water temperature and salinity and was calculated according to Weiss (1974). The *k* coefficient also significantly controls air-water FCO_2 since it directly takes turbulence processes at the air-water exchange

interface into account (Polsenaere et al., 2013). In this study, k (or k_{660}) was calculated according to both Raymond and Cole (2001) (RC01; Eq. 4) and Wanninkhof et al. (2022) (W22; Eq. 5) corresponding to closed environments and more open coastal environments, respectively. These two parametrization methods for the k exchange coefficient were applied in order to compare the results.

For closed freshwater environments (Raymond and Cole, 2001):

$$k_{600} = 1.91 \times \exp[0.35 \times U_{10}] \quad (4)$$

For more open coastal environments (Wanninkhof et al., 2022):

$$k_{600} = 0.31 \times (U_{10})^2 \quad (5)$$

The gas transfer coefficients normalized to a Schmidt number of 600 (k_{600}) obtained with the two parametrization were then converted to the gas transfer velocity of CO_2 at the in situ temperature and salinity (k_{660}) according to Jähne et al. (1987) following Eq. (6):

$$k_{660} = k_{600} / (660/Sc)^{-0.5} \quad (6)$$

where k_{660} (cm h^{-1}) is the gas transfer velocity of CO_2 at the in situ temperature and salinity according to the parametrizations of RC01 or W22, U_{10} (m s^{-1}) is the wind speed normalized to 10 m (Amorocho and DeVries, 1980) and Sc is the Schmidt number which describes both the water viscosity and the molecular diffusion of the subsurface layer (Bade, 2009). In summer 2019 and winter 2020, wind speeds were measured by the Eddy Covariance (station *e;* Fig. 2.1) at a height of 3.15 m; for all other periods, wind data were obtained from the Infoclimat station (Fig. 2.1) measured at a height of 10 m (distances of 6.20, 4.85, 4.30 and 8.40 km from stations *a*, *b*, *c* and *d*, respectively).

2.5. Chl a concentrations and fluorometer data calibration

In situ Chl *a* concentrations (µg L^{-1}) were measured from sub-surface water samples collected only at stations *c* and *d*. Water samples (50-100 mL) were filtered through GF/F filters (Whatman® Nuclepore™, porosity of 0.7 µm) and stored at -20°C until analysis. In the dark, Chl *a* was extracted in 90% acetone with a glass rod. After 12 h of stirring at 4°C to continue the extraction, Chl *a* was analysed by monochromatic spectrophotometry at 665 nm (Aminot and Kérouel, 2004).

For the fluorometer data, the calibration procedure was applied to derive Chl *a* values from our water fluorescence measurements (Aminot & Kérouel, 2004). Chl *a* could be calculated only at station *d* through the significant linear regressions ($p < 0.05$) between the fluorometer values and the in situ Chl *a* values sampled simultaneously in the marsh waters.

2.6. Statistical tools and analysis

For all measured variables, the high-frequency data (i.e. 1 min) did not respect a normal distribution (Shapiro-Wilk tests, $p < 0.05$). Non-parametric comparisons such as the Mann-Whitney and Kruskal-Wallis tests were carried out with 0.05 level of significance. A Dunn test was used to perform a post-hoc multiple comparison of the Kruskal-Wallis test to detect significant differences among groups. The statistical tests as well as temporal graphs, linear regressions, boxplot and barplot were performed with the GraphPad Prism 7 software. The R-studio software was used to perform the principal component analysis (PCA) with the "FactoMineR" package (Lê et al., 2008) and the correlation matrices with the "corrplot" package (Wei and Simko, 2017). The PCA allows to study the seasonal distribution of data along the studied continuums (Fig. 2.2). It is based on the seasonal means of the temperature, salinity, turbidity, DO and pCO_2 measured (i) once every two weeks at station *F* and (ii) once every minute over 24-h cycles at stations *a*, *b*, *c* and *d*. Stepwise multilinear regression analysis were performed to test the contribution of measured physicochemical variables (salinity, temperature, turbidity and oxygen) on water pCO_2 variations through the percentage of explained variance (adjusted R^2; Harrell, 2015). Within each 24-h cycle, the selected multilinear model ($p < 0.001$, $n = 1441$) had the highest adjusted R^2 with all variables explaining at least 5% of the pCO_2 variation. Analysis were performed with Statgraphics Centurion 19 software.

3. Results

3.1. Biogeochemical overview of the aquatic continuums

Over our measurement periods, thermal conditions for the years 2018 and 2019 were similar following a classical seasonal trend. However, July 2018, July 2019 and February 2020 were warmer than the 1990-2020 reference period (Table 2.1). Annual cumulative precipitations in 2018 and 2019 were higher than the historical data with March 2018 and October 2019 as the rainiest months (Table 2.1). Salinity at station *F* as the water source flowing into the two studied continuums did not vary significantly between the years 2018, 2019, 2020 and the 2000-2017 reference period (Kruskal-Wallis test, $p = 0.77$; Fig. S2).

At station *F*, over the biweekly measurements in 2018, water temperatures varied from 7.5 (winter) to 21.7°C (summer) whereas at station *a* over our seasonal 24-h cycles, values varied from 9.1 (winter) to 26.9°C (summer). Along the aquatic continuum, water temperatures significantly increased from station *a* to stations *b* and *c* (Mann-Whitney tests, $p < 0.05$). Salinity ranged from 28.9 (winter) to 35.4 (autumn) at station *F* whereas, values varied from 31.4 (winter) to 35.7 (autumn) at station *a*, from 27.5 (winter) to 36.9 (autumn) at station *b*, from 27.0 (winter) to 42.6 (summer) at station *c* and from 21.3 (winter) to 38.4 (autumn) at station *d* with largest salinity gradients recorded at stations *c* and *d* (Table 2.2). In average over the year, station *a* waters were slightly oversaturated in oxygen compared to the atmosphere with DO saturation levels ranging between 70 (LT during dawn) and 150% (LT during dusk) during the summer cycle (Fig. 2.3). Simultaneously, station *b* waters were close to the saturation value with the atmosphere with a lower maximum value (120%) during the summer cycle (Fig. 2.4). Larger amplitudes of DO saturation level were recorded in the artificial salt marshes with values ranging from 36 to 176% at station *c* (summer; Fig. 2.5) and from 49 to 150% at station *d* (summer; Fig. 2.6). The annual levels of water CO_2 undersaturation with respect to the atmosphere were 48%, 16%, 65% and 86% at stations *a*, *b*, *c* and *d*, respectively, with a strong annual CO_2 oversaturation at station *b* (Fig. 2.4). The greatest amplitude in water pCO_2 was recorded at station *c* with values varying from 6 (spring) to 721 ppmv (autumn; Fig. 2.5).

At station *F*, over the year 2018, Chl *a* values increased from winter (0.7 ± 0.1 µg L^{-1}) to spring-summer (2.5 ± 1.6 and 1.6 ± 1.0 µg L^{-1}, respectively), before decreasing in autumn (0.8 ± 0.5 µg L^{-1}). At station *c*, the highest and lowest Chl *a* values were recorded in autumn 2019 (8.1 ± 0.4 µg L^{-1}) and winter 2020 (1.3 ± 0.3 µg L^{-1}), respectively, whereas at station *d*, the highest and lowest values were recorded in winter 2020 (3.4 ± 0.4 µg L^{-1}) and summer 2019

(1.9 ± 0.3 µg L^{-1}), respectively. Moreover, at station *c*, from spring to autumn 2019, a free floating macroalgae development (*Ulva spp.*) was observed in the sub-surface waters and on sediments (Fig. S3). On the contrary, at station *d*, no macroalgae development occurred, allowing for the seagrass growth (*Ruppia spp*.) in the marsh (Fig. S3).

Table 2.1: Meteorological conditions (air temperature in °C and cumulative precipitation in mm) obtained from the "Infoclimat" station on Ré Island (Fig. 1; https://www.infoclimat.fr) at the monthly and annual scales over our measurement periods in 2018, 2019 and 2020 in bold compared to the reference period (1990-2020).

Year	Season	Month	Mean air temperature (°C)	Difference with the reference period (°C)	Cumulative precipitation (mm)	Difference with the reference period (mm)
2018	Winter	March	**9.1**	-0.7	**127**	+70
	Spring	April	**13.4**	+1.4	**58**	-3
	Summer	July	**22.2**	+1.7	**59**	+19
	Autumn	September	**19.0**	+1.0	**9**	-51
		Annual	**14.3**	+0.8	**786**	+32
2019	Spring	April	**11.9**	-0.1	**57**	-4
	Summer	July	**22.5**	+2.0	**33**	-7
	Autumn	October	**15.8**	+1.1	**117**	+33
		Annual	**14.1**	+0.6	**827**	+73
2020	Winter	February	**10.4**	+3.1	**68**	+12

Table 2.2: Seasonal means (± SD) and ranges (min - max) of temperature (°C), salinity, DO (µmol L^{-1}), pH (NBS scale) and pCO_2 (ppmv) values measured (i) once every two weeks in 2018 at station *F* (Coignot et al., 2020) and (ii) during each 24-h cycle from 2018 to 2020 at stations *a*, *b*, *c* and *d* in this study.

		Temperature (°C)	**Salinity**	**DO (µmol L^{-1})**	**pH (NBS)**	**pCO_2 (ppmv)**
Winter 2018	*F*	**9.1 ± 1.3** (7.5 - 10.6)	**31.4 ± 1.8** (28.9 - 33.0)	**269.6 ± 29.7** (225.0 - 285.3)	**8.04 ± 0.17** (7.79 - 8.17)	**619 ± 285** (415 - 1040)
March 2018	*a*	**9.5 ± 0.4** (9.1 - 10.4)	**32.5 ± 0.2** (31.9 - 32.9)	**278.7 ± 7.7** (257.2 - 288.8)	-	**441 ± 21** (377 - 510)
March 2018	*b*	**9.8 ± 0.5** (9.0 - 11.3)	**31.0 ± 1.4** (27.5 - 32.5)	**269.7 ± 9.3** (251.6 - 307.5)	-	**450 ± 33** (337 - 518)
February 2020	*c*	**11.5 ± 0.7** (10.2 - 12.9)	**27.8 ± 0.7** (27.0 - 29.7)	**287.5 ± 22.0** (256.9 - 350.0)	**8.20 ± 0.14** (7.94 - 8.53)	**343 ± 87** (130 - 519)
February 2020	*d*	**10.2 ± 0.6** (9.2 - 11.1)	**21.4 ± 0.0** (21.3 - 21.5)	**314.5 ± 15.9** (293.1 - 343.8)	**8.27 ± 0.04** (8.16 - 8.32)	**347 ± 30** (302 - 438)
Spring 2018	*F*	**16.0 ± 2.5** (13.2 - 19.1)	**32.4 ± 1.5** (30.8 - 34.2)	**270.0 ± 28.5** (245.3 - 308.2)	**8.23 ± 0.09** (8.11 - 8.33)	**379 ± 89** (279 - 495)
April 2018	*a*	**15.0 ± 0.7** (14.1 - 16.5)	**31.5 ± 0.0** (31.4 - 31.5)	**265.8 ± 16.4** (221.9 - 285.3)	**8.17 ± 0.03** (8.09 - 8.21)	**390 ± 40** (342 - 505)
April 2018	*b*	**15.5 ± 0.9** (14.1 - 16.9)	**31.2 ± 0.3** (30.3 - 31.6)	**252.2 ± 20.1** (200.3 - 279.4)	**8.05 ± 0.02** (7.98 - 8.09)	**443 ± 44** (371 - 551)
May 2019	*c*	**17.1 ± 1.8** (14.3 - 19.9)	**33.7 ± 0.2** (33.3 - 34.0)	**287.5 ± 78.4** (168.4 - 415.0)	**8.78 ± 0.43** (8.12 - 9.23)	**135 ± 165** (6 - 425)
-	*d*	-	-	-	-	-
Summer 2018	*F*	**19.9 ± 1.5** (18.2 - 21.7)	**34.6 ± 0.6** (34.0 - 35.2)	**235.6 ± 22.3** (204.4 - 253.1)	**8.20 ± 0.12** (8.05 - 8.34)	**410 ± 130** (270 - 572)
July 2018	*a*	**22.9 ± 1.6** (21.0 - 26.9)	**34.2 ± 0.3** (33.6 - 34.9)	**249.4 ± 35.9** (153.4 - 306.6)	**8.22 ± 0.07** (8.12 - 8.39)	**385 ± 60** (267 - 522)
July 2018	*b*	**23.9 ± 1.3** (21.9 - 26.1)	**34.7 ± 0.5** (33.9 - 35.6)	**211.8 ± 33.9** (139.7 - 291.9)	**8.02 ± 0.05** (7.89 - 8.12)	**454 ± 55** (374 - 590)
July 2019	*c*	**23.5 ± 2.5** (20.1 - 28.4)	**36.8 ± 2.3** (33.5 - 42.6)	**206.8 ± 58.5** (76.9 - 339.7)	**8.31 ± 0.23** (8.01 - 8.94)	**242 ± 116** (25 - 430)
July 2019	*d*	**23.3 ± 1.6** (21.2 - 28.1)	**35.8 ± 1.4** (33.3 - 38.1)	**202.4 ± 70.4** (108.8 - 314.4)	**7.97 ± 0.09** (7.84 - 8.11)	**377 ± 85** (250 - 508)
Autumn 2018	*F*	**14.7 ± 3.2** (10.3 - 17.5)	**34.3 ± 2.1** (30.6 - 35.4)	**249.1 ± 23.5** (225.0 - 284.4)	**8.09 ± 0.06** (8.04 - 8.18)	**510 ± 70** (403 - 580)
September 2018	*a*	**18.9 ± 1.5** (17.6 - 22.0)	**35.2 ± 0.1** (35.1 - 35.7)	**267.4 ± 25.9** (204.7 - 323.4)	**7.98 ± 0.07** (7.90 - 8.16)	**460 ± 58** (334 - 569)
September 2018	*b*	**20.8 ± 1.2** (18.8 - 23.1)	**35.9 ± 0.5** (35.1 - 36.9)	**232.1 ± 30.3** (153.8 - 275.3)	**7.84 ± 0.05** (7.74 - 7.94)	**503 ± 46** (422 - 630)
October 2019	*c*	**17.1 ± 0.9** (15.1 - 18.5)	**35.0 ± 0.3** (34.6 - 35.7)	**194.3 ± 24.4** (152.2 - 236.9)	**7.82 ± 0.04** (7.74 - 7.91)	**622 ± 57** (522 - 721)
October 2019	*d*	**15.9 ± 0.4** (15.4 - 16.8)	**38.2 ± 0.1** (38.0 - 38.4)	**255.8 ± 39.9** (210.6 - 331.9)	**8.17 ± 0.07** (8.07 - 8.28)	**155 ± 30** (110 - 218)

3.2. Seasonal variations and controls along the aquatic continuums

Seasonally, the PCA reveals that stations along the aquatic continuums were vertically distinguished according to pCO_2, turbidity and DO saturation within PC2 explaining 35.5% of the total variance (Fig. 2.2). Within this axis, our results confirmed that water pCO_2 were seasonally negatively correlated with DO saturation ($r_{Pearson}$ = -0.56; n = 19; $p < 0.05$) and positively correlated with turbidity ($r_{Pearson}$ = 0.54; n = 19; $p < 0.05$) (Fig. 2.2). Station *b* recorded the highest water pCO_2 values and the lowest DO saturation levels compared to the three other studied stations (except in autumn; Table 2.2 and Fig. 2.2). Station *b* was also characterized by the highest turbidity values along the aquatic continuums (from 1.6 to 41 NTU). The PCA also shows that seasonal data were horizontally distinguished according to salinity and temperature within PC1 explaining 42.3% of the total variance (Fig. 2.2). Generally, the highest and lowest salinity values were recorded in summer and winter, respectively (Fig. 2.2), except at station *d* where the highest salinity were recorded in autumn (Table 2.2). At all studied stations, temperature and salinity values significantly varied between each seasonal 24-h cycles (Kruskal-Wallis tests, $p < 0.0001$).

Along the aquatic continuums, the PCA reveals contrasted seasonal variations of water pCO_2, particularly in artificial salt marshes (Fig. 2.2). At station *F*, in 2018, no significant difference in water pCO_2 were recorded at the seasonal scale (Kruskal-Wallis test, $p = 0.13$), although the highest and lowest seasonal means were recorded in winter and spring, respectively (Table 2.2 and Fig. 2.7). At station *a*, in 2018, water pCO_2 showed the same seasonal pattern decreasing from winter to summer before increasing in autumn, whereas station *b* showed lower seasonal variations over the same measurement periods (Table 2.2 and Fig. 2.7). In contrast, stations *c* and *d* showed larger seasonal pCO_2 variations (Fig. 2.7). Station *c* waters were undersaturated in CO_2 in spring 2019, summer 2019 and winter 2020 but oversaturated in CO_2 in autumn 2019 (622 ± 57 ppmv). At the same time, station *d* waters were undersaturated in CO_2 in summer, autumn and winter with the largest water CO_2 undersaturation recorded in autumn (155 ± 30 ppmv) in contrast to station *c* (Fig. 2.7). At all studied stations, water pCO_2 significantly differed between seasons (Kruskal-Wallis tests, $p < 0.05$), except for station *a* between spring and summer (Dunn's post-test, $p > 0.99$).

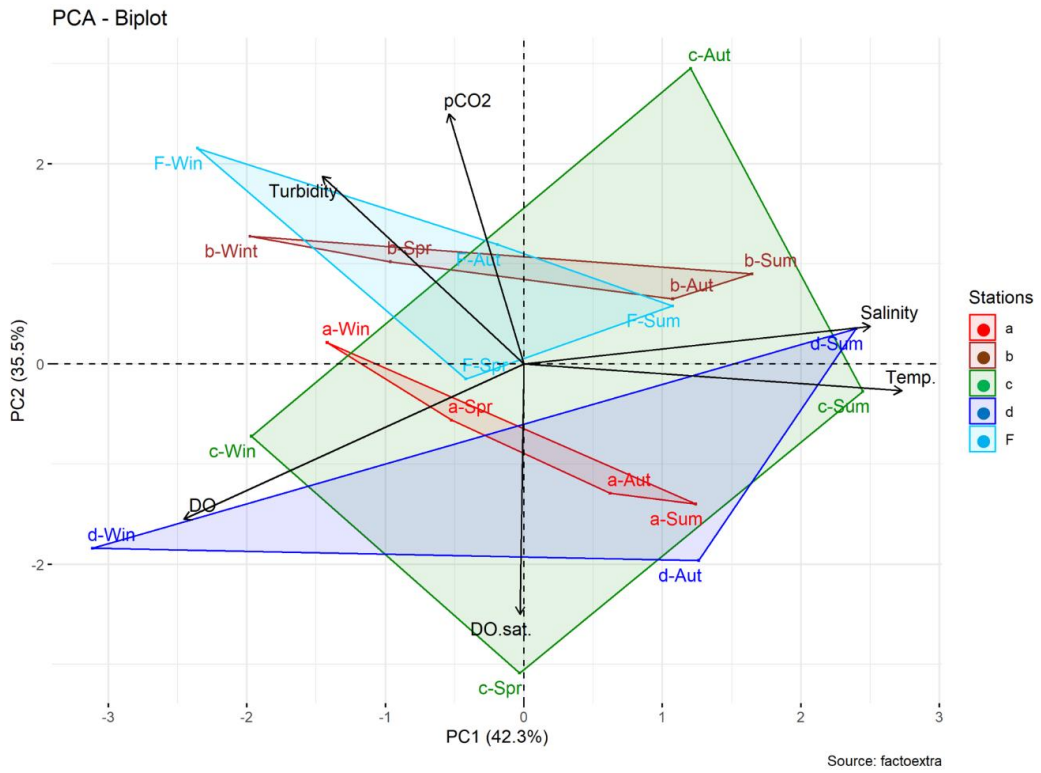

Figure 2.2: Principal Component Analysis (PCA) of the biogeochemical parameters measured at each season along the studied aquatic continuums (stations *a*, *b*, *c* and *d*). The PCA is based on temperature (Temp), salinity, turbidity, dissolved oxygen concentration (DO), dissolved oxygen saturation level (DO-sat.) and pCO_2 mean values for each 24-h cycle. Stations *a*, *b*, *c* and *d* are represented in red, brown, green and blue, respectively. The additional station *F* is represented in light blue. Win: Winter; Spr: Spring; Sum: Summer; Aut: Autumn.

The same seasonal $NpCO_2$ variations were observed at stations *a* and *b* in 2018, with a decrease from winter (595 and 624 ppmv, respectively) to summer (296 and 347 ppmv, respectively) and an increase towards autumn (420 and 439 ppmv, respectively; Fig. 2.7). At station *c*, the seasonal mean $NpCO_2$ value increased sharply from summer 2019 (193 ppmv) to autumn 2019 (630 ppmv) and then decreased towards winter 2020 (441 ppmv) whereas at station *d*, values slightly decreased from summer (286 ppmv) to autumn 2019 (160 ppmv) before increasing towards winter 2020 (453 ppmv; Fig. 2.7). Regarding temperature effects on water pCO_2, the highest and lowest seasonal $TpCO_2$ values were measured in summer and winter, respectively, with seasonal $TpCO_2$ values followed systematically by seasonal water temperature variations (Fig. 2.7). At station *a*, $\Delta TpCO_2$ offset recorded from winter to summer 2018 ($\Delta TpCO_2$ = 240 ppmv, from 310 to 550 ppmv) concomitantly to the water temperature increase of 13.4 °C partly compensated non-thermal effects on water pCO_2 during this period ($\Delta NpCO_2$ = 299 ppmv, from 595 to 296 ppmv).

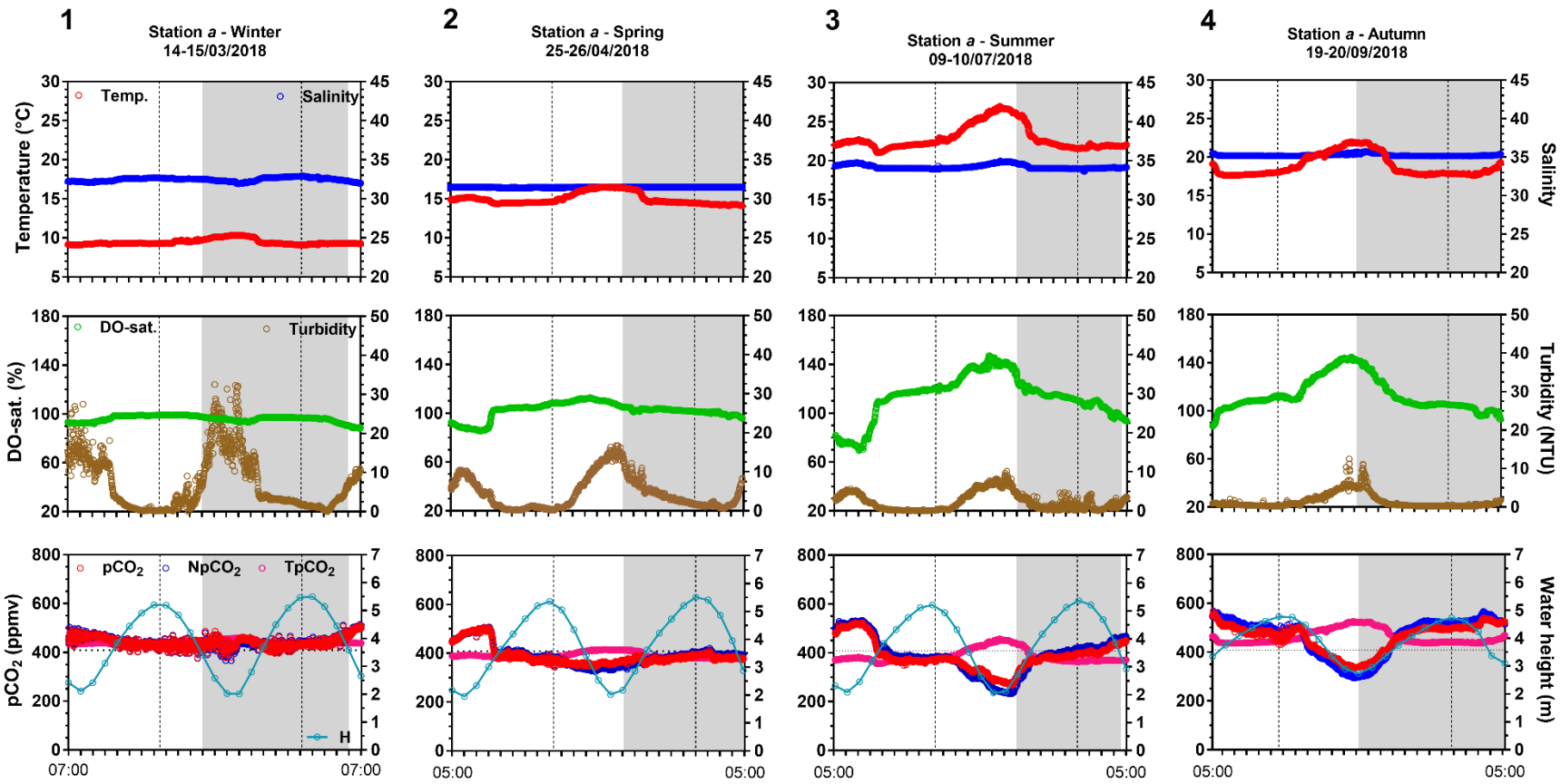

Figure 2.3: Temporal variations at station *a* (tidal estuary) of water temperature (°C), salinity, DO saturation level (DO-sat., %), turbidity (NTU), pCO_2, $NpCO_2$ (pCO_2 variations related to non-temperature effects, ppmv) and $TpCO_2$ (pCO_2 variations related to temperature physical effects, ppmv) during each 24-h cycle from winter 2018 to autumn 2018. Parameters were autonomously measured once per minute by *in situ* probes. Water heights (H, m) were retrieved from the SHOM station (9 km away; Fig. 2.1). Grey areas correspond to night-time periods. Vertical dotted lines correspond to high tides. Horizontal dotted lines correspond to the CO_2 atmospheric concentration (411 ppm; NOAA 2018). Each graduation of the x-axis corresponds to one hour.

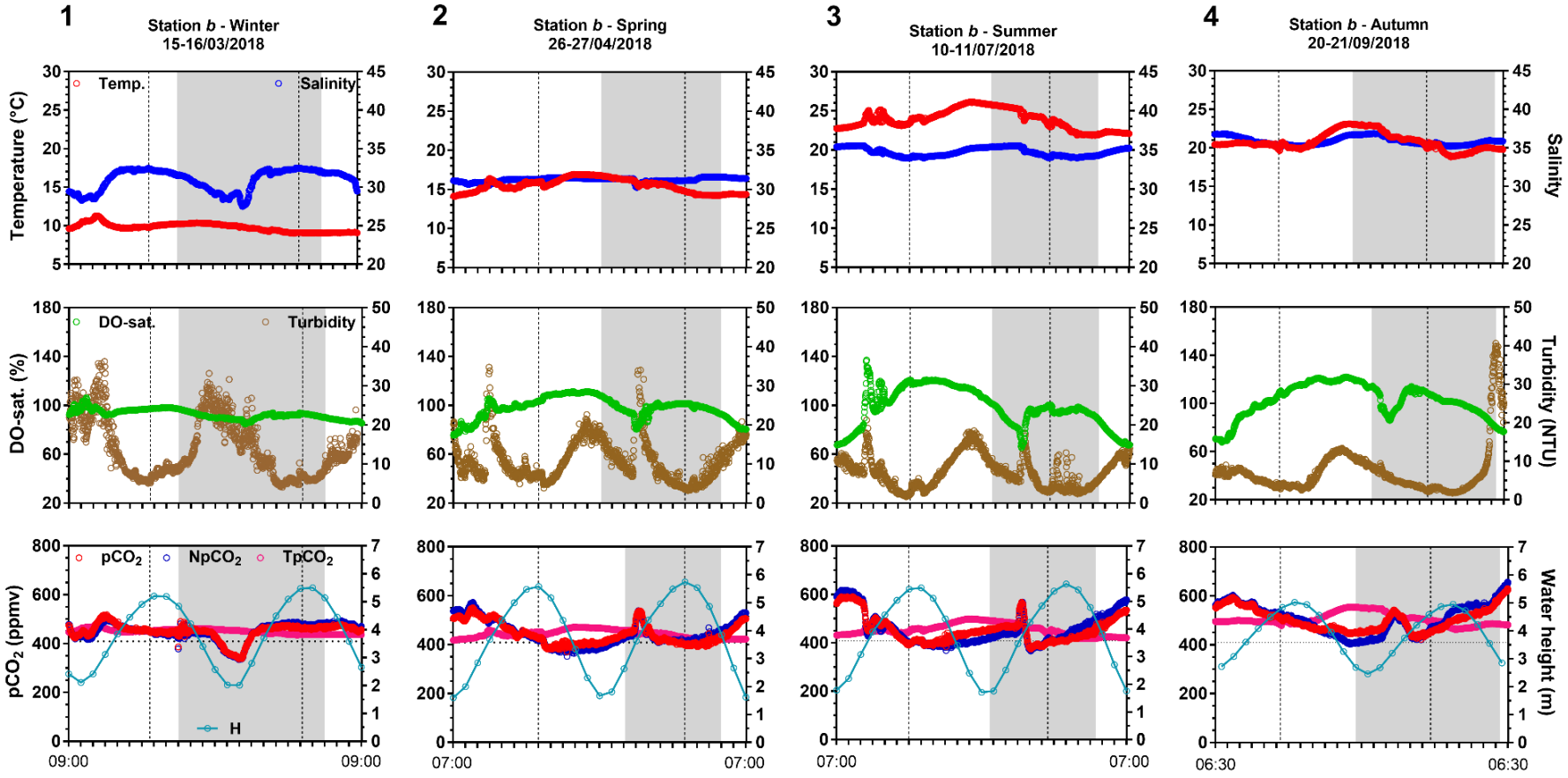

Figure 2.4: Temporal variations at station *b* (channel) of water temperature (°C), salinity, DO saturation level (DO-sat., %), turbidity (NTU), pCO_2, $NpCO_2$ and $TpCO_2$ (ppmv) during each 24-h cycle from winter 2018 to autumn 2018. See the Fig. 2.3 caption for more details.

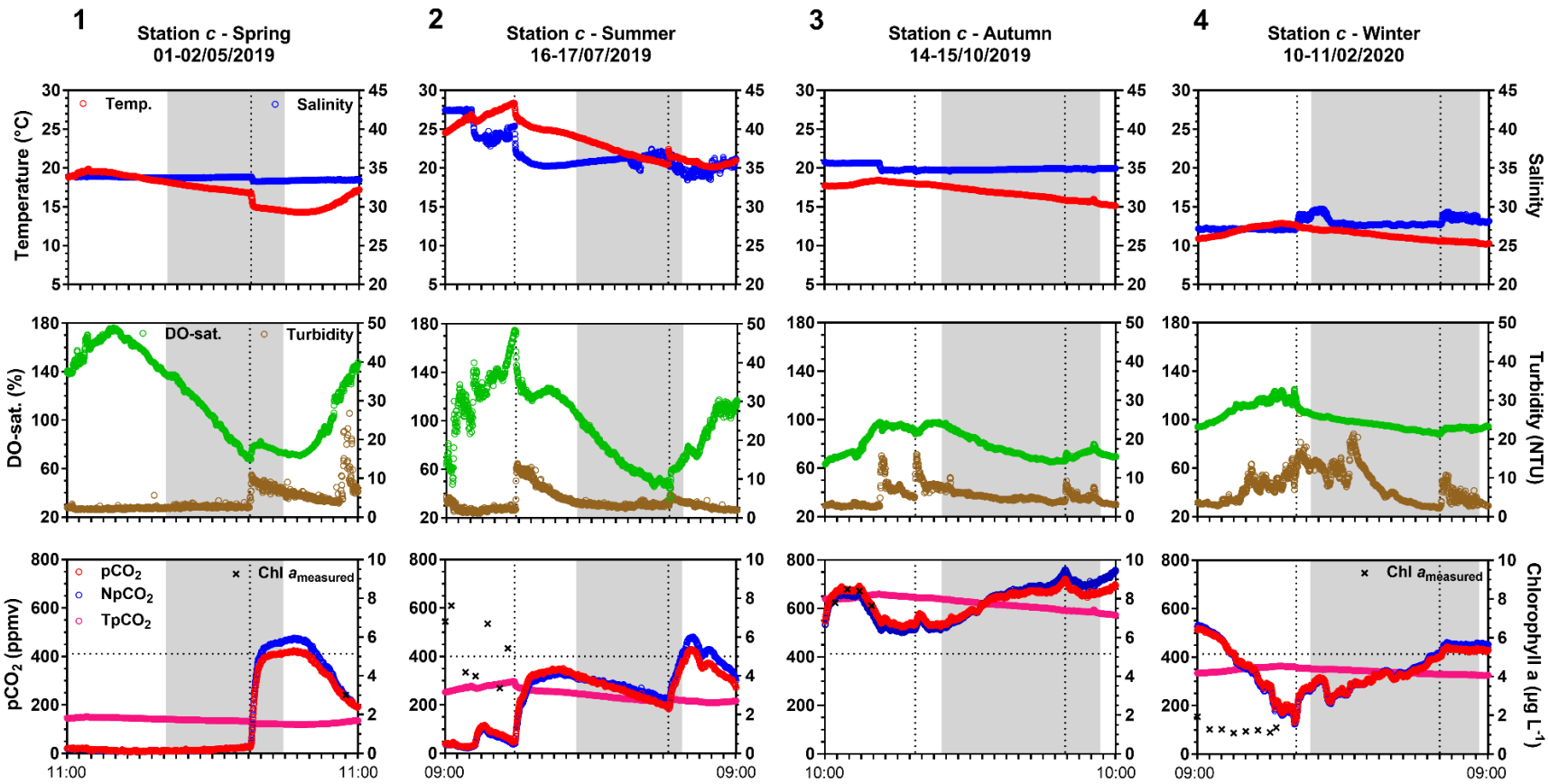

Figure 2.5: Temporal variations at station *c* (rewilded artificial salt marsh) of water temperature (°C), salinity, DO saturation level (DO-sat., %), turbidity (NTU), pCO_2, $NpCO_2$ and $TpCO_2$ (ppmv) and *in situ* Chl *a* (µg L^{-1}) during each 24-h cycle from spring 2019 to winter 2020. Vertical dotted lines correspond to coastal water inflows to the marsh during incoming tide. Horizontal dotted lines correspond to the atmospheric CO_2 concentration simultaneously measured (i) by the Eddy Covariance (station *e*) during the summer and winter cycles and (ii) by NOAA during the spring and autumn cycles. *In situ* Chl *a* values are represented by black crosses (Chl $a_{measured}$); no water samples could be taken in spring 2019. See the Fig. 2.3 caption for more details.

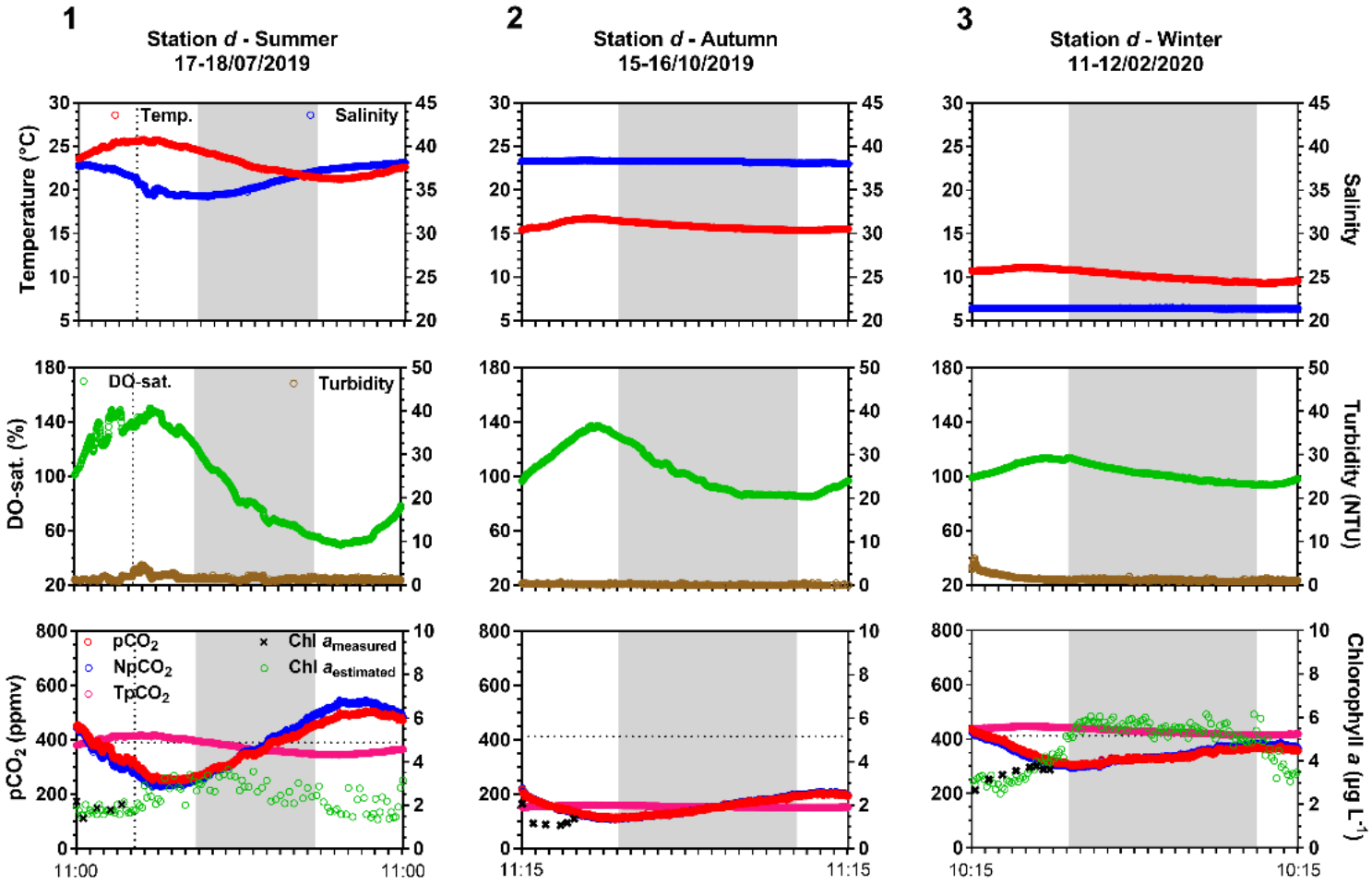

Figure 2.6: Temporal variations at station *d* (working artificial salt marsh) of water temperature (°C), salinity, DO saturation level (DO-sat., %), turbidity (NTU), pCO_2, $NpCO_2$ and $TpCO_2$ (ppmv) and *in situ* Chl *a* (µg L^{-1}) during each 24-h cycle from summer 2019 to winter 2020. Chl *a* values in green were derived from the C3-fluorometer every 10 min. (Chl $a_{estimated}$). See the Fig. 2.3 caption for more details.

3.3. Diurnal/tidal variations and controls along the aquatic continuums

At stations *a* and *b* in winter, salinity varied at the tidal scale with the lowest values at LT and the highest values at HT whereas from spring to autumn, the opposite pattern was recorded with salinity decreases at each incoming tide from the shelf (Figs. 2.3 and 2.4). At stations *c* and *d*, even stronger salinity gradients were recorded, especially in summer with decreases of 9 and 5 salinity units, respectively (Figs. 2.5 and 2.6). At station *c*, coastal water inflows led to an increase in salinity only in winter (Fig. 2.5). At station *d*, salinity and turbidity did not vary neither in autumn or in winter (Fig. 2.6).

The largest diurnal/tidal variations in water pCO_2 and DO concentrations occurred during summer with pCO_2 ranges of 255, 216, 405 and 258 ppmv at stations *a*, *b*, *c* and *d*, respectively, and DO ranges of 153.2, 152.2, 262.8 and 205.6 µmol L^{-1} at stations *a*, *b*, *c* and *d*, respectively. At stations *a* and *b*, the low tide periods during the day (LT/D) occurring at dawn showed higher water pCO_2 values and lower DO saturation levels than the low tide periods during the night (LT/N) occurring at dusk under similar salinity ranges, particularly in summer (Figs. 2.3 and 2.4). In general, our diurnal cycles showed a pCO_2 decrease that was negatively correlated to a DO increase during daytime (except at station *c* in spring; Fig. 2.5) and an opposite pattern during night-time (except at station *c* in summer; Fig. 2.5). At station *c*, in winter during LT periods (no salinity variation), water pCO_2 decreased of 390 ppmv during the day (from 09:00 to 17:00) and increased of 230 ppmv during the night (from 20:00 to 05:00) while, simultaneously, DO increased of 76.6 µmol L^{-1} and decreased of 29.0 µmol L^{-1}, respectively (Fig. 2.5). At station *d*, the same diurnal water pCO_2 and DO patterns were recorded at each 24-h cycle (Fig. 2.6). However, these strong diurnal pCO_2 and DO variations were significantly disrupted once coastal water advection and marsh management practices occurred.

Strong tidal variations in water pCO_2 were recorded during all seasonal cycles, except at station *d* both in autumn and winter (Fig. 2.6). At stations *a* and *b*, incoming tides from the shelf during the day produced rapid water pCO_2 decreases from an oversaturation to a slight water undersaturation, particularly in spring (-121 and -167 ppmv, respectively) and in summer (-139 and -115 ppmv, respectively; Figs. 2.3 and 2.4). Only at station *a*, ebbing tides during the day generated an additional pCO_2 decrease to reach the lowest values (Fig. 2.3). At station *a*, in summer and autumn and at station *b* over the four seasons, incoming tides during the night produced pCO_2 increases leading to water oversaturation periods (Figs. 2.3 and 2.4). Along the continuum, at station *c* during the night, higher water pCO_2 values were recorded at

HT than at LT, especially in spring (363 ± 85 and 16 ± 5 ppmv at HT/N and LT/N, respectively) and in winter (431 ± 6 and 323 ± 53 ppmv at HT/N and LT/N, respectively; Fig. 2.8). The same tidal pCO_2 pattern was also recorded at station *c* in summer during the day (323 ± 88 and 197 ± 141 ppmv at HT/D and LT/D, respectively; Fig. 2.8). In spring, the station *c* marsh recorded the lowest water pCO_2 values both the day and the night during the marsh confinement but coastal water inflows at HT from the station *b* channel instantly produced a large and rapid increase in water pCO_2 (+395 ppmv) within a two-hour period (Fig. 2.8).

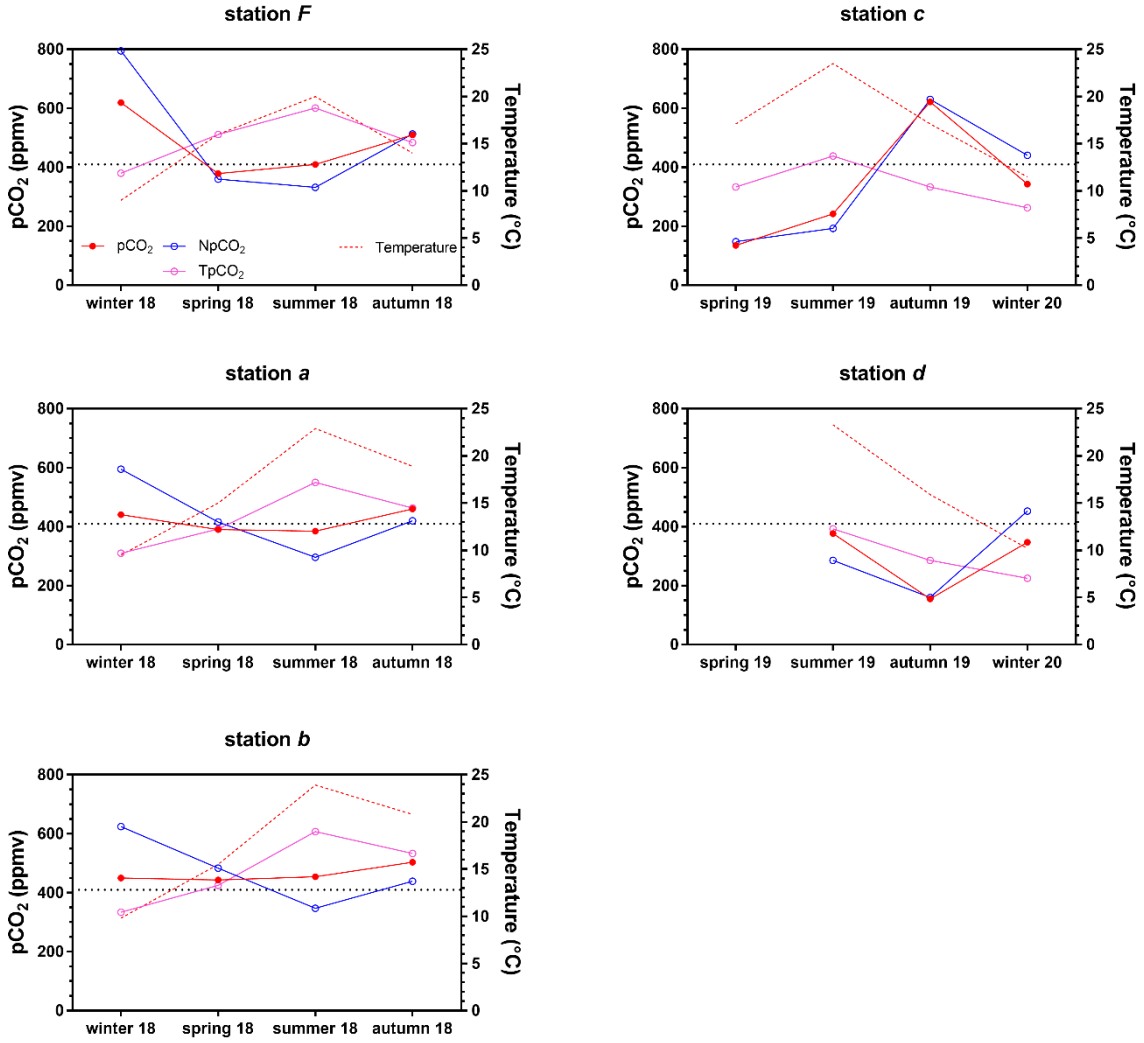

Figure 2.7: Derived temperature-normalized pCO_2 (seasonal $NpCO_2$, blue curves with empty blue dots) and thermally forced pCO_2 (seasonal $TpCO_2$, pink curves with empty pink dots) at the seasonal scale at stations *F*, *a*, *b*, *c* and *d*. Seasonal means of water temperature (in red dotted lines) and pCO_2 (red curves with filled red dots) are also represented. Horizontal dotted lines correspond to CO_2 atmospheric concentration (411 ppm; NOAA 2018).

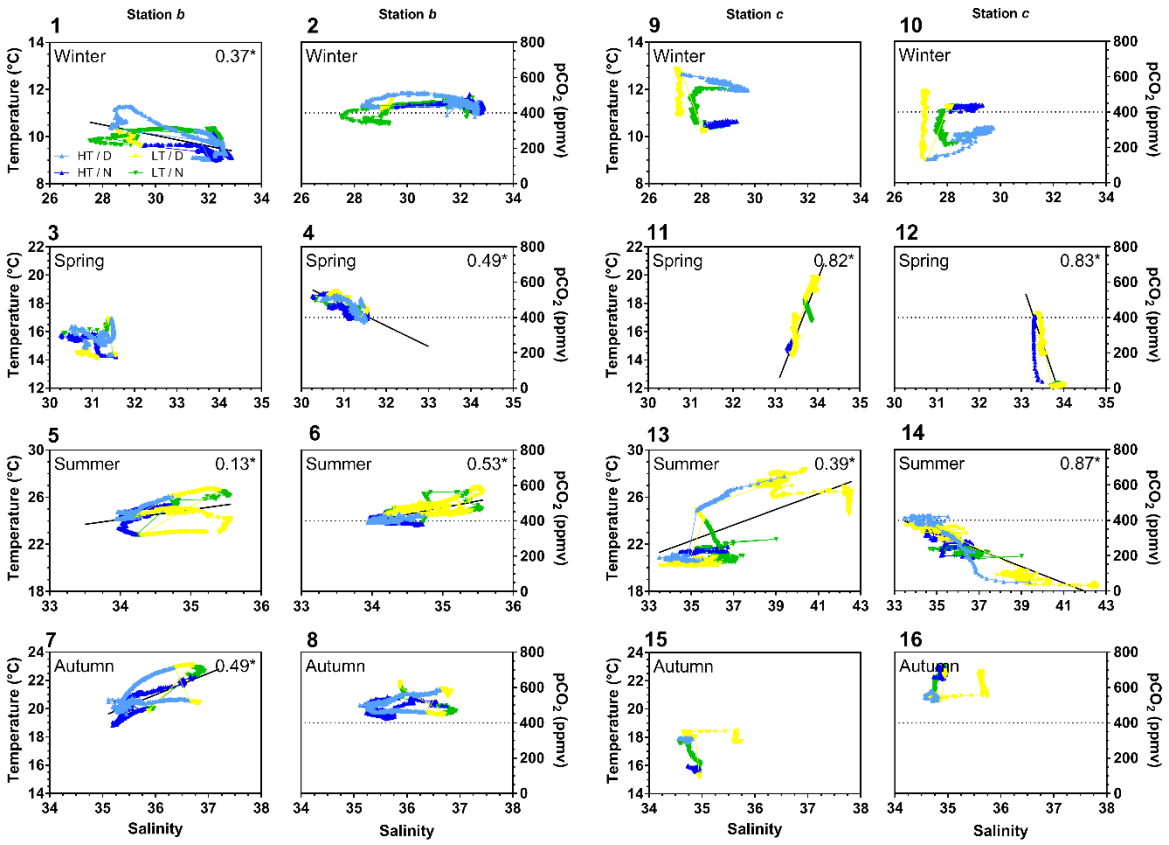

Figure 2.8: Diurnal/tidal correlation plots of temperature *vs.* salinity and water pCO_2 *vs.* salinity at stations *b* and *c* for each season. Only significant R^2 (slopes significantly different from zero; n = 1441; $p < 0.05$) are showed. HT/D: high tide day; LT/D: low tide day; HT/N: high tide night; LT/N: low tide night. At station *c*, HT periods correspond to coastal water inflows to the marsh. Note that the temperature and salinity ranges across the seasons are not the same. Horizontal dotted lines correspond to the atmospheric CO_2 concentration.

For all 24-h cycles, strong and significant correlations between pCO_2 and $NpCO_2$ were computed (Figs. 2.3-2.6). Similarly, water pCO_2 values were negatively correlated with DO saturation levels (n = 1441, $p < 0.05$), with $r_{Spearman}$ ranging from -0.67 (winter) to -0.97 (autumn) at station *a*, from -0.63 (summer) to -0.87 (autumn) at station *b*, from -0.54 (winter) to -0.86 (autumn) at station *c* and from -0.59 (winter) to -0.80 (autumn) at station *d*. At station *d*, negative correlations were obtained between measured pCO_2 and estimated Chl *a* in summer ($r_{Spearman}$ = -0.44; n = 105; $p < 0.05$) and winter ($r_{Spearman}$ = -0.60; n = 144; $p < 0.05$) (Fig. 2.6). At station *a*, in winter, the multilinear regression analyses highlighted that water pCO_2 were controlled by DO, temperature and salinity whereas over other seasons, pCO_2 were strongly controlled only by DO with the highest R^2 values (Table 2.4). At station *a*, in spring and summer, estimated TA values were weakly correlated with measured pCO_2 and pH values (Fig. S4) whereas in autumn, stronger correlations TA *versus* pCO_2 were recorded (R^2

= 0.89 and R^2 = 0.71, respectively; n = 1441; $p < 0.05$). At station *c*, water pCO_2 were mainly controlled by both salinity and DO in spring, by salinity in summer and by DO in autumn (Table 2.4). Finally, at station *d*, pCO_2 were mostly explained by salinity and DO in summer (salt farming period) and by DO and temperature in autumn/winter (total marsh confinement periods) (Table 2.4).

3.4. Air-water CO_2 flux variations

Annual means of air-water CO_2 fluxes (FCO_2) according to the W22 parametrization were estimated to be -0.01 ± 0.22, 0.22 ± 0.40, 0.18 ± 1.37 and -1.22 ± 1.71 mmol m^{-2} h^{-1} at stations *a* (sink), *b* (source), *c* (source) and *d* (sink), respectively, whereas station *F* waters behaved as a CO_2 source (0.30 ± 1.04 mmol m^{-2} h^{-1}). Large seasonal and diurnal variations were observed at the studied stations (Fig. 2.9). On average, station *a* showed positive FCO_2 values in winter and autumn (slight CO_2 source) and negative values in spring and summer (slight CO_2 sink; Table 2.3 and Fig. 2.9). At station *b*, positive FCO_2 values were estimated with maximum and minimum FCO_2 mean values occurring in winter and summer, respectively (Table 2.3 and Fig. 2.9). Station *c* behaved as a CO_2 sink in spring, summer and winter and as a strong CO_2 source in autumn (Table 2.3). At this marsh station, FCO_2 varied between -3.00 and 0.03 mmol m^{-2} h^{-1} in spring and between 0.61 and 4.61 mmol m^{-2} h^{-1} in autumn (Fig. 2.9). Station *d* behaved as a CO_2 sink in summer, autumn and winter with the largest atmospheric CO_2 uptake in autumn (Table 2.3) where FCO_2 varied between -6.03 and -1.79 mmol m^{-2} h^{-1} (Fig. 2.9).

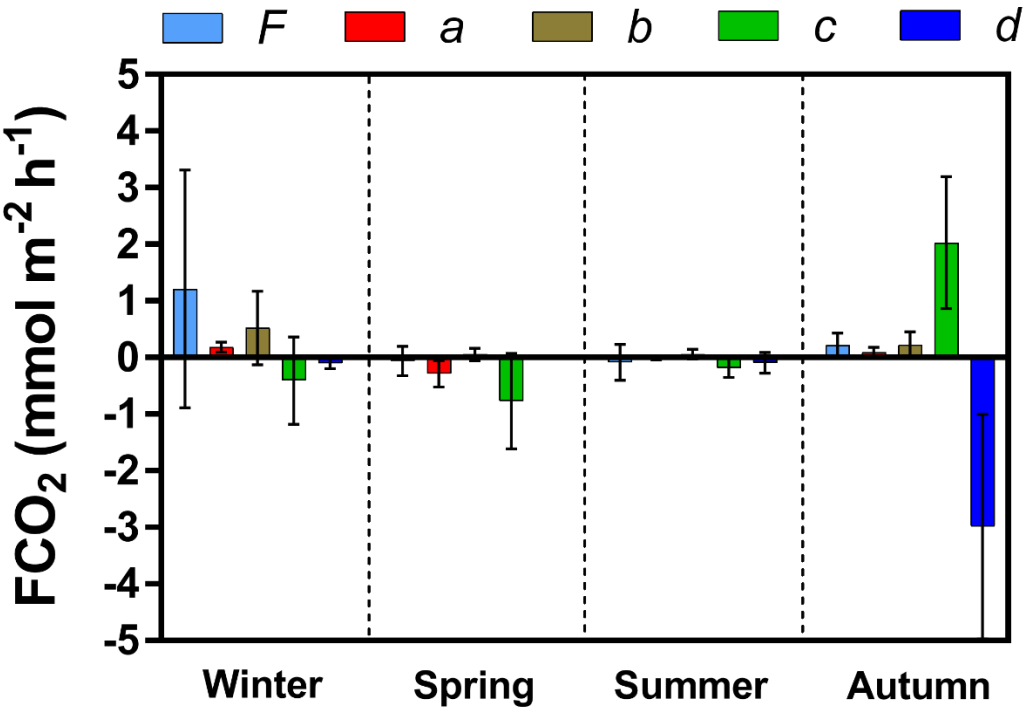

Figure 2.9: Seasonal and spatial variations in estimated CO_2 fluxes (FCO_2, in mmol m^{-2} h^{-1}) at the water-atmosphere interface at stations *F*, *a*, *b*, *c* and *d*. The means and associated standard deviations over each 24-h cycle are shown. k_{660} and FCO_2 estimations were calculated according to the R22 parametrization. FCO_2 values at stations *a* and *b* are only given for high tide periods.

Table 2.3: Seasonal means (± SD) and ranges (min - max) of wind speed (km h^{-1}), gas transfer velocity (k_{660}, cm h^{-1}) and estimated water-atmosphere CO_2 flux (FCO_2, mmol m^{-2} h^{-1}) values measured (i) once every two weeks in 2018 at station *F* (Coignot et al., 2020) and (ii) during each 24-h cycle from 2018 to 2020 at stations *a*, *b*, *c* and *d* in the present study. Air CO_2 concentrations used for FCO_2 calculations are: 408 ppm (stations *a*, *b* and *F* in 2018), 411 ppm (station *c* in spring 2019), 413 ppm (stations *c* and *d* in autumn 2019), 400 ppm (stations *c* and *d* in summer 2019) and 403 ppm (stations *c* and *d* in winter 2020; see M&M sections).

		Wind speed (km h^{-1})	**k_{660} (cm h^{-1})**		**FCO_2 (mmol m^{-2} h^{-1})**	
			W22	**RC01**	**W22**	**RC01**
Winter 2018	*F*	**19 ± 10** (7 - 29)	**7.45 ± 6.30** (0.91 - 14.24)	**11.29 ± 8.83** (2.79 - 21.62)	**1.21 ± 2.10** (0.01 - 4.35)	**1.85 ± 3.18** (0.02 - 6.60)
March 2018	*a*	**29 ± 4** (22 - 37)	**14.93 ± 4.04** (8.63 - 24.68)	**24.75 ± 9.92** (12.08 - 52.53)	**0.18 ± 0.09** (0.09 - 0.42)	**0.28 ± 0.14** (0.13 - 0.69)
March 2018	*b*	**32 ± 12** (13 - 54)	**21.39 ± 15.99** (3.02 - 54.68)	**66.17 ± 87.62** (5.06 - 285.40)	**0.52 ± 0.65** (-0.31 - 2.13)	**1.91 ± 3.45** (-0.46 - 11.11)
February 2020	*c*	**27 ± 5** (16 - 34)	**23.17 ± 10.28** (6.93 - 39.66)	**30.36 ± 13.28** (9.21 - 50.44)	**-0.40 ± 0.77** (-2.02 - 0.94)	**-0.68 ± 1.31** (-3.58 - 1.58)
February 2020	*d*	**15 ± 5** (4 - 24)	**6.92 ± 3.17** (2.15 - 14.23)	**9.46 ± 4.34** (2.96 - 19.78)	**-0.10 ± 0.09** (-0.31 - 0.09)	**-0.15 ± 0.13** (-0.41 - 0.13)
Spring 2018	*F*	**15 ± 20** (11 - 20)	**5.35 ± 3.44** (2.41 - 9.32)	**7.78 ± 3.91** (4.43 - 12.40)	**-0.06 ± 0.26** (-0.40 - 0.22)	**-0.09 ± 0.34** (-0.54 - 0.30)
April 2018	*a*	**33 ± 7** (24 - 43)	**24.01 ± 9.56** (11.85 - 38.49)	**51.64 ± 32.90** (16.94 - 108.70)	**-0.29 ± 0.23** (-0.71 - 0.11)	**-0.66 ± 0.65** (-1.81 - 0.18)
April 2018	*b*	**14 ± 5** (4 - 22)	**4.62 ± 2.96** (0.35 - 10.44)	**7.23 ± 3.46** (2.55 - 13.62)	**0.05 ± 0.11** (-0.06 - 0.33)	**0.08 ± 0.15** (-0.08 - 0.46)
May 2020	*c*	**18 ± 7** (6 - 31)	**8.99 ± 6.31** (0.86 - 22.99)	**12.86 ± 9.09** (3.17 - 37.67)	**-0.77 ± 0.84** (-3.00 - 0.03)	**-1.21 ± 1.30** (-5.09 - 0.04)
-	*d*	-	-	-	-	-
Summer 2018	*F*	**20 ± 12** (4 - 32)	**12.85 ± 10.75** (0.36 - 24.50)	**20.41 ± 17.10** (2.56 - 40.89)	**-0.09 ± 0.31** (-0.34 - 0.31)	**-0.08 ± 0.49** (-0.50 - 0.51)
July 2018	*a*	**11 ± 3** (6 - 17)	**3.50 ± 1.97** (0.89 - 7.21)	**6.35 ± 2.13** (3.55 - 10.40)	**-0.02 ± 0.03** (-0.08 - 0.08)	**-0.03 ± 0.06** (-0.14 - 0.16)
July 2018	*b*	**18 ± 7** (7 - 30)	**9.69 ± 6.37** (1.29 - 23.89)	**14.66 ± 9.28** (4.15 - 39.18)	**0.06 ± 0.08** (-0.07 - 0.22)	**0.09 ± 0.13** (-0.11 - 0.37)
July 2019	*c*	**13 ± 4** (4 - 19)	**4.56 ± 2.59** (0.43 - 9.46)	**7.59 ± 2.92** (3.16 - 13.32)	**-0.19 ± 0.17** (-0.70 - 0.01)	**-0.33 ± 0.24** (-1.01 - 0.02)
July 2019	*d*	**15 ± 6** (2 - 23)	**7.12 ± 4.60** (0.11 - 14.77)	**10.77 ± 5.72** (2.41 - 20.96)	**-0.09 ± 0.18** (-0.43 - 0.20)	**-0.12 ± 0.27** (-0.60 - 0.29)
Autumn 2018	*F*	**17 ± 5** (11 - 22)	**6.37 ± 4.09** (2.25 - 10.83)	**9.01 ± 4.98** (4.08 - 14.46)	**0.21 ± 0.22** (-0.02 - 0.56)	**0.30 ± 0.29** (-0.02 - 0.75)
September 2018	*a*	**11 ± 6** (4 - 20)	**3.55 ± 3.27** (0.36 - 8.98)	**6.21 ± 3.66** (2.65 - 12.53)	**0.09 ± 0.09** (0.01 - 0.30)	**0.15 ± 0.11** (0.01 - 0.41)
September 2018	*b*	**17 ± 6** (11 - 32)	**7.32 ± 5.46** (2.90 - 24.27)	**9.46 ± 7.91** (4.02 - 42.48)	**0.22 ± 0.23** (0.07 - 1.00)	**0.28 ± 0.33** (0.05 - 1.75)
October 2019	*c*	**35 ± 8** (20 - 48)	**27.39 ± 11.52** (9.01 - 48.79)	**63.79 ± 42.95** (12.58 - 179.80)	**2.03 ± 1.17** (0.61 - 4.61)	**4.86 ± 4.22** (0.85 - 16.98)
October 2019	*d*	**42 ± 7** (31 - 54)	**38.22 ± 12.55** (20.54 - 62.36)	**122.80 ± 84.13** (34.76 - 325.40)	**-3.43 ± 1.09** (-6.03 - -1.79)	**-10.91 ± 7.35** (-31.46 - -3.03)

Table 2.4: Stepwise multilinear regression analyses to test the contribution of physicochemical variables on water pCO_2 variations through the percentage of explained variance (adjusted R^2). Each selected multilinear model ($p < 0.001$, $n = 1441$) had the highest adjusted R^2 value with all variables explaining at least 5% of the pCO_2 variation. In bold is indicated the parameter explaining at least 50% of the pCO_2 variation. Input variables: DO-sat. (dissolved oxygen saturation level), T (water temperature), S (salinity) and TU (turbidity). The statistic (F) and adjusted R^2 (adj. R^2) are given.

			Equations	**F**	**adj. R^2**
Winter	March 2018	*a*	pCO_2 = 2227.7 - 3.7 **DO-sat.** - 19.9 T - 38.2 S	1004	67.7%
	March 2018	*b*	pCO_2 = -373.8 + 21.1 S + 0.8 TU + 15.9 T	377	43.9%
	February 2020	*c*	pCO_2 = 1460.5 - 158.3 **T** + 7.0 DO-sat.	1180	62.1%
	February 2020	*d*	pCO_2 = 446.6 - 10.8 DO-sat. + 99.1 T	4723	86.8%
Spring	April 2018	*a*	pCO_2 = 949.8 - 5.5 **DO-sat.**	8255	85.2%
	April 2018	*b*	pCO_2 = 2542.0 - 4.0 **DO-sat.** - 61.7 S + 14.2 T	1923	80.0%
	May 2019	*c*	pCO_2 = 21777.7 - 640.8 **S** - 0.6 DO-sat.	3668	83.6%
	-	*d*	-		-
Summer	July 2018	*a*	pCO_2 = 747.2 - 3.2 **DO-sat.**	30524	95.5%
	July 2018	*b*	pCO_2 = -2440.0 + 100.8 **S** - 25.4 T	3330	82.7%
	July 2019	*c*	pCO_2 = 1961.5 - 46.7 **S**	9401	86.8%
	July 2019	*d*	pCO_2 = -961.8 + 40.1 **S** - 1.2 DO-sat.	47983	98.5%
Autumn	September 2018	*a*	pCO_2 = 923.1 - 4.1 **DO-sat.**	34905	96.4%
	September 2018	*b*	pCO_2 = 782.0 - 2.8 **DO-sat.** + 1.1 TU	3066	81.0%
	October 2019	*c*	pCO_2 = 1009.3 - 4.9 **DO-sat.**	8831	86.0%
	October 2019	*d*	pCO_2 = 1932.7 + 1.6 **DO-sat.** - 122.7 T	3253	81.9%

4. Discussion

4.1. Biogeochemical parameter relationships and pCO_2 controls along the shelf - estuary - marsh continuums

At the tidal estuary (*a*) and its associated channel (*b*), seasonal non-thermal effects (biological and tidal effects) inducing heterotrophy in winter and autotrophy in summer were offset by thermal effects and resulted in low seasonal variations of water pCO_2 (Fig. 2.7). Similar observations were reported in two marine-dominated estuaries (Jiang et al., 2008) and in the Arcachon coastal lagoon (Polsenaere et al., 2022). In the estuarine waters here, thermal effects decreased and increased in situ pCO_2 values of 30 and 40% in winter and summer, respectively. On the contrary, at the rewilded artificial salt marsh (*c*), seasonal water pCO_2 were strongly controlled by non-thermal effects promoting autotrophy both in spring and summer and heterotrophy in autumn, mostly due to macroalgae activity whereas at the working artificial salt marsh (*d*), thermal effects in summer and biological effects in autumn strongly controlled seasonal water pCO_2 (Fig. 2.7).

At the diurnal scale, the biological influence on continuum water pCO_2 dynamics through autotrophic and heterotrophic processes was significant at each station as endorsed by strong linear relationships between pCO_2 and DO, especially in autumn (Table 2.4). At the tidal estuary (*a*), from spring to autumn, diurnal pCO_2 variations were mostly controlled by the photosynthesis versus respiration balance of planktonic communities; indeed, more than 80% of the pCO_2 variance was modelled with DO only (Table 2.4). Dai et al. (2009) highlighted that CO_2 biogeochemical processes in coastal environments such as our estuary are generally controlled by non-thermal effects, like biological activity, compared to more open systems. Several studies have shown a major biological control on diurnal pCO_2 variations in coastal systems such as the temperate Bay of Brest (France; Bozec et al., 2011), the temperate Arcachon lagoon (France; Polsenaere et al., 2022), the shallow subtropical estuary in Tampa Bay (USA; Yates et al., 2007) and the tropical coastal embayment at Guanabara Bay (Brazil; Cotovicz Jr. et al., 2015). At the rewilded marsh (*c*), while in spring and summer, the high primary production of macroalgae induced large periods of water CO_2 undersaturation with respect to the atmosphere, winter pCO_2 variations were rather induced by planktonic community activity (ciliates > $2\ 10^4$ cell L^{-1}; unpublish result). At the working marsh (*d*), the negative correlations between pCO_2 and Chl *a* associated with strong non-thermal contributions ($\Delta NpCO_2$ = 318 ppmv in summer for instance) showed a major biological influence on diurnal pCO_2 variations as well. By comparison, in a *Zostera marina* meadow (South Bay, USA), Berg et al. (2019) measured similar diurnal fluctuations of water pCO_2

that were directly controlled by seagrass metabolism with diurnal ranges of 528 and 603 ppmv in spring and summer, respectively.

Tidal advection of waters between continental shelf and salt marshes also significantly controlled pCO_2 dynamics and associated station biogeochemical status. This control was supported by the linear relationships between water pCO_2 and salinity as observed at each station from winter to summer whereas, relationships with turbidity were rather related to the hydrodynamic forcing on water pCO_2 (Table 2.4). At the tidal estuary (*a*) and its associated channel (*b*), daytime incoming tides created a significant decrease in water pCO_2 since the advected shelf waters were CO_2 undersaturated with respect to the atmosphere contrary to estuarine waters. In the Arcachon lagoon, seasonal measurement cycles also showed a strong tidal control on inorganic C parameters with lower pCO_2 values measured at high tide than at low tide irrespective of day or night status (Polsenaere et al., 2022). Even stronger tidal influences on water pCO_2 (from 1380 to 4770 ppmv) were observed during a summer cycle in the Gaderu Creek mangrove (Borges et al., 2003). In summer, the large pCO_2 decrease in the studied estuarine waters at ebbing tide the day, associated with strong DO saturation level increase, was probably due to CO_2 undersaturated water exports from the productive salt marshes upstream. Indeed, in spring and summer, the rewilded marsh waters (*c*) were CO_2 depleted due to strong autotrophy activity. Conversely, more CO_2-enriched coastal water inflows from the shelf and the estuary into the marsh instantly produced significant salinity decreases and pCO_2 increases (Table 2.4). Therefore, at each semi-diurnal tidal cycle, horizontal advection had significant effects on water pCO_2 dynamics (except during marsh confinement) but variations strongly depended on the biogeochemical state (CO_2 sink/source) of advected waters from upstream/downstream and the ecosystem typology (estuary, marsh, channel).

4.2. Continuum typologies revealed from measured biogeochemical parameters

In the coastal ocean, a strong influence of ecosystem typology (continental shelf, estuary, marsh) on biogeochemistry is generally observed and particularly, on inorganic C (Bauer et al., 2013). In our study, in 2018, watershed-influenced shelf waters (*F*) were characterized by lower salinity values than the Atlantic Ocean (35.6; Vandermeirsch, 2012), confirmed over the 2000-2017 reference period (Belin et al., 2021: REPHY, 2021). However, shelf waters showed a rather weak influence of terrestrial inputs on water pCO_2 dynamics (annual non-

significant salinity and pCO_2 relationship, p = 0.88). At this shelf station, phytoplankton bloom with centric diatoms generally occurs in spring and summer (Guarini et al., 2004) and can induce water CO_2 undersaturation as also observed on the Belgian continental shelf (Borges and Frankignoulle, 1999). Along the continuum, the tidal estuary (*a*) influenced by buffered shelf waters was CO_2 undersaturated at 4% in winter and 82% in spring/summer that could be attributed to coastal water autotrophic activity at this period. A previous study carried out in the same estuarine waters measured Chl *a* concentrations from 0.2 (winter) to 3.5 µg L^{-1} (spring/summer) and a Chl *a* export suggesting a net primary production within this tidal estuary (Bel Hassen, 2001). Additionally, Savelli et al. (2019) observed in a nearby intertidal zone that microphytobenthos (MPB) may also contribute to water CO_2 undersaturation and to the overall water column Chl *a* concentration through tidal resuspension. Due to the small insulary catchement area (1200 ha) consisting only of salt marshes (no terrestrial water input), the CO_2 dynamics in the tidal estuary (*a*) is different from other estuaries worldwide (Borges and Abril, 2011). Similarly, the marine-dominated estuary of Sapelo Sound (USA) was also characterized by lower water pCO_2 values than river-dominated ones (Borges and Abril, 2011) but bacterial remineralization of organic carbon produced by *Spartina* in nearby salt marshes strongly increased water pCO_2 in summer (Jiang et al., 2008) contrarily to our studied estuary.

Overall, channel (*b*) waters between the estuary and salt marshes showed the longest periods of CO_2 oversaturation with respect to the atmosphere. At this channel station, strong hydrodynamic forcings during incoming and ebbing tides produced more turbid waters due to organic matter resuspension from muds (Guarini et al., 2008). It probably limited the primary production (phytoplankton, MPB) by low light availability in water column (Cloern, 1987) and, on the contrary, favoured heterotrophic processes (Polsenaere et al., 2022). In channel waters, we recorded lower DO concentrations (-10%) and higher pCO_2 values (+10%) than in estuarine waters under similar salinity ranges and meteorological conditions. In channels at the same location, Tortajada (2011) measured POC/Chl *a* > 200 mg mg^{-1} throughout the year and even POC/Chl *a* > 600 mg mg^{-1} in autumn. This detrital/heterotrophic organic material may indicate microbial mineralization processes from MPB and confirm the water CO_2 oversaturation periods. However, our studied channel (*b*) showed lower water pCO_2 values than those from other coastal channel systems probably due to low terrestrial water inputs upstream/downstream over the estuary (*a*). The Sancti Petri Channel waters and its nearby salt marshes between the Atlantic Ocean and the Cadiz Bay (Spain) were also mainly CO_2

oversaturated (281 - 862 ppmv), due to DIC inputs from diagenetic processes of organic matter in mudflats that constitute a CO_2 source to water column (Burgos et al., 2018). Indeed, within the Duplin River salt marsh-estuary coastal system (USA), higher summer pCO_2 and DIC values were recorded at low tide in channel waters (12000 ppmv and 4300 µmol L^{-1}, respectively) than at high tide in marsh waters (1600 ppmv and 2200 µmol L^{-1}, respectively; Wang et al., 2018).

Contrary to estuarine and channel waters, artificial salt marshes (*c* and *d*) waters were characterized by the lowest turbidity and highest salinity values due to longer water residence times. These lower hydrodynamic conditions promoted the development of primary producers and as a result, biological CO_2 uptake associated with the highest DO saturation levels. In turn, the salt marshes showed lower water pCO_2 values and longer water CO_2 undersaturation periods mainly due to a strong macrophyte activity (macroalgae at rewilded marsh and seagrasses at working marsh) than the tidal estuary and elsewhere similar wetland typologies (Borges et al., 2003; Burgos et al., 2018; Wang et al., 2018; Berg et al., 2019; Polsenaere et al., 2022; Song et al., 2023). Unlike seagrasses which are known to be important blue C systems (Mcleod et al., 2011), macroalgae developing in coastal wetlands have a limited capacity to store C over the long-term. However, studies have shown their potential contribution to coastal blue C by (i) storing large organic matter quantities in their living biomass through their high primary production (Raven, 2018) and (ii) transferring it to adjacent systems through tides and storage in coastal sediments (Duarte and Cebrián, 1996; Hill et al., 2015; Krause-Jensen and Duarte, 2016). Our pCO_2 observations are in accordance with these reports with the role of C storage by macrophytes in these shallow salt marshes.

4.3. Temporal carbon modulation by management practices

Management practices at the artificial salt marshes correspond to specific water lock actions linked to anthropogenic activities. They can strongly modulate water fluxes from the estuary and thereby influence marsh pCO_2 dynamics. At the rewilded marsh (*c*), the specific management practice by the NNR produced favourable conditions for free floating macroalgae development from early spring to late summer under low water marsh hydrodynamic and high air and water temperature conditions (Newton and Thornber, 2013). These macroalgae indicate a degraded-eutrophic status of the marsh waters with excess nutrient inputs, as described for other coastal ecosystems (Teichberg et al., 2010; Le Fur et al.,

2018). In our study, nearby marsh aquafarming activities occurring upstream from the estuary (Paticat, 2007; Tortajada, 2011) can communicate with the rewilded marsh (*c*) through channels and result in high nutrient conditions which could explain observed macroalgae blooms. Indeed, at the station *b* channel in September 2018, high DIN concentrations were reported (60 µmol L^{-1}; unpublished results). Moreover, shelf waters influenced by terrestrial inputs in winter could also lead to nutrient inputs at the rewilded marsh. Indeed, at the station *F* shelf in winter 2019, NO_3^- ranged between 29 and 107 µmol L^{-1} (Belin et al., 2021; REPHY, 2021). Consequently, these fast-growing macroalgae probably prevented the growth of phytoplankton and seagrasses by nutrient and oxygen competition and light limitation in the water column (Sand-Jensen and Borum, 1991; Le Fur et al., 2018). Simultaneously, in spring and summer, the large water CO_2 undersaturation periods due to the macroalgae autotrophy were maintained through occasional inflows of CO_2 oversaturated channel waters (weak tidal amplitudes). This result is confirmed by significantly higher salinity values in the rewilded marsh waters than in the channel waters during the spring and summer sampling periods (Table 2.2). On the contrary, macroalgae degradation in autumn probably by microbial remineralization processes (Hill et al., 2015) produced in turn the highest pCO_2 values and the longest oversaturation periods recorded in marsh waters. These heterotrophic processes were confirmed by high NH_4^+ levels (62 µmol L^{-1}; unpublished results) and low DO saturation levels recorded at this period and as described by Newton and Thornber (2013).

Contrarily to the rewilded marsh (*c*), the working marsh (*d*) is managed for salt production in the upstream ponds along the continuum and is directly connected to the estuary (*a*) with no channel in between (Fig. 2.10). Salt production requires a subtle lock hydraulic management of the marsh depending on the frequency of the coastal water supplies that are mainly controlled by the salt manufacturer and meteorological conditions (rainfall, sunshine and wind) to favour the evaporation process (Paticat, 2007). Therefore, contrary to rewilded marsh, coastal water inflows to the working marsh were performed sparingly with small daily volumes to limit these water mixing effects (i.e. rapid accumulation of large water volumes through rainfall events or spring tides stop the increase in temperature and salinity in marsh waters; Paticat, 2007). At the working marsh in summer, water pCO_2 were significantly higher than those measured at the same period at the rewilded marsh but reflected those from the estuary (Table 2.2). This could also be linked to a lower activity of the primary producers during the summer period dedicated to salt production as confirmed by higher thermal than non-thermal effects on water pCO_2 (Fig. 2.7). On the other hand, in autumn and winter, lower

hydrodynamic conditions due to lock closure (standstill salt farming activity) led to low water turbidity (< 2.0 NTU) and nutrient input into the marsh (DIN < 2.0 µmol L^{-1}; unpublished results) and the growth of seagrasses and phytoplankton produced, in turn, the lowest water pCO_2 values. Overall, in Mediterranean poly-euhaline lagoons, Le Fur et al. (2018) confirmed that nutrient pollution influence the contribution of primary producers from perennial seagrasses in oligotrophic waters to fast-growing macroalgae in eutrophic waters. Similarly, other studies have suggested that the coastal ecosystem management by reducing anthropogenic nutrients could favour blue C ecosystems such as seagrasses and salt marshes (Macreadie et al., 2017, Palacios et al., 2021).

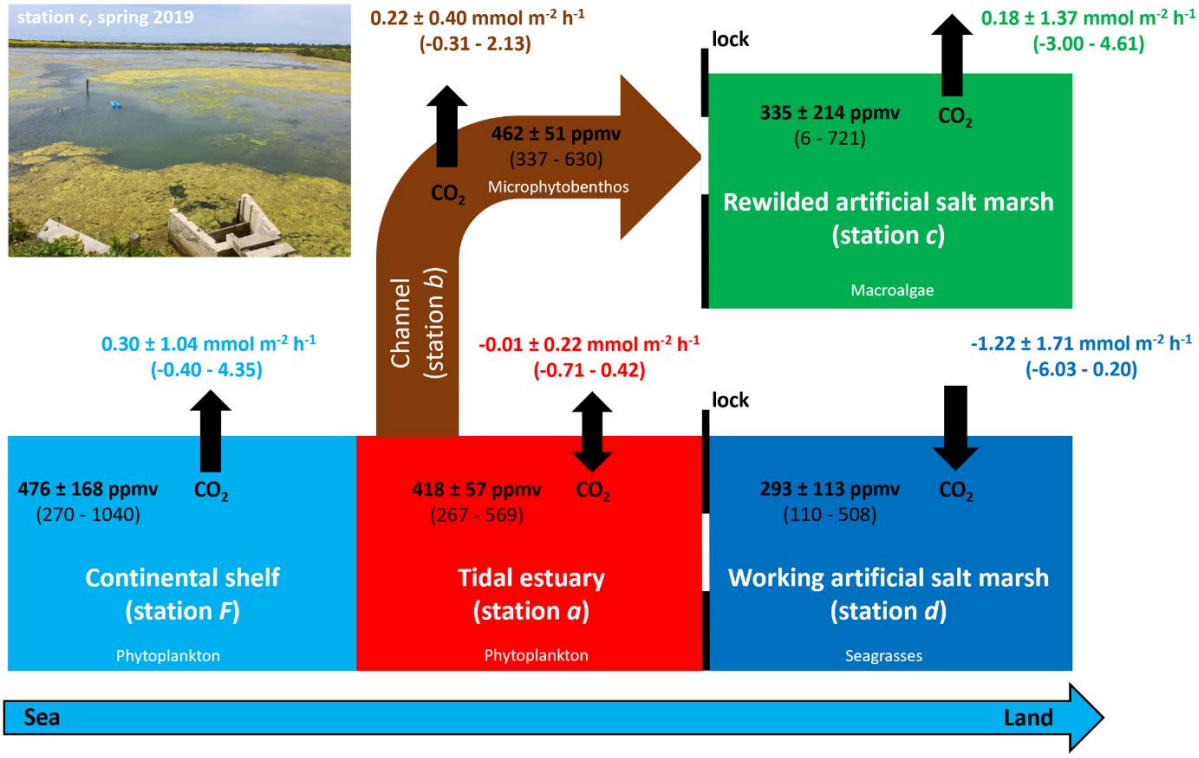

Figure 2.10: CO_2 budget over the two aquatic sea - land continuums: (1) continental shelf - estuary - channel - rewilded artificial salt marsh and (2) continental shelf - estuary - working artificial salt marsh. Annual means (± SD) and ranges (min - max) of water pCO_2 (ppmv) and air-water FCO_2 (mmol m^{-2} h^{-1}) are showed. The picture of station *c* in spring 2019 (© P. Polsenaere) allows to visualize the macroalgae bloom.

4.4. Metabolism assessment of the sea-land continuums

The tidal estuary (*a*) behaved on average as a yearly CO_2 sink close to the atmospheric equilibrium (Fig. 2.10), although a significant sink was measured in the spring/summer due to autotrophic activity of phytoplankton in coastal waters. Conversely, over the same meteorological periods, the channel (*b*) was a net annual source from its turbid waters to the atmosphere due to several water CO_2 oversaturation periods (Fig. 2.10), particularly in winter, characterized by high gas transfer velocities (Table 2.3). In the Arcachon lagoon, estimated atmospheric CO_2 sources were higher with seasonal means ranging from 0.06 ± 0.04 (winter) to 0.62 ± 0.66 mmol m^{-2} h^{-1} (summer) with significant diurnal fluctuations (Polsenaere et al., 2022). In our study, eutrophic waters of the rewilded marsh (*c*) behaved as a yearly source of atmospheric CO_2 (Fig. 2.10), when macroalgae degradation produced strong atmospheric CO_2 effluxes. On the contrary, oligotrophic waters of the working marsh (*d*) behaved as a large yearly CO_2 sink (Fig. 2.10), favoured by low tidal advection in the absence of salt-farming activities. Within the Duplin River salt marsh-estuary system, both channel and marsh waters degassed CO_2 to the atmosphere and, unlike our stations, the highest and lowest sources were recorded in summer (5.50 and 3.90 mmol m^{-2} h^{-1} from channel and marsh waters, respectively) and in winter (0.70 and 0.60 mmol m^{-2} h^{-1} from channel and marsh waters, respectively), respectively (Wang et al., 2018). Overall, the Duplin system emits more atmospheric CO_2 than the Fier d'Ars system, probably due to its more intense estuarine heterotrophic metabolism.

In autumn, the lack of variations in wind speeds between stations *a* and *b* in 2018 and between stations *c* and *d* in 2019, whereas atmospheric CO_2 exchanges significantly changed, highlighted the predominance of air-water CO_2 gradients in the control of flux directions either as a sink or a source (Table 2.3). However, at the seasonal scale, turbulence processes measured at the air-water interface played an important role in CO_2 flux variability and magnitude. For instance, at station *a* between spring and summer and at station *b* between winter and summer, wind speed variability produced significant FCO_2 variations although no significant air-water CO_2 gradients were measured (Table 2.3). Atmospheric exchanges in salt marshes are therefore dependent on the CO_2 saturation state of the water column considering that the wind only acts as a driver of the flux (Polsenaere et al., 2022). Moreover, the methodological calculations and associated differences chosen for the exchange coefficient parameterizations (higher fluxes with RC01 than with W22; Table 2.3) may produce even

more contrasts in the estimated air-water FCO_2 (Cotovicz Jr. et al., 2015; Polsenaere et al., 2022).

By scaling-up and considering stations *a* and *b* together along the continuum, estuarine and channel waters behaved as an annual atmospheric CO_2 source of 7.3 g C m^{-2} yr^{-1}. The rewilded marsh emitted 17.5 g C m^{-2} yr^{-1} to the atmosphere whereas, the working marsh absorbed 97.7 g C m^{-2} yr^{-1} from the atmosphere. A larger scale study along three shelf – estuary – tidal wetland continuums on the Atlantic coast of the United States also showed strong spatial variations in atmospheric CO_2 fluxes with uptake to wetland and shelf waters (523.2 ± 148.1 and 10.5 ± 1.8 g C m^{-2} yr^{-1}, respectively) and a source from estuarine waters (110.0 ± 44.5 g C m^{-2} yr^{-1}; Najjar et al., 2018). During our study, contrasting coastal stations were sampled via seasonal 24-h cycles to estimate the air-water CO_2 exchanges. However, longer seasonal measurement periods would be more representative of the strong temporal variability in k_{660}, water pCO_2 and other biogeochemical parameters. At the nearby tidal salt marsh (*e*), emerged for 75% of time during low tides and neap tides, another flux methodology using the atmospheric Eddy Covariance technique was deployed to continuously measure in situ CO_2 fluxes at the ecosystem scale coming from all habitats (aquatic and terrestrial vegetations, mudflats, channels). Over the year 2020, a net uptake of 483 g C m^{-2} yr^{-1} from the atmosphere was measured, indicating a stronger CO_2 sink in tidal marshes than artificial marshes due to higher halophytic plant photosynthesis activity. However, it is also important to study the whole marsh metabolism taking terrestrial and aquatic compartments into account and distinguishing their respective contributions to atmospheric fluxes and the regional C budgets of the associated marshes (Mayen et al., 2023).

5. Conclusion

Along the continuums, estuarine and channel waters were slightly oversaturated in CO_2 characterized by seasonal compensations of thermal and non-thermal effects whereas, upstream marsh waters were mostly undersaturated in CO_2 due to stronger biological activity and longer water residence times. At the diurnal/tidal scale, our high-resolution analyses highlighted large water pCO_2 variations in salt marshes, controlled by production and respiration of macrophytes and coastal water inflows. However, anthropogenic management in salt marshes could strongly influence the contribution and turnover of macrophytes and, consequently, the marsh CO_2 sink/source behaviour. Due to eutrophication in the rewilded

marsh, development of the fast-growing macroalgae produced an overall net annual atmospheric CO_2 source through their degradation. Our results suggest a winter marsh confinement follow by drying up to limit nutrient inputs and macroalgae development and on the contrary, favour rather slow-growing macrophytes (i.e. seagrasses) which could ultimately contribute to blue C sequestration.

Acknowledgements

We would like to sincerely thank the oyster farmers for their help with taking samples at station *a*, Julien Gernigon from the Lilleau des Niges NNR (LPO) and Brice Collonier from the Loix Ecomuseum for their help and the information given at stations *b*, *c*, *d* and *e*. We are grateful to our colleagues Jean-Michel Chabirand, James Grizon and Philippe Geairon for their help with field sensor deployments and QGIS work. We also thank Quentin Ternon, Gabriel Devique and Jonathan Deborde for their contribution in the field. This paper is a contribution to the Master and Ph.D. thesis of Jérémy Mayen (Ifremer funding), the ANR-PAMPAS project (Agence Nationale de la Recherche « Evolution de l'identité patrimoniale des marais des Pertuis Charentais en réponse à l'aléa de submersion marine », ANR-18-CE32-0006) and the CNRS-INSU LEFE-DYCIDEMAIM project (DYnamique du Carbone aux Interfaces D'Échange des MArais tIdaux teMpérés). The English language was edited by Sara Mullin (Ph.D.).

Credit authorship contribution statement

Jérémy Mayen: Methodology, Software, Validation, Formal analysis, Investigation, Writing – original draft, Writing – review & editing. **Pierre Polsenaere:** Conceptualization, Methodology, Software, Validation, Formal analysis, Investigation, Resources, Writing – review & editing, Supervision, Project Administration, Funding acquisition. **Aurore Regaudie de Gioux:** Writing – review & editing, Supervision, Funding acquisition. **Christine Dupuy:** Validation, Writing – review & editing. **Marie Vagner:** Writing – review & editing, Funding acquisition. **Jean-Christophe Lemesle:** Resources. **Benoit Poitevin:** Resources. **Philippe Souchu:** Validation, Writing – review & editing, Supervision, Funding acquisition.

Supplementary materials (Mayen et al., 2023)

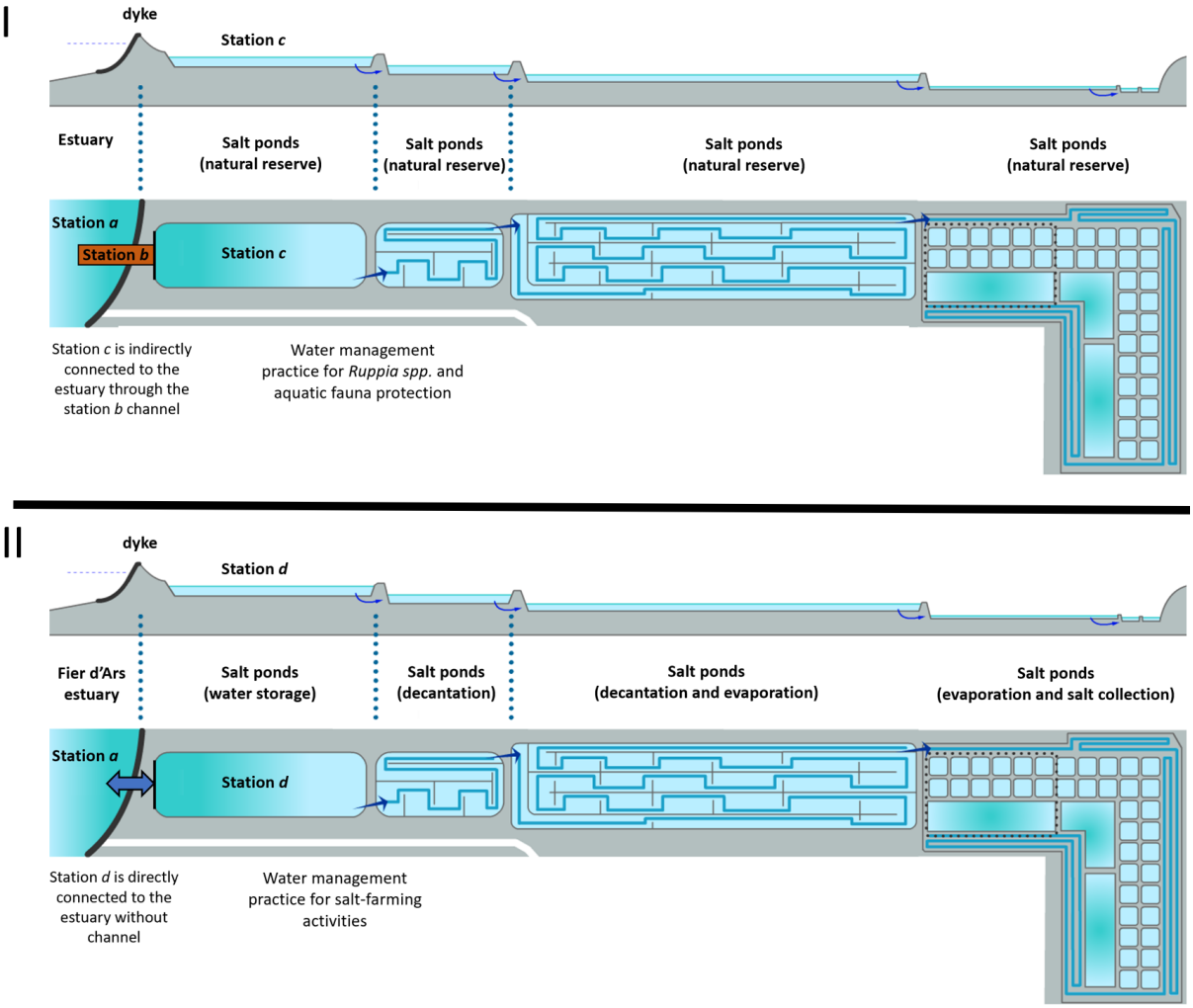

Figure S1: Artificial salt marsh complexes within the National Natural Reserve (I; location of station *c*) and within a salt-farm (II; location of station *d*). Station *c* is a rewilded marsh for which water management practices depend on the protection of *Ruppia spp.* and aquatic fauna in upstream ponds. Station *d* is a working marsh used for water storage and for which water management practices depend on the salt-farming activities in upstream ponds.

Table S1: In situ 24-h measurements carried out in the present study across seasons from 2018 to 2020 at stations *a*, *b*, *c* and *d* along the two aquatic continuums on Ré Island (France). High tide and low tide for each 24-h cycle are indicated. Tidal information is taken from the SHOM station (9 km away from studied stations; Fig. 1; www.shom.fr). The same diurnal/tidal synchronism (high and low tides at the same period of the day) during each season and station was adopted. Over the Breton Sound continental shelf at station *F*, the same biogeochemical parameters were used for the present study and biweekly measured at high tide by Coignot et al. (2020) over the year 2018: four samplings in winter (17/01/2018 14:15; 30/01/2018 13:55; 15/02/2018 14:03; 03/03/2018 13:40), four samplings in spring (17/04/2018 14:25; 26/04/2018 12:20; 29/05/2018 13:40; 14/06/2018 14:00); four samplings in summer (28/06/2018 13:05; 11/07/2018 12:45; 09/08/2018 10:45; 11/09/2018 08:50) and five samplings in autumn (26/09/2018 13:45; 09/10/2018 13:25; 24/10/2018 12:50; 08/11/2018 08:15; 11/12/2018 09:50). U.T. Universal time.

		Date	24-h cycle start-end (U.T.)	Tidal amplitudes	High/Low tide hours (U.T.)
Winter	*a*	14/03- 15/03/2018	07:00 - 07:00	61	14:28 / 20:23
				67	02:34 / 08:41
	b	15/03 - 16/03/2018	09:00 - 09:00	73	14:57 / 21:01
				78	03:05 / 09:19
	c	10/02 - 11/02/2020	09:00 - 09:00	106	16:49 / 22:55
				108	05:05 / 11:25
	d	11/02 - 12/02/2020	10:15 - 10:15	108	17:30 / 23:41
				107	05:47 / 12:10
Spring	*a*	25/04 - 26/04/2018	05:00 - 05:00	58	12:52 / 18:16
				64	01:17 / 06:58
	b	26/04 - 27/04/2018	07:00 - 07:00	70	13:42 / 19:20
				76	02:05 / 07:54
	c	01/05 - 02/05/2019	11:00 - 11:00	61	14:06 / 20:01
				66	02:12 / 08:18
	d	-	-	-	-
Summer	*a*	09/07 - 10/07/2018	05:00 - 05:00	57	12:46 / 18:26
				63	01:09 / 06:55
	b	10/07 - 11/07/2018	07:00 - 07:00	68	13:38 / 19:26
				75	02:04 / 07:52
	c	16/07 - 17/07/2019	09:00 - 09:00	75	15:31 / 21:50
				76	03:57 / 10:07
	d	17/07 - 18/07/2019	11:00 - 11:00	77	16:04 / 22:29
				78	04:28 / 10:37
Autumn	*a*	19/09 - 20/09/2018	05:00 - 05:00	33	12:24 / 17:53
				37	01:03 / 06:30
	b	20/09 - 21/09/2018	06:30 - 06:30	43	13:13 / 19:00
				49	01:46 / 07:27
	c	14/10 - 15/10/2019	10:00 - 10:00	87	15:51 / 22:20
				88	04:03 / 10:37
	d	15/10 - 16/10/2019	11:15 - 11:15	87	16:16 / 22:50
				86	04:28 / 11:08

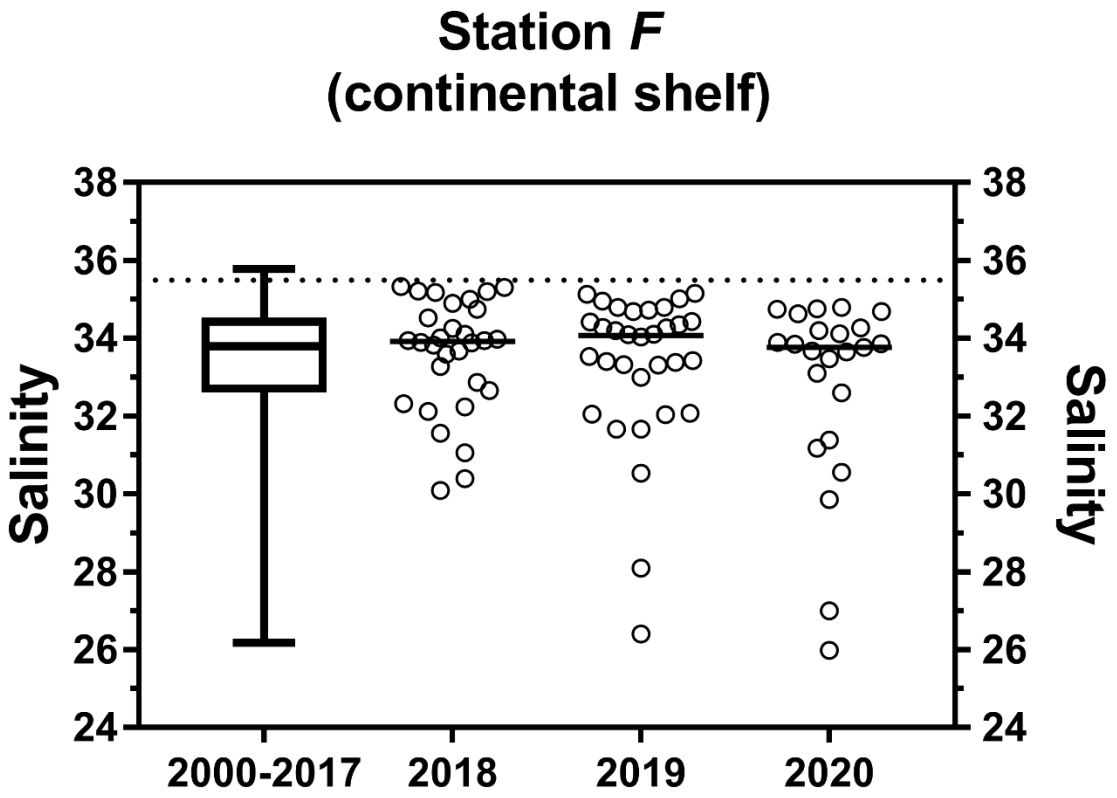

Figure S2: Water salinity at station *F* over the Breton Sound continental shelf (France) measured biweekly by the REPHY monitoring network (Belin et al., 2021) over the 2000-2017 period (boxplot) and over the years 2018, 2019 and 2020 (values and medians). The horizontal dotted line corresponds to the salinity of the Atlantic Ocean (35.6; Vandermeirsch, 2012).

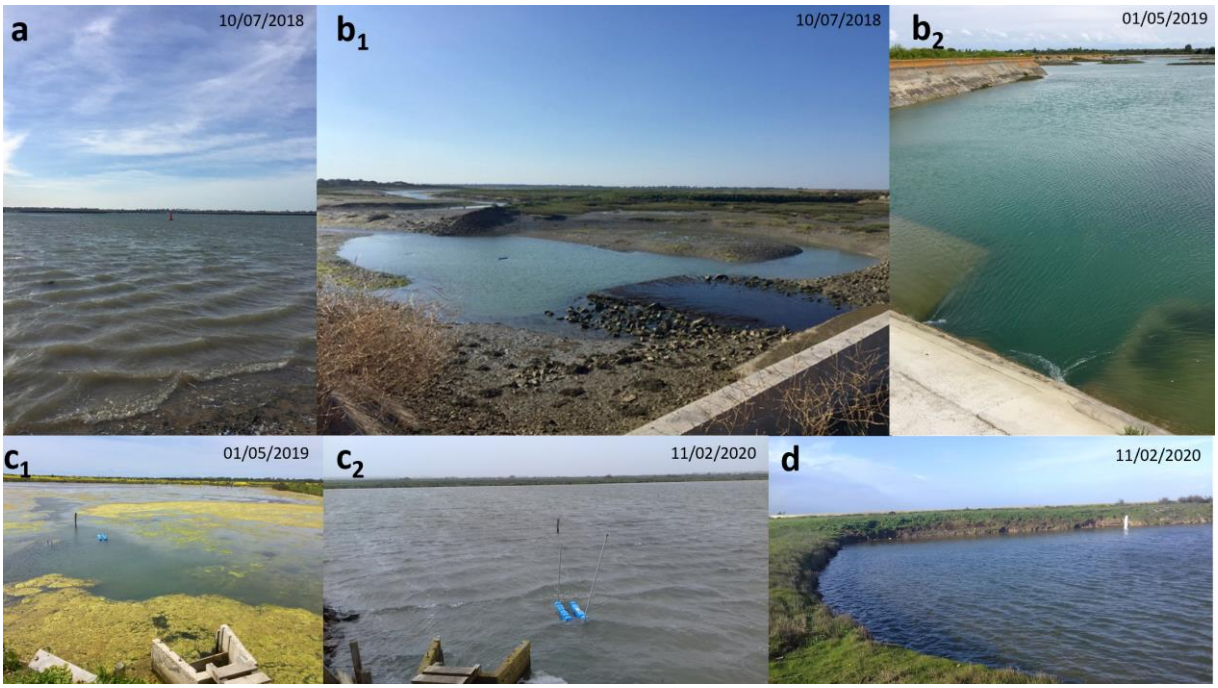

Figure S3: Station *a*, *b*, *c* and *d* pictures (© P. Polsenaere). **a** shows station *a* (Fier d'Ars estuary at low tide). **b1** and **b2** show station *b* (channel) at low and high tide, respectively. **c1** and **c2** show station *c* (rewilded artificial salt marsh) at two contrasting seasons with and without macroalgae bloom, respectively. **d** shows station *d* (working artificial salt marsh).

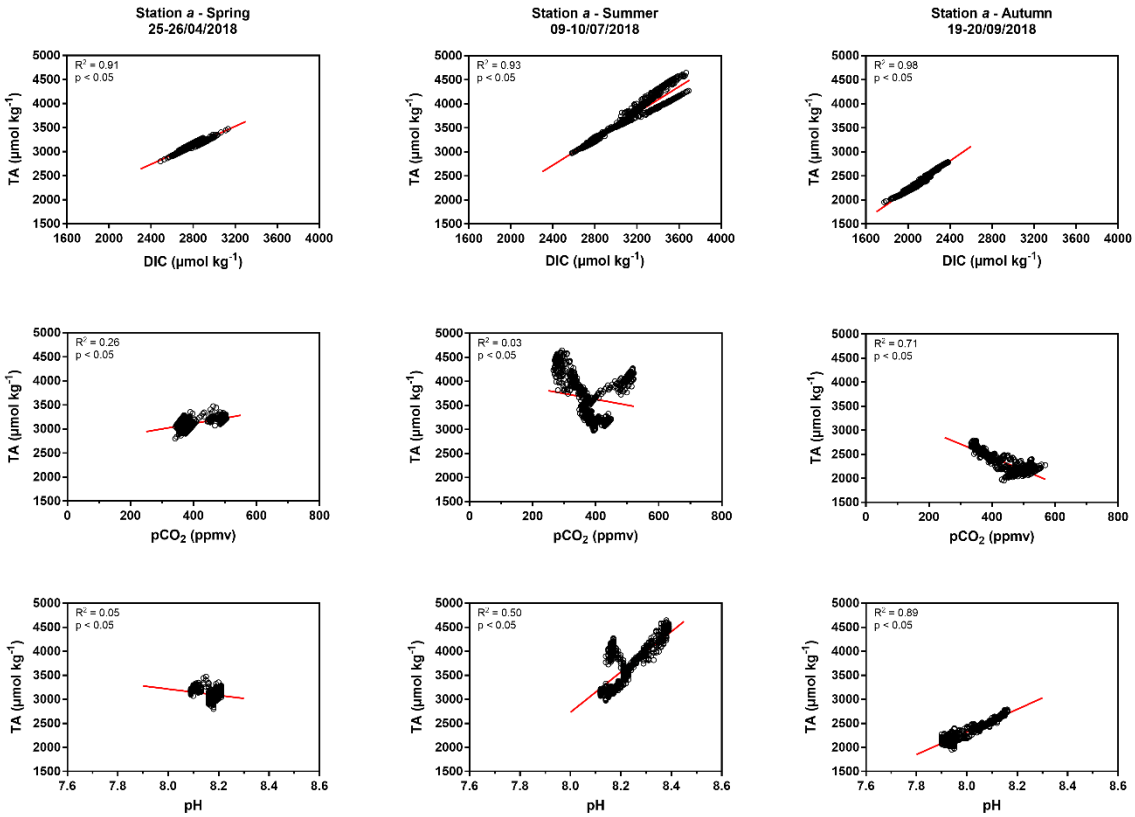

Figure S4: Significant linear regressions (slopes significantly different from zero; n = 1441; $p < 0.05$) between estimated TA and estimated DIC values, between estimated TA and measured pCO_2 values and between estimated TA and measured pH values from spring to autumn 2018 at station *a* estuary. See M&M section for TA and DIC estimations.

Chapitre III

Échanges nets de CO_2 atmosphérique d'un pré-salé par des mesures à l'échelle de l'écosystème (technique de l'Eddy Covariance) et influence des facteurs de contrôles biotiques et abiotiques associés

Station d'Eddy Covariance sur le marais tidal des Bossys perdus (île de Ré, Fier d'Ars) pendant l'immersion de la végétation (marée haute, 27/04/2021). © Polsenaere.

Atmospheric CO_2 exchanges measured by Eddy Covariance over a temperate salt marsh and influence of environmental controlling factors

Jérémy Mayen[1,2*], Pierre Polsenaere[1], Éric Lamaud[3], Marie Arnaud[1,4], Pierre Kostyrka[1,5], Jean-Marc Bonnefond[3], Philippe Geairon[1], Julien Gernigon[6], Romain Chassagne[7], Thomas Lacoue-Labarthe[8], Aurore Regaudie de Gioux[5], Philippe Souchu[2]

*Correspondence to: Jérémy Mayen (jeremy.mayen@ifremer.fr)

[1]IFREMER, Littoral, Laboratoire Environnement Ressources des Pertuis Charentais (LER/PC), BP 133, 17390, La Tremblade, France
[2]IFREMER, Littoral, Laboratoire Environnement Ressources Morbihan Pays de Loire (LER/MPL), BP 21105, 44311, Nantes, France
[3]INRAE, Bordeaux Sciences Agro, ISPA, F-33140 Villenave d'Ornon, France
[4]Institute of Ecology and Environmental Sciences Paris (iEES-Paris), Sorbonne University, Paris 75005, France
[5]IFREMER, Dyneco, Pelagos, ZI de la Pointe du Diable - CS 10070 - 29280 Plouzané, France
[6]LPO, Réserve Naturelle de Lilleau des Niges, 17880, Les Portes en Ré, France
[7]BRGM, 3 avenue Claude-Guillemin, BP 36009, 45060 Orléans, Cedex 02, Orléans, France
[8]Littoral Environnement et Sociétés (LIENSs), UMR 7276, CNRS, La Rochelle Université, 2 Rue Olympe de Gouge, 17000 La Rochelle, France

A research article published in Biogeosciences (Mayen et al., 2024).
https://doi.org/10.5194/bg-21-993-2024

Abstract

Within the coastal zone, salt marshes are atmospheric CO_2 sinks and represent an essential component of biological carbon (C) stored on earth due to a strong primary production. Significant amounts of C are processed within these tidal systems which requires a better understanding of the temporal CO_2 flux dynamics, the metabolic processes involved and the controlling factors. Within a temperate salt marsh (French Atlantic coast), continuous CO_2 fluxes measurements were performed by the atmospheric eddy covariance technique to assess the net ecosystem exchange (NEE) at diurnal, tidal and seasonal scales as well as the associated relevant biophysical drivers. To study marsh metabolic processes, measured NEE were partitioned into gross primary production (GPP) and ecosystem respiration (R_{eco}) during marsh emersion allowing to estimate NEE at the marsh-atmosphere interface (NEE_{marsh} = GPP - R_{eco}). During the year 2020, the net C balance from measured NEE was -483 g C m^{-2} yr^{-1} while GPP and R_{eco} absorbed and emitted 1019 and 533 g C m^{-2} yr^{-1}, respectively. The highest CO_2 uptake was recorded in spring during the growing season for halophyte plants in relationships with favourable environmental conditions for photosynthesis whereas in summer, higher temperatures and lower humidity rates increased ecosystem respiration. At the diurnal scale, the salt marsh was a CO_2 sink during daytime, mainly driven by light, and a CO_2 source during night-time, mainly driven by temperature, irrespective of emersion or immersion periods. However, daytime immersion strongly affected NEE fluxes by reducing marsh CO_2 uptake up to 90%. During night-time immersion, marsh CO_2 emissions could be completely suppressed, even causing a change in metabolic status from source to sink under certain situations, especially in winter when R_{eco} rates were lowest. At the annual scale, tidal immersion did not significantly affect the net C uptake of the studied salt marsh since similar annual balances of measured NEE (with tidal immersion) and estimated NEE_{marsh} (without tidal immersion) were recorded.

Key words

Eddy Covariance, net ecosystem exchange, net ecosystem production, ecosystem respiration, salt marsh, biophysical controlling factors, tidal effects, temporal variations.

1. Introduction

Salt marshes are intertidal coastal ecosystems dominated by salt-tolerant herbaceous plants located at the terrestrial-aquatic interface. Despite their low surface area at the global scale (54650 km^2; Mcowen et al., 2017), salt marshes provide important ecosystem services such as an erosion protection (natural buffer zones), a water purification, a nursery for fisheries (Gu et al., 2018) and a high capacity for atmospheric CO_2 uptake and carbon (C) sequestration in their organic matter (OM) enriched sediments and soils (Mcleod et al., 2011; Alongi, 2020). In salt marshes, emersion at low tide and slow immersion at high tide favour this CO_2 fixation through photosynthesis of terrestrial and aquatic vegetations and also a strong benthic-pelagic coupling (Cai, 2011; Wang et al., 2016; Najjar et al., 2018). The high net primary production (NPP) rate of salt marshes on the Atlantic coast of the United States (1070 g C m^{-2} yr^{-1}; Wang et al., 2016) makes marshes one of the most productive ecosystems on earth (Duarte et al., 2005; Gedan et al., 2009). According to Artigas et al. (2015), approximately 22% of C fixed through this marsh NPP is then buried in sediments as "blue C" thus allowing salt marshes to be a large biological C pool (Chmura et al., 2003; Mcleod et al., 2011). However, tidal immersion can generate strong lateral exports of organic and inorganic C to the coastal ocean (Wang et al., 2016), inducing in turn atmospheric CO_2 emissions from coastal ecosystems downstream (Wang and Cai, 2004; Jiang et al., 2008). Salt marshes represent a biogeochemically active interface area within the coastal zone but are also threatened by sea level rise and global warming (Gu et al., 2018) which could significantly alter their capacity to sink and store C (Campbell et al., 2022). Thus, atmospheric CO_2 exchanges need to be accurately measured and better understood, especially the influence of biotic and abiotic controlling factors, in order to be included in regional and global C budgets (Borges et al., 2005; Cai, 2011) and to predict future mash C sinks within the context of climate change.

In temperate salt marshes, actual and historical land and water management, plant species, tidal influence and environmental conditions have been shown to play an important role in the C cycle. Generally, strong seasonal variations in the net ecosystem CO_2 exchange (NEE) were recorded with a marsh CO_2 sink during the hottest and brightest months and a CO_2 source during the rest of the year (Schäfer et al., 2014; Artigas et al., 2015). At a smaller scale, in urban salt marshes (USA), the highest CO_2 uptake generally occurred at midday whereas the systems emitted CO_2 throughout the night-time, illustrating the major role of net solar radiations in the marsh metabolic status (Schäfer et al., 2014, 2019). Tidal immersion over salt marshes can also strongly influence both daytime and night-time NEE fluxes, especially

during spring tides (Forbrich and Giblin, 2015). For instance, negative correlations between NEE and tidal effects were computed in a temperate salt marsh (USA) with *Spartina alterniflora* and *Phragmites australis*, especially in summer and winter, with negative (sink) and positive (source) NEE fluxes during incoming and ebbing tides, respectively (Schäfer et al., 2014). Wang et al. (2006) showed a competitive advantage for the growth and productivity of *S. alterniflora* plants under a moderate level of salinity (15‰) and immersion conditions. These different eddy covariance (EC) studies highlight the complexity of the C cycle over salt marshes and the associated biophysical factors driving CO_2 fluxes that require more *in situ* and integrative NEE measurements within and between all compartments at the different temporal scales to better understand the biogeochemical functioning of these ecosystems under changing sea level conditions.

Within coastal wetlands, CO_2 fluxes at the sediment-atmosphere interface can be accurately assessed with static chambers by repeating measurements over different intertidal habitats (Xi et al., 2019; Wei et al., 2020a). Yet, a major limitation of this method is that it can hardly include the temporal and spatial CO_2 flux variability across different vegetations and habitats (Migné et al., 2004). In heterogeneous intertidal systems, the eddy covariance (EC) technique can be used to measure ecosystem-scale CO_2 fluxes (NEE) based on the covariance between fluctuations in the vertically velocity and air CO_2 concentration (Baldocchi et al., 1988; Aubinet et al., 1999; Baldocchi, 2003). This direct and non-invasive micrometeorological technique has been of growing interest over the coastal zone to obtain NEE time series through accurate, continuous and high-frequency CO_2 flux measurements (Schäfer et al., 2014; Artigas et al., 2015; Forbrich and Giblin, 2015). This method has been deployed over blue C systems such as mangroves (Rodda et al., 2016; Gnanamoorthy et al., 2020), seagrass meadows (Polsenaere et al., 2012; Van Dam et al., 2021) and salt marshes (Artigas et al., 2015; Forbrich et al., 2018; Schäfer et al., 2019) to assess their capacity of CO_2 uptake. In intertidal systems like salt marshes, the major advantage of the EC method is to measure NEE fluxes at the ecosystem scale, coming from all habitats inside the footprint, at various timescales from hours to years and at both the sediment-air and water-air interfaces (i.e. low and high tides, respectively) (Kathilankal et al., 2008; Wei et al., 2020b). Although many studies have used this method to assess tidal effects on NEE fluxes over salt marshes, only a limited number have looked at the loss of CO_2 uptake due to tidal effects. Moreover, NEE can be partitioned into marsh metabolic fluxes (gross primary production, GPP and ecosystem respiration, R_{eco}) during emersion periods through modelling approaches (Kowalski et al., 2003; Reichstein et al., 2005; Lasslop et al., 2010). However, use of the EC

method requires significant qualitative and quantitative processing and data correction applied to each specific site since this method relies on the physical and theoretical backgrounds (Baldocchi et al., 1988; Burba, 2021) and is adapted (technically and scientifically) to the coastal systems.

Our study focused on the atmospheric CO_2 uptake capacity of a tidal salt marsh (old anthropogenic marsh) under the influence of biophysical factors and its potential role in global and regional C budgets. For this purpose, we deployed an atmospheric EC station to measure vertical CO_2 fluxes (NEE) during the year 2020 at the ecosystem scale on the Bossys perdus salt marsh on Ré Island connected to the French continental shelf of the Atlantic Ocean. Here, we aim to (a) describe NEE flux temporal series measured at different temporal scales (diurnal, tidal and seasonal scales) using the EC technique, (b) evaluate the relevant environmental factors that control atmospheric CO_2 exchanges (i.e. NEE) and (c) accurately qualify and quantify the effects of tides on the marsh CO_2 metabolism.

2. Materials and methods

2.1. Study site

The study was conducted at the Bossys perdus salt marsh situated along the French Atlantic coast on Ré Island (Fig. 3.1). It corresponds to a vegetated intertidal area of 52.5 ha that has been protected inside the National Natural Reserve (NNR) (Fig. 3.1). Between the 17^{th} century and the most of the 20^{th} century, the salt marsh experienced successive periods of intensive land use (salt harvesting and oyster farming) and returned to natural conditions before becoming a permanent part of the NNR in 1981 for the biodiversity protection without major restoration work (J. Gernigon, personal communication). It is currently managed to restore its natural hydrodynamics while conserving the site's specific typology due to past human activities (channel networks, humps and dykes; Fig. 3.2). This salt marsh is linked to the Fier d'Ars tidal estuary that exchanges between 2.4 and 10.2×10^6 m^3 of coastal waters with the Breton Sound continental shelf allowing a maximal tidal range of 5 m in the estuary (Bel Hassen, 2001). This communication allows (1) drainage of the intertidal zone of the estuary including mudflats (slikke) and tidal salt marshes (schorre) and (2) supply of coastal water to a large complex of artificial salt marshes (i.e. salt ponds) located upstream of the dyke (Fig. 3.1). The artificial marsh waters managed by the NNR for biodiversity protection (Mayen et al., 2023) are flushed back to the estuary downstream through the Bossys perdus channel (Fig. 3.1).

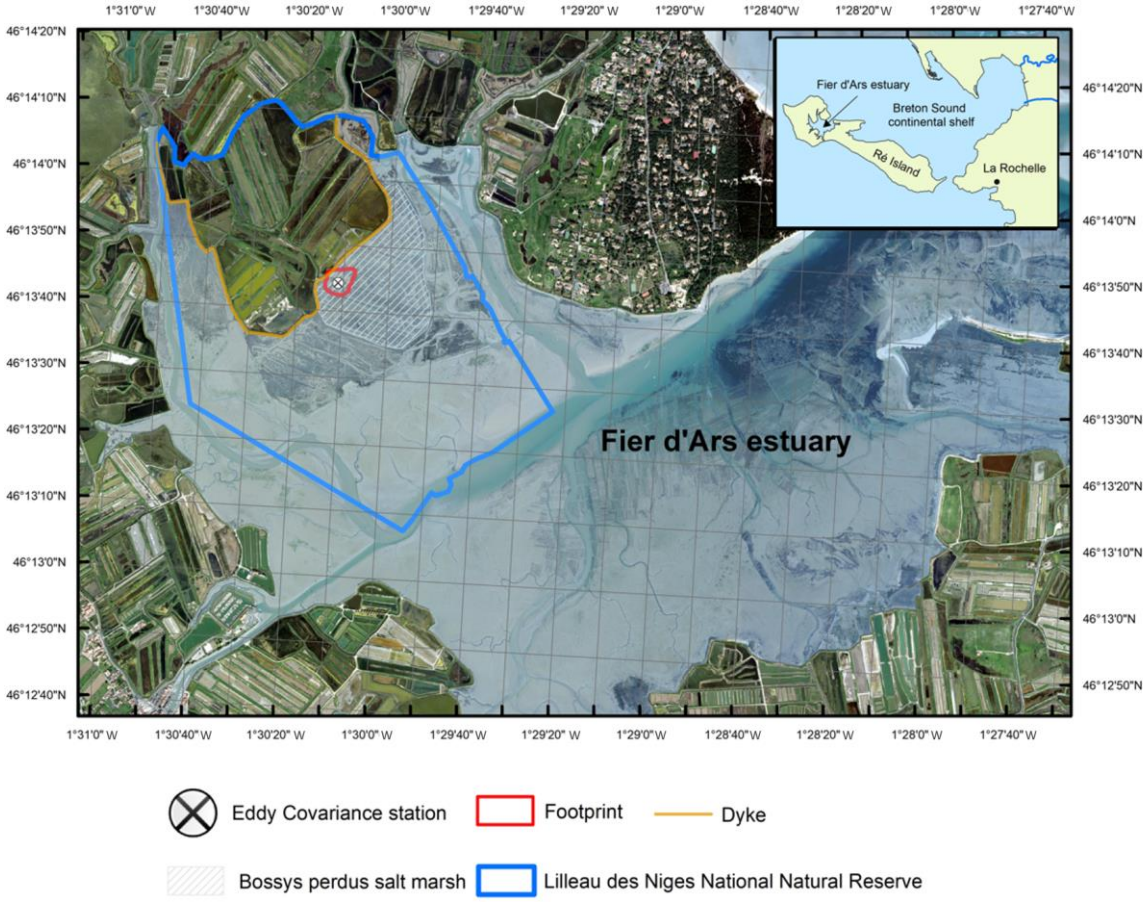

Figure 3.1: The studied Bossys perdus salt marsh located on the French Atlantic coast within the National Natural Reserve (blue line delimitation) on Ré Island. The salt marsh is connected to the Fier d'Ars tidal estuary (light blue). The dyke separates terrestrial and maritime marsh areas (orange line). The eddy covariance system and associated estimated footprint are indicated (black cross and red line; see Fig. 3.2). From geo-referenced IGN orthogonal images (IGN 2019).

The Bossys perdus salt marsh, located upstream of the estuary (schorre), is subjected to semi-diurnal tides from the Breton Sound continental shelf (Fig. 3.1) allowing the marsh immersion by two main channels differently in space, time and frequency according to the tidal periods (Fig. 3.2). At high tide, advected coastal waters can completely fill channels (Fig. S1-B in the Supplement) and immerse the marsh through variable water heights depending on tidal amplitudes and meteorological conditions (Fig. S1-C). In contrast, at low tide, the marsh vegetation at the benthic interface is emerged into the atmosphere without any coastal waters (Fig. S1-A). During this time, Bossys perdus channels allow drainage of upstream artificial marsh waters to the estuary (Fig. 3.2). The marsh vegetation assemblage was mainly composed by three halophytic species as perennial plants (*Halimione portulacoides*, *Spartina maritima* and *Suaeda vera*; Fig. 3.2) that associated with different metabolic pathways (the C3-type photosynthesis for *H. portulacoides* and *S. vera* and the C4-type photosynthesis for *S. maritima*; Duarte et al., 2013, 2014). Whereas *H. portulacoides* and *S. vera* are evergreen plants throughout the year, the growing season for *S. maritima* was shorter (from spring) with a flowering period between August and October (plants persist only in the form of rhizomes in winter and fall; J. Gernigon, personal communication).

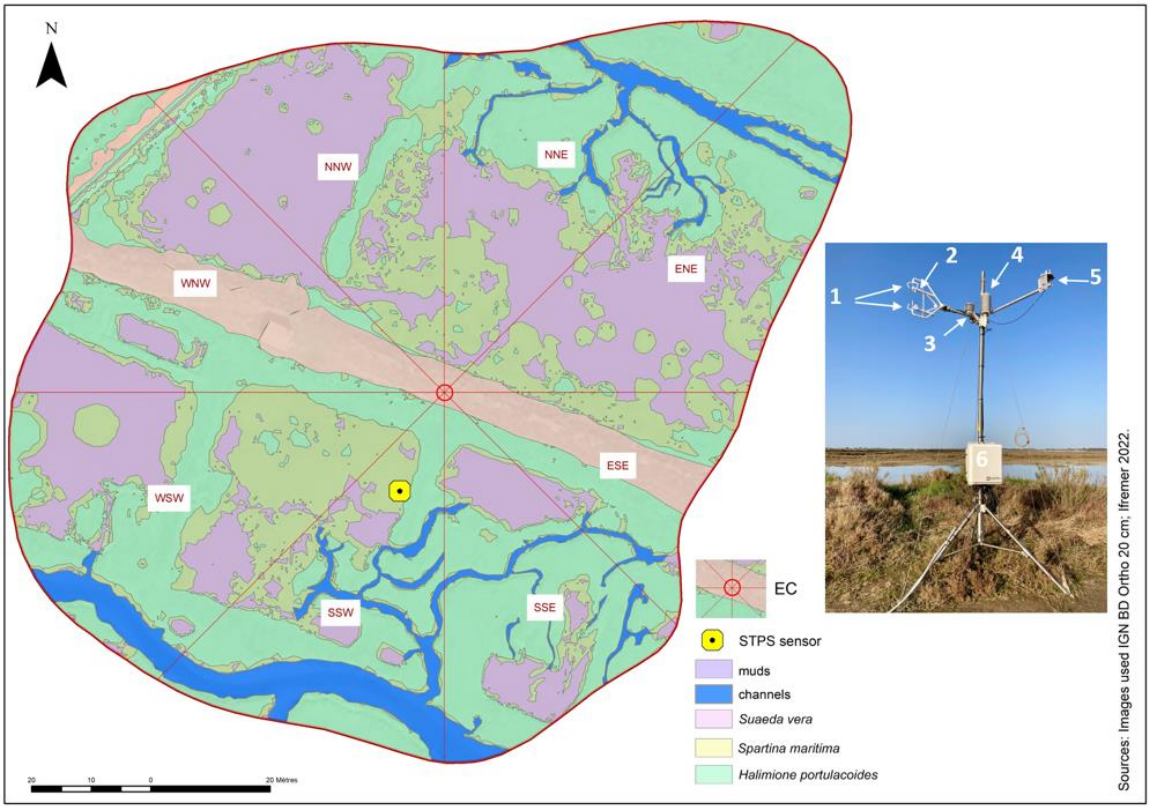
N
NNW
NNE
ENE
WNW
ESE
WSW
SSW
SSE
EC
STPS sensor
muds
channels
Suaeda vera
Spartina maritima
Halimione portulacoides
1
2
3
4
5
6
Sources: Images used IGN BD Ortho 20 cm; Ifremer 2022.

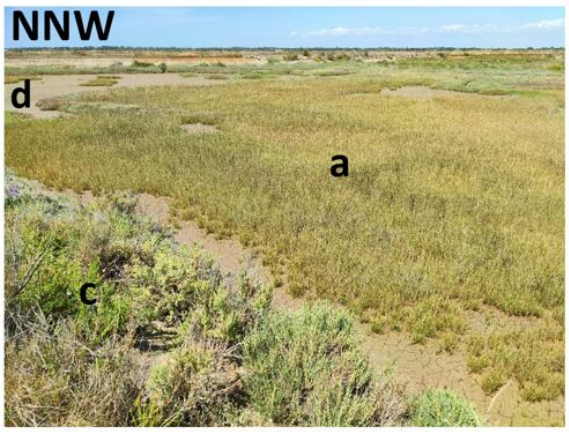
NNW
d
a
c

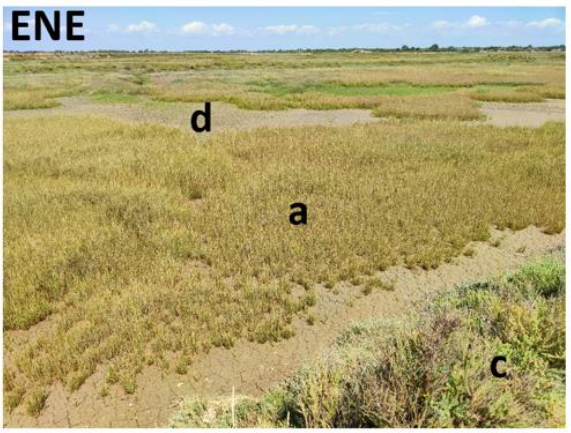
ENE
d
a
c

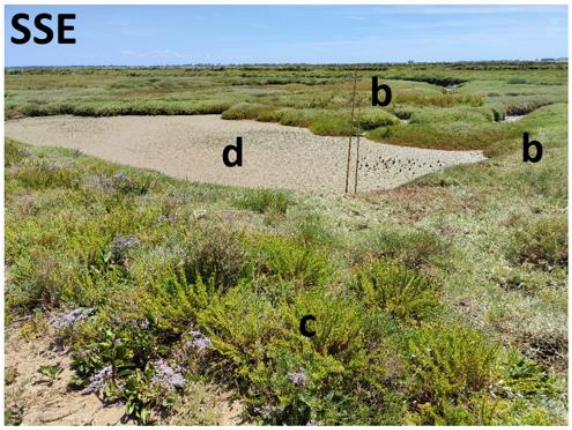
SSE
b
d
b
c

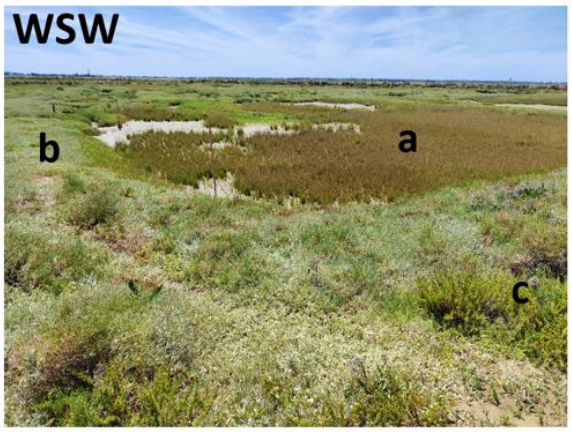
WSW
b
a
c

Figure 3.2: Location and set-up of the eddy covariance (EC) system within the Bossys perdus salt marsh and its associated footprint estimated from Kljun et al. 2015 and averaged over the year 2020 (70% contour line, i.e. 13042 m^2). Wind sectors (45°) and marsh habitats (see Table 3.1) are represented. The canopy height of the studied marsh is short and constant (from 0.15 m for *H. portulacoides* to 0.30 m for *S. maritima*). The STPS sensor (in yellow), measuring water heights (Hw) and temperatures (Tw), was located in the SSW sector. The EC system includes (1) the ultrasonic anemometer (CSAT3), (2) the open-path infrared gas analyser (EC150), (3) the temperature probe (100K6A1A), (4) the temperature/relative humidity sensor (HMP155A), (5) the silicon quantum sensor (SKP215) and (6) the central acquisition system (CR6) and the electronics module (EC100). A rainfall sensor (TE525MM) simultaneously measured the cumulative precipitation. From geo-referenced IGN orthogonal images (IGN 2019). Photographs of four wind sectors within the studied footprint area (NNW, ENE, WSW and SSE) were taken from the EC system during an emersion period in summer 2021 when all the marsh habitats were emerged into the atmosphere: (a) *Spartina maritima*, (b) *Halimione portulacoides*, (c) *Suaeda vera* and (d) mudflat. © S.-C. Zech.

2.2. Eddy covariance and micrometeorological measurements

The atmospheric eddy covariance (EC) technique allows us to quantify the net CO_2 fluxes at the ecosystem-atmosphere interface through micrometeorological measurements of the vertical component of atmospheric turbulent eddies (Aubinet et al., 1999; Baldocchi, 2003; Burba, 2021). The averaged vertical flux of any gas (F, µmol m^{-2} s^{-1}) can be expressed as the covariance between the vertical wind speed (w, m s^{-1}), air density (ρ, kg m^{-3}) and the dry mole fraction (s) of the gas of interest as

$$F = \overline{\rho\, w\, s} \approx \overline{p'}\,\overline{w's'} \quad (1)$$

where the overbar represents the time average of the parameter (i.e. 10 minutes in this study due to strong fluctuations at the tidal scale; Polsenaere et al., 2012) and the apostrophe indicates the instantaneous turbulent fluctuations in these parameters relative to their temporal average (Reynolds, 1883). The Reynold's decomposition was used to break the instantaneous term down into its mean and deviation (e.g. $w = \overline{w} + w'$) (Reynolds, 1883; Burba, 2021). This equation (Eq. 1) is obtained by assuming, on a flat and homogeneous surface, that (1) the variation in air density is negligible, (2) there is no divergence or convergence of large-scale vertical air motion and (3) atmospheric conditions are stable and stationary (Aubinet et al., 2012). A negative flux of atmospheric CO_2 is directed towards the ecosystem, and is therefore characterized as a sink, and *vice versa* for positive fluxes qualified as sources of CO_2 to the atmosphere.

An EC system was continuously deployed at the Bossys perdus salt marsh to measure the net ecosystem CO_2 exchange (NEE, µmol m^{-2} s^{-1}). The set of EC sensors (Fig. 3.2), at a height of 3.15 m, was composed of an open-path infrared gas analyser (model EC150; Campbell Scientific) to measure the CO_2 (mg m^{-3}) and H_2O (g m^{-3}) concentrations in the air as well as the atmospheric pressure (kPa) and an ultrasonic anemometer (model CSAT3; Campbell Scientific) to measure the three-dimensional components of wind speed (U, V and W; m s^{-1}) at a frequency of 20 Hz and averaged every 10 minutes (Fig. 3.2). The EC150 gas analyser also measured the air temperature using a thermistor probe (model 100K6A1A; BetaTherm). The EC100 electronics module (model EC100; Campbell Scientific) allowed us to synchronize high-frequency measurements and rapid communications between the CR6 datalogger (model CR6; Campbell Scientific) and EC devices including EC150 and CSAT3A (Fig. 3.2). The CR6 datalogger is a powerful core component for the data acquisition system. Additional meteorological data, such as relative humidity (RH, %), air temperature (Ta, °C) and photosynthetically active radiation (PAR, µmol m^{-2} s^{-1}) were recorded every 10 minutes simultaneously and at the same height as the EC sensors, by a temperature/relative humidity sensor (HMP155A, with RAD14 natural ventilation shelter; Campbell Scientific) and a silicon quantum sensor (SKP215; Skye Instruments), respectively (Fig. 3.2). The vapour pressure deficit (VPD, Pa) was calculated every 10 minutes from saturated vapour pressure (calculated from Ta) and from actual vapour pressure (calculated from RH). A rainfall sensor (TE525MM; Rain gauge, Texas Electronics), located 10 m away and connected to the EC station, simultaneously measured the cumulative precipitation at a height of 1 m (rainfall, mm). All high-frequency EC data were recorded on a SD micro-card (2 Go; Campbell Scientific) that was replaced every 2 weeks, whereas meteorological data were recorded and stored in the central acquisition system (CR6). The EC system was connected to two rechargeable batteries (12 volts and 260 amperes per hour; AGM) powered by a monocrystalline solar panel (24 volts, 200Wp module with MPPT 100V/30A controller; Victron Energy). The EC sensors were checked and cleaned every 2 weeks and the EC150 was calibrated each season with a zero-air calibration of 0 ppm (Campbell Scientific) and a certificated CO_2 standard of 520 ppm (Gasdetect). Water height (Hw; ± 0.3 m) and water temperature (Tw; ± 0.1°C) were also measured every 10 minutes along with EC data using a STPS probe (NKE Instrumentation) located 20 m away from the EC system (Fig. 3.2). The sensor was checked every two months at the laboratory to verify possible derivations in the measured parameters.

2.3. Footprint estimation and immersion/emersion marsh heterogeneity

Footprints were estimated using the model of Kljun et al. (2015) applied to data from the year 2020 to obtain an annual averaged footprint from the constant measurement height (Zm = 3.15 m), the constant displacement height (d = 0.1 m; estimated from 0.67 times the canopy height; LI-COR Environmental), mean wind velocities (u_mean, m s^{-1}), standard deviations of the lateral velocity fluctuations after rotation [sigma_v, m s^{-1}], the Obukhov length (L), friction velocities (u^*, m s^{-1}) and wind directions (°) obtained from the EC measurements and the processing software (EddyPro® v7.0.8; LI-COR Environmental) output. For verification, we performed the footprint estimations both with variable Zm from water height measurements and with constant Zm from data at emersion and we obtained the same footprint shapes and extends. For all calculations (i.e. habitat coverage, relationships with CO_2 fluxes, etc.), we used the 70% footprint contour line that corresponds to an average footprint of 13042 m^2 of the studied salt marsh area of interest (Fig. 3.2). A land-use map was also created (Fig. 3.2) from geo-referenced IGN BD orthogonal images with a resolution of 20 cm (2019) using ArcGIS 10.2 (ESRI). The spatial analysis tool of ArcGIS 10.2 was used to perform an unsupervised classification of the BD orthogonal images. We checked the resulting map by selecting 20 random locations within the footprint of the studied salt marsh and compared their land use on the ground and on the map.

In some situations, based on the tide (neap tides), due to meteorology influence (wind direction and atmospheric pressure) and the local altimetry heterogeneity, our one-location Hw measurements could not accurately account for the whole spatial emersion and immersion of the marsh in the EC footprint (Fig. 3.2). At incoming tide, when coastal waters begin to fill the channel and then overflow over the marsh (from 0.5 h in spring tides to 2.5 h in neap tides; data not shown), the SSW sector (Fig. 3.2) was first immersed and a non-zero Hw value was measured. However, although some marsh sectors were immersed at the same time, others were still emerged. Indeed, lowest marsh levels (56% of the footprint area), mainly composed of mudflats and *S. maritima* (Table 3.1 and Fig. 3.2), were quickly immersed from Hw > 0 m (south), whereas the whole marsh immersion (muds and all plants) only occurred 0.75 h later from Hw > 1.0 m at high tide during spring tide. Thus, the highest marsh levels (44% of the footprint area), mainly composed of *H. portulacoides* and *S. vera* (Table 3.1 and Fig. 3.2), were still emerged for 0 < Hw < 1.0 m. Conversely, at neap tide, this footprint immersion versus emersion marsh heterogeneity could still be present even at high tide due to insufficient water levels. Although a digital field model for water heights could not be performed in 2020 to have a better spatial representation of the immersion/emersion footprint,

all these important considerations were considered in our computations and analyses in this study.

2.4. EC data processing and quality control

Raw EC data measured at high-frequency were processed following Aubinet et al. (2000) with the EddyPro software. First, different correcting steps were applied to our raw data according to the procedures given by Vickers and Mahrt (1997) and Polsenaere et al. (2012) for intertidal systems: (1) unit conversion to check that the units for instantaneous data are appropriate and consistent to avoid any errors in the calculation and correction of CO_2 fluxes; (2) despiking to remove outliers in the instantaneous data from the anemometer and gas analyser due to electronic and physical noise and replaced the detected spikes with a linear interpolation of the neighbouring values; (3) amplitude resolution to identify situations in which the signal variance is too low with respect to the instrumental resolution; (4) double coordinate rotation to align the *x* axis of the anemometer to the current mean streamlines, nullifying the vertical and cross-wind components; (5) time delay removal by detecting discontinuities and time shifts in the signal acquisition from the anemometer and gas analyser; (6) detrending with removal of short-term linear trends to suppress the impact of low-frequency air movements and (7) performing the Webb-Pearman-Leuning (WPL) correction to take into account the effects of temperature and water vapour fluctuations on the measured fluctuations in the CO_2 and H_2O densities (Burba, 2021). The turbulent fluctuations of CO_2 fluxes were calculated with EddyPro using the linear detrending method (Gash and Culf, 1996) which involves calculating deviations from around any linear trend evaluated (i.e. over the whole flux averaged period). High-frequency CO_2 fluxes were processed and averaged over intervals of 10 min. (shorter than in terrestrial ecosystems) to detect fast NEE variations with the tide (Polsenaere et al., 2012; Van Dam et al., 2021). During the EC data processing by EddyPro, a correction for flux spectral losses in the low frequency range was performed according to Moncrieff et al. (2004).

A strict quality control was applied on EddyPro processed CO_2 flux data to remove bad data related to instrument malfunctions, processing and mathematical artefacts, ambient conditions that do not satisfy the requirements for the EC method, wind that is not from the footprint and heavy precipitation for the open-path IRGA (Burba, 2021). Processed data were screened using tests for steady state and turbulent conditions (Foken and Wichura, 1996; Foken et al., 2004; Göckede et al., 2004). In this study, we did not apply a ustar filter in our

EC data processing because we measured only 11% of night-time data corresponding to a ustar threshold below 0.1 m s^{-1} and above which NEE does not increase anymore with ustar values (threshold close to values found in grassland; Gu et al., 2005). Contrary to terrestrial ecosystems (Gu et al., 2005), the low canopy height of the studied marsh strongly limited the CO_2 storage in the vegetation and favours the atmospheric CO_2 circulation. If the signal to noise ratio of the EC150 gas analyser was less than 0.7 and/or the percentage of high-frequency missing values over 10 min. exceeded 10% (i.e. data absent in the raw data file or removed through the quality screening procedures), no flux was calculated. This choice was the best compromise between removing poor-quality data and keeping as much of measured CO_2 flux data as possible (data and associated tests not shown). Then, we used the method of Papale et al. (2006) to detect and remove outliers in the 10-min. flux data. The median and median absolute deviation (MAD) were calculated over a 2-week window separating daytime and night-time periods. Data above 5.2×MAD were removed. After all post-processing and quality controls, 18.3% of the EC data were removed and gap-filled through a machine learning approach to obtain continuous flux data in 2020.

2.5. Flux gap filling and statistic tools

The random forest (RF) model was used to gap-fill our EC dataset. Random forest is a supervised machine learning technique proposed by Breiman (2001) that can model a non-linear relationship with no assumption about the underlying distribution of the data population. This method has been shown to be particularly suited to gap-fill EC data (Kim et al., 2020; Cui et al., 2021). Random forest builds multiple decision trees, each of which is based on a bootstrap aggregated data sample (i.e. bagging of the EC data) and a random subset of predictors (i.e. the selected environmental data; Table S1). We build RF models with environmental predictors that have been identified in the literature to control CO_2 fluxes in salt marshes and which were available during the gaps and with measurements recorded between 2019 and 2020 (Table S1). Each random forest model was built from a trained bagging ensemble of 400 randomly generated decision trees (Kim et al., 2020) with the "randomForest" package in the R software (Liaw and Wiener, 2022). In this study, we used the RF2 model with PAR, air temperature, water height and relative humidity as environmental predictors because its performance indicators showed a high Pearson correlation coefficient (R^2 = 0.88) and low values of root mean square error (RMSE = 1.27) and model bias (0.0024) allowing us to correctly gap-fill a large EC data (Table S1). The

calculated uncertainty of the RF2 model on the resulting annual C budget was 0.43%. Each tree was trained from bagged samples including 70% of the initial dataset. The remaining 30% of the data were used to estimate the fit of each random forest model. The model used was then able to explain 88% of the variability in the test data. Daytime data were better explained than night-time data (59% versus 38%), with light being the main parameter of the model. However, only 20% of the night-time EC data were gap-filled with the random forest model. Using a partial dependence analysis and an ondelette analysis, we concluded that the relationships and temporal dynamics modelled allowed us to correctly fill the gaps in our dataset. However, extreme values of some predictors (i.e. PAR > 1000 µmol m^{-2} s^{-1}) can reduce the random forest model performance for estimation of EC data. This observation is common for random forest models, as they show poor results for extreme values. Other models, such as artificial neural networks, were also tested but showed poorer results (Table S1).

For all measured variables, the 10 min. data did not follow a normal distribution (Shapiro-Wilk tests, $p < 0.05$). Non-parametric comparisons, such as the Mann-Whitney and Kruskal-Wallis tests, were carried out with a 0.05 level of significance. To assess the influence of meteorological and hydrological drivers on NEE fluxes at different temporal scales, we performed a pairwise Spearman's correlation analysis on the 10-min. values and monthly mean values ("cor function" in R).

2.6. Temporal analysis of NEE fluxes and partitioning

During the year 2020, temporal variations in NEE fluxes were studied at the seasonal and diurnal/tidal scales. Seasons were defined based on calendar dates: the winter period from 01/01/2020 to 19/03/2020 and from 21/12/2020 to 31/12/2020, the spring period from 20/03/2020 to 19/06/2020, the summer period from 20/06/2020 to 21/09/2020 and the fall period from 22/09/2020 to 20/12/2020. Daytime and night-time were separated into PAR > 10 and PAR ≤ 10 µmol m^{-2} s^{-1}, respectively. For the NEE flux analysis according to environmental drivers, NEE fluxes were grouped into five PAR groups ($0 < PAR \leq 10$, $10 < PAR \leq 500$, $500 < PAR \leq 1000$, $1000 < PAR \leq 1500$ and $1500 < PAR \leq 2000$ µmol m^{-2} s^{-1}) to reduce NEE fluctuations due to PAR variations. Water heights (Hw) measured at one location over the marsh (Fig. 3.2) relative to the mean sea level were used to distinguish emersion (Hw = 0 m at low tide) and immersion (Hw > 0 m at high tide) periods (see Sect. 2.3) and thus, the influence of tides on NEE fluxes.

To study marsh metabolism related to photosynthesis and respiration processes, measured NEE fluxes were partitioned into gross primary production (GPP) and ecosystem respiration (R_{eco}), respectively. During marsh emersion, NEE fluxes occur at the marsh-atmosphere interface involving only benthic metabolism (or marsh metabolism) resulting in NEE = GPP - R_{eco}. During marsh immersion, NEE fluxes are the result of benthic metabolism, planktonic metabolism and lateral C exchanges by tides thereby making it more difficult to study the marsh metabolism (Polsenaere et al., 2012). Negative NEE values indicated a marsh CO_2 uptake from the atmosphere and positive values indicated a marsh CO_2 source into the atmosphere. GPP was expressed in negative values and R_{eco} was expressed in positive values. In this study, NEE flux partitioning into marsh metabolic fluxes (NEE_{marsh}) was performed according to the following equation using the model of Kowalski et al. (2003):

$$NEE_{marsh} = GPP - R_{eco} = \frac{a1\ PAR}{a2+PAR} - R_{eco} \quad (2)$$

where a_1 is the maximal photosynthetic CO_2 uptake at light saturation (µmol CO_2 m^{-2} s^{-1}) and a_2 is the PAR at half of the maximal photosynthetic CO_2 uptake (µmol photon m^{-2} s^{-1}). The a_1/a_2 ratio corresponds to photosynthetic efficiency (Kowalski et al., 2003). R_{eco} was calculated as follows (Eq. 3) according to Wei et al. (2020b):

$$R_{eco} = R_0 \exp(bTa) \quad (3)$$

where R_{eco} is the night-time ecosystem respiration (µmol CO_2 m^{-2} s^{-1}), R_0 is the ecosystem respiration rate at 0°C (µmol CO_2 m^{-2} s^{-1}), Ta is the air temperature (°C) and *b* is a response coefficient of the temperature variation (Wei et al., 2020b).

For NEE flux partitioning, estimations of the GPP coefficients (a_1 and a_2; Eq. 2) and R_{eco} coefficients (R_0 and *b*; Eq. 3) were performed by the least squares method ("minpack.lm" package in R) at the monthly scale only during emersion periods where measured NEE fluxes corresponded to estimated NEE_{marsh} fluxes. First, for each month, R_0 and *b* were estimated during night-time emersion periods where NEE = R_{eco} following Eq. (3) (Wei et al., 2020b). Then, a_1 and a_2 were estimated during daytime emersion periods using night-time respiration coefficients (R_0 and *b*) where NEE = GPP - R_{eco} following Eq. (2) and Eq. (3) (Kowalski et al., 2003). Finally, NEE_{marsh} (net marsh metabolic fluxes without tidal influence) were calculated from PAR and Ta values measured at a 10-min. frequency throughout the year using the monthly coefficients calculated for the partitioning (Eq. 2). As our ecosystem had a low phenological variation (Table S2), we concluded that a monthly time step for the

coefficient estimation was sufficient to answer our study objectives. During emersion periods, monthly net C balances (i.e. budgets) of measured NEE and estimated NEE_{marsh}, as well as the monthly mean fluxes, were very similar (Table S3), confirming the correct NEE flux partitioning calculations done in this study.

3. Results

3.1. Habitat covering of the footprint

Within the EC footprint, halophyte marsh vegetation (66%) composed of *Halimione portulacoides*, *Spartina maritima* and *Suaeda vera* mainly dominated, whereas muds and channels only accounted for 27 and 7%, respectively (Fig. 3.2). The area occupied by *S. vera*, crossing the EC footprint from WNW to ESE (Table 3.1), corresponded to the highest marsh level that was partly immersed only during the highest tidal amplitudes (Fig. 3.2). *H. portulacoides* and *S. maritima* occupied mostly the NNE (70%), SSE (69%), WSW (68%) and SSW (67%) wind sectors. In contrast, mud habitats mostly covered the NNW sector, where the lowest vegetation cover was found (Table 3.1 and Fig. 3.2). The highest channel area was found in the SSW sector (Table 3.1 and Fig. 3.2).

Table 3.1: Bossys perdus marsh habitat (percentages are in bold and associated surface area, in square metres, are in brackets) within each 45° wind sector in the corresponding footprint areas (Fig. 3.2) and the whole averaged footprint for the year 2020 (13042 m^2, 70% contour line). *Negligible surfaces on the total area of the sector.

Wind sectors		*Halimione portulacoides*	*Spartina maritima*	*Suaeda vera*	Muds	Channels
NNE	0-45	**48** (850)	**22** (390)	**1*** (9)	**22** (386)	**8** (150)
ENE	45-90	**31** (590)	**26** (492)	**1** (22)	**37** (704)	**4** (80)
ESE	90-135	**37** (335)	**21** (190)	**31** (288)	**9** (82)	**2** (22)
SSE	135-180	**60** (803)	**9** (124)	**0*** (4)	**21** (275)	**8** (113)
SSW	180-225	**48** (734)	**19** (283)	**0*** (2)	**8** (122)	**25** (388)
WSW	225-270	**33** (689)	**35** (745)	**0*** (6)	**25** (530)	**6** (132)
WNW	270-315	**30** (580)	**11** (216)	**29** (570)	**30** (588)	**0** (0)
NNW	315-360	**16** (249)	**26** (401)	**2** (31)	**56** (867)	**0** (0)
Total footprint (70% contour line)		**37** (4830)	**22** (2841)	**7** (932)	**27** (3554)	**7** (885)

3.2. Seasonal variations of environmental conditions and NEE fluxes

Throughout the year 2020, the full seasonal range in solar radiation was measured with an increase in daytime PAR from winter (lowest light season) to summer (brightest season; Fig. 3.3-A). A similar seasonal pattern was recorded for air temperatures (Ta) with values ranging from 1.5°C in winter (coldest season) to 33.6°C in summer (warmest season; Fig. 3.3-B). On average, the winter and fall seasons were the wettest (RH > 82%), associated with the lowest vapour pressure deficit (VPD) values, whereas spring and summer were the driest ones (RH < 75%), associated with the highest VPD values (Fig. 3.3-B). Indeed, the highest and lowest cumulative rainfalls were recorded in fall (342 mm) and summer (62 mm), respectively. The highest mean seasonal wind speed was measured in winter (4.9 ± 2.3 m s^{-1}) with maximal speeds up to 13 m s^{-1} (Fig. 3.3-C). Winds came mostly from the SSW-WSW sectors both in winter (55%) and summer (41%) and from the NNE-ENE sectors both in spring (51%) and fall (31%) (Fig. 3.2).

Tidal activities reflected the typical hydrological conditions of the Atlantic coasts with a bi-monthly succession of spring tides and neap tides (Fig. 3.3-D). Water heights (Hw) strongly varied according to tidal amplitudes with a maximal Hw of 1.4 m during neap tides and 2.0 m during spring tides (overall annual mean of 0.6 ± 0.4 m; Fig. 3.3-D). Throughout the year, 25.5% of the EC data were measured when the salt marsh was immersed through variable immersion durations and water heights (Table 3.2). On average, the daily immersion durations ranged between 5.7 h d^{-1} in winter (23.7% of the EC data) and 6.5 h d^{-1} in fall (28% of the EC data). In winter, the EC data during immersion were split into 19% for 0 < Hw < 1 m and 4.7% for 1 < Hw < 2 m, whereas in fall, these latter were split into 20% for 0 < Hw < 1 m and 8% for 1 < Hw < 2 m. In summer, the lowest marsh immersion was measured with no Hw value higher than 1.5 m (Table 3.2).

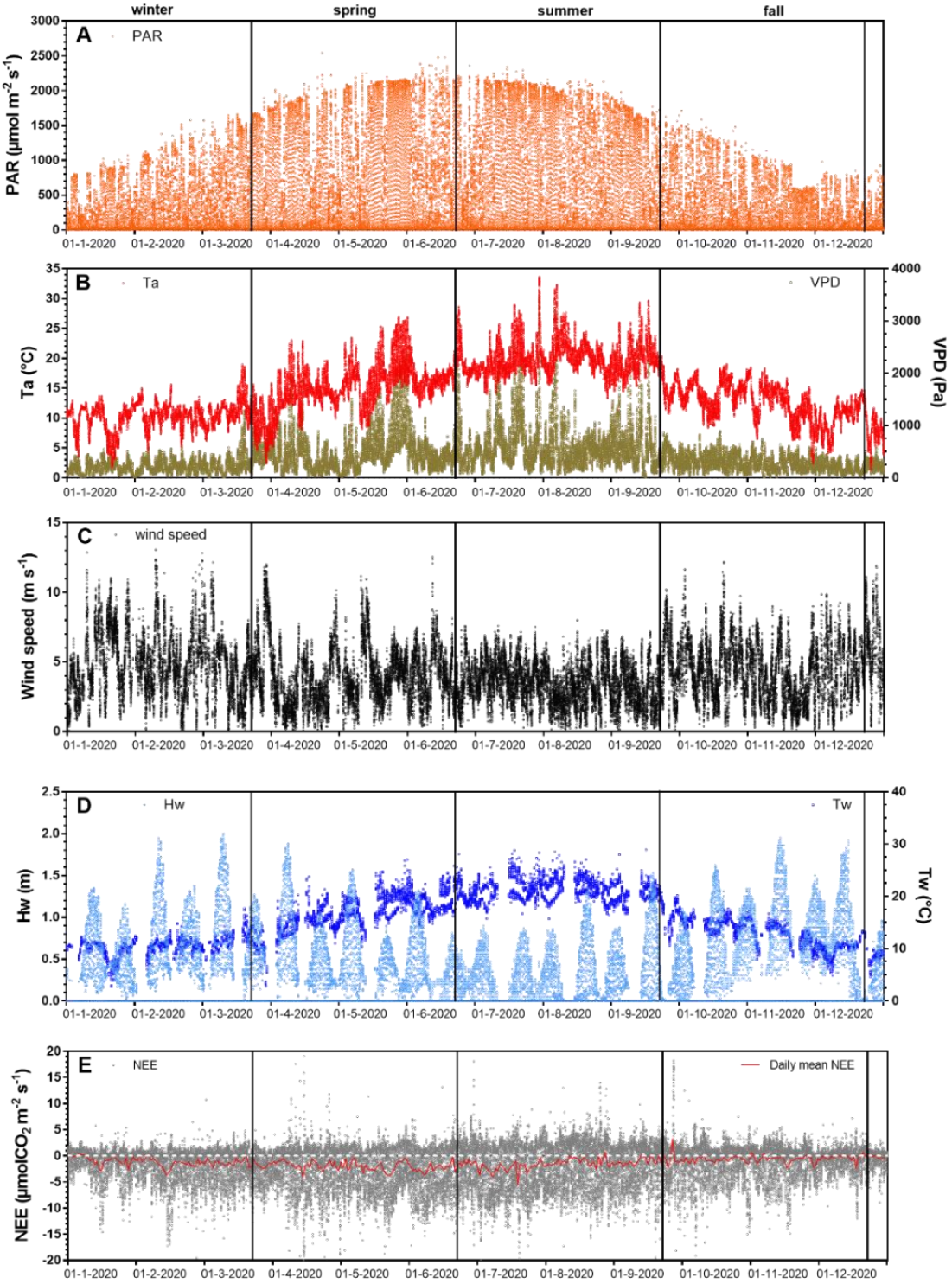

Figure 3.3: Net ecosystem exchanges and associated environmental parameters measured every 10 min throughout the year 2020. The measured environmental parameters include (A) the photosynthetically active radiation (PAR, µmol m^{-2} s^{-1}), (B) air temperature (Ta, °C), vapour pressure deficit (VPD, Pa), (C) wind speed (m s^{-1}), (D) water height (Hw, m), water temperature (Tw, °C) and (E) the net ecosystem exchanges (NEE, µmol CO_2 m^{-2} s^{-1}) computed from the 20 Hz atmospheric CO_2 and wind speed measurements with the EddyPro software. The red line in E is the moving average of NEE (daily mean). Seasons are delimited by vertical lines.

Table 3.2: Emersion and immersion periods (percentage in bold) at the studied salt marsh for four water height ranges of 0.5 m during the year 2020 and at the seasonal scale. The emersion and immersion durations in hours per day (h d^{-1}) were calculated (shown in brackets).

	Emersion	**Immersion**			
	Hw = 0	0 < Hw < 0.5	0.5 < Hw < 1	1 < Hw < 1.5	1.5 < Hw < 2
Year 2020	**74.5** (17.9)	**12.4** (2.9)	**8.7** (2.1)	**3.6** (0.9)	**0.8** (0.2)
Winter	**76.3** (18.0)	**10.4** (2.5)	**8.6** (2.0)	**3.6** (0.9)	**1.1** (0.3)
Spring	**74.5** (18.0)	**13.7** (3.2)	**8.2** (2.0)	**3.0** (0.7)	**0.6** (0.1)
Summer	**75.1** (18.5)	**17.1** (4.2)	**5.9** (1.6)	**1.3** (0.3)	**0.0** (0.0)
Fall	**72.0** (17.0)	**8.5** (1.9)	**11.5** (2.7)	**6.4** (1.5)	**1.6** (0.4)

The annual mean NEE value was -1.27 ± 3.48 µmol m^{-2} s^{-1} with strong temporal variabilities recorded over both long and short timescales (Fig. 3.3-E). Significant NEE variations were highlighted between each season (Kruskal-Wallis test, $p < 0.001$) where, on average, the highest and lowest atmospheric CO_2 sinks were recorded in spring (-1.93 ± 3.84 µmol m^{-2} s^{-1}) and fall (-0.59 ± 2.83 µmol m^{-2} s^{-1}), respectively (Fig. 3.4). NEE flux partitioning gave an annual mean NEE_{marsh} value of -1.28 ± 3.16 µmol m^{-2} s^{-1} (see Sect. 2.6), ranging from -2.00 ± 3.49 µmol m^{-2} s^{-1} in spring to -0.53 ± 2.51 µmol m^{-2} s^{-1} in fall (Fig. 3.4). On average, in winter and fall, the measured NEE values were more negative than the estimated NEE_{marsh} values whereas in spring and summer, the opposite trend was recorded (Fig. 3.4). Contrary to NEE and NEE_{marsh}, the highest seasonal values of GPP and R_{eco} were estimated in summer whereas the lowest seasonal values were estimated in winter (Fig. 3.4). The highest and lowest photosynthetic efficiencies (a_1/a_2 ratio) were found in winter (-2.08 10^{-2}) and summer (-1.36 10^{-2}), respectively.

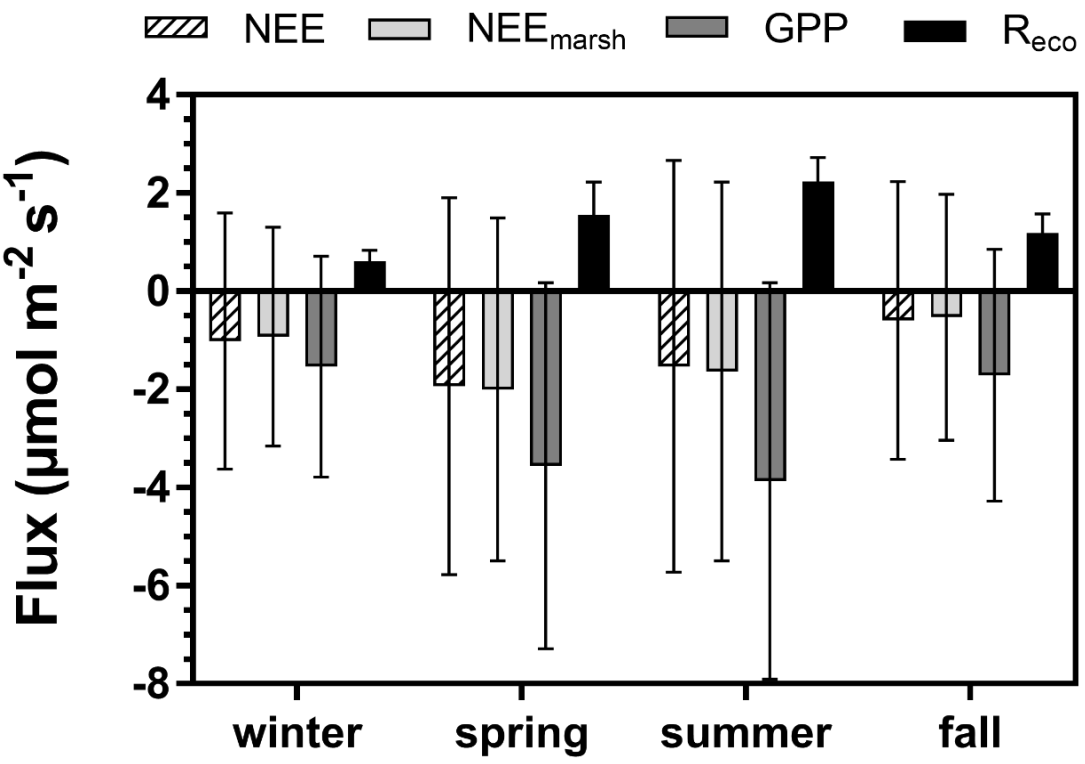

Figure 3.4: Seasonal variations (means ± SD) of the measured NEE, estimated NEE_{marsh}, estimated GPP and estimated R_{eco} (µmol CO_2 m^{-2} s^{-1}) recorded throughout the year 2020. NEE: net ecosystem exchange, NEE_{marsh}: net ecosystem exchange at the marsh-atmosphere interface without coastal water, GPP: gross primary production, R_{eco}: ecosystem respiration. The NEE fluxes were partitioned into GPP and R_{eco} according to Kowalski et al. (2003) and Wei et al. (2020b) (see section 2.6).

3.3. Environmental parameter and NEE flux variations at diurnal and tidal scales

At each season, significant diurnal differences in NEE fluxes were highlighted (Mann-Whitney tests, $p < 0.05$) with, on average, an atmospheric CO_2 sink during daytime and an atmospheric CO_2 source during night-time, irrespective of emersion or immersion periods (Table 3.3). For instance, in spring, NEE flux means were -3.93 ± 3.72 and 1.06 ± 1.09 µmol m^{-2} s^{-1} during daytime and night-time, respectively (Fig. 3.5-B). Over all seasons, similar diurnal variations in measured NEE and estimated NEE_{marsh} were recorded with, on average, a rapid increase in CO_2 uptake during the morning up to the middle of the day (low Ta and VPD values) and then, a decrease in CO_2 uptake during the afternoon (high Ta and VPD values) to become a CO_2 source during night-time (Figs. 3.5 and S2). On average, during the afternoon, the GPP decreases and R_{eco} increases explained the measured decrease in CO_2 uptake (Fig. 3.5). For each season, the highest marsh CO_2 uptakes were measured during daytime emersion periods between 12:00 U.T. and 13:00 U.T. (maximal PAR levels), with the

latter increasing from winter (-4.84 ± 2.87 µmol m^{-2} s^{-1}) to spring-summer (-6.94 ± 2.80 µmol m^{-2} s^{-1}; Fig. 3.5).

At each season, the tidal rhythm strongly disrupted NEE fluxes with, in general, no change in the marsh metabolism status (sink/source). During daytime, significantly lower CO_2 uptakes were recorded during immersion than during emersion (Mann-Whitney tests, $p < 0.05$) when marsh plants were mostly immersed in tidal waters and during night-time, a similar tidal pattern was recorded for CO_2 emissions (Mann-Whitney tests, $p < 0.05$; Table 3.3). For instance, in spring, NEE means were -4.39 ± 3.76 and -2.59 ± 3.24 µmol m^{-2} s^{-1} during daytime emersion and daytime immersion, respectively, and were 1.25 ± 0.98 and 0.51 ± 1.22 µmol m^{-2} s^{-1} during night-time emersion and night-time immersion, respectively. In winter, during some night-time periods, weak CO_2 sinks were recorded both during emersion (-0.79 ± 0.84 µmol m^{-2} s^{-1}; 137 hours over 71 days) and immersion (-0.82 ± 0.91 µmol m^{-2} s^{-1}; 143 hours over 55 days associated with a mean Hw of 0.80 m; Fig. S2). The maximal CO_2 uptakes were -4.80 and -5.31 µmol m^{-2} s^{-1} during night-time emersion and night-time immersion, respectively (Table 3.3).

Table 3.3: Diurnal/tidal variations (means ± SD in bold) of NEE fluxes (µmol CO_2 m^{-2} s^{-1}) during each season in 2020. The associated ranges (min/max) are indicated in brackets. Daytime and night-time periods were separated into PAR > 10 and PAR ≤ 10 µmol m^{-2} s^{-1}, respectively, whereas emersion and immersion periods were separated into Hw = 0 m and Hw > 0 m, respectively.

	Daytime emersion	**Night-time emersion**	**Daytime immersion**	**Night-time immersion**	**Seasonal**
Winter	**-3.15 ± 2.96** (-19.55/10.73)	**0.61 ± 0.86** (-4.80/5.40)	**-2.03 ± 2.30** (-16.06/6.49)	**-0.10 ± 0.99** (-5.31/3.34)	**-1.01 ± 2.61** (-19.55/10.73)
Spring	**-4.39 ± 3.76** (-25.67/19.09)	**1.25 ± 0.98** (-4.54/7.01)	**-2.59 ± 3.24** (-29.68/17.62)	**0.51 ± 1.22** (-4.60/6.04)	**-1.93 ± 3.84** (-29.68/19.09)
Summer	**-4.42 ± 3.88** (-23.71/18.07)	**2.11 ± 1.34** (-5.93/9.25)	**-2.22 ± 3.26** (-25.23/13.01)	**1.18 ± 1.44** (-4.86/9.36)	**-1.53 ± 4.19** (-25.23/18.07)
Fall	**-3.00 ± 3.32** (-21.54/17.74)	**1.12 ± 1.03** (-4.19/6.09)	**-1.53 ± 2.60** (-18.15/18.21)	**0.29 ± 1.07** (-3.97/5.50)	**-0.59 ± 2.83** (-21.54/18.21)

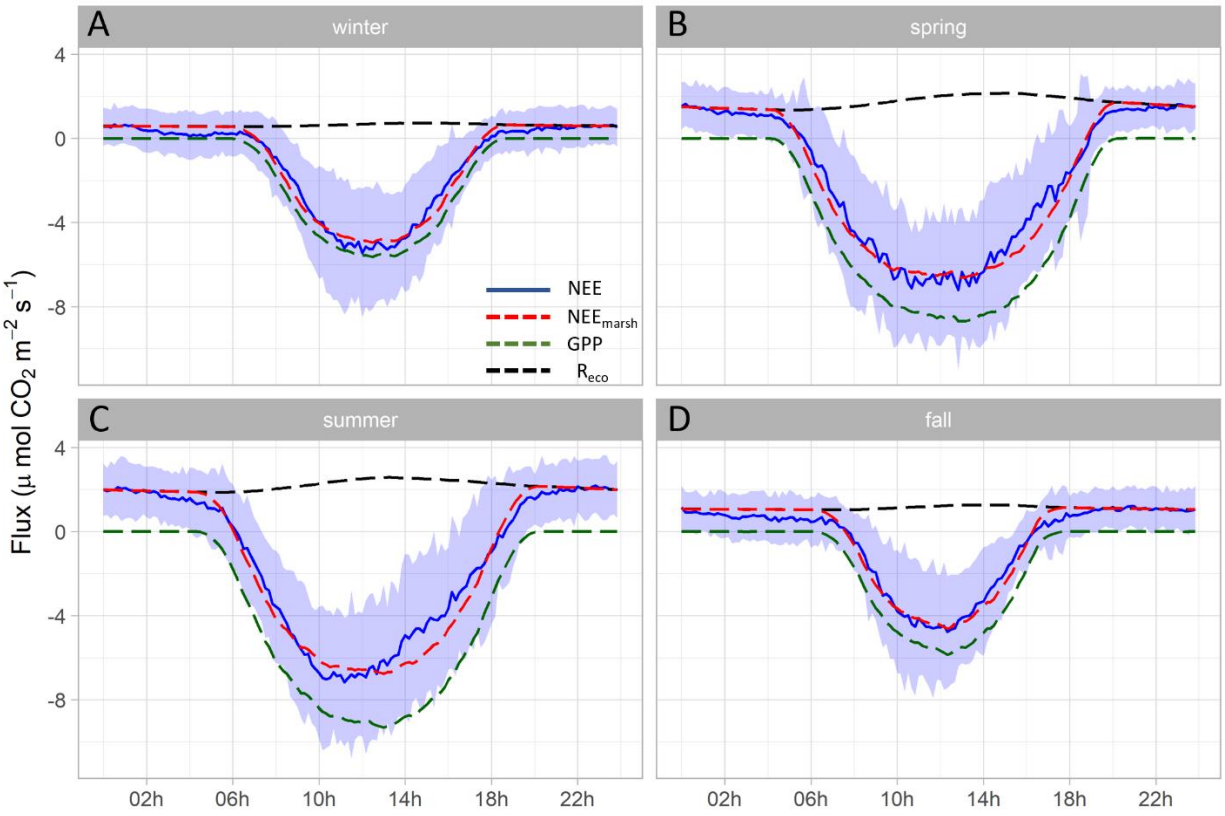

Figure 3.5: Hourly plots of the measured NEE, estimated NEE_{marsh}, estimated GPP and estimated R_{eco} diurnal variations obtained every 10 minutes in winter (A), spring (B), summer (C) and fall (D) for the year 2020. NEE averages are represented by solid blue lines and standard deviations are represented by blue areas. The NEE_{marsh}, GPP and R_{eco} averages are represented by dotted red, green and black lines, respectively. The measured NEE fluxes were partitioned into GPP and R_{eco} according to Kowalski et al. (2003) using monthly coefficients (see the "Materials and methods" section). Night-time periods correspond to GPP = 0 µmol m^{-2} s^{-1} and $NEE_{marsh} = R_{eco}$. All values are in µmol CO_2 m^{-2} s^{-1}.

3.4. Influence of environmental drivers on temporal NEE variations

Throughout the year, NEE fluxes were significantly controlled by solar radiations and air temperatures at the multiple timescales studied, thereby favouring marsh CO_2 uptake. During daytime (PAR > 10 µmol m^{-2} s^{-1}), PAR and Ta displayed the strongest negative correlations with NEE at both the monthly scale (-0.87 and -0.65, respectively; n = 12, $p < 0.05$) and the 10-min. scale (-0.77 and -0.21, respectively; n = 27160, $p < 0.05$). The highest and lowest correlations between NEE and PAR were recorded for $10 < PAR \leq 500$ and for $1500 < PAR \leq 2000$ µmol m^{-2} s^{-1}, respectively, confirming the rapid increase or decrease in CO_2 uptake for low daytime PAR values (Fig. 3.6-A). During daytime, vapour pressure deficit (VPD) was negatively correlated with NEE (-0.31; n = 27160, $p < 0.05$) producing a large reduction in CO_2 uptake for all PAR levels and even led to a switch from sink to source of atmospheric

CO_2 from VPD > 1200 Pa for low PAR levels (PAR ≤ 500 µmol m^{-2} s^{-1}; Fig. 3.6-B). During night-time and daytime, air temperature (Ta) was positively (0.54; n = 27190, $p < 0.05$) and negatively (-0.21; n = 25544, $p < 0.05$) correlated with NEE, respectively. However, from PAR > 500 µmol m^{-2} s^{-1}, high Ta values (> 20°C) decreased CO_2 uptake for all PAR levels (Fig. 3.6-C). Water temperature (Tw) did not influence NEE during immersion (Fig. 3.6-D). Indeed, for PAR > 500 µmol m^{-2} s^{-1} and Hw > 0.5 m, no significant relationships was found between NEE and Tw (n = 1215; $p = 0.26$). For low PAR levels (PAR ≤ 500 µmol m^{-2} s^{-1}), wind speeds quickly increased CO_2 uptake whereas for high PAR levels (PAR > 500 µmol m^{-2} s^{-1}), CO_2 uptake was increased only for wind speeds higher than 7 m s^{-1} (Fig. 3.6-E). For wind directions, a spatial heterogeneity of NEE was recorded according to wind sectors both during daytime and night-time (Fig. 3.6-F).

Within the footprint area composed of an assemblage of plants and muds (Fig. 3.2), the highest CO_2 uptakes were generally recorded from the southern sectors (high vegetation:mud ratios) whereas, the lowest CO_2 uptakes were generally recorded from the northern sectors (low vegetation:mud ratios; Fig. 3.7). For instance, our sectorial NEE analysis during daytime emersion showed that the SSE sector (vegetation:mud ratio of 2.4; Table 3.1) did uptake 32% (winter), 25% (spring) and 50% (fall) times more atmospheric CO_2 than the NNW sector (vegetation:mud ratio of 0.8; Table 3.1). Moreover, in winter and fall, we highlighted that CO_2 uptake rates of *H. portulacoides* (C3 species) were significantly higher than *S. maritima* (C4 species) ones by comparing the SSE (60% of *H. portulacoides* and 9% of *S. maritima*) and WSW (33% of *H. portulacoides* and 35% of *S. maritima*) sectors during daytime emersion (Mann-Whitney tests, $p < 0.0001$). In contrast, in summer, no significant difference in NEE fluxes was recorded between these two sectors (Mann-Whitney test, $p = 0.06$; Fig. 3.7) and, more generally, between the different wind sectors (Table 3.1 and Fig. 3.7). For all seasons, during night-time emersion, we recorded that southern sectors (ESE, SSE and SSW) emitted higher atmospheric CO_2 than northern sectors (NNE and ENE), especially in winter and fall (Table 3.1 and Fig. 3.7).

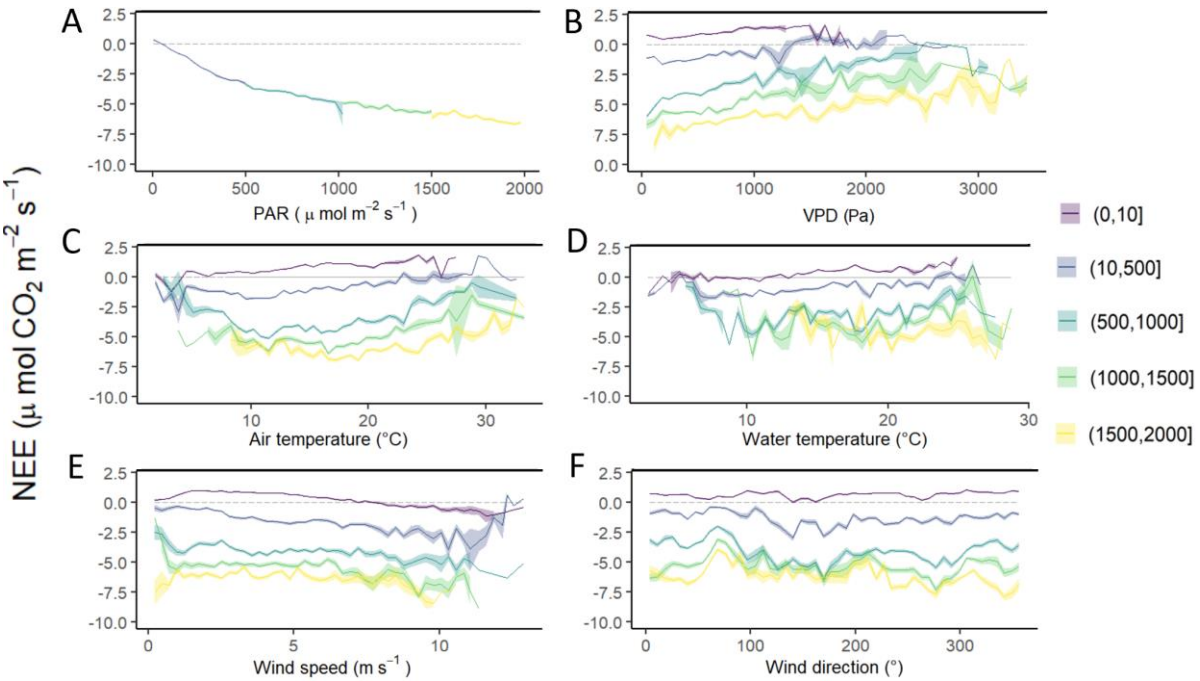

Figure 3.6: Diurnal variations of NEE fluxes (µmol CO_2 m^{-2} s^{-1}) measured every 10 min according to different variables within five PAR groups: 0-10 (night-time), 10-500, 500-1000, 1000-1500 and 1500-2000 µmol m^{-2} s^{-1}. Panel (A) shows PAR (µmol m^{-2} s^{-1}), (B) VPD (Pa), (C) air temperature (°C), (D) water temperature (°C), (E) wind speed (m s^{-1}) and (F) wind direction (°). NEE fluxes are averaged after separating each variable into five classes and the coloured area is the standard error at the mean.

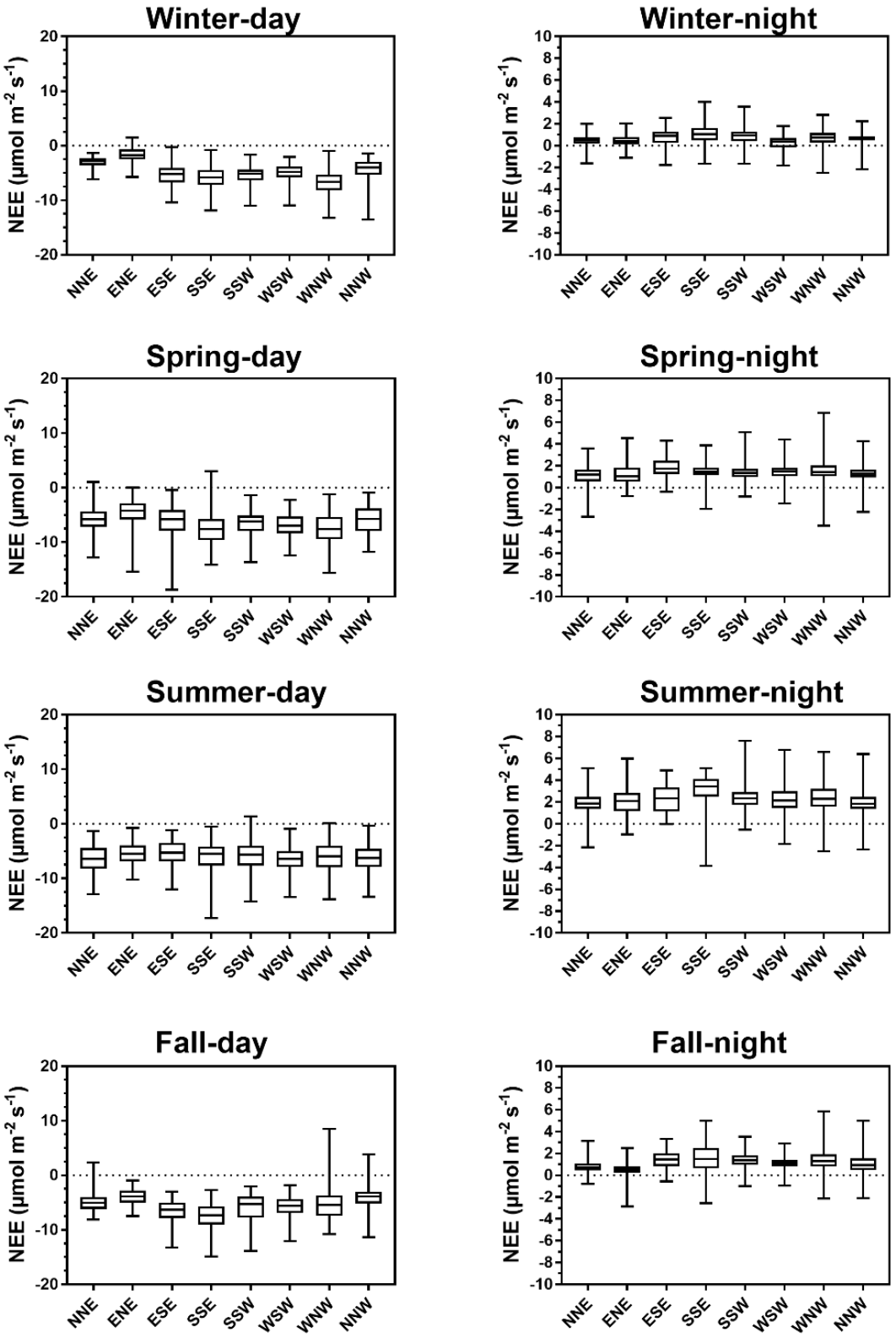

Figure 3.7: Spatial split of NEE fluxes (µmol CO_2 m^{-2} s^{-1}) within each 45° wind sector (Fig. 3.2) during emersion periods (Hw = 0 m) at the seasonal and diurnal scales. During daytime, the brightest emersion periods (PAR ≥ 500 µmol m^{-2} s^{-1}) were chosen to reduce NEE fluctuations due to PAR influence (see Fig. 3.6-a).

The tidal rhythm strongly influenced NEE fluxes during immersion depending on water heights (Hw) and PAR levels (Figs. 3.8 and S3). Throughout the year, NEE were positively correlated with Hw during the day but negatively correlated during the night (Fig. 3.8). More precisely, night-time immersion strongly reduced CO_2 emissions and even led to a switch from source to sink of atmospheric CO_2 from Hw > 0.4 m in winter (Fig. 3.8-A), Hw > 0.7 m in spring (Fig. 3.8-B), Hw > 1.4 m in summer (Fig. 3.8-C) and Hw > 1 m in fall (Fig. 3.8-D), on average. For low daytime PAR levels (PAR ≤ 500 µmol m^{-2} s^{-1}), immersion only slightly reduced CO_2 uptake (Fig. 3.8-C). On the contrary, for higher daytime PAR levels (PAR > 500 µmol m^{-2} s^{-1}), immersion strongly reduced CO_2 uptake, especially from Hw > 0.5 m, to reach the lowest CO_2 sinks from Hw > 1.0 m, irrespective of the PAR levels (Fig. 3.8-C).

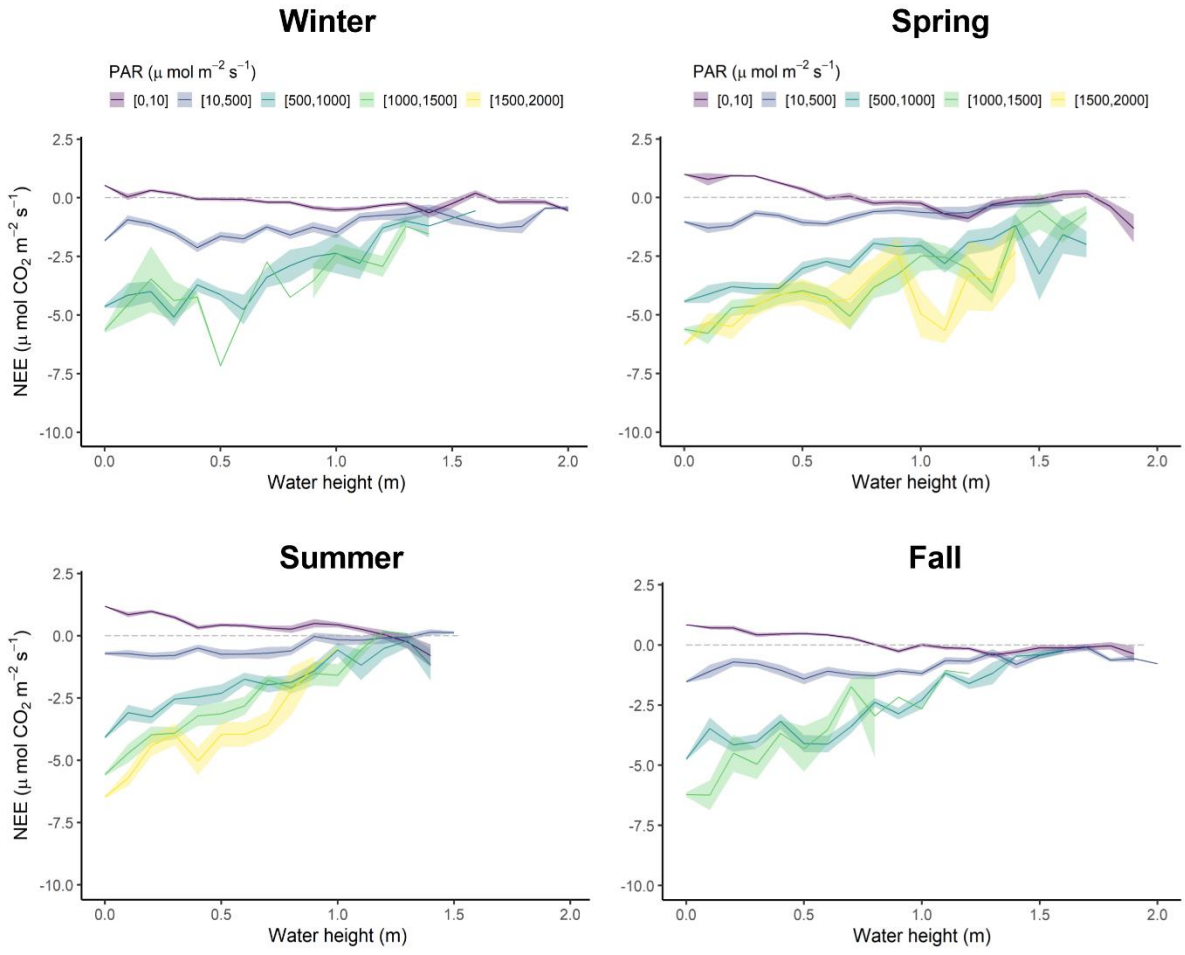

Figure 3.8: Diurnal variations of NEE fluxes (µmol CO_2 m^{-2} s^{-1}) measured every 10 minutes according to water height (Hw, m) within five PAR groups (see caption of Fig. 3.6) in winter (A), spring (B), summer (C) and fall (D). NEE values were averaged every 0.1 m. The coloured areas represent the standard error of the mean.

3.5. Annual carbon budgets

Throughout the year, the annual NEE value was -483.6 g C m^{-2} yr^{-1}, associated with immersion duration of 6.1 h d^{-1}, on average. Simultaneously, estimated GPP and R_{eco} (marsh metabolic fluxes without tidal influence) absorbed and emitted 1019.4 and 533.2 g C m^{-2} yr^{-1}, respectively, resulting in an annual estimated NEE_{marsh} value similar to the measured NEE value (Fig. 3.9). At the seasonal scale, the highest CO_2 uptakes occurred in spring and summer, associated with the lowest marsh immersion levels, and the lowest CO_2 uptakes occurred in winter and fall, associated with the highest marsh immersion levels (Tables 3.2 and 3.4). In winter and fall, when the daytime immersion periods were the shortest, net C balances from measured NEE gave higher values than net C balances from estimated NEE_{marsh} (+7.9 and +6.2 g C m^{-2}, respectively; Table 3.4). Conversely, in spring and summer when the daytime immersion periods were the longest, the opposite pattern was observed between measured NEE values and estimated NEE_{marsh} values (-7.3 and -9.9 g C m^{-2}, respectively; Table 3.4).

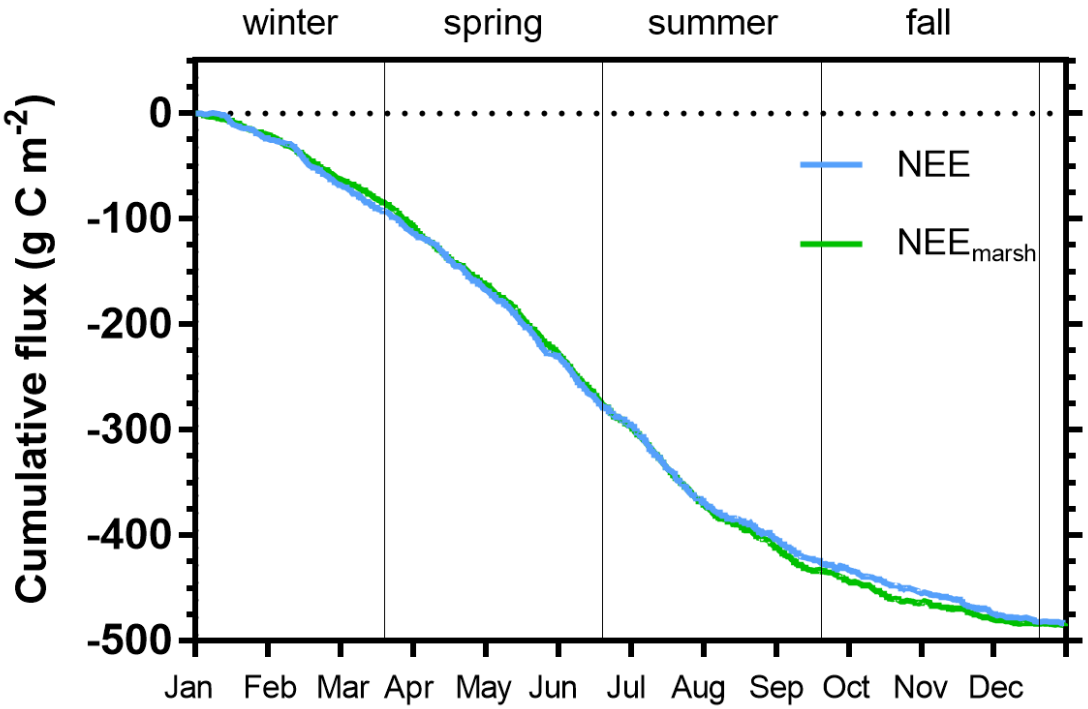

Figure 3.9: Cumulative carbon fluxes (g C m^{-2}) of the measured NEE (in blue) and estimated NEE_{marsh} (in green) throughout the year 2020. Vertical lines are used to delimit the four seasons. NEE fluxes correspond to net vertical CO_2 exchanges measured by EC whereas NEE_{marsh} fluxes correspond to net vertical CO_2 exchanges estimated from NEE partitioning at the benthic interface only, without any tidal influence.

Table 3.4: Net seasonal carbon balances for the measured NEE and estimated NEE_{marsh} values (g C m^{-2}). Corresponding seasonal percentages (%) of marsh immersion and daytime marsh immersion are indicated. NEE corresponds to net vertical CO_2 exchanges measured by EC whereas NEE_{marsh} corresponds to net vertical CO_2 exchanges estimated at the benthic interface without any tidal influence.

	Cumulative NEE (g C m^{-2})	**Cumulative NEE_{marsh} (g C m^{-2})**	**NEE – NEE_{marsh} (g C m^{-2})**	**Immersion time (%)**	**Daytime immersion time (%)**
Year 2020	483.6	485.9	-2.3	25.5	52.2
Winter	94.4	86.5	7.9	23.7	41.5
Spring	184.5	191.8	-7.3	25.5	63.4
Summer	149.3	159.2	-9.9	24.9	64.5
Fall	55.5	49.3	6.2	27.9	39.5

Table 3.5: Comparison of the annual NEE budget (g C m^{-2} yr^{-1}) using EC measurements across the salt, brackish and freshwater marshes of the coastal zone.

Study site	Location	Annual NEE budget (g C m^{-2} yr^{-1})	Reference
Tidal salt marsh*	Fier d'Ars tidal estuary, France	-483	This study
Tidal salt marsh*	Virginia, USA	-130[a]	Kathilankal et al., 2008
Urban tidal marsh*	Hudson-Raritan estuary, New-Jersey, USA	From +894 to -310	Schäfer et al., 2014
Restored salt marsh*	Hudson-Raritan estuary, New-Jersey, USA	-213	Artigas et al., 2015
Tidal salt marsh	Plum Island Sound estuary, Massachusetts, USA	From -104 to -233 (-176 ± 32)[b]	Forbrich et al., 2018
Tidal salt marsh	Duplin River salt marsh-estuary, Georgia, USA	From -139 to -309	Nahrawi, 2019
Urban tidal wetlands	Hudson-Raritan estuary, New-Jersey, USA	-307[c]	Schäfer et al., 2019
Brackish tidal marsh	San Francisco Bay, California, USA	-225	Knox et al., 2018
Brackish marsh	Louisiana, USA	171	Krauss et al., 2016
Para-dominated subtropical marsh	Taiwan	-376	Lee et al., 2015
Reed-dominated marsh	Taiwan	-53	Lee et al., 2015
Freshwater marsh	Louisiana, USA	-337	Krauss et al., 2016
Freshwater wetland	Everglades National Park, Florida, USA	From -91 to +3 (-21 ± 17)[d]	Zhao et al., 2019

*Managed and protected marshes, [a]NEE budget during the growing season (from May to October 2007), [b]Mean of annual NEE budgets over a five-year period (from 2013 to 2017), [c]Annual NEE budget of three tidal marshes with different restoration histories, [d]Mean of annual NEE budgets over a nine-year period (from 2008 to 2016).

4. Discussion

4.1. Marsh CO_2 uptake and influence of management practice

In the present EC study, the salt marsh absorbed 483 g C m^{-2} yr^{-1} from the atmosphere. This net C balance (i.e. budget) was lower than the values estimated for global tidal wetlands (1125 g C m^{-2} yr^{-1}; Bauer et al., 2013) and for tidal marshes on the Atlantic coast of the United State (775 g C m^{-2} yr^{-1}; Wang et al., 2016) but similar to the C balance estimated by Alongi (2020) for global salt marshes (382 g C m^{-2} yr^{-1}).

Currently, an increasing number of EC measurements are being taken in salt marshes in order to obtain continuous NEE data series as well as to increase knowledge about the associated metabolic processes and fluxes for these tidal systems (Schäfer et al., 2014; Forbrich et al., 2018; Knox et al., 2018) (Table 3.5). These EC studies confirmed the estimates of CO_2 sinks in salt marshes (Wang et al., 2016; Alongi, 2020) but also revealed strong NEE flux heterogeneities according to climatic conditions and anthropogenic influences (Herbst et al., 2013; Schäfer et al., 2019). For instance, NEE measured in a natural salt marsh (*S. alterniflora*, *S. maritima* and *D. spicata*) showed a net C uptake from the atmosphere with high interannual variations in C balances (Table 3.5) mainly due to rainfall during the growing season for marsh plants (Forbrich et al., 2018). By comparison, in an urban tidal marsh, Schäfer et al. (2014) reported a higher interannual variability from 984 g C m^{-2} in 2009 to -310 g C m^{-2} in 2012 due to management practices and plant species (*P. australis* and *S. alterniflora* in 2009 and total elimination of *P. australis* in 2012; Table 3.5). In the same area, in another restored salt marsh in which the *P. australis* monoculture was replaced by a high diversity of emergent marsh plants (*S. patens*, *S. cynosuroides*, *S. alterniflora* and *D. spicata*), a net CO_2 uptake was recorded (Table 3.5) which once again confirms the importance of land management practices in marsh C balances (Artigas et al., 2015). In our studied salt marsh, the natural management for several decades has allowed for a return to the natural site hydrodynamics and the development of productive marsh halophytes, mainly composed of *H. portulacoides* and *S. maritima* (59% of the footprint area). However, past human activities and water management practices for salt farming have shaped the marsh typology (channel network, humps and dykes), producing a time-delayed immersion of plants and muds between high and low marsh areas during spring tides. Thus, due to this emersion/immersion heterogeneity, mud and *S. maritima* were quickly immersed by coastal waters, whereas the whole immersion of marsh habitats only occurred during the highest tidal amplitudes favouring a higher atmospheric CO_2 uptake by *H. portulacoides* and *S. vera*. During the year 2020, our rewilded salt marsh took up more C from the atmosphere

mainly due to strong plant photosynthesis than the other salt, brackish and freshwater marshes reported in the literature (Table 3.5). However, the net C balances calculated with the EC method are still too scarce to be able to take all temporal and spatial variabilities of salt marshes into account. Based on biomass production measurements in salt marshes, Sousa et al. (2010) estimated that the NPP of *H. portulacoides* was 505 g C m^{-2} yr^{-1} whereas the NPP of *S. maritima* varied between 367 and 959 g C m^{-2} yr^{-1} depending on the chemical-physical characteristics and marsh maturity. Thus, the net metabolism of these halophytic plants could play an important role in our net C balance but, according to "the marsh CO_2 pump" (Wang et al., 2016), a significant proportion of marsh NPP was respirated by heterotrophic processes and then (1) emitted as atmospheric CO_2 (38 ± 11%) and (2) exported by tides as DIC (37 ± 15%; Song et al., 2023).

Moreover, despite a lower benthic metabolism (photosynthesis and respiration) of muds than evergreen plants (Fig. 3.7), the microphytobenthos which can develop on mudflats (27% of the footprint area) may also contribute to marsh production during daytime emersion, as highlighted in our studied marsh where static chamber measurements performed in March 2023 at midday showed a net CO_2 uptake to a non-vegetated mudflat (NEE mean of -2.92 µmol m^{-2} s^{-1}; unpublished results) and confirmed in an estuarine wetland in China (Xi et al., 2019). On an intertidal flat (France), EC measurements even showed a higher daily benthic metabolism with microphytobenthos (1.72 g C m^{-2} d^{-1}; September/October 2007) than with *Zostera noltei* (1.25 g C m^{-2} d^{-1}; July and September 2008), confirming the high biological productivity of mudflats (Polsenaere et al., 2012). However, due to the specific assemblage of our studied marsh (Fig. 3.2), it remains complex to accurately study these habitat effects (plants *vs.* microphytobenthos) on NEE fluxes at the marsh scale and draw more general conclusions. Thus, the microphytobenthos could play a significant role in the atmospheric CO_2 uptake of salt marshes but also, more generally, in the carbon cycle of the coastal ocean because the resuspension of the microphytobenthos primary production during tidal immersion induce a large export of organic carbon from muds to coastal waters (up to 60% of the benthic primary production in a nearby tidal flat; Savelli et al., 2019). These fast-growing primary producers with high labile organic carbon could also be quickly degraded locally by microbial remineralization (Ruttenberg, 1992; De Brouwer & Stal, 2001; Morelle et al., 2022) contrary to evergreen plants contributing to long-term "blue carbon" burial in sediments (Mcleod et al., 2011).

4.2. Metabolism processes and controlling factors at multiple timescales

4.2.1. Seasonal scale

In a tidal salt marsh, the average monthly budgets from Forbrich et al. (2018) showed a net CO_2 sink during the growing season for marsh plants from June to September and a net CO_2 source to the atmosphere during the rest of the year, indicating a strong seasonal variability in marsh metabolic fluxes. In urban salt marshes, the growing season was longer switching from source to sink in May (Schäfer et al., 2014; Artigas et al., 2015) and even in April in a brackish marsh (Knox et al., 2018). In our studied marsh, the halophyte vegetation, mostly composed of evergreen species, was autotrophic throughout the year allowing a net C uptake from the atmosphere during both the growing and non-growing seasons (between 9 g C m^{-2} in December and 73 g C m^{-2} in July), whereas the senescence of smooth cordgrass plants in some salt marshes (*S. alterniflora* and *S. cynosuroides*, for instance) from October produced a marsh heterotrophy and a net C source to the atmosphere in winter and fall (Schafer et al., 2014; Artigas et al. 2015; Forbrich et al., 2018). In our case, *S. maritima* is a perennial species with a relatively short growing period. Indeed, during winter and fall, the metabolism of this halophytic plant could have a significantly lower influence on marsh C uptake than *H. portulacoides* and *S. vera*. The spatial NEE analysis showed that, in summer during daytime emersion, CO_2 uptake rates of the north sectors (high mudflats areas) were close to ones of the south sectors (high plants areas) which suggests a low heterotrophic respiration in the mudflats during this period. The low R_{eco} rates related to plant and soil respiration processes resulted in lower atmospheric CO_2 emissions in the studied salt marsh than in urban salt marshes (Artigas et al., 2015) and brackish marshes (Knox et al., 2018), thus allowing a net CO_2 sink from winter to summer. Moreover, our low R_{eco} is also likely linked to the low OM decomposition observed at our site, notably due to recalcitrant OM (Arnaud et al., submitted). Furthermore, it is also important to better understand the direct and indirect effects of meteorological conditions and tidal immersion on photosynthesis and respiration processes and the associated marsh C balances (Knox et al., 2018).

Our study showed the predominant role of PAR and Ta on NEE variations in the salt marsh as has already been highlighted elsewhere by Wei et al. (2020b). Our correct NEE flux partitioning into GPP and R_{eco} during emersion indicated that plant photosynthesis was mainly driven by light, while ecosystem respiration was mainly driven by temperature. At the seasonal scale, the strongest CO_2 sinks were measured during warm and bright periods such as spring and summer, which were responsible for 70% of the annual C uptake (Table 3.4). However, although the highest seasonal rate of GPP was measured in summer during the

brightest months, the simultaneously recorded high Ta values instead favoured ecosystem respiration producing a lower net CO_2 uptake in summer than in spring (Table 3.4). For instance, in two urban salt marshes, the Ta values above 30°C reduced CO_2 uptake by increasing respiration and atmospheric CO_2 emissions (Schäfer et al., 2019). These two meteorological parameters controlled short- and long-term NEE variations, as confirmed in urban salt marshes where significant and strong pairwise correlations of NEE with net radiation and temperature were recorded on half hourly, daily and monthly averages (Schäfer et al., 2019).

At the studied salt marsh, we showed a significant influence of VPD and RH on daytime NEE variations favouring plant CO_2 uptake for the lowest VPD values (< 1000 Pa) and the highest RH values (> 80%). The lack of a significant relationship between NEE and RH at night indicated that humidity influenced plant photosynthesis, by decreasing VPD and stomata opening, rather than their respiration. In a similar tidal salt marsh, Forbrich et al. (2018) showed a link between rainfall and C budgets on interannual variations in NEE, i.e. during the early growing season in spring, rainfall events produced a decrease in soil salinity and favoured CO_2 uptake through an increase in plant productivity. In a salt marsh in the Yellow River Delta, significant NEE increases and GPP decreases were recorded with high soil salinities during emersion using static chamber measurements (Wei et al., 2020a). High levels of soil salinity in salt marshes are a stressor for plants such as *Spartina spp.* and can lead to reduce biomass production by inhibiting nutrient and CO_2 uptake throughout stomatal closure (Morris, 1984; Hwang and Morris, 1994). Thus, in our studied marsh, we believe that the increase in dryness periods, especially in summer, with a decrease in rainfall events could profoundly modify plant productivity and marsh C uptake. This was confirmed by a significant reduction in the CO_2 sink at the studied salt marsh with low RH and high Ta values.

4.2.2. Diurnal and tidal scale influences

High-frequency EC measurements demonstrated that diurnal variations in NEE fluxes were driven by light rather than air temperature (Xi et al., 2019; Wei et al., 2020b) with no significant time delay recorded between NEE and PAR variations (Fig. S2). At our studied site, the highest negative correlations between NEE and PAR were highlighted for low daytime PAR values, indicating that the increases in light during the morning strongly favoured CO_2 uptake mainly through plant photosynthesis up to the middle of the day. During

the afternoon, the high Ta and VPD values (warm and dry periods) produced a reduction in photosynthetic rates through stomatal closure of the C3 plants (Lasslop et al., 2010). This GPP decrease associated with a R_{eco} increase in afternoon reduced the net CO_2 uptake up to reach CO_2 emissions during night-time (Knox et al., 2018; Xi et al., 2019). In another tidal salt marsh, Kathilankal et al. (2008) confirmed the PAR importance on *Spartina* photosynthesis and diurnal NEE fluxes. In a restored salt marsh, EC measurements also showed that the time of day has a major influence on atmospheric CO_2 exchanges during the growing season, accounting for 49% of NEE variability (Artigas et al., 2015). Moreover, in some cases, soil respiration can also be controlled by PAR or photosynthesis at the diurnal scale (Vargas et al., 2011; Jia et al., 2018; Mitra et al., 2019), once again highlighting the major role played by light in diurnal NEE variations (Kathilankal et al., 2008; Wei et al., 2020b). In winter, negative NEE fluxes were measured during some night-time emersion periods in the absence of any photosynthetic processes (18.5% in January, 18.1% in February and 10.7% in March). These negative fluxes could have two main sources: (1) an inorganic CO_2 diffusion and dissolution processes in saline/alkaline soils over mudflats (Ma et al., 2013) and (2) an inflow of coastal waters undersaturated in CO_2 with respect to the atmosphere within the footprint area (in channel; Fig. 3.2) but not seen by the STPS probe due to our one-location water height measurement and immersion marsh heterogeneity (see Sect. 2.2). The negative values during night-time emersion could reduce the night-time random forest model performance for EC data gap-filling and produce an underestimation of respiration coefficients for NEE flux partitioning (particularly *b*) even causing a negative coefficient (February; Table S2).

At the daily scale, the intensity of atmospheric CO_2 exchanges and the metabolic status of the marsh (sink/source) were also significantly influenced by the tidal rhythm (Fig. 3.8). Tides produced a significant decrease in daytime CO_2 uptake with maximal reductions up to 90% for the highest tidal amplitudes. In a *S. alterniflora* salt marsh, a mean reduction of 46 ± 26% was measured during immersion, although large CO_2 amounts were still assimilated at a reduced rate (Kathilankal et al., 2008). In some cases, daytime NEE fluxes could be completely suppressed during immersion in salt marshes (Moffett et al., 2010; Forbrich and Giblin, 2015; Wei et al., 2020a) and brackish marshes (Knox et al., 2018). This drop in CO_2 uptake could be related to a physiological stress for plants under tidal immersion conditions resulting in a reduction in the effective photosynthetic leaf area and photosynthesis rates (Kathilankal et al., 2008; Moffett et al., 2010). Moreover, the physical barrier created by tidal waters could limit the CO_2 diffusion from waters to plants, thereby resulting in fewer CO_2

exchanges between the atmosphere and the benthic compartment (sediments and soil). Using chamber measurements at different tidal stages, Wei et al. (2020a) also highlighted the importance of water heights and marsh immersion levels in NEE variations and confirmed a significant GPP decrease during immersion. However, tidal effects on daytime NEE fluxes may be more variable depending on the immersion level of the marsh and the biogeochemistry state of the tidal waters. Indeed, during the brightest periods in winter and spring, the temporary increases in CO_2 uptake recorded during incoming tides could be related to (1) an increase in the GPP of *H. portulacoides* and *S. vera* (highest marsh levels) favoured by VPD and Ta decreases due to tidal conditions and/or (2) tidal waters advected from the shelf that are undersaturated in CO_2 with respect to the atmosphere due to phytoplankton blooms (Mayen et al., in prep.). Moreover, when the salt marsh was fully immersed at high tide during spring tides, NEE fluxes were mostly controlled by ecosystem respiration and/or inorganic processes (carbonate and physicochemical pumps) rather than by photosynthesis, as light was no longer a major controlling factor for CO_2 uptake in tidal waters.

During night-time, CO_2 emissions from the salt marsh were inhibited by tidal effects through a significant decrease in ecosystem respiration (Han et al., 2015; Knox et al., 2018; Wei et al., 2020a). The physical barrier formed by tidal waters limits the atmospheric CO_2 releases via respiration from plants and soils (Wei et al., 2020b). Moreover, saturation of surface soils in tidal waters during immersion could reduce oxygen availability in the soil and limit OM microbial decomposition and CO_2 emissions through aerobic respiration (Nyman and DeLaune, 1991; Miller et al., 2001; Jimenez et al., 2012; Han et al., 2015). In our case, night-time CO_2 exchanges were reduced up to 100% (completely suppressed), sometimes even causing a change in metabolic status of atmospheric CO_2 from source to sink, especially in winter when the R_{eco} rates were the lowest. The presence of tidal waters advected from the shelf during the night and CO_2 undersaturated with respect to the atmosphere due to previous phytoplankton production and/or $CaCO_2$ dissolution in the water column during the day (Gattuso et al., 1999; Polsenaere et al., 2012), could induce a sink which may lead to a net uptake of CO_2 at night (Fig. 3.8). The results of our study indicate that tidal NEE variations may be mainly related to the marsh immersion level, the PAR level and the time of the growing cycle of plants as reported in Nahrawi et al. (2020).

4.3. Salt marsh carbon budgets for future research perspectives

At the annual scale in 2020, the tidal rhythm did not significantly affect the net C balance of the studied salt marsh since similar annual measured NEE and estimated NEE_{marsh} values were recorded (Fig. 3.9). The loss of CO_2 uptake measured during daytime immersion due to a GPP decrease could be compensated by night-time immersion where CO_2 emissions and R_{eco} were inhibited. However, strong temporal variabilities were measured, especially between the growing and non-growing seasons. In winter and fall, the salt marsh did uptake more C from the atmosphere with the tidal influence (measured NEE) than without (estimated NEE_{marsh}), especially in December (+35.7%), November (+19.7%) and January (+15.4%), associated with the highest photosynthetic efficiencies. An opposite trend was observed in spring and summer with a reduction in net C uptake under tidal influence, especially in August (-16.9%) and September (-9.8%). This significant difference in the seasonal C balances could be mainly related to the photoperiod of immersion periods. We demonstrated that daytime immersion decreased CO_2 uptake, whereas night-time immersion decreased CO_2 emissions up to a change in metabolic status for the highest immersion levels. Thus, during seasons where daytime immersion primarily occurs, such as spring and summer, the salt marsh did uptake less atmospheric CO_2 with tidal influence, whereas seasons that mostly have night-time immersion did uptake more atmospheric CO_2 with tidal influence (Table 3.4). However, this unpublished result was only possible provided that the salt marsh switched from a source to a sink of CO_2 during night-time immersion due to water undersaturation with respect to the atmosphere. In a salt marsh on Sapelo Island (USA), Nahrawi et al. (2020) highlighted tidal CO_2 flux reductions all year round by distinguishing neap tide and spring tide periods. Their results showed that the highest and lowest reductions in C uptake occurred in spring (-34%) and summer (-13%), respectively, with a similar but greater tidal influence on the C uptake values compared with our study.

To better constrain the tidal influence on the metabolism of the salt marsh, further investigations have been carried out in 2021 in parallel with our EC measurements, with the construction of a digital field model for water heights that can be used to spatially determine, over the whole EC footprint, the exact areas of immersion and emersion (especially for the low water levels) of the marsh in each sector at a 10-min. step. Similarly, during marsh immersion, EC measurements do not directly capture CO_2 fluxes from benthic metabolism because of the physical barrier of the water and the lower CO_2 diffusion rates in water than in air. Consequently, at the same time as when the NEE measurements were taken, water pCO_2, inorganic and organic carbon concentrations associated with planktonic metabolism were

determined each season through 24-h cycles to provide essential information on the contribution of planktonic communities and plants to CO_2 fluxes during immersion (Mayen et al., in prep.). The lateral carbon export from salt marshes by tides plays a significant role in the coastal ocean carbon cycle (Guo et al., 2009; Wang et al., 2016). Plant respiration and microbial mineralization of marsh NPP could generate DIC in waters associated with a strong benthic-pelagic coupling. Thus, our 2021 measurements of the carbon parameters, planktonic metabolism (production and respiration) and other relevant biogeochemical variables over 24-h diurnal cycles, along with measurements of the soil compartment (root OM production versus mineralization; Arnaud et al., submitted) carried out in the EC footprint would allow for a more integrative calculation of the studied marsh carbon budget (Mayen et al., in prep.). One advantage of the EC measurements is the aggregation of CO_2 fluxes from all compartments (waterbodies, soil, plants and atmosphere) in salt marshes. Yet, through this flux aggregation, we cannot mechanistically understand each marsh compartment, and therefore it can be challenging to predict CO_2 fluxes under multiple global changes. Therefore, future contributions should try to simultaneously quantify all these compartments, especially soil as it is where most of the carbon is stored in salt marshes (Arnaud et al., submitted). Ongoing atmospheric CO_2 exchange measurements are actually carried out since January 2023 up north over the Aiguillon intertidal Bay in France where we precisely deployed an EC station at the edge between the tidal mud flat on the west side and salt marsh habitats on the east side of the footprint along with benthic chamber flux and water, sediment, soil carbon measurements and satellite analysis at each season to specially address questions on relative habitat (mudflat versus salt marshes) influence on atmospheric CO_2 exchanges (P. Polsenaere, personal communication).

5. Conclusion

In this study, we used the micrometeorological eddy covariance technique to investigate the net ecosystem CO_2 exchanges (NEE) at different timescales and to determine the major biophysical drivers of a rewilded tidal salt marsh. During the year 2020, the net C uptake from the atmosphere (-483 g C m^{-2} yr^{-1}) was mainly related to a low OM decomposition rate coupled with an intense autotrophic metabolism of halophyte plants, especially during the growing season, driven by light, temperature and VPD. In summer, the brightest days increased the plant GPP and simultaneously, high temperature and VPD values favoured R_{eco} resulting in a lower net CO_2 uptake in summer than in spring. At the daily scale, the tidal

rhythm significantly influenced NEE fluxes according to the level of marsh immersion and PAR. During daytime, tides strongly limited atmospheric CO_2 uptake, up to 90% reductions whereas night-time immersion inhibited atmospheric CO_2 emissions through plant and soil respiration, sometimes even causing a change in metabolic status from source to sink. However, at the annual scale, NEE flux partitioning into NEE_{marsh} highlighted that the tidal rhythm did not significantly affect the net marsh C balance. Our continuous NEE measurements have made it possible to better understand the biogeochemical functioning of salt marshes over a wide range of environmental conditions and have provided essential information on NEE fluxes in marshes undergoing potential future changes such as global warming or sea level rise.

Data availability

All raw data can be provided by the corresponding authors upon request.

Author contribution

TLL and PP facilitated the funding acquisition. PP, EL and JMB conceptualized and designed the study. JM and PP compiled and prepared the datasets. JM and PK performed statistical and time-series analyses. JM, PP, EL and PK investigated and analysed the data. PK and RC executed the random forest model. JM, PP, EL, PK, ARG and PS confirmed the data. PP, EL, MA, JMB, PG, JG and RC provided resources. JM performed the graphics and wrote the manuscript draft. PP, EL, MA, PK, RC, ARG and PS reviewed and edited the manuscript. PP, ARG and PS supervised the PhD thesis of JM.

Competing interests

The authors declare that they have no conflict of interest.

Acknowledgements

Jérémy Mayen thanks Ifremer (the French research institute for exploitation of the sea) for financing his PhD thesis (2020-2023). We are grateful to our colleagues (Didier Garrigou, Jean-Michel Chabirand, Jean-Christophe Lemesle and Jonathan Deborde) who contributed to the fieldwork carried out during this study. We thank Susann-Catrin Zech for her contribution in the field (photographs) and trainees (Camille Pery, Maxime Coutantin and Maxime Paschal) for their contributions to data analysis. Our grateful acknowledgements also go to the two reviewers (Francisco Artigas and an anonymous referee) for their constructive comments

and suggestions. The proofreading of the manuscript and the correcting of the English content were carried out by Sara Mullin (PhD; freelance translator). This work is a contribution to the Jérémy Mayen's PhD thesis and the ANR-PAMPAS project (Agence Nationale de la Recherche « Evolution de l'identité patrimoniale des marais des Pertuis Charentais en réponse à l'aléa de submersion marine », ANR-18-CE32-0006).

Supplementary materials (Mayen et al., 2024)

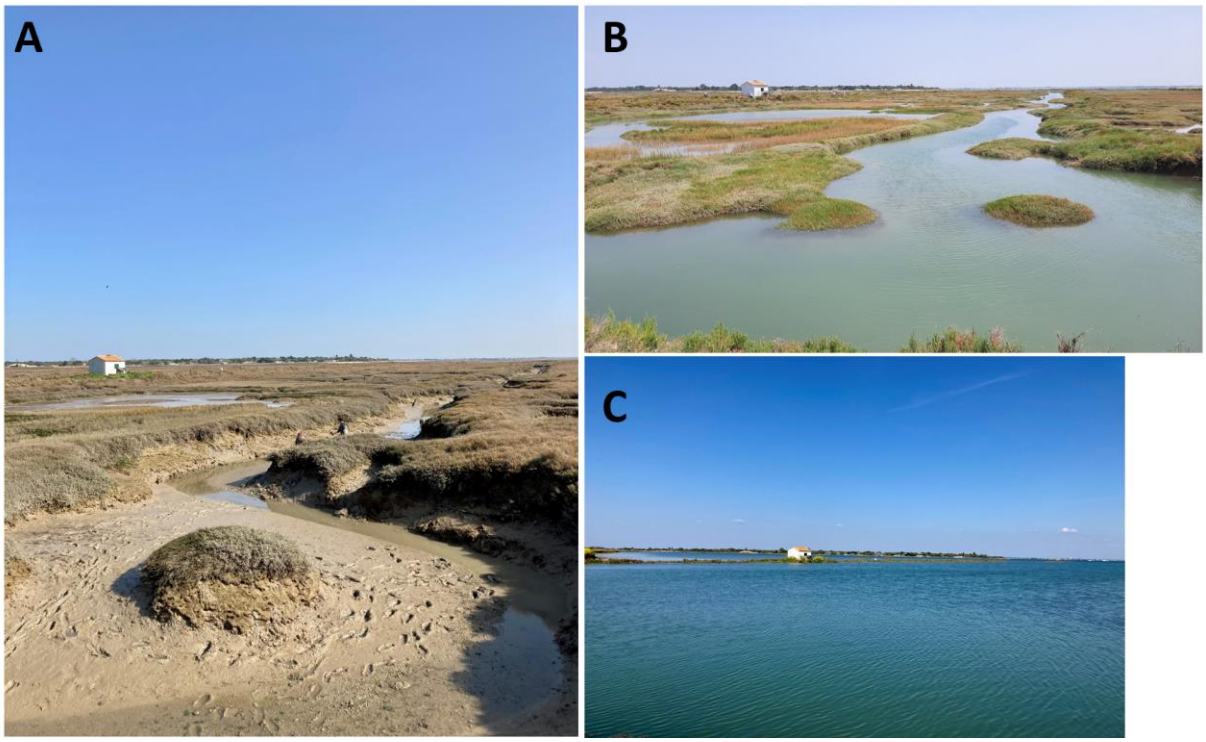

Figure S1: Pictures of the Bossys perdus salt marsh during emersion (A; 01/03/2021 15:00, Hw = 0 m) and immersion (B, 22/07/2021 13:00, Hw = 0.3 m; C, 27/04/2021 16:00, Hw = 1.8 m). Picture A was taken at low tide when all the marsh plants were emerged into the atmosphere. During this time, the channel drains the upstream marsh waters to the estuary. Picture B was taken during incoming tide when advected coastal waters completely fill the channel and immerse the marsh. Picture C was taken at high tide during the highest tidal amplitude when all the marsh plants were immersed by coastal waters. Water heights (Hw) were measured from the STPS sensor located on the salt marsh and not in the channel (see M&M section and Figure 3.2). © P. Polsenaere.

Table S1: Performance indicators for each model (RF: Random Forest, ANN: Artificial Neural Network) tested to gap fill the CO_2 fluxes. Predictor variables are PAR (Photosynthetically active radiation, µmol m^{-2} s^{-1}), Ta (air temperature, °C), Hw (water height, m), RH (Relative Humidity, %) and Vd (wind direction, m s^{-1}). The performance indicators are the coefficient of linear determination Pearson which shows the level of variability captured by the model (R^2), the racine of the error quadratic average which gives an overview of the uncertainty of the result (RMSE: Root Mean Square Error), as well as the bias of the model.

Models	**Predictor variable**	**RMSE**	**Bias**	**R^2**
RF1	PAR, Ta, Hw	1.42	0.0039	0.85
RF2	PAR, Ta, Hw, RH	1.27	0.0024	0.88
RF3	PAR, Ta, Hw, Vd	1.19	0.0029	0.90
ANN1	PAR, Ta, Hw	1.95	-0.0003	0.71
ANN2	PAR, Ta, Hw, RH	1.89	0.0021	0.73
ANN3	PAR, Ta, Hw, Vd	1.81	0.0041	0.75

Table S2: Estimation of the parameters used for NEE flux partitioning (a_1, a_2, R_0 and *b*) during emersion at the monthly scale. The a_1 coefficient is directly linked to the phenology of the ecosystem.

	a_1	**a_2**	**R_0**	***b***
January	-7.82	370	0.34	0.04
February	-9.89	435	0.64	-0.03
March	-9.38	506	0.17	0.15
April	-12.51	787	0.24	0.12
May	-13.41	812	0.35	0.10
June	-14.68	846	0.68	0.06
July	-14.98	934	0.84	0.05
August	-17.91	1397	0.56	0.07
September	-16.86	1419	0.32	0.09
October	-13.08	766	0.58	0.06
November	-14.37	783	0.19	0.14
December	-7.60	360	0.31	0.09

Table S3: Monthly mean (µmol CO_2 m^{-2} s^{-1}) and monthly cumulative (g C m^{-2} $month^{-1}$) fluxes of the measured NEE and estimated NEE_{marsh} during marsh emersion periods (Hw = 0 m). These comparisons between measured NEE and estimated NEE_{marsh} only during marsh emersion allowed to confirm the correct NEE flux partitioning (see M&M section).

	Mean NEE (µmol CO_2 m^{-2} s^{-1})	**Mean NEE_{marsh} (µmol CO_2 m^{-2} s^{-1})**	**Cumulative NEE (g C m^{-2})**	**Cumulative NEE_{marsh} (g C m^{-2})**
January	-0.75	-0.77	-18.2	-18.7
February	-1.55	-1.56	-34.8	-35.0
March	-1.53	-1.53	-37.3	-37.3
April	-1.95	-1.93	-45.2	-44.9
May	-2.16	-2.16	-53.0	-53.2
June	-2.29	-2.30	-50.6	-50.9
July	-2.34	-2.33	-57.7	-57.6
August	-1.24	-1.27	-29.9	-30.6
September	-1.14	-1.13	-27.2	-26.9
October	-0.80	-0.80	-18.4	-18.4
November	-0.63	-0.61	-14.8	-14.4
December	-0.40	-0.40	-6.3	-6.2

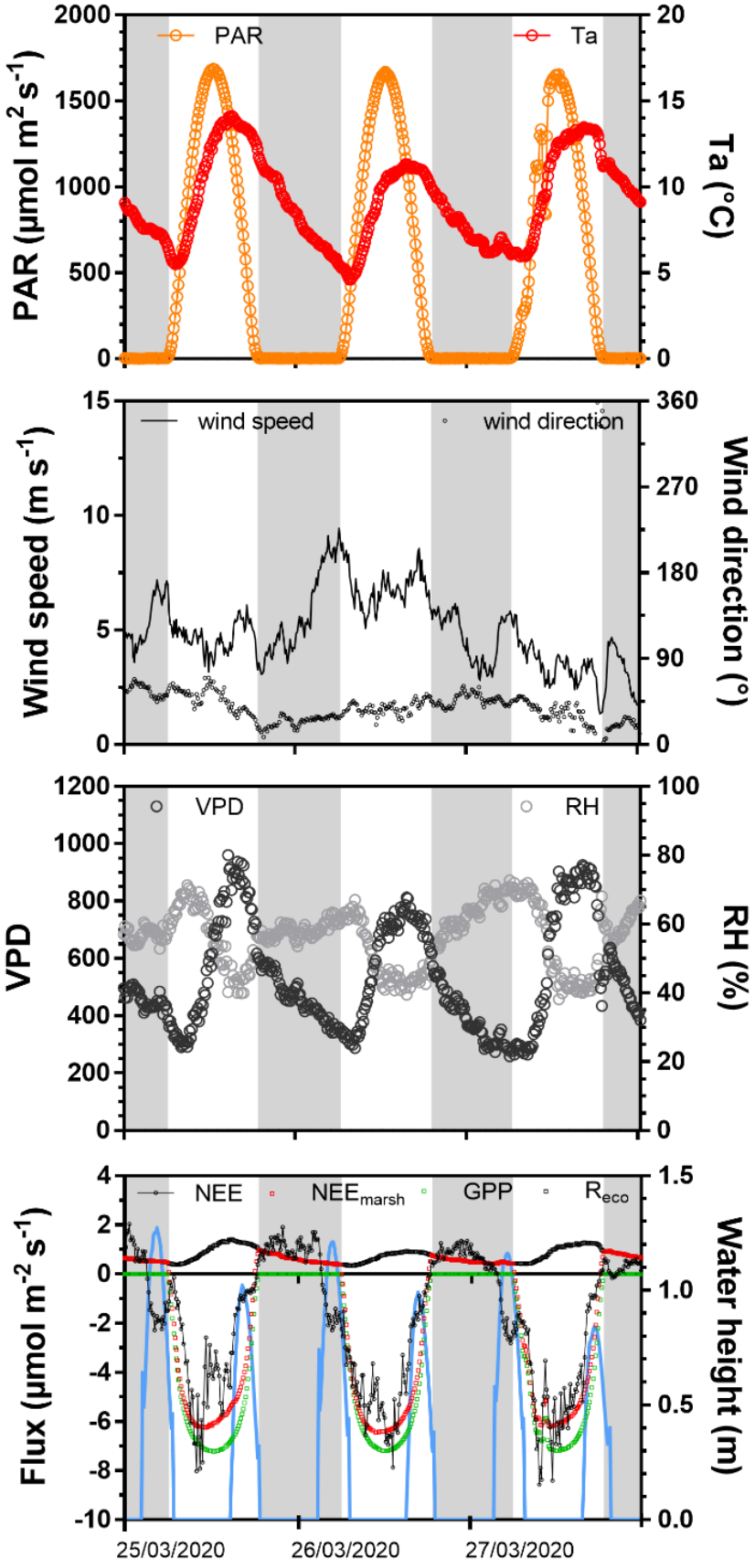
PAR
Ta
PAR (µmol m-2 s-1)
Ta (°C)
wind speed
wind direction
Wind speed (m s-1)
Wind direction (°)
VPD
RH
VPD
RH (%)
NEE
NEEmarsh
GPP
Reco
Flux (µmol m-2 s-1)
Water height (m)
25/03/2020
26/03/2020
27/03/2020

Figure S2: Temporal variations of PAR (µmol m^{-2} s^{-1}), Ta (°C), wind speed (m s^{-1}), wind direction (°), VPD (Pa), RH (%), measured NEE, estimated NEE_{marsh}, estimated GPP and estimated R_{eco} (µmol CO_2 m^{-2} s^{-1}) and water height (Hw, m) values measured at a 10-minute frequency in early spring 2020 from 25/03/2020 (00:00 am) to 27/03/2020 (23:50 pm). Grey areas correspond to night-time periods (PAR ≤ 10 µmol m^{-2} s^{-1}). This temporal window in March 2020 was chosen to highligh the marsh CO_2 sink during night-time immersion, the rapid decrease of CO_2 uptake during daytime immersion and the negative correlation between NEE and PAR.

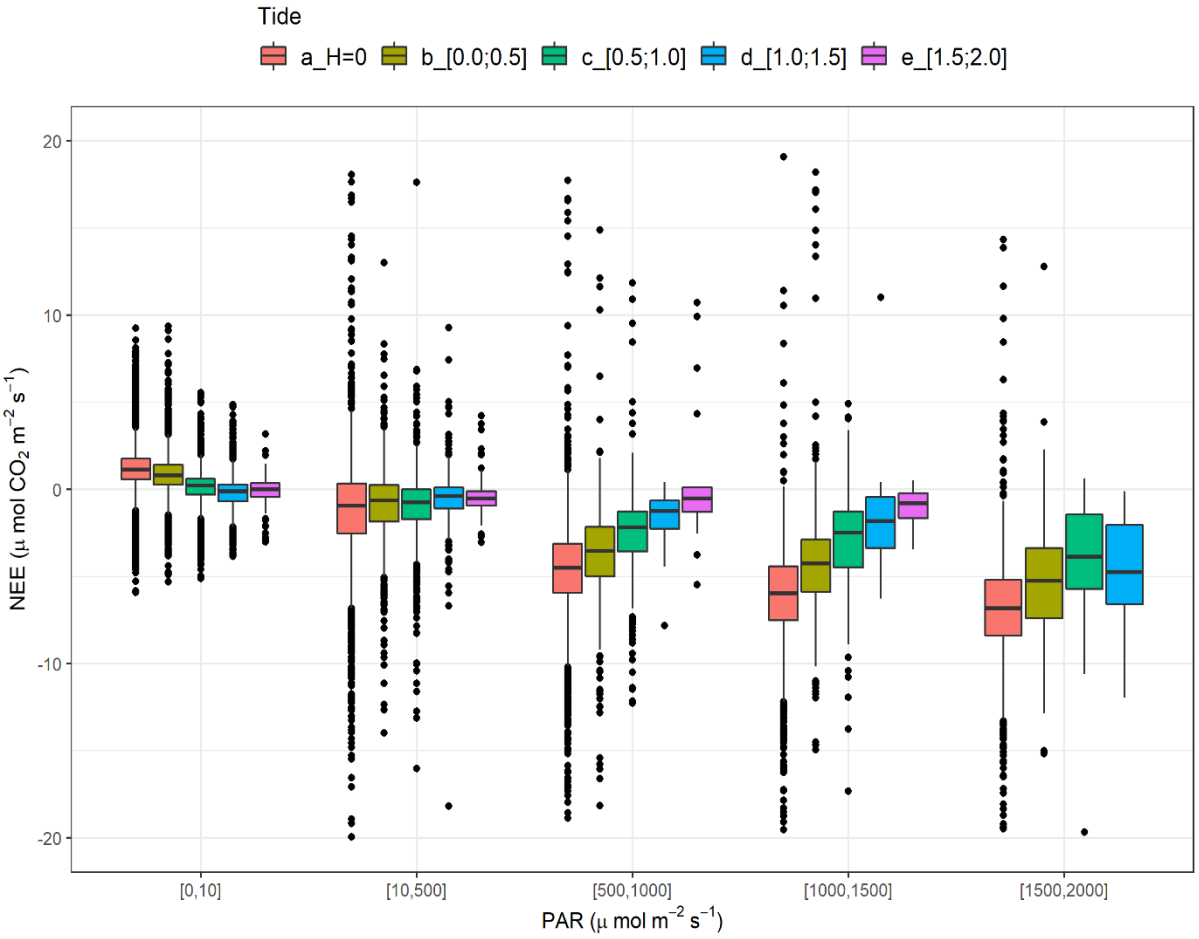

Figure S3: Diurnal/tidal variations (boxplots) of NEE fluxes (µmol CO_2 m^{-2} s^{-1}) during marsh emersion (Hw = 0 m) and at four water level ranges of 0.5 m within five PAR groups. The five PAR groups are 0 < PAR ≤ 10 (night), 10 < PAR ≤ 500, 500 < PAR ≤ 1000, 1000 < PAR ≤ 1500, 1500 < PAR ≤ 2000 µmol m^{-2} s^{-1}.

Chapitre IV

Influence du métabolisme aquatique des marais littoraux sur la dynamique temporelle du carbone

Début d'immersion au marais tidal des Bossys perdus (île de Ré, Fier d'Ars) lors d'une marée montante (26/07/2021). © Mayen.

Influence of aquatic metabolism on temporal marsh carbon dynamics and associated atmospheric CO_2 fluxes

Jérémy Mayen[1,2], Pierre Polsenaere[2], Aurore Regaudie de Gioux[3], Jonathan Deborde[2], Karine Collin[1], Yoann Le Merrer[1], Élodie Foucault[4], Vincent Ouisse[4], Laurent André[5,6], Éric Lamaud[7] and Philippe Souchu[1]

Corresponding author: Jérémy Mayen (jeremy.mayen@ifremer.fr).

[1]Ifremer, LITTORAL, F-44000 Nantes, France

[2]Ifremer, LITTORAL, F-17390 La Tremblade, France

[3]Ifremer, DYNECO, F-29280 Plouzané, France

[4]MARBEC, Univ. Montpellier, CNRS, Ifremer, IRD, Sète, France

[5]BRGM, F-45060 Orléans, France

[6]ISTO, UMR7327, Université d'Orléans, CNRS, BRGM, F-45071 Orléans

[7]INRAE, Bordeaux Sciences Agro, ISPA, F-33140 Villenave d'Ornon, France

A research paper in preparation for Limnology and Oceanography (Mayen et al., in prep.).

Abstract

Salt marshes are highly productive coastal ecosystems allowing atmospheric CO_2 uptake through primary production of halophyte plants. These tidal systems also export large and variable amounts of organic and inorganic carbon (C) processed by marsh metabolism. However, the strong temporal variations of vertical and horizontal C fluxes need to study the whole marsh metabolism taking terrestrial and aquatic compartments into account and distinguishing their contributions to atmospheric CO_2 exchanges measured by Eddy Covariance. Within a temperate salt marsh, seasonal 24-hour cycles were performed to measure relevant biogeochemical parameters (water pCO_2, organic and inorganic C and nutrients), planktonic metabolism and net ecosystem CO_2 exchanges (NEE) at the diurnal and tidal scales. In this study, water pCO_2 were mainly controlled by biological activity inducing water CO_2 oversaturation in winter due to heterotrophic processes and water CO_2 undersaturation in spring and summer due to autotrophic processes. In winter, the highest concentrations in DIC, TA and nutrients (NH_4^+ and PO_4^{3-}) measured at low tides could come from sediment heterotrophy and exported to channel waters by tidal pumping. On the contrary, in spring and summer, the significant water pCO_2 decreases and DOC increases from high to low tides could be related to a strong marsh primary production including plants, macroalgae and phytoplankton. At low tides, planktonic metabolism had a significant influence to water pCO_2 inducing a net uptake in winter and spring and a net source in summer and fall but planktonic communities did not play a significant role in marsh C balances at the ecosystem scale.

Key words

salt marsh, 24-hour cycles, water pCO_2, net ecosystem CO_2 exchanges, organic and inorganic carbon, nutrients, planktonic metabolism.

Graphical Abstract

Marsh influenced by coastal waters

Coastal influence → Salt marsh influence

Channel influenced by the salt marsh

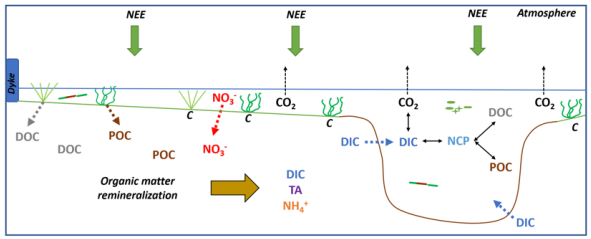

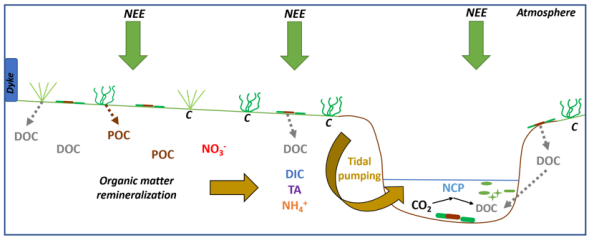

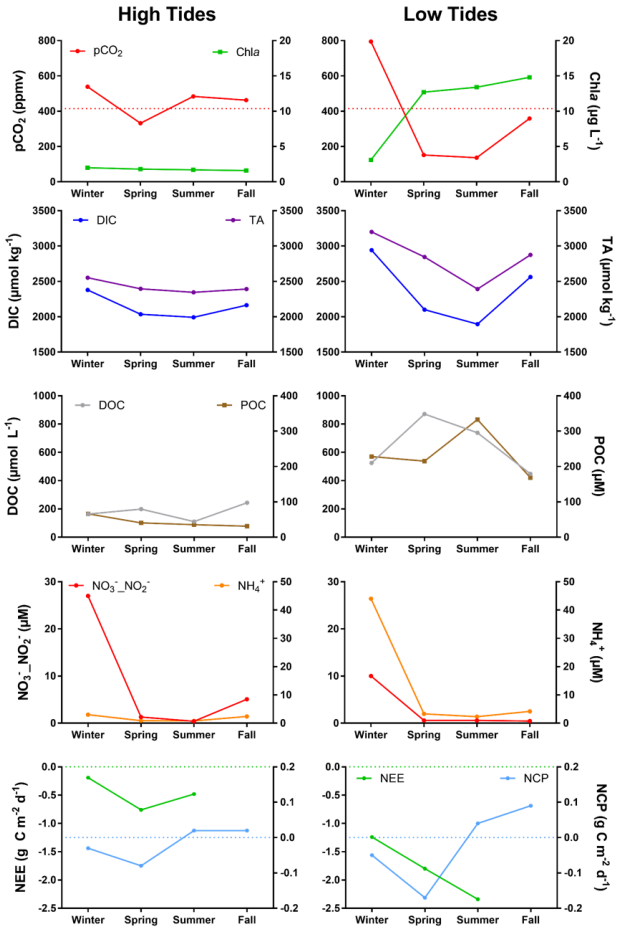

- March waters oversaturated in CO_2 (except in spring)
- Large allochthonous NO_3^-_NO_2^- inputs
- Weak planktonic activity (NCP)
- Low marsh CO_2 uptake (NEE)

- Channel waters undersaturated in CO_2 (except in winter)
- Large increases in DIC, TA and NH_4^+
- Strong planktonic activity (NCP)
- High marsh CO_2 uptake (NEE)

1. Introduction

Since several decades, atmospheric CO_2 emissions by anthropogenic activities strongly modified biogeochemical equilibrium of the global carbon cycle (Friedlingstein et al. 2019) favouring global warming and sea level rise (Lee et al., 2021). Significant amounts of anthropogenic CO_2 have been taken up by terrestrial and marine environments through photosynthesis of vegetation and phytoplankton (Canadell et al., 2021). However, some uncertainties yet remain on the redistribution of these CO_2 fluxes within coastal systems such as salt marshes that play a significant role in the carbon biogeochemical processes at the terrestrial-aquatic-atmospheric exchange interfaces (Cai 2011; Bauer et al. 2013; Alongi 2020).

Salt marshes are among the most productive ecosystems in the biosphere with gross primary production (GPP) rates ranging from 1900 to 3600 g C m^{-2} yr^{-1} and net ecosystem production (NEP) rates ranging from 150 to 1600 g C m^{-2} yr^{-1} (Duarte et al. 2005; Hopkinson and Smith 2005; Gedan et al. 2009), allowing to behave as significant CO_2 sinks (Cai 2011). A part of marsh primary production (~10%) can be buried as “blue carbon” in sediments and/or plant living biomass (Chmura et al. 2003; Macreadie et al. 2017) helping to offset anthropogenic CO_2 emissions. Blue carbon burial rates in coastal wetlands such as salt marshes (218 ± 24 g C m^{-2} yr^{-1}), mangroves (226 ± 39 g C m^{-2} yr^{-1}) and seagrass beds (138 ± 38 g C m^{-2} yr^{-1}), are among the highest, making a major contribution to the global carbon cycle compared with terrestrial ecosystems (Mcleod et al. 2011). The majority of the marsh primary production (> 70%) is respired by heterotrophic processes and exported out of the system through horizontal and vertical carbon fluxes whose dynamics depends on seasonal, diurnal and tidal rhythms (Wang et al. 2016). Various respiration processes in marsh sediments produce and export important quantities of dissolved inorganic carbon (DIC) and total alkalinity (TA) from high to low tides strongly influencing in turn partial pressures of CO_2 (pCO_2) or more generally the carbonate systems of tidal waters (Wang et al. 2018; Song et al. 2023; Reithmaier et al. 2023) and the carbon balance of downstream coastal systems (Cai 2011; Bauer et al. 2013). The "marsh CO_2 pump" hypothesis proposes that atmospheric CO_2 uptake by salt marshes and the export of inorganic carbon would be one of the main mechanisms making adjacent coastal waters sources of CO_2 for the atmosphere (Wang and Cai 2004). The second pathway for marsh carbon loss is vertical carbon fluxes with the atmosphere both from emerged and immerged marsh respirations (Song et al. 2023). In salt marshes, strong heterogeneity of horizontal and vertical carbon fluxes due to seasonal, diurnal

and tidal rhythms (Cai 2011; Wang et al. 2016) requires integrative measurements of net ecosystem CO_2 exchanges (NEE) simultaneously with organic and inorganic carbon of tidal waters to evaluate marsh carbon dynamics at all different temporal scales (Wang et al. 2018; Alongi 2020).

In terrestrial ecosystems, NEE measured by atmospheric Eddy Covariance (EC) generally correspond to NEP (Kowalski et al. 2003; Chapin et al. 2006). However, in salt marshes, the later relationship is more complex and NEE does not fully correspond to NEP since lateral DIC exports are not captured by EC measurements, especially during transient tidal phases (flooding/ebbing) (Wang et al. 2018; Mayen et al. 2024). During marsh emersion, NEE mainly occurs at the soil-atmosphere interface, implying a strong contribution from benthic NEP (plants and sediments) to atmospheric CO_2 exchanges. Indeed, salt marshes, with a large halophyte vegetation cover, have high rates of primary production and respiration (Schäfer et al. 2014; Forbrich and Giblin 2015) inducing net CO_2 uptake during daytime emersion (-3.86 ± 3.62 µmol m^{-2} s^{-1}) and net CO_2 emission during night-time emersion (1.22 ± 1.18 µmol m^{-2} s^{-1}; Mayen et al. 2024). In addition, the microphytobenthos (MPB) on sediments, composed of benthic microalgae, can migrate to the surface of muddy sediments during daytime emersion to use photosynthetically active radiation (PAR) and contribute to benthic NEP (Migné et al. 2007; Xi et al. 2019). On the contrary, marsh sediments can also behave as a net source of atmospheric CO_2, especially during non-growing season for plants, mainly related to microbial decomposition of soil organic carbon (Gong et al. 2023). During marsh immersion, advected coastal waters create a physical barrier between benthic and atmospheric compartments which strongly influences NEE (Chapin et al. 2006; Mayen et al. 2024). In this situation, NEE involves cumulated contributions from benthic NEP, planktonic NEP and horizontal carbon exchanges by tidal advection. In addition, during immersion, the organic carbon produced at emersion can be transferred to the water column and contribute to planktonic NEP such as MBP (Polsenaere et al. 2012; Savelli et al. 2019). The shallowness of salt marshes can favour primary production of planktonic communities through a significant light penetration in waters (Gazeau et al. 2004) and also strong benthic exchanges producing DIC in waters (Wang and Cai 2004; Wang et al. 2016; Gong et al. 2023). In salt marshes, previous studies highlighted CO_2 emissions at the water-atmosphere interface due to heterotrophy of aquatic metabolism (0.06 and 0.02 mol C m^{-2} d^{-1} in summer and winter, respectively, in the Duplin salt marsh estuary; Wang et al. 2018). However, a limited number of studies showed the contribution of water CO_2 biogeochemical status and planktonic

communities on marsh metabolic fluxes at the ecosystem scale (Song et al. 2023). Thus, it is of paramount importance to more precisely study the whole marsh metabolism taking terrestrial and aquatic compartments into account at the different spatio-temporal scales and distinguishing their respective contributions to ecosystem CO_2 exchanges (sink/source).

This biogeochemical study focuses on the aquatic metabolism influence on carbon dynamics (horizontal and vertical fluxes) in a temperate salt marsh. For this purpose, we performed four seasonal 24-hour cycles, measuring relevant biogeochemical parameters (water pCO_2, organic and inorganic carbon and nutrients), planktonic metabolism and atmospheric CO_2 fluxes in a main channel of the studied salt marsh connected to upstream artificial marsh and downstream shelf waters. The main focuses of this paper are (1) to highlight biotic and abiotic controlling factors on water carbon variations and particularly water pCO_2, (2) to study the metabolic status of planktonic communities in the marsh as sink or source of CO_2 and (3) to identify the contribution of biogeochemical water signatures on NEE fluxes.

2. Materials and methods

2.1. Study site

The Bossys perdus salt marsh is a vegetated intertidal wetland (52.5 ha) along the French Atlantic coast on Ré Island (Fig. 4.1-A). After an intensive land-use (salt harvesting, oyster farming), the salt marsh is now protected inside a National Natural Reserve (NNR) since 1981 to restore its natural hydrodynamics and its halophile vegetation (Champion et al. 2012). The salt marsh is located within the Fier d'Ars tidal estuary that exchanges coastal waters with the Breton Sound continental shelf (Bel Hassen 2001) allowing to (1) flood the intertidal zone of the estuary including mudflats (slikke) and salt marshes (schorre) and (2) supply the artificial salt marshes (i.e. salt ponds) upstream of the dyke (Fig. 4.1-A). The water residence times in salt ponds vary from few hours to fifteen days according to the seasonal management practice (Mayen et al. 2023). The Bossys perdus salt marsh is subjected to semi-diurnal tides from the shelf (Fig. 4.1-A) allowing the marsh immersion through channels differently in space, in time and frequency according to tidal periods. During high tide (HT) periods, imported coastal waters gradually fill the sampling channel (southern sector; Fig. 4.1-B) and can immerge the salt marsh through variable water heights depending on tidal amplitudes and meteorological conditions (Mayen et al. 2024, Fig. S1). On the contrary, during low tide (LT) periods, the

vegetation cover of the marsh, mainly composed by *Halimione portulacoides*, *Spartina maritima* and *Suaeda vera*, is emerged and exposed to the atmosphere (Mayen et al. 2024, Fig. S1). At that time (LT), waters remaining in the sampling channel are influenced and exported from upstream salt ponds to the downstream estuary (Fig. 4.1-B) with constant water heights. Generally, macroalgae blooms (*Ulva spp.*) colonized each year artificial salt marsh ponds from April to October during each year (Mayen et al. 2023).

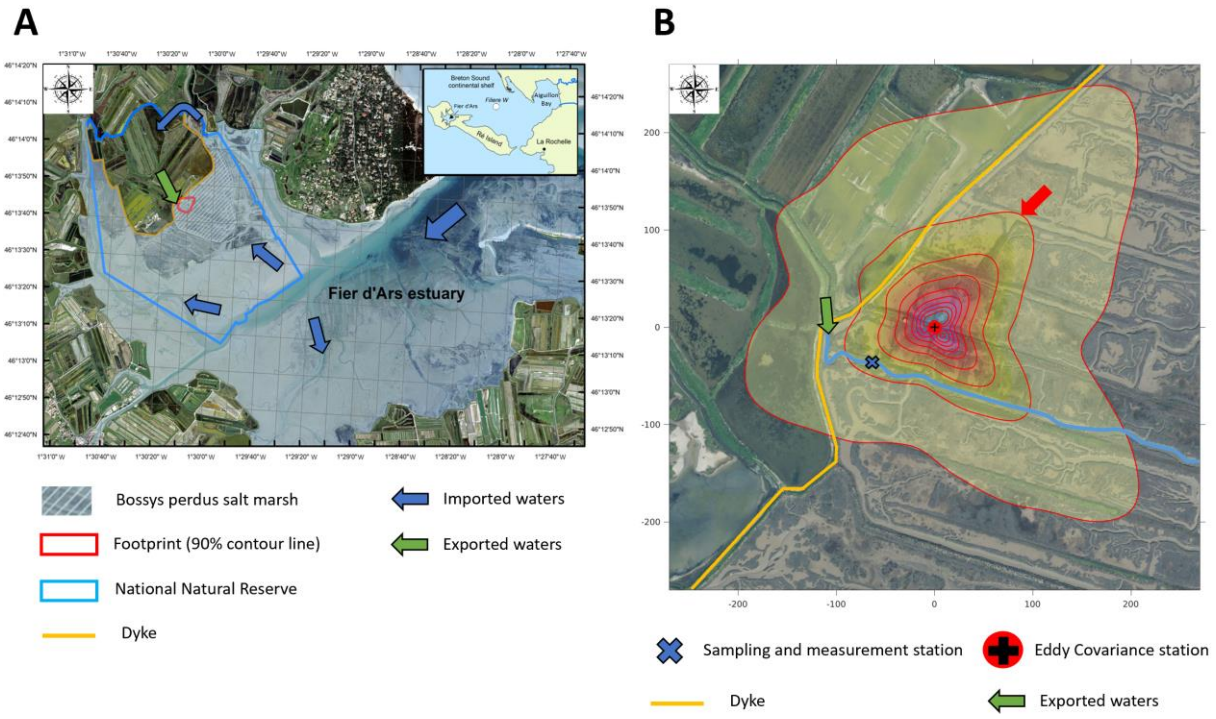

Figure. 4.1: (A) The Bossys perdus salt marsh located on the French Atlantic coast within the National Natural Reserve on Ré Island. This intertidal salt marsh is connected to the downstream Fier d'Ars estuary (light blue under tidal immersion) and the upsteam artificial salt marshes (salt ponds). The dyke (orange line) separates terrestrial and maritime marsh areas. Blue arrows represents coastal water inputs from the estuary and the continental shelf at high tides (tidal marsh flooding and artificial marsh supplying) and green arrows represents exported waters from artificial salt marshes to the estuary through the Bossys perdus channel at low tides. The studied footprint area (80% countour line) of the Bossys perdus marsh is indicated (red line). **(B)** Location and set-up of the eddy covariance (EC) system within the Bossys perdus salt marsh at low tide (marsh emersion) and its associated footprints averaged over the year 2021 (Kljun et al., 2015). The red arrows corresponds to the studied 80% footprint countour line encompassing the water sampling location (blue cross).

2.2. Sampling strategy and field techniques

Four 24-h cycles were performed at the seasonal scale from March to December 2021 (Tables 4.1 and 4.2) in the main tidal channel to the south of the Bossys perdus salt marsh (Fig. 4.1-B). For each 24-h cycle, our sampling strategy consisted of measuring relevant biogeochemical parameters and the associated planktonic metabolism simultaneously with atmospheric CO_2 fluxes at diurnal (daytime and night-time) and tidal (low tide and high tide) scales through discrete samplings and continuous real-time measurements, respectively. At the same station, the discrete sampling of sub-surface waters was performed every hour or two hours during each 24-h cycle (n = 13 over C1-winter, n = 15 over C2-spring and C3-summer and n = 16 over C4-fall) with a large variation in water heights: from the bottom of the channel at low tide (Hw = 0.5 m) to the full marsh immersion at high tide (Hw > 2.5 m) (Fig. 4.2). These discrete samplings allowed the analysis of photosynthetic pigments (Chl*a*), carbonate system parameters (DIC and TA), nutrients (NO_3^-_NO_2^-, NH_4^+, DIP and DSi) and dissolved and particulate organic matter parameters (DOC, DON, POC and PON) (Table 4.3). Water samples were collected with a 5 L glass bottle, directly filtered on the field and then conditioned for chemical analysis at the laboratory. For the organic matter, the sampling equipment was pre-washed with HCl 10% (for 12h), rinsed with de-ionised water and dried. The glassware (filter holders, filtration funnels, GF/F filters, vials and syringe) was pre-combusted (for 4h at 450°C). These two treatments eliminated any trace of inorganic and organic carbon (Lorrain et al. 2003). For the planktonic metabolism measurements, water samples were collected every six hours during each 24-h cycle (n = 4) successively at LT (channel waters) and HT (marsh waters). Additionally, in sub-surface waters, partial pressure of CO_2 (pCO_2), temperature, salinity and dissolved oxygen concentration (DO) were autonomously measured every 10 min. by *in situ* probes (C-sense and EXO2 probes). These measurements were performed at the same frequency during 4 days before each 24-h cycle (i.e. 5 days of continuous measurements per season).

The sampling strategy successively at LT (channel waters influenced by salt marsh) and at HT (marsh waters influenced by shelf) both at day and night allowed to take into account all temporal variability during 24-h cycles (LT/Day, HT/Day, LT/Night, HT/Night; Fig. 4.2).

Table 4.1: *In situ* 24-h cycles and associated meteorological parameters measured by the EC station (means and standard deviations in bold and ranges in brackets) across the seasons of the year 2021 at the Bossys perdus salt marsh. Dates and times of start and end of each 24-hour cycles were indicated (times in universal time). Cumulated rain over 7 days before cycles were done. Meteorological parameter averages over each 24-h cycle were compared to a longer seasonal reference period (Table S1). NA: wind data could not be measured over the C4-fall. Ta: air temperature; RH: relative humidity.

24-h cycle	Season	Date	Time (start-end)	Ta (°C)	Daytime PAR (µmol m^{-2} s^{-1})	Wind speed (m s^{-1})	RH (%)	7-day cumulated rain (mm)
C1	**winter**	01-02 March	09:00-09:00	**11.4 ± 1.9** (8.7 – 15.3)	**762 ± 465** (10 – 1335)	**2.33 ± 1.19** (0.45 – 5.09)	**75.2 ± 10.0** (54.8 – 89.5)	**2.1**
C2	**spring**	27-28 April	08:00-08:00	**13.8 ± 2.9** (9.4 – 20.1)	**1134 ± 668** (10 – 1964)	**3.80 ± 1.29** (0.38 – 6.27)	**65.6 ± 14.4** (31.5 – 84.1	**0.2**
C3	**summer**	26-27 July	08:00-08:00	**19.6 ± 0.6** (18.5 – 20.8)	**976 ± 728** (10 – 2216)	**3.11 ± 0.83** (1.14 – 5.05)	**78.6 ± 2.6** (73.2 – 88.9)	**4.5**
C4	**fall**	06-07 December	09:00-09:00	**10.3 ± 0.7** (7.9 – 11.3)	**160 ± 93** (10 – 340)	NA	**87.8 ± 6.5** (73.4 – 97.5)	**25.0**

Table 4.2: *In situ* 24-h cycles and associated tidal rhythm parameters corresponding to each seasonal sampling period. The same diurnal/tidal synchronism (low and high tides at the same period of the day) during each 24-h cycle was adopted. Hw ranges (m) correspond to the water height amplitudes measured for each tidal cycle in the sampling channel (Fig. 4.1-B). The daytime and night-time marsh immersion duration corresponded to hours per day (h d^{-1}) where coastal waters completely fill the channel and flood the habitats of the Bossys perdus salt marsh. See the Table 4.1 caption for more information.

24-h cycle	Season	Date	Time (start-end)	Low/High tide hours	Hw range (m)	Daytime marsh immersion (h d^{-1})	Night-time marsh immersion (h d^{-1})
C1	**winter**	01-02 March	09:00-09:00	11:22 / 17:18	0.50 – 2.50	4	4
				23:37 / 05:34	0.50 – 2.65		
C2	**spring**	27-28 April	08:00-08:00	09:51 / 16:00	0.50 – 2.70	5	5
				22:11 / 04:20	0.50 – 2.80		
C3	**summer**	26-27 July	08:00-08:00	11:19 / 17:27	0.50 – 1.90	4	4
				23:46 / 05:50	0.50 – 1.75		
C4	**fall**	06-07 December	09:00-09:00	11:01 / 17:14	0.50 – 2.40	5	5
				23:23 / 05:37	0.50 – 2.60		

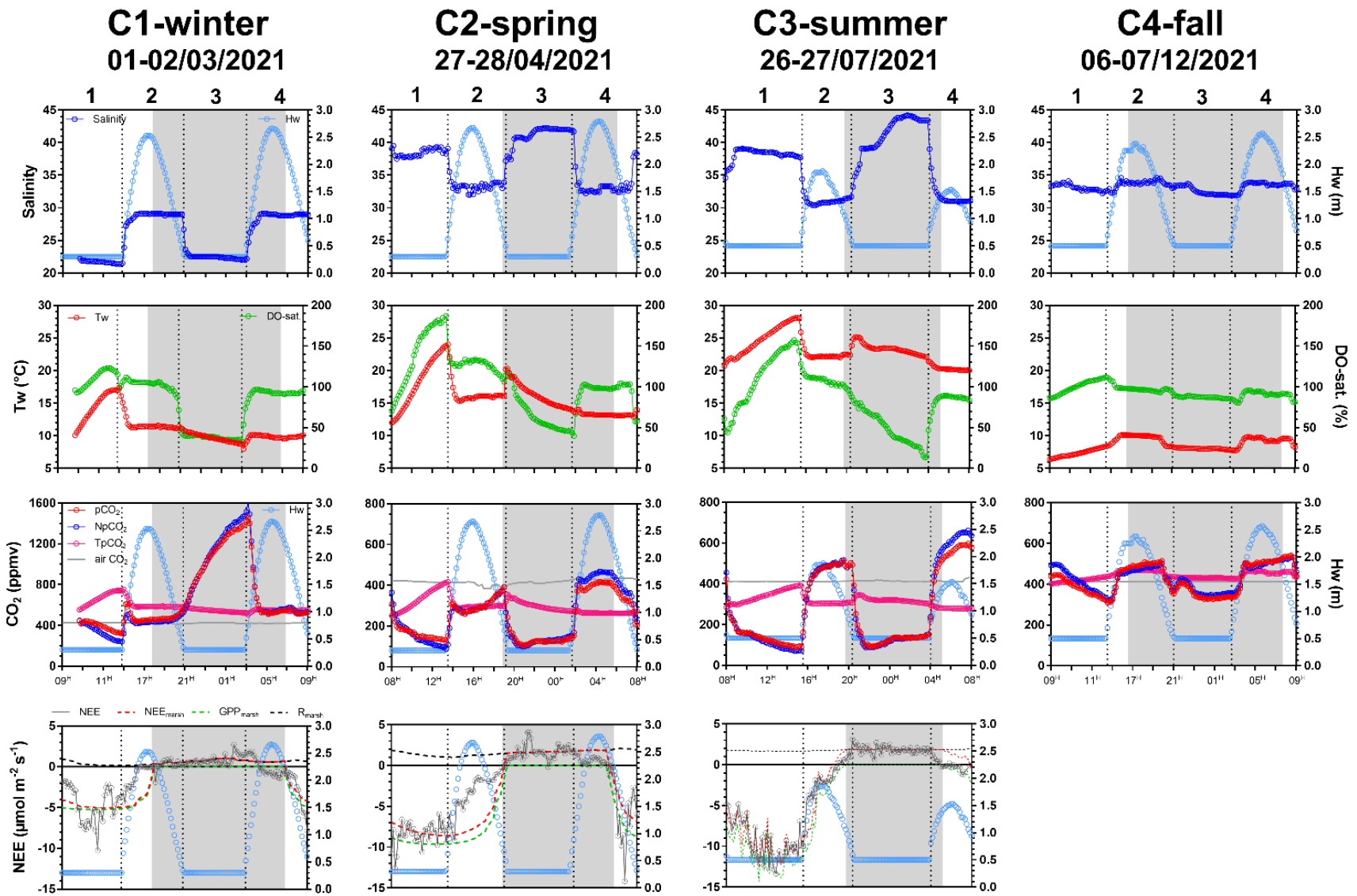
C1-winter
01-02/03/2021
C2-spring
27-28/04/2021
C3-summer
26-27/07/2021
C4-fall
06-07/12/2021
1
2
3
4
Salinity
Hw
Hw (m)
Tw
DO-sat
Tw (°C)
DO-sat. (%)
pCO2
NpCO2
TpCO2
air CO2
CO2 (ppmv)
NEE
NEEmarsh
GPPmarsh
Rmarsh
NEE (µmol m-2 s-1)

Figure 4.2: Temporal variations of biogeochemical parameters measured during each 24-h cycle from winter to fall: water salinity, water height (Hw, m), water temperature (Tw; °C), DO saturation level (DO-sat.; %), pCO_2 (ppmv), $NpCO_2$ (pCO_2 variations related to non-temperature effects; ppmv), $TpCO_2$ (pCO_2 variations related to temperature effects; ppmv), air CO_2 concentration (ppm) and NEE fluxes (µmol CO_2 m^{-2} s^{-1}). Estimated NEE_{marsh}, GPP_{marsh} and R_{marsh} fluxes (µmol CO_2 m^{-2} s^{-1}) are presented simultaneously with NEE fluxes measured by EC. All parameters were measured or estimated every 10 min. during each 24-h cycle. White and grey areas correspond to daytime and night-time, respectively. No variation of Hw (Hw = 0.50 m) corresponds to low tides and increase/decrease of Hw (Hw > 0.50 m) correspond to high tides. Vertical dotted lines distinguish low tide day (LT/Day, 1), high tide day (HT/Day, 2), low tide night (LT/Night, 3) and high tide night (HT/Night, 4) (see M&M section for further information). Each graduation of the x-axis corresponds to two hours.

2.3. Online parameters

2.3.1. Water pCO_2 measurements and associated physicochemical parameters

A C-sense™ probe (PME/Turner Designs) and an EXO2 multiparameter probe (YSI) were deployed to measure continuously every 10 min. water pCO_2 and physicochemical parameters, respectively. The measurement range of the C-sense probe is 0-2000 ppmv with an absolute accuracy of 60 ppmv (3% of the full scale; Turner Designs). The C-sense probe was calibrated by the manufacturer before the study. A water pCO_2 correction was applied taking into account the total dissolved gas pressure (TDGP), the atmospheric pressure during the calibration (1009 hPa) and the measured pCO_2 values (Mayen et al. 2023). The EXO2 probe was used to measure water temperature (± 0.1°C), salinity (± 0.2 salinity unit), DO concentration (± 3.1 µmol L^{-1}) and DO saturation level (± 1%). Simultaneously, water heights (Hw, ± 0.3 m) were measured every 10 min. by a STPS probe (NKE Instrumentation) located in the sampling channel (Fig. 4.1-B). Water heights (Hw) measured at one location in the channel relative to the mean sea level were used to distinguish LT periods with constant water heights (Hw = 0.50 m; Fig. 4.2) and HT periods with increases (flooding tide) or decreases (ebbing tide) of water heights (Hw > 0.50 m; Fig. 4.2).

2.3.2. Atmospheric eddy covariance measurements

Over the year 2021 and simultaneously to our water samplings, an atmospheric Eddy Covariance (EC) system (*Campbell Scientific Inc.*) was deployed at the Bossys perdus salt marsh as described in Mayen et al. (2024). The EC station continuously measured the net ecosystem CO_2 exchanges (NEE, µmol m^{-2} s^{-1}) within the annual averaged footprint (90% contour line, i.e. 12069 m^2; Fig. 4.1-B). EC data were recorded at a frequency of 20 Hz and

averaged every 10 min. over each 24-h cycle except for the C4-fall where no EC measurement was possible due to an anemometer malfunction and revision. In addition, photosynthetically active radiation (PAR, µmol m^{-2} s^{-1}), air temperature (Ta, °C), relative humidity (RH, %) and cumulative precipitation (rainfall, mm) were also recorded at the same frequency of NEE. Daytime and night-time were separated into PAR > 10 and PAR ≤ 10 µmol m^{-2} s^{-1}, respectively (Fig. 4.2). The set of EC sensors (the open-path infrared gas analyser, the ultrasonic anemometer, the meteorological station), footprint estimation, EC data processing, quality control and gap-filling model are fully described in Mayen et al. (2024). The random forest model, using PAR, Ta, RH and Hw values, allowed to gap-fill the missing EC data over each 24-h cycle (0, 20 and 2% over C1-winter, C2-spring and C3-summer, respectively). The studied footprint area was mainly dominated by halophyte plants, composed by *H. portulacoides* (37%), *S. maritima* (22%) and *S. vera* (7%) at the benthic interface. Negative NEE fluxes represent a marsh CO_2 uptake (atmospheric sink) whereas, positive NEE fluxes represent a marsh CO_2 emission (atmospheric source). To study marsh metabolism related to photosynthesis and respiration processes, NEE were partitioned during LT periods into ecosystem gross primary production (GPP_{marsh}) and ecosystem respiration (R_{marsh}), respectively (Kowalski et al. 2003; Wei et al. 2020). In this study, NEE correspond to net vertical CO_2 exchanges measured by EC whereas, NEE_{marsh} ($GPP_{marsh} - R_{marsh}$) correspond to net vertical CO_2 exchanges estimated at the marsh-atmosphere interface without tidal immersion (Mayen et al. 2024).

2.4. Analytical procedures

2.4.1. Discrete parameters

For dissolved inorganic nitrogen (DIN = NO_3^-_NO_2^- + NH_4^+) and phosphorus (DIP = PO_4^{3-}), 300 mL water samples were pre-filtered through cellulose acetate membrane filters (Minisart Sartorius© 0.45 µm pore size) directly after the sampling and stored at -20°C until analysis. For dissolved silicate (DSi = $Si(OH)_4^-$), 100 mL filtered water samples were stored at 4°C until analysis. Samples were analysed using an auto-analyser (Seal analytical AA3) following standard protocols (Aminot and Kérouel, 2007). Nitrate and nitrite were analysed together and grouped as NO_3^-_NO_2^-. The limits of quantification (LQ) were 0.4 µM for DSi, 0.2 µM for NO_3^-_NO_2^- and 0.05 µM for DIP and NH_4^+. Measurement uncertainties were 4% for DSi and 8% for NO_3^-_NO_2^-, NH_4^+ and DIP.

For dissolved organic and inorganic matter (DOC, DIC and DON), 50 mL water samples were filtered through precombusted GF/F filters (Whatman® Nuclepore™, 0.7 µm pore size) in opaque vials using a glass syringe. Total dissolved carbon (TDC) concentration was measured using the 680°C combustion catalytic oxidation method on a TOC meter (Shimadzu TOC-$_{LCPH/CPN}^{TM}$). Furthermore, by acidifying the sample (HCl, pH < 3.0), all DIC in the sample is converted to CO_2 and DIC concentrations were obtained with an infrared gas analyzer (Shimadzu TOC-$_{LCPH/CPN}^{TM}$). DOC concentrations were then calculated by subtracting the DIC concentration from the obtained TDC concentration. Total dissolved nitrogen (TDN) concentration was measured with a combustion (720°C) where TDN in the sample was decomposed to nitrogen monoxide. The nitrogen gas was cooled, dehumidified and then, the nitrogen monoxide was detected by a chemiluminescence gas analyser on a TOC meter (Shimadzu TOC-$_{LCPH/CPN}^{TM}$). DON concentrations were calculated by the difference between TDN and DIN. Measurement uncertainties were 3.0% for TDC and TDN and 7.0% for DIC.

For particulate organic matter (POC and PON), 30–200 mL water samples were gently filtered through precombusted GF/F filters (Whatman® Nuclepore™, 0.7 µm pore size). Filters were dried (12 h at 60°C), enclosed within clean glass vials and stored in the dark protected from humidity until analysis (Lorrain et al. 2003). After removal of carbonates with phosphoric acid, filters were treated using a CHN element analyser (Thermo Fisher Scientific, Waltham, USA) to measure POC and PON concentrations following Aminot and Kérouel (2004).

TA analyses were performed with an automatic titration system (Titroline 7000 from SI Analytics) using HCl 0.01 N on 25 g of filtered samples (Dickson et al. 2007). The equivalent point for the TA measurement was calculated by linearizing the Gran function (Gran, 1952). Measurements were compared to certified reference material (CRM, provided by A. G. Dickson from Scripps Institution of Oceanography). The maximal precision level was ± 0.44%.

Phytoplankton biomass was estimated through Chl*a* concentrations. Water samples (30–200 mL) were filtered through GF/F filters (Whatman® Nuclepore™, 0.7 µm pore size) and stored at -20°C until analysis. Chl*a* was extracted in 10 mL of 90% acetone in the dark at 4°C for 12 h and analysed by monochromatic spectrophotometry (Aminot and Kérouel, 2004). Microphytoplankton (>20 µm) abundance and community diversity were assessed using an inverted microscope (Zeiss, Axio Observer). 1000 mL water samples were fixed with

Lugol iodine solution (2%) and stored in the dark at 4°C. Samples were gently homogenised before settling in 10 mL sub-sample for 12 h in Hydro-Bios counting chambers (Utermöhl, 1958). Limits of quantification was 100 cells L^{-1}. For bacterial and phytoplanktonic abundances by flow cytometry, 2 mL water samples were fixed with glutaraldehyde (0.25% final concentration; SIGMA-ALDRICH) and stored at -80°C until analysis. Enumeration was carried out using a flow cytometer (NovoCyte, Agilent Tech.).

2.4.2. Planktonic metabolism parameters

For planktonic metabolism measurements (net community production, NCP, gross primary production, GPP and community respiration, CR), 5 L water samples were pre-filtrated through 100 µm pores to remove larger grazers, larges particles or large phytoplankton colonies and carefully siphoned into fifteen 125 mL narrow-mouth Winkler glass bottles with a silicon tube avoiding air oxygen bubbles. Water samples were protected from solar irradiation before the onset of the incubation. Five replicates bottles were used to determine the initial oxygen concentrations and five transparent "light" and five opaque "dark" replicates bottles were used for *in situ* incubations in the sub-surface waters for six hours (Carpenter 1965; Carritt and Carpenter). Dissolved oxygen concentration was measured using the spectrophotometric Winkler approach which shows a standard deviation of 0.45% for inter-repeatability and 0.73% for reproducibility near 250 µmol L^{-1} (Labasque et al. 2004). CR and NCP rates were calculated from changes in dissolved oxygen concentrations after incubation of samples under light and dark conditions, respectively, relative to the initial oxygen concentrations. GPP were then calculated as the sum of CR and NCP following the mass balance equation GPP = NCP + CR. Occasionally, metabolism experiments failed and yielded negative CR rates (i.e. production of oxygen in the dark) or negative GPP (i.e. CR > NCP). These estimated were further not considered in the analysis.

The temporal evolution of the metabolic status of the planktonic community is described by the GPP/CR ratio, where GPP/CR > 1 represents a net autotrophy, GPP/CR = 1 is a metabolic balance and GPP/CR < 1 represents a net heterotrophy. In order to convert planktonic metabolism rates from oxygen to carbon, we used an average photosynthetic quotient (PQ = 1.3) from similar coastal systems and a typical respiratory quotient (RQ = 1.0) used in most studies (Laws 1991; Caffrey 2004; Gazeau et al. 2004; Wielgat-Rychert et al. 2017). Results are expressed in µmol CO_2 L^{-1} h^{-1}.

For each HT period, an integrated NCP rate (mmol CO_2 m^{-2} h^{-1}) was estimated from the volumetric NCP rate (µmol CO_2 L^{-1} h^{-1}) and the Hw mean above the marsh to compare planktonic metabolism with net aquatic ecosystem production and air-water CO_2 fluxes (see below). For each 24-h cycle, a daily net C balance (g C m^{-2} d^{-1}) was obtained taking into account the four NCP rates measured every 6 h successively at LT and HT.

2.5. Calculations

To distinguish temperature *vs.* non-temperature effects on water pCO_2 variations, $TpCO_2$ (ppmv) and $NpCO_2$ (ppmv) were calculated, respectively, following Takahashi et al. (2002) and Polsenaere et al. (2022). In this study, $TpCO_2$ studied pCO_2 variations around the annual or seasonal mean pCO_2 that would be expected only from temperature effects whereas, $NpCO_2$ represented pCO_2 variations due to biological and non-temperature effects (horizontal advection, tidal pumping, benthic exchanges) with a temperature normalization to an annual or seasonal mean (Mayen et al. 2023).

Over the 24-h cycles, air-water CO_2 fluxes (FCO_2) and net aquatic ecosystem production ($NEP_{aquatic}$) were simultaneously estimated for each HT period during highest immersion levels with limited horizontal exchanges (for 2 h over C1-winter and C3-summer and for 3.5 h over C2-spring and C4-fall).

2.5.1. Air-water CO_2 fluxes

Diffusive CO_2 fluxes (FCO_2, mmol m^{-2} h^{-1}) at the air-water interface were estimated each hour following Eq. (1) from Polsenaere et al. (2022) and Mayen et al. (2023):

$$FCO_2 = k.\alpha.\Delta pCO_2 \quad (1)$$

where k (cm h^{-1}) is the CO_2 gas transfer velocity, α (mol kg^{-1} atm^{-1}) is the CO_2 solubility coefficient in saltwater (Weiss, 1974) and ΔpCO_2 (ppmv) is the gradient between mean water and air pCO_2. Water pCO_2 were measured by the C-sense probe while air pCO_2 and wind speeds were measured by the Eddy Covariance system. In this study, we used the k-wind parametrization of Wanninkhof et al. (2022), which was a coefficient specific for oceanic and coastal waters (Wang et al. 2018; Polsenaere et al. 2022). The gas transfer coefficients, normalized to a Schmidt number of 600 (k_{600}) obtained from Wanninkhof et al. (2022), were

converted to the gas transfer velocity of CO_2 at the *in situ* temperature and salinity (k_{660}) following the procedure of Jähne et al. (1987).

2.5.2. Net ecosystem production of water column ($NEP_{aquatic}$)

The $NEP_{aquatic}$ was calculated by considering the changes in DIC concentrations between two discrete samplings during HT periods and corrected for $CaCO_3$ production/dissolution and air-water CO_2 flux (Cotovicz et al. 2021), following Eq. (2):

$$NEP_{aquatic} = ((DIC_1 - DIC_2)\rho d) / \Delta t - ((TA_1 - TA_2)\rho d) / \Delta t - FCO_2 \quad (2)$$

where DIC_1 and DIC_2 are DIC concentrations (mmol kg^{-1}) between two discrete samplings normalized to the mean salinity, TA_1 and TA_2 are TA concentrations (mmol kg^{-1}) between two discrete samplings normalized to the mean salinity, ρ is the sampled seawater density (kg m^{-3}), d is the mean depth above the marsh (m), Δt is the time interval (h) and FCO_2 is the mean CO_2 flux (mmol m^{-2} h^{-1}) across the air-water interface. In this study, $NEP_{aquatic}$ estimated the overall aquatic metabolism (benthic and planktonic) whereas, NCP studied the planktonic aquatic metabolism only (section 2.3.3).

2.6. Data analysis and statistical analysis

For each 24-h cycle, a linear regression between TA and DIC normalized to a salinity constant (nTA and nDIC) was performed to highlight the dominant biogeochemical processes affecting DIC and TA concentrations (Borges et al. 2003). For this, DIC and TA were normalised according to Friis et al. (2003) with a mean salinity value from all samples (25.0, 36.7, 36.0 and 33.2 at C1-winter, C2-spring, C3-summer and C4-fall, respectively) in order to reduce evaporation and dilution processes on these parameters (Koné and Borges 2008; Saderne et al. 2019). For each 24-h cycle, DIC was partitioned into dissolved CO_2, HCO_3^- and CO_3^{2-} ions from salinity, temperature, DSi, DIP, DIC and TA using the carbonic acid constant from Mehrbach et al. (1973) as modified by Dickson and Millero (1987), the $KHSO_4$ constant from Dickson (1990) and the borate acidity constant from Lee et al. (2010). The CO_2 system calculation program (version 2.1.) performed these calculations (Lewis and Wallace, 1998).

Discrete sampling data did not respect a normal distribution (Shapiro-Wilk tests, $p < 0.05$). Non-parametric comparisons such as the Mann-Whitney and Kruskal-Wallis tests were carried out with 0.05 level of significance. A Dunn test was used to perform a post-hoc

multiple comparison of the Kruskal-Wallis test to detect significant differences among groups. For a better data representation, high-frequency data were done in means (meteorological data, water pCO_2 and atmospheric CO_2 fluxes) whereas, discrete sampling data were done in medians (inorganic carbon, organic matter, nutrients). The statistical tests, Spearman's correlation matrix as well as figures (temporal graphs, barplots, boxplots) were performed with the GraphPad Prism 7 software. Since the biogeochemical data did not follow a normal distribution, non-metric multidimensional scaling (NMDS) were conducted to assess temporal variabilities at the seasonal scale (between 24-h cycles), at the tidal scale (low tide *vs* high tide) and at the diurnal scale (daytime *vs* night-time) using the "vegan" package (Oksanen et al., 2022) for the R software. At the global scale (all sampling data, n = 59), multiple factor variance analyses were performed to test the contribution of seasonal, diurnal and tidal factors on measured biogeochemical variables (Table 4.4). For variance analysis, data that did not respect a normal distribution were transformed into $\log_{10}(x)$ or $\log_{10}(x+1)$. These statistical analyses were performed with Statgraphics Centurion 19 software.

3. Results

3.1. Meteorological and environmental settings

The air temperature (Ta) averages over the 24-h cycles (Table 4.1) were within the standard deviations of the 3-year seasonal averages (continuous measurements during three full seasons; Table S1) although, C1-winter was significantly warmer (+2.1°C) and C4-fall was significantly colder (-2.4°C) than the seasonal reference period (Mann-Whitney tests, $p < 0.05$). C3-summer was the warmest period whereas, similar thermal conditions were recorded between C1-winter and C4-fall (Table 4.1). Similarly, the full seasonal range in solar radiations was captured over our 24-h cycles although, the daytime period of C1-winter was brighter and the one of C4-fall less bright than the seasonal reference period (Tables 4.1 and S1). C2-spring and C3-summer were the brightest periods with no significant variation in daytime PAR values (Mann-Whitney, $p = 0.10$; Table 4.1). Globally, 24-h cycles were characterized as bright/cold over C1-winter, very bright/warm over C2-spring, very bright/very warm over C3-summer, no bright/cold over C4-fall. In average, over C2-spring and C3-summer, wind speeds were similar to the seasonal reference periods whereas over C1-winter, wind speeds were lower (Tables 4.1 and S1). Over C1-winter, winds came from northeast whereas over C2-spring and C3-summer, higher wind rotations were recorded with winds mainly came from west (Fig. 4.1-B). The driest and wettest periods were the C2-spring

and C4-fall, respectively, associated to the lowest and highest 7-day cumulative rains (Table 4.1).

Over the year 2021, salinity of shelf waters as water source flooding the studied salt marsh were bimonthly measured at a close marine station (Filiere W; Fig. 4.1-A) and ranged from 27.6 (winter) to 34.8 (summer). At Filiere W station, salinity did no significantly varied between the year 2021 and the 2000-2020 reference period (Mann-Whitney test, $p = 0.50$) according to Belin et al. (2021) (Table S2). At the studied salt marsh, salinity measured at high tides (marsh waters) was similar to the shelf whereas, salinity measured at low tides (channel waters) showed stronger variations ranging from 21.4 (C1-winter) to 44.2 (C3-summer; Fig. 4.2). The whole duration of high tide periods was 8 h d^{-1} over C1-winter and C3-summer (lowest tidal ranges) and 10 h d^{-1} over C2-spring and C4-fall (highest tidal ranges; Table 4.2). Water temperatures varied between 6.4°C (C4-fall) and 28.1°C (C3-summer). Similarly, large amplitudes of DO and water pCO_2 were measured over the 24-h cycles, with DO-sat. ranging between 13% (C3-summer) and 187% (C2-spring) and water pCO_2 ranging between 83 ppmv (C3-summer) and 1461 ppmv (C1-winter). For each variable, these extreme values were measured at low tide in channel waters between the day (LT/Day) and the night (LT/Night; Fig. 4.2).

3.2. Temporal variations of water pCO_2 and atmospheric CO_2 exchanges

During each 24-h cycle, the average water pCO_2 was within the standard deviations of the 5-day seasonal average (Table S3). In average at the seasonal scale, waters were oversaturated in CO_2 with respect to the atmosphere over C1-winter and C4-fall (669 ± 327 and 422 ± 73 ppmv, respectively) and undersaturated in CO_2 over C2-spring and C3-summer (239 ± 105 and 271 ± 182 ppmv, respectively). Water pCO_2 significantly differed between each 24-h cycle (Kruskal-Wallis test, $p < 0.0001$), except between C2-spring and C3-summer (Dunn's test, $p = 0.16$). The average $NpCO_2$ decreased sharply from C1-winter (802 ± 440 ppmv) to C3-summer (200 ± 146 ppmv) and then increased towards C4-fall (546 ± 80 ppmv) whereas, the highest and lowest average $TpCO_2$ were calculated over C3-summer (562 ± 57 ppmv) and C1-winter (342 ± 35 ppmv), respectively.

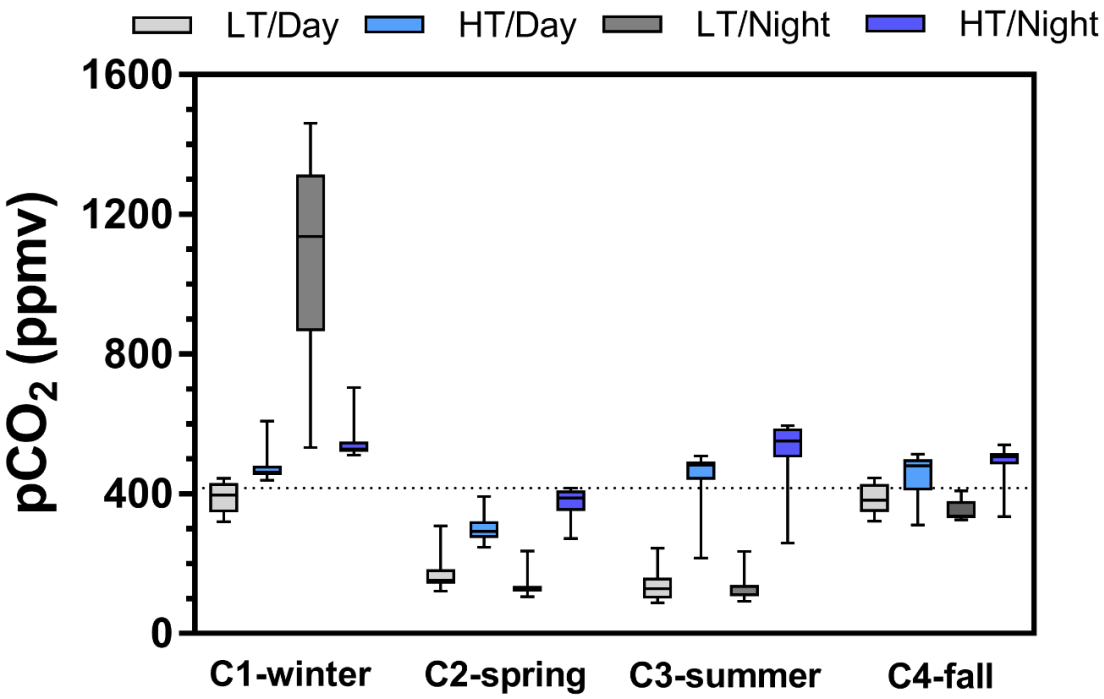

Figure 4.3: Boxplot distribution of water pCO_2 variations measured every 10-min. at the diurnal/tidal scales within each seasonal 24-h cycles. Horizontal dotted line corresponds to the CO_2 atmospheric concentration measured by the EC station and averaged over the four seasonal 24-h cycles (416 ppm). LT/Day: low tide day; HT/Day: high tide day; LT/Night: low tide night; HT/Night: high tide night. Daytime and night-time periods were separated into PAR > 10 and PAR ≤ 10 µmol m^{-2} s^{-1}, respectively, whereas low tide (LT) and high tide (HT) periods were separated into Hw = 0.50 m and Hw > 0.50 m, respectively (see Fig. 4.2 and M&M section for further information on these temporal periods).

Water pCO_2 also significantly varied within each 24-h cycle depending on diurnal and tidal scales with, generally, (1) pCO_2 decreases during daytime and pCO_2 increases during night-time and (2) lower pCO_2 values at low tides than at high tides (Figs. 4.2 and 4.3). Over C1-winter, the largest diurnal/tidal variation of water pCO_2 was recorded ranging from 321 ppmv at LT/Day (undersaturation period in CO_2) to 1461 ppmv at LT/Night (oversaturation period in CO_2; Fig. 4.3). Over C2-spring and C3-summer at low tide (LT/Day and LT/Night), water was strongly undersaturated in CO_2 whereas at high tide (HT/Day and HT/Night), water was slightly undersaturated and oversaturated in CO_2 over C2-spring and C3-summer, respectively (Fig. 4.3). Finally, over C4-fall, the lowest diurnal/tidal variation was recorded (from 311 to 541 ppmv) associated with a slightly water CO_2 undersaturation at low tide and a slightly water CO_2 oversaturation at high tide (Fig. 4.3). For each 24-h cycle, significant differences in water pCO_2 were highlighted at the diurnal/tidal scales (Kruskall-Wallis tests, $p < 0.0001$), except (1) between LT/Day and LT/Night and (2) between HT/Day and HT/Night

both over C3-summer (Dunn's tests, p = 0.90 and p = 0.60, respectively) and C4-fall (Dunn's tests, p = 0.21 and p = 0.07, respectively; Fig. 4.3). At the global scale (all pCO_2 values, n = 570), the variance analysis highlighted a significant effect of seasonal (F = 194.6, p < 0.0001) and tidal (F = 243.6, p < 0.0001) factors on $\log_{10}(pCO_2)$ but no significant diurnal effect (F = 0.9, p = 0.33).

During high tide periods, mean air-water FCO_2 from k_{660} and water pCO_2 were estimated to be 0.09 ± 0.09 (source), -0.13 ± 0.11 (sink), 0.12 ± 0.08 (source) and 0.30 ± 0.20 (source) mmol m^{-2} h^{-1} over C1-winter, C2-spring, C3-summer and C4-fall, respectively. Significant variations of air-water FCO_2 were recorded between the 24-h cycles (Kruskal-Wallis, p < 0.0001), except between C1-winter and C3-summer (Dunn's test, p = 0.65). We recorded a significant higher mean air-water CO_2 source at night than at day only over C1-winter (t test, p < 0.0001).

3.3. Planktonic biomass, abundance and metabolism

Median values of Chl*a* concentrations increased from C1-winter to C4-fall (Table 4.3). Over C1-winter, Chl*a* varied between 1.2 and 5.0 µg L^{-1} independently of the tidal status whereas during the other 24-h cycles, higher Chl*a* were recorded at low tide than at high tide (Fig. 4.4 and Fig. S1). Over the 24-h cycles, microphytoplankton (> 20 µm) was mainly composed of pennate diatoms (except over C3-summer where a dinoflagellate bloom occurred) with an increase of abundances from high to low tides both over C2-spring and C3-summer (Fig. 4.4). For smaller cells (< 20 µm), nanophytoplankton was also more abundant at low tides than at high tides from C2-spring to C4-fall (Fig. 4.4). Higher bacteria abundances were also recorded at low tides with the highest and lowest tidal variations during C2-spring/C3-summer and C1-winter/C4-fall, respectively (Fig. 4.4).

Over the 24-h cycles, NCP rates strongly varied according to light (daytime *vs.* night-time) and water height (low tide *vs.* high tide). Planktonic community was net autotrophic during daytime (except for C2-HT/Day and C4-HT/Day) and net heterotrophic during night-time (except for C2-HT/Night) irrespective of the water height (Fig. 4.5-A). Systematically, a stronger planktonic metabolism (net production and respiration) was recorded at low tides than at high tides (Fig. 4.5-A,B). The highest net autotrophy rates (NCP > 0) were recorded at low tide during daytime ranging from 0.54 ± 0.10 (C4-LT/Day) to 5.24 ± 0.39 µmol L^{-1} h^{-1} (C2-LT/Day) and the highest net heterotrophy rates (NCP < 0) were recorded at low tide

during night-time ranging from -0.92 ± 0.64 (C1-LT/Night) to -2.15 ± 0.35 µmol L^{-1} h^{-1} (C3-LT/Night). At low tide, CR rates ranged from 0.92 ± 0.64 (C1-LT/Night) to 3.23 ± 0.62 µmol L^{-1} h^{-1} (C3-LT/Day) whereas at high tide, CR rates slighter varied from 0.26 ± 0.13 (C4-HT/Day) to 1.99 ± 0.07 µmol L^{-1} h^{-1} (C2-HT/Day; Fig. 4.5-B). Consequently, the strongest daytime GPP rates were also recorded at low tide, especially over C2-LT/Day and C3-LT/Day (Fig. 4.5-C). The NCP *vs.* CR relationship was significant only without LT/Day periods (R^2 = 0.43, $p < 0.05$, n = 12). At the global scale with all rates, CR were significantly related to bacteria abundance (R^2 = 0.50, $p < 0.05$, n = 16) but not to Chl*a* concentrations (p = 0.14, n = 16) (data not shown here).

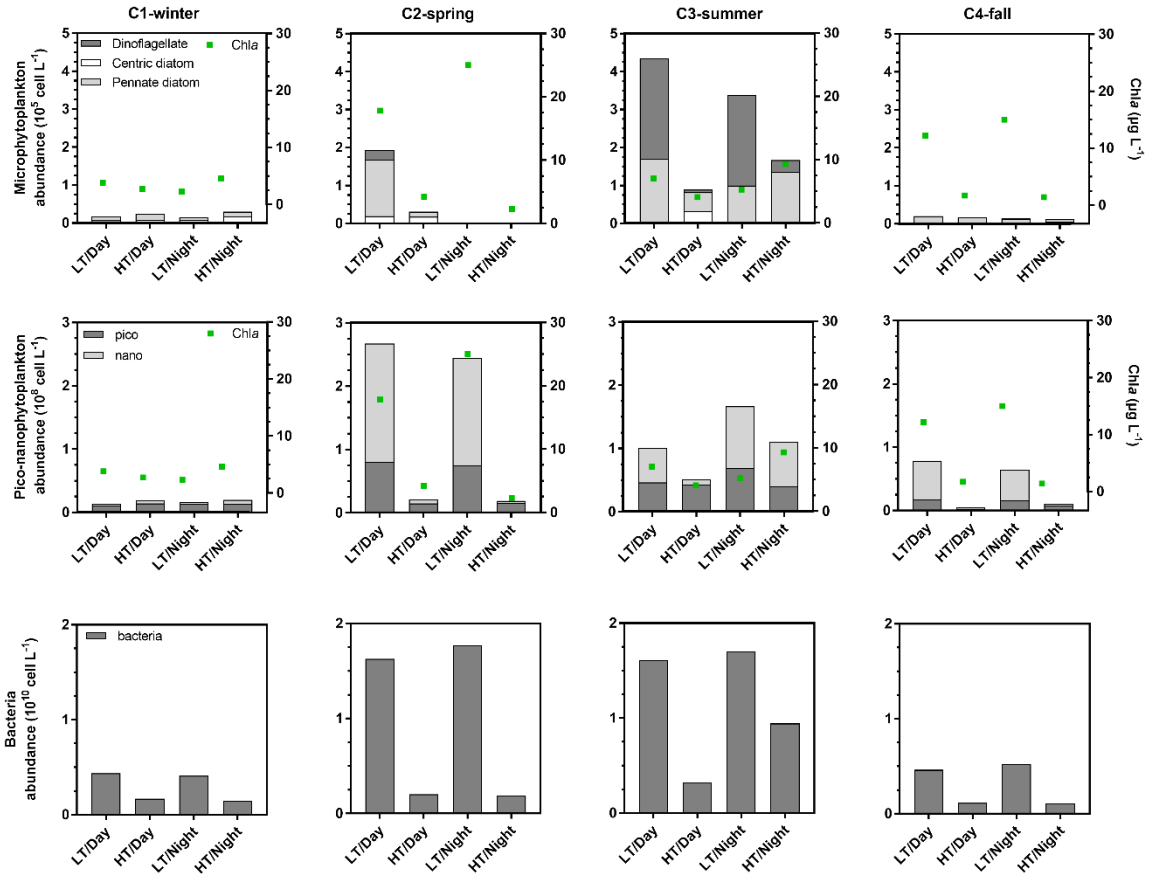

Figure 4.4: Abundance of microphytoplankton (10^5 cell L^{-1}), pico-nanophytoplankton (10^8 cell L^{-1}) and bacteria (10^{10} cell L^{-1}) sampled at the diurnal/tidal scales during each 24-h cycle simultaneously with NCP measurements. Contrary to the biogeochemical parameters sampled every hour or two hours over 24-h cycles, planktonic communities were sampled every 6 h once of each period of LT/Day, HT/Day, LT/Night and HT/Night (n = 4). The Chl*a* concentration associated to each sampled planktonic community was added in green. Microphytoplankton was separated into centric diatoms, pennate diatoms and dinoflagellates. LT/Day: low tide day; HT/Day: high tide day; LT/Night: low tide night; HT/Night: high tide night (see Fig. 4.2 for further information on these temporal periods).

Table 4.3: Medians (in bold) and associated ranges (in brackets) of biogeochemical parameters measured during our 24-h cycles (n = 13 over C1-winter, n = 15 over C2-spring and C3-summer and n = 16 over C4-fall; see Fig. S1).

	code	C1-winter	C2-spring	C3-summer	C4-fall	Transformation for variance analysis
Chlorophyll *a* (µg L^{-1})	Chl*a*	**2.6** (1.2 – 5.0)	**4.2** (1.4 – 25)	**7.0** (1.3 – 17)	**11.4** (1.0 – 29)	$\log_{10}(x)$
Dissolved Inorganic Carbon (µmol kg^{-1})	DIC	**2850** (2313 – 3869)	**2068** (1886 – 2342)	**1963** (1663 – 2278)	**2520** (2124 – 2793)	$\log_{10}(x)$
Total Alkalinity (µmol kg^{-1})	TA	**3076** (2508 – 4016)	**2757** (2379 – 2947)	**2385** (2228 – 2812)	**2804** (2351 – 3047)	$\log_{10}(x)$
Nitrate + Nitrite (µM)	NO_3^-_NO_2^-	**19.0** (8.4 – 31)	**1.0** (0.37 – 1.7)	**0.60** (0.20 – 0.80)	**1.5** (0.35 – 5.3)	$\log_{10}(x + 1)$
Ammonium (µM)	NH_4^+	**33** (2.5 – 60)	**2.9** (0.51 – 7.7)	**2.1** (0.59 – 4.0)	**3.3** (1.59 – 6.6)	$\log_{10}(x + 1)$
Phosphate (µM)	DIP	**1.06** (0.56 – 2.3)	**0.19** (0.05 – 0.88)	**0.75** (0.12 – 1.73)	**0.25** (0.11 – 0.39)	$\log_{10}(x + 1)$
Silicate (µM)	DSi	**27** (21 – 94)	**14.4** (2.2 – 27)	**23** (8.4 – 40)	**7.2** (5.2 – 12.5)	$\log_{10}(x + 1)$
Dissolved Organic Carbon (µM)	DOC	**288** (124.0 – 596)	**519** (161.9 – 1040)	**358** (97.4 – 1010)	**289** (93.1 – 529)	$\log_{10}(x)$
Particulate Organic Carbon (µM)	POC	**188** (41.8 – 581)	**151** (27.4 – 560)	**166** (29.6 – 1048)	**101** (21.3 – 270)	$\log_{10}(x)$
Dissolved Organic Nitrogen (µM)	DON	**16** (5.4 – 45)	**44** (12.3 – 85)	**56** (23.3 – 117)	**39** (18.6 – 57)	$\log_{10}(x)$
Particulate Organic Nitrogen (µM)	PON	**16** (3.2 – 39)	**17** (2.7 – 68)	**28** (3.7 – 131)	**15** (3.8 – 36)	$\log_{10}(x)$

Over the 24-h cycles, we examined also the variation of planktonic metabolism standardized to Chl*a* biomass in order to observe if the variation of the planktonic metabolism is due to its productivity or to its biomass (Fig. 4.5). Chl*a* specific NCP rates (NCP_{Chla}) showed the highest mean value at C1-LT/Day whereas lower and similar specific NCP_{Chla} rates were recorded both at C2-LT/Day and C3-LT/Day (Fig. 4.5-D). At low tide, the highest and lowest specific CR_{Chla} rates were recorded over C1-winter/C3-summer and C2-spring/C4-fall, respectively (Fig. 4.5-E). Over C2-spring, specific CR_{Chla} rates were higher at high tide than at low tide whereas over C3-summer, the opposite trend was recorded (Fig. 4.5-E). The increases in specific GPP_{Chla} and CR_{Chla} rates from C2-LT/Day to C3-LT/Day could associated with a bloom of dinoflagellate that appeared in summer at low tide (42% of *Lingulodium polyedra*, 18% of *Gymnodinium* and 10% of *Prorocentrum micans*) whereas, abundance of pennate diatoms did no varied between spring and summer (Fig. 4.4). The highest specific CR rates standardized per cell of bacteria (CR_{bac}) were recorded over C1-HT/Night and C2-HT/Day (Fig. 4.5-G).

During high tide periods, planktonic metabolism (NCP) was compared with overall aquatic metabolism ($NEP_{aquatic}$; Table 4.6). Planktonic community was net autotrophic at C1-HT/Day and C3-HT/Day (NCP = 0.89 and 0.43 mmol m^{-2} h^{-1}, respectively) whereas, overall aquatic community was net autotrophic only at C3-HT/Day ($NEP_{aquatic}$ = 95.91 mmol m^{-2} h^{-1}). At high tides, overall aquatic community produced higher inorganic carbon to water column by heterotrophy at night than at day (except to the C2-spring). Generally, NCP rates were lower than $NEP_{aquatic}$ rates and similar metabolic status (autotrophy *vs.* heterotrophy) were recorded except over C1-HT/Day and C2-HT/Night (Table 4.6).

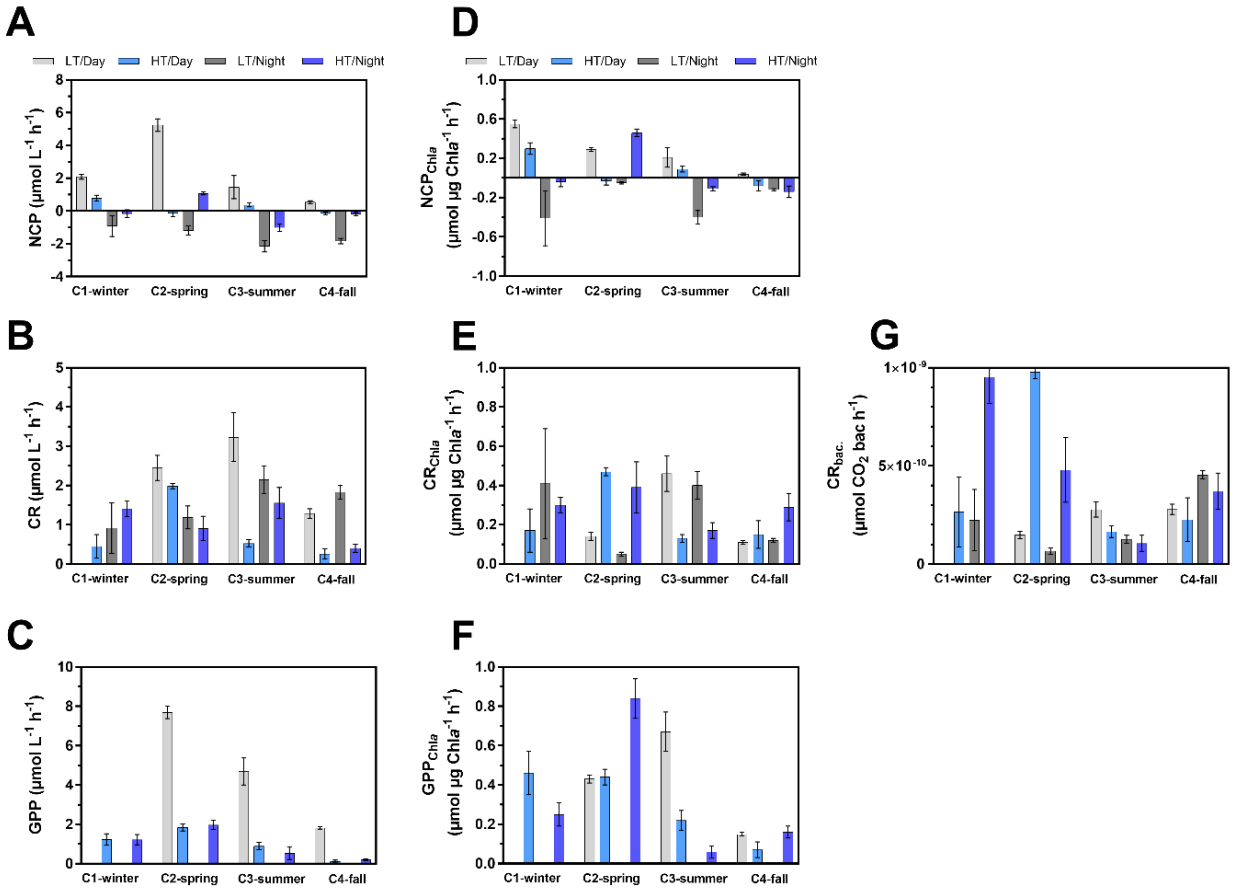

Figure 4.5: Planktonic metabolism and associated standard errors at diurnal/tidal scale over the four seasonal 24-h cycles: net community production (NCP, µmol CO_2 L^{-1} h^{-1}), community respiration (CR, µmol CO_2 L^{-1} h^{-1}) and gross primary production (GPP, µmol CO_2 L^{-1} h^{-1}). Specific rates of NCP (D), CR (E) and GPP (F) were standardized per unit of Chl*a* (µmol CO_2 µg Chl*a* h^{-1}). Specific CR rates standardized per abundance of bacteria (G) were also indicated (µmol CO_2 cell h^{-1}). Planktonic metabolism rates were measured by the Winkler method with *in situ* water incubation in transparent and dark bottles. LT/Day: low tide day; HT/Day: high tide day; LT/Night: low tide night; HT/Night: high tide night (see M&M section for further information on these temporal periods).

3.4. Analytical biogeochemical measurements from water samples

DIC and TA concentrations followed similar seasonal and tidal variations with decreases from C1-winter to C3-summer and increases from high tides to low tides (Table 4.3). Over each 24-h cycle, the highest DIC and TA concentrations were recorded in channel waters at low tides, especially over C1-winter at night (Table 4.3 and Fig. S1). Significant linear relationship between salinity-normalized TA (nTA) and salinity-normalized DIC (nDIC) was found over each 24-h cycle with slopes ranging from 0.39 over C2-spring (R^2 = 0.58, n = 12, $p < 0.001$; Fig. 6-B) to 1.10 over C4-fall (R^2 = 0.99, n = 16, $p < 0.001$; Fig. 4.6-D).

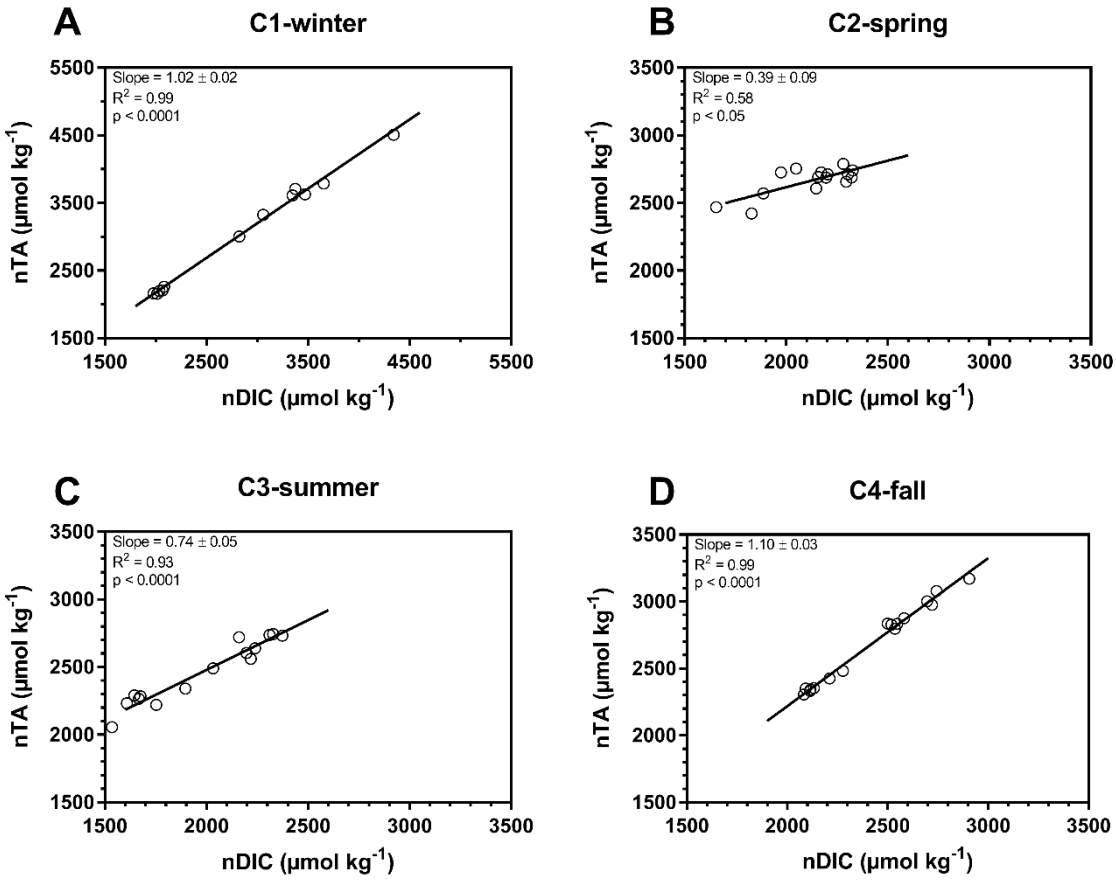

Figure 4.6: Linear regressions between normalized DIC (nDIC) *versus* normalized TA (nTA) for each 24-h cycle at the seasonal scale. For each cycle, nTA and nDIC data were calculated from Friis et al. (2003) with a mean salinity value from all samples (25.0, 36.7, 36.0 and 33.2 at C1-winter, C2-spring, C3-summer and C4-fall, respectively; see section 2.6.).

Nutrients significantly varied between seasons (Kruskal-Wallis tests, $p < 0.05$), with a strong decrease of NO_3^-_NO_2^- and NH_4^+ concentrations from C1-winter to C2-spring. DIP and DSi concentrations also decreased from C1-winter to C2-spring before increasing toward C3-summer (Table 4.3). At a shorter timescale (hourly sampling), significant higher concentrations of NH_4^+, DSi and DIP were recorded at low tides than at high tides (Mann-Whitney tests, $p < 0.05$) whatever diurnal status, especially (1) over C1-winter for NH_4^+ (Fig. 4.7-B), (2) over C2-spring and C3-summer for DSi (Fig. 4.7-C) and (3) over C1-winter and C3-summer for DIP (Fig. 4.7-D) where the greatest amplitudes were recorded. On the contrary, NO_3^-_NO_2^- concentrations were significantly lower at low tide at high tide (Mann-Whitney tests, $p < 0.05$), especially over C1-winter (Fig. 4.7-A). Over the 24-h cycles, the highest and lowest DIN:DIP and DIN:DSi ratio were recorded over C1-winter (medians of 45 and 1.5, respectively) and C3-summer (medians of 3.3 and 0.1, respectively), respectively, whereas, no seasonal variation in DSi:DIP ratio (overall median of 37, Table S4).

Organic matter also strongly varied at the seasonal scale (Table 4.3) with the highest POC and DOC concentrations recorded over C1-winter and C2-spring, respectively. Over 24-h cycles, the highest concentrations were recorded at low tides and the lowest ones were recorded at high tides. For instance, over C2-spring, median values of POC and DOC ranged from 40 to 231 µM and from 199 to 873 µM, respectively, from high to low tides. For each 24-h cycle, total carbon (TC) and total nitrogen (TN) was calculated at high tides and at low tides (Fig. 4.8) and most of TC was as inorganic forms whereas, most of TN was as organic forms (except for C1-winter). Systematically, significant increases in TC and TN were recorded from high tide to low tide (Fig. 4.8) with (1) mainly increases of dissolved inorganic matter over C1-winter (especially, HCO_3^- and NH_4^+) and (2) mainly increases of dissolved organic matter over C2-spring and C3-summer (especially, DOC). Over all 24-h cycles at low tides, POC:PON ratios varied between 6 and 8 (except to C1-winter where the highest POC:PON ratios were recorded; Fig. 4.9-A). Discrete samplings showed that particulate organic matter was mainly detrital (POC:Chl*a* > 200 mg mg^{-1}; (Savoye et al. 2003) with the highest and lowest POC:Chl*a* ratios recorded at low tide over C1-winter and C4-fall, respectively. Over C2-spring, significant lower POC:Chl*a* ratios were recorded at low tide than at high tide whereas over C3-summer, the opposite tidal trend was recorded (Mann-Whitney tests, $p < 0.05$; Fig. 4.9-B).

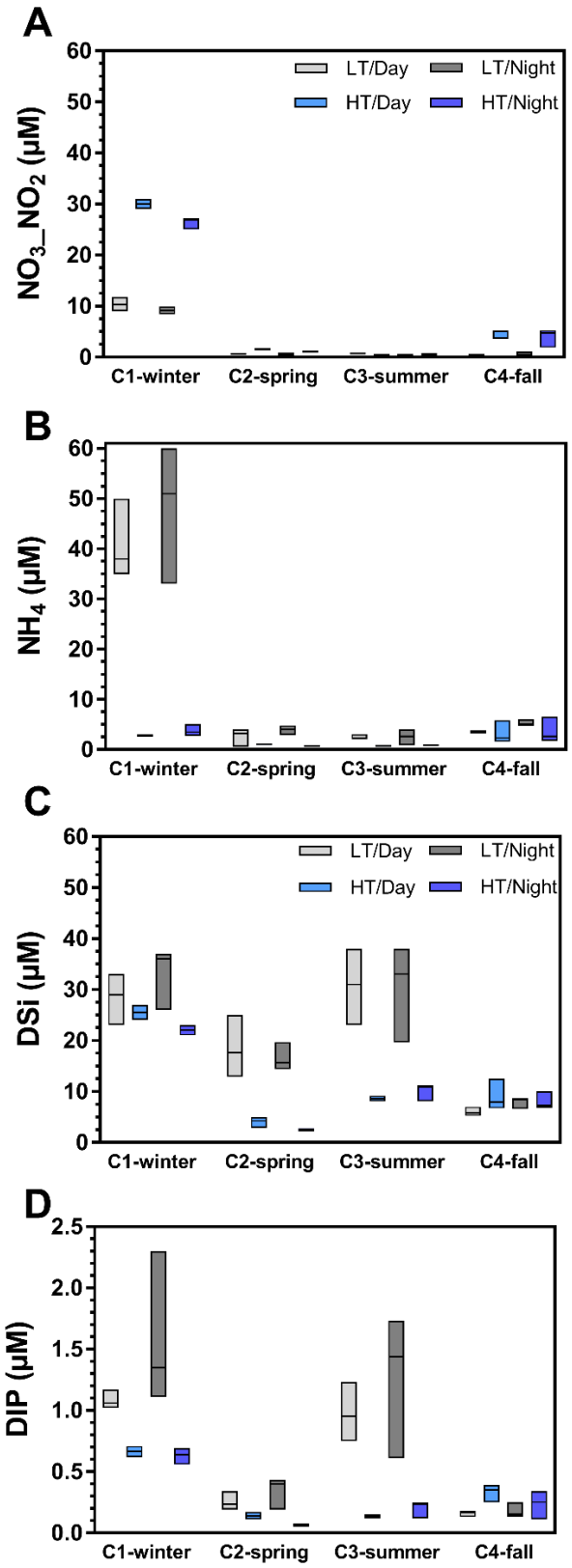

Figure 4.7: Boxplot distribution (median, minimum and maximum) of inorganic nutrients (µM) at the diurnal/tidal scales within each seasonal 24-h cycle: NO_3^-_NO_2^- **(A)**, NH_4^+ **(B)**, DSi **(C)** and DIP **(D)**. LT/Day: low tide day; HT/Day: high tide day; LT/Night: low tide night; HT/Night: high tide night.

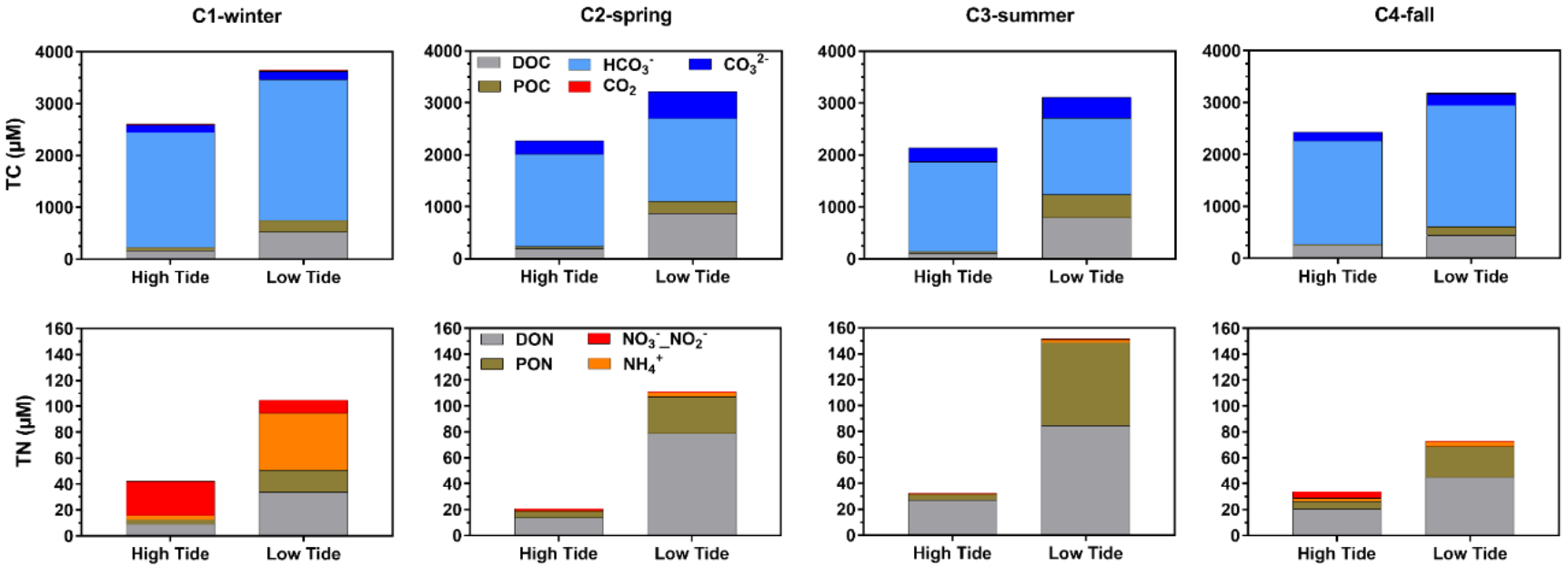

Figure 4.8: Median concentrations of total carbon (TC; in µM) and total nitrogen (TN; in µM) at high tides and low tides over the four 24-h cycle from winter to fall 2021. The sum of DOC, POC, HCO_3^-, CO_3^{2-} and CO_2 correspond to total carbon (TC) and the sum of DON, PON, NO_3^-_NO_2^- and NH_4^+ correspond to total nitrogen (TN). The DIC partitioning into CO_2, HCO_3^- and CO_3^{2-} was described in the M&M section.

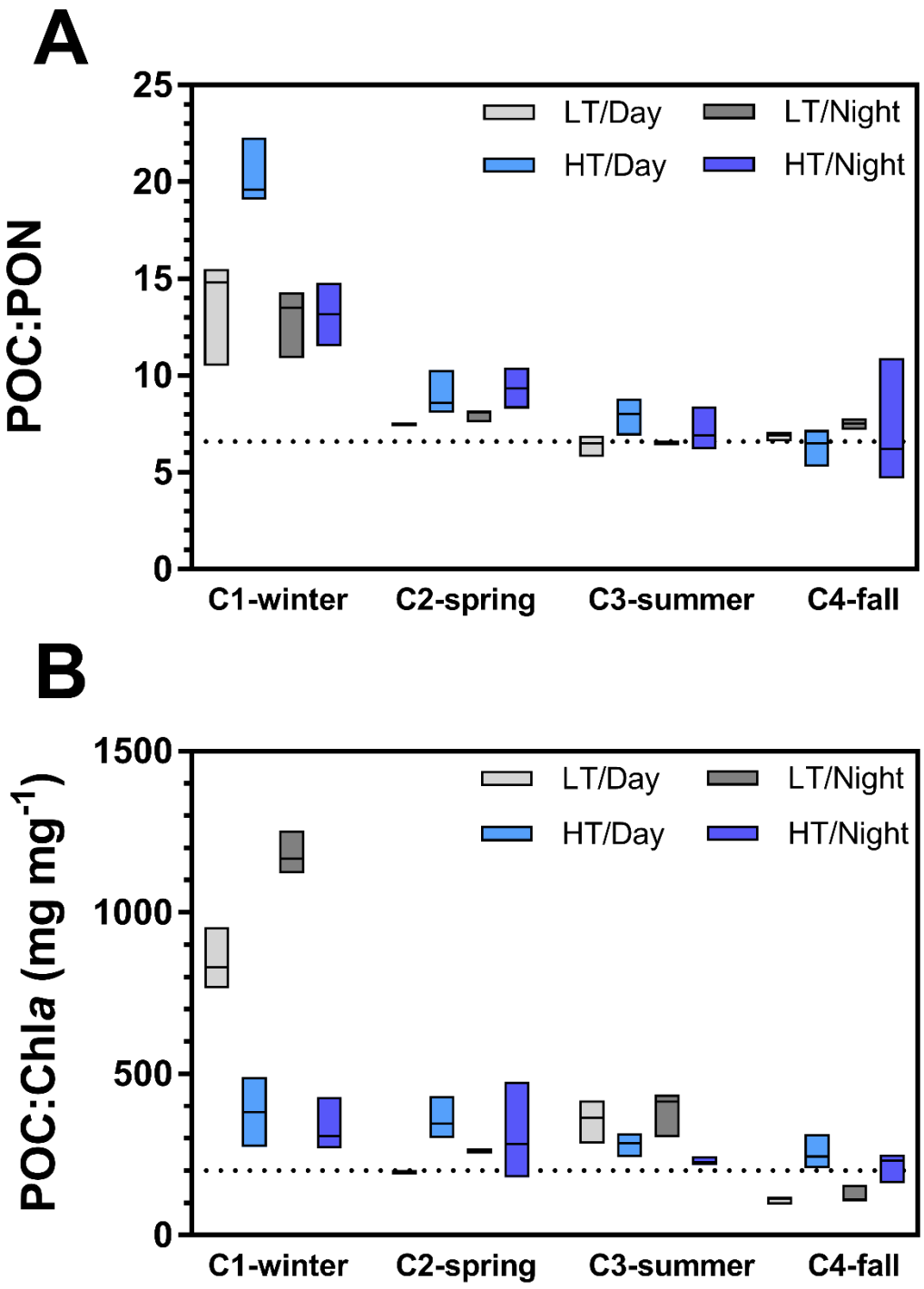

Figure 4.9: Boxplot distribution (median, minimum and maximum) of POC:PON molar ratio (**A**) and POC:Chl*a* mass ratio (**B**; in mg mg^{-1}) at the diurnal/tidal scales within each seasonal 24-h cycle. The horizontal dotted line in **(A)** corresponds to the Redfield ratio (i.e. theorical molar ratio for plankton; POC:PON = 6.6) (Redfield, 1958). The horizontal dotted line in **(B)** allows characterizing particulate organic matter either as autotrophic (POC:Chl*a* < 200 mg mg^{-1}, dominance of "fresh" living phytoplankton) or heterotrophic (POC:Chl*a* > 200 mg mg^{-1}, dominance of detrital organic material; Savoye et al., 2003). LT/Day: low tide day; HT/Day: high tide day; LT/Night: low tide night; HT/Night: high tide night.

3.5. Statistical analysis

At the scale of all 24-h cycles (all samples, n = 59), NMDS showed higher temporal variations of measured biogeochemical parameters at seasonal and tidal scales than at diurnal scale (Fig. 4.10). More precisely, variance analyses on dissolved inorganic matter showed that TA, NH_4^+ and DSi were more strongly explained by tidal factor in comparison with seasonal factor whereas, the opposite trend was found for NO_3^-_NO_2^- and DIC (Table 4.4). Regarding dissolved organic matter, DOC and DON were mostly controlled by tidal factor (weak seasonal influence) whereas for particulate organic matter, POC was only controlled by tidal factor (Table 4.4). Diurnal factor did not significantly explained variance of biogeochemical parameters at the global scale (except for DIP; Table 4.4) but significantly affected carbonate system (DIC, TA and pCO_2) over C1-winter only (Fig. S1). At the global scale (n = 59), correlation analyses highlighted that dissolved organic matter (DOC and DON) and photosynthetic pigments (Chl*a*) displayed strong negative correlations with water pCO_2 whereas, dissolved inorganic matter (DIC and NO_3^-_NO_2^-) displayed weak positive correlations with water pCO_2 (Table 4.5). We showed that organic carbon (POC and DOC) were significantly positively correlated with Chl*a* whereas, NO_3^-_NO_2^- were significantly negatively correlated with Chl*a*. Increases in NH_4^+ from high to low tides were strongly positively correlated with TA and DIC (Fig. S1 and Table 4.5).

3.6. Net ecosystem CO_2 exchanges and daily C balances

Significant seasonal variations of NEE were highlighted between each 24-cycle (Kruskal-Wallis test, $p < 0.001$). In average, the highest and lowest atmospheric CO_2 sinks within the EC footprint were measured over C3-summer (-2.70 ± 5.00 µmol m^{-2} s^{-1}) and C1-winter (-1.37 ± 2.66 µmol m^{-2} s^{-1}), respectively (Fig. 4.2). Over the 24-h cycles, the highest CO_2 uptake and CO_2 emission were recorded at low tides during daytime and night-time, respectively, associated with a major influence of marsh benthic metabolism (i.e. measured NEE = estimated NEE_{marsh}; Fig. 4.2). However, at high tides, immersion strongly disrupted NEE though, in general, no change in the marsh metabolism status (sink/source) was noticed. Indeed, at HT/Day, significant differences were recorded between measured NEE and estimated NEE_{marsh} over C1-winter and C2-spring (Wilcoxon tests, $p < 0.05$), where tides decreased net marsh CO_2 uptake of 80% and 68%, respectively. On the contrary, no significant difference between NEE and NEE_{marsh} was recorded over C3-summer at HT/Day (Wilcoxon test, $p = 0.41$; NEE = NEE_{marsh}) though a water CO_2 oversaturation was measured

at this time (Fig. 4.2). At HT/Night, lower marsh CO_2 emissions were measured with measured NEE than with estimated NEE_{marsh} (Wilcoxon tests, $p < 0.05$) inducing even a switch from source to sink over C1-winter, though a water CO_2 oversaturation was measured at the same time (Fig. 4.2).

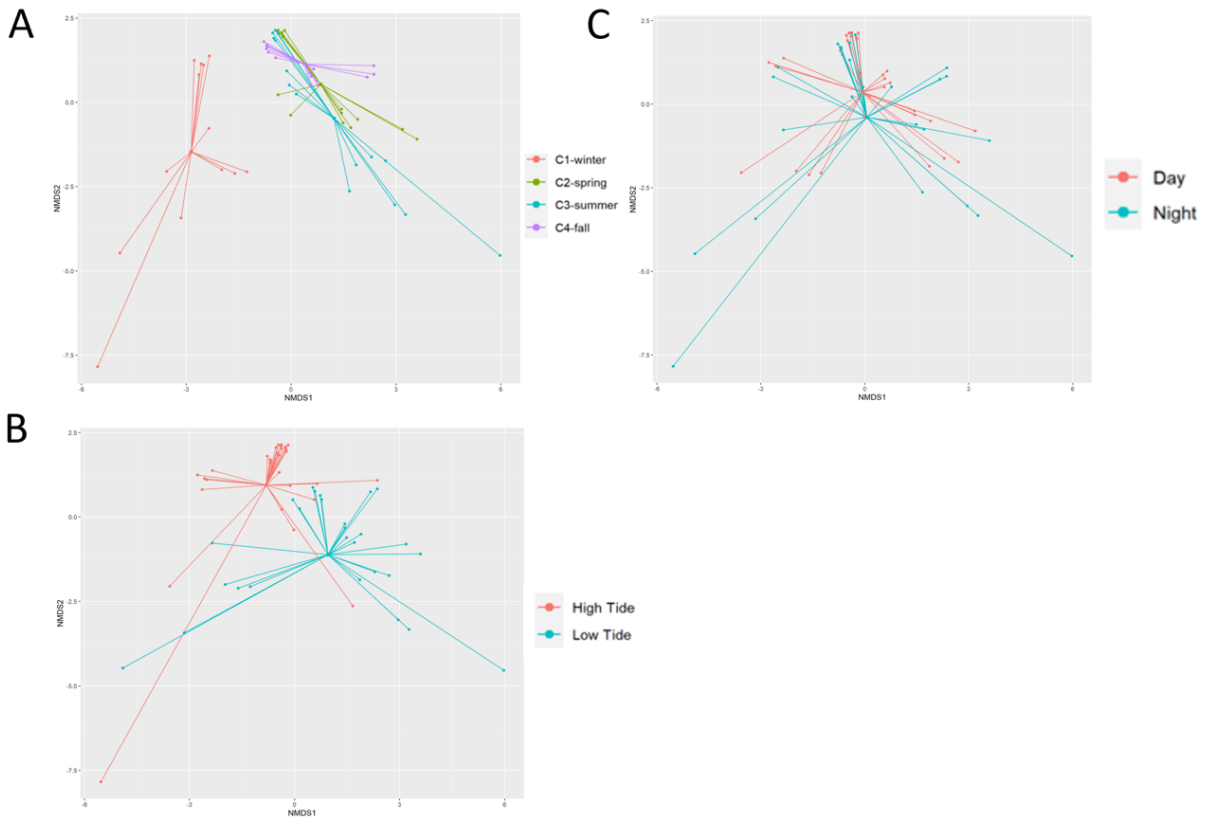

Figure 4.10: Non-metric multidimensional scaling (NMDS) using Euclidean distance of the biogeochemical parameters measured from hourly water samples (n = 59) at the seasonal **(A)**, tidal **(B)** and diurnal **(C)** scales (stress of 0.08). Each NMDS is based on pCO_2, DIC, DOC, POC, PON, DON, TA, Chl*a*, NO_3^-_NO_2^-, NH_4^+, DSi and DIP values. Biogeochemical data were reported in table 4.3. Seasonal factor assesses variability between 24-h cycles (C1-winter, C2-spring, C3-summer and C4-fall); tidal factor assesses variability between high tides (Hw > 0.50 m) and low tides (Hw = 0.50 m); diurnal factor assesses variability between daytime (PAR > 10 µmol m^{-2} s^{-1}) and night-time (PAR < 10 µmol m^{-2} s^{-1}).

Table 4.4: Multiple factor variance analysis of biogeochemical parameters measured from hourly water samples during all 24-h cycles (n = 59). Seasonal factor assesses variability between 24-h cycles (C1-winter, C2-spring, C3-summer and C4-fall); tidal factor assesses variability between high tides (Hw > 0.50 m) and low tides (Hw = 0.50 m); diurnal factor assesses variability between daytime (PAR > 10 µmol m^{-2} s^{-1}) and night-time (PAR < 10 µmol m^{-2} s^{-1}). Parameters that did not respect a normal distribution were transformed into $log_{10}(x)$ or $log_{10}(x+1)$ for variance analysis. The F values of the Fisher test were added. The higher the value of F, the greater the influence of the factor on the parameter.

	Seasonal factor	**Tidal factor**	**Diurnal factor**
log_{10}(Chl*a*)	**Yes** F = 5.9 p < 0.001	**Yes** F = 30.2 p < 0.0001	No F = 0.1 p = 0.74
log_{10}(DIC)	**Yes** F = 47.9 p < 0.0001	**Yes** F = 18.1 p < 0.0001	No F = 0.3 p = 0.61
log_{10}(TA)	**Yes** F = 25.9 p < 0.0001	**Yes** F = 91.0 p < 0.0001	No F = 0.1 p = 0.79
log_{10}(POC)	No F = 2.2 p = 0.10	**Yes** F = 161.2 p < 0.0001	No F = 0.8 p = 0.37
log_{10}(DOC)	**Yes** F = 4.2 p < 0.05	**Yes** F = 188.5 p < 0.0001	No F = 0.8 p = 0.36
log_{10}(PON)	**Yes** F = 5.1 p < 0.05	**Yes** F = 174.3 p < 0.0001	No F = 0.7 p = 0.41
log_{10}(DON)	**Yes** F = 23.3 p < 0.0001	**Yes** F = 170.9 p < 0.0001	No F = 0.2 p = 0.65
$log_{10}(NO_3\_NO_2 + 1)$	**Yes** F = 151.6 p < 0.0001	**Yes** F = 53.8 p < 0.0001	No F = 1.8 p = 0.19
$log_{10}(NH_4 + 1)$	**Yes** F = 39.2 p < 0.0001	**Yes** F = 60.0 p < 0.0001	No F = 0.8 p = 0.39
log_{10}(DIP + 1)	**Yes** F = 25.7 p < 0.0001	**Yes** F = 23.2 p < 0.0001	**Yes** F = 6.3 p < 0.05
log_{10}(DSi +1)	**Yes** F = 28.0 p < 0.0001	**Yes** F = 40.8 p < 0.0001	No F = 1.1 p = 0.31

Table 4.5: Spearman's rank correlations of biogeochemical parameters and phytoplankton biomass recorded from hourly water samples during the four 24-h cycles at the Bossys perdus salt marsh (n = 59). Asterisks designate significant correlations (*** $p < 0.001$, ** $p < 0.01$, * $p < 0.05$, NA $p > 0.05$).

Spearman	**pCO_2**	**Chl*a***	**DIC**	**TA**	**NO_3^-_NO_2^-**	**NH_4^+**	**DIP**	**DSi**	**DOC**	**POC**	**PON**	**DON**
pCO_2	1.00	-0.61^{***}	0.42^{***}	NA	0.59^{***}	NA	NA	NA	-0.68^{***}	-0.56^{***}	-0.64^{***}	-0.69^{***}
Chl*a*			0.11^{***}	0.45^{***}	-0.50^{***}	0.32^{*}	NA	0.25^{*}	0.69^{***}	0.78^{***}	0.84^{***}	0.77^{***}
DIC				0.79^{***}	0.43^{***}	0.74^{***}	NA	NA	NA	NA	NA	NA
TA					NA	0.87^{***}	0.27^{*}	0.37^{**}	0.49^{***}	0.57^{***}	0.42^{**}	0.26^{*}
NO_3^-_NO_2^-						0.25^{*}	0.37^{**}	NA	-0.39^{**}	NA	-0.43^{**}	-0.68^{***}
NH_4^+							0.47^{***}	0.46^{***}	0.40^{**}	0.49^{***}	0.35^{**}	NA
DIP								0.87^{***}	0.36^{*}	0.50^{***}	0.37^{**}	0.22^{*}
DSi									0.46^{***}	0.68^{***}	0.50^{***}	NA
DOC										0.80^{***}	0.85^{***}	0.83^{***}
POC											0.92^{***}	0.71^{***}
PON												0.87^{***}
DON												1.00

Table 4.6: Diurnal comparison (day *vs* night) of planktonic metabolism (NCP) and overall aquatic metabolism ($NEP_{aquatic}$) during marsh immersion over each 24-h cycle at the Bossys perdus salt marsh. Simultaneously, water-air CO_2 fluxes (FCO_2) estimated from water pCO_2 measurements and net ecosystem CO_2 exchanges (NEE) measured by EC were simultaneously recorded (means and SD in bold, ranges in brackets) and related to planktonic and aquatic metabolism. Wind direction (wind dir.) measured by the EC station was added for each immersion period. NA: EC data could not be measured for C4-fall.

		Planktonic metabolism		**Overall aquatic metabolism**	**Water-air CO_2 fluxes**	**Net ecosystem CO_2 exchanges (NEE)**	
		GPP/CR	NCP (mmol m^{-2} h^{-1})	$NEP_{aquatic}$ (mmol m^{-2} h^{-1})	FCO_2 (mmol m^{-2} h^{-1})	NEE (mmol m^{-2} h^{-1})	Wind dir.
C1-winter	HT/Day	**3.31**	**0.89**	**-6.68**	**0.01 ± 0.00** (0.00 – 0.02)	**-0.43 ± 2.22** (-6.80 – 2.80)	ENE ESE
	HT/Night	**0.84**	**-0.23**	**-16.70**	**0.17 ± 0.04** (0.11 – 0.22)	**-3.18 ± 1.03** (-5.02 – -1.55)	ESE
C2-spring	HT/Day	**0.91**	**-0.20**	**-27.81**	**-0.23 ± 0.08** (-0.31 – -0.11)	**-10.84 ± 4.72** (-19.33 – -5.29)	WNW NNW
	HT/Night	**2.52**	**1.77**	**-1.32**	**-0.06 ± 0.09** (-0.22 – 0.00)	**0.96 ± 2.16** (-4.25 – 3.71)	NNW
C3-summer	HT/Day	**1.91**	**0.43**	**95.91**	**0.07 ± 0.03** (0.03 – 0.10)	**-8.03 ± 2.87** (-15.84 – -5.08)	NNE
	HT/Night	**0.12**	**-0.73**	**-20.89**	**0.21 ± 0.02** (0.18 – 0.22)	**0.06 ± 1.09** (-1.24 – 1.56)	NNW
C4-fall	HT/Day	**0.29**	**-0.18**	**-1.30**	**0.38 ± 0.06** (0.32 – 0.44)	NA	NA
	HT/Night	**0.39**	**-0.27**	**-5.87**	**0.29 ± 0.26** (0.00 – 0.62)	NA	NA

Table 4.7: Daily net C balances (g C m^{-2} d^{-1}) of measured NCP rates (planktonic metabolism), measured NEE fluxes (atmospheric CO_2 exchanges) and estimated NEE_{marsh}, GPP_{marsh} and R_{marsh} fluxes (marsh metabolic fluxes) during the four seasonal 24-h cycles at the Bossys perdus salt marsh. For daily NCP rates, negative balances correspond to an autotrophy (net C sink for waters) and positive balances correspond to a heterotrophy (net C source for waters). For net marsh metabolism with immersion (NEE) and without immersion (NEE_{marsh}), negative balances correspond to an atmospheric C uptake by the marsh. NA: EC data could not be measured for C4-fall.

	Daily NCP (g C m^{-2} d^{-1})	**Daily NEE (g C m^{-2} d^{-1})**	**Daily NEE_{marsh} (g C m^{-2} d^{-1})**	**Daily GPP_{marsh} (g C m^{-2} d^{-1})**	**Daily R_{marsh} (g C m^{-2} d^{-1})**
C1-winter	-0.07	-1.43	-1.64	-2.22	0.58
C2-spring	-0.25	-2.56	-3.32	-4.96	1.64
C3-summer	0.06	-2.82	-2.62	-4.49	1.87
C4-fall	0.11	NA	NA	NA	NA

Over the 24-h cycles, net C balances of planktonic metabolism (NCP) ranged from -0.25 (C2-spring) to 0.11 g C m^{-2} d^{-1} (C4-fall) whereas, net C balances of the salt marsh (NEE) ranged from -1.43 (C1-winter) to -2.82 g C m^{-2} d^{-1} (C3-summer; (Table 4.7). Indeed, net C balances from estimated NEE_{marsh}, considering only the marsh metabolism at emersion, ranged from -1.64 (C1-winter) to -3.32 g C m^{-2} d^{-1} (C2-spring). The highest GPP_{marsh} and R_{marsh} rates were recorded over C2-spring and C3-summer, respectively (Table 4.7). At emersion, a significant proportion of the marsh primary production (GPP_{marsh}) was respired and re-emitted as atmospheric CO_2 (R_{marsh}) over our 24-h cycles (26%, 33% and 42% over C1-winter, C2-spring and C3-summer, respectively; Table 4.7).

4. Discussion

4.1. Temporal variations of water pCO_2 and controlling factors

The four 24-h cycles with continuous water measurements following the different tidal phases (at high tide with marsh waters influenced by shelf and at low tide with channel waters influenced by salt marsh) showed large and significant seasonal and tidal variations of water biogeochemical parameters related to carbon cycle (Fig. 4.10), especially water pCO_2 (Fig. 4.3). For illustrate this, we observed a maximal pCO_2 variation of 430 ppmv at the seasonal scale (between 24-h cycles) and a maximal pCO_2 variation of 1140 ppmv at the tidal scale (between high tide and low tide).

Seasonal water pCO_2 were strongly controlled by non-thermal effects (biological activity, tidal exchange and benthic exchanges) inducing a water CO_2 oversaturation in winter and a water CO_2 undersaturation in spring and summer. In the salt marsh, the water temperature increased of 11.9°C from winter to summer whereas simultaneously, seasonal $NpCO_2$ values decreased (from 802 to 200 ppmv) concomitantly to pCO_2 values (from 669 to 271 ppmv) confirming a stronger control of non-thermal components than thermal components on water pCO_2. In winter, during the lowest marsh primary production (Mayen et al., 2024), aquatic heterotrophy through microbial respiration of organic matter in the channel was favoured inducing the highest seasonal $NpCO_2$ value. On the contrary, in spring and summer during the growing period of marsh plants (Mayen et al., 2024), aquatic autotrophy through photosynthesis was favoured inducing the lowest seasonal $NpCO_2$ values (winter heterotrophy and spring/summer autotrophy are more discussed in the next sections). In fall, non-thermal effects consisted in more heterotrophy were offset by thermal effects producing a mean water

pCO_2 value nearby to atmospheric equilibrium. Fall thermal effects decreased water pCO_2 of 23% due to a water colding limiting water CO_2 oversaturation. In upstream artificial salt marshes with higher water residence times, a strong biological control of macroalgae was recorded on water pCO_2 inducing water CO_2 undersaturation in spring and summer due to autotrophy (135 ± 165 and 242 ± 116 ppmv, respectively) and water CO_2 oversaturation in fall due to heterotrophy (622 ± 57 ppmv; (Mayen et al. 2023). On the contrary, in the downstream estuarine waters, a strong seasonal compensation of thermal and non-thermal effects seemed to occur throughout the year producing low seasonal water pCO_2 variations (between 441 ± 21 ppmv in winter and 385 ± 60 ppmv in summer; (Mayen et al. 2023). Thus, in closed coastal environments, CO_2 biogeochemical processes in waters are likely to be controlled by non-thermal effects, like biological activity (Borges et al. 2003; Cotovicz Jr. et al. 2015; Berg et al. 2019), compared to more open systems where thermal effect can be more dominant (Jiang et al. 2008; Dai et al. 2009; Polsenaere et al. 2022).

In the salt marsh, a stronger influence of the tide (i.e. water height) was recorded on water pCO_2 which may be due to higher biological activity (production and respiration) at low tide in channel waters than at high tide in marsh waters (see next sections) as showed by Wang et al. (2018). In winter at low tide, low daytime autotrophic processes in channel waters induced the lowest pCO_2 decrease whereas high night-time heterotrophic processes in channel waters induced the highest pCO_2 increase. On the contrary, in spring and summer both at day and night, the strong channel autotrophy induced the lowest water pCO_2 values (Fig. 4.3). Thus, during transient tidal phases, lateral exchanges with buffered shelf waters produced instantaneously variations of channel water pCO_2 leading to strong increases during incoming tides (i.e. channel filing), except in winter at night, and strong decreases during ebbing tides (i.e. channel emptying; Fig. 4.2). To investigate the role of primary producers on the chemical composition of channel waters, geochemical calculations had been done with PHREEQC (Parkhurst and Appelo, 2013), a geochemical code able to calculate the speciation of dissolved species in waters as well as the solid-water-gas equilibria in aqueous systems. The objectives of these simulations were mainly to investigate the calco-carbonic equilibrium according to the season and to recalculate the equivalent water pCO_2 according to temperature, pH and DIC concentrations and to compare with field measurements. These calculations also allowed defining the saturation indices of solid phases and predicting the risk of dissolution/precipitation of minerals. The results highlight that, during daytime low tides periods in winter and fall, calculated pCO_2 in channel waters are very close to the

atmospheric pCO_2 (about $10^{-3.5}$ atm) which could indicate that pCO_2 are partially controlled by the calco-carbonic equilibrium. In spring and summer, calculated pCO_2 in channel waters are one order of magnitude lower than the atmospheric pCO_2 (about $10^{-4.3}$ atm), which could signify that the calco-carbonic equilibrium is influenced by other mechanisms, like a strong biological driver playing the role of carbon sink. Our results can confirm the strong contribution of biological activity in water inorganic carbon in salt marshes (Wang and Cai 2004; Wang et al. 2016; Gong et al. 2023), especially in water pCO_2 (Wang et al. 2018; Song et al. 2023). Others studies in coastal wetlands (seagrasses, mangroves and salt marshes) showed a strong tidal control on inorganic carbon but, unlike to our results, the highest pCO_2 values were measured at low tide irrespective of day or night status (Polsenaere et al. 2022). The mineralization of organic carbon in sediments followed by efflux of porewaters oversaturated in CO_2 to water column by tidal pumping induced large water pCO_2 increases at low tide (Borges et al. 2003; Burgos et al. 2018). For instance, within the Duplin River salt marsh-estuary coastal system (USA), water pCO_2 values varied from 1600 ppmv (high tide) to 12000 ppmv (low tide) in summer (Wang et al. 2018). Thus, horizontal exchanges of coastal waters with salt marshes strongly modified water CO_2 biogeochemical status (sink/source) with respect to the atmosphere due to a strong marsh metabolism (production and respiration).

4.2. Marsh primary producer influence on water pCO_2 and DOC

At the sampling station, water pCO_2 decreases and DOC concentration increases from high to low tides, especially in spring (-54% and +77%, respectively) and summer (-71% and +85%, respectively), were related to a strong marsh primary production. In the salt marsh, a large part of water inorganic carbon can be fixed by photosynthesis of primary producers (negative correlations between Chl*a* biomass and water pCO_2), including phytoplankton, benthic microalgae, macroalgae and halophyte plants and it could be processed and exported to channel waters as organic carbon form (negative correlations between DOC and water pCO_2; Table 4.5).

Within the 24-h cycles, the strong increases of phytoplankton abundance from high to low tides, especially in spring and summer (Fig. 4.4), indicated a development of planktonic communities under non-limiting nutrient conditions (Fig. 4.7). During low tide periods (except in winter), POC:PON ratios were close to the Redfield value (Fig. 4.9-A) suggesting

living phytoplanktonic biomass in waters. In the sampling planktonic communities, the high abundance of pennate diatoms in spring and summer could indicate the presence of resuspended benthic microalgal mats (microphytobenthos: MPB) whose strong metabolism can influence water pCO_2 variations (Polsenaere et al. 2022). During low tide periods, daily planktonic metabolism influenced inorganic C variations in channel waters inducing a net autotrophy in winter and spring (0.05 and 0.17 g C m^{-2} d^{-1}, respectively) and a net heterotrophy in summer and fall (-0.04 and -0.09 g C m^{-2} d^{-1}, respectively). These planktonic communities behaved as a net CO_2 sink for channel waters during daytime and as a net CO_2 source for channel waters during night-time (Fig. 4.5-A). During daytime low tides, the highest planktonic CO_2 uptake (NCP) was recorded in spring (high PAR and intermediate Tw) through a significant autotrophic activity of pennate diatoms and nanophytoplankton whereas, the decrease of planktonic CO_2 uptake towards summer (high PAR and Tw) could be liked to higher temperatures, which leads to an increase in respiration, and more generally, heterotrophic processes. Moreover, in summer, the dinoflagellate bloom in channel waters, some species of which are known to be mixotrophic or even heterotrophic (Stoecker 1999; Jeong et al. 2010), could be responsible to the lower net planktonic CO_2 uptake in summer than in spring. Thus, planktonic metabolism can be a significant controlling factor of water pCO_2, especially in spring, inducing high daytime decreases and low night-time increases (Fig. 4.5-A). Moreover, since Chl*a* concentrations significantly varied according to seasons and tides (Table 4.4), variations in NCP rates also reflected changes in phytoplankton biomass rather than physiological responses to community compositions or environmental conditions. At low tides, the highest net autotrophy of planktonic metabolism standardized to Chl*a* biomass (NCP_{Chla}) was recorded in winter inducing a daytime decrease of water pCO_2 probably by MPB activity. The metabolic activity of planktonic communities in channel waters can be an important source of DOC (positive correlation between Chl*a* and DOC) as recorded at low tides (Fig. 4.8) by extracellular releases commonly accounting 5-30% of their primary production (Karl et al. 1998). Planktonic communities can also produce DOC by phytoplankton cell lysis in summer, which is an important process during physiological stress conditions such as nutriment limitation (Van Boekel et al. 1992). In the salt marsh, pennate diatoms and nanophytoplankton are fast-growing primary producers releasing high labile DOC (De Brouwer and Stal 2001; Morelle et al. 2022) which could be degraded in CO_2 by bacterial remineralization (Oakes and Eyre 2014).

In spring and summer at low tides, the strong daytime increases (up 190%) and night-time decreases (up to 10%) of DO-sat in channel waters (Fig. 4.2) could indicate a strong biological influence of aquatic macroalgae and/or benthic microalgae which have typically higher rates of production and respiration than phytoplankton (Borum and Sand-Jensen 1996; Hill et al. 2015). The fast-growing macroalgae bloom recorded in the upstream artificial marsh waters, related to eutrophication conditions (Teichberg et al. 2010; Le Fur et al. 2018), can induce and maintain large water CO_2 undersaturation both at day and at night, especially during warm and bright periods (Mayen et al. 2023). These macroalgae can largely contributed to CO_2 depleted and DOC concentrated waters recorded in the sampling channel which received all upstream marsh waters at low tides. Previous studies have reported that the primary production of macroalgae favours a large DOC exportation by horizontal exchanges, a part of which can be sequestered in coastal and marine sediments (Hill et al. 2015; Krause-Jensen and Duarte 2016; Raven 2018).

At the salt marsh, the strong net primary production of emerged plants, especially in spring and summer (Mayen et al. 2024), could induce a large organic matter production by roots (Duarte et al. 2005; Schiebel et al. 2018). A major part of this marsh primary production can be exported to channel waters (Santos et al. 2009) favouring the highest DOC concentrations (Fig. 4.8). The mostly DOC leached from marsh plants like *Spartina* is labile and highly biodegradable by bacterial activity, especially polysaccharides. However, because of its long residence time, lignin-derived DOC is a potentially important source of aquatic humic substances in salt marshes (Moran and Hodson 1990; Wang et al. 2014). Thus, CO_2-depleted and DOC-concentrated water exportation from high to low tides highlighted a significant role of marsh primary production in the carbon cycle of the coastal ocean.

4.3. Aquatic marsh respiration processes as source of DIC

Over 24-h cycles, significant temporal variations of DIC and TA were recorded (Fig. 4.6), mainly driven by tidal factor. During high tide periods (marsh immersion), net ecosystem production of water column was heterotrophic both during daytime and night-time (except in summer at day) inducing DIC additions and water pCO_2 increases (Table 4.6). The low contribution of planktonic metabolism (NCP) to net ecosystem production of water column ($NEP_{aquatic}$) suggested a major influence of immersed plant respiration and benthic exchanges in water inorganic carbon. Previous studies in intertidal wetlands showed that benthic

respiration produced strong sediment-to-water DIC transports by diffusion during immersion inducing, in turn, water CO_2 oversaturation (Song et al. 2023; Gong et al. 2023).

During low tide periods, the largest DIC and TA increases were measured in channel waters, especially in winter (Table 4.3 and Fig. S1), highlighting a strong control of tidal forcing on water carbonate chemistry. In most of intertidal systems such as salt marshes and mangroves, strong metabolic processes occur in sediments and can induced the highest DIC and TA concentrations in surface waters at low tide through porewater exports driven by tides (Koné and Borges 2008; Reithmaier et al. 2023). In winter, during the lowest biological activity of *S. maritima* (Mayen et al. 2024), the highest POC:PON and POC:Chl*a* ratios (Fig. 4.9) could suggest a refractory organic matter from decaying vegetation and could constitute an energy source for bacterial activity inducing, in turn, the highest increases of DIC concentrations and water pCO_2 in the channel. In an intertidal wetland (China), a large biological addition of DIC was also recorded in sediments at low tides mainly by aerobic respiration and fermentation of organic carbon derived from *S. alterniflora* (Gong et al. 2023). Over the winter 24-h cycle, the strong relationship between DIP and NH_4^+ from high to low tide ($R^2 = 0.66$, $p < 0.001$; Fig. 4.7) can confirm a microbial respiration of organic matter in sediments and a lateral export of DIC and nutrients from porewaters to channel waters by tidal pumping (Deborde et al. 2008; Liu et al. 2017; Santos et al. 2019). As marsh sediments are anoxic from first millimetres (Wiebe et al. 1981), anaerobic respirations can be dominant metabolic processes in intertidal salt marshes producing DIC and TA (Wang et al. 2016; Reithmaier et al. 2023). In winter and fall, the slope of the nTA:nDIC regression (Fig. 4.6) suggests a major control of sulfate reduction in the DIC and TA additions (mainly HCO_3^-) according to theorical stoichiometric ratios of metabolic processes as deduced by Krumins et al. 2013. Due to salinity, sulfate is abundant in coastal waters considering sulfate reduction as among the most important organic carbon mineralisation pathways in intertidal salt marshes (Wang et al. 2018; Reithmaier et al. 2023). However, variations in nutrient concentrations could highlight other anaerobic processes producing DIC and TA in channel waters, further confirming the major role of sediments in the water inorganic carbon dynamics. In winter, we recorded the highest DIN:DIP ratios, especially at high tides, showing typically conditions of terrestrial inputs of NO_3^-_NO_2^- in shelf waters by the Aiguillon Bay watershed (Belin et al. 2021). Over the 24-h cycle, NO_3^-_NO_2^- decrease from high to low tides was significantly related to NH_4^+ increase ($R^2 = 0.90$, $p < 0.001$; Fig. 4.7). This strong relationship could highlight a dissimilatory nitrate reduction to ammonium (DNRA) in anoxic sediments which

is an important fermentative process in salt marshes producing DIC and TA (Hopkinson and Giblin 2008; Giblin et al. 2013). Under low autotrophy conditions in winter, NO_3^-_NO_2^- can diffuse into marsh sediments during immersion (Boynton et al. 2018) and can be reduce in NH_4^+ by fermentative DNRA (Koop-Jakobsen and Giblin 2010) before its transfer to channel waters through tidal pumping (Zheng et al. 2016). However, DNRA measurements are unavailable to confirm the importance of this process.

In spring and summer, a larger increase of DIC than TA (Fig. 4.6) was recorded since both aerobic and anaerobic respirations produced DIC whereas, only anaerobic respiration produced TA (Krumins et al. 2013). Contrary to winter, DIC and TA productions in spring and summer at low tide did not induced a significant water pCO_2 variation (Fig. 4.3). In spring, the nTA *vs* nDIC regression was slightly significant ($R^2 = 0.58$, $p < 0.05$; Fig. 4.6-B) suggesting a large contribution of aerobic respiration to DIC production in surface waters. On the contrary, in summer, the nTA *vs* nDIC regression was highly significant ($R^2 = 0.93$, $p < 0.0001$; Fig. 4.6-C) and the slope was close to the theorical stoichiometric ratio of denitrification as deduced by Krumins et al. 2013. At low tides in summer, the values of POC:Chl*a* ratios (from 300 to 450 mg mg^{-1}; Fig. 4.9) suggest a large contribution of detrital phytoplanktonic biomass to DIC and nutriment productions in waters. Over the summer 24-h cycle, the strong increase of DIP and DSi from high to low tides (Fig. 4.7) could confirm strong sediment-water fluxes (Boynton et al. 2018; Borawska et al. 2022), especially at low tide night where hypoxia conditions were occurred (Fig. 4.2). Moreover, the lowest DIN:DIP ratios in summer (from 0.2 to 8.4) could suggest a denitrification and/or iron oxy-hydroxide respiration in sediments promoting DIC releases in channel waters (Boynton et al. 2018). In this salt marsh, a shift from refractory decomposed organic matter in winter to labile fresh phytoplankton in spring/summer probably occurred. The sources of POC and PON were sampled for identification; unfortunately, results are unavailable to validate the organic matter composition.

4.4. Influence of aquatic and benthic metabolism on marsh ecosystem CO_2 exchanges

To study the contribution of planktonic communities taking into account both high tide and low tides on marsh CO_2 uptake in the integrative way, daily C balances were calculated from planktonic metabolism in waters and from atmospheric CO_2 exchanges in the EC footprint (Table 4.7). The daily planktonic metabolism was autotrophic in winter and spring

due to higher daytime CO_2 uptake than night-time CO_2 source whereas, it was heterotrophic in summer and fall due to lower daytime CO_2 uptake than night-time CO_2 source (Fig. 4.5-A). Simultaneously, NEE fluxes measured by EC indicated a strong marsh autotrophy from winter to summer allowing a net daily C uptake from the atmosphere (Table 4.7) with a major contribution of marsh habitats (NEE_{marsh}) and a minor one of planktonic communities (NCP). For instance, in spring, tidal immersion reduced the marsh C uptake (-0.76 g C m^{-2} d^{-1}) despite a planktonic autotrophy whereas in summer, immersion slightly increased the marsh C balance (0.20 g C m^{-2} d^{-1}) despite a planktonic heterotrophy (Table 4.7). Therefore, our study indicated a low contribution of planktonic communities in daily C balances with a contribution account up to 10% over a spring 24-h cycle. Moreover, over the 24-h cycles, NEE flux partitioning allowed to study the influence of benthic metabolism on marsh metabolic fluxes (photosynthesis and respiration). In an intertidal wetland (China), Gong et al. (2023) showed that the microbial addition of DIC in sediments at low tide induced large atmospheric CO_2 emissions from emerged sediments (0.95 ± 0.24 g C m^{-2} d^{-1}). However, at the ecosystem scale, our EC measurements estimated a low R_{marsh}:GPP_{marsh} ratio in winter (i.e. 0.26; Table 4.7) suggesting a weak contribution of the sediment heterotrophy and associated DIC and TA exports on marsh C uptake whereas, the high R_{marsh}:GPP_{marsh} ratio in summer (i.e. 0.42; Table 4.7) could indicate a high influence of phytoplankton heterotrophy and associated benthic microalgae remineralisation on marsh C uptake.

Over the 24-h cycles, strong variabilities in net ecosystem CO_2 exchanges (NEE) were recorded by atmospheric EC with generally daytime CO_2 uptake and night-time CO_2 emission associated with higher metabolic fluxes at low tides than at high tides (Fig. 4.2). During low tide periods, the channel water CO_2 oversaturation (winter) and undersaturation (spring/summer) did not significantly influence NEE fluxes measured within the EC footprint. Indeed, the emerged marsh remained a daytime CO_2 sink and a night-time CO_2 source, especially in spring and summer, due to a strong terrestrial plant metabolism (Fig. 4.2). Thus, at emersion, the CO_2 biogeochemical status (sink/source) of channel waters related to heterotrophic metabolism (winter) and autotrophic metabolism (spring/summer) was not a major controlling factor in marsh metabolic fluxes. However, due to wind directions did not come from the sectors most represented by the channel, it remains complex to study precisely the effect of the biogeochemical status of channel waters (sink/source of atmospheric CO_2) on NEE fluxes at the marsh scale.

During high tide periods, coastal waters advected from the shelf immersed the salt marsh (mudflats and plants) and quickly disrupted NEE fluxes since waters created a physical barrier between the marsh and the atmosphere limiting the CO_2 diffusion. During immersion, atmosphere-water CO_2 fluxes estimated from water pCO_2 could be compared with NEE fluxes from EC measurements at the same time to go further on the contribution of aquatic metabolism on marsh metabolic fluxes (uptake/emission) at the footprint scale. During the highest immersion levels of plants (winter and spring), aquatic metabolism and associated water-atmosphere CO_2 fluxes significantly influenced marsh CO_2 uptake within the EC footprint. Indeed, during daytime immersion in winter, the water CO_2 oversaturation (source) strongly reduced the marsh CO_2 uptake at the ecosystem scale whereas in spring, the water CO_2 undersaturation allowed to maintain a weak marsh CO_2 uptake (Fig. 4.2). On the contrary, during the lowest immersion levels of plants (summer), the water CO_2 oversaturation and associated atmospheric CO_2 emissions did not significantly influence marsh CO_2 uptake which was mainly controlled by terrestrial metabolism of emerged plants (*Suaeda vera*). During night-time, tidal immersion completely suppressed the atmospheric CO_2 emissions from ecosystem respiration (plants and sediments) even causing a change in metabolic status from source to sink of atmospheric CO_2 in winter despite an aquatic heterotrophy and a water CO_2 oversaturation. This weak night-time CO_2 sink during marsh immersion could suggest important spatial variations in water pCO_2 with coastal waters undersaturated in CO_2 compared to the atmosphere due to previous phytoplankton production in the downstream shelf and estuary (Mayen et al. 2024). For instance, in spring 2022 (from 01/04 to 03/04/2022), atmospheric CO_2 uptake were recorded during night-time immersion and could be related to a centric diatom bloom ($\approx 1.10^6$ cell L^{-1}) a few days earlier in the downstream shelf waters (station Filiere W; Fig. 4.1-A). To conclude, during high tides periods, marsh metabolic fluxes are strongly controlled by terrestrial vegetation since emerged plants located on the highest marsh levels can maintain a strong atmospheric CO_2 uptake despite an immersion by coastal waters oversaturated in CO_2. Under future environmental conditions, the continuous sea level increase will induce a significant decrease of atmospheric CO_2 uptake through higher immersion levels of marsh plants.

Data availability

All raw data can be provided by the corresponding authors upon request.

Author contribution

PP and PS allowed the funding acquisition. PP, ARG, PS and JM conceptualized and designed the study. JM, PP, ARG and JD performed the 24-h cycles. JM, KC, YLM and EF performed labwork. JM prepared the dataset and performed statistical analyses. JM, PP, ARG and PS investigated and analysed the data. JM, PP, ARG, JD, VO, LA, EL and PS confirmed the data. JM performed the graphics and wrote the manuscript draft. All authors reviewed and edited the manuscript. PP, ARG and PS supervised the PhD thesis of JM.

Competing interests

The authors declare that they have no conflict of interest.

Acknowledgements

Jérémy Mayen would like to thank Ifremer (the French research institute for exploitation of the sea) for financing his PhD thesis (2020-2023). We are grateful to Marie Arnaud, Pierre Kostyrka and Philippe Geairon for their important contribution to the fieldwork carried out during this study. We thank Julien Gernignon and Jean-Christophe Lemesle for your help on the field. We would like to sincerely thank our colleagues at Ifremer for their labwork (Olivier Pierre-Duplessix for nutrient analysis, Anne Schmitt for phytoplanktonic community analysis, Clarisse Hubert for POC and PON analysis and Marie Latimier for flow cytometry analysis). This work is a contribution to the Jérémy Mayen's PhD thesis, the ANR-PAMPAS project (Agence Nationale de la Recherche « évolution de l'identité PAtrimoniale des Marais des Pertuis charentais en réponse à l'Aléa de Submersion marine », ANR-18-CE32-0006) and the CNRS-INSU LEFE-DYCIDEMAIM project (DYnamique du Carbone aux Interfaces D'Échange des MArais tIdaux teMpérés).

Supplementary materials (Mayen et al. in prep.).

Table S1. Seasonal comparisons of meteorological parameters measured by the EC station at the Bossys perdus salt marsh between 3-year reference periods and our 24-h cycles. Each meteorological parameter measured during 24-hour cycles was compared to a mean and standard deviation of the parameter measured continuously over three full reference seasons (2020, 2021 and 2022). For all parameters, means and standard deviations were done in bold and ranges were done in brackets. Ta: air temperature (°C), PAR: photosynthetically active radiation (µmol photon m^{-2} s^{-1}), RH: relative humidity (%).

		Ta (°C)	**Daytime PAR (µmol m^{-2} s^{-1})**	**Wind speed (m s^{-1})**	**RH (%)**
Winter	3-year reference period	**9.3 ± 2.7** (-0.7 – 19.1)	**454 ± 375** (10 – 1770)	**4.59 ± 2.21** (0.05 – 14.01)	**83.3 ± 10.2** (41.4 – 99.5)
	C1-winter	**11.4 ± 1.9** (8.7 – 15.3)	**762 ± 465** (10 – 1335)	**2.33 ± 1.19** (0.45 – 5.09)	**75.2 ± 10.0** (54.8 – 89.5)
Spring	3-year reference period	**14.8 ± 4.4** (2.5 – 35.7)	**946 ± 668** (10 – 2539)	**3.94 ± 1.96** (0.04 – 14.29)	**72.8 ± 14.2** (24.5 – 99.4)
	C2-spring	**13.8 ± 2.9** (9.4 – 20.1)	**1134 ± 668** (10 – 1964)	**3.80 ± 1.29** (0.38 – 6.27)	**65.6 ± 14.4** (31.5 – 84.1)
Summer	3-year reference period	**19.9 ± 3.1** (12.2 – 36.3)	**970 ± 662** (10 – 2428)	**3.56 ± 1.54** (0.03 – 10.49)	**74.0 ± 13.9** (16.6 – 99.6)
	C3-summer	**19.6 ± 0.6** (18.5 – 20.8)	**976 ± 728** (10 – 2216)	**3.11 ± 0.83** (1.14 – 5.05)	**78.6 ± 2.6** (73.2 – 88.9)
Fall	3-year reference period	**12.7 ± 4.1** (-0.5 – 23.7)	**476 ± 393** (10 – 2062)	NA	**81.9 ± 9.5** (42.2 – 99.4)
	C4-fall	**10.3 ± 0.7** (7.9 – 11.3)	**160 ± 93** (10 – 340)	NA	**87.8 ± 6.5** (73.4 – 97.5)

Table S2. Hydrological and biogeochemical setting of station Filiere W (continental shelf; Fig. 1-A) as source water flooding the Bossys perdus salt marsh for (i) the year 2021 (year of water sampling) and (ii) a reference period (2000-2020 for salinity, temperature and turbidity; 2006-2020 for Chl*a* concentrations and 2016-2020 for nutrient concentrations). For all parameters, means and standard deviations were done in bold whereas ranges were done in brackets. Parameters were measured biweekly at station Filiere W according to REPHY monitoring network (Belin et al., 2021). The highest and lowest values (except Chl*a* concentrations) were recorded in winter and summer, respectively (Belin et al., 2021; REPHY, 2021).

	Reference periods (REPHY monitoring network)			**Year of water sampling**
	2000-2020 period	2006-2020 period	2016-2020 period	2021
Salinity	**33.3 ± 1.8** (26.0 – 35.8) N = 575			**33.3 ± 2.2** (27.6 – 34.8) N = 23
Temperature (°C)	**14.8 ± 4.3** (5.5 – 23.7) N = 573			**14.8 ± 4.6** (7.5 – 20.7) N = 23
Chl*a* (µg L^{-1})		**2.1 ± 1.7** (0.3 – 11.2) N = 380		**1.3 ± 0.9** (0.4 – 4.1) N = 25
NO_3^-_NO_2^- (µM)			**16.9 ± 23.0** (0.2 – 107) N = 114	**15.6 ± 23.2** (0.2 – 78) N = 21
NH_4^+ (µM)			**1.5 ± 1.4** (0.1 – 5.9) N = 114	**1.6 ± 1.2** (0.2 – 4.1) N = 24
DSi (µM)			**13.7 ± 10.1** (0.9 – 50) N = 114	**12.8 ± 11.4** (0.4 – 44) N = 25
DIP (µM)			**0.42 ± 0.48** (0.10 – 4.3) N = 114	**0.36 ± 0.30** (0.10 – 1.21) N = 22

Table S3. Seasonal comparisons in 2021 of water pCO_2 measured every 10 min. at the Bossys perdus salt marsh between 5-day reference periods and our 24-h cycles (see section 2.2). Means and standard deviations were done in bold and ranges were done in brackets. NA: water pCO_2 could not measure during low tide periods over the winter reference period (from 26/02 to 01/03/2021).

		Water pCO_2 (ppmv)
Winter	**Winter reference period** 26/02-02/03/2021	NA
	C1-winter 01/03-02/03/2021	**669 ± 327** (321 – 1461)
Spring	**Spring reference period** 23/04-28/04/2021	**296 ± 113** (106 – 596)
	C2-spring 27/04-28/04/2021	**239 ± 105** (106 – 416)
Summer	**Summer reference period** 23/07-27/07/2021	**307 ± 178** (85 – 668)
	C3-summer 26/07-27/07/2021	**271 ± 182** (89 – 597)
Fall	**Fall reference period** 03/12-07/12/2021	**452 ± 88** (260 – 753)
	C4-fall 06/12-07/12/2021	**422 ± 73** (311 – 541)

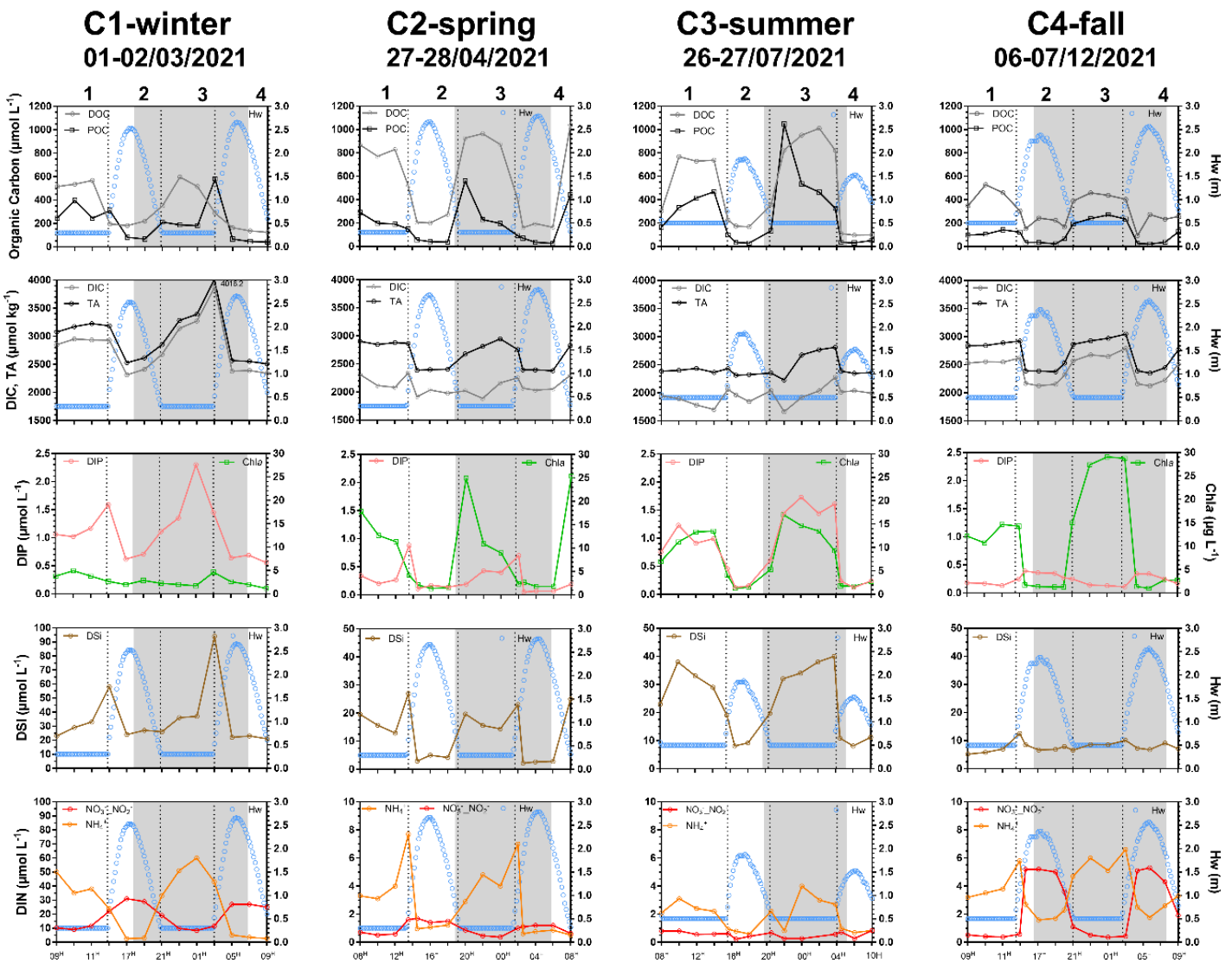
C1-winter
01-02/03/2021
C2-spring
27-28/04/2021
C3-summer
26-27/07/2021
C4-fall
06-07/12/2021
1
2
3
4
DOC
POC
Hw
Organic Carbon (µmol L-1)
DIC
TA
DIC, TA (µmol kg-1)
DIP
Chla
DIP (µmol L-1)
Chla (µg L-1)
DSi
DSi (µmol L-1)
NO3-_NO2-
NH4+
DIN (µmol L-1)
Hw (m)

Fig. S1. Hourly variations of biogeochemical parameters sampled during each 24-h cycle from March to December 2021: DOC and POC (µmol L^{-1}) as organic carbon parameters, DIC and TA (µmol kg^{-1}) as carbonate system parameters, Chl*a* (µg L^{-1}) as biological parameter, DSi, DIP and DIN as ecological parameters (nutrients, µmol L^{-1}). Simultaneously, water heights (Hw, m) were also measured every 10 mins by the STPS probe (Fig. 1). Grey areas correspond to night-time periods. Each graduation of the x-axis corresponds to two hours. Graduations of DSi and DIN were not the same between C1-winter and other cycles to a better visualization of tidal variations. Vertical dotted lines allow to distinguish the periods of low tide day (LT/Day, 1), high tide day (HT/Day, 2), low tide night (LT/Night, 3) and high tide night (HT/Night, 4).

Table S4. Seasonal medians of DIN:DIP, DIN:DSi and DSI:DIP molar ratios (ranges in brackets) measured from water samplings at the Bossys perdus salt marsh in 2021.

	DIN:DIP	**DIN:DSi**	**DSi:DIP**
C1-winter	**45.1** (29 – 57)	**1.5** (0.6 – 2.6)	**33.3** (16 – 65)
C2-spring	**17.0** (6.0 – 34)	**0.3** (0.0 – 0.9)	**37.1** (26 – 132)
C3-summer	**3.3** (0.2 – 8.4)	**0.1** (0.0 – 0.2)	**32.3** (20 – 67)
C4-fall	**23.1** (19 – 64)	**0.7** (0.5 – 1.0)	**31.7** (19 – 92)

Chapitre V

Synthèse générale de la thèse

Immersion du marais tidal des Bossys perdus (île de Ré, Fier d'Ars) lors d'une marée haute (08/12/2021). © Polsenaere.

Les zones humides côtières telles que les marais salés sont des écosystèmes végétalisés d'une importance majeure sur Terre puisqu'ils sont reconnus comme « des écosystèmes à carbone bleu » grâce à la captation et à la séquestration de grandes quantités de carbone atmosphérique dans les sédiments permettant de lutter contre le changement climatique (Cai, 2011 ; McLeod et al., 2011 ; Macreadie et al., 2017). Les taux d'accumulation de carbone organique y sont parmi les plus élevés sur Terre (McLeod et al., 2011) et constitue un argument de poids en faveur de leur protection et de leur restauration (Gu et al., 2018 ; Campbell et al., 2022 ; Pétillon et al., 2023).

1. Synthèse des pCO_2 de l'eau dans les marais Charentais

Mes travaux de thèse ont permis de montrer que la typologie (tidal ou rétro-littoral) et le mode de gestion (protégé ou exploité) des marais littoraux Charentais (Fier d'Ars, Brouage et Tasdon ; Fig. 1.20) influencent significativement la dynamique des pCO_2 de l'eau et le statut métabolique du compartiment aquatique (puits ou source de CO_2 atmosphérique).

1.1. Influence de la typologie des marais littoraux sur la dynamique des pCO_2 de l'eau

Les marais salés sont naturellement des écosystèmes intertidaux végétalisés qui sont localisés à l'interface entre le milieu terrestre et le milieu aquatique (chapitre III, Mayen et al., 2024). Nos mesures biogéochimiques au marais tidal des Bossys perdus ont montré de fortes variations saisonnières des pCO_2 de l'eau avec, en moyenne, des eaux sursaturées en CO_2 en hiver et en automne ($pCO_{2eau} > pCO_{2air}$) et des eaux sous-saturées en CO_2 au printemps et en été ($pCO_{2eau} < pCO_{2air}$), associées à une forte variabilité à l'échelle tidale (Tableau 5.1). À marée haute, lors de l'immersion du marais par les eaux côtières, la faible activité des communautés planctoniques associée à un métabolisme aquatique hétérotrophe ont induit des sursaturations en CO_2 de l'eau et des émissions de CO_2 à l'interface eau-atmosphère en hiver, en été et en automne (chapitre IV ; Tableau 4.6). Cependant, l'activité photosynthétique des producteurs primaires immergés (plantes et algues) peut jouer un rôle important sur les pCO_2 de l'eau des marais en contribuant à réduire les émissions de CO_2 atmosphérique provenant du compartiment aquatique en moyenne de 31% (i.e. 52 ± 60 g C m^{-2} an^{-1} ; Song et al., 2023). Au sein des marais tidaux, le temps de résidence très court des eaux côtières (de quelques

minutes à quelques heures selon les coefficients de marée) induit une immersion courte du marais et favorise un renouvellement rapide de la colonne d'eau. À marée basse, lors de l'émersion du marais, les chenaux permettent d'exporter des eaux sursaturées en CO_2 en hiver (pCO_2 > 1400 ppmv ; Tableau 5.1) dominées par une forte respiration aquatique en conditions de dessalure (Sal = 22) et des eaux sous-saturées en CO_2 au printemps et en été (pCO_2 < 100 ppmv ; Tableau 5.1) influencées par la production primaire aquatique en conditions hypersalines (Sal ≈ 40) (chapitre IV ; Mayen et al., in prep.). Cependant, certains marais tidaux dans le monde sont localisés à proximité des estuaires turbides qui sont généralement hétérotrophes (Frankignoulle et al., 1998 ; Borges et Abril, 2011) induisant des valeurs très élevées des pCO_2 de l'eau notamment à marée basse lorsque l'eau est restreinte au niveau des rivières (Wang et Cai, 2004). Par exemple, dans un système de marais salés en milieu estuarien (île de Sapelo, USA), les pCO_2 de l'eau ont montré de fortes variations saisonnières et tidales avec des valeurs variant de 500 à 4000 ppmv entre la marée haute et la marée basse en hiver et de 1600 à 12000 ppmv entre la marée haute et la marée basse en été (Wang et al., 2018). Ces valeurs sont significativement plus élevées que celles mesurées au marais des Bossys perdus (Tableau 5.1). Ainsi, au sein des marais tidaux, le rythme de la marée induit des variations importantes des pCO_2 qui peuvent être différents d'un site à l'autre (Wang et al., 2018 ; Song et al., 2023), nécessitant de continuer à réaliser des mesures *in situ* sur des cycles de 24 heures afin de mieux comprendre toutes les variabilités spatiales et temporelles liées au cycle du carbone et de prendre en compte la contribution du compartiment aquatique des marais dans les budgets globaux de carbone.

Tableau 5.1 : Moyennes saisonnières (± écart-type et min-max entre parenthèses) des pressions partielles de CO_2 de l'eau (pCO_2 en ppmv) mesurées sur des cycles de 24 heures dans les marais littoraux Charentais (Fier d'Ars, Brouage et Tasdon ; Fig. 1.20). Les pCO_2 de l'eau ont été mesurées toutes les minutes par une sonde autonome *in situ* (C-sense™, PME/Turner Designs) sauf en automne à MAD, les pCO_2 ont été estimées à partir du système des carbonates en utilisant les mesures de DIC et de TA. En rouge, les eaux de marais en moyenne sursaturées en CO_2 sur 24 heures et en bleu, les eaux de marais en moyenne sous-saturées en CO_2 sur 24 heures. Au sein de chaque cycle de 24 heures, les amplitudes (min-max) des pCO_2 de l'eau correspondent aux variations diurne (jour/nuit) et tidale (marée haute/marée basse). Aux stations *c* et *d* (Fier d'Ars), les mesures ont été réalisées entre 2019 et 2020 tandis qu'aux autres stations, les mesures ont été réalisées au cours de l'année 2021 (après la renaturation pour le marais de Tasdon). À MAS et MAD, les mesures ont été réalisées en simultané (chapitre I, section 6.1). Les salinités sont données dans le chapitre II pour les stations *c* et *d* au Fier d'Ars, dans le chapitre IV pour les Bossys perdus, dans le chapitre V (Fig. 5.3) pour les stations T7, T6 et T2 à Tasdon.

	Fier d'Ars			**Brouage**		**Tasdon**		
	Station *c*	Station *d*	Bossys perdus	MAD	MAS	T7	T6	T2
Hiver	**343 ± 87** (130 - 519)	**347 ± 30** (302 - 438)	**669 ± 327** (321 - 1461)	**346 ± 58** (272 - 481)	**259 ± 11** (241 - 289)	**954 ± 175** (722 - 1303)	**282 ± 138** (109 - 637)	**606 ± 103** (461 - 784)
Printemps	**135 ± 165** (6 - 425)	NA	**239 ± 105** (106 - 416)	**1666 ± 533** (869 - 2423)	**326 ± 38** (256 - 392)	**438 ± 168** 164 - 822	**953 ± 287** (562 - 1460)	**400 ± 47** (336 - 553)
Été	**242 ± 116** (25 - 430)	**377 ± 85** (250 - 508)	**271 ± 182** (89 - 597)	**83 ± 53** (25 - 312)	**482 ± 119** (310 - 688)	**291 ± 190** (91 - 681)	**1332 ± 615** (628 - 3464)	**3034 ± 398** (1974 - 3568)
Automne	**622 ± 57** (522 - 721)	**155 ± 30** (110 - 218)	**422 ± 73** (311 - 541)	**192 ± 58** (117 - 283)	**122 ± 6** (108 - 137)	**1143 ± 139** (741 - 1578)	**124 ± 36** (79 - 233)	**294 ± 50** (222 - 393)

Depuis le Moyen Âge, les marais tidaux ont subi des grands aménagements par l'Homme (endiguement, poldérisation) principalement le long des côtes Atlantique Françaises et des estuaires (ex : Charente Maritime). Le principal but était de gagner des étendues de terre sur la mer pour y développer des activités agricoles et d'élevages mais aussi pour le contrôle du temps de résidence de l'eau avec des écluses pour la production de sel (Verger, 2005). Les marais salés rétro-littoraux, situés en arrière des digues, sont donc alimentés en eaux côtières par la marée mais de façon gérée par rapport aux activités socio-économiques qui s'y déroulent (Paticat, 2007 ; Tortajada, 2011). Le temps de résidence plus long de l'eau (de quelques heures à quelques semaines selon le mode de gestion) favorise généralement le développement des producteurs primaires aquatiques (phytoplancton, herbier, macroalgue) induisant des périodes prolongées de sous-saturation en CO_2 de l'eau et des puits de CO_2 atmosphérique pendant la majorité de l'année (Tableau 5.1) (chapitre II, Mayen et al., 2023). Ainsi, les marais rétro-littoraux pourraient être associés aux valeurs de pCO_2 de l'eau les plus faibles par comparaison à d'autres typologies de zones humides côtières similaires comme les marais tidaux (Wang et al. 2018 ; Song et al. 2023), les mangroves (Borges et al., 2003 ; Borges et Koné, 2007) et les herbiers marins (Berg et al., 2019 ; Polsenaere et al. 2022) mais davantage de mesures intégrées au sein de ces systèmes « carbone bleu » sont nécessaire aux différentes échelles temporelles pour confirmer ces résultats. Cependant, les modes de gestion des marais rétro-littoraux, au travers des apports en eaux côtières et en nutriments, pourraient fortement influencer les pCO_2 de l'eau et modifier le statut métabolique du compartiment aquatique (puits/source de CO_2 atmosphérique).

1.2. Influence du mode de gestion des marais littoraux sur la dynamique pCO_2 de l'eau

Au sein du Fier d'Ars (Fig. 1.21), deux marais salés rétro-littoraux ont été étudiés avec des modes de gestion actuels contrastés : un marais « réensauvagé » à la station *c* (27,0 < salinité < 42,6) au sein de la réserve naturelle nationale (RNN) des Lilleau des Niges géré pour une conservation de l'identité patrimoniale (voir définitions de réensauvagement dans Pettorelly et al., 2019) et un marais salicole à la station *d* (21,3 < salinité < 38,4) au sein de l'écomusée de Loix géré pour une production de sel (chapitre I, section 5). Des périodes de sous-saturations importantes en CO_2 de l'eau ont été mesurées dans les marais salés rétro-littoraux du Fier d'Ars au printemps et en été (Tableau 5.1) favorisées par des macrophytes aquatiques et des modes de gestion différents de l'écluse (chapitre II, Mayen et al., 2023). À

la station *c*, le bloom de macroalgues flottantes du début du printemps jusqu'à la fin de l'été, probablement lié à une pollution en nutriments et à un faible hydrodynamique du marais (Newton et Thornber, 2013), a favorisé de fortes sous-saturations en CO_2 de l'eau tandis que la reminéralisation de ces macroalgues à croissante rapide en automne a induit une augmentation des pCO_2 et une sursaturation en CO_2 de l'eau (Tableau 5.1). Simultanément, en été, la station *d* a présenté une sous-saturation en CO_2 de l'eau plus faible provenant des entrées d'eau côtière tamponnée nécessaire à la saliculture (ouverture régulière de l'écluse à la mer). Au contraire, en automne, une forte sous-saturation en CO_2 de l'eau a été mesurée pendant l'arrêt de la saliculture et le confinement du marais (fermeture de l'écluse à la mer) favorisant probablement le développement des herbiers de *Ruppia* et le puits de CO_2 atmosphérique (Tableau 5.1). Les entrées d'eau côtière au sein des marais rétro-littoraux selon les différents modes de gestion peuvent donc fortement perturber la dynamique des pCO_2 de l'eau en réduisant instantanément les périodes de sous-saturation en CO_2 au printemps et en été lors de la saison de croissance des producteurs primaires (chapitre II, Mayen et al., 2023).

À Brouage, deux marais rétro-littoraux avec une histoire salicole commune (aménagés pour la production de sel) mais des modes de gestion actuels contrastés (saumatre *vs.* salé) ont été suivis en simultanée aux différentes saisons au sein de la RNN de Moëze-Oléron : le marais saumâtre MAD (2,4 < salinité < 6,6) et le marais salé MAS (13,6 < salinité < 50,3) (chapitre I, section 5 ; Fig. 1.20). En moyenne, ces deux marais ont été caractérisés par de longues périodes de sous-saturation en CO_2 de l'eau sauf (1) au printemps pour MAD (forte sursaturation) probablement liée à une pollution en nutriments et à l'eutrophisation du marais et (2) en été pour MAS (faible sursaturation) probablement liée à une reminéralisation du phytoplancton (Tableau 5.1 et Fig. S1). Les cycles de 24 heures réalisés à MAD (non présentés dans cette thèse) ont montré une communauté planctonique hétérotrophe au printemps (-0,19 g C m^{-2} j^{-1}) associée à une matière organique particulaire détritique (POC:Chl*a* = 570 mg mg^{-1} ; Savoye et al., 2003) et une communauté planctonique autotrophe en automne (0,41 g C m^{-2} j^{-1}) associée à une matière organique particulaire proche du phytoplancton (POC:Chl*a* = 110 mg mg^{-1}). Une analyse multidimensionnelle (ACP) a été réalisée afin d'étudier la distribution temporelle des paramètres biogéochimiques mesurés à l'échelle diurne (dans les cycles de 24 h) et à l'échelle saisonnière (entre les cycles de 24 h) et d'évaluer les principaux facteurs de contrôle des pCO_2 de l'eau (Fig. 5.1). L'ACP a montré que les cycles de 24 h se sont principalement distingués de façon horizontale le long de l'axe PC1 en fonction des paramètres biogéochimiques du carbone (pCO_2, DIC, TA et POC), des nutriments (DIN) et de la biomasse phytoplanctonique (Chl*a*). Au sein de cet axe, les résultats

ont indiqué que l'hétérotrophie planctonique au printemps (salinité de 5,3) a été associée aux concentrations les plus élevées en DIC (6499 ± 344 µmol kg^{-1}) et en NH_4^+ (86 ± 6 µM) favorisant une forte sursaturation en CO_2 de l'eau par respiration (source de CO_2 atmosphérique). Du printemps à l'automne, la Chl*a* a été négativement corrélée au DIC et au NH_4^+ permettant une assimilation des pCO_2 et des nutriments de la colonne d'eau par la production primaire phytoplanctonique (Fig. 5.1). Ainsi, l'autotrophie planctonique en automne (salinité de 6,6) lors d'un bloom de nanophytoplancton et de chlorophytes (> 20 µm) a été associée aux concentrations les plus faibles en DIC (4344 ± 370 µmol kg^{-1}) et en NH_4^+ (0,53 ± 0,39 µM) induisant un puits de CO_2 atmosphérique par la photosynthèse du phytoplancton. L'ACP permet également d'observer une forte variation temporelle (diurne et saisonnière) des paramètres biogéochimiques (carbone et nutriments) indiquant la nécessité de réaliser des cycles de 24 h sur plusieurs périodes de l'année afin de prendre en compte toute la variabilité temporelle liée au cycle du carbone dans les marais (Fig. 5.1).

Au marais salé MAS, nos mesures à hautes fréquences des pCO_2 de l'eau sur 24 h ont montré une forte sous-saturation en CO_2 de la colonne d'eau en hiver et en automne associée à de faibles variations diurnes (Tableau 5.1 et Fig. S1), probablement liées au métabolisme lent de l'herbier de *Ruppia*. Dans la lagune d'Arcachon, Polsenaere et al. (2022) ont aussi montré de faibles variations des pCO_2 de l'eau sur 24 h, principalement liées à l'activité des herbiers de *Zostère*. Au contraire, en été, les mesures à MAS ont montré une sursaturation en CO_2 de la colonne d'eau associée à de fortes variations diurnes des pCO_2 (Tableau 5.1 et Fig. A.1), probablement liées à des producteurs primaires avec un métabolisme plus rapide. L'échantillonnage de l'eau pendant l'été a suggéré que le phytoplancton (Chl*a* = 85 µg L^{-1}) était la principale source de matière organique particulaire (POC:PON = 6,6 ; Redfield, 1958). Cependant, cette biomasse phytoplanctonique était en majorité détritique (POC:Chl*a* > 650 mg mg^{-1} ; Savoye et al., 2003) indiquant une probable reminéralisation du phytoplancton sur les sédiments et une production associée du CO_2 et de nutriments dans l'eau. En effet, les concentrations élevées en DSi (91 µM) et en DIP (21 µM) et la faible concentration en DIN (1,3 µM) ont induis des ratios DIN:DIP et DIN:DSi bien inférieurs à ceux de Redfield (< 0,1) pouvant suggérer une contribution de l'interface eau-sédiment (Boynton et al., 2017), notamment la nuit lorsque des conditions d'hypoxies se sont produites dans le marais. Sur des cycles de 24 h à chaque saison à MAS, des mesures de chambre benthique couplées à des incubations des communautés planctoniques permettraient de préciser la contribution respectivement du phytoplancton et de l'herbier de *Ruppia* sur les pCO_2 de l'eau. Si les herbiers marins sont reconnus pour la captation de CO_2 atmosphérique en zone intertidale et

subtidale (Polsenaere et al., 2012 ; Berg et al., 2019 ; Van Dam et al., 2019), peu d'études existent concernent l'influence du métabolisme des herbiers sur les flux de CO_2 atmosphérique des marais salés.

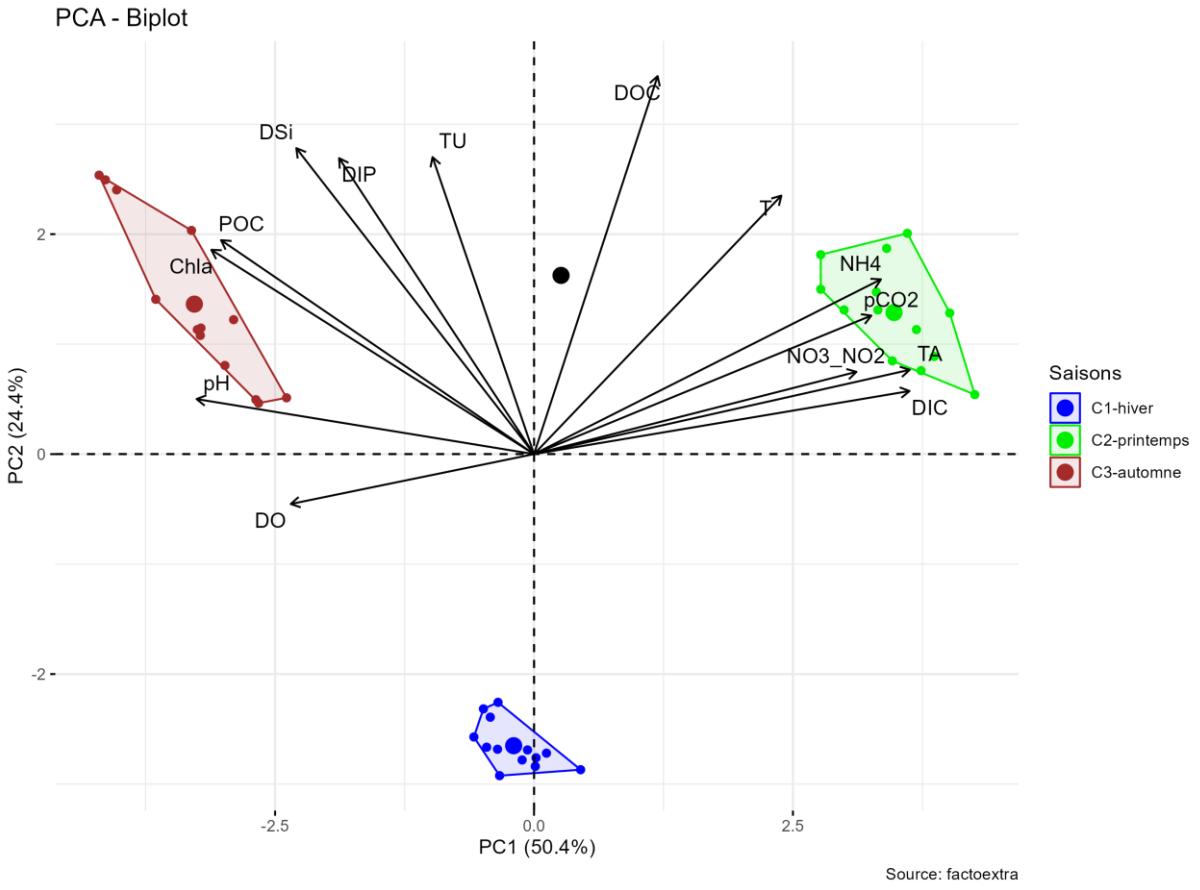

Figure 5.1 : Analyse en Composante Principale (ACP) des paramètres biogéochimiques de l'eau échantillonnés à l'échelle diurne au cours de trois cycles de 24 heures (C1-hiver, C2-printemps et C3-automne) au marais saumâtre MAD à Brouage. Les plus petits points représentent les échantillons horaires au sein de chaque cycle de 24 h (n = 12) et les plus gros points représentent les barycentres. L'ACP est basée sur les valeurs de température (T, °C), turbidité (TU, FNU), oxygène dissous (DO, µM), pression partielle de CO_2 (pCO_2, ppmv), carbone inorganique dissous (DIC, µmol kg^{-1}), carbone organique dissous (DOC, µM), carbone organique particulaire (POC, µM), azote organique particulaire (PON, µM), alcalinité totale (TA, µmol kg^{-1}), chlorophylle-*a* (Chl*a* ; µg L^{-1}), nitrate_nitrite (NO_3^-_NO_2^- ; µM), ammonium (NH_4^+ ; µM), silicates (DSi, µM) et phosphate (DIP, µM). Les trois cycles de 24 h ont été réalisés en hiver (février 2021, salinité de 2,4), au printemps (mai 2021, salinité de 5,3) et en automne (novembre 2021, salinité de 6,6) ; l'été a été associé uniquement à des mesures biogéochimiques *in situ* des pCO_2 de l'eau (voir Tableau 5.1). Pour chaque cycle de 24 h, la stratégie d'échantillonnage et les différentes méthodes analytiques ont été entièrement décrites au sein du chapitre IV (Mayen et al., in prep.). Le logiciel R-studio et le package "FactoMineR" (Lê et al., 2008) ont été utilisés pour réaliser l'ACP.

Dans le cadre de mon travail de thèse et des mesures à hautes fréquences des pCO_2 de l'eau, nous avons suggéré que l'état trophique des marais rétro-littoraux influence le type de producteur primaire et le statut puits/source de CO_2 atmosphérique du compartiment aquatique. Dans les marais au stade de développement en conditions eutrophes (station *c* au Fier d'Ars et station MAD à Brouage), les producteurs primaires à croissantes rapides (macroalgues opportunistes et phytoplancton), souvent associés à des rapports production (P) sur biomasse (B) élevés, ont tendance à se développer rapidement (Sand-Jensen et Borum, 1990 ; Le Fur et al., 2017) et à favoriser des sous-saturation en CO_2 de l'eau pendant la saison de croissance. Cependant, ils sont rapidement reminéralisés par les micro-organismes induisant des augmentations importantes des pCO_2 de l'eau et probablement une source annuelle nette de CO_2 atmosphérique (Fig. 5.2). Au contraire, dans les marais au stade mature en conditions oligotrophes (station *d* au Fier d'Ars et station MAS à Brouage), les producteurs primaires à croissance lente (herbiers de *Ruppia*), avec des rapports P:B souvent plus faibles, maintiennent des sous-saturations généralement toute l'année, en particulier en hiver et en automne favorisant une captation annuelle nette de CO_2 atmosphérique (chapitre II, Mayen et al., 2023) (Fig. 5.2). Ainsi, le mode de gestion anthropique des marais influence fortement la contribution et le renouvellement des producteurs primaires et, par conséquent, le comportement puits/source de CO_2 atmosphérique des marais. Ces résultats recommandent une gestion adaptée des marais littoraux permettant de limiter l'eutrophisation par les apports en nutriments et, au contraire, de favoriser les macrophytes à croissance lente qui contribuent à une meilleure séquestration du carbone bleu (McLeod et al., 2011).

Au sein des marais tidaux, le stade mature associé à de faibles apports en nutriments permet le développement d'une forte végétation halophyle (Spartines, Obiones, Soudes) et une faible reminéralisation de la matière organique (MO) du sol favorisant une captation optimale du CO_2 atmosphérique par photosynthèse (Fig. 5.2. ; Mayen et al., 2024). Au contraire, dans les marais tidaux au stade de développement, les apports imports de nitrates par les eaux côtières favorisent la reminéralisation de la MO du sol (biomasse souterraine des plantes), entrainant une déstabilisation de la végétation et une augmentation de la surface des chenaux (Deegan et al., 2013). Cette modification des habitats (d'une surface végétalisée à une surface peu végétalisée) pourrait avoir des impacts négatifs sur la capacité de captation de CO_2 atmosphérique par les végétaux du marais (Fig. 5.2).

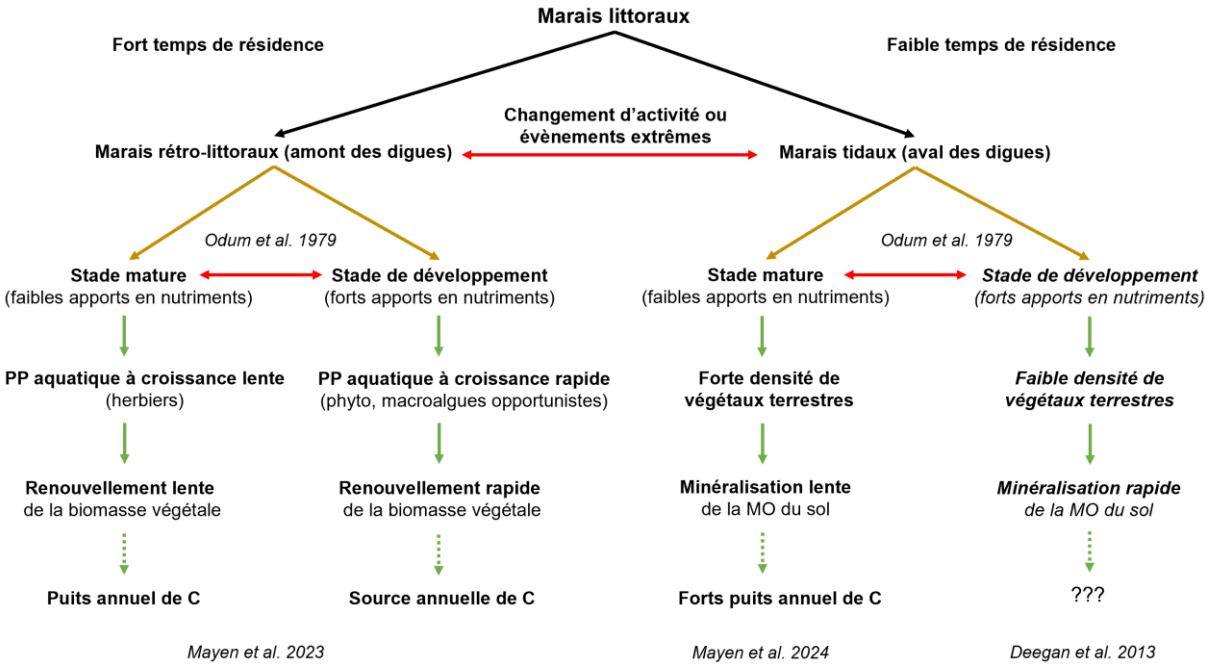

Figure 5.2 : Influence de la typologie (marais rétro-littoraux vs marais tidaux) et du mode de gestion (stade mature vs stade de développement) des marais littoraux sur leur statut comme puits ou source de CO_2 atmosphérique. Les flèches noires correspondent à la typologie, les flèches marrons correspondent au mode de gestion et les flèches vertes correspondent aux producteurs primaires dominants. Les flèches rouges correspondent au changement de typologie ou de mode de gestion selon les activités humaines (changements d'activités par exemple) ou les évènements extrêmes (submersion par exemple).

1.3. Influence de la renaturation des marais littoraux sur le statut puits/source de CO_2 de l'eau : cas du marais de Tasdon

L'étude biogéochimique concernant l'influence de la renaturation du marais de Tasdon sur les flux de CO_2 atmosphérique n'a pas été traitée dans ce manuscrit de thèse mais les résultats sont présentés et discutés dans cette section. Le marais de Tasdon est une ancienne zone humide d'eau douce abandonnée et eutrophisée (concentration maximale en NO_3^- de 1260 µM en 2019 ; Xaus, 2023) qui a connu un projet de renaturation (réaménagement des bassins, implantation de végétation et reconnexion à la mer ; chapitre I, section 5) afin de préserver la biodiversité et de restaurer les fonctions écologiques du marais (Bergeon et al., in prep.). Dans le cadre de cette thèse et des différents projets associées (PAMPAS, LRTZC), nous avons étudié les variations diurnes (jour/nuit) et saisonnières des pCO_2 de l'eau et des flux de CO_2 eau-air estimés au sein des trois stations du marais (T7, T6 et T2 ; Fig. 1.22) pour mieux comprendre les variations temporelles du cycle du carbone et l'influence de la renaturation du marais sur le comportement puits ou source de CO_2 atmosphérique du compartiment

aquatique. Sur nos périodes de mesure entre 2019 et 2022, les pCO_2 de l'eau ont significativement varié à l'échelle saisonnière mais aussi à l'échelle spatiale avant et après renaturation (tests de Kruskal-Wallis, $p < 0.05$). Au printemps et en automne 2019 avant la renaturation, les valeurs moyennes des pCO_2 de l'eau étaient respectivement de 899 ± 358 et 2084 ± 324 ppmv à la station T7, de 1649 ± 228 et 3294 ± 312 ppmv à la station T6 et de 1881 ± 85 et 3065 ± 159 ppmv à la station T2. Les trois stations étaient fortement sursaturées en CO_2, particulièrement en automne 2019, entrainant ainsi un dégazage important de CO_2 vers l'atmosphère à cette saison (Fig. 5.3).

Suite à la renaturation du marais à partir du printemps 2021, les stations T7 et T6 (initialement d'eau douce) ont progressivement été ouvertes à la mer par des entrées régulières d'eaux côtières lors de marées de vives-eaux (Fig. 5.3). La station T2 est un marais d'eau douce et la renaturation n'a pas influencé sa salinité. En moyenne sur 24 heures, la station T7 a été sous-saturée en CO_2 uniquement en été 2021 (291 ± 190 ppmv) et sursaturée en CO_2 au printemps 2021 (438 ± 138 ppmv), en automne 2021 (1143 ± 139 ppmv) et en hiver 2022 (954 ± 175 ppmv). Cette sous-saturation de la station T7 pendant l'été a induit un puits de CO_2 atmosphérique (-0,7 g C m^{-2} j^{-1}) contrairement aux autres saisons (Fig. 5.3). Suite à la renaturation de la station T6, les pCO_2 de l'eau ont légèrement augmenté du printemps 2021 (953 ± 287 ppmv) à l'été 2021 (1332 ± 615 ppmv) avant de fortement diminuer en automne 2021 et en hiver 2022 (124 ± 36 et 282 ± 138 ppmv, respectivement ; Fig. 5.3). Ainsi, la station T6 s'est comportée comme un puits de CO_2 atmosphérique uniquement à l'automne 2021 (-0,3 g C m^{-2} j^{-1}). Pour finir, la station T2 a été en moyenne sous-saturée en CO_2 au printemps et en automne 2021 (400 ± 47 et 294 ± 50 ppmv, respectivement) et fortement sursaturée en été 2021 (3034 ± 398 ppmv) entrainant des émissions de CO_2 vers l'atmosphère (1,5 g C m^{-2} j^{-1} ; Fig. 5.3).

À la fois au printemps et à l'automne, aux trois stations étudiées, la renaturation du marais de Tasdon a entrainé une diminution significative des pCO_2 de l'eau et des émissions de CO_2 atmosphérique (tests de Mann-Whitney, $p < 0.05$). Au printemps, entre 2019 et 2021, les pCO_2 ont diminué en moyenne de 51% (station T7), 42% (station T6) et 79% (station T2) tandis qu'en automne, entre 2019 et 2021, les pCO_2 ont diminué en moyenne de 45% (station T7), 96% (station T6) et 90% (station T2) (Fig. 5.3). Nos résultats ont donc montré que la renaturation du marais a limité le dégazage de CO_2 atmosphérique aux trois stations et dates étudiées et a permis un passage de source à puits de CO_2 à l'automne à la station T6 (de 20,2 à -0,3 g C m^{-2} j^{-1}) et à la station T2 (de 29,9 à -0,3 g C m^{-2} j^{-1}). La renaturation du marais de Tasdon au travers d'une ouverture progressive à la mer et de l'implantation d'une végétation

aquatique dense a probablement enclenché une transition d'un système aquatique globalement hétérotrophe qui émet du CO_2 atmosphérique vers un système aquatique globalement autotrophe qui capte du CO_2 atmosphérique. Cependant, de grandes incertitudes persistent concernant l'influence de la renaturation du marais sur les flux de CO_2 atmosphérique en prenant en compte l'évolution de la diversité et de l'abondance des communautés planctoniques (bactéries, phytoplancton et zooplancton). Ainsi, un stage de Master 2 a été réalisé en 2023 (Xaus, 2023) et une publication est en cours de préparation permettant d'approfondir le lien entre le comportement du CO_2 des marais (puits/source) et les réseaux trophiques planctoniques associés (Xaus et al., in prep.) en continuité des travaux de thèse de L. Bergeon (2020-2023) sur ce site (Bergeon et al., in prep.). Un lien important a été mis en évidence entre la typologie du réseau trophique planctonique et la dynamique des pCO_2 de l'eau montrant que trois typologies de réseau trophique stable (hiver biologique, réseau microbien, et multivore) sont associées à des pCO_2 élevés (source) tandis que deux typologies de réseau trophique transitoire (multivore faible et herbivore faible) sont associées à des valeurs de pCO_2 plus faibles (puits) (Xaus, 2023). Par exemple, après la renaturation, le réseau « hiver biologique » à la station T7 en hiver et à la station T6 au printemps a été associé à des pCO_2 moyens de 954 ± 175 et 953 ± 287 ppmv, respectivement, tandis que le réseau « faible herbivore » à la station T6 en automne et en hiver a été associé à des pCO_2 moyens de 124 ± 36 et de 282 ± 138 ppmv, respectivement (Tableau 5.1 ; Xaus, 2023). Cependant, les fortes variabilités diurne, saisonnière et interannuelle observées nécessite de poursuivre les mesures *in situ* des pCO_2 de l'eau afin de confirmer ou pas le passage d'un système hétérotrophe vers un système autotrophe permettant une captation et séquestration de carbone.

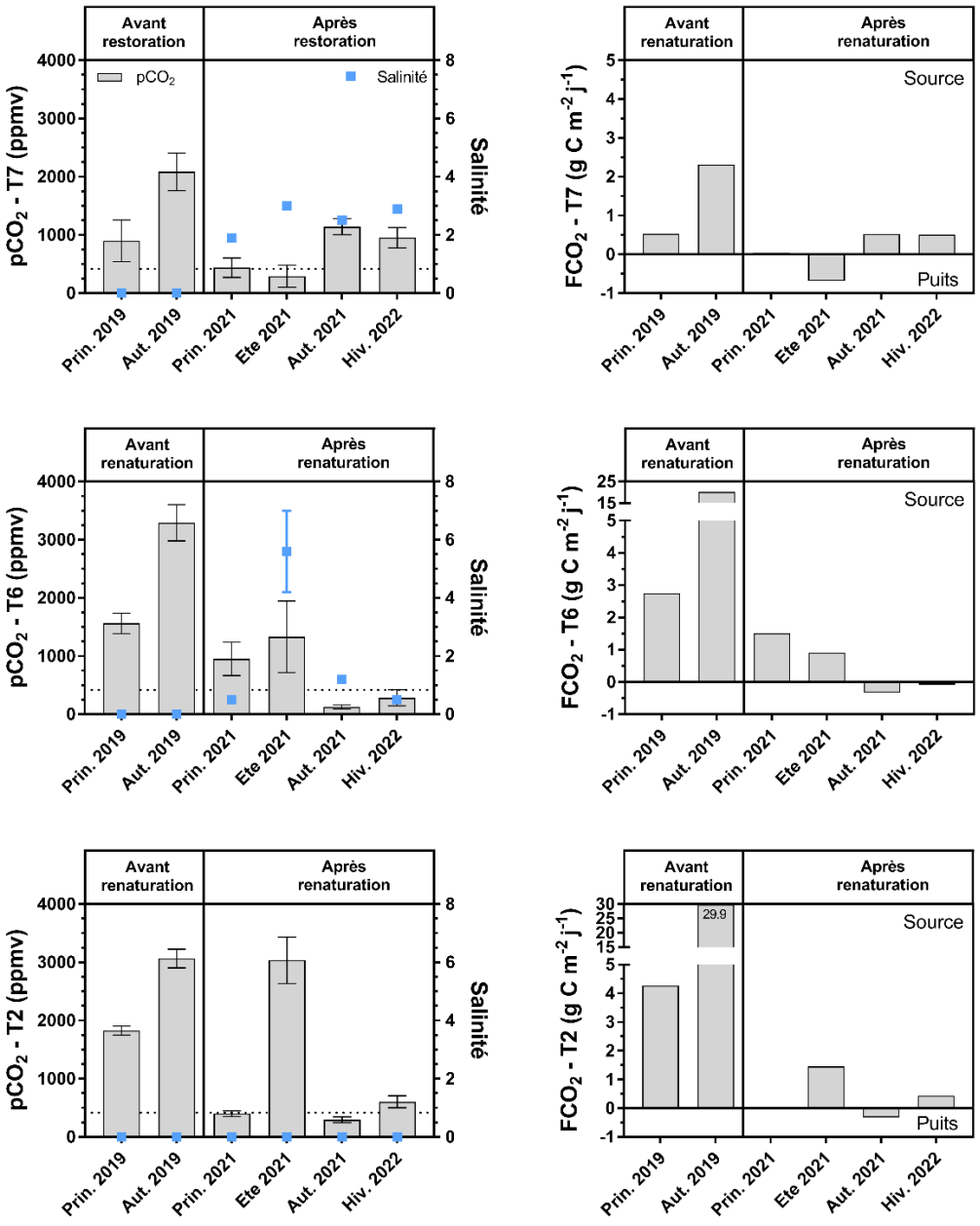

Figure 5.3 : Variations spatiales et saisonnières des pCO_2 de l'eau (moyenne ± écart-type, en ppmv) et des flux de carbone atmosphérique (g C m^{-2} j^{-1}) aux stations T7, T6 et T2 avant (2019) et après (2021 et 2022) la renaturation du marais de Tasdon. Les valeurs de salinité sont indiquées en bleu. Les lignes horizontales en pointillé correspondent à la pCO_2 de l'air pour chaque période (NOAA). Les pCO_2 de l'eau inférieures à la pCO_2 de l'air indiquent une sous-saturation en CO_2 de l'eau par rapport à l'atmosphère et les pCO_2 de l'eau supérieures à la pCO_2 de l'air indiquent une sursaturation en CO_2 de l'eau par rapport à l'atmosphère. Les flux de CO_2 à l'interface eau-air (mmol CO_2 m^{-2} h^{-1}), estimés avec la paramétrisation de Raymond et Cole (2001), ont été cumulés sur 24 h et convertis en flux de carbone atmosphérique (g C m^{-2} j^{-1}). Des flux de C cumulés négatifs à l'interface eau-air indiquent un puits net de C atmosphérique sur 24 h et des flux de C cumulés positifs à l'interface eau-air indiquent une source nette de C atmosphérique sur 24 h. La stratégie de mesure des pCO_2 de l'eau et la méthode d'estimation des flux de CO_2 atmosphérique ont été décrites au sein du chapitre II (Mayen et al., 2023).

2. Variations des échanges nets de CO_2 atmosphérique au sein d'un marais tidal

Une partie majeure de mon travail de thèse a concerné l'étude des variations spatio-temporelles et des facteurs de contrôle associés des flux verticaux de CO_2 entre le marais tidal des Bossys perdus et l'atmosphère (chapitre III, Mayen et al., 2024). Pour cela, la technique de l'Eddy Covariance (EC) atmosphérique a permis de mesurer les échanges nets de CO_2 à l'échelle de l'écosystème (NEE, µmol m^{-2} s^{-1}) à un pas de temps court (10 mins) et de manière intégrative au sein de l'empreinte (footprint), à la fois à l'interface sédiment-air à marée basse et à l'interface eau-air à marée haute.

2.1. Aspects methodologies

La première étape s'est focalisée sur le traitement des données d'EC par le logiciel EddyPro qui nécessite une longue séquence d'opérations comprenant le filtrage des données brutes, la calibration et d'autres algorithmes de calculs et de corrections des flux (chapitre III, section 2.4). Au sein de notre étude, les fluctuations turbulentes des flux de CO_2 atmosphérique à 20 Hz ont été traitées et moyennées sur des intervalles de temps de 10 mins (soit une moyenne de 12 000 mesures) contre 30 mins en général. En effet, nous avons choisi une moyenne temporelle plus courte que pour les écosystèmes terrestres (Kowalski et al., 2003 ; Lasslop et al., 2010 ; Burba, 2021) et certains marais salés (Schäfer et al., 2014 ; Forbrich et al., 2018 ; Nahrawi et al., 2020 ; Wei et al., 2020) afin de mieux détecter les variations rapides de la NEE pendant les périodes transitoires de marées montantes et de marées descendantes. Lors du traitement des données d'EC, une correction pour les pertes spectrales des flux de CO_2 dans la gamme des basses fréquences a été effectuée selon Moncrieff et al. (2004). Pour vérifier cette correction, deux périodes temporelles sur plusieurs jours sans immersion et avec des variations importantes dans les vitesses du vent ont été choisies et utilisées pour comparer les flux de CO_2 moyennés sur un pas de temps de 10 mins par rapport à ceux moyennés sur un pas de temps de 30 mins. Nous avons calculé le rapport entre la moyenne des trois valeurs de flux à 10 mins et la valeur de flux à 30 mins et nous avons enregistré un rapport moyen proche de 1 à la fois pour les vitesses de vent les plus élevées (1,07 ± 0,88 pour 5 < vitesses < 10 m s^{-1}) et pour les vitesses de vent les plus faibles (1,01 ± 0,13 pour 0 < vitesses < 5 m s^{-1}). Ainsi, dans notre étude, nous avons pu faire l'hypothèse qu'il n'y a pas eu de perte significative à basse fréquence dans les flux de CO_2 atmosphérique moyennés sur 10 mins en utilisant la correction de Moncrieff et al. (2004).

D'autres auteurs ont également choisi une moyenne temporelle de 10 mins comme Polsenaere et al. (2012) dans la lagune d'Arcachon où il n'a pas été montré de perte significative des basses fréquences en utilisant cette moyenne temporelle. Mon travail de thèse a permis de valider les mesures de flux de CO_2 atmosphérique par EC sur des intervalles de 10 mins dans les zones humides côtières telles que les marais salés intertidaux afin de quantifier avec précision leur taux de captation de CO_2 atmosphérique et leur contribution au cycle global du carbone (chapitre III, Mayen et al., 2024).

Un contrôle strict de la qualité des données a été appliqué aux traitements des flux de CO_2 par EddyPro afin d'éliminer les données qualifiées de mauvaises qualités liées aux dysfonctionnements de l'instrument, aux artefacts mathématiques et de traitement, aux conditions ambiantes qui ne correspondent pas à la méthode EC, aux vents qui ne proviennent pas de l'empreinte et aux fortes précipitations pour l'IRGA (analyseur de gaz infrarouge ; Burba, 2021). Un diagnostic sur la force du signal de l'IRGA a été appliqué pour toutes les mesures à 20 Hz avec un indicateur variant de 0 (mauvaise qualité) à 1 (bonne qualité). Si ce rapport signal/bruit de l'IRGA était inférieur à 0,7 et/ou si le pourcentage de valeurs manquantes sur 10 mins dépassait 10% (valeurs non mesurées ou supprimées à cause de l'indicateur de qualité), aucun flux de CO_2 n'a été calculé. Ce travail a permis de montrer que ce choix a été le meilleur équilibre entre supprimer la majorité des données de mauvaises qualités et conserver un maximum de données de flux de CO_2 mesurés (tests et résultats non présentés dans ce manuscrit). Ensuite, nous avons utilisé la méthode de Papale et al. (2006) pour détecter et supprimer les valeurs aberrantes dans les données de flux à 10 min (Kostyrka, 2021). Suite à l'ensemble des contrôles de qualité et de post-traitement sur l'année 2020, environ 18% des données EC ont été supprimées et comblées par une approche d'apprentissage automatique (machine learning) afin d'obtenir des données de flux de CO_2 (NEE) en continue sur 2020. Un modèle de Random Forest (RF) (Kim et al., 2020 ; Cui et al., 2021) a été développé avec des variables environnementales disponibles ou mesurées et identifiées dans la littérature pour contrôler de manière significative les flux de CO_2 dans les marais salés (Kostyrka, 2021). Cependant, le modèle RF a moins bien estimé les flux de CO_2 la nuit (38%) que le jour (59%). Pendant la nuit, la faible performance du modèle RF pourrait être liée aux flux de CO_2 négatifs mesurés à la fois à l'émersion et à l'immersion du marais. Ces faibles puits de CO_2 nocturne peuvent être expliqués par des apports d'eau côtière sous-saturée en CO_2 par rapport à l'atmosphère et/ou par la dissolution de $CaCO_3$ dans les eaux ou les sédiments (chapitre III, Mayen et al., 2024). Ces processus aquatiques et/ou benthiques pourraient contribuer à la difficulté du modèle RF à combler les flux de CO_2 atmosphérique

pendant la nuit. Une étude récente montre qu'à l'échelle diurne (jour/nuit), les modèles de machine learning pour prédire les flux de CO_2, même sur les écosystèmes terrestres, sont particulièrement compliqués à appliquer de façon efficace en raison des non-stationnarités provenant de processus multiples (Bartolomeis et al., 2023). Cependant, ce travail de thèse a permis de mettre en évidence que ce modèle RF a induit seulement une faible incertitude sur le bilan de carbone annuel au marais tidal des Bossys perdus au cours de l'année 2020 (i.e. 0,43%), ce qui traduit la bonne performance du modèle pour combler les données EC en zone de marais.

Enfin, dans le but d'étudier le métabolisme du marais tidal des Bossys perdus (photosynthèse *vs* respiration), un travail de modélisation a été mené dans cette thèse (en collaboration avec l'INRAE) pour partitionner les échanges nets de l'écosystème (NEE) en production primaire brute (GPP) et respiration de l'écosystème (R_{eco}) selon Kowalski et al. (2003) et Wei et al. (2020), respectivement (chapitre III, Mayen et al., 2024).

2.2. Variations temporelles de la NEE d'un marais tidal

Une deuxième étape a été d'évaluer les différentes variations temporelles de la NEE mesurée par EC au marais tidal des Bossys perdus afin de mieux comprendre le fonctionnement biogéochimique de ces systèmes côtiers face à l'immersion tidale et de les intégrer dans les budgets de carbone. Au cours de l'année 2020, nos mesures en continu (10 mins) ont montré que le marais s'est comporté en moyenne comme un puits de CO_2 atmosphérique (-1,27 ± 3,48 µmol m^{-2} s^{-1} ; Fig. 3.3) permettant une captation nette de 483 g C m^{-2} an^{-1}, au travers d'une forte autotrophie des plantes halophytes terrestres (*Spartina maritima*, *Halimione portulacoides* et *Suaeda vera*) (chapitre III, Mayen et al., 2024). L'augmentation du taux de captation de CO_2 atmosphérique en 2021 et 2022 (551 et 527 g C m^{-2} an^{-1}, respectivement) a été liée aux conditions environnementales plus favorables à la photosynthèse (conditions plus froides et plus humides en 2021) et à une augmentation de la couverture végétale de *S. maritima* sur les zones de vase qui peuvent assurer une forte production primaire au printemps et en été (Coutantin, 2023). D'après nos mesures, les marais tidaux pourraient avoir des taux de captation de CO_2 atmosphérique supérieurs à ceux des herbiers marins (Polsenaere et al., 2012 ; Van Dam et al., 2021), des mangroves (Rodda et al., 2016 ; Gnanamoorthy et al., 2020) et des vasières intertidales (Xi et al., 2019 ; Polsenaere et al., 2012 ; Polsenaere, 2022 ; Pery, 2023) permettant de jouer un rôle important dans le cycle

global du carbone et de contribuer à la compensation des émissions de CO_2 d'origine anthropique (chapitre I, section 1.1).

Les mesures EC ont également révélé de fortes variabilités saisonnières dans les flux de NEE. La captation nette de CO_2 la plus importante a été mesurée au printemps pendant la saison de croissance des plantes halophytes avec des conditions environnementales favorables à la photosynthèse tandis qu'en été, les températures de l'air plus élevées et les taux d'humidité plus faibles ont limité la production primaire et ont, au contraire, favorisé la respiration de l'écosystème (plantes, microphytobenthos et bactéries). Concernant cette saisonnalité, l'utilisation de modèles linéaires dynamiques (DLM) appliquée aux trois années de mesures (de 2020 à 2022) a permis de montrer des variations saisonnières de l'ordre de 200% entre la saison la plus productive (fin printemps/début été) et la saison la moins productive (l'hiver) (Coutantin, 2023). Des variations temporelles encore plus importantes de la NEE ont été enregistrées sur des échelles de temps plus courtes au cours d'une journée avec un puits de CO_2 atmosphérique le jour contrôlé par la photosynthèse des producteurs primaires et une source de CO_2 atmosphérique la nuit contrôlée par la respiration de l'écosystème (rôle majeur de la lumière). Cependant, les mesures ont montré que l'immersion tidale a affecté instantanément la NEE en réduisant la captation de CO_2 de jour sans modifier le statut métabolique de l'écosystème. Les eaux côtières advectées forment en général une barrière physique entre les plantes et l'atmosphère limitant les échanges de CO_2 avec l'atmosphère (Polsenaere et al., 2012 ; Nahrawi et al., 2020 ; Wei et al., 2020). La nuit, lors des niveaux immersions les plus élevés, les émissions de CO_2 atmosphérique ont été entièrement supprimées entrainant même un passage de source vers puits de CO_2 dans certaines situations, notamment l'hiver lorsque la respiration de l'écosystème est la plus faible. Pendant la nuit, la présence d'eau côtière advectée sous-saturée en CO_2 par rapport à l'atmosphère en raison de la production primaire phytoplanctonique dans l'estuaire du Fier d'Ars ou/et dans le Pertuis Breton pendant la journée, a pu induire une captation nette de CO_2 (Fig. 3.8). Le passage de source à puits de CO_2 atmosphérique pendant l'immersion nocturne du marais est possible uniquement si les eaux côtières advectées sont sous-saturée en CO_2, ce qui n'est généralement pas le cas pour la plupart des marais salés en milieu estuarien où le métabolisme aquatique hétérotrophe prédomine (Wang et al., 2018). Au cours de l'année 2020, la comparaison des bilans nets de carbone entre la NEE mesurée par EC (-483 g C m^{-2} an^{-1}) et la NEE modélisée à l'interface benthique entre le marais et l'atmosphère sans présence d'eau (-486 g C m^{-2} an^{-1}) a permis de montrer que l'immersion du marais (30% du temps sur l'année) n'a pas eu d'impact significatif sur la captation annuelle de CO_2

atmosphérique. Ce résultat important a été confirmé sur les années 2021 et 2022 au même site d'étude (Coutantin, 2023). Au marais étudié, pendant une année de mesure, la perte de captation de CO_2 pendant l'immersion jour en raison de la diminution de la GPP a pu être compensée par l'immersion de nuit où les émissions de CO_2 ont été inhibées. Ces travaux de thèse permettent de confirmer que les marais salés tidaux avec une forte couverture végétale terrestre sont de bons candidats au sein de la zone côtière pour la captation et la séquestration de carbone.

2.3. Variations spatiales de la NEE au sein d'un marais tidal

Au sein de l'emprise de l'EC (Fig. 3.2), l'analyse spatiale de la NEE en fonction des directions de vent pendant l'émersion du marais a généralement indiqué que les secteurs avec une forte densité de végétation ont été associés à une captation de CO_2 diurne et une émission de CO_2 nocturne plus importantes que les secteurs avec une forte densité de vase (Fig. 3.7). Ainsi, les zones de vase, plutôt occupées par du microphytobenthos (MPB) (Savelli et al., 2019), pourraient présenter un métabolisme benthique (production *vs.* respiration) plus faible que les zones dominées par les plantes vasculaires terrestres (chapitre III, Mayen et al., 2024). Cependant, en raison de la forte hétérogénéité spatiale du marais des Bossys perdus (Fig. 3.2), il a été complexe d'étudier plus précisément l'effet des habitats (vasière *vs.* macrophyte) sur les flux de NEE à l'échelle de l'écosystème et d'en tirer des conclusions plus générales. Dans le cadre du projet La Rochelle Territoire Zéro Carbone (LRTZC), une station EC a été déployée depuis février 2023 au sein de la Baie de l'Aiguillon (France), à la limite entre la partie vasière intertidale et la partie occupée par les habitats de marais salé, afin justement de répondre aux interrogations concernant l'influence des habitats sur les échanges de CO_2 atmosphérique (Pery, 2023). Sur les mesures réalisées à l'émersion entre janvier et mai 2023, les résultats ont mis en évidence une plus forte captation de CO_2 atmosphérique par la vasière ($-1{,}47 \pm 2{,}79$ µmol m^{-2} s^{-1}) que par le marais salé ($-0{,}98 \pm 3{,}56$ µmol m^{-2} s^{-1} ; Pery, 2023) nécessitant d'évaluer plus précisément les flux de NEE des vasières sur des séries à long terme pour mieux comprendre leur capacité de captation de CO_2 atmosphérique dans les systèmes intertidaux tels que les marais salés et les estrans (Polsenaere et al., 2012 ; Savelli et al., 2019, 2021). De plus, le MPB (producteurs à croissance rapide) est principalement constitué de carbone organique labile (De Brouwer et Stal, 2001 ; Morelle et al., 2022) qui peut être rapidement reminéralisé en CO_2 par la respiration hétérotrophe, alors que les plantes à feuilles persistantes (producteurs à croissance lente) sont principalement constituées de carbone

organique réfractaire comme la lignine (Benner, 2011 ; Jiao et al., 2011) permettant un renouvellement lent de sa biomasse et ainsi, de sa reminéralisation en CO_2. Ainsi, contrairement au MPB sur les vases, une forte densité de plantes vasculaires dans les marais salés pourrait être considérée comme une "pratique de gestion souhaitable" pour une meilleur captation et séquestration de carbone dans un contexte de lutte contre le changement climatique (Francisco Artigas, communication personnelle).

De plus, en hiver et en automne à l'émersion, l'analyse spatiale de la NEE a montré des taux de captation de CO_2 significativement plus élevés pour *H. portulacoides* que pour *S. maritima* alors qu'en été, aucune différence significative n'a été enregistrée entre ces deux espèces végétales (Fig. 3.7). Cette différence saisonnière pourrait être liée à la phénologie des plantes puisque *H. portulacoides* est une plante à feuilles persistantes tout au long de l'année, alors que la saison de croissance de *S. maritima* est restreinte du printemps et à l'été. Ainsi, cette analyse a permis de conclure d'une plus grande efficacité de *H. portulacoides* dans la captation de CO_2 atmosphérique par rapport à *S. maritima* (chapitre III, Mayen et al., 2024).

Dans le marais salé des Bossys perdus, les activités salicoles passées ont modifié la typologie du site avec un ensemble de digues, de bosses et de petits chenaux produisant une immersion plus longue pour les zones basses du marais (vases et *S. maritima*) que pour les zones hautes du marais (*H. portulacoides* et *S. vera*). Ainsi, cette immersion différée dans le temps a probablement favorisé une plus forte captation de CO_2 atmosphérique par *H. portulacoides* et *S. vera*. Nous avons pu faire l'hypothèse que la micro-topologie des marais salés liée aux activités anthropiques récentes favoriserait une captation de CO_2 plus importante qu'un marais salé sans activité anthropique depuis très longtemps dont la surface plane permet l'immersion rapide de l'ensemble des habitats (Pery, 2023). Dans le contexte de l'augmentation du niveau des océans et de l'altération des digues, les marais rétro-littoraux façonnés pour un usage salicole seront probablement submergés et remplacés par des marais tidaux avec à une forte densité de plantes terrestres halophytes et une micro-topologie spécifique qui favorisera une plus forte captation de carbone atmosphérique. Dans le cadre du projet de l'ANR-PAMPAS, une étude est en cours de préparation afin de mieux comprendre les effets des submersions marines sur les marais littoraux Charentais au travers à travers une approche multidisciplinaire intégrant les liens entre la géomorphologie, les producteurs primaires (plancton), les consommateurs (poissons, amphibiens, arthropodes), et les fonctions de captation et de séquestration de carbone (Amann et al., in prep.).

3. Influence du métabolisme aquatique sur les flux horizontaux et verticaux de carbone

Les marais salés sont des écosystèmes côtiers productifs qui favorisent la captation de CO_2 atmosphérique grâce à une forte production primaire des plantes halophytes terrestres (Schäfer et al., 2014 ; Artigas et al., 2015 ; Forbrich et Giblin, 2015). De plus, le métabolisme intense de ces systèmes intertidaux exporte horizontalement des quantités importantes et variables de carbone (C) organique et inorganique au travers du compartiment aquatique (Cai, 2011 ; Wang et al., 2016 ; Reithmaier et al., 2023). Cependant, les fortes variations temporelles de ces flux verticaux et horizontaux de C nécessitent d'étudier l'ensemble du métabolisme des marais en prenant en compte les compartiments terrestre et aquatique et en distinguant leurs contributions respectives aux échanges de CO_2 atmosphérique mesurés par Eddy Covariance (EC). Au cours de nos quatre cycles de 24 heures au marais tidal des Bossys perdus, les formes organiques et inorganiques du C, les nutriments et le métabolisme planctonique ont été mesurés en simultané avec les pCO_2 de l'eau et les flux de CO_2 atmosphérique associés. Ces mesures ont permis d'apporter des informations essentielles sur les variations temporelles du C, des nutriments et du métabolisme planctonique entre les phases de marée haute et celles de marée basse et d'étudier l'influence du compartiment aquatique des marais sur les échanges nets de CO_2 à l'échelle de l'écosystème (NEE) (chapitre IV, Mayen et al., in prep.).

Figure 5.4 : Schéma de la dynamique du carbone entre la marée haute (immersion du marais par les eaux côtières) et la marée basse (émersion du marais et exportation des eaux vers le chenal) au cours de nos cycles de 24 h au marais tidal des Bossys perdus. Les eaux des marais rétro-littoraux en amont sont évacuées dans le chenal uniquement lors des périodes de marée basse. Les bilans de carbone en hiver, au printemps et en été pour la NEE (échanges de CO_2 atmosphérique mesurés par EC), la NEE_{marsh} (flux métabolique du marais sans immersion) et la NCP (métabolisme planctonique) sont donnés en g C m^{-2} j^{-1}. Pour les taux journaliers de NCP, les bilans négatifs correspondent à une autotrophie (puits net de C pour les eaux) et les bilans positifs correspondent à une hétérotrophie (source nette de C pour les eaux). Pour le métabolisme net du marais avec immersion (NEE) et sans immersion (NEE_{marsh}), les bilans négatifs correspondent à une captation de C atmosphérique par le marais. Les valeurs en DIC, DOC et POC sont les concentrations moyennes à marée basse et à marée haute (en µM) pour chaque cycle de 24 h. NA : les données EC n'ont pas pu être mesurées pour C4-fall.

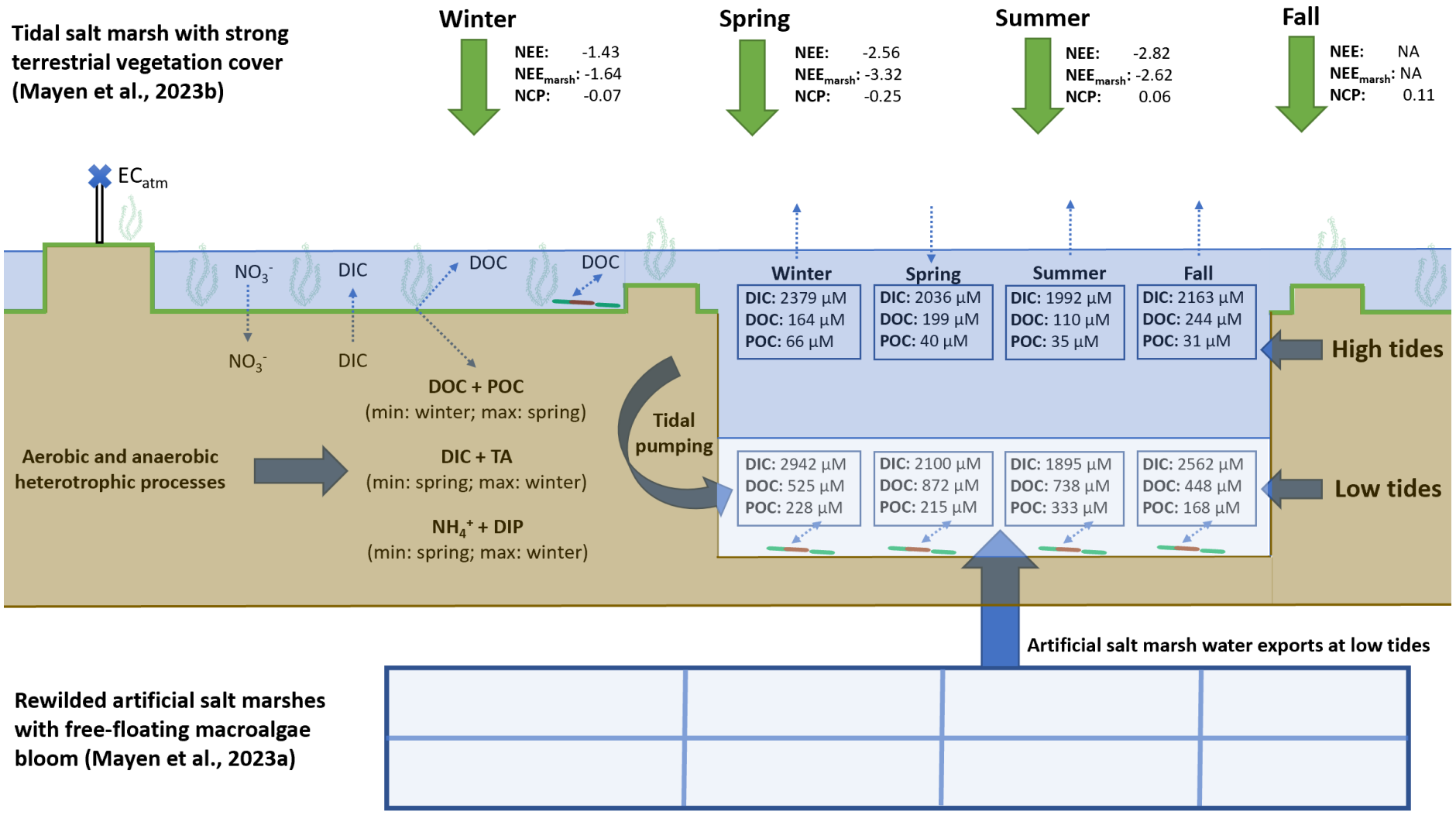
Tidal salt marsh with strong terrestrial vegetation cover (Mayen et al., 2023b)
Winter
NEE: -1.43
NEE$_{marsh}$: -1.64
NCP: -0.07
Spring
NEE: -2.56
NEE$_{marsh}$: -3.32
NCP: -0.25
Summer
NEE: -2.82
NEE$_{marsh}$: -2.62
NCP: 0.06
Fall
NEE: NA
NEE$_{marsh}$: NA
NCP: 0.11
EC$_{atm}$
NO$_3^-$
DIC
DOC
DOC
NO$_3^-$
DIC
DOC + POC
(min: winter; max: spring)
DIC + TA
(min: spring; max: winter)
NH$_4^+$ + DIP
(min: spring; max: winter)
Aerobic and anaerobic heterotrophic processes
Tidal pumping
Winter
DIC: 2379 µM
DOC: 164 µM
POC: 66 µM
Spring
DIC: 2036 µM
DOC: 199 µM
POC: 40 µM
Summer
DIC: 1992 µM
DOC: 110 µM
POC: 35 µM
Fall
DIC: 2163 µM
DOC: 244 µM
POC: 31 µM
High tides
DIC: 2942 µM
DOC: 525 µM
POC: 228 µM
DIC: 2100 µM
DOC: 872 µM
POC: 215 µM
DIC: 1895 µM
DOC: 738 µM
POC: 333 µM
DIC: 2562 µM
DOC: 448 µM
POC: 168 µM
Low tides
Artificial salt marsh water exports at low tides
Rewilded artificial salt marshes with free-floating macroalgae bloom (Mayen et al., 2023a)

Tableau 5.2 : Bilans nets de carbone journaliers (g C m^{-2} j^{-1}) à l'échelle tidale (marée haute/marée basse) des taux de NCP mesurés par la méthode Winkler (métabolisme planctonique), des flux de NEE mesurés par EC (échanges de CO_2 atmosphérique) et des flux de NEE_{marsh}, GPP_{marsh} et R_{marsh} estimés à partir du partitionnement de Kowalski et al. (2003) (flux métabolique du marais sans immersion) au cours des quatre cycles de 24 heures au marais salé de Bossys perdus. Pour les taux journaliers de NCP, les bilans négatifs correspondent à une autotrophie (puits net de C pour l'eau) et les bilans positifs correspondent à une hétérotrophie (source nette de C pour l'eau). Pour le métabolisme net du marais avec immersion (NEE) et sans immersion (NEE_{marsh}), les bilans négatifs correspondent à une captation de C atmosphérique par le marais (chapitre IV, Mayen et al., in prep.). NA : les données EC n'ont pas pu être mesurées pour C4-fall.

			C1-winter	C2-spring	C3-summer	C4-fall
High Tides	**NEE**	Benthic and aquatic metabolism	-0.19	-0.76	-0.48	NA
	NEE_{marsh}	Benthic metabolism	-0.40	-1.52	-0.29	NA
	GPP_{marsh}	Benthic metabolism	-0.60	-2.23	-1.00	NA
	R_{marsh}	Benthic metabolism	0.20	0.71	0.71	NA
	NCP	Planktonic metabolism in marsh waters	-0.03	-0.08	0.02	0.02
Low Tides	**NEE**	Benthic metabolism	-1.24	-1.80	-2.34	NA
	NEE_{marsh}	Benthic metabolism	-1.24	-1.80	-3.34	NA
	GPP_{marsh}	Benthic metabolism	-1.62	2.73	-3.49	NA
	R_{marsh}	Benthic metabolism	0.38	0.93	1.16	NA
	NCP	Planktonic metabolism in channel water	-0.05	-0.17	0.04	0.09

Lors de l'immersion du marais par les eaux côtières du Pertuis Breton (Fig. 1.21), les mesures du métabolisme aquatique ont généralement indiqué une hétérotrophie de la colonne d'eau produisant du DIC et des augmentations de pCO_2 de l'eau. En absence d'une forte activité des communautés planctoniques à marée haute, cette hétérotrophie aquatique pourrait être liée à la respiration des plantes immergées et/ou à un couplage benthique-pélagique (Fig. 5.4). Les fortes concentrations en nitrate dans les eaux côtières en hiver (> 30 µM ; Belin et al., 2021), influencées par le bassin versant de la Baie de l'Aiguillon, ont été advectées vers le marais des Bossys perdus lors des marées hautes (DIN:DIP > 50). Les nitrates ont ensuite probablement diffusé dans les sédiments où ils ont été réduits pour la respiration de la matière organique produisant un flux diffusif de DIC des sédiments vers la colonne d'eau (chapitre IV, Mayen et al., in prep.). Cette hétérotrophie aquatique mesurée a probablement favorisé les sursaturations en CO_2 de l'eau et les émissions de CO_2 atmosphérique par le compartiment aquatique (Fig. 5.4). À marée haute, les flux de NEE principalement à l'interface entre l'eau et l'air ont montré une faible captation nette de CO_2 atmosphérique au cours des cycles de 24 heures (Tableau 5.2 et Fig. 5.4). En hiver et au printemps, les bilans nets de C mesurés par EC lors de l'immersion (i.e. NEE) ont été deux fois plus faibles que ceux estimés pour le compartiment benthique du marais sans immersion (i.e. NEE_{marsh}) induisant une perte dans la captation de CO_2 atmosphérique lors des marées hautes tandis que, l'inverse a été mesurée en été (Tableau 5.2). Simultanément, les incubations de la colonne d'eau ont montré que les communautés planctoniques, essentiellement composés de diatomées pennées et de picophytoplancton, se sont comportées comme un puits net de CO_2 pour la colonne d'eau en hiver et au printemps (autotrophie) et comme une source nette de CO_2 pour la colonne d'eau en été et en automne (hétérotrophie) (Tableau 5.2). Cependant, les faibles taux du métabolisme planctonique (NCP) par comparaison à la captation nette de CO_2 du compartiment aquatique (NEE) suggère une contribution importante du compartiment benthique (NEE_{marsh}) où le métabolisme terrestre des plantes émergées sur les zones les plus hautes du marais pourraient maintenir un puits de CO_2 atmosphérique pendant l'immersion malgré des eaux sursaturées en CO_2 par rapport à l'atmosphère (Tableau 5.2 et Fig. 5.4).

Lors de l'émersion, les eaux influencées par les marais salés sont drainées vers les chenaux permettant d'exporter des eaux sursaturées en CO_2 en hiver (hétérotrophie aquatique) et des eaux sous-saturées en CO_2 au printemps et en été (autotrophie aquatique). Les augmentations importantes et significatives des concentrations en carbone total dans l'eau (TC = DOC + POC + DIC) de la marée haute vers la marée basse (1087, 912, 830 et 740 µM en hiver, printemps, été et automne, respectivement) peuvent mettre en évidence un

métabolisme intense du marais (Tableau 5.2 et Fig. 5.4). En hiver, les plus fortes augmentations en DIC, en TA et en nutriments (NH_4^+ et PO_4^{3-}) pendant la marée basse de nuit (chapitre IV, Mayen et al., in prep.) sont probablement liées à des apports sédimentaires par la pompe tidale et une exportation associée d'eaux porales vers le chenal (Lui et al., 2017 ; Santos et al., 2019 ; Reithmaier et al., 2023). Plusieurs processus de respiration anaérobie se produisent en simultanée dans les sédiments des marais salés (sulfato-réduction, dénitrification, etc.) produisant du DIC et du TA dans les eaux de surface (Wang et al., 2016). En hiver, la forte relation entre les diminutions de NO_3^-_NO_2^- et les augmentations de NH_4^+ de la marée haute vers la marée basse ont pu indiquer une réduction dissimilatrice des nitrates en ammonium dont le processus a déjà été mis en évidence dans les marais salés tidaux (Hopkinson et Giblin, 2008 ; Giblin et al., 2013 ; Zhen et al., 2016). Au contraire, au printemps et en été, les diminutions significatives des pCO_2 de l'eau et les augmentations significatives du DOC au cours de la marée basse ont pu être liées à une forte production primaire du marais dont celle des plantes halophytes, des macroalgues, du MPB et du phytoplancton qui se développent dans le chenal (Fig. 5.4). Ainsi, les taux associés au métabolisme planctonique (NCP) ont été plus élevés à marée basse dans les eaux du chenal variant de -0,17 g C m^{-2} j^{-1} au printemps (puits de CO_2) à 0,09 g C m^{-2} j^{-1} en automne (source de CO_2). Cependant, lors des périodes de marée basse, la forte captation de CO_2 mesurée par EC au sein de l'emprise a sans doute été principalement contrôlée par le compartiment benthique du marais constitué à 70% de plantes halophytes terrestres qui assurent une forte production primaire à l'émersion (Tableau 5.2).

Les exportations horizontales de DIC par les marais salés pourraient induire un dégazage de CO_2 atmosphérique dans les eaux côtières adjacentes (Wang et al., 2016) alors que les exportations horizontales de TA favoriseraient la capacité tampon des eaux côtières et le puits de carbone à long terme puisque l'alcalinité totale reste généralement sous forme dissoute (Middelburg et al., 2020). Les données liées aux exportations de TA au sein de plusieurs marais salés autour du monde ont été récoltées afin de les intégrer au budget de carbone des marais et permettre d'augmenter la plus-value de ces écosystèmes intertidaux dans la séquestration de carbone (Reithmaier et al., 2023).

Conclusions de la thèse

Ces travaux de thèse ont permis d'apporter des connaissances concernant les processus biologiques, physiques et chimiques contrôlant les flux de carbone aux interfaces terrestre-aquatique-atmosphérique des marais Charentais au travers de mesures *in situ* (pCO_2 de l'eau et flux de CO_2 atmosphérique) et d'échantillonnages de la colonne d'eau (POC, DOC, DIC, TA et nutriments) aux différentes échelles temporelles (diurne, tidale, saisonnière) et spatiales (marais salés et doux). Une étude de la balance métabolique des communautés planctoniques a également été menée afin d'étudier la contribution du phytoplancton dans les flux horizontaux et verticaux de carbone dans les marais.

Face aux enjeux environnementaux que représente la préservation des marais littoraux dans la captation de CO_2 atmosphérique, il a été fondamental d'apporter une meilleure compréhension du cycle du carbone et du comportement du CO_2 dans ces écosystèmes végétalisés selon leur typologie et leur mode de gestion. Le long d'un continuum aquatique (île de Ré), nos mesures biogéochimiques à haute fréquence ont montré un fort contrôle de la typologie de l'écosystème sur la dynamique du carbone inorganique, avec des pCO_2 de l'eau significativement plus faibles dans les marais salés rétro-littoraux en amont, en raison d'une activité biologique plus forte et d'un temps de résidence de l'eau plus long, que dans l'estuaire tidal en aval. En effet, les pCO_2 de l'eau des marais salés ont été fortement contrôlées par le métabolisme des producteurs primaires aquatiques (phytoplancton et macrophytes) induisant des périodes importantes de sous-saturation en CO_2 de l'eau par rapport à l'atmosphère. Cependant, les entrées d'eau côtière tamponnée dans les marais salés selon les différents modes de gestion (naturel *vs.* anthropique) ont significativement perturbé la dynamique des pCO_2 de l'eau en diminuant instantanément les périodes de sous-saturation en CO_2 de la colonne d'eau. De plus, ces travaux de thèse ont également permis d'établir un lien entre le type de producteur primaire dans le marais et le statut métabolique du compartiment aquatique comme source ou puits de CO_2 atmosphérique. Les apports en nutriments interagissent de façon significative avec le cycle du carbone des marais en favorisant principalement des producteurs primaires à croissance rapide (macroalgues flottantes et phytoplancton) dont le renouvellement rapide au cours de l'année ne permet pas une captation nette de CO_2 atmosphérique à l'échelle annuelle contrairement aux macrophytes à croissance lente (herbiers marins ou plantes vasculaires). Ainsi, ce travail de thèse indique que la gestion des marais peut être un levier important afin de limiter les nutriments et de

privilégier des producteurs primaires avec un faible taux de renouvellement permettant une meilleur captation et séquestration de carbone à plus long terme.

Les marais tidaux sont des zones humides végétalisés à l'interface entre le milieu terrestre et le milieu aquatique associées à des temps de résidence plus court de l'eau lors de l'immersion par les eaux côtières. Un système d'Eddy Covariance atmosphérique a été déployé pendant trois ans (2019-2022) au niveau d'un marais tidal des Bossys perdus (ancien marais salants) afin de mesurer en continu les échanges nets de CO_2 de l'écosystème (NEE) et évaluer l'influence des principaux facteurs de contrôle environnementaux (biotiques et abiotiques). Les résultats de ces travaux ont montré un fort puits annuel de CO_2 atmosphérique principalement lié à une faible respiration de l'écosystème (plantes, MPB, sédiments) couplée à une forte activité photosynthétique des plantes terrestres émergés, principalement au printemps et en été, contrôlée par la lumière, la température et le VPD. Cette étude a fourni également des informations importantes sur les variations temporelles des flux de NEE pendant l'immersion tidale en diminuant significativement la captation de CO_2 atmosphérique le jour et les émissions de CO_2 atmosphérique la nuit au cours d'une journée alors que l'immersion n'a pas affecté significativement le bilan annuel de carbone du marais.

Au cours des cycles de 24 heures menés au marais tidal des Bossys perdus, les pCO_2 de l'eau ont été contrôlées par l'activité biologique induisant en moyenne une sursaturation en CO_2 de l'eau en hiver et une sous-saturation en CO_2 de l'eau au printemps et en été. Lors des marées hautes, le métabolisme hétérotrophe de la colonne d'eau a favorisé la production de DIC et des augmentations de pCO_2 de l'eau. Ainsi, les eaux sursaturées en CO_2 par rapport à l'atmosphère (en plus de l'effet barrière de la colonne d'eau sur les échanges eau-air) ont pu réduire de manière significative la captation de CO_2 atmosphérique à l'échelle du marais mesurée par Eddy Covariance pendant les niveaux d'immersion des plantes les plus élevés. De la marée haute à la marée basse, le marais s'est comporté comme une source importante de DIC, de TA et de nutriments (NH_4^+ et PO_4^{3-}), notamment en hiver, probablement liée à des processus métaboliques anaérobies importants dans le chenal et les sédiments induisant une augmentation significative des pCO_2 de l'eau. Au contraire, au printemps et en été, la forte production primaire du marais incluant le phytoplancton, les microalgues benthiques (MPB) et les macroalgues ont favorisé des plus faibles valeurs des pCO_2 de l'eau dans le chenal de jour comme de nuit, associées à de fortes productions de DOC. À marée basse, le métabolisme planctonique a eu une influence significative sur les pCO_2 de l'eau, induisant une captation nette en hiver et au printemps et une source nette en été et en automne. Cependant, les communautés planctoniques n'ont pas joué un rôle significatif dans les bilans

nets de carbone du marais à l'échelle de l'écosystème qui sont contrôlés majoritairement par la végétation terrestre. Ces résultats soulignent que les échanges horizontaux d'eau côtière avec les marais salés ont modifié de manière significative la dynamique du carbone et l'état biogéochimique du CO_2 de l'eau par rapport à l'atmosphère au travers d'une forte activité biologique des marais (production et respiration).

Dans le contexte du changement climatique, ce travail a permis une avancée dans la compréhension écologique et biogéochimique des marais et pourra fournir une aide à la gestion de ces écosystèmes littoraux pour favoriser les puits de carbone en zone côtière.

Perspectives de thèse

MNT et Eddy Covariance atmosphérique

En raison de la micro-topologie spécifique du marais tidal des Bossys perdus liée aux anciennes salines, les mesures de hauteur d'eau à une seule localisation sur le marais n'ont pas permis de prendre en compte précisément toute la variabilité spatiale du site entre les secteurs émergés (zones hautes du marais) et ceux immergés (zones basses du marais) au sein du footprint (Fig. 3.2). En effet, plusieurs secteurs de vent sont rapidement immergés par les eaux côtières lors de la marée montante (vases) alors qu'en même temps, d'autres secteurs sont encore émergés (sources) complexifiant l'étude de l'influence de l'immersion tidale sur les flux de NEE mesurés par Eddy Covariance (chapitre III). Nos visualisations sur le terrain lors des plus gros coefficients de marée ont indiqué que certains secteurs de vent sont encore émergés ou partiellement émergés dans l'atmosphère pour une hauteur d'eau mesurée inférieure à 1 m (Fig. 3.8). Pour mieux contraindre l'influence de l'immersion tidale sur les flux métabolique du marais, un modèle numérique de terrain (MNT) pour les hauteurs d'eau permettrait de déterminer spatialement les zones précises d'immersion et d'émersion dans chaque secteur de vent du footprint et à chaque valeur de flux de NEE à 10 mins. Ce MNT a été réalisé pour les années 2021 et 2022 mais il nécessite des améliorations, notamment du fait des imprécisions liées au capteur STPS pour les mesures de hauteur d'eau (plusieurs capteurs STPS dans différents secteurs du footprint seraient nécessaires). Associé à la connaissance des habitats des Bossys perdus au sein du footprint (Tableau 3.1), nous pourrions ainsi calculer la proportion relative des secteurs immergés et émergés par rapport à la surface totale correspondantes et leurs contributions respectives quant aux flux de CO_2 atmosphérique mesurés par Eddy Covariance en termes de photosynthèse et respiration lors de ces phrases d'immersion variables suivant la marée.

Matière organique particulaire des marais salés

Compte tenu de l'importance de la matière organique particulaire dans le cycle du carbone des environnements côtiers, il est nécessaire d'échantillonner le carbone organique particulaire (POC) et l'azote organique particulaire (NOP) afin d'élucider son rôle sur les pCO_2 de l'eau et échanges de CO_2 atmosphérique associés dans les marais. Au cours des cycles de 24 h au marais tidal des Bossys perdus, les ratios POC:PON (molaire) et POC:Chl*a*

(atomique) ont permis de donner des indications sur les caractéristiques la matière organique particulaire dans l'eau (origine, composition, état de dégradation) (Savoye et al., 2003). En hiver, les valeurs les plus élevées des ratios POC:PON (entre 11 et 15) et POC:Chl*a* (entre 1300 et 1600 mg mg^{-1}) ont été mesurées au cours de la marée basse de nuit et pourraient indiquer une minéralisation de la matière organique végétale en décomposition dans les eaux du chenal induisant les plus fortes augmentations des pCO_2 de l'eau et des concentrations en DIC. Au contraire, aux autres saisons échantillonnées à marée basse, les ratios POC:PON ont été proche de la valeur théorique de Redfield (106:16) indiquant une matière organique phytoplanctonique dégradée à l'été (POC:Chl*a* > 300 mg mg^{-1}) et peu dégradée à l'automne (POC:Chl*a* < 150 mg mg^{-1}). Cependant, des mesures par signature isotopiques permettraient d'identifier les sources de la matière organique particulaire dans l'eau avec une meilleure précision (Savoye et al., 2003 ; Bristow et al., 2012). En biogéochimie et écologie aquatique, les rapports isotopiques stables du carbone ($\delta^{13}C$) et de l'azote ($\delta^{15}N$) sont largement utilisés pour déterminer l'origine (macrophytes terrestres ou aquatiques, phytoplancton d'eaux douces ou d'eaux marines ou eaux usées) et le devenir de la matière organique particulaire en suspension. Dans cette thèse, les sources de POC et de PON (eau et producteurs primaires) ont été échantillonnées lors de nos cycles de 24 h pour l'identification de la matière organique ; les analyses sont prévues et les résultats à venir.

Budget de carbone des marais salés

Au sein des marais salés tidaux de la côte nord-est des États-Unis, le budget de carbone a été construit sur la base de flux horizontaux et verticaux de carbone mesurés au sein de plusieurs études et compilées au sein d'un même budget (Fig. 1.16 ; Song et al., 2023). Ainsi, la GPP a été calculée comme la somme des exports latérales de DIC (Wang et al., 2016), de DOC et de POC (Herrmann et al., 2015 ; Najjar et al., 2018), de séquestration de carbone bleu (Chmura et al., 2003) et de dégazage de CO_2 atmosphérique par les compartiments terrestre (Forbrich et Giblin, 2015 ; Carey et al., 2022) et aquatique (Song et al., 2023). Cependant, le manque de mesures *in situ* sur les échanges de CO_2 atmosphérique à grande échelle par Eddy Covariance en simultanée avec des mesures de la balance métabolique des communautés planctoniques et des flux horizontaux de carbone entraine encore des incertitudes dans les budgets de carbone des marais (Wang et al., 2018 ; Song et al., 2023) et sur leur contribution aux cycles régional et global du carbone (Bauer et al., 2013 ; Najjar et al., 2018).

Au cours de nos cycles de 24 h au marais tidal des Bossys perdus (chapitre IV), des mesures courantométriques à hautes fréquences (10 mins) ont donc été réalisées dans le chenal à chaque saison en simultanée avec les mesures du carbone organique et inorganique de l'eau (DIC, DOC, POC) dans le but de calculer précisément les flux horizontaux de carbone lors des différentes phases de marée en simultanée avec les mesures des échanges nets de CO_2 de l'écosystème (NEE) par Eddy Covariance. Ces mesures/résultats (qui viennent de nous être transmis) de volumes d'eau et de débits associés transitant au marais étudié, soit advectés depuis le Pertuis Breton à marée haute, soit exportés depuis le marais vers le Pertuis Breton à marée basse permettront de tendre vers un premier budget de carbone en prenant en compte des flux de NEE en continu. De plus, nos mesures en simultanée entre les pCO_2 de l'eau et les flux de CO_2 atmosphérique par Eddy Covariance lors des périodes d'immersion offre la possibilité de calculer avec précision le coefficient d'échange du CO_2 à l'interface eau-air (k ; chapitre I, section 4.1) suivant Polsenaere et al. (2013) afin d'apporter des précisions concernant les dégazages de CO_2 par le compartiment aquatique du marais à marée haute. Pour finir, dans le cadre de deux post-doctorats, le compartiment sol du marais a également été suivi la même année par des mesures de séquestration de carbone (Amann et al., soumis) et aussi de production et de dégradation racinaire des plantes halophiles en fonction du rythme tidal (Arnaud et al., soumis) et permettent d'apporter des précisons majeurs dans la construction du budget de carbone du marais tidal des Bossys perdus.

De plus, dans les marais tidaux, les valeurs de NEP (production de l'écosystème nette ; chapitre I, section 3.1) ne peuvent pas être directement estimées par des mesures Eddy Covariance atmosphérique (Chapin et al., 2006 ; Mayen et al., 2024). En effet, pendant les phases de marée descendante, les exportations latérales de DIC liées à la respiration hétérotrophe du marais, la minéralisation de la matière organique, la dissolution des carbonates et le couplage benthique-pélagique (Wang et al., 2016) ne peuvent pas être prise en compte par des mesures d'échanges de CO_2 atmosphérique. Ainsi, des mesures d'exports latérales de DIC doivent être menées en simultanée avec des mesures Eddy Covariance afin d'estimer avec précision la NEP des marais.

Pour finir, des incertitudes persistent encore quant à la contribution des réseaux trophiques dans les flux horizontaux et verticaux de carbone suivant la typologie des marais littoraux. Un travail de post-doctorat au sein du projet LRTZC propose de mesurer des flux de CO_2 atmosphérique aux différentes interfaces d'échange des marais (sédiment-air, eau-air et sédiment-eau) afin d'établir des bilans de carbone à l'échelle de l'écosystème *via* une

approche de modélisation des réseaux trophiques tout en prenant en compte les variabilités saisonnières. Face à l'enjeu que représente la préservation et la gestion des marais littoraux pour la captation et la séquestration de carbone, il est fondamental de mieux comprendre le fonctionnement biogéochimique de ces écosystèmes d'interface et notamment, la contribution des réseaux trophiques dans les flux horizontaux et verticaux de carbone.

Lien entre eutrophisation des marais et les bilans de carbone

Ces travaux ont permis d'établir une première relation entre le niveau trophique des marais littoraux et leur statut métabolique comme puits ou source de CO_2 atmosphérique (chapitre V, section 1.2). Les fortes valeurs de pCO_2 de l'eau dans les marais pourraient être ainsi liées à l'eutrophisation du milieu et au renouvellement rapide des producteurs primaires à croissance rapide. Dans un contexte de hausse de l'anthropisation des environnements côtiers, il serait nécessaire d'approfondir les connaissances concernant l'influence des apports en nutriments dans les marais sur les échanges de CO_2 atmosphérique et sur leur capacité de captation de carbone. Il serait intéressant de déployer une station d'Eddy Covariance à la station MAD (Brouage) afin de quantifier les flux de NEE à l'interface entre l'eau et l'atmosphère à l'échelle de l'écosystème et d'apporter des précisions concernant l'influence de l'eutrophisation d'un marais sur la capacité de captation de CO_2 atmosphérique aux différentes échelles temporelles.

Dans les mangroves, l'eutrophisation liée aux apports importants de matière organique labile comme les algues pourrait (1) renforcer la boucle microbienne de dégradation de la matière organique peu biodégradable et altérer la séquestration de carbone bleu dans les sédiments (Cheynel et al., 2022) et (2) augmenter les émissions de CO_2 atmosphérique provenant des sédiments émergés (Barroso et al., 2022). Au sein des marais tidaux, les niveaux élevés en nutriments (NO_3^-) associés à l'eutrophisation côtière augmentent la décomposition microbienne de la matière organique par dénitrification au niveau de la biomasse souterraine des plantes altérant la structure des marais et favorisant le passage d'un couvert végétal à un couvert vaseux (Deegan et al., 2012). Ces augmentations de la respiration de l'écosystème pourraient être mis en évidence par des mesures d'Eddy Covariance atmosphérique en utilisant le partitionnement des flux de NEE en flux métabolique du marais.

Annexes chapitre V

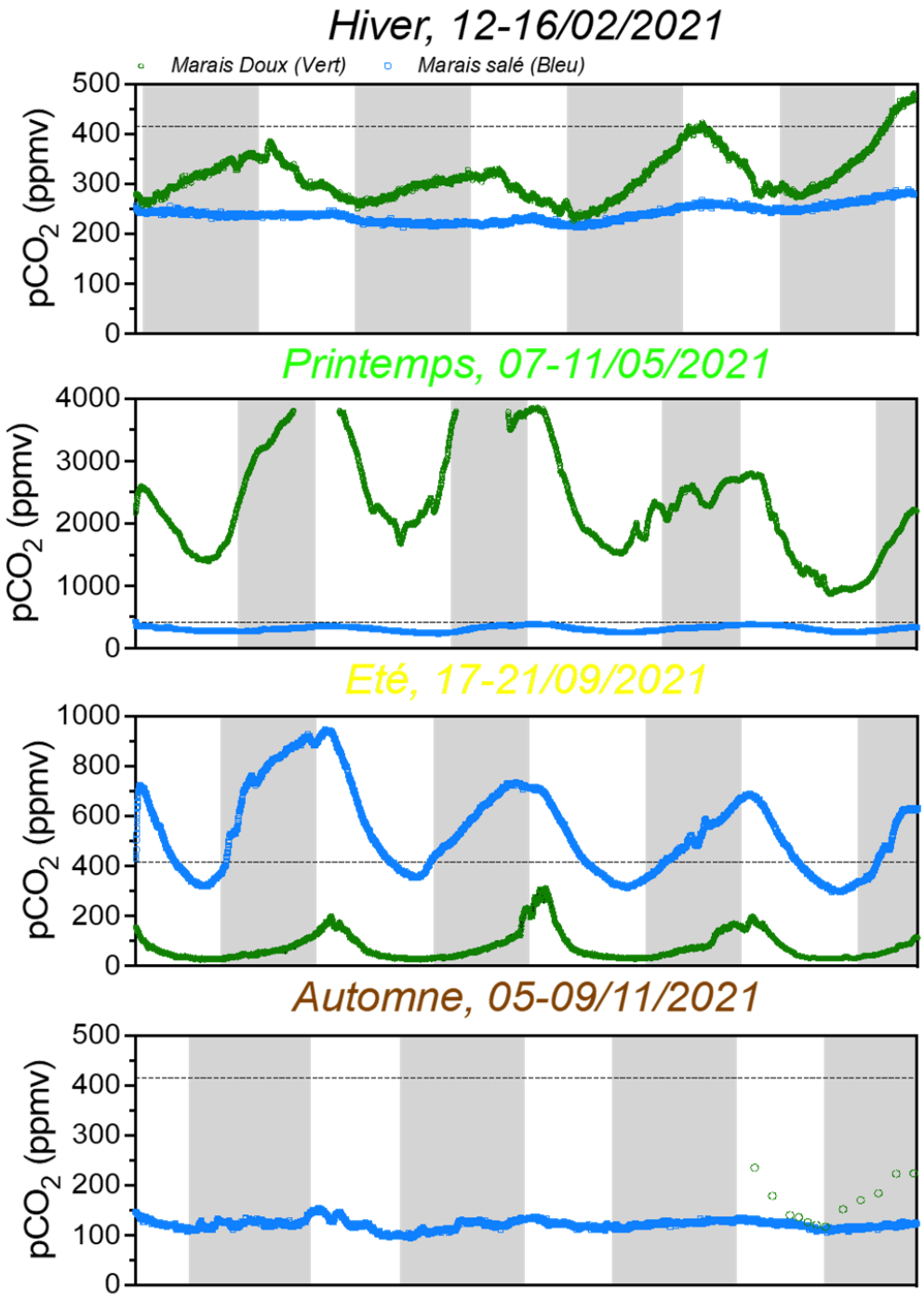

Figure S1 : Pression partielle de CO_2 de l'eau (pCO_2 en ppmv) mesurées à hautes fréquences (i.e. 1 minute) au marais saumatre (MAD en vert) et au marais salé (MAS en bleu) aux quatre saisons en 2021 en simultané durant quatre jours consécutifs (hiver en noir, printemps en vert, été en jaune et automne en marron) ; les bandes claires et foncées représentent les périodes de jour et de nuit, respectivement ; le trait pointillé à 415 ppmv correspond à la pCO_2 moyenne de l'atmosphère en 2021 ; à MAD en automne, les pCO_2 de l'eau ont été estimées à partir des mesures de pH et d'alcalinité de l'eau toutes les deux heures lors des dernières 24 heures de mesures. Polsenaere, 2023.

Des analyses statistiques complémentaires ont été réalisées telles que des régressions linéaires multiples à l'échelle saisonnière (cycle de 24 heures ; 12 < n < 16) afin de tester la contribution des variables biogéochimiques mesurées (Tableau 4.3) sur les variations des pCO_2 de l'eau au travers du pourcentage de variance expliquée (R^2 ajusté ; Tableau 5.3). En hiver et en automne, les analyses de régression multilinéaire ont montré que les pCO_2 ont été significativement expliquées par les variations de DIC, de TA et de nutriments (NO_3^-_NO_2^- et NH_4^+), ce qui pourrait confirmer une forte contribution des processus hétérotrophes sur les pCO_2 de l'eau. Au contraire, au printemps et en été, les pCO_2 ont été fortement corrélées avec DOC (Tableau 5.3) permettant de confirmer une forte contribution des processus autotrophes sur les pCO_2 de l'eau. Ces analyses statistiques peuvent venir compléter les résultats et les conclusions du chapitre IV (Mayen et al., in prep) concernant l'influence des processus métaboliques de la colonne d'eau sur les pCO_2 mesurées.

Tableau S5.3 : Analyses de régression linéaire multiple (méthode pas à pas) à l'échelle saisonnière (cycles de 24 heures ; 12 < n < 16) (Harrell, 2015). Pour chaque modèle multilinéaire sélectionné ($p < 0,001$), la valeur du R^2 ajustée est la plus élevée avec toutes les variables expliquant au moins 5% de la variation des pCO_2 de l'eau. En gras est indiqué le paramètre expliquant au moins 50% de la variation de la pCO_2. La statistique F de Fisher et le R^2 ajusté (R^2 adj.) sont indiqués. Ces analyses statistiques ont été réalisées avec le logiciel Statgraphics Centurion 19.

	Équation	**F**	**Adj. R^2**
Hiver	pCO_2 = -1349,5 **+ 4,1 DIC** - 3,2 TA - 0,9 POC + 11,3 NO_3^-_NO_2^-	103,9	97,1%
Printemps	pCO_2 = 415,4 **- 0,4 DOC** - 0,8 POC + 22,7 Chl*a*	15,2	75,3%
Été	pCO_2 = 527,6 **- 0,5 DOC**	59,7	80,7%
Automne	pCO_2 = 668,2 **+ 0,7 DIC - 6,7 TA - 37,1 NH_4^+**	57,6	91,9%

Bibliographie

- **A**

Abril, G., M.-V. Commarieu, A. Sottolichio, P. Bretel, and F. Guérin. 2009. Turbidity limits gas exchange in a large macrotidal estuary. Estuarine, Coastal and Shelf Science **83**: 342–348. doi:10.1016/j.ecss.2009.03.006

Abril, G., M. Nogueira, H. Etcheber, G. Cabeçadas, E. Lemaire, and M. J. Brogueira. 2002. Behaviour of Organic Carbon in Nine Contrasting European Estuaries. Estuarine, Coastal and Shelf Science 54: 241–262. doi:10.1006/ecss.2001.0844

AcclimaTerra, 2018. Le Treut, H. (dir). Anticiper les changements climatiques en Nouvelle-Aquitaine. Pour agir dans les territoires. Éditions Région Nouvelle-Aquitaine, 488 p.

Adam, P., 2019. Salt Marsh Restoration, in: Coastal Wetlands. Elsevier, pp. 817–861. https://doi.org/10.1016/B978-0-444-63893-9.00023-X

Aller, R. C. 1994. Bioturbation and remineralization of sedimentary organic matter: effects of redox oscillationl. Chemical Geology.

Alpine, A. E. and J. E. Cloern. 1988. Phytoplankton Growth-Rates in a Light-Limited Environment, San-Francisco Bay, Mar. Ecol. Prog. Ser., 44, 167–173

Alongi, D. M. 2020. Carbon Balance in Salt Marsh and Mangrove Ecosystems: A Global Synthesis. JMSE **8**: 767. doi:10.3390/jmse8100767

Altor, A. E., and W. J. Mitsch. 2008. Pulsing hydrology, methane emissions and carbon dioxide fluxes in created marshes: A 2-year ecosystem study. Wetlands **28**: 423–438. doi:10.1672/07-98.1

Aminot, A., and R. Kérouel. 2004. In: Ifremer, Plouzané (Ed.), Hydrologie des écosystèmes marins: paramètres et analyses in French, (France).

Aminot, A., and R. Kérouel. 2007. In: Ifremer, Plouzané (Ed.), Dosage automatique des nutriments dans les eaux marines : méthodes en flux continu in French, (France).

Amorocho, J., and J. J. DeVries. 1980. A new evaluation of the wind stress coefficient over water surfaces. J. Geophys. Res. **85**: 433. doi:10.1029/JC085iC01p00433

Ara, K., K. Yamaki, K. Wada, S. Fukuyama, T. Okutsu, S. Nagasaka, A. Shiomoto, and J. Hiromi. 2011. Temporal variability in physicochemical properties, phytoplankton standing crop and primary production for 7 years (2002–2008) in the neritic area of Sagami Bay, Japan. J Oceanogr **67**: 87–111. doi:10.1007/s10872-011-0010-y

Archibald, K. M., S. Dutkiewicz, C. Laufkötter, and H. V. Moeller. 2022. Thermal Responses in Global Marine Planktonic Food Webs Are Mediated by Temperature Effects on Metabolism. JGR Oceans **127**: e2022JC018932. doi:10.1029/2022JC018932

Arnaud, M., A. J. Baird, P. J. Morris, T. H. Dang, and T. T. Nguyen. 2020. Sensitivity of mangrove soil organic matter decay to warming and sea level change. Global Change Biology **26**: 1899–1907. doi:10.1111/gcb.14931

Artigas, F., J. Y. Shin, C. Hobble, A. Marti-Donati, K. V. R. Schäfer, and I. Pechmann. 2015. Long term carbon storage potential and CO_2 sink strength of a restored salt marsh in New Jersey. Agricultural and Forest Meteorology **200**: 313–321. doi:10.1016/j.agrformet.2014.09.012

Aubinet, M., Grelle, A., Ibrom, A., Rannik, Ü., Moncrieff, J., Foken, T., Kowalski, A. S., Martin, P. H., Berbigier, P., Bernhofer, Ch., Clement, R., Elbers, J., Granier, A., Grünwald, T., Morgenstern, K., Pilegaard, K., Rebmann, C., Snijders, W., Valentini, R., and Vesala, T.: Estimates of the Annual Net Carbon and Water Exchange of Forests: The EUROFLUX Methodology, in: Advances in Ecological Research, vol. 30, Elsevier, 113–175, https://doi.org/10.1016/S0065-2504(08)60018-5, 1999.

Aubinet, M., Vesala, T., and Papale, D. (Eds.): Eddy Covariance: A Practical Guide to Measurement and Data Analysis, Springer Netherlands, Dordrecht, https://doi.org/10.1007/978-94-007-2351-1

Aufdenkampe, A. K., E. Mayorga, P. A. Raymond, J. M. Melack, S. C. Doney, S. R. Alin, R. E. Aalto, and K. Yoo. 2011. Riverine coupling of biogeochemical cycles between land, oceans, and atmosphere. Frontiers in Ecology and the Environment **9**: 53–60. doi:10.1890/100014

- **B**

Bade, D.L., 2009. Gas Exchange at the Air–Water Interface, in: Encyclopedia of Inland Waters. Elsevier, pp. 70–78. https://doi.org/10.1016/B978-012370626-3.00213-1

Baldocchi, D. D., B. B. Hincks, and T. P. Meyers. 1988. Measuring Biosphere-Atmosphere Exchanges of Biologically Related Gases with Micrometeorological Methods. Ecology **69**: 1331–1340. doi:10.2307/1941631

Baldocchi, D. D. 2003. Assessing the eddy covariance technique for evaluating carbon dioxide exchange rates of ecosystems: past, present and future: CARBON BALANCE and EDDY COVARIANCE. Global Change Biology **9**: 479–492. doi:10.1046/j.1365-2486.2003.00629.x

Baldocchi, D. D., B. B. Hincks, and T. P. Meyers. 1988. Measuring Biosphere-Atmosphere Exchanges of Biologically Related Gases with Micrometeorological Methods. Ecology **69**: 1331–1340. doi:10.2307/1941631

Barroso, G. C., G. Abril, W. Machado, and others. 2022. Linking eutrophication to carbon dioxide and methane emissions from exposed mangrove soils along an urban gradient. Science of The Total Environment **850**: 157988. doi:10.1016/j.scitotenv.2022.157988

Bauer, J. E., W.-J. Cai, P. A. Raymond, T. S. Bianchi, C. S. Hopkinson, and P. A. G. Regnier. 2013. The changing carbon cycle of the coastal ocean. Nature **504**: 61–70. doi:10.1038/nature12857

Bel Hassen, M. 2000. Fonctionnement des marais maritimes Atlantiques: échanges d'énergie et effets des flux aquacoles diffus. Thèse. Bretagne Occidentale.

Bel Hassen, M. 2001. Spatial and Temporal Variability in Nutrients and Suspended Material Processing in the Fier d'Ars Bay (France). Estuarine, Coastal and Shelf Science **52**: 457–469. doi:10.1006/ecss.2000.0754

Belin, C., D. Soudant, and Z. Amzil. 2021. Three decades of data on phytoplankton and phycotoxins on the French coast: Lessons from REPHY and REPHYTOX. Harmful Algae 102, 101733. https://doi.org/10.1016/j.hal.2019.101733

Benner, R., and K. Kaiser. 2011. Biological and photochemical transformations of amino acids and lignin phenols in riverine dissolved organic matter. Biogeochemistry **102**: 209–222. doi:10.1007/s10533-010-9435-4

Berg, P., M. L. Delgard, P. Polsenaere, K. J. McGlathery, S. C. Doney, and A. C. Berger. 2019. Dynamics of benthic metabolism, O_2 , and pCO_2 in a temperate seagrass meadow. Limnol Oceanogr **64**: 2586–2604. doi:10.1002/lno.11236

Borawska, Z., B. Szymczycha, M. J. Silberberger, K. Koziorowska-Makuch, M. Szczepanek, and M. Kędra. 2022. Benthic fluxes of dissolved silica are an important component of the marine Si cycle in the coastal zone. Estuarine, Coastal and Shelf Science **273**: 107880. doi:10.1016/j.ecss.2022.107880

Borges, A. V., and G. Abril. 2011. Carbon Dioxide and Methane Dynamics in Estuaries, p. 119–161. *In* Treatise on Estuarine and Coastal Science. Elsevier.

Borges, A. V., B. Delille, and M. Frankignoulle. 2005. Budgeting sinks and sources of CO_2 in the coastal ocean: Diversity of ecosystems counts: COASTAL CO $_2$ SINKS AND SOURCES. Geophys. Res. Lett. **32**: LI4601. doi:10.1029/2005GL023053

Borges, A. V., B. Delille, L. Schiettecatte, F. Gazeau, G. Abril, and M. Frankignoulle. 2004. Gas transfer velocities of CO_2 in three European estuaries (Randers Fjord,Scheldt, and Thames). Limnology & Oceanography **49**: 1630–1641. doi:10.4319/lo.2004.49.5.1630

Borges, A. V., S. Djenidi, G. Lacroix, J. Théate, B. Delille, and M. Frankignoulle. 2003. Atmospheric CO_2 flux from mangrove surrounding waters. Geophysical Research Letters **30**: 2003GL017143. doi:10.1029/2003GL017143

Borges, A. V., and M. Frankignoulle. 1999. Daily and seasonal variations of the partial pressure of CO_2 in surface seawater along Belgian and southern Dutch coastal areas. Journal of Marine Systems **19**: 251–266. doi:10.1016/S0924-7963(98)00093-1

Borum, J., and K. Sand-Jensen. 1996. Is Total Primary Production in Shallow Coastal Marine Waters Stimulated by Nitrogen Loading? Oikos **76**: 406. doi:10.2307/3546213

Boynton, W. R., M. A. C. Ceballos, E. M. Bailey, C. L. S. Hodgkins, J. L. Humphrey, and J. M. Testa. 2018. Oxygen and Nutrient Exchanges at the Sediment-Water Interface: a Global Synthesis and Critique of Estuarine and Coastal Data. Estuaries and Coasts **41**: 301–333. doi:10.1007/s12237-017-0275-5

Bozec, Y., L. Merlivat, A.-C. Baudoux, and others. 2011. Diurnal to inter-annual dynamics of pCO_2 recorded by a CARIOCA sensor in a temperate coastal ecosystem (2003–2009). Marine Chemistry **126**: 13–26. doi:10.1016/j.marchem.2011.03.003

Breiman, L. 2001. Random Forests, Mach. Learn., 45, 5–32, https://doi.org/10.1023/A:1010933404324

Bridgham, S. D., J. P. Megonigal, J. K. Keller, et al. 2006. The carbon balance of North American wetlands. Wetlands 26: 889–916

Bristow, L. A., T. D. Jickells, K. Weston, A. Marca-Bell, R. Parker, and J. E. Andrews. 2013. Tracing estuarine organic matter sources into the southern North Sea using C and N isotopic signatures. Biogeochemistry **113**: 9–22. doi:10.1007/s10533-012-9758-4

Brzezinski, M. A. 1985. The Si V C V N ratio of marine diatoms: Interspecific variability and the effect of some environmental variables, J. Phycol., 21, 347–357, https://doi.org/10.1111/j.0022- 3646.1985.00347.x

Burba, G. 2021. Atmospheric flux measurements, in: Advances in Spectroscopic Monitoring of the Atmosphere, edited by: Chen, W., Venables, D. S., and Sigrist, M. W., Elsevier, 443–520, https://doi.org/10.1016/B978-0-12-815014-6.00004-X

Burgos, M., T. Ortega, and J. Forja. 2018. Carbon Dioxide and Methane Dynamics in Three Coastal Systems of Cadiz Bay (SW Spain). Estuaries and Coasts **41**: 1069–1088. doi:10.1007/s12237-017-0330-2

- **C**

Cai, W., and Y. Wang. 1998. The chemistry, fluxes, and sources of carbon dioxide in the estuarine waters of the Satilla and Altamaha Rivers, Georgia. Limnology & Oceanography **43**: 657–668. doi:10.4319/lo.1998.43.4.0657

Cai, W.-J. 2011. Estuarine and Coastal Ocean Carbon Paradox: CO_2 Sinks or Sites of Terrestrial Carbon Incineration? Annu. Rev. Mar. Sci. **3**: 123–145. doi:10.1146/annurev-marine-120709-142723

Caffrey, J. M. 2004. Factors controlling net ecosystem metabolism in U.S. estuaries. Estuaries **27**: 90–101. doi:10.1007/BF02803563

Calbet, A. 2001. Mesozooplankton grazing effect on primary production: A global comparative analysis in marine ecosystems, Limnol. Oceanogr., 46, 1824–1830.

Canadell, J. G. et al., 2021. Global Carbon and other Biogeochemical Cycles and Feedbacks. In Climate Change 2021: The Physical Science Basis. Contribution of Working Group I to the Sixth Assessment Report of the Intergovernmental Panel on Climate Change [Masson-Delmotte, V., P. Zhai, A. Pirani, S.L. Connors, C. Péan, S. Berger, N. Caud, Y. Chen, L. Goldfarb, M.I. Gomis, M. Huang, K. Leitzell, E. Lonnoy, J.B.R. Matthews, T.K. Maycock, T. Waterfield, O. Yelekçi, R. Yu, and B. Zhou (eds.)]. Cambridge University Press, Cambridge, United Kingdom and New York, NY, USA, pp. 673–816, doi:10.1017/9781009157896.007.

Campbell, A. D., L. Fatoyinbo, L. Goldberg, and D. Lagomasino. 2022. Global hotspots of salt marsh change and carbon emissions. Nature **612**: 701–706. doi:10.1038/s41586-022-05355-z

Canfield, D. E., and B. Thamdrup. 2009. Towards a consistent classification scheme for geochemical environments, or, why we wish the term ‘suboxic’ would go away. Geobiology **7**: 385–392. doi:10.1111/j.1472-4669.2009.00214.x

Carey, J. C., K. D. Kroeger, and J. Tang. 2022. Higher Temperature Sensitivity of Ecosystem Respiration in Low Marsh Compared to High Elevation Marsh Ecosystems. JGR Biogeosciences **127**: e2022JG006832. doi:10.1029/2022JG006832

Carpenter, J. H. 1965. THE CHESAPEAKE BAY INSTITUTE TECHNIQUE FOR THE WINKLER DISSOLVED OXYGEN METHOD. Limnology & Oceanography **10**: 141–143. doi:10.4319/lo.1965.10.1.0141

Carritt, D. E., and J. H. Carpenter. 1966. Comparison and evaluation of currently employed modifications of the Winkler method for determining dissolved oxygen in sea-water, J. Mar. Res., 24, 286–318

Champion, E., J. Gernigon, J.-C. Lemesle, J. Terrisse, and S. Maisonhaute. 2012. 3ème Plan de gestion 2013-2017 de la réserve naturelle nationale de Lilleau des Niges

Chapin, F. S., G. M. Woodwell, J. T. Randerson, and others. 2006. Reconciling Carbon-cycle Concepts, Terminology, and Methods. Ecosystems **9**: 1041–1050. doi:10.1007/s10021-005-0105-7

Chmura, G. L., S. C. Anisfeld, D. R. Cahoon, and J. C. Lynch. 2003. Global carbon sequestration in tidal, saline wetland soils. Global Biogeochemical Cycles **17**: 2002GB001917. doi:10.1029/2002GB001917

Chynel, M., S. Rockomanovic, G. Abril, and others. 2022. Contrasting organic matter composition in pristine and eutrophicated mangroves revealed by fatty acids and stable isotopes (Rio de Janeiro, Brazil). Estuarine, Coastal and Shelf Science **277**: 108061. doi:10.1016/j.ecss.2022.108061

Cloern, J. E. 1987. Turbidity as a control on phytoplankton biomass and productivity in estuaries. Continental Shelf Research **7**: 1367–1381. doi:10.1016/0278-4343(87)90042-2

Cloern, J. E., S. Q. Foster, and A. E. Kleckner. 2014. Phytoplankton primary production in the world's estuarine-coastal ecosystems. Biogeosciences **11**: 2477–2501. doi:10.5194/bg-11-2477-2014

Coignot, E., P. Polsenaere, P. Soletchnik, O. Le Moine, P. Souchu, E. Joyeux, Y. Le Roy, J.-P. Guéret, L. Froud, R. Gallais, E. Chourré, and L. Chaigneau. 2020. Variabilité spatio-temporelle des nutriments et du carbone et flux associés le long d'un continuum terrestre-aquatique tempéré (Marais poitevin – Baie de l'Aiguillon – Pertuis Breton). Rapport final (suivi 2017-2018) - Projet Aiguillon (2016–2020). 111pp. https://archimer.ifremer.fr/doc/00618/73003/.

Cole, J. J., Y. T. Prairie, N. F. Caraco, and others. 2007. Plumbing the Global Carbon Cycle: Integrating Inland Waters into the Terrestrial Carbon Budget. Ecosystems **10**: 172–185. doi:10.1007/s10021-006-9013-8

Consalvey, M., B. Jesus, R. G. Perkins, V. Brotas, G. J. C. Underwood, and D. M. Paterson. 2004. Monitoring Migration and Measuring Biomass in Benthic Biofilms: The Effects of Dark/far-red Adaptation and Vertical Migration on Fluorescence Measurements. Photosynthesis Research **81**: 91–101. doi:10.1023/B:PRES.0000028397.86495.b5

Costanza, R., R. D'Arge, R. de Groots, S. Farber, M. Grasso, B. Hannon, K. Limburg, S. Naeem, R. O'Neill, J. Paruelo, R.G. Raskin, P. Sutton, and M. van den Belt. 1997. The value of the world's ecosystem services and natural capital. Nature 387, 253–260

Couvillion, B. R., J. A. Barras, G. D. Steyer, W. Sleavin, M. Fischer, H. Beck, N. Trahan, B. Griffin, and D. Heckman. 2011. Land change in coastal Louisiana from 1932 to 2010. In: U.S. Geological Survey, Scientific Investigations Map 3164 (12 pp.)

Cotovicz Jr., L. C., B. A. Knoppers, N. Brandini, S. J. Costa Santos, and G. Abril. 2015. A strong CO2 sink enhanced by eutrophication in a tropical coastal embayment (Guanabara Bay, Rio de Janeiro, Brazil). Biogeosciences **12**: 6125–6146. doi:10.5194/bg-12-6125-2015

Cotovicz, L. C., B. A. Knoppers, C. R. Régis, D. Tremmel, S. Costa-Santos, and G. Abril. 2021. Eutrophication overcoming carbonate precipitation in a tropical hypersaline coastal lagoon acting as a CO2 sink (Araruama Lagoon, SE Brazil). Biogeochemistry **156**: 231–254. doi:10.1007/s10533-021-00842-3

Coutantin, M. 2023. Variabilités temporelle et spatiale des échanges de CO_2 atmosphérique en pré-salé tempéré : processus, facteurs de contrôle et potentiel de captation associés. Rapport de Stage d'Initiation à la Recherche et au Développement. 4ème année Master I, Génie Énergétique et Environnement. INSA Lyon.

Crosswell, J. R., I. C. Anderson, J. W. Stanhope, and others. 2017. Carbon budget of a shallow, lagoonal estuary: Transformations and source-sink dynamics along the river-estuary-ocean continuum. Limnology and Oceanography **62**: S29–S45. doi:10.1002/lno.10631

Cui, X., T. Goff, S. Cui, and others. 2021. Predicting carbon and water vapor fluxes using machine learning and novel feature ranking algorithms. Science of The Total Environment **775**: 145130. doi:10.1016/j.scitotenv.2021.145130

- D

Dai, M., Z. Lu, W. Zhai, B. Chen, Z. Cao, K. Zhou, W.-J. Cai, and C.-T. A. Chenc. 2009. Diurnal variations of surface seawater pCO_2 in contrasting coastal environments. Limnol. Oceanogr. **54**: 735–745. doi:10.4319/lo.2009.54.3.0735

Dai, M., J. Su, Y. Zhao, and others. 2022. Carbon Fluxes in the Coastal Ocean: Synthesis, Boundary Processes, and Future Trends. Annu. Rev. Earth Planet. Sci. **50**: 593–626. doi:10.1146/annurev-earth-032320-090746

De Brouwer, J., and L. Stal. 2001. Short-term dynamics in microphytobenthos distribution and associated extracellular carbohydrates in surface sediments of an intertidal mudflat. Mar. Ecol. Prog. Ser. **218**: 33–44. doi:10.3354/meps218033

Deborde, J., P. Anschutz, I. Auby, C. Glé, M.-V. Commarieu, D. Maurer, P. Lecroart, and G. Abril. 2008. Role of tidal pumping on nutrient cycling in a temperate lagoon (Arcachon Bay, France). Marine Chemistry **109**: 98–114. doi:10.1016/j.marchem.2007.12.007

Deegan, L. A., D. S. Johnson, R. S. Warren, B. J. Peterson, J. W. Fleeger, S. Fagherazzi, and W. M. Wollheim. 2012. Coastal eutrophication as a driver of salt marsh loss. Nature **490**: 388–392. doi:10.1038/nature11533

Del Giorgio, P. A., and C. M. Duarte. 2002. Respiration in the open ocean. Nature **420**: 379–384. doi:10.1038/nature01165

Delmer, S. 2022. Dynamique temporelle du carbone au sein d'un marais tidal tempéré. Rapport de stage de L3 Université Paris Est Créteil.

Denman, K. L. et al., 2007. Couplings Between Changes in the Climate System and Biogeochemistry, In: Climate Change 2007: The Physical Science Basis. Contribution of Working Group I to the Fourth Assessment Report of the Intergovernmental Panel on Climate Change [Solomon, S., D. Qin, M. Manning, Z. Chen, M. Marquis, K.B. Averyt, M.Tignor and H.L. Miller (eds.)], Cambridge University Press, Cambridge, United Kingdom and New York, NY, USA, 500-587

Dickson, A. G., and F. J. Millero. 1987. A comparison of the equilibrium constants for the dissociation of carbonic acid in seawater media. *Deep-Sea Research* 34: 1733–1743.

Dickson, A. G. 1990. Standard potential of the reaction: $AgCl(s) + 1/2H_2(g) = Ag(s) + HCl(aq)$, and the standard acidity constant of the ion HSO_4^- in synthetic sea water from 273.15 to 318.15 K. Journal of Chemical Thermodynamics 22: 113–127.

Dickson, A. G., C. L. Sabine, J. R. Christian, C. P. Bargeron, and North Pacific Marine Science Organization, eds. 2007. Guide to best practices for ocean CO_2 measurements, North Pacific Marine Science Organization.

Duarte, C. M., and J. Cebrián. 1996. The fate of marine autotrophic production. Limnol. Oceanogr. **41**: 1758–1766. doi:10.4319/lo.1996.41.8.1758

Duarte, C. M., S. Agustí, P. del Giorgio, and J. J. Cole. 1999. Regional carbon imbalances in the oceans. Science 284:17–35

Duarte, C. M., S. Agustí, J. Arístegui, N. González, and R. Anadón. 2001. Evidence for a heterotrophic subtropical northeast Atlantic. Limnology & Oceanography **46**: 425–428. doi:10.4319/lo.2001.46.2.0425

Duarte, C. M., J. J. Middelburg, and N. Caraco. 2005. Major role of marine vegetation on the oceanic carbon cycle. Biogeosciences 2: 1–8. doi:10.5194/bg-2-1-2005

Duarte, C. M., W. C. Dennison, R. J. W. Orth, and T. J. B. Carruthers. 2008. The charisma of coastal ecosystems: addressing the imbalance. Estuary Coast 31: 233–38

Duarte, C. M., I. J. Losada, I. E. Hendriks, I. Mazarrasa, and N. Marbà. 2013. The role of coastal plant communities for climate change mitigation and adaptation. Nature Clim Change **3**: 961–968. doi:10.1038/nclimate1970

Duarte, B., T., Couto, J., Freitas, J., Valentim, H., Silva, J. C., Marques, J.M., Dias, and I., Caçador. 2013. Abiotic modulation of Spartina maritima photobiology in different latitudinal populations, Estuarine, Coastal and Shelf Science, 130, 127–137, https://doi.org/10.1016/j.ecss.2013.02.008

Duarte, B., D., Santos, H., Silva, J.C., Marques, and I., Caçador. 2014. Photochemical and biophysical feedbacks of C3 and C4 Mediterranean halophytes to atmospheric CO2 enrichment confirmed by their stable isotope signatures, Plant Physiology and Biochemistry, 80, 10–22, https://doi.org/10.1016/j.plaphy.2014.03.016

Dürr, H. H., G. G. Laruelle, C. M. van Kempen, C. P. Slomp, M. Meybeck, and H. Middelkoop. 2011. Worldwide Typology of Nearshore Coastal Systems: Defining the Estuarine Filter of River Inputs to the Oceans. Estuaries and Coasts **34**: 441–458. doi:10.1007/s12237-011-9381-y

- **F**

Foken, T., M. Gockede, M. Mauder, L. Mahrt, B. Amiro, and W. Munger. 2004. POST-FIELD DATA QUALITY CONTROL. HANDBOOK OF MICROMETEOROLOGY 28.

Foken, Th., and B. Wichura. 1996. Tools for quality assessment of surface-based flux measurements. Agricultural and Forest Meteorology **78**: 83–105. doi:10.1016/0168-1923(95)02248-1

Forbrich, I., and A. E. Giblin. 2015. Marsh-atmosphere CO_2 exchange in a New England salt marsh. J. Geophys. Res. Biogeosci. **120**: 1825–1838. doi:10.1002/2015JG003044

Forbrich, I., A. E. Giblin, and C. S. Hopkinson. 2018. Constraining Marsh Carbon Budgets Using Long-Term C Burial and Contemporary Atmospheric CO_2 Fluxes. J. Geophys. Res. Biogeosci. **123**: 867–878. doi:10.1002/2017JG004336

Frankignoulle, M., G. Abril, A. Borges, I. Bourge, C. Canon, B. Delille, E. Libert, and J.-M. Théate. 1998. Carbon Dioxide Emission from European Estuaries. Science, New Series **282**: 434–436.

Frankignoulle, M., R. Biondo, J.-M. Théate, and A. V. Borges. 2003. Carbon dioxide daily variations and atmospheric fluxes over the open waters of the Great Bahama Bank and Norman's Pond using a novel autonomous measuring system, Caribbean Journal of Science, 39, 257-264

Friedlingstein, P., and others. 2019. Global Carbon Budget 2019. Earth Syst. Sci. Data **11**: 1783–1838. doi:10.5194/essd-11-1783-2019

Friis, K., A. Körtzinger, and D. W. R. Wallace. 2003. The salinity normalization of marine inorganic carbon chemistry data. Geophysical Research Letters **30**: 2002GL015898. doi:10.1029/2002GL015898

- **G**

Gash, J. H. C., and A. D. Culf. 1996. Applying a linear detrend to eddy correlation data in realtime. Boundary-Layer Meteorol **79**: 301–306. doi:10.1007/BF00119443

Gattuso, J.-P., M. Frankignoulle, and R. Wollast. 1998. CARBON AND CARBONATE METABOLISM IN COASTAL AQUATIC ECOSYSTEMS. Annu. Rev. Ecol. Syst. **29**: 405–434. doi:10.1146/annurev.ecolsys.29.1.405

Gattuso, J.-P., M. Frankignoulle, and S. V. Smith. 1999. Measurement of community metabolism and significance in the coral reef CO_2 source-sink debate. Proc. Natl. Acad. Sci. U.S.A. **96**: 13017–13022. doi:10.1073/pnas.96.23.13017

Gazeau, F., S. V. Smith, B. Gentili, M. Frankignoulle, and J.-P. Gattuso. 2004. The European coastal zone: characterization and first assessment of ecosystem metabolism. Estuarine, Coastal and Shelf Science **60**: 673–694. doi:10.1016/j.ecss.2004.03.007

Gedan, K. B., B. R. Silliman, and M. D. Bertness. 2009. Centuries of Human-Driven Change in Salt Marsh Ecosystems. Annu. Rev. Mar. Sci. **1**: 117–141. doi:10.1146/annurev.marine.010908.163930

Giblin, A., C. Tobias, B. Song, N. Weston, G. Banta, and V. Rivera-Monroy. 2013. The Importance of Dissimilatory Nitrate Reduction to Ammonium (DNRA) in the Nitrogen Cycle of Coastal Ecosystems. oceanog **26**: 124–131. doi:10.5670/oceanog.2013.54

Gnanamoorthy, P., V. Selvam, P. K. Deb Burman, and others. 2020. Seasonal variations of net ecosystem (CO_2) exchange in the Indian tropical mangrove forest of Pichavaram. Estuarine, Coastal and Shelf Science **243**: 106828. doi:10.1016/j.ecss.2020.106828

Göckede, M., C. Rebmann, and T. Foken. 2004. A combination of quality assessment tools for eddy covariance measurements with footprint modelling for the characterisation of complex sites. Agricultural and Forest Meteorology **127**: 175–188. doi:10.1016/j.agrformet.2004.07.012

Gong, J.-C., B.-H. Li, J.-W. Hu, X.-J. Ding, C.-Y. Liu, and G.-P. Yang. 2023. Tidal effects on carbon dioxide emission dynamics in intertidal wetland sediments. Environmental Research **238**: 117110. doi:10.1016/j.envres.2023.117110

Gran, G. 1952. Determination of the equivalence point in potentiometric titrations. Part II, Analyst, 77, 661-671.

Gu, J., M. Luo, X. Zhang, G. Christakos, S. Agusti, C. M. Duarte, and J. Wu. 2018. Losses of salt marsh in China: Trends, threats and management. Estuarine, Coastal and Shelf Science **214**: 98–109. doi:10.1016/j.ecss.2018.09.015

Guo, H., A. Noormets, B. Zhao, J. Chen, G. Sun, Y. Gu, B. Li, and J. Chen. 2009. Tidal effects on net ecosystem exchange of carbon in an estuarine wetland. Agricultural and Forest Meteorology **149**: 1820–1828. doi:10.1016/j.agrformet.2009.06.010

Guarini, J. M. 1998. Modélisation de la dynamique du microphytobenthos des vasières intertidales du bassin de Marennes-Oléron, Thèse de Doctorat, Université Pierre et Marie Curie, 177 pp

Guarini, J.-M., P. Gros, G. Blanchard, P. Richard, and A. Fillon. 2004. Benthic contribution to pelagic microalgal communities in two semi-enclosed, European-type littoral ecosystems (Marennes-Oléron Bay and Aiguillon Bay, France). Journal of Sea Research **52**: 241–258. doi:10.1016/j.seares.2004.04.003

Guarini, J.-M., N. Sari, and C. Moritz. 2008. Modelling the dynamics of the microalgal biomass in semi-enclosed shallow-water ecosystems. Ecological Modelling **211**: 267–278. doi:10.1016/j.ecolmodel.2007.09.011

- **H**

Han, G., X. Chu, Q. Xing, and others. 2015. Effects of episodic flooding on the net ecosystem CO_2 exchange of a supratidal wetland in the Yellow River Delta. J. Geophys. Res. Biogeosci. **120**: 1506–1520. doi:10.1002/2015JG002923

Hansell, D. A. 2013. Recalcitrant Dissolved Organic Carbon Fractions. Annu. Rev. Mar. Sci. **5**: 421–445. doi:10.1146/annurev-marine-120710-100757

Harrell , F. E. 2015. Regression Modeling Strategies: With Applications to Linear Models, Logistic and Ordinal Regression, and Survival Analysis, Springer International Publishing.

Herbst, M., T. Friborg, K. Schelde, R. Jensen, R. Ringgaard, V. Vasquez, A. G. Thomsen, and H. Soegaard. 2013. Climate and site management as driving factors for the atmospheric greenhouse gas exchange of a restored wetland. Biogeosciences **10**: 39–52. doi:10.5194/bg-10-39-2013

Herrmann, M., R. G. Najjar, W. M. Kemp, and others. 2015. Net ecosystem production and organic carbon balance of U.S. East Coast estuaries: A synthesis approach. Global Biogeochemical Cycles **29**: 96–111. doi:10.1002/2013GB004736

Hill, R., A. Bellgrove, P. I. Macreadie, K. Petrou, J. Beardall, A. Steven, and P. J. Ralph. 2015. Can macroalgae contribute to blue carbon? An Australian perspective: Can macroalgae contribute to blue carbon? Limnol. Oceanogr. **60**: 1689–1706. doi:10.1002/lno.10128

Ho, D. T., V. C. Engel, S. Ferrón, B. Hickman, J. Choi, and J. W. Harvey. 2018. On factors influencing air-water gas exchange in emergent wetlands. Journal of Geophysical Research: Biogeosciences, 123(1), 178–192. https://doi.org/10.1002/2017JG004299

Hopkinson, C. S. 1988. Patterns of organic carbon exchange between coastal ecosystems—the mass balance approach in salt marsh ecosystems. In B.-O. Jansson [ed.], Coastal-offshore ecosystem interactions. Lecture notes on coastal and estuarine studies. Springer.

Hopkinson, C. S., and E. M. Smith. 2005. Estuarine respiration: an overview of benthic, pelagic, and whole system respiration, p. 122–146. *In* P. Del Giorgio and P. Williams [eds.], Respiration in Aquatic Ecosystems. Oxford University Press.

Hopkinson, C. S., and A. E. Giblin. 2008. Nitrogen Dynamics of Coastal Salt Marshes, p. 991–1036. *In* Nitrogen in the Marine Environment. Elsevier.

Hubas, C., D. Davoult, T. Cariou, and L. Artigas. 2006. Factors controlling benthic metabolism during low tide along a granulometric gradient in an intertidal bay (Roscoff Aber Bay, France). Mar. Ecol. Prog. Ser. **316**: 53–68. doi:10.3354/meps316053

Hulot, V., E. Metzger, A. Thibault De Chanvalon, and others. 2023. Impact of an exceptional winter flood on benthic oxygen and nutrient fluxes in a temperate macrotidal estuary: Potential consequences on summer deoxygenation. Front. Mar. Sci. **10**: 1083377. doi:10.3389/fmars.2023.1083377

Hussenot, J. 1998. L'eau et l'aquaculture en marais salé selon le niveau d'intensification : besoins quantitatifs et modifications qualitatives. In: Hussenot J, Buchet, V. (ed) Marais Maritimes et aquaculture. Activité durable pour la préservation et l'exploitation des zones humides littorales. IFREMER, Rochefort, p 278

Hwang, Y.-H., and J. T. Morris. 1994. Whole-plant gas exchange responses of *S partina alterniflora* (Poaceae) to a range of constant and transient salinities. American Journal of Botany **81**: 659–665. doi:10.1002/j.1537-2197.1994.tb15500.x

- **J**

Jähne, B., K. O. Münnich, R. Bösinger, A. Dutzi, W. Huber, and P. Libner. 1987. On the parameters influencing air-water gas exchange. J. Geophys. Res. **92**: 1937. doi:10.1029/JC092iC02p01937

Jeong, H. J., Y. D. Yoo, J. S. Kim, K. A. Seong, N. S. Kang, and T. H. Kim. 2010. Growth, feeding and ecological roles of the mixotrophic and heterotrophic dinoflagellates in marine planktonic food webs. Ocean Sci. J. **45**: 65–91. doi:10.1007/s12601-010-0007-2

Jia, X., T. Zha, S. Wang, C. P.-A. Bourque, B. Wang, S. Qin, and Y. Zhang. 2018. Canopy photosynthesis modulates soil respiration in a temperate semi-arid shrubland at multiple timescales. Plant Soil **432**: 437–450. doi:10.1007/s11104-018-3818-z

Jiang, L.-Q., W.-J. Cai, and Y. Wang. 2008. A comparative study of carbon dioxide degassing in river- and marine-dominated estuaries. Limnol. Oceanogr. **53**: 2603–2615. doi:10.4319/lo.2008.53.6.2603

Jiao, N., G. J. Herndl, D. A. Hansell, and others. 2010. Microbial production of recalcitrant dissolved organic matter: long-term carbon storage in the global ocean. Nat Rev Microbiol **8**: 593–599. doi:10.1038/nrmicro2386

Jimenez, K. L., G. Starr, C. L. Staudhammer, J. L. Schedlbauer, H. W. Loescher, S. L. Malone, and S. F. Oberbauer. 2012. Carbon dioxide exchange rates from short- and long-hydroperiod Everglades freshwater marsh: EVERGLADES MARSH CARBON DYNAMICS. J. Geophys. Res. **117**: n/a-n/a. doi:10.1029/2012JG002117

- **K**

Karl, D. M., D. V. Hebel, K. Björkman, and R. M. Letelier. 1998. The role of dissolved organic matter release in the productivity of the oligotrophic North Pacific Ocean. Limnology & Oceanography **43**: 1270–1286. doi:10.4319/lo.1998.43.6.1270

Kathilankal, J. C., T. J. Mozdzer, J. D. Fuentes, P. D'Odorico, K. J. McGlathery, and J. C. Zieman. 2008. Tidal influences on carbon assimilation by a salt marsh. Environ. Res. Lett. **3**: 044010. doi:10.1088/1748-9326/3/4/044010

Keller, A. A., C. Taylor, C. Oviatt, T. Dorrington, G. Holcombe, and L. Reed. 2001. Phytoplankton production patterns in Massachusetts Bay and the absence of the 1998 winter-spring bloom, Mar. Biol., 138, 1051–1062

King, S. E., and J. N. Lester. 1995. The value of salt marsh as a sea defence. Mar. Poll. Bull. 30:180–89

Kim, Y., M. S. Johnson, S. H. Knox, T. A. Black, H. J. Dalmagro, M. Kang, J. Kim, and D. Baldocchi. 2020. Gap-filling approaches for eddy covariance methane fluxes: A comparison of three machine learning algorithms and a traditional method with principal component analysis. Global Change Biology **26**: 1499–1518. doi:10.1111/gcb.14845

Kljun, N., P. Calanca, M. W. Rotach, and H. P. Schmid. 2015. A simple two-dimensional parameterisation for Flux Footprint Prediction (FFP). Geosci. Model Dev. **8**: 3695–3713. doi:10.5194/gmd-8-3695-2015

Knox, S. H., L. Windham-Myers, F. Anderson, C. Sturtevant, and B. Bergamaschi. 2018. Direct and Indirect Effects of Tides on Ecosystem-Scale CO_2 Exchange in a Brackish Tidal Marsh in Northern California. J. Geophys. Res. Biogeosci. **123**: 787–806. doi:10.1002/2017JG004048

Koné, Y. J. M., G. Abril, K. N. Kouadio, B. Delille, and A. V. Borges. 2009. Seasonal Variability of Carbon Dioxide in the Rivers and Lagoons of Ivory Coast (West Africa). Estuaries and Coasts **32**: 246–260. doi:10.1007/s12237-008-9121-0

Koné, Y. J.-M., and A. V. Borges. 2008. Dissolved inorganic carbon dynamics in the waters surrounding forested mangroves of the Ca Mau Province (Vietnam). Estuarine, Coastal and Shelf Science **77**: 409–421. doi:10.1016/j.ecss.2007.10.001

Koop-Jakobsen, K., and A. E. Giblin. 2010. The effect of increased nitrate loading on nitrate reduction via denitrification and DNRA in salt marsh sediments. Limnology & Oceanography **55**: 789–802. doi:10.4319/lo.2010.55.2.0789

Kostyrka, P. 2021. Dynamique des échanges de CO_2 atmosphérique mesurés par covariance des turbulences et facteurs de contrôle associés dans un marais salé tempéré / Eddy covariance atmospheric CO_2 flux dynamic and associated controlling factors in a temperate salt marsh. Mémoire de Master Sciences de la Mer. Université Sorbonne.

Kowalski, S., M. Sartore, R. Burlett, P. Berbigier, and D. Loustau. 2003. The annual carbon budget of a French pine forest (*Pinus pinaster*) following harvest: ANNUAL CARBON BUDGET OF A PINE FOREST AFTER HARVEST. Global Change Biology **9**: 1051–1065. doi:10.1046/j.1365-2486.2003.00627.x

Krauss, K. W., G. O. Holm, B. C. Perez, and others. 2016. Component greenhouse gas fluxes and radiative balance from two deltaic marshes in Louisiana: Pairing chamber techniques and eddy covariance: Gas Fluxes From Louisiana Marshes. J. Geophys. Res. Biogeosci. **121**: 1503–1521. doi:10.1002/2015JG003224

Krause-Jensen, D., and C. M. Duarte. 2016. Substantial role of macroalgae in marine carbon sequestration. Nature Geosci **9**: 737–742. doi:10.1038/ngeo2790

Kristensen, E., S. Bouillon, T. Dittmar, and C. Marchand. 2008. Organic carbon dynamics in mangrove ecosystems: A review. Aquatic Botany **89**: 201–219. doi:10.1016/j.aquabot.2007.12.005

Kroeger, K., and others. 2012. Fluxes in tidal wetlands, p. 10– 11. In R. G. Najjar, M.A.M. Friedrichs and W.-J. Cai [eds.], Report of the U.S. East Coast carbon cycle synthesis workshop. January 19-20, 2012. Ocean Carbon and Biogeochemistry Program and North American Carbon Program.

Krumins, V., M. Gehlen, S. Arndt, P. Van Cappellen, and P. Regnier. 2013. Dissolved inorganic carbon and alkalinity fluxes from coastal marine sediments: model estimates for different shelf environments and sensitivity to global change. Biogeosciences **10**: 371–398. doi:10.5194/bg-10-371-2013

- **L**

Labasque, T., C. Chaumery, A. Aminot, and G. Kergoat. 2004. Spectrophotometric Winkler determination of dissolved oxygen: re-examination of critical factors and reliability. Marine Chemistry **88**: 53–60. doi:10.1016/j.marchem.2004.03.004

Lasslop, G., M. Reichstein, D. Papale, A. D. Richardson, A. Arneth, A. Barr, P. Stoy, and G. Wohlfahrt. 2010. Separation of net ecosystem exchange into assimilation and respiration using a light response curve approach: critical issues and global evaluation: SEPARATION OF NEE INTO GPP AND RECO. Global Change Biology **16**: 187–208. doi:10.1111/j.1365-2486.2009.02041.x.

Laws, E. A. 1991. Photosynthetic quotients, new production and net community production in the open ocean. Deep Sea Research Part A. Oceanographic Research Papers **38**: 143–167. doi:10.1016/0198-0149(91)90059-O

Lee, K., Kim, T.-W., Byrne, R.H., Millero, F.J., Feely, R.A., Liu, Y.-M., 2010. The universal ratio of boron to chlorinity for the North Pacific and North Atlantic oceans Geochimica et Cosmochimica Acta 74, 1801–1811. https://doi.org/10.1016/j.gca.2009.12.027

Lee, S.-C., C.-J. Fan, Z.-Y. Wu, and J.-Y. Juang. 2015. Investigating effect of environmental controls on dynamics of CO_2 budget in a subtropical estuarial marsh wetland ecosystem. Environ. Res. Lett. **10**: 025005. doi:10.1088/1748-9326/10/2/025005

Lee, J. Y. et al., 2021. Future Global Climate: Scenario-Based Projections and Near- Term Information. In Climate Change 2021. The Physical Science Basis. Contribution of Working Group I to the Sixth Assessment Report of the Intergovernmental Panel on Climate Change [Masson-Delmotte, V., P. Zhai, A. Pirani, S.L. Connors, C. Péan, S. Berger, N. Caud, Y. Chen, L. Goldfarb, M.I. Gomis, M. Huang, K. Leitzell, E. Lonnoy, J.B.R. Matthews, T.K. Maycock, T. Waterfield, O. Yelekçi, R. Yu, and B. Zhou (eds.)]. Cambridge University Press, Cambridge, United Kingdom and New York, NY, USA, pp. 553–672, doi:10.1017/9781009157896.006.

Le Fur, I., R. De Wit, M. Plus, J. Oheix, M. Simier, and V. Ouisse. 2018. Submerged benthic macrophytes in Mediterranean lagoons: distribution patterns in relation to water chemistry and depth. Hydrobiologia **808**: 175–200. doi:10.1007/s10750-017-3421-y

Lê, S., J. Josse, and F. Husson. 2008. **FactoMineR** : An *R* Package for Multivariate Analysis. J. Stat. Soft. **25**. doi:10.18637/jss.v025.i01

Lewis, E. and D. Wallace. 1998. Program developed for CO_2 system calculations. Carbon dioxide information analysis center. Oak Ridge National Laboratory

Liaw, A. and M. Wiener. 2022. Classification and Regression by randomForest. R news 2, 18–22

Liu, Y., J. J. Jiao, W. Liang, and X. Luo. 2017. Tidal Pumping-Induced Nutrients Dynamics and Biogeochemical Implications in an Intertidal Aquifer. JGR Biogeosciences **122**: 3322–3342. doi:10.1002/2017JG004017

Lønborg, C., C. Carreira, T. Jickells, and X. A. Álvarez-Salgado. 2020. Impacts of Global Change on Ocean Dissolved Organic Carbon (DOC) Cycling. Front. Mar. Sci. **7**: 466. doi:10.3389/fmars.2020.00466

Lorrain, A., N. Savoye, L. Chauvaud, Y.-M. Paulet, and N. Naulet. 2003. Decarbonation and preservation method for the analysis of organic C and N contents and stable isotope ratios of low-carbonated suspended particulate material. Analytica Chimica Acta **491**: 125–133. doi:10.1016/S0003-2670(03)00815-8

Luo, M., J.-F. Huang, W.-F. Zhu, and C. Tong. 2017. Impacts of increasing salinity and inundation on rates and pathways of organic carbon mineralization in tidal wetlands: a review. Hydrobiologia **827**: 31–49. doi:10.1007/s10750-017-3416-8

- **M**

Macreadie, P. I., Q. R. Ollivier, J. J. Kelleway, and others. 2017. Carbon sequestration by Australian tidal marshes. Sci Rep **7**: 44071. doi:10.1038/srep44071

Macreadie, P.I., Nielsen, D.A., Kelleway, J.J., Atwood, T.B., Seymour, J.R., Petrou, K., Connolly, R.M., Thomson, A.C., Trevathan-Tackett, S.M., Ralph, P.J., 2017. Can we manage coastal ecosystems to sequester more blue carbon? 8. https://doi.org/10.1002/fee.1484

Maltby, E., D. V. Hogan and, R. J. McInnes. 1996. Functional Analysis of European Wetland Ecosystems Phase 1 (FAEWE): The Function of River Marginal Wetland Ecosystems; Improving the Science Base for the Development of Procedures of Functional Analysis; Final Report EC DG XII STEP-CT90- 0084. Ecosystems Research Report 18. Luxembourg: Off. for Official Publ. of the European Communities

Marchand, C., J. R. Disnar, E. Lallier-Vergès, and N. Lottier. 2005. Early diagenesis of carbohydrates and lignin in mangrove sediments subject to variable redox conditions (French Guiana). Geochimica et Cosmochimica Acta **69**: 131–142. doi:10.1016/j.gca.2004.06.016

Masclaux, H., S. Tortajada, O. Philippine, F.-X. Robin, and C. Dupuy. 2015. Planktonic food web structure and dynamic in freshwater marshes after a lock closing in early spring. Aquat Sci **77**: 115–128. doi:10.1007/s00027-014-0376-1

Mayen, J. 2019. Variabilité temporelle des pressions partielles de CO_2 dans l'eau et flux eau-atmosphère associés au niveau des marais du Fier d'Ars (île de Ré). https://archimer.ifremer.fr/doc/00505/61678/

Mayen, J. 2020. Spatial and temporal variations in pCO_2 and atmospheric CO_2 exchanges in a temperate salt marsh system. Master's degree 2 internship report: Chemistry and Life Sciences, speciality Molecular Biology and Environmental Microbiology. https://archimer.ifremer.fr/doc/00636/74772/

Mayen, J., P. Polsenaere, A. Regaudie De Gioux, C. Dupuy, M. Vagner, J.-C. Lemesle, B. Poitevin, and P. Souchu. 2023. Influence of typology and management practices on water pCO_2 and atmospheric CO_2 fluxes over two temperate shelf–estuary–marsh water continuums. Regional Studies in Marine Science **67**: 103209. doi:10.1016/j.rsma.2023.103209

Mayen, J., Polsenaere, P., Lamaud, É., Arnaud, M., Kostyrka, P., Bonnefond, J.-M., Geairon, P., Gernigon, J., Chassagne, R., Lacoue-Labarthe, T., Regaudie de Gioux, A., and P. Souchu. 2024. Atmospheric CO_2 exchanges measured by eddy covariance over a temperate salt marsh and influence of environmental controlling factors, Biogeosciences, 21(4), 993-1016. Publisher's official version: https://doi.org/10.5194/bg-21-993-2024, Open Access version: https://archimer.ifremer.fr/doc/00882/99396/

McGillis, W. R., J. B. Edson, Hare, J. E., and C. W. Fairall. 2001. Direct covariance air-sea CO_2 fluxes. Journal of Geophysical Research, 106(C8), 16,729–16,745. https://doi.org/10.1029/2000JC000506

McGlathery, K. J., K. Sundbäck, and I. C. Anderson. 2004. The Importance Of Primary Producers For Benthic Nitrogen And Phosphorus Cycling In Nielsen, S. L., G. T. Banta, & M. F. Pedersen (eds), Estuarine Nutrient Cycling: The Influence of Primary Producers. Springer Netherlands: 231–261.

Mcleod, E., G. L. Chmura, S. Bouillon, and others. 2011. A blueprint for blue carbon: toward an improved understanding of the role of vegetated coastal habitats in sequestering CO2. Frontiers in Ecology and the Environment **9**: 552–560. doi:10.1890/110004

Mcowen, C., L. Weatherdon, J.-W. Bochove, and others. 2017. A global map of saltmarshes. BDJ **5**: e11764. doi:10.3897/BDJ.5.e11764

Mehrbach, C., C. H. Culberson, J. E. Hawley, and R. M. Pytkowicz. 1973. Measurement of the Apparent Dissociation Constants of Carbonic Acid in Seawater at Atmospheric Pressure. Limnology and Oceanography **18**: 897–907.

Meybeck, M. 1993. Riverine transport of atmospheric carbon: sources, global typology and budget. Water Air Soil Pollut. 70:443–63

Middelburg, J. J., K. Soetaert, and M. Hagens. 2020. Ocean Alkalinity, Buffering and Biogeochemical Processes. Reviews of Geophysics **58**: e2019RG000681. doi:10.1029/2019RG000681

Migné, A., N. Spilmont, and D. Davoult. 2004. In situ measurements of benthic primary production during emersion: seasonal variations and annual production in the Bay of Somme (eastern English Channel, France). Continental Shelf Research **24**: 1437–1449. doi:10.1016/j.csr.2004.06.002

Migné, A., F. Gévaert, A. Créach, N. Spilmont, E. Chevalier, and D. Davoult. 2007. Photosynthetic activity of intertidal microphytobenthic communities during emersion: in situ measurements of chlorophyll fluorescence (PAM) and CO_2 flux (IRGA) [1]. Journal of Phycology **43**: 864–873. doi:10.1111/j.1529-8817.2007.00379.x

Miller, W. D., S. C. Neubauer, and I. C. Anderson. 2001. Effects of Sea Level Induced Disturbances on High Salt Marsh Metabolism. Estuaries **24**: 357. doi:10.2307/1353238

Mitra, B., G. Miao, K. Minick, S. G. McNulty, G. Sun, M. Gavazzi, J. S. King, and A. Noormets. 2019. Disentangling the Effects of Temperature, Moisture, and Substrate Availability on Soil CO_2 Efflux. J. Geophys. Res. Biogeosci. **124**: 2060–2075. doi:10.1029/2019JG005148

Mitsch, W. J., and J. G. Gosselink. 2015. Tidal Marshes. Wetlands, 5th ed. Wiley, Hoboken, 259 310

Moeller, I., T. Spencer, and J. R. French. 1996. Wind wave attenuation over saltmarsh surfaces: Preliminary results from Norfolk, England. J. Coast. Res. 12:1009–16

Moncrieff, J., R. Clement, J. Finnigan, and T. Meyers. 2004. Averaging, Detrending, and Filtering of Eddy Covariance Time Series, p. 7–31. *In* X. Lee, W. Massman, and B. Law [eds.], Handbook of Micrometeorology. Kluwer Academic Publishers.

Moran, M., and R. Hodson. 1990. Contributions of degrading Spartina alterniflora lignocellulose to the dissolved organic carbon pool of a salt marsh. Mar. Ecol. Prog. Ser. **62**: 161–168. doi:10.3354/meps062161

Morelle, J., C. Roose-Amsaleg, and A. M. Laverman. 2022. Microphytobenthos as a source of labile organic matter for denitrifying microbes. Estuarine, Coastal and Shelf Science **275**: 108006. doi:10.1016/j.ecss.2022.108006

Moffett, K. B., A. Wolf, J. A. Berry, and S. M. Gorelick. 2010. Salt marsh–atmosphere exchange of energy, water vapor, and carbon dioxide: Effects of tidal flooding and biophysical controls. Water Resour. Res. **46**: 2009WR009041. doi:10.1029/2009WR009041

Morris, J. T. 1984. Effects of oxygen and salinity on ammonium uptake by Spartina alterniflora Loisel. and Spartina patens (Aiton) Muhl. Journal of Experimental Marine Biology and Ecology **78**: 87–98. doi:https://doi.org/10.1016/0022-0981(84)90071-6

- **N**

Nahrawi, H. 2019. Exchange of Carbon Dioxide between a Southeastern Salt Marsh and the Atmosphere. Ph.D thesis. The University of Georgia.

Nahrawi, H., M. Y. Leclerc, S. Pennings, G. Zhang, N. Singh, and R. Pahari. 2020. Impact of tidal inundation on the net ecosystem exchange in daytime conditions in a salt marsh. Agricultural and Forest Meteorology **294**: 108133. doi:10.1016/j.agrformet.2020.108133

Najjar, R. G., M. Herrmann, R. Alexander, and others. 2018. Carbon Budget of Tidal Wetlands, Estuaries, and Shelf Waters of Eastern North America. Global Biogeochem. Cycles **32**: 389–416. doi:10.1002/2017GB005790

Navarro, N., S. Agustí, and C. Duarte. 2004. Plankton metabolism and dissolved organic carbon use in the Bay of Palma, NW Mediterranean Sea. Aquat. Microb. Ecol. **37**: 47–54. doi:10.3354/ame037047

Newton, C., and C. Thornber. 2013. Ecological Impacts of Macroalgal Blooms on Salt Marsh Communities. Estuaries and Coasts **36**: 365–376. doi:10.1007/s12237-012-9565-0

Nixon, S. W., S. L. Granger, and B. L. Nowicki. 1995. An assessment of the annual mass balance of carbon, nitrogen, and phosphorus in Narragansett Bay. Biogeochemistry **31**. doi:10.1007/BF00000805

Nyman, J. A., and R. D. DeLaune. 1991. CO_2 emission and soil Eh responses to different hydrological conditions in fresh, brackish, and saline marsh soils. Limnol. Oceanogr. **36**: 1406–1414. doi:10.4319/lo.1991.36.7.1406

- **O**

Oakes, J. M., and B. D. Eyre. 2014. Transformation and fate of microphytobenthos carbon in subtropical, intertidal sediments: potential for long-term carbon retention revealed by ^{13}C-labeling. Biogeosciences **11**: 1927–1940. doi:10.5194/bg-11-1927-2014

Oksanen, J., F. G. Blanchet, M. Friendly, R. Kindt, P. Legendre, D. McGlinn, P. R. Minchin, R. B. O'Hara, G. L. Simpson, P. Solymos, M. Henry, H. Stevens, E. Szoecs, and H. Wagner. 2019. Vegan: Community ecology package. R Package Version 2.5-6.

Odum, W. E. 1988. Comparative ecology of tidal freshwater and salt marshes. Annu. Rev. Ecol. Syst. 19, 147–176.

Odum, E. P., Finn, J. T. and Franz, E. H. 1979. Perturbation Theory and the Subsidy-Stress Gradient, BioScience, https://doi.org/10.2307/1307690

Ouisse, V., A. Migné, and D. Davoult. 2011. Community-level carbon flux variability over a tidal cycle in Zostera marina and Z. noltii beds. Mar. Ecol. Prog. Ser. **437**: 79–87. doi:10.3354/meps09274

Oustin, D. 2003. Étude et cartographie de la végétation des marais salés de l'anse d'Yffiniac. Réserve naturelle nationale de la Baie de Saint-Brieuc, Université de Rennes I. Rapport : 63 p.

- **P**

Palacios, M. M., S. M. Trevathan-Tackett, M. E. Malerba, and P. I. Macreadie. 2021. Effects of a nutrient enrichment pulse on blue carbon ecosystems. Marine Pollution Bulletin **165**: 112024. doi:10.1016/j.marpolbul.2021.112024

Parkhurst, D. L., and C. A. J. Appelo. 2013. Description of input and examples for PHREEQC version 3—A computer program for speciation, batch-reaction, one-dimensional transport, and inverse geochemical calculations: U.S. Geological Survey Techniques and Methods, book 6, chap. A43, 497 p., available only at http://pubs.usgs.gov/tm/06/a43/

Papale, D., M. Reichstein, M. Aubinet, and others. 2006. Towards a standardized processing of Net Ecosystem Exchange measured with eddy covariance technique: algorithms and uncertainty estimation. Biogeosciences **3**: 571–583. doi:10.5194/bg-3-571-2006

Paticat, F. 2007. Flux et usages de l'eaude mer dans les marais salés endigués Charentais: Cas du marais salé endigué de l'île de Ré. Thèse. Nantes.

Pery, C. 2023. Dynamique des échanges de CO_2 atmosphérique à grande échelle en limite pré-salé - vasière d'une baie intertidale tempérée. Rapport de stage. Master 1 en Science de l'eau. Université de Pau et des Pays de l'Adour

Pernetta, J. C., and J. D. Milliman. 1995. Land-Ocean interactions in the coastal zone. Implementation plan, IGPB Rep., 33, 1-215

Pétillon, J., E. McKinley, M. Alexander, and others. 2023. Top ten priorities for global saltmarsh restoration, conservation and ecosystem service research. Science of The Total Environment **898**: 165544. doi:10.1016/j.scitotenv.2023.165544

Petton, S., F. Pernet, V. Le Roy, and others. 2024. French coastal network for carbonate system monitoring: the CocoriCO2 dataset. Earth Syst. Sci. Data 16: 1667–1688. doi:10.5194/essd-16-1667-2024

Pennock, J. R. 1985. Chlorophyll distributions in the Delaware estuary: Regulation by light-limitation, Estuar. Coast. Shelf S., 21, 711–725.

Philippe, A., C. Plumejeaud-Perreau, J. Jourde, P. Pineau, N. Lachaussée, E. Joyeux, F. Corre, P. Delaporte and, P. Bocher. 2017. Building a database for long-term monitoring of benthic macrofauna in the Pertuis- Charentais (2004-2014). Biodiversity Data Journal. 5:e10288

Polsenaere, P. 2011. Echanges de CO_2 atmosphérique dans la lagune d'Arcachon et relations avec le métabolisme intertidal. Biogéochimie et Ecosystèmes. Université de Bordeaux I.

Polsenaere, P., E. Lamaud, V. Lafon, J.-M. Bonnefond, P. Bretel, B. Delille, J. Deborde, D. Loustau and G. Abril. 2012. Spatial and temporal CO_2 exchanges measured by Eddy Covariance over a temperate intertidal flat and their relationships to net ecosystem production. Biogeosciences **9**: 249–268. doi:10.5194/bg-9-249-2012

Polsenaere, P., J. Deborde, G. Detandt, L. O. Vidal, M. A. P. Pérez, V. Marieu, and G. Abril. 2013. Thermal enhancement of gas transfer velocity of CO_2 in an Amazon floodplain lake revealed by eddy covariance measurements: GAS TRANSFER VELOCITY IN AN AMAZON LAKE. Geophys. Res. Lett. **40**: 1734–1740. doi:10.1002/grl.50291

Polsenaere, P., P. Soletchnik, O. Le Moine, and others. 2017. Potential environmental drivers of a regional blue mussel mass mortality event (winter of 2014, Breton Sound, France). Journal of Sea Research **123**: 39–50. doi:10.1016/j.seares.2017.03.005

Polsenaere, P., B. Delille, D. Poirier, C. Charbonnier, J. Deborde, A. Mouret, and G. Abril. 2022. Seasonal, Diurnal, and Tidal Variations of Dissolved Inorganic Carbon and pCO_2 in Surface Waters of a Temperate Coastal Lagoon (Arcachon, SW France). Estuaries and Coasts. doi:10.1007/s12237-022-01121-6

Polsenaere, P. 2022. Dynamique à grande échelle des échanges de CO_2 atmosphérique au sein de la zone côtière des Pertuis Charentais. Colloque de restitution du projet LIFE Baie de l'Aiguillon : Restauration et de préservation des espaces littoraux. 6 et 7 avril 2022, La Rochelle.

Polsenaere Pierre (2018). Rôle des marais littoraux dans les budgets de Carbone : processus et flux associés. Colloque international « Adaptation des marais littoraux au changement climatique ». 27, 28 et 29 novembre 2018, La Rochelle.

- **R**

Ragotzkie, R. A. 1959. Plankton productivity in estuarine waters of Georgia. Publ. Inst. Mar. Sci. Univ. Texas 6: 146–158

Rassmann, J., E. M. Eitel, B. Lansard, C. Cathalot, C. Brandily, M. Taillefert, and C. Rabouille. 2020. Benthic alkalinity and dissolved inorganic carbon fluxes in the Rhône River prodelta generated by decoupled aerobic and anaerobic processes. Biogeosciences **17**: 13–33. doi:10.5194/bg-17-13-2020

Raven, J. 2018. Blue carbon: past, present and future, with emphasis on macroalgae. Biol. Lett. **14**: 20180336. doi:10.1098/rsbl.2018.0336

Raymond, P. A., and J. J. Cole. 2001. Gas Exchange in Rivers and Estuaries: Choosing a Gas Transfer Velocity. Estuaries **24**: 312. doi:10.2307/1352954

Redfield, A. C. 1958. The biological control of chemical factors in the environment, Am. Sci., 46, 205–221

Regaudie-de-Gioux, A., and C. M. Duarte. 2012. Temperature dependence of planktonic metabolism in the ocean. Global Biogeochemical Cycles **26**: 2010GB003907. doi:10.1029/2010GB003907

Reichstein, M., E. Falge, D. Baldocchi, and others. 2005. On the separation of net ecosystem exchange into assimilation and ecosystem respiration: review and improved algorithm. Global Change Biol **11**: 1424–1439. doi:10.1111/j.1365-2486.2005.001002.x

Reithmaier, G. M. S., A. Cabral, A. Akhand, and others. 2023. Carbonate chemistry and carbon sequestration driven by inorganic carbon outwelling from mangroves and saltmarshes. Nat Commun **14**: 8196. doi:10.1038/s41467-023-44037-w

REPHY – French Observation and Monitoring program for Phytoplankton and Hydrology in coastal waters. 2021. REPHY dataset - French Observation and Monitoring program for Phytoplankton and Hydrology in coastal waters. Metropolitan data. SEANOE. https://doi.org/10.17882/47248

Reynolds, O. 1883. An Experimental Investigation of the Circumstances Which Determine Whether the Motion of Water Shall Be Direct or Sinuous, and of the Law of Resistance in Parallel Channels. Philosophical Transactions of the Royal Society of London **17**: 935–982.

Ribas-Ribas, M., A. Gómez-Parra, and J. M. Forja. 2011. Air–sea CO_2 fluxes in the north-eastern shelf of the Gulf of Cádiz (southwest Iberian Peninsula). Marine Chemistry **123**: 56–66. doi:10.1016/j.marchem.2010.09.005

Riley, G., 1967. The plankton of estuaries, in: Estuaries, edited by: Lauff, G., American Association for the Advancement of Science, Publication, No. 83, Washington, DC, 316–328.

Rodda, S., K. Thumaty, C. Jha, and V. Dadhwal. 2016. Seasonal Variations of Carbon Dioxide, Water Vapor and Energy Fluxes in Tropical Indian Mangroves. Forests **7**: 35. doi:10.3390/f7020035

Ruttenberg, K. C. 1992. Development of a sequential extraction method for different forms of phosphorus in marine sediments, Limnology & Oceanography, 37, 1460–1482, https://doi.org/10.4319/lo.1992.37.7.1460

- **S**

Saderne, V., K. Baldry, A. Anton, S. Agustí, and C. M. Duarte. 2019. Characterization of the CO_2 System in a Coral Reef, a Seagrass Meadow, and a Mangrove Forest in the Central Red Sea. JGR Oceans **124**: 7513–7528. doi:10.1029/2019JC015266

Sand-Jensen, K., and J. Borum. 1991. Interactions among phytoplankton, periphyton, and macrophytes in temperate freshwaters and estuaries. Aquatic Botany **41**: 137–175. doi:10.1016/0304-3770(91)90042-4

Santos, I. R., W. C. Burnett, T. Dittmar, I. G. N. A. Suryaputra, and J. Chanton. 2009. Tidal pumping drives nutrient and dissolved organic matter dynamics in a Gulf of Mexico subterranean estuary. Geochimica et Cosmochimica Acta **73**: 1325–1339. doi:10.1016/j.gca.2008.11.029

Santos, I. R., D. T. Maher, R. Larkin, J. R. Webb, and C. J. Sanders. 2019. Carbon outwelling and outgassing vs. burial in an estuarine tidal creek surrounded by mangrove and saltmarsh wetlands. Limnology & Oceanography **64**: 996–1013. doi:10.1002/lno.11090

Savelli, R., X. Bertin, F. Orvain, and others. 2019. Impact of Chronic and Massive Resuspension Mechanisms on the Microphytobenthos Dynamics in a Temperate Intertidal Mudflat. J. Geophys. Res. Biogeosci. **124**: 3752–3777. doi:10.1029/2019JG005369

Savelli, R., C. Dupuy, L. Barillé, and others. 2018. On biotic and abiotic drivers of the microphytobenthos seasonal cycle in a temperate intertidal mudflat: a modelling study. Biogeosciences **15**: 7243–7271. doi:10.5194/bg-15-7243-2018

Savoye, N., A. Aminot, P. Tréguer, M. Fontugne, N. Naulet, and R. Kérouel. 2003. Dynamics of particulate organic matter d15N and d13C during spring phytoplankton blooms in a macrotidal ecosystem (Bay of Seine, France). Mar. Ecol. Prog. Ser. **255**: 27–41. doi:10.3354/meps255027

Schäfer, K. V. R., R. Tripathee, F. Artigas, T. H. Morin, and G. Bohrer. 2014. Carbon dioxide fluxes of an urban tidal marsh in the Hudson-Raritan estuary: Carbon dioxide fluxes of an wetland. J. Geophys. Res. Biogeosci. **119**: 2065–2081. doi:10.1002/2014JG002703

Schäfer, K. V. R., T. Duman, K. Tomasicchio, R. Tripathee, and C. Sturtevant. 2019. Carbon dioxide fluxes of temperate urban wetlands with different restoration history. Agricultural and Forest Meteorology **275**: 223–232. doi:10.1016/j.agrformet.2019.05.026

Schiebel, H. N., G. B. Gardner, X. Wang, F. Peri, and R. F. Chen. 2018. Seasonal Export of Dissolved Organic Matter from a New England Salt Marsh. Journal of Coastal Research **344**: 939–954. doi:10.2112/JCOASTRES-D-16-00196.1

Schramm, W. 1999. Factors influencing seaweed responses to eutrophication: some results from EU-project EUMAC. Journal of applied Phycology 11: 69–78.

Schramm, W., and P. Nienhuis. 1996. Marine Benthic Vegetation: Recent Changes and the Effects of Eutrophication. Springer, NewYork.

Shen, Y., and R. Benner. 2018. Mixing it up in the ocean carbon cycle and the removal of refractory dissolved organic carbon. Sci Rep **8**: 2542. doi:10.1038/s41598-018-20857-5

Soletchnik, P., P. Polsenaere, O. Le Moine, S. Guesdon, and C. Bechemin. 2014. Interactions between river freshwater inputs and the shellfish farming (oysters and mussels) in the Pertuis Charentais (France).

Song, S., Z. A. Wang, K. D. Kroeger, M. Eagle, S. N. Chu, and J. Ge. 2023. High-frequency variability of carbon dioxide fluxes in tidal water over a temperate salt marsh. Limnology & Oceanography **68**: 2108–2125. doi:10.1002/lno.12409

Sousa, A. I., A. I. Lillebø, M. A. Pardal, and I. Caçador. 2010. Productivity and nutrient cycling in salt marshes: Contribution to ecosystem health. Estuarine, Coastal and Shelf Science **87**: 640–646. doi:10.1016/j.ecss.2010.03.007

Stanisiere, J.-Y., F. Dumas, M. Plus, D. Maurer, and S. Robert. 2006. Hydrodynmaic characterization of a semi-enclosed coastal system : Marennes Oleron (France) basin. Rapport.

Stoecker, D. K. 1999. Mixotrophy among Dinoflagellates1. J Eukaryotic Microbiology **46**: 397–401. doi:10.1111/j.1550-7408.1999.tb04619.x

Sun, M.-Y., C. Lee, and R. C. Aller. 1993. Laboratory studies of oxic and anoxic degradation of chlorophyll-a in Long Island Sound sediments. Geochimica et Cosmochimica Acta **57**: 147–157. doi:10.1016/0016-7037(93)90475-C

- **T**

Takahashi, T., S. C. Sutherland, C. Sweeney, and others. 2002. Global sea–air CO2 flux based on climatological surface ocean pCO2, and seasonal biological and temperature effects. Deep Sea Research Part II: Topical Studies in Oceanography **49**: 1601–1622. doi:10.1016/S0967-0645(02)00003-6

Teichberg, M., S. E. Fox, Y. S. Olsen, and others. 2010. Eutrophication and macroalgal blooms in temperate and tropical coastal waters: nutrient enrichment experiments with *Ulva* spp. Global Change Biology **16**: 2624–2637. doi:10.1111/j.1365-2486.2009.02108.x

Tobias, C., Neubauer, S.C., 2019. Salt Marsh Biogeochemistry—An Overview, in: Coastal Wetlands. Elsevier, pp. 539–596. https://doi.org/10.1016/B978-0-444-63893-9.00016-2

Tortajada, S. 2011. De l'étude du fonctionnement des réseaux trophiques planctoniques des marais de Charente Maritime vers la recherche d'indicateurs. Océanologie Biologie et Environnement Marin. Université de La Rochelle.

Tortajada, S., V. David, A. Brahmia, and others. 2011. Variability of fresh- and salt-water marshes characteristics on the west coast of France: A spatio-temporal assessment. Water Research **45**: 4152–4168. doi:10.1016/j.watres.2011.05.024

- **U**

Upstill-Goddard, R. C. 2006. Air–sea gas exchange in the coastal zone. Estuarine, Coastal and Shelf Science **70**: 388–404. doi:10.1016/j.ecss.2006.05.043

Uterm¨ohl, H. 1958. Zur vervollkommnung der quantitativen phytoplankton methodik. Mitteilungen-Internationale Vereiningung fur Limnologie. 9, 1–38.

- **V**

Van Boekel, W., F. Hansen, R. Riegman, and R. Bak. 1992. Lysis-induced decline of a Phaeocystis spring bloom and coupling with the microbial foodweb. Mar. Ecol. Prog. Ser. **81**: 269–276. doi:10.3354/meps081269

Van Dam, B., P. Polsenaere, A. Barreras-Apodaca, and others. 2021. Global Trends in Air-Water CO_2 Exchange Over Seagrass Meadows Revealed by Atmospheric Eddy Covariance. Global Biogeochem Cycles **35**. doi:10.1029/2020GB006848

Van Dam, B. R., J. B. Edson, and C. Tobias. 2019. Parameterizing Air-Water Gas Exchange in the Shallow, Microtidal New River Estuary. J. Geophys. Res. Biogeosci. **124**: 2351–2363. doi:10.1029/2018JG004908

Vandermeirsch, F. 2012. ÉTAT PHYSIQUE ET CHIMIQUE Caractéristiques physiques.

Vargas, R., D. D. Baldocchi, M. Bahn, P. J. Hanson, K. P. Hosman, L. Kulmala, J. Pumpanen, and B. Yang. 2011. On the multi-temporal correlation between photosynthesis and soil CO_2 efflux: reconciling lags and observations. New Phytologist **191**: 1006–1017. doi:10.1111/j.1469-8137.2011.03771.x

Verger, F. (ed) (2005) Marais et estuaires du littoral français, Paris, France

Vickers, D., and L. Mahrt. 1997. Quality Control and Flux Sampling Problems for Tower and Aircraft Data. J. Atmos. Oceanic Technol. **14**: 512–526. doi:10.1175/1520-0426(1997)014<0512:QCAFSP>2.0.CO;2

- **W**

Wang, Q., C. H. Wang, B. Zhao, Z. J. Ma, Y. Q. Luo, J. K. Chen, and B. Li. 2006. Effects of growing conditions on the growth of and interactions between salt marsh plants: implications for invasibility of habitats. Biol Invasions **8**: 1547–1560. doi:10.1007/s10530-005-5846-x

Wang, S. R., D. Di Iorio, W. Cai, and C. S. Hopkinson. 2018. Inorganic carbon and oxygen dynamics in a marsh-dominated estuary. Limnol. Oceanogr. **63**: 47–71. doi:10.1002/lno.10614

Wang, X., R. F. Chen, J. E. Cable, and J. Cherrier. 2014. Leaching and microbial degradation of dissolved organic matter from salt marsh plants and seagrasses. Aquat Sci **76**: 595–609. doi:10.1007/s00027-014-0357-4

Wang, Z. A., and W.-J. Cai. 2004. Carbon dioxide degassing and inorganic carbon export from a marsh-dominated estuary (the Duplin River): A marsh CO_2 pump. Limnol. Oceanogr. **49**: 341–354. doi:10.4319/lo.2004.49.2.0341

Wang, Z. A., K. D. Kroeger, N. K. Ganju, M. E. Gonneea, and S. N. Chu. 2016. Intertidal salt marshes as an important source of inorganic carbon to the coastal ocean. Limnol. Oceanogr. **61**: 1916–1931. doi:10.1002/lno.10347

Wanninkhof, R., and W. R. Mcgillis. 1999. A cubic relationship between air-sea CO_2 exchange and wind speed. Geophysical Research Letters, 26(13), 1889–1892. https://doi.org/10.1029/1999GL900363

Wanninkhof, R., D. Pierrot, K. Sullivan, P. Mears, and L. Barbero. 2022. Comparison of discrete and underway CO_2 measurements: Inferences on the temperature dependence of the fugacity of CO_2 in seawater. Marine Chemistry **247**: 104178. doi:10.1016/j.marchem.2022.104178

Wei, T., Simko, V., 2017. R package "corrplot": Visualization of a Correlation Matrix. https://github.com/taiyun/corrplot

Wei, S., G. Han, X. Jia, W. Song, X. Chu, W. He, J. Xia, and H. Wu. 2020. Tidal effects on ecosystem CO_2 exchange at multiple timescales in a salt marsh in the Yellow River Delta. Estuarine, Coastal and Shelf Science **238**: 106727. doi:10.1016/j.ecss.2020.106727

Wiebe, W. J., R. R. Christian, J. A. Hansen, G. King, B. Sherr, and G. Skyring. 1981. Anaerobic respiration and fermentation, p. 137–159. In L. R. Pomeroy, and R. G. Wiegert [eds.], The ecology of a salt marsh. Springer

Weiss, R. F. 1974. Carbon dioxide in water and seawater: the solubility of a non-ideal gas. Marine Chemistry **2**: 203–215. doi:10.1016/0304-4203(74)90015-2

Wielgat-Rychert, M., K. Rychert, Z. Witek, and M. Zalewski. 2017. CALCULATION OF THE PHOTOSYNTHETIC QUOTIENT (PQ) IN THE GULF OF GDAŃSK (SOUTHERN BALTIC).

Woodwell, G. M., and P. H. Whittaker. 1968. Primary production in terrestrial communities, Am. Zool., 8, 19-30

Wofsy, S. C. 1983. A simple model to predict extinction coefficients and phytoplankton biomass in eutrophic waters, Limnol. Oceanogr.,28, 1144–1155

- **X**

Xaus, L. 2023. Relationship between water carbon and planktonic food webs in “blue carbon” ecosystem. Rapport de stage de Master 2. Gestion des Littoraux et des Mers. Université de Montpellier.

Xi, M., X. Zhang, F. Kong, Y. Li, X. Sui, and X. Wang. 2019. CO_2 exchange under different vegetation covers in a coastal wetland of Jiaozhou Bay, China. Ecological Engineering **137**: 26–33. doi:10.1016/j.ecoleng.2018.12.025

- **Y**

Yates, K. K., C. Dufore, N. Smiley, C. Jackson, and R. B. Halley. 2007. Diurnal variation of oxygen and carbonate system parameters in Tampa Bay and Florida Bay. Marine Chemistry **104**: 110–124. doi:10.1016/j.marchem.2006.12.008

- **Z**

Zeebe, R. E. 2012. History of Seawater Carbonate Chemistry, Atmospheric CO_2, and Ocean Acidification. Annu. Rev. Earth Planet. Sci. **40**: 141–165. doi:10.1146/annurev-earth-042711-105521

Zeebe, R. E., and D. Wolf-Gladrow. 2001. CO_2 in Seawater: Equilibrium, Kinetics, Isotopes. Amsterdam: Elsevier. 346 pp.

Zhao, J., S. L. Malone, S. F. Oberbauer, P. C. Olivas, J. L. Schedlbauer, C. L. Staudhammer, and G. Starr. 2019. Intensified inundation shifts a freshwater wetland from a CO_2 sink to a source. Global Change Biology **25**: 3319–3333. doi:10.1111/gcb.14718

Zheng, Y., L. Hou, M. Liu, and others. 2016. Tidal pumping facilitates dissimilatory nitrate reduction in intertidal marshes. Sci Rep **6**: 21338. doi:10.1038/srep21338

Regional Studies in Marine Science 67 (2023) 103209

Contents lists available at ScienceDirect

Regional Studies in Marine Science

journal homepage: www.elsevier.com/locate/rsma

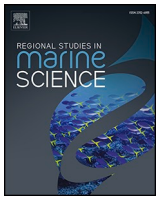

Influence of typology and management practices on water pCO_2 and atmospheric CO_2 fluxes over two temperate shelf–estuary–marsh water continuums☆

Jérémy Mayen [a,b,*], Pierre Polsenaere [a], Aurore Regaudie de Gioux [c], Christine Dupuy [d], Marie Vagner [e], Jean-Christophe Lemesle [f], Benoit Poitevin [g], Philippe Souchu [b]

[a] IFREMER, Littoral, Laboratoire Environnement Ressources des Pertuis Charentais (LER/PC), BP 133, 17390, La Tremblade, France
[b] IFREMER, Littoral, Laboratoire Environnement Ressources Morbihan-Pays de Loire (LER/MPL), BP 21105, 44311, Nantes, France
[c] IFREMER, Dyneco, Pelagos, ZI de la Pointe du Diable - CS 10070, 29280 Plouzané, France
[d] UMR 7266 Littoral Environnement et Société (LIENSs), CNRS – La Rochelle Université, France
[e] LEMAR, UMR 6539 CNRS/Univ Brest/IRD/Ifremer, ZI pointe du diable, 29 280, Plouzané, France
[f] LPO, Réserve Naturelle de Lilleau des Niges, 17880, Les Portes en Ré, France
[g] Pôle-Nature de l'Ecomusée du Marais Salant, route de Loix, 17111, Loix en Ré, France

ARTICLE INFO

Keywords:
Shelf–estuary–marsh continuums
Water pCO_2
Air–water CO_2 fluxes
Diurnal
Tidal
Seasonal scales
Marsh management practices
Macrophytes

ABSTRACT

Within the coastal zone, salt marshes often behave as atmospheric CO_2 sinks, allowing for blue carbon (C) sequestration associated with intense autotrophic metabolism. However, C dynamics over salt marshes are complex since various biogeochemical processes and fluxes occur at different terrestrial–aquatic–atmospheric exchange interfaces and spatiotemporal scales. This study focuses on seasonal, tidal and diurnal variations of water pCO_2, estimated water–air CO_2 fluxes and controlling factors along two temperate shelf–estuary–marsh continuums. The latter include typical coastal systems with artificial salt marshes that have contrasting water management practices and primary producer types. Our high-frequency biogeochemical measurements (seasonal 24-hour cycles) highlighted a strong control of ecosystem typology on inorganic C dynamics with lower water pCO_2 values in the artificial salt marshes, due to stronger biological activity and longer water residence times, than in the tidal estuary. In the marine-dominated estuary, water pCO_2 variations (267 - 569 ppmv) were strongly controlled by tidal effects and phytoplankton activity particularly in spring/summer. On the contrary, the greatest amplitudes in water pCO_2 were recorded in the artificial salt marshes (6 - 721 ppmv) due to intense macrophyte activity. In the rewilded marsh, eutrophication favoured spring/summer fast-growing macroalgae produced, in turn, strong fall atmospheric CO_2 outgassing from degraded algae waters and thus a net annual source of CO_2 to the atmosphere (17.5 g C m^{-2} yr^{-1}). Conversely, specific management practices at the working marsh for salt-farming activity favoured rather slow-growing macrophytes (i.e. seagrasses) which greatly contribute to the yearly observed atmospheric CO_2 sink (-97.7 g C m^{-2} yr^{-1}). In this work, we suggest that salt marsh management can be used to control the contribution of primary producers to marsh C budget as atmospheric CO_2 (sink and/or source).

1. Introduction

Marine coastal environments, which only account for 7% of the global ocean, perform major ecological functions such as primary production, bacterial mineralization and organic matter burial (Gattuso et al., 1998). The coastal zone presents a wide diversity of geomorphological types and ecosystems (shelves, estuaries, bays, wetlands) shaping the biogeochemical cycle coupling between land, ocean and atmosphere (Aufdenkampe et al., 2011; Bauer et al., 2013). These dynamics and heterogeneous ecosystems vertically exchanges large and variable quantities of carbon (C) with the atmosphere (Cole et al., 2007; Polsenaere et al., 2012). At the global scale, continental shelves behave

☆ A research paper submitted to the Regional Studies in Marine Science.

* Corresponding author at: IFREMER, Littoral, Laboratoire Environnement Ressources des Pertuis Charentais (LER/PC), BP 133, 17390, La Tremblade, France.
E-mail address: jeremy.mayen@ifremer.fr (J. Mayen).

https://doi.org/10.1016/j.rsma.2023.103209
Received 19 October 2022; Received in revised form 26 May 2023; Accepted 18 September 2023
Available online 22 September 2023

as atmospheric CO_2 sinks and absorb 0.25 ± 0.05 Pg C yr^{-1} due to phytoplankton primary production (Bauer et al., 2013; Dai et al., 2022). On the contrary, CO_2 supersaturated estuarine waters emit 0.25 ± 0.05 Pg C yr^{-1} to the atmosphere (Bauer et al., 2013) due to a strong mineralization of organic matter from the land (Frankignoulle et al., 1998; Borges and Abril, 2011). These atmospheric C exchanges within the coastal zone are heterogeneous (Borges et al., 2005) and need to be better taken into account in regional and global C budgets (Najjar et al., 2018). For instance, coastal wetlands, including salt marshes located along inner shelf–estuary–marsh continuums, absorb 0.55 ± 0.05 Pg C yr^{-1} from the atmosphere (Bauer et al., 2013) and may play a major role in atmospheric CO_2 uptake and associated organic C burial on Earth (Cai, 2011; Mcleod et al., 2011).

In salt marshes, inorganic C dynamics and water pCO_2 are influenced by several physicochemical and biological processes within and between each ecosystem compartment such as tidal exchanges, calcium carbonate precipitation/dissolution, benthic-pelagic coupling, air–water exchanges and photosynthesis/respiration balance (Cai, 2011; Bauer et al., 2013; Macreadie et al., 2017). Due to high photoautotrophy rates of both aquatic (phytoplankton and seagrasses) and terrestrial (vascular plants) primary producers (Tobias and Neubauer, 2019), these highly productive ecosystems mostly behave as net atmospheric C sinks (Schäfer et al., 2014; Artigas et al., 2015; Forbrich and Giblin, 2015). A refractory part of organic C produced through photosynthesis in these vegetated coastal ecosystems can then be sequestered in sediments or/and plant biomass (Chmura et al., 2003) and stored as blue C, and greatly contribute to the regional/global C cycle in comparison with terrestrial ecosystems (Mcleod et al., 2011). Salt marshes also produce and horizontally export significant quantities of C through tidal water advection (Najjar et al., 2018) which could, in turn, strongly influence the C balance of the system itself as well as the estuary and shelf systems (Cai, 2011). The "marsh CO_2 pump" hypothesis proposes that atmospheric CO_2 uptake by marsh primary producers and the export of a part of the associated C may be one of the major mechanisms making adjacent coastal waters sources of CO_2 to the atmosphere (Wang and Cai, 2004). For instance, in a tidal marsh area (USA; 12 300 km^2), Wang et al. (2016) estimated that 56% of the atmospheric C uptake by the marsh net primary production (NPP) was exported to the coastal ocean by tides (39% inorganic and 17% organic C forms). Nevertheless, despite these major ecological potentials (storm protection, nursery areas, long-term C storage), these interface areas are the most threatened in the world by land-use changes, climate changes and sea level rise (Gu et al., 2018). Moreover, coastal eutrophication causes the loss of salt marshes by decreasing the below-ground biomass of plant roots through microbial degradation processes thereby producing a decrease in the geomorphic stability of marshes (Deegan et al., 2012). Since the 1800s, salt marshes have lost about 25% of their global area with negative effects on the atmospheric CO_2 sink and the associated C sequestration (Mcleod et al., 2011). Their importance as ecosystem service reservoirs has made it possible to implement protection and restoration policies that contribute to their better management and to the development of their ecological and economic potentials (Gu et al., 2018; Adam, 2019).

The high heterogeneity in biogeochemical processes within coastal systems at spatial and temporal scales (Cai, 2011; Bauer et al., 2013) requires more integrative C process and exchange measurements at the various terrestrial–aquatic–atmospheric interfaces over different time scales (tidal, diurnal and seasonal) to better understand the ecological functioning of these ecosystems facing global changes. Some studies in coastal wetlands such as salt marshes or seagrasses have taken water pCO_2 measurements at different temporal scales allowing the study of in situ CO_2 dynamics in relation to other biotic and abiotic processes (Berg et al., 2019; Burgos et al., 2018; Polsenaere et al., 2022; Wang et al., 2018). For instance, in an intertidal mangrove (Gaderu Creek, India), Borges (2003) showed a strong control of diurnal pCO_2 variations by tides and biological activity (primary production and respiration). However, still too few studies have taken high-frequency water pCO_2 measurements in salt marshes at the diurnal and tidal scales to better understand the biogeochemical status of marsh waters which are still little studied from a C point of view (Song et al., 2023). These temporal variations in water pCO_2 strongly affect associated air–water CO_2 fluxes that can, in turn, be estimated from the CO_2 gas transfer velocity, CO_2 solubility in the water and air–water CO_2 gradient (Borges, 2003; Crosswell et al., 2017). The atmospheric Eddy Covariance technique represents an alternative way to directly measure atmospheric CO_2 fluxes at the ecosystem scale (Baldocchi et al., 1988; Schäfer et al., 2014). This non-intrusive micrometeorological technique allows to study the metabolism of coastal ecosystems (sink or source) under real field conditions and to integrate them into regional C budgets (Polsenaere et al., 2012; Van Dam et al., 2021).

The purpose of this study was to better understand CO_2 dynamics at different temporal scales and locations over two aquatic sea–land continuums along the Atlantic French coast on Ré Island. These continuums include coastal systems (shelf, estuary, marsh) such as those studied elsewhere by Cai (2011) and Bauer et al. (2013) with regards to horizontal and vertical C exchanges in the coastal ocean. Unlike tidal salt marshes, which are more generally discussed in the literature (Cai, 2011; Wang et al., 2016), here we studied two artificial salt marshes (i.e. salt ponds) in which water exchanges are controlled by dykes and locks for human uses (biodiversity protection or anthropogenic activities (Tortajada et al., 2011)). Through in situ high-frequency measurements of biogeochemical parameters in waters and estimations of atmospheric CO_2 fluxes from 2018 to 2020, we sought to (1) identify biophysical controlling factors of water pCO_2 by establishing biogeochemical relationships both at the seasonal and diurnal/tidal scales, (2) highlight the influence of continuum typologies on measured biogeochemical parameters and (3) identify role of station typologies and salt marsh management practices on temporal pCO_2 dynamics and associated CO_2 budgets. The results allowed us to contextualize the associated continuum metabolism among other studied systems from a C dynamics and budget point of view.

2. Materials and methods

2.1. Study sites

2.1.1. Tidal estuary (station a) and channel (station b)

The Fier d'Ars estuary is a semi-closed maritime area of 750 ha on Ré Island within the French Atlantic Ocean and connected to the Breton Sound continental shelf (Fig. 1). It corresponds to a type II temperate tidal estuary according to Dürr et al.'s (2011) coastal system typology. At low tide (LT), its subtidal zone (in light blue; Fig. 1) is composed of mudflats (slikke) and tidal salt marshes (schorre) traversed by numerous channels of different sizes. At high tide (HT), the subtidal zone is flooded by coastal waters from the shelf up to the dykes (Fig. 1), managed to control water exchanges between the estuary and upstream artificial salt marshes. Station *a*, with a maximum water height of 6.5 m, is located within the subtidal zone of the estuary along the main channel connected to slikke (Fig. 1). Station *b* is a secondary tidal channel associated to the schorre and located at the back of the estuary before the dyke. With a maximum water height of 5.3 m, it is connected to station *a* (distance of 1.6 km) enabling the supply of coastal waters to artificial salt marshes upstream from the dyke (Fig. 1).

Artificial salt marshes are old tidal salt marshes divided into multiple ponds by dykes mainly located along European coasts for which water residence times (from a few hours to fifteen days according to the management practices; Bel Hassen, 2001) were originally controlled for salt-farming through locks (Tortajada et al., 2011).

2.1.2. Rewilded artificial salt marsh (station c)

Station *c* is a rewilded artificial salt marsh upstream from the dyke (surface area of 40 100 m^2, depth of 60 cm), protected and managed inside a National Natural Reserve (NNR). During HT periods, this

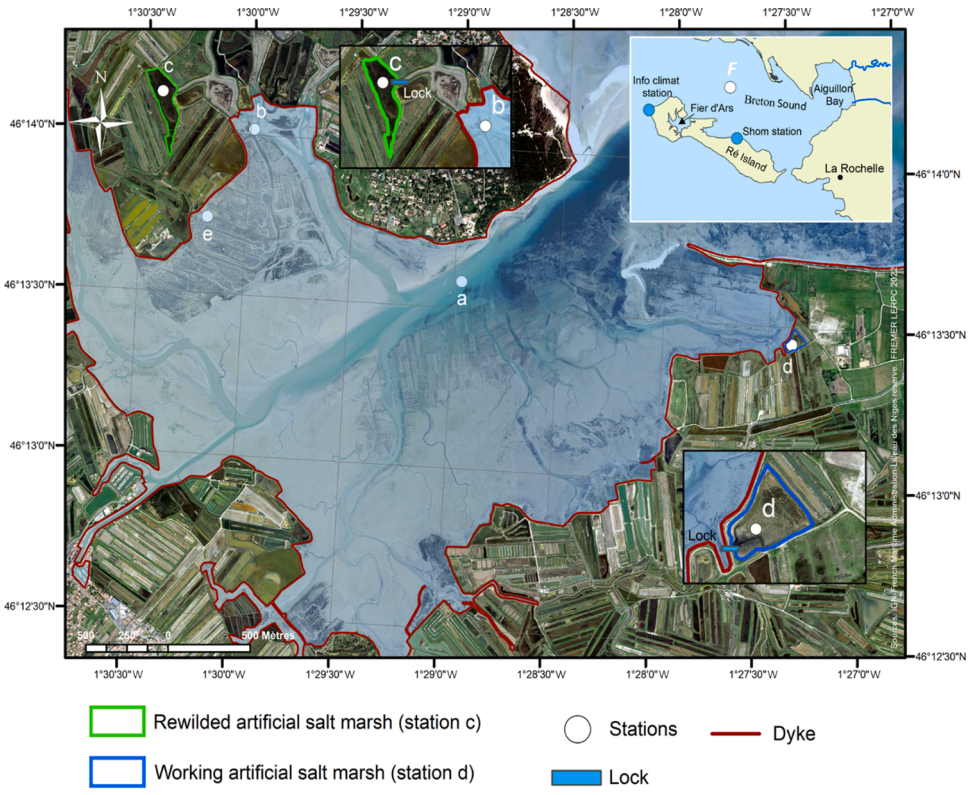

Fig. 1. The Fier d'Ars estuary (Ré Island, French Atlantic coast) and locations of the four studied stations along aquatic continuums: tidal estuary at station *a*, channel at station *b*, rewilded artificial salt marsh at station *c* (countour line in green) and working artificial salt marsh at station *d* (countour line in blue). The dyke (red line) delimits terrestrial and maritime (subtidal) areas. The locks in the two studied artificial marshes are represented within the two map expansions. An atmospheric Eddy Covariance station was deployed at station *e* on the tidal salt marsh downstream from the dyke. Station *F* is located in the centre of the Breton Sound continental shelf; station *a* is located at the entry of the estuary; stations *b*, *c* and *e* are within the National Natural Reserve to the west of the estuary; station *d* to the east of the estuary is within a salt-farm. (For interpretation of the references to colour in this figure legend, the reader is referred to the web version of this article.)

rewilded marsh is supplied indirectly with coastal waters from the estuary by the station *b* channel (distance of 500 m between stations *b* and *c*; Fig. 1) through a lock management practice to promote biodiversity protection (former salt farm that has been rewilded; Fig. A.1). From November to March (winter period), the lock is open only during the highest tidal amplitudes in order to have the best compromise between salt- and fresh-mixing waters (salinity around 30) to allow aquatic fauna passing from the continental shelf to the marsh. From April to October (summer period) with lower tidal amplitudes, the lock is permanently open to avoid large salinity fluctuations in marsh waters and favour the development of *Ruppia spp.* seagrass beds in the marsh (salinity between 30 and 45). Lately, this rewilded marsh is characterized by significant macroalgae development from early spring to late summer each year thereby preventing seagrass development (Champion et al., 2012).

2.1.3. *Working artificial salt marsh (station d)*

Station *d* is a working artificial salt marsh upstream from the dyke (surface area of 8 500 m^2, depth of 75 cm) directly communicating (no channel in between) with coastal waters at HT from the estuary through a lock (distance of 2 km between stations *a* and *d*; Fig. 1). This working marsh was chosen for its specific management practice of the lock related to a salt-farming activity. In spring and summer, the lock is regularly open to store salt waters and then allow to supply a succession of upstream ponds during neap tides for the salt production through the evaporation process (Fig. A.1). Moreover, the use of this working marsh requires a drying up and a cleaning once a year in early spring before the start of the salt production period to remove seagrass, macroalgae and organic matter in the marsh (Poitevin, personal communication).

2.1.4. *Additional station: continental shelf (station F)*

The Breton Sound corresponds to a coastal maritime area located on the French continental shelf, characterized by a surface area of 425 km^2 (Fig. 1). The Breton Sound continental shelf exchanges salt waters with the Atlantic Ocean to the west at each semi-diurnal tidal cycle and receives continental inputs through the Aiguillon Bay discharges to the east depending on hydrodynamic and meteorological conditions (Stanisière et al., 2006; Soletchnik et al., 2015). The highest and lowest river water flows were recorded in winter and summer, respectively, influencing salinity of the shelf waters differently. Station *F* in the centre of the Breton Sound (Fig. 1) is located in a predominantly marine environment with a low freshwater contribution (Stanisière et al., 2006; Soletchnik et al., 2015). At each HT, the continental shelf supplies our studied stations (*a*, *b*, *c* and *d*) with various water masses based on the tidal amplitudes and seasonal periods along two aquatic sea–land continuums: (1) continental shelf (station *F*)–estuary (station *a*)–channel (station *b*)–rewilded salt marsh (station *c*) and (2) continental shelf (station *F*)–estuary (station *a*)–working salt marsh (station *d*). Conversely, at each LT, different water masses from salt marshes are exported (indirectly through the station *b* channel for station *c* or directly for station *d*) to the estuary and then to continental shelf (Fig. 1).

In this study, meteorological parameters (air temperature, rain, wind speed) corresponding to our measurement cycles were used from the Eddy Covariance station (Campbell Scientific) deployed on a nearby tidal salt marsh (station *e*; Fig. 1).

2.2. *Measurement strategy and biogeochemical measurements*

In the sub-surface waters (~30 cm depth), partial pressure of CO_2 (pCO_2), temperature, salinity, turbidity, dissolved oxygen concentration

(DO) and pH were autonomously measured with in situ probes at a frequency of 1 min. during fifteen 24-h cycles at stations *a*, *b*, *c* and *d* during each season (Table A.1). These high frequency measurements allowed to record relevant temporal (diurnal, tidal and seasonal) and spatial (continuums) variations of water pCO_2 and associated physico-chemical parameters. The diurnal scale corresponds to fluctuations occurring between daytime and night-time whereas, the tidal scale corresponds to fluctuations between LT and HT. The seasonal measurement cycles were performed in 2018 at stations *a* and *b* and in 2019/2020 at stations *c* and *d*. Measurements could not be taken at station *d* in spring 2020 due to the Covid pandemic. At station *F*, the same biogeochemical measurements were taken biweekly over the year 2018 (Table A.1) by Coignot et al. (2020).

A pCO_2 underwater probe (C-Sense™; PME/Turner Designs), a multiparameter probe (EXO2; YSI) and a submersible fluorometer (C3™; Turner Designs) were deployed to measure water pCO_2, physicochemical parameters and fluorescence, respectively. The measurement range of the C-Sense probe is 0–2000 ppmv with an absolute accuracy of 60 ppmv (3% of the full scale; Turner Designs). The C-Sense probe was calibrated by the manufacturer before the study. The EXO2 probe was used to measure temperature (±0.1 °C), salinity (± 0.5 salinity unit), turbidity (± 0.3 NTU), DO concentration (±3.1 µmol L^{-1}), DO saturation level (± 1%) and pH (± 0.01 pH unit). The pH was calibrated before and after each 24-h cycle using three YSI buffer solutions (pH 4.01, pH 7.00 and pH 10.01) as outlined by Aminot and Kérouel (2004). It was not possible to measure pH at stations *a* and *b*. The C3-fluorometer was used to estimate the sub-surface Chl *a* values from the 10-min. fluorescence data. This latter was deployed only at station *c* and *d* in summer 2019 and winter 2020.

Water pCO_2 measured by the C-Sense probe are influenced by the total dissolved gas pressure (TDGP) which corresponds to the total pressure exhibited by all gases within the water column. When this pressure greatly exceeded the pressure at which the C-Sense probe was calibrated, the output needed to be corrected. Then, a pCO_2 correction was applied taking both TDGP, atmospheric pressure during sensor calibration (1009 hPa) and the measured pCO_2 by the C-Sense probe into account, as per equation ($pCO_{2measured}$ × 1009)/TDGP (Turner Designs). Over all 24-h cycles, the corrected pCO_2 values with TDGP were 2.6 ± 0.9% lower than the measured pCO_2 values. Total alkalinity (TA) and dissolved inorganic carbon (DIC) were estimated from salinity, temperature, pH and water pCO_2 using the carbonic acid constant from Mehrbach et al. (1973) as modified by Dickson and Millero (1987), the K_{HSO4} constant from Dickson (1990) and the borate acidity constant from Lee et al. (2010). The CO_2 system calculation program (version 2.1.) performed these calculations (Lewis and Wallace, 1998).

2.3. Temperature and non-temperature effects on pCO_2 variations

To distinguish between the temperature and non-temperature effects on in situ pCO_2 variations at the seasonal and diurnal scales, $TpCO_2$ (pCO_2 variations related to temperature physical effects, in ppmv) and $NpCO_2$ (pCO_2 variations related to non-temperature effects, in ppmv) were calculated respectively, following Eq. (1) and Eq. (2) from Takahashi et al. (2002):

$$TpCO_2 = pCO_{2mean} \times exp[0.0423 \times (T_{obs} - T_{mean})] \quad (1)$$

$$NpCO_2 = pCO_{2obs} \times exp[0.0423 \times (T_{mean} - T_{obs})] \quad (2)$$

where T_{obs} and pCO_{2obs} are the temperature and pCO_2 values measured by the probes at each time step (1 min.), respectively. T_{mean} and pCO_{2mean} are the temperature and pCO_2 averaged either at the seasonal (annual mean) or diurnal scale (means per 24-h cycle). $TpCO_2$ is only associated with the physical pump whereas, $NpCO_2$ is associated with biological processes, tidal advection and benthic-pelagic coupling (Cotovicz et al., 2015; Polsenaere et al., 2022).

2.4. Calculations of air–water CO_2 fluxes

For all 24-h measurement cycles, the gas transfer velocity (k_{600}) and hourly CO_2 fluxes (FCO_2) at the air–water interface were estimated following Ribas-Ribas et al. (2011) and Polsenaere et al. (2022) in coastal environments. At stations *a* and *b*, only air–water FCO_2 during HT periods (four hours around each HT) were calculated whereas at stations *c* and *d*, all hourly FCO_2 were calculated using the following Eq. (3):

$$FCO_2 = \alpha \times k \times \Delta pCO_2 \quad (3)$$

where FCO_2 (mmol m^{-2} h^{-1}) is the estimated air–water CO_2 fluxes, α (mol kg^{-1} atm^{-1}) is the CO_2 solubility coefficient in saltwater, k (cm h^{-1}) is the gas transfer velocity of CO_2 and ΔpCO_2 (ppmv) is the gradient between mean water and air pCO_2. Water pCO_2 were measured by the C-Sense probe. Atmospheric CO_2 concentrations were measured by (1) the Eddy Covariance (station *e*; Fig. 1) for summer 2019 and winter 2020 and (2) the National Oceanic and Atmospheric Administration (NOAA) at the Mauna Loa Observatory for all other periods (see values caption Table 3). The α coefficient depends on water temperature and salinity and was calculated according to Weiss (1974). The k coefficient also significantly controls air–water FCO_2 since it directly takes turbulence processes at the air–water exchange interface into account (Polsenaere et al., 2013). In this study, k (or k_{660}) was calculated according to both Raymond and Cole (2001) (RC01; Eq. (4)) and Wanninkhof et al. (2022) (W22; Eq. (5)) corresponding to closed environments and more open coastal environments, respectively. These two parametrization methods for the k exchange coefficient were applied in order to compare the results.

For closed freshwater environments (Raymond and Cole, 2001):

$$k_{600} = 1.91 \times exp[0.35 \times U_{10}] \quad (4)$$

For more open coastal environments (Wanninkhof et al., 2022):

$$k_{600} = 0.31 \times (U_{10})^2 \quad (5)$$

The gas transfer coefficients normalized to a Schmidt number of 600 (k_{600}) obtained with the two parametrization were then converted to the gas transfer velocity of CO_2 at the in situ temperature and salinity (k_{660}) according to Jähne et al. (1987) following Eq. (6):

$$k_{660} = k_{600} \Big/ (660/Sc)^{-0.5} \quad (6)$$

where k_{660} (cm h^{-1}) is the gas transfer velocity of CO_2 at the in situ temperature and salinity according to the parametrizations of RC01 or W22, U_{10} (m s^{-1}) is the wind speed normalized to 10 m (Amorocho and DeVries, 1980) and Sc is the Schmidt number which describes both the water viscosity and the molecular diffusion of the subsurface layer (Bade, 2009). In summer 2019 and winter 2020, wind speeds were measured by the Eddy Covariance (station *e;* Fig. 1) at a height of 3.15 m; for all other periods, wind data were obtained from the Infoclimat station (Fig. 1) measured at a height of 10 m (distances of 6.20, 4.85, 4.30 and 8.40 km from stations *a*, *b*, *c* and *d*, respectively).

2.5. Chl *a* concentrations and fluorometer data calibration

In situ Chl *a* concentrations (µg L^{-1}) were measured from sub-surface water samples collected only at stations *c* and *d*. Water samples (50–100 mL) were filtered through GF/F filters (Whatman® Nuclepore™, porosity of 0.7 µm) and stored at −20 °C until analysis. In the dark, Chl *a* was extracted in 90% acetone with a glass rod. After 12 h of stirring at 4 °C to continue the extraction, Chl *a* was analysed by monochromatic spectrophotometry at 665 nm (Aminot and Kérouel, 2004).

For the fluorometer data, the calibration procedure was applied to

Table 1
Meteorological conditions (air temperature in °C and cumulative precipitation in mm) obtained from the Infoclimat station on Ré Island (Fig. 1; https://www.infoclimat.fr) at the monthly and annual scales over our measurement periods in 2018, 2019 and 2020 in bold compared to the reference period (1990–2020).

Year	Season	Month	Mean air temperature (°C)	Difference with the reference period (°C)	Cumulative precipitation (mm)	Difference with the reference period (mm)
2018	Winter	March	**9.1**	−0.7	**127**	+70
	Spring	April	**13.4**	+1.4	**58**	−3
	Summer	July	**22.2**	+1.7	**59**	+19
	Autumn	September	**19.0**	+1.0	**9**	−51
		Annual	**14.3**	+0.8	**786**	+32
2019	Spring	April	**11.9**	−0.1	**57**	−4
	Summer	July	**22.5**	+2.0	**33**	−7
	Autumn	October	**15.8**	+1.1	**117**	+33
		Annual	**14.1**	+0.6	**827**	+73
2020	Winter	February	**10.4**	+3.1	**68**	+12

derive Chl *a* values from our water fluorescence measurements (Aminot and Kérouel, 2004). Chl *a* could be calculated only at station *d* through the significant linear regressions ($p < 0.05$) between the fluorometer values and the in situ Chl *a* values sampled simultaneously in the marsh waters.

2.6. Statistical tools and analysis

For all measured variables, the high-frequency data (i.e. 1 min) did not respect a normal distribution (Shapiro–Wilk tests, $p < 0.05$). Non-parametric comparisons such as the Mann–Whitney and Kruskal–Wallis tests were carried out with 0.05 level of significance. A Dunn test was used to perform a post-hoc multiple comparison of the Kruskal–Wallis test to detect significant differences among groups. The statistical tests as well as temporal graphs, linear regressions, boxplot and barplot were performed with the GraphPad Prism 7 software. The R-studio software was used to perform the principal component analysis (PCA) with the "FactoMineR" package (Lê et al., 2008) and the correlation matrices with the "corrplot" package (Wei and Simko, 2017). The PCA allows to study the seasonal distribution of data along the studied continuums (Fig. 2). It is based on the seasonal means of the temperature, salinity, turbidity, DO and pCO_2 measured (i) once every two weeks at station *F* and (ii) once every minute over 24-h cycles at stations *a*, *b*, *c* and *d*. Stepwise multilinear regression analysis were performed to test the contribution of measured physicochemical variables (salinity, temperature, turbidity and oxygen) on water pCO_2 variations through the percentage of explained variance (adjusted R^2; Harrell, 2015). Within each 24-h cycle, the selected multilinear model ($p < 0.001$, $n = 1441$) had the highest adjusted R^2 with all variables explaining at least 5% of the pCO_2 variation. Analysis were performed with Statgraphics Centurion 19 software.

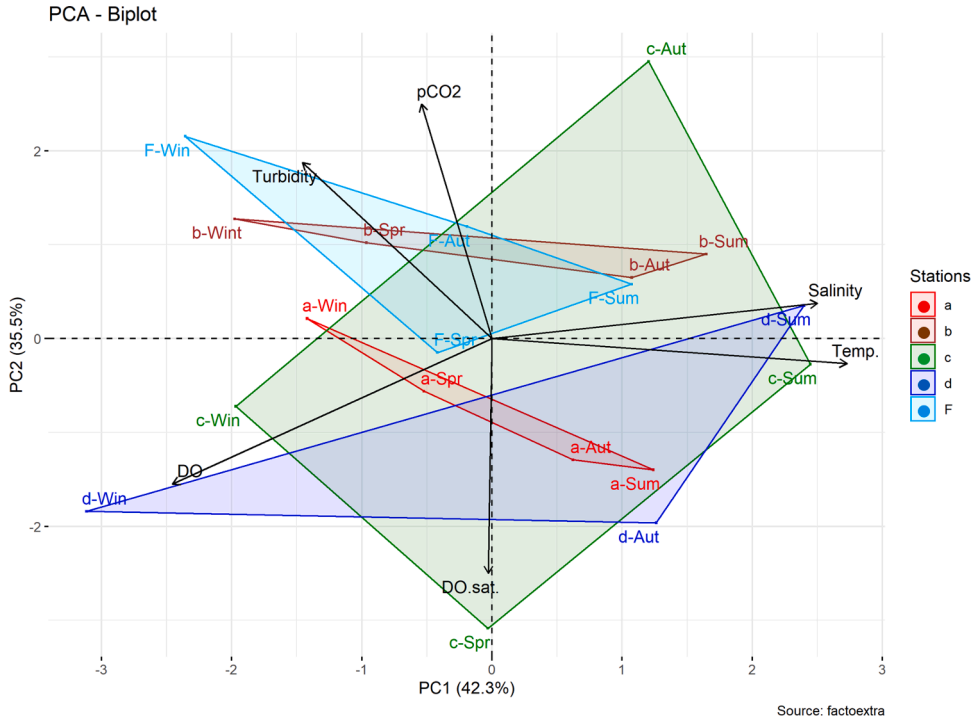

Fig. 2. Principal Component Analysis (PCA) of the biogeochemical parameters measured at each season along the studied aquatic continuums (stations *a*, *b*, *c* and *d*). The PCA is based on temperature (Temp), salinity, turbidity, dissolved oxygen concentration (DO), dissolved oxygen saturation level (DO-sat.) and pCO_2 mean values for each 24-h cycle. Stations *a*, *b*, *c* and *d* are represented in red, brown, green and blue, respectively. The additional station *F* is represented in light blue. Win: Winter; Spr: Spring; Sum: Summer; Aut: Autumn. (For interpretation of the references to colour in this figure legend, the reader is referred to the web version of this article.)

3. Results

3.1. Biogeochemical overview of the aquatic continuums

Over our measurement periods, thermal conditions for the years 2018 and 2019 were similar following a classical seasonal trend. However, July 2018, July 2019 and February 2020 were warmer than the 1990–2020 reference period (Table 1). Annual cumulative precipitations in 2018 and 2019 were higher than the historical data with March 2018 and October 2019 as the rainiest months (Table 1). Salinity at station *F* as the water source flowing into the two studied continuums did not vary significantly between the years 2018, 2019, 2020 and the 2000–2017 reference period (Kruskal–Wallis test, $p = 0.77$; Fig. A.2).

At station *F*, over the biweekly measurements in 2018, water temperatures varied from 7.5 (winter) to 21.7 °C (summer) whereas at station *a* over our seasonal 24-h cycles, values varied from 9.1 (winter) to 26.9 °C (summer). Along the aquatic continuum, water temperatures significantly increased from station *a* to stations *b* and *c* (Mann–Whitney tests, $p < 0.05$). Salinity ranged from 28.9 (winter) to 35.4 (autumn) at station *F* whereas, values varied from 31.4 (winter) to 35.7 (autumn) at station *a*, from 27.5 (winter) to 36.9 (autumn) at station *b*, from 27.0 (winter) to 42.6 (summer) at station *c* and from 21.3 (winter) to 38.4 (autumn) at station *d* with largest salinity gradients recorded at stations *c* and *d* (Table 2). In average over the year, station *a* waters were slightly oversaturated in oxygen compared to the atmosphere with DO saturation levels ranging between 70 (LT during dawn) and 150% (LT during dusk) during the summer cycle (Fig. 3). Simultaneously, station *b* waters were close to the saturation value with the atmosphere with a lower maximum value (120%) during the summer cycle (Fig. 4). Larger amplitudes of DO saturation level were recorded in the artificial salt marshes with values ranging from 36 to 176% at station *c* (summer; Fig. 5) and from 49 to 150% at station *d* (summer; Fig. 6). The annual levels of water CO_2 undersaturation with respect to the atmosphere were 48%, 16%, 65% and 86% at stations *a*, *b*, *c* and *d*, respectively, with a strong annual CO_2 oversaturation at station *b* (Fig. 4). The greatest amplitude in water pCO_2 was recorded at station *c* with values varying from 6 (spring) to 721 ppmv (autumn; Fig. 5).

At station *F*, over the year 2018, Chl *a* values increased from winter

Table 2
Seasonal means (±SD) and ranges (min–max) of temperature (°C), salinity, DO (μmol L^{-1}), pH (NBS scale) and pCO_2 (ppmv) values measured (i) once every two weeks in 2018 at station *F* (Coignot et al., 2020) and (ii) during each 24-h cycle from 2018 to 2020 at stations *a*, *b*, *c* and *d* in this study.

		Temperature (°C)	Salinity	DO (μmol L^{-1})	pH (NBS)	pCO_2 (ppmv)
Winter 2018	*F*	**9.1 ± 1.3** (7.5–10.6)	**31.4 ± 1.8** (28.9–33.0)	**269.6 ± 29.7** (225.0–285.3)	**8.04 ± 0.17** (7.79–8.17)	**619 ± 285** (415–1040)
March 2018	*a*	**9.5 ± 0.4** (9.1–10.4)	**32.5 ± 0.2** (31.9–32.9)	**278.7 ± 7.7** (257.2–288.8)	–	**441 ± 21** (377–510)
March 2018	*b*	**9.8 ± 0.5** (9.0–11.3)	**31.0 ± 1.4** (27.5–32.5)	**269.7 ± 9.3** (251.6–307.5)	–	**450 ± 33** (337–518)
February 2020	*c*	**11.5 ± 0.7** (10.2–12.9)	**27.8 ± 0.7** (27.0–29.7)	**287.5 ± 22.0** (256.9–350.0)	**8.20 ± 0.14** (7.94–8.53)	**343 ± 87** (130–519)
February 2020	*d*	**10.2 ± 0.6** (9.2–11.1)	**21.4 ± 0.0** (21.3–21.5)	**314.5 ± 15.9** (293.1–343.8)	**8.27 ± 0.04** (8.16–8.32)	**347 ± 30** (302–438)
Spring 2018	*F*	**16.0 ± 2.5** (13.2–19.1)	**32.4 ± 1.5** (30.8–34.2)	**270.0 ± 28.5** (245.3–308.2)	**8.23 ± 0.09** (8.11–8.33)	**379 ± 89** (279–495)
April 2018	*a*	**15.0 ± 0.7** (14.1–16.5)	**31.5 ± 0.0** (31.4–31.5)	**265.8 ± 16.4** (221.9–285.3)	**8.17 ± 0.03** (8.09–8.21)	**390 ± 40** (342–505)
April 2018	*b*	**15.5 ± 0.9** (14.1–16.9)	**31.2 ± 0.3** (30.3–31.6)	**252.2 ± 20.1** (200.3–279.4)	**8.05 ± 0.02** (7.98–8.09)	**443 ± 44** (371–551)
May 2019	*c*	**17.1 ± 1.8** (14.3–19.9)	**33.7 ± 0.2** (33.3–34.0)	**287.5 ± 78.4** (168.4–415.0)	**8.78 ± 0.43** (8.12–9.23)	**135 ± 165** (6–425)
–	*d*	–	–	–	–	–
Summer 2018	*F*	**19.9 ± 1.5** (18.2–21.7)	**34.6 ± 0.6** (34.0–35.2)	**235.6 ± 22.3** (204.4–253.1)	**8.20 ± 0.12** (8.05–8.34)	**410 ± 130** (270–572)
July 2018	*a*	**22.9 ± 1.6** (21.0–26.9)	**34.2 ± 0.3** (33.6–34.9)	**249.4 ± 35.9** (153.4–306.6)	**8.22 ± 0.07** (8.12–8.39)	**385 ± 60** (267–522)
July 2018	*b*	**23.9 ± 1.3** (21.9–26.1)	**34.7 ± 0.5** (33.9–35.6)	**211.8 ± 33.9** (139.7–291.9)	**8.02 ± 0.05** (7.89–8.12)	**454 ± 55** (374–590)
July 2019	*c*	**23.5 ± 2.5** (20.1–28.4)	**36.8 ± 2.3** (33.5–42.6)	**206.8 ± 58.5** (76.9–339.7)	**8.31 ± 0.23** (8.01–8.94)	**242 ± 116** (25–430)
July 2019	*d*	**23.3 ± 1.6** (21.2–28.1)	**35.8 ± 1.4** (33.3–38.1)	**202.4 ± 70.4** (108.8–314.4)	**7.97 ± 0.09** (7.84–8.11)	**377 ± 85** (250–508)
Autumn 2018	*F*	**14.7 ± 3.2** (10.3–17.5)	**34.3 ± 2.1** (30.6–35.4)	**249.1 ± 23.5** (225.0–284.4)	**8.09 ± 0.06** (8.04–8.18)	**510 ± 70** (403–580)
September 2018	*a*	**18.9 ± 1.5** (17.6–22.0)	**35.2 ± 0.1** (35.1–35.7)	**267.4 ± 25.9** (204.7–323.4)	**7.98 ± 0.07** (7.90–8.16)	**460 ± 58** (334–569)
September 2018	*b*	**20.8 ± 1.2** (18.8–23.1)	**35.9 ± 0.5** (35.1–36.9)	**232.1 ± 30.3** (153.8–275.3)	**7.84 ± 0.05** (7.74–7.94)	**503 ± 46** (422–630)
October 2019	*c*	**17.1 ± 0.9** (15.1–18.5)	**35.0 ± 0.3** (34.6–35.7)	**194.3 ± 24.4** (152.2–236.9)	**7.82 ± 0.04** (7.74–7.91)	**622 ± 57** (522–721)
October 2019	*d*	**15.9 ± 0.4** (15.4–16.8)	**38.2 ± 0.1** (38.0–38.4)	**255.8 ± 39.9** (210.6–331.9)	**8.17 ± 0.07** (8.07–8.28)	**155 ± 30** (110–218)

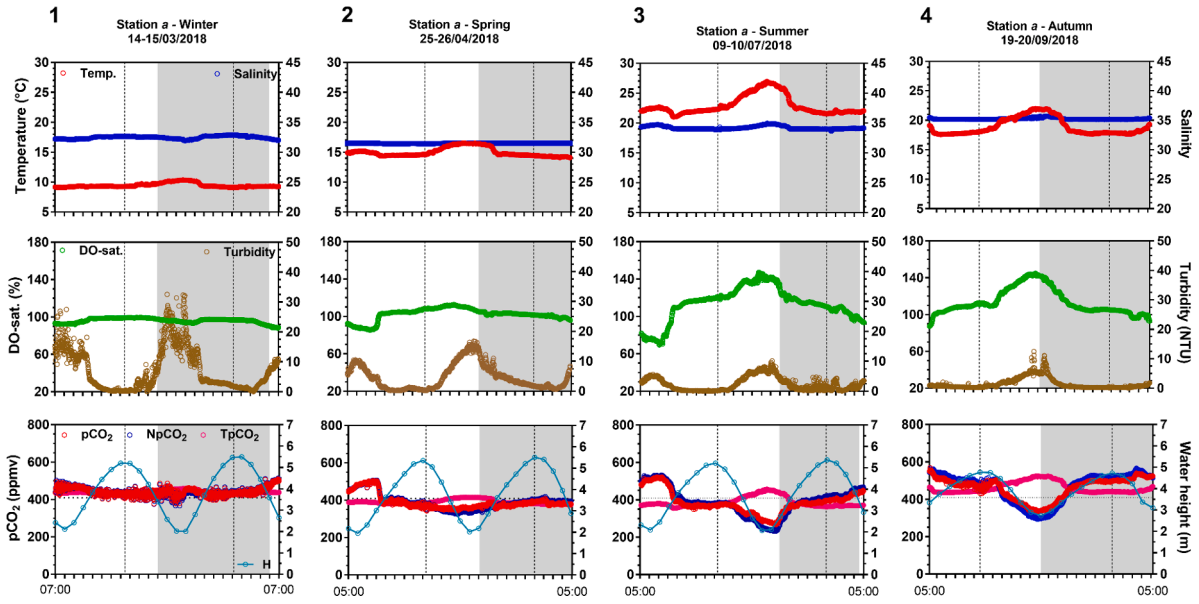

Fig. 3. Temporal variations at station *a* (tidal estuary) of water temperature (°C), salinity, DO saturation level (DO-sat., %), turbidity (NTU), pCO_2, $NpCO_2$ (pCO_2 variations related to non-temperature effects, ppmv) and $TpCO_2$ (pCO_2 variations related to temperature physical effects, ppmv) during each 24-h cycle from winter 2018 to autumn 2018. Parameters were autonomously measured once per minute by in situ probes. Water heights (H, m) were retrieved from the SHOM station (9 km away; Fig. 1). Grey areas correspond to night-time periods. Vertical dotted lines correspond to high tides (HT). Horizontal dotted lines correspond to the CO_2 atmospheric concentration (411 ppm; NOAA 2018). Each graduation of the *x*-axis corresponds to one hour.

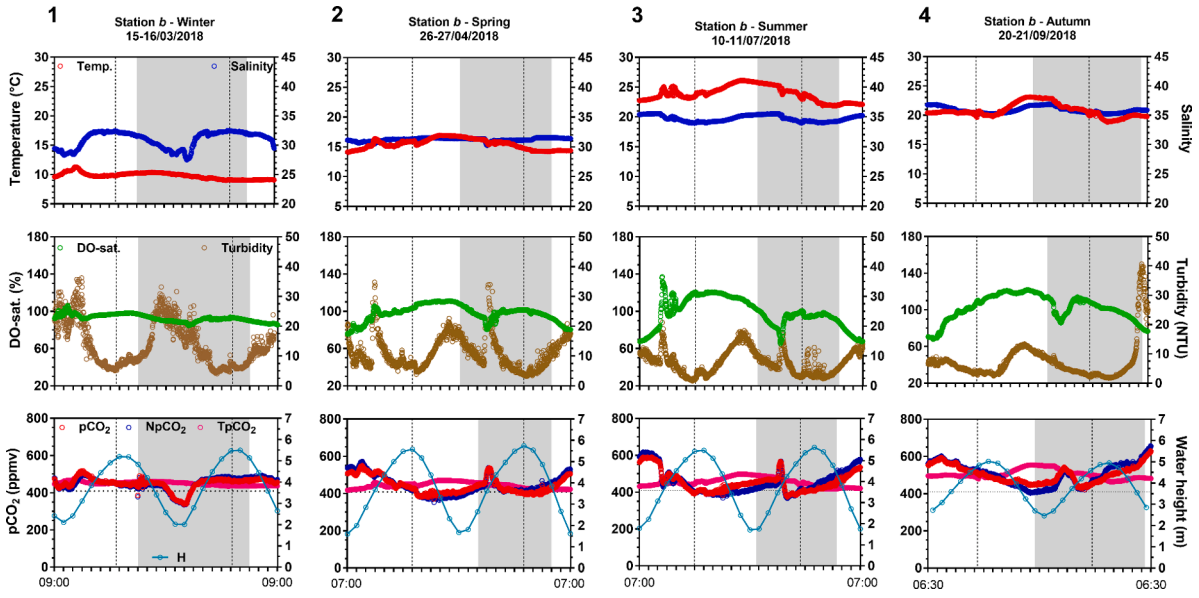

Fig. 4. Temporal variations at station *b* (channel) of water temperature (°C), salinity, DO saturation level (DO-sat., %), turbidity (NTU), pCO_2, $NpCO_2$ and $TpCO_2$ (ppmv) during each 24-h cycle from winter 2018 to autumn 2018. See Fig. 3 caption for more details.

(0.7 ± 0.1 µg L^{-1}) to spring–summer (2.5 ± 1.6 and 1.6 ± 1.0 µg L^{-1}, respectively), before decreasing in autumn (0.8 ± 0.5 µg L^{-1}). At station *c*, the highest and lowest Chl *a* values were recorded in autumn 2019 (8.1 ± 0.4 µg L^{-1}) and winter 2020 (1.3 ± 0.3 µg L^{-1}), respectively, whereas at station *d*, the highest and lowest values were recorded in winter 2020 (3.4 ± 0.4 µg L^{-1}) and summer 2019 (1.9 ± 0.3 µg L^{-1}), respectively. Moreover, at station *c*, from spring to autumn 2019, a free floating macroalgae development (*Ulva spp.*) was observed in the sub-surface waters and on sediments (Fig. A.3). On the contrary, at station *d*, no macroalgae development occurred, allowing for the seagrass growth (*Ruppia spp.*) in the marsh (Fig. A.3).

3.2. Seasonal variations and controls along the aquatic continuums

Seasonally, the PCA reveals that stations along the aquatic continuums were vertically distinguished according to pCO_2, turbidity and DO saturation within PC2 explaining 35.5% of the total variance (Fig. 2). Within this axis, our results confirmed that water pCO_2 were seasonally negatively correlated with DO saturation ($r_{Pearson} = -0.56$; $n = 19$; $p < 0.05$) and positively correlated with turbidity ($r_{Pearson} = 0.54$; $n = 19$; $p < 0.05$) (Fig. 2). Station *b* recorded the highest water pCO_2 values and the lowest DO saturation levels compared to the three other studied stations (except in autumn; Table 2 and Fig. 2). Station *b* was also characterized by the highest turbidity values along the aquatic

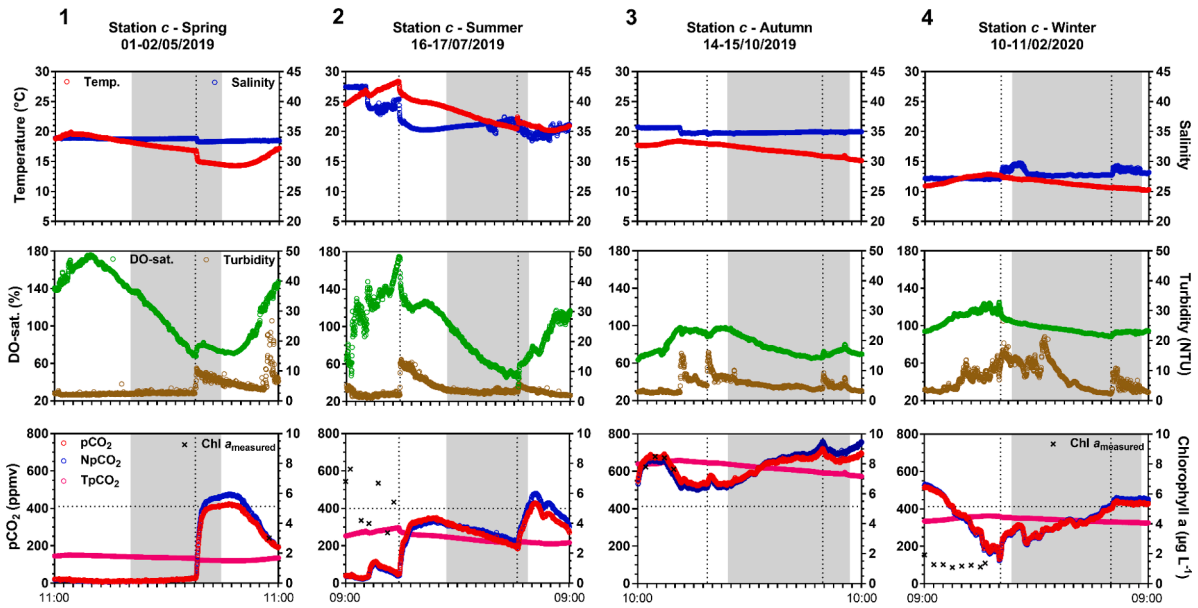

Fig. 5. Temporal variations at station *c* (rewilded artificial salt marsh) of water temperature (°C), salinity, DO saturation level (DO-sat., %), turbidity (NTU), pCO_2, $NpCO_2$ and $TpCO_2$ (ppmv) and *in situ* Chl *a* (µg L^{-1}) during each 24-h cycle from spring 2019 to winter 2020. Vertical dotted lines correspond to coastal water inflows to the marsh during incoming tide. Horizontal dotted lines correspond to the atmospheric CO_2 concentration simultaneously measured (i) by the Eddy Covariance (station *e*) during the summer and winter cycles and (ii) by NOAA during the spring and autumn cycles. *In situ* Chl *a* values are represented by black crosses (Chl $a_{measured}$); no water samples could be taken in spring 2019. See Fig. 3 caption for more details.

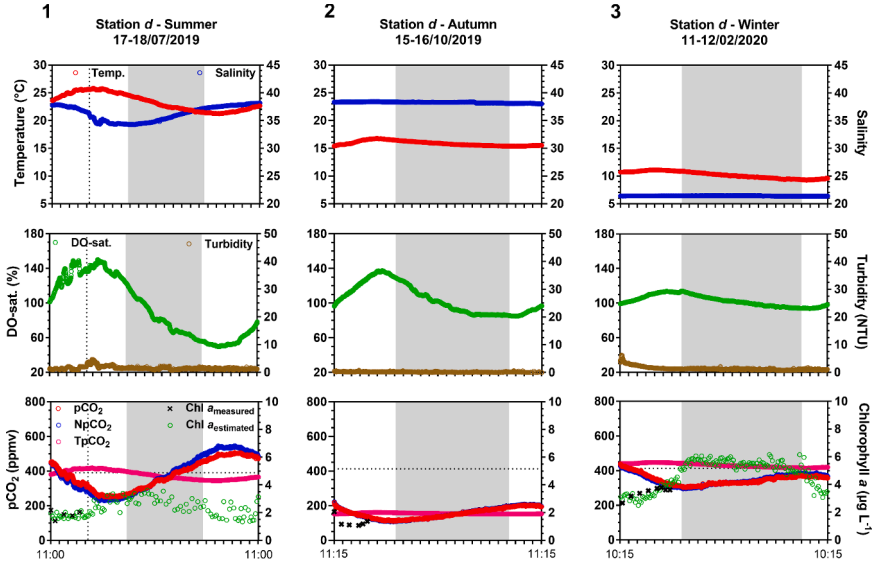

Fig. 6. Temporal variations at station *d* (working artificial salt marsh) of water temperature (°C), salinity, DO saturation level (DO-sat., %), turbidity (NTU), pCO_2, $NpCO_2$ and $TpCO_2$ (ppmv) and *in situ* Chl *a* (µg L^{-1}) during each 24-h cycle from summer 2019 to winter 2020. Chl *a* values in green were derived from the C3-fluorometer every 10 min. (Chl $a_{estimated}$). See Fig. 3 caption for more details. (For interpretation of the references to colour in this figure legend, the reader is referred to the web version of this article.)

continuums (from 1.6 to 41 NTU). The PCA also shows that seasonal data were horizontally distinguished according to salinity and temperature within PC1 explaining 42.3% of the total variance (Fig. 2). Generally, the highest and lowest salinity values were recorded in summer and winter, respectively (Fig. 2), except at station *d* where the highest salinity were recorded in autumn (Table 2). At all studied stations, temperature and salinity values significantly varied between each seasonal 24-h cycles (Kruskal–Wallis tests, $p < 0.0001$).

Along the aquatic continuums, the PCA reveals contrasted seasonal variations of water pCO_2, particularly in artificial salt marshes (Fig. 2). At station *F*, in 2018, no significant difference in water pCO_2 were recorded at the seasonal scale (Kruskal–Wallis test, $p = 0.13$), although the highest and lowest seasonal means were recorded in winter and spring, respectively (Table 2 and Fig. 7). At station *a*, in 2018, water pCO_2 showed the same seasonal pattern decreasing from winter to summer before increasing in autumn, whereas station *b* showed lower seasonal variations over the same measurement periods (Table 2 and Fig. 7). In contrast, stations *c* and *d* showed larger seasonal pCO_2 variations (Fig. 7). Station *c* waters were undersaturated in CO_2 in spring 2019, summer 2019 and winter 2020 but oversaturated in CO_2 in autumn 2019 (622 ± 57 ppmv). At the same time, station *d* waters were undersaturated in CO_2 in summer, autumn and winter with the largest

water CO_2 undersaturation recorded in autumn (155 ± 30 ppmv) in contrast to station *c* (Fig. 7). At all studied stations, water pCO_2 significantly differed between seasons (Kruskal–Wallis tests, $p < 0.05$), except for station *a* between spring and summer (Dunn's post-test, $p > 0.99$).

The same seasonal $NpCO_2$ variations were observed at stations *a* and *b* in 2018, with a decrease from winter (595 and 624 ppmv, respectively) to summer (296 and 347 ppmv, respectively) and an increase towards autumn (420 and 439 ppmv, respectively; Fig. 7). At station *c*, the seasonal mean $NpCO_2$ value increased sharply from summer 2019 (193 ppmv) to autumn 2019 (630 ppmv) and then decreased towards winter 2020 (441 ppmv) whereas at station *d*, values slightly decreased from summer (286 ppmv) to autumn 2019 (160 ppmv) before increasing towards winter 2020 (453 ppmv; Fig. 7). Regarding temperature effects on water pCO_2, the highest and lowest seasonal $TpCO_2$ values were measured in summer and winter, respectively, with seasonal $TpCO_2$ values followed systematically by seasonal water temperature variations (Fig. 7). At station *a*, $\Delta TpCO_2$ offset recorded from winter to summer 2018 ($\Delta TpCO_2 = 240$ ppmv, from 310 to 550 ppmv) concomitantly to the water temperature increase of 13.4 °C partly compensated non-thermal effects on water pCO_2 during this period ($\Delta NpCO_2 = 299$ ppmv, from 595 to 296 ppmv).

3.3. Diurnal/tidal variations and controls along the aquatic continuums

At stations *a* and *b* in winter, salinity varied at the tidal scale with the lowest values at LT and the highest values at HT whereas from spring to autumn, the opposite pattern was recorded with salinity decreases at each incoming tide from the shelf (Figs. 3 and 4). At stations *c* and *d*, even stronger salinity gradients were recorded, especially in summer with decreases of 9 and 5 salinity units, respectively (Figs. 5 and 6). At station *c*, coastal water inflows led to an increase in salinity only in winter (Fig. 5). At station *d*, salinity and turbidity did not vary neither in autumn or in winter (Fig. 6).

The largest diurnal/tidal variations in water pCO_2 and DO concentrations occurred during summer with pCO_2 ranges of 255, 216, 405 and 258 ppmv at stations *a*, *b*, *c* and *d*, respectively, and DO ranges of 153.2, 152.2, 262.8 and 205.6 $\mu mol\ L^{-1}$ at stations *a*, *b*, *c* and *d*, respectively. At stations *a* and *b*, the low tide periods during the day (LT/D) occurring at dawn showed higher water pCO_2 values and lower DO saturation levels than the low tide periods during the night (LT/N) occurring at dusk under similar salinity ranges, particularly in summer (Figs. 3 and 4). In general, our diurnal cycles showed a pCO_2 decrease that was negatively correlated to a DO increase during daytime (except at station *c* in spring; Fig. 5) and an opposite pattern during night-time (except at station *c* in summer; Fig. 5). At station *c*, in winter during LT periods (no

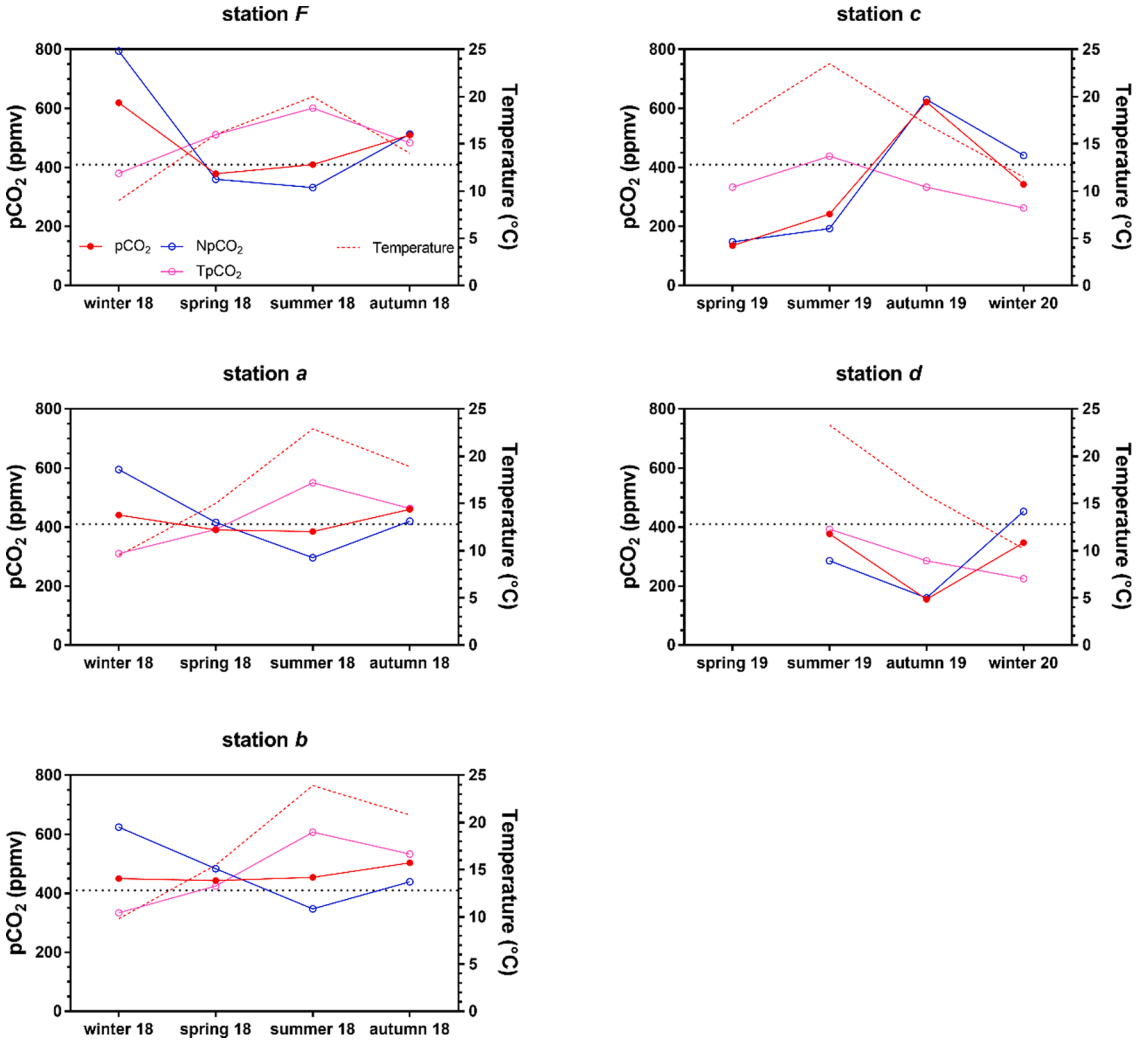

Fig. 7. Derived temperature-normalized pCO_2 (seasonal $NpCO_2$, blue curves with empty blue dots) and thermally forced pCO_2 (seasonal $TpCO_2$, pink curves with empty pink dots) at the seasonal scale at stations *F*, *a*, *b*, *c* and *d*. Seasonal means of water temperature (in red dotted lines) and pCO_2 (red curves with filled red dots) are also represented. Horizontal dotted lines correspond to CO_2 atmospheric concentration (411 ppm; NOAA 2018). (For interpretation of the references to colour in this figure legend, the reader is referred to the web version of this article.)

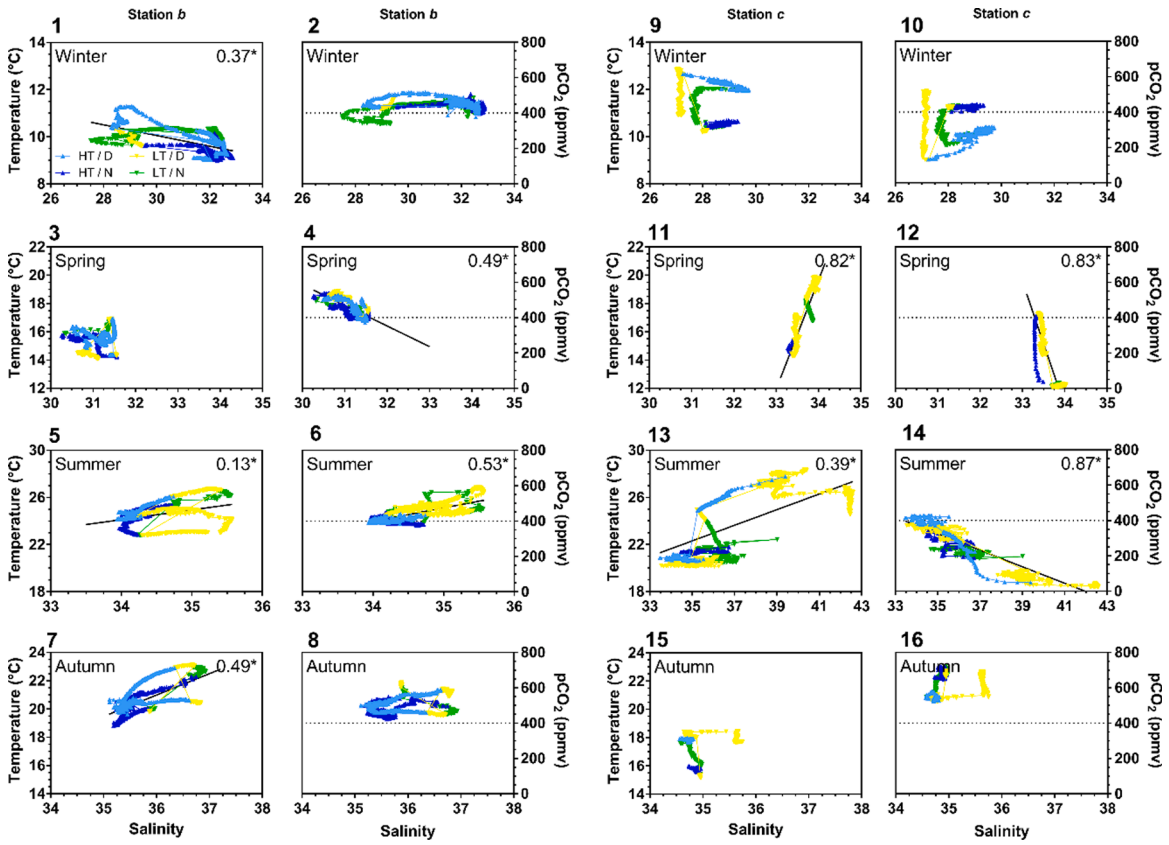

Fig. 8. Diurnal/tidal correlation plots of temperature vs. salinity and water pCO_2 vs. salinity at stations *b* and *c* for each season. Only significant R^2 (slopes significantly different from zero; n = 1441; $p < 0.05$) are showed. HT/D: high tide day; LT/D: low tide day; HT/N: high tide night; LT/N: low tide night. At station *c*, HT periods correspond to coastal water inflows to the marsh. Note that the temperature and salinity ranges across the seasons are not the same. Horizontal dotted lines correspond to the atmospheric CO_2 concentration.

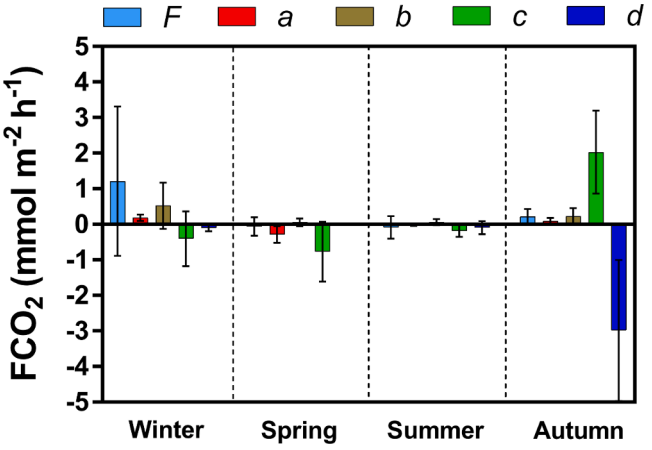

Fig. 9. Seasonal and spatial variations in estimated CO_2 fluxes (FCO_2, in mmol m^{-2} h^{-1}) at the water–atmosphere interface at stations *F*, *a*, *b*, *c* and *d*. The means and associated standard deviations over each 24-h cycle are shown. k_{660} and FCO_2 estimations were calculated according to the R22 parametrization. FCO_2 values at stations *a* and *b* are only given for high tide periods.

salinity variation), water pCO_2 decreased of 390 ppmv during the day (from 09:00 to 17:00) and increased of 230 ppmv during the night (from 20:00 to 05:00) while simultaneously, DO increased of 76.6 μmol L^{-1} and decreased of 29.0 μmol L^{-1}, respectively (Fig. 5). At station *d*, the same diurnal water pCO_2 and DO patterns were recorded at each 24-h cycle (Fig. 6). However, these strong diurnal pCO_2 and DO variations were significantly disrupted once coastal water advection and marsh management practices occurred.

Strong tidal variations in water pCO_2 were recorded during all seasonal cycles, except at station *d* both in autumn and winter (Fig. 6). At stations *a* and *b*, incoming tides from the shelf during the day produced rapid water pCO_2 decreases from an oversaturation to a slight water undersaturation, particularly in spring (−121 and −167 ppmv, respectively) and summer (−139 and −115 ppmv, respectively; Figs. 3 and 4). Only at station *a*, ebbing tides during the day generated an additional pCO_2 decrease to reach the lowest values (Fig. 3). At station *a*, in summer and autumn and at station *b* over the four seasons, incoming tides during the night produced pCO_2 increases leading to water oversaturation periods (Figs. 3 and 4). Along the continuum, at station *c* during the night, higher water pCO_2 values were recorded at HT than at LT, especially in spring (363 ± 85 and 16 ± 5 ppmv at HT/N and LT/N, respectively) and in winter (431 ± 6 and 323 ± 53 ppmv at HT/N and LT/N, respectively; Fig. 8). The same tidal pCO_2 pattern was also recorded at station *c* in summer during the day (323 ± 88 and 197 ± 141 ppmv at HT/D and LT/D, respectively; Fig. 8). In spring, the station *c* marsh recorded the lowest water pCO_2 values both the day and the night during the marsh confinement but coastal water inflows at HT from the station *b* channel instantly produced a large and rapid increase in water pCO_2 (+ 395 ppmv) within a two-hour period (Fig. 8).

For all 24-h cycles, strong and significant correlations between pCO_2 and $NpCO_2$ were computed (Figs. 3–6). Similarly, water pCO_2 values were negatively correlated with DO saturation levels ($n = 1441$, $p < 0.05$), with $r_{Spearman}$ ranging from −0.67 (winter) to −0.97 (autumn) at station *a*, from −0.63 (summer) to −0.87 (autumn) at station *b*, from −0.54 (winter) to −0.86 (autumn) at station *c* and from −0.59 (winter) to −0.80 (autumn) at station *d*. At station *d*, negative correlations were obtained between measured pCO_2 and estimated Chl *a* in summer

($r_{Spearman} = -0.44$; $n = 105$; $p < 0.05$) and winter ($r_{Spearman} = -0.60$; $n = 144$; $p < 0.05$) (Fig. 6). At station *a*, in winter, the multilinear regression analyses highlighted that water pCO_2 were controlled by DO, temperature and salinity whereas over other seasons, pCO_2 were strongly controlled only by DO with the highest R^2 values (Table 4). At station *a*, in spring and summer, estimated TA values were weakly correlated with measured pCO_2 and pH values (Fig. A.4) whereas in autumn, stronger correlations TA versus pCO_2 were recorded ($R^2 = 0.89$ and $R^2 = 0.71$, respectively; $n = 1441$; $p < 0.05$). At station *c*, water pCO_2 were mainly controlled by both salinity and DO in spring, by salinity in summer and by DO in autumn (Table 4). Finally, at station *d*, pCO_2 were mostly explained by salinity and DO in summer (salt farming period) and by DO and temperature in autumn/winter total (marsh confinement periods) (Table 4).

3.4. Air–water CO_2 flux variations

Annual means of air–water CO_2 fluxes (FCO_2) according to the W22 parametrization were estimated to be -0.01 ± 0.22, 0.22 ± 0.40, 0.18 ± 1.37 and -1.22 ± 1.71 mmol m^{-2} h^{-1} at stations *a* (sink), *b* (source), *c* (source) and *d* (sink), respectively, whereas station *F* waters behaved as a CO_2 source (0.30 ± 1.04 mmol m^{-2} h^{-1}). Large seasonal and diurnal variations were observed at the studied stations (Fig. 9). On average, station *a* showed positive FCO_2 values in winter and autumn (slight CO_2 source) and negative values in spring and summer (slight CO_2 sink; Table 3 and Fig. 9). At station *b*, positive FCO_2 values were estimated with maximum and minimum FCO_2 mean values occurring in winter and summer, respectively (Table 3 and Fig. 9). Station *c* behaved as a CO_2 sink in spring, summer and winter and as a strong CO_2 source in autumn (Table 3). At this marsh station, FCO_2 varied between −3.00 and 0.03 mmol m^{-2} h^{-1} in spring and between 0.61 and 4.61 mmol m^{-2} h^{-1}

Table 3
Seasonal means (±SD) and ranges (min–max) of wind speed (km h^{-1}), gas transfer velocity (k_{660}, cm h^{-1}) and estimated water–atmosphere CO_2 flux (FCO_2, mmol m^{-2} h^{-1}) values measured (i) once every two weeks in 2018 at station *F* (Coignot et al., 2020) and (ii) during each 24-h cycle from 2018 to 2020 at stations *a*, *b*, *c* and *d* in the present study. Air CO_2 concentrations used for FCO_2 calculations are: 408 ppm (stations *a*, *b* and *F* in 2018), 411 ppm (station *c* in spring 2019), 413 ppm (stations *c* and *d* in autumn 2019), 400 ppm (stations *c* and *d* in summer 2019) and 403 ppm (stations *c* and *d* in winter 2020; see M&M sections).

		Wind speed	k_{660} (cm h^{-1})		FCO_2 (mmol m^{-2} h^{-1})	
		(km h^{-1})	W22	RC01	W22	RC01
Winter 2018	*F*	**19 ± 10** (7–29)	**7.45 ± 6.30** (0.91–14.24)	**11.29 ± 8.83** (2.79–21.62)	**1.21 ± 2.10** (0.01–4.35)	**1.85 ± 3.18** (0.02–6.60)
March 2018	*a*	**29 ± 4** (22–37)	**14.93 ± 4.04** (8.63–24.68)	**24.75 ± 9.92** (12.08–52.53)	**0.18 ± 0.09** (0.09–0.42)	**0.28 ± 0.14** (0.13–0.69)
March 2018	*b*	**32 ± 12** (13–54)	**21.39 ± 15.99** (3.02–54.68)	**66.17 ± 87.62** (5.06–285.40)	**0.52 ± 0.65** (−0.31–2.13)	**1.91 ± 3.45** (−0.46–11.11)
February 2020	*c*	**27 ± 5** (16–34)	**23.17 ± 10.28** (6.93–39.66)	**30.36 ± 13.28** (9.21–50.44)	**−0.40 ± 0.77** (−2.02–0.94)	**−0.68 ± 1.31** (−3.58–1.58)
February 2020	*d*	**15 ± 5** (4–24)	**6.92 ± 3.17** (2.15–14.23)	**9.46 ± 4.34** (2.96–19.78)	**−0.10 ± 0.09** (−0.31–0.09)	**−0.15 ± 0.13** (−0.41–0.13)
Spring 2018	*F*	**15 ± 20** (11–20)	**5.35 ± 3.44** (2.41–9.32)	**7.78 ± 3.91** (4.43–12.40)	**−0.06 ± 0.26** (−0.40–0.22)	**−0.09 ± 0.34** (−0.54–0.30)
April 2018	*a*	**33 ± 7** (24–43)	**24.01 ± 9.56** (11.85–38.49)	**51.64 ± 32.90** (16.94–108.70)	**−0.29 ± 0.23** (−0.71–0.11)	**−0.66 ± 0.65** (−1.81–0.18)
April 2018	*b*	**14 ± 5** (4–22)	**4.62 ± 2.96** (0.35–10.44)	**7.23 ± 3.46** (2.55–13.62)	**0.05 ± 0.11** (−0.06–0.33)	**0.08 ± 0.15** (−0.08–0.46)
May 2020	*c*	**18 ± 7** (6–31)	**8.99 ± 6.31** (0.86–22.99)	**12.86 ± 9.09** (3.17–37.67)	**−0.77 ± 0.84** (−3.00–0.03)	**−1.21 ± 1.30** (−5.09–0.04)
–	*d*	–	–	–	–	–
Summer 2018	*F*	**20 ± 12** (4–32)	**12.85 ± 10.75** (0.36–24.50)	**20.41 ± 17.10** (2.56–40.89)	**−0.09 ± 0.31** (−0.34–0.31)	**−0.08 ± 0.49** (−0.50–0.51)
July 2018	*a*	**11 ± 3** (6–17)	**3.50 ± 1.97** (0.89–7.21)	**6.35 ± 2.13** (3.55–10.40)	**−0.02 ± 0.03** (−0.08–0.08)	**−0.03 ± 0.06** (−0.14–0.16)
July 2018	*b*	**18 ± 7** (7–30)	**9.69 ± 6.37** (1.29–23.89)	**14.66 ± 9.28** (4.15–39.18)	**0.06 ± 0.08** (−0.07–0.22)	**0.09 ± 0.13** (−0.11–0.37)
July 2019	*c*	**13 ± 4** (4–19)	**4.56 ± 2.59** (0.43–9.46)	**7.59 ± 2.92** (3.16–13.32)	**−0.19 ± 0.17** (−0.70–0.01)	**−0.33 ± 0.24** (−1.01–0.02)
July 2019	*d*	**15 ± 6** (2–23)	**7.12 ± 4.60** (0.11–14.77)	**10.77 ± 5.72** (2.41–20.96)	**−0.09 ± 0.18** (−0.43–0.20)	**−0.12 ± 0.27** (−0.60–0.29)
Autumn 2018	*F*	**17 ± 5** (11–22)	**6.37 ± 4.09** (2.25–10.83)	**9.01 ± 4.98** (4.08–14.46)	**0.21 ± 0.22** (−0.02–0.56)	**0.30 ± 0.29** (−0.02–0.75)
September 2018	*a*	**11 ± 6** (4–20)	**3.55 ± 3.27** (0.36–8.98)	**6.21 ± 3.66** (2.65–12.53)	**0.09 ± 0.09** (0.01–0.30)	**0.15 ± 0.11** (0.01–0.41)
September 2018	*b*	**17 ± 6** (11–32)	**7.32 ± 5.46** (2.90–24.27)	**9.46 ± 7.91** (4.02–42.48)	**0.22 ± 0.23** (0.07–1.00)	**0.28 ± 0.33** (0.05–1.75)
October 2019	*c*	**35 ± 8** (20–48)	**27.39 ± 11.52** (9.01–48.79)	**63.79 ± 42.95** (12.58–179.80)	**2.03 ± 1.17** (0.61–4.61)	**4.86 ± 4.22** (0.85–16.98)
October 2019	*d*	**42 ± 7** (31–54)	**38.22 ± 12.55** (20.54–62.36)	**122.80 ± 84.13** (34.76–325.40)	**−3.43 ± 1.09** (−6.03–−1.79)	**−10.91 ± 7.35** (−31.46–−3.03)

Table 4
Stepwise multilinear regression analyses to test the contribution of physico-chemical variables on water pCO_2 variations through the percentage of explained variance (adjusted R^2). Each selected multilinear model ($p < 0.001$, $n = 1441$) had the highest adjusted R^2 value with all variables explaining at least 5% of the pCO_2 variation. In bold is indicated the parameter explaining at least 50% of the pCO_2 variation. Input variables: DO-sat. (dissolved oxygen saturation level), T (water temperature), S (salinity) and TU (turbidity). The statistic (F) and adjusted R^2 (adj. R^2) are given.

			Equations	F	adj. R^2
Winter	March 2018	*a*	$pCO_2 = 2227.7 - 3.7$ **DO-sat.** $- 19.9\ T - 38.2\ S$	1004	67.7%
	March 2018	*b*	$pCO_2 = -373.8 + 21.1\ S + 0.8\ TU + 15.9\ T$	377	43.9%
	February 2020	*c*	$pCO_2 = 1460.5 - 158.3$ **T** $+ 7.0$ DO-sat.	1180	62.1%
	February 2020	*d*	$pCO_2 = 446.6 - 10.8$ DO-sat. $+ 99.1\ T$	4723	86.8%
Spring	April 2018	*a*	$pCO_2 = 949.8 - 5.5$ **DO-sat.**	8255	85.2%
	April 2018	*b*	$pCO_2 = 2542.0 - 4.0$ **DO-sat.** $- 61.7\ S + 14.2\ T$	1923	80.0%
	May 2019	*c*	$pCO_2 = 21\,777.7 - 640.8$ **S** $- 0.6$ DO-sat.	3668	83.6%
	–	*d*	–		–
Summer	July 2018	*a*	$pCO_2 = 747.2 - 3.2$ **DO-sat.**	30 524	95.5%
	July 2018	*b*	$pCO_2 = -2440.0 + 100.8$ **S** $- 25.4\ T$	3330	82.7%
	July 2019	*c*	$pCO_2 = 1961.5 - 46.7$ **S**	9401	86.8%
	July 2019	*d*	$pCO_2 = -961.8 + 40.1$ **S** $- 1.2$ DO-sat.	47 983	98.5%
Autumn	September 2018	*a*	$pCO_2 = 923.1 - 4.1$ **DO-sat.**	34 905	96.4%
	September 2018	*b*	$pCO_2 = 782.0 - 2.8$ **DO-sat.** $+ 1.1$ TU	3066	81.0%
	October 2019	*c*	$pCO_2 = 1009.3 - 4.9$ **DO-sat.**	8831	86.0%
	October 2019	*d*	$pCO_2 = 1932.7 + 1.6$ **DO-sat.** $- 122.7\ T$	3253	81.9%

in autumn (Fig. 9). Station *d* behaved as a CO_2 sink in summer, autumn and winter with the largest atmospheric CO_2 uptake in autumn (Table 3) where FCO_2 varied between -6.03 and -1.79 mmol m^{-2} h^{-1} (Fig. 9).

4. Discussion

4.1. Biogeochemical parameter relationships and pCO_2 controls along the shelf–estuary–marsh continuums

At the tidal estuary (*a*) and its associated channel (*b*), seasonal non-thermal effects (biological and tidal affects) inducing heterotrophy in winter and autotrophy in summer were offset by thermal effects and resulted in low seasonal variations of water pCO_2 (Fig. 7). Similar observations were reported in two marine-dominated estuaries (Jiang et al., 2008) and in the Arcachon coastal lagoon (Polsenaere et al., 2022). In the estuarine waters here, thermal effects decreased and increased in situ pCO_2 values of 30 and 40% in winter and summer, respectively. On the contrary, at the rewilded artificial salt marsh (*c*), seasonal water pCO_2 were strongly controlled by non-thermal effects promoting autotrophy both in spring and summer and heterotrophy in autumn, mostly due to macroalgae activity whereas at the working artificial salt marsh (*d*), thermal effects in summer and biological effects in autumn strongly controlled seasonal water pCO_2 (Fig. 7).

At the diurnal scale, the biological influence on continuum water pCO_2 dynamics through autotrophic and heterotrophic processes was significant at each station as endorsed by strong linear relationships between pCO_2 and DO, especially in autumn (Table 4). At the tidal estuary (*a*), from spring to autumn, diurnal pCO_2 variations were mostly controlled by the photosynthesis versus respiration balance of planktonic communities; indeed, more than 80% of the pCO_2 variance was modelled with DO only (Table 4). Dai et al. (2009) highlighted that CO_2 biogeochemical processes in coastal environments such as our estuary are generally controlled by non-thermal effects, like biological activity, compared to more open systems. Several studies have shown a major biological control on diurnal pCO_2 variations in coastal systems such as the temperate Bay of Brest (France; Bozec et al., 2011), the temperate Arcachon lagoon (France; Polsenaere et al., 2022), the shallow subtropical estuary in Tampa Bay (USA; Yates et al., 2007) and the tropical coastal embayment at Guanabara Bay (Brazil; Cotovicz et al., 2015). At the rewilded marsh (*c*), while in spring and summer, the high primary production of macroalgae induced large periods of water CO_2 undersaturation with respect to the atmosphere, winter pCO_2 variations were rather induced by planktonic community activity (ciliates $> 2\ 10^4$ cell L^{-1}; unpublish result). At the working marsh (*d*), the negative correlations between pCO_2 and Chl *a* associated with strong non-thermal contributions ($\Delta NpCO_2 = 318$ ppmv in summer for instance) showed a major biological influence on diurnal pCO_2 variations as well. By comparison, in a *Zostera marina* meadow (South Bay, USA), Berg et al. (2019) measured similar diurnal fluctuations of water pCO_2 that were directly controlled by seagrass metabolism with diurnal ranges of 528 and 603 ppmv in spring and summer, respectively.

Tidal advection of waters between continental shelf and salt marshes also significantly controlled pCO_2 dynamics and associated station biogeochemical status. This control was supported by the linear relationships between water pCO_2 and salinity as observed at each station from winter to summer whereas, relationships with turbidity were rather related to the hydrodynamic forcing on water pCO_2 (Table 4). At the tidal estuary (*a*) and its associated channel (*b*), daytime incoming tides created a significant decrease in water pCO_2 since the advected shelf waters were CO_2 undersaturated with respect to the atmosphere contrary to estuarine waters. In the Arcachon lagoon, seasonal measurement cycles also showed a strong tidal control on inorganic C parameters with lower pCO_2 values measured at high tide than at low tide irrespective of day or night status (Polsenaere et al., 2022). Even stronger tidal influences on water pCO_2 (from 1380 to 4770 ppmv) were observed during a summer cycle in the Gaderu Creek mangrove (Borges, 2003). In summer, the large pCO_2 decrease in the studied estuarine waters at ebbing tide the day, associated with strong DO saturation level increase, was probably due to CO_2 undersaturated water exports from the productive salt marshes upstream. Indeed, in spring and summer, the rewilded marsh waters (*c*) were CO_2 depleted due to strong autotrophy activity. Conversely, more CO_2-enriched coastal water inflows from the shelf and the estuary into the marsh instantly produced significant salinity decreases and pCO_2 increases (Table 4). Therefore, at each semi-diurnal tidal cycle, horizontal advection had significant effects on water pCO_2 dynamics (except during marsh confinement) but variations strongly depended on the biogeochemical state (CO_2 sink/source) of advected waters from upstream/downstream and the ecosystem typology (estuary, marsh, channel).

4.2. Continuum typologies revealed from measured biogeochemical parameters

In the coastal ocean, a strong influence of ecosystem typology (continental shelf, estuary, marsh) on biogeochemistry is generally observed and particularly, on inorganic C (Bauer et al., 2013). In our study, in 2018, watershed-influenced shelf waters (*F*) were characterized by lower salinity values than the Atlantic Ocean (35.6; Vandermeirsch, 2012), confirmed over the 2000–2017 reference period (Belin et al., 2021; REPHY, 2021). However, shelf waters showed a rather weak influence of terrestrial inputs on water pCO_2 dynamics (annual non-significant salinity and pCO_2 relationship, $p = 0.88$). At this shelf station, phytoplankton bloom with centric diatoms generally occurs in

spring and summer (Guarini et al., 2004) and can induce water CO_2 undersaturation as also observed on the Belgian continental shelf (Borges and Frankignoulle, 1999). Along the continuum, the tidal estuary (*a*) influenced by buffered shelf waters was CO_2 undersaturated at 4% in winter and 82% in spring/summer that could be attributed to coastal water autotrophic activity at this period. A previous study carried out in the same estuarine waters measured Chl *a* concentrations from 0.2 (winter) to 3.5 μg L^{-1} (spring/summer) and a Chl *a* export suggesting a net primary production within this tidal estuary (Bel Hassen, 2001). Additionally, Savelli et al. (2019) observed in a nearby intertidal zone that microphytobenthos (MPB) may also contribute to water CO_2 undersaturation and to the overall water column Chl *a* concentration through tidal resuspension. Due to the small insulary catchement area (1200 ha) consisting only of salt marshes (no terrestrial water input), the CO_2 dynamics in the tidal estuary (*a*) is different from other estuaries worldwide (Borges and Abril, 2011). Similarly, the marine-dominated estuary of Sapelo Sound (USA) was also characterized by lower water pCO_2 values than river-dominated ones (Borges and Abril, 2011) but bacterial remineralization of organic carbon produced by *Spartina* in nearby salt marshes strongly increased water pCO_2 in summer (Jiang et al., 2008) contrarily to our studied estuary.

Overall, channel (*b*) waters between the estuary and salt marshes showed the longest periods of CO_2 oversaturation with respect to the atmosphere. At this channel station, strong hydrodynamic forcings during incoming and ebbing tides produced more turbid waters due to organic matter resuspension from muds (Guarini et al., 2008). It probably limited the primary production (phytoplankton, MPB) by low light availability in water column (Cloern, 1987) and, on the contrary, favoured heterotrophic processes (Polsenaere et al., 2022). In channel waters, we recorded lower DO concentrations (−10%) and higher pCO_2 values (+ 10%) than in estuarine waters under similar salinity ranges and meteorological conditions. In channels at the same location, Tortajada (2011) measured POC/Chl $a > 200$ mg mg^{-1} throughout the year and even POC/Chl $a > 600$ mg mg^{-1} in autumn. This detrital/heterotrophic organic material may indicate microbial mineralization processes from MPB and confirm the water CO_2 oversaturation periods. However, our studied channel (*b*) showed lower water pCO_2 values than those from other coastal channel systems probably due to low terrestrial water inputs upstream/downstream over the estuary (*a*). The Sancti Petri Channel waters and its nearby salt marshes between the Atlantic Ocean and the Cadiz Bay (Spain) were also mainly CO_2 oversaturated (281–862 ppmv), due to DIC inputs from diagenetic processes of organic matter in mudflats that constitute a CO_2 source to water column (Burgos et al., 2018). Indeed, within the Duplin River salt marsh-estuary coastal system (USA), higher summer pCO_2 and DIC values were recorded at low tide in channel waters (12 000 ppmv and 4300 μmol L^{-1}, respectively) than at high tide in marsh waters (1600 ppmv and 2200 μmol L^{-1}, respectively; Wang et al., 2018).

Contrary to estuarine and channel waters, artificial salt marshes (*c* and *d*) waters were characterized by the lowest turbidity and highest salinity values due to longer water residence times. These lower hydrodynamic conditions promoted the development of primary producers and as a result, biological CO_2 uptake associated with the highest DO saturation levels. In turn, the salt marshes showed lower water pCO_2 values and longer water CO_2 undersaturation periods mainly due to a strong macrophyte activity (macroalgae at rewilded marsh and seagrasses at working marsh) than the tidal estuary and elsewhere similar wetland typologies (Borges, 2003; Burgos et al., 2018; Wang et al., 2018; Berg et al., 2019; Polsenaere et al., 2022; Song et al., 2023). Unlike seagrasses which are known to be important blue C systems (Mcleod et al., 2011), macroalgae developing in coastal wetlands have a limited capacity to store C over the long-term. However, studies have shown their potential contribution to coastal blue C by (i) storing large organic matter quantities in their living biomass through their high primary production (Raven, 2018) and (ii) transferring it to adjacent systems through tides and storage in coastal sediments (Duarte and Cebrián, 1996; Hill et al., 2015; Krause-Jensen and Duarte, 2016). Our pCO_2 observations are in accordance with these reports with the role of C storage by macrophytes in these shallow salt marshes.

4.3. Temporal carbon modulation by management practices

Management practices at the artificial salt marshes correspond to specific water lock actions linked to anthropogenic activities. They can strongly modulate water fluxes from the estuary and thereby influence marsh pCO_2 dynamics. At the rewilded marsh (*c*), the specific management practice by the NNR produced favourable conditions for free floating macroalgae development from early spring to late summer under low water marsh hydrodynamic and high air and water temperature conditions (Newton and Thornber, 2013). These macroalgae indicate a degraded-eutrophic status of the marsh waters with excess nutrient inputs, as described for other coastal ecosystems (Teichberg et al., 2010; Le Fur et al., 2018). In our study, nearby marsh aquafarming activities occurring upstream from the estuary (Paticat, 2007; Tortajada, 2011) can communicate with the rewilded marsh (*c*) through channels and result in high nutrient conditions which could explain observed macroalgae blooms. Indeed, at the station *b* channel in September 2018, high DIN concentrations were reported (60 μmol L^{-1}; unpublished results). Moreover, shelf waters influenced by terrestrial inputs in winter could also lead to nutrient inputs at the rewilded marsh. Indeed, at the station *F* shelf in winter 2019, NO_3^- ranged between 29 and 107 μmol L^{-1} (Belin et al., 2021; REPHY, 2021). Consequently, these fast-growing macroalgae probably prevented the growth of phytoplankton and seagrasses by nutrient and oxygen competition and light limitation in the water column (Sand-Jensen and Borum, 1991; Le Fur et al., 2018). Simultaneously, in spring and summer, the large water CO_2 undersaturation periods due to the macroalgae autotrophy were maintained through occasional inflows of CO_2 oversaturated channel waters (weak tidal amplitudes). This result is confirmed by significantly higher salinity values in the rewilded marsh waters than in the channel waters during the spring and summer sampling periods (Table 2). On the contrary, macroalgae degradation in autumn probably by microbial remineralization processes (Hill et al., 2015) produced in turn the highest pCO_2 values and the longest oversaturation periods recorded in marsh waters. These heterotrophic processes were confirmed by high NH_4^+ levels (62 μmol L^{-1}; unpublished results) and low DO saturation levels recorded at this period and as described by Newton and Thornber (2013).

Contrarily to the rewilded marsh (*c*), the working marsh (*d*) is managed for salt production in the upstream ponds along the continuum and is directly connected to the estuary (*a*) with no channel in between (Fig. 10). Salt production requires a subtle lock hydraulic management of the marsh depending on the frequency of the coastal water supplies that are mainly controlled by the salt manufacturer and meteorological conditions (rainfall, sunshine and wind) to favour the evaporation process (Paticat, 2007). Therefore, contrary to rewilded marsh, coastal water inflows to the working marsh were performed sparingly with small daily volumes to limit these water mixing effects (i.e. rapid accumulation of large water volumes through rainfall events or spring tides stop the increase in temperature and salinity in marsh waters; Paticat, 2007). At the working marsh in summer, water pCO_2 were significantly higher than those measured at the same period at the rewilded marsh but reflected those from the estuary (Table 2). This could also be linked to a lower activity of the primary producers during the summer period dedicated to salt production as confirmed by higher thermal than non-thermal effects on water pCO_2 (Fig. 7). On the other hand, in autumn and winter, lower hydrodynamic conditions due to lock closure (standstill salt farming activity) led to low water turbidity (< 2 NTU) and nutrient input into the marsh (DIN < 2 μmol L^{-1}; unpublished results) and the growth of seagrasses and phytoplankton produced, in turn, the lowest water pCO_2 values. Overall, in Mediterranean poly-euhaline lagoons, Le Fur et al. (2018) confirmed that nutrient

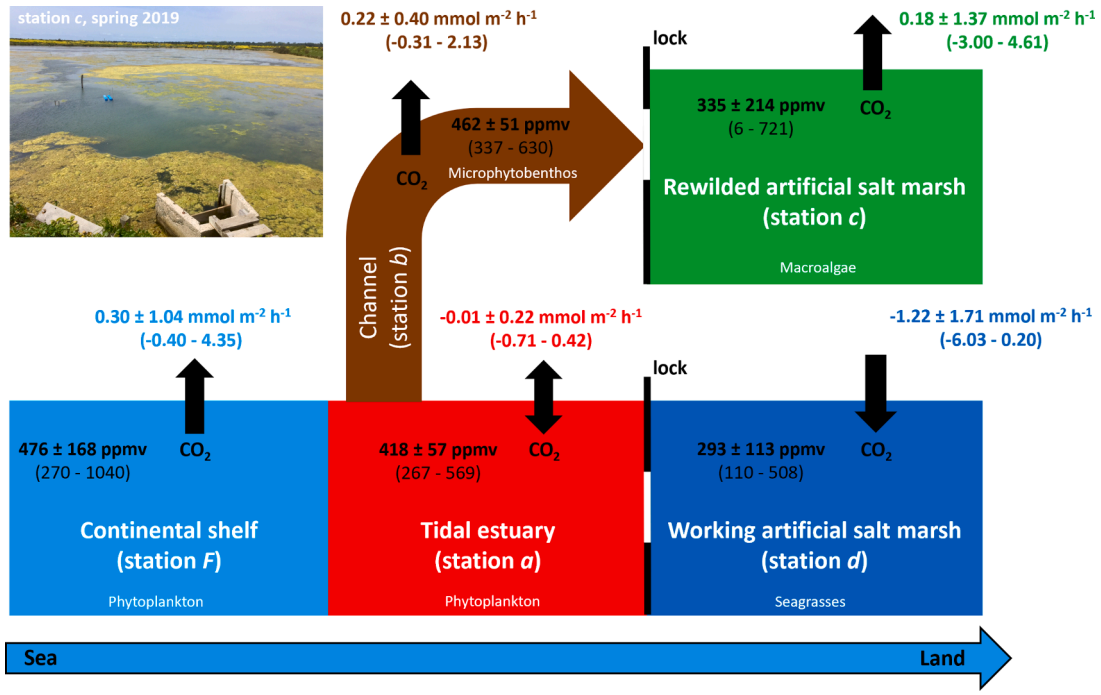

Fig. 10. CO_2 budget over the two aquatic sea - land continuums: (1) continental shelf - estuary - channel - rewilded artificial salt marsh and (2) continental shelf - estuary - working artificial salt marsh. Annual means (± SD) and ranges (min–max) of water pCO_2 (ppmv) and air–water FCO_2 (mmol m^{-2} h^{-1}) are showed. The picture of station *c* in spring 2019 (© P. Polsenaere) allows to visualize the macroalgae bloom.

pollution influence the contribution of primary producers from perennial seagrasses in oligotrophic waters to fast-growing macroalgae in eutrophic waters. Similarly, other studies have suggested that the coastal ecosystem management by reducing anthropogenic nutrients could favour blue C ecosystems such as seagrasses and salt marshes (Macreadie et al., 2017; Palacios et al., 2021).

4.4. Metabolism assessment of the sea–land continuums

The tidal estuary (*a*) behaved on average as a yearly CO_2 sink close to the atmospheric equilibrium (Fig. 10), although a significant sink was measured in the spring/summer due to autotrophic activity of phytoplankton in coastal waters. Conversely, over the same meteorological periods, the channel (*b*) was a net annual source from its turbid waters to the atmosphere due to several water CO_2 oversaturation periods (Fig. 10), particularly in winter, characterized by high gas transfer velocities (Table 3). In the Arcachon lagoon, estimated atmospheric CO_2 sources were higher with seasonal means ranging from 0.06 ± 0.04 (winter) to 0.62 ± 0.66 mmol m^{-2} h^{-1} (summer) with significant diurnal fluctuations (Polsenaere et al., 2022). In our study, eutrophic waters of the rewilded marsh (*c*) behaved as a yearly source of atmospheric CO_2 (Fig. 10), when macroalgae degradation produced strong atmospheric CO_2 effluxes. On the contrary, oligotrophic waters of the working marsh (*d*) behaved as a large yearly CO_2 sink (Fig. 10), favoured by low tidal advection in the absence of salt-farming activities. Within the Duplin River salt marsh-estuary system, both channel and marsh waters degassed CO_2 to the atmosphere and, unlike our stations, the highest and lowest sources were recorded in summer (5.50 and 3.90 mmol m^{-2} h^{-1} from channel and marsh waters, respectively) and in winter (0.70 and 0.60 mmol m^{-2} h^{-1} from channel and marsh waters, respectively), respectively (Wang et al., 2018). Overall, the Duplin system emits more atmospheric CO_2 than the Fier d'Ars system, probably due to its more intense estuarine heterotrophic metabolism.

In autumn, the lack of variations in wind speeds between stations *a* and *b* in 2018 and between stations *c* and *d* in 2019, whereas atmospheric CO_2 exchanges significantly changed, highlighted the predominance of air–water CO_2 gradients in the control of flux directions either as a sink or a source (Table 3). However, at the seasonal scale, turbulence processes measured at the air–water interface played an important role in CO_2 flux variability and magnitude. For instance, at station *a* between spring and summer and at station *b* between winter and summer, wind speed variability produced significant FCO_2 variations although no significant air–water CO_2 gradients were measured (Table 3). Atmospheric exchanges in salt marshes are therefore dependent on the CO_2 saturation state of the water column considering that the wind only acts as a driver of the flux (Polsenaere et al., 2022). Moreover, the methodological calculations and associated differences chosen for the exchange coefficient parameterizations (higher fluxes with RC01 than with W22; Table 3) may produce even more contrasts in the estimated air–water FCO_2 (Cotovicz et al., 2015; Polsenaere et al., 2022).

By scaling-up and considering stations *a* and *b* together along the continuum, estuarine and channel waters behaved as an annual atmospheric CO_2 source of 7.3 g C m^{-2} yr^{-1}. The rewilded marsh emitted 17.5 g C m^{-2} yr^{-1} to the atmosphere whereas, the working marsh absorbed 97.7 g C m^{-2} yr^{-1} from the atmosphere. A larger scale study along three shelf–estuary–tidal wetland continuums on the Atlantic coast of the United States also showed strong spatial variations in atmospheric CO_2 fluxes with uptake to wetland and shelf waters (523.2 ± 148.1 and 10.5 ± 1.8 g C m^{-2} yr^{-1}, respectively) and a source from estuarine waters (110.0 ± 44.5 g C m^{-2} yr^{-1}; Najjar et al., 2018). During our study, contrasting coastal stations were sampled via seasonal 24-h cycles to estimate the air–water CO_2 exchanges. However, longer seasonal measurement periods would be more representative of the strong temporal variability in k_{660}, water pCO_2 and other biogeochemical parameters. At the nearby tidal salt marsh (*e*), emerged for 75% of time during low tides and neap tides, another flux methodology using the atmospheric Eddy Covariance technique was deployed to continuously measure in situ CO_2 fluxes at the ecosystem scale coming from all habitats (aquatic and terrestrial vegetations, mudflats, channels). Over the year 2020, a net uptake of 483 g C m^{-2} yr^{-1} from the atmosphere was measured, indicating a stronger CO_2 sink in tidal marshes than artificial

marshes due to higher halophytic plant photosynthesis activity. However, it is also important to study the whole marsh metabolism taking terrestrial and aquatic compartments into account and distinguishing their respective contributions to atmospheric fluxes and the regional C budgets of the associated marshes (Mayen et al., 2017).

5. Conclusion

Along the continuums, estuarine and channel waters were slightly oversaturated in CO_2 characterized by seasonal compensations of thermal and non-thermal effects whereas, upstream marsh waters were mostly undersaturated in CO_2 due to stronger biological activity and longer water residence times. At the diurnal/tidal scale, our high-resolution analyses highlighted large water pCO_2 variations in salt marshes, controlled by production and respiration of macrophytes and coastal water inflows. However, anthropogenic management in salt marshes could strongly influence the contribution and turnover of macrophytes and, consequently, the marsh CO_2 sink/source behaviour. Due to eutrophication in the rewilded salt marsh, development of the fast-growing macroalgae produced an overall net annual atmospheric CO_2 source through their degradation. Our results suggest a winter marsh confinement follow by drying up to limit nutrient inputs and macroalgae development and on the contrary, favour rather slow-growing macrophytes (i.e. seagrasses) which could ultimately contribute to blue C sequestration.

CRediT authorship contribution statement

Jérémy Mayen: Methodology, Software, Validation, Formal analysis, Investigation, Writing – original draft, Writing – review & editing. **Pierre Polsenaere:** Conceptualization, Methodology, Software, Validation, Formal analysis, Investigation, Resources, Writing – review & editing, Supervision, Project Administration, Funding acquisition. **Aurore Regaudie de Gioux:** Writing – review & editing, Supervision, Funding acquisition. **Christine Dupuy:** Validation, Writing – review & editing. **Marie Vagner:** Writing – review & editing, Funding acquisition. **Jean-Christophe Lemesle:** Resources. **Benoit Poitevin:** Resources. **Philippe Souchu:** Validation, Writing – review & editing, Supervision, Funding acquisition.

Declaration of competing interest

The authors declare that they have no known competing financial interests or personal relationships that could have appeared to influence the work reported in this paper.

Data availability

Data will be made available on request

Acknowledgements

We would like to sincerely thank the oyster farmers for their help with taking samples at station *a*, Julien Gernigon from the Lilleau des Niges NNR (LPO) and Brice Collonier from the Loix Ecomuseum for their help and the information given at stations *b*, *c*, *d* and *e*. We are grateful to our colleagues Jean-Michel Chabirand, James Grizon and Philippe Geairon for their help with field sensor deployments and QGIS work. We also thank Quentin Ternon, Gabriel Devique and Jonathan Deborde for their contribution in the field. This paper is a contribution to the Master and Ph.D. thesis of Jérémy Mayen (Ifremer funding, France), the ANR-PAMPAS project (Agence Nationale de la Recherche, France «Evolution de l'identité patrimoniale des marais des Pertuis Charentais en réponse à l'aléa de submersion marine », ANR-18-CE32-0006) and the CNRS-INSU LEFE-DYCIDEMAIM project (DYnamique du Carbone aux Interfaces D'Échange des MArais tIdaux teMpérés, France). Our grateful acknowledgements also go to the two anonymous reviewers for their constructive comments and suggestions. The English language was edited by Sara Mullin (Ph.D.).

Appendix A. Supplementary data

Supplementary material related to this article can be found online at https://doi.org/10.1016/j.rsma.2023.103209.

References

Adam, P., 2019. Salt marsh restoration. In: Coastal WetlandS. Elsevier, pp. 817–861. https://doi.org/10.1016/B978-0-444-63893-9.00023-X.

Aminot, A., Kérouel, R., 2004. Hydrologie des écosystèmes marins. In: Ifremer (Ed.), Paramètres Et Analyses.

Amorocho, J., DeVries, J.J., 1980. A new evaluation of the wind stress coefficient over water surfaces. J. Geophys. Res. 85 (433) https://doi.org/10.1029/JC085iC01p00433.

Artigas, F., Shin, J.Y., Hobble, C., Marti-Donati, A., Schäfer, K.V.R., Pechmann, I., 2015. Long term carbon storage potential and CO_2 sink strength of a restored salt marsh in New Jersey. Agricult. Forest Meteorol. 200, 313–321. https://doi.org/10.1016/j.agrformet.2014.09.012.

Aufdenkampe, A.K., Mayorga, E., Raymond, P.A., Melack, J.M., Doney, S.C., Alin, S.R., Aalto, R.E., Yoo, K., 2011. Riverine coupling of biogeochemical cycles between land, oceans, and atmosphere. Front. Ecol. Environ. 9, 53–60. https://doi.org/10.1890/100014.

Bade, D.L., 2009. Gas exchange at the air–water interface. In: Encyclopedia of Inland Waters. Elsevier, pp. 70–78. https://doi.org/10.1016/B978-012370626-3.00213-1.

Baldocchi, D.D., Hincks, B.B., Meyers, T.P., 1988. Measuring biosphere-atmosphere exchanges of biologically related gases with micrometeorological methods. Ecology 69, 1331–1340. https://doi.org/10.2307/1941631.

Bauer, J.E., Cai, W.-J., Raymond, P.A., Bianchi, T.S., Hopkinson, C.S., Regnier, P.A.G., 2013. The changing carbon cycle of the coastal ocean. Nature 504, 61–70. https://doi.org/10.1038/nature12857.

Bel Hassen, M., 2001. Spatial and temporal variability in nutrients and suspended material processing in the fier d'ars bay (France). Estuar. Coast. Shelf Sci. 52, 457–469. https://doi.org/10.1006/ecss.2000.0754.

Belin, C., Soudant, D., Amzil, Z., 2021. Three decades of data on phytoplankton and phycotoxins on the French coast: Lessons from rephy and rephytox. Harmful Algae 102, 101733. https://doi.org/10.1016/j.hal.2019.101733.

Berg, P., Delgard, M.L., Polsenaere, P., McGlathery, K.J., Doney, S.C., Berger, A.C., 2019. Dynamics of benthic metabolism, O_2, and pCO_2 in a temperate seagrass meadow. Limnol. Oceanogr. 64, 2586–2604. https://doi.org/10.1002/lno.11236.

Borges, A.V., 2003. Atmospheric CO_2 flux from mangrove surrounding waters. Geophys. Res. Lett. 30 (1558) https://doi.org/10.1029/2003GL017143.

Borges, A.V., Abril, G., 2011. Carbon dioxide and methane dynamics in estuaries. In: Treatise on Estuarine and Coastal Science. Elsevier, pp. 119–161. https://doi.org/10.1016/B978-0-12-374711-2.00504-0.

Borges, A.V., Delille, B., Frankignoulle, M., 2005. Budgeting sinks and sources of CO_2 in the coastal ocean: Diversity of ecosystems counts: Coastal CO_2 Sinks and sources. Geophys. Res. Lett. 32 (LI4601) https://doi.org/10.1029/2005GL023053.

Borges, A.V., Frankignoulle, M., 1999. Daily and seasonal variations of the partial pressure of CO_2 in surface seawater along Belgian and southern Dutch coastal areas. J. Mar. Syst. 19, 251–266. https://doi.org/10.1016/S0924-7963(98)00093-1.

Bozec, Y., Merlivat, L., Baudoux, A.-C., Beaumont, L., Blain, S., Bucciarelli, E., Danguy, T., Grossteffan, E., Guillot, A., Guillou, J., Répécaud, M., Tréguer, P., 2011. Diurnal to inter-annual dynamics of pCO_2 recorded by a CARIOCA sensor in a temperate coastal ecosystem (2003–2009). Mar. Chem. 126, 13–26. https://doi.org/10.1016/j.marchem.2011.03.003.

Burgos, M., Ortega, T., Forja, J., 2018. Carbon dioxide and methane dynamics in Three Coastal systems of cadiz bay (SW Spain). Estuar. Coasts 41, 1069–1088. https://doi.org/10.1007/s12237-017-0330-2.

Cai, W.-J., 2011. Estuarine and coastal ocean carbon paradox: CO_2 sinks or sites of terrestrial carbon incineration? Annu. Rev. Mar. Sci. 3, 123–145. https://doi.org/10.1146/annurev-marine-120709-142723.

Champion, E., Gernigon, J., Lemesle, J.-C., Terrisse, J., Maisonhaute, S., 2012. 3Ème Plan de gestion 2013–2017 de la réserve naturelle nationale de Lilleau des Niges.

Chmura, G.L., Anisfeld, S.C., Cahoon, D.R., Lynch, J.C., 2003. Global carbon sequestration in tidal, saline wetland soils. In: Global Biogeochem. Cycles, Vol. 17, p. 1111. https://doi.org/10.1029/2002GB001917.

Cloern, J.E., 1987. Turbidity as a control on phytoplankton biomass and productivity in estuaries. Cont. Shelf Res. 7, 1367–1381. https://doi.org/10.1016/0278-4343(87)90042-2. Dynamics of Turbid Coastal Environments.

Coignot, E., Polsenaere, P., Soletchnik, O., Le Moine, P., Souchu, E., Joyeux, Y., Le Roy, J.-P., Guéret, L., Froud, R., Gallais, E., Chourré, P., Chaigneau, L., 2020. Variabilité spatio-temporelle des nutriments et du carbone et flux associés le long d'un continuum terrestre-aquatique tempéré (Marais poitevin – Baie de l'Aiguillon – Pertuis Breton). In: Rapport Final (Suivi 2017-2018) - Projet Aiguillon (2016–2020), p. 111. https://archimer.ifremer.fr/doc/00618/73003/.

Cole, J.J., Prairie, Y.T., Caraco, N.F., McDowell, W.H., Tranvik, L.J., Striegl, R.G., Duarte, C.M., Kortelainen, P., Downing, J.A., Middelburg, J.J., Melack, J., 2007. Plumbing the global carbon cycle: Integrating inland waters into the terrestrial

carbon budget. Ecosystems 10, 172–185. https://doi.org/10.1007/s10021-006-9013-8.
Cotovicz Jr., L.C., Knoppers, B.A., Brandini, N., Costa Santos, S.J., Abril, G., 2015. A strong CO_2 sink enhanced by eutrophication in a tropical coastal embayment (Guanabara Bay, Rio de Janeiro, Brazil). Biogeosciences 12, 6125–6146. https://doi.org/10.5194/bg-12-6125-2015.
Crosswell, J.R., Anderson, I.C., Stanhope, J.W., Dam, B.V., Brush, M.J., Ensign, S., Piehler, M.F., McKee, B., Bost, M., Paerl, H.W., 2017. Carbon budget of a shallow, lagoonal estuary: Transformations and source–sink dynamics along the river-estuary-ocean continuum. Limnol. Oceanogr. 62, S29–S45. https://doi.org/10.1002/lno.10631.
Dai, M., Lu, Z., Zhai, W., Chen, B., Cao, Z., Zhou, K., Cai, W.-J., Chenc, C.-T.A., 2009. Diurnal variations of surface seawater pCO_2 in contrasting coastal environments. Limnol. Oceanogr. 54, 735–745. https://doi.org/10.4319/lo.2009.54.3.0735.
Dai, M., Su, J., Zhao, Y., Hofmann, E.E., Cao, Z., Cai, W.-J., Gan, J., Lacroix, F., Laruelle, G.G., Meng, F., Müller, J.D., Regnier, P.A.G., Wang, G., Wang, Z., 2022. Carbon fluxes in the coastal ocean: Synthesis, boundary processes, and future trends. Annu. Rev. Earth Planet. Sci. 50, 593–626. https://doi.org/10.1146/annurev-earth-032320-090746.
Deegan, L.A., Johnson, D.S., Warren, R.S., Peterson, B.J., Fleeger, J.W., Fagherazzi, S., Wollheim, W.M., 2012. Coastal eutrophication as a driver of salt marsh loss. Nature 490, 388–392. https://doi.org/10.1038/nature11533.
Dickson, A.G., 1990. Standard potential of the reaction: $AgCl(s) + 1/2H_2(g) = Ag(s) + HCl(aq)$, and the standard acidity constant of the ion HSO_4^- in synthetic sea water from 273.15 to 318.15 K. J. Chem. Thermodyn. 22, 113–127.
Dickson, A.G., Millero, F.J., 1987. A comparison of the equilibrium constants for the dissociation of carbonic acid in seawater media. Deep-Sea Res. 34, 1733–1743.
Duarte, C.M., Cebrián, J., 1996. The fate of marine autotrophic production. Limnol. Oceanogr. 41, 1758–1766. https://doi.org/10.4319/lo.1996.41.8.1758.
Dürr, H.H., Laruelle, G.G., van Kempen, C.M., Slomp, C.P., Meybeck, M., Middelkoop, H., 2011. Worldwide typology of Nearshore Coastal systems: Defining the estuarine filter of river inputs to the oceans. Estuar. Coasts 34, 441–458. https://doi.org/10.1007/s12237-011-9381-y.
Forbrich, I., Giblin, A.E., 2015. Marsh-atmosphere CO_2 exchange in a New England salt marsh. J. Geophys. Res. Biogeosci. 120, 1825–1838. https://doi.org/10.1002/2015JG003044.
Frankignoulle, M., Abril, G., Borges, A., Bourge, I., Canon, C., Delille, B., Libert, E., Théate, J.-M., 1998. Carbon dioxide emission from European estuaries. Sci. New Ser. 282, 434–436.
Gattuso, J.-P., Frankignoulle, M., Wollast, R., 1998. Carbon and carbonate metabolism in coastal aquatic ecosystems. Annu. Rev. Ecol. Syst. 29, 405–434. https://doi.org/10.1146/annurev.ecolsys.29.1.405.
Gu, J., Luo, M., Zhang, X., Christakos, G., Agusti, S., Duarte, C.M., Wu, J., 2018. Losses of salt marsh in China: Trends, threats and management. Estuar. Coast. Shelf Sci. 214, 98–109. https://doi.org/10.1016/j.ecss.2018.09.015.
Guarini, J.-M., Gros, P., Blanchard, G., Richard, P., Fillon, A., 2004. Benthic contribution to pelagic microalgal communities in two semi-enclosed, European-type littoral ecosystems (Marennes-Oléron Bay and Aiguillon Bay, France). J. Sea Res. 52, 241–258. https://doi.org/10.1016/j.seares.2004.04.003.
Guarini, J.-M., Sari, N., Moritz, C., 2008. Modelling the dynamics of the microalgal biomass in semi-enclosed shallow-water ecosystems. Ecol. Model. 211, 267–278. https://doi.org/10.1016/j.ecolmodel.2007.09.011.
Harrell, F.E., 2015. In: Regression Modeling Strategies: With Applications To Linear Models, Logistic and Ordinal Regression, and Survival Analysis. Springer Series in Statistics.. Springer International Publishing, Cham. https://doi.org/10.1007/978-3-319-19425-7.
Hill, R., Bellgrove, A., Macreadie, P.I., Petrou, K., Beardall, J., Steven, A., Ralph, P.J., 2015. Can macroalgae contribute to blue carbon? An Australian perspective: Can macroalgae contribute to blue carbon? Limnol. Oceanogr. 60, 1689–1706. https://doi.org/10.1002/lno.10128.
Jähne, B., Münnich, K.O., Bösinger, R., Dutzi, A., Huber, W., Libner, P., 1987. On the parameters influencing air–water gas exchange. J. Geophys. Res. 92 (1937) https://doi.org/10.1029/JC092iC02p01937.
Jiang, L.-Q., Cai, W.-J., Wang, Y., 2008. A comparative study of carbon dioxide degassing in river- and marine-dominated estuaries. Limnol. Oceanogr. 53, 2603–2615. https://doi.org/10.4319/lo.2008.53.6.2603.
Krause-Jensen, D., Duarte, C.M., 2016. Substantial role of macroalgae in marine carbon sequestration. Nat. Geosci. 9, 737–742. https://doi.org/10.1038/ngeo2790.
Lê, S., Josse, J., Husson, F., 2008. FactoMineR: An *R* package for multivariate analysis. J. Stat. Soft. 25 https://doi.org/10.18637/jss.v025.i01.
Le Fur, I., De Wit, R., Plus, M., Oheix, J., Simier, M., Ouisse, V., 2018. Submerged benthic macrophytes in Mediterranean lagoons: distribution patterns in relation to water chemistry and depth. Hydrobiologia 808, 175–200. https://doi.org/10.1007/s10750-017-3421-y.
Lee, K., Kim, T.-W., Byrne, R.H., Millero, F.J., Feely, R.A., Liu, Y.-M., 2010. The universal ratio of boron to chlorinity for the North Pacific and North Atlantic oceans. Geochim. Cosmochim. Acta 74, 1801–1811. https://doi.org/10.1016/j.gca.2009.12.027.
Lewis, E., Wallace, D., 1998. Program Developed for CO_2 System Calculations. Carbon dioxide information analysis center. Oak Ridge National Laboratory.
Macreadie, P.I., Nielsen, D.A., Kelleway, J.J., Atwood, T.B., Seymour, J.R., Petrou, K., Connolly, R.M., Thomson, A.C., Trevathan-Tackett, S.M., Ralph, P.J., 2017. Can we manage coastal ecosystems to sequester more blue carbon?. pp. 8. https://doi.org/10.1002/fee.1484.
Mayen, J., Polsenaere, P., Lamaud, É., Arnaud, M., Kostyrka, P., Bonnefond, J.-M., Geairon, P., Gernigon, J., Chassagne, R., Lacoue-Labarthe, T., Regaudie de Gioux, A., Souchu, P., 2017. Atmospheric CO_2 exchanges measured by Eddy Covariance over a temperate salt marsh and influence of environmental controlling factors, EGUsphere [preprint]. https://doi.org/10.5194/egusphere-2023-1641.
Mcleod, E., Chmura, G.L., Bouillon, S., Salm, R., Björk, M., Duarte, C.M., Lovelock, C.E., Schlesinger, W.H., Silliman, B.R., 2011. A blueprint for blue carbon: toward an improved understanding of the role of vegetated coastal habitats in sequestering CO_2. Front. Ecol. Environ. 9, 552–560. https://doi.org/10.1890/110004.
Mehrbach, C., Culberson, C.H., Hawley, J.E., Pytkowicz, R.M., 1973. Measurement of the apparent dissociation constants of carbonic acid in seawater at atmospheric pressure. Limnol. Oceanogr. 18, 897–907.
Najjar, R.G., Herrmann, M., Alexander, R., Boyer, E.W., Burdige, D.J., Butman, D., Cai, W.-J., Canuel, E.A., Chen, R.F., Friedrichs, M.A.M., Feagin, R.A., Griffith, P.C., Hinson, A.L., Holmquist, J.R., Hu, X., Kemp, W.M., Kroeger, K.D., Mannino, A., McCallister, S.L., McGillis, W.R., Mulholland, M.R., Pilskaln, C.H., Salisbury, J., Signorini, S.R., St-Laurent, P., Tian, H., Tzortziou, M., Vlahos, P., Wang, Z.A., Zimmerman, R.C., 2018. Carbon budget of tidal wetlands, estuaries, and shelf waters of Eastern North America. In: Global Biogeochem. Cycles, Vol. 32, pp. 389–416. https://doi.org/10.1002/2017GB005790.
Newton, C., Thornber, C., 2013. Ecological impacts of macroalgal blooms on salt marsh communities. Estuar. Coasts 36, 365–376. https://doi.org/10.1007/s12237-012-9565-0.
Palacios, M.M., Trevathan-Tackett, S.M., Malerba, M.E., Macreadie, P.I., 2021. Effects of a nutrient enrichment pulse on blue carbon ecosystems. Mar. Pollut. Bull. 165, 112024 https://doi.org/10.1016/j.marpolbul.2021.112024.
Paticat, F., 2007. Flux Et Usages De L'eau De Mer Dans Les Marais Salés Endigués Charentais: Cas Du Marais Salé Endigué De L'île De Ré (Thèse). Université Nantes.
Polsenaere, P., Deborde, J., Detandt, G., Vidal, L.O., Pérez, M.A.P., Marieu, V., Abril, G., 2013. Thermal enhancement of gas transfer velocity of CO_2 in an Amazon floodplain lake revealed by eddy covariance measurements: Gas transfer velocity in an amazon lake. Geophys. Res. Lett. 40, 1734–1740. https://doi.org/10.1002/grl.50291.
Polsenaere, P., Delille, B., Poirier, D., Charbonnier, C., Deborde, J., Mouret, A., Abril, G., 2022. Seasonal, diurnal, and tidal variations of dissolved inorganic carbon and pCO_2 in surface waters of a Temperate Coastal lagoon (Arcachon, SW France). Estuar. Coasts. https://doi.org/10.1007/s12237-022-01121-6.
Polsenaere, P., Lamaud, E., Lafon, V., Bonnefond, J.-M., Bretel, P., Delille, B., Deborde, J., Loustau, D., Abril, G., 2012. Spatial and temporal CO_2 exchanges measured by Eddy Covariance over a temperate intertidal flat and their relationships to net ecosystem production. Biogeosciences 9, 249–268. https://doi.org/10.5194/bg-9-249-2012.
Raven, J., 2018. Blue carbon: past, present and future, with emphasis on macroalgae. Biol. Lett. 14, 20180336 https://doi.org/10.1098/rsbl.2018.0336.
Raymond, P.A., Cole, J.J., 2001. Gas exchange in rivers and estuaries: Choosing a gas transfer velocity. Estuaries 24 (312). https://doi.org/10.2307/1352954.
REPHY – French observation and monitoring program for phytoplankton and hydrology in coastal waters. In: REPHY Dataset - French Observation and Monitoring Program for Phytoplankton and Hydrology in Coastal Waters, 2021. Metropolitan data. SEANOE. https://doi.org/10.17882/47248.
Ribas-Ribas, M., Gómez-Parra, A., Forja, J.M., 2011. Air–sea CO_2 fluxes in the north-eastern shelf of the Gulf of Cádiz (southwest Iberian Peninsula). Mar. Chem. 123, 56–66. https://doi.org/10.1016/j.marchem.2010.09.005.
Sand-Jensen, K., Borum, J., 1991. Interactions among phytoplankton, periphyton, and macrophytes in temperate freshwaters and estuaries. Aquat. Bot. 41, 137–175. https://doi.org/10.1016/0304-3770(91)90042-4.
Savelli, R., Bertin, X., Orvain, F., Gernez, P., Dale, A., Coulombier, T., Pineau, P., Lachaussée, N., Polsenaere, P., Dupuy, C., Le Fouest, V., 2019. Impact of chronic and massive resuspension mechanisms on the microphytobenthos dynamics in a temperate intertidal mudflat. J. Geophys. Res. Biogeosci. 124, 3752–3777. https://doi.org/10.1029/2019JG005369.
Schäfer, K.V.R., Tripathee, R., Artigas, F., Morin, T.H., Bohrer, G., 2014. Carbon dioxide fluxes of an urban tidal marsh in the Hudson-Raritan estuary: Carbon dioxide fluxes of a wetland. J. Geophys. Res. Biogeosci. 119, 2065–2081. https://doi.org/10.1002/2014JG002703.
Soletchnik, P., Polsenaere, P., Le Moine, O., Guesdon, S., Béchemin, C., 2015. Relations entre apports terrigènes et conchyliculture dans les pertuis charentais. pp. 1–53. http://archimer.ifremer.fr/doc/00248/35964/.
Song, S., Wang, Z.A., Kroeger, K.D., Eagle, M., Chu, S.N., Ge, J., 2023. High-frequency variability of carbon dioxide fluxes in tidal water over a temperate salt marsh. Limnol. Oceanogr. 12409. https://doi.org/10.1002/lno.12409.
Stanisière, J.Y., Dumas, F., Plus, M., Maurer, D., Robert, S., 2006. Caractérisation des composantes hydrodynamiques d'un système côtier semi-fermé: le bassin de marennes-oléron. pp. 1–112. http://archimer.ifremer.fr/doc/00000/2353/.
Takahashi, T., Sutherland, S.C., Sweeney, C., Poisson, A., Metzl, N., Tilbrook, B., Bates, N., Wanninkhof, R., Feely, R.A., Sabine, C., Olafsson, J., Nojiri, Y., 2002. Global sea–air CO_2 flux based on climatological surface ocean pCO_2, and seasonal biological and temperature effects. Deep Sea Res. II 49, 1601–1622. https://doi.org/10.1016/S0967-0645(02)00003-6.
Teichberg, M., Fox, S.E., Olsen, Y.S., Valiela, I., Martinetto, P., Iribarne, O., Muto, E.Y., Petti, M.A.V., Corbisier, T.N., Soto-Jiménez, M., Páez-Osuna, F., Castro, P., Freitas, H., Zitelli, A., Cardinaletti, M., Tagliapietra, D., 2010. Eutrophication and macroalgal blooms in temperate and tropical coastal waters: nutrient enrichment experiments with *Ulva* spp. Global Change Biol. 16, 2624–2637. https://doi.org/10.1111/j.1365-2486.2009.02108.x.
Tobias, C., Neubauer, S.C., 2019. Salt marsh biogeochemistry—An overview. In: Coastal WetlandS. Elsevier, pp. 539–596. https://doi.org/10.1016/B978-0-444-63893-9.00016-2.

Tortajada, S., 2011. De L'étude Du Fonctionnement Des Réseaux Trophiques Planctoniques Des Marais de Charente Maritime Vers la Recherche D'Indicateurs (Thèse). Université La Rochelle.

Tortajada, S., David, V., Brahmia, A., Dupuy, C., Laniesse, T., Parinet, B., Pouget, F., Rousseau, F., Simon-Bouhet, B., Robin, F.-X., 2011. Variability of fresh- and salt-water marshes characteristics on the west coast of France: A spatio-temporal assessment. Water Res. 45, 4152–4168. https://doi.org/10.1016/j.watres.2011.05.024.

Van Dam, B., Polsenaere, P., Barreras-Apodaca, A., Lopes, C., Sanchez-Mejia, Z., Tokoro, T., Kuwae, T., Loza, L.G., Rutgersson, A., Fourqurean, J., Thomas, H., 2021. Global trends in air-water CO_2 exchange over seagrass meadows revealed by atmospheric eddy covariance. In: Global Biogeochem Cycles, p. 35. https://doi.org/10.1029/2020GB006848.

Vandermeirsch, F., 2012. État physique et chimique caractéristiques physiques.

Wang, Z.A., Cai, W.-J., 2004. Carbon dioxide degassing and inorganic carbon export from a marsh-dominated estuary (the Duplin River): A marsh CO_2 pump. Limnol. Oceanogr. 49, 341–354. https://doi.org/10.4319/lo.2004.49.2.0341.

Wang, S.R., Di Iorio, D., Cai, W., Hopkinson, C.S., 2018. Inorganic carbon and oxygen dynamics in a marsh-dominated estuary. Limnol. Oceanogr. 63, 47–71. https://doi.org/10.1002/lno.10614.

Wang, Z.A., Kroeger, K.D., Ganju, N.K., Gonneea, M.E., Chu, S.N., 2016. Intertidal salt marshes as an important source of inorganic carbon to the coastal ocean. Limnol. Oceanogr. 61, 1916–1931. https://doi.org/10.1002/lno.10347.

Wanninkhof, R., Pierrot, D., Sullivan, K., Mears, P., Barbero, L., 2022. Comparison of discrete and underway CO_2 measurements: Inferences on the temperature dependence of the fugacity of CO_2 in seawater. Mar. Chem. 247, 104178 https://doi.org/10.1016/j.marchem.2022.104178.

Wei, T., Simko, V., 2017. R package corrplot: Visualization of a correlation matrix. https://github.com/taiyun/corrplot.

Weiss, R.F., 1974. Carbon dioxide in water and seawater: the solubility of a non-ideal gas. Mar. Chem. 2, 203–215. https://doi.org/10.1016/0304-4203(74)90015-2.

Yates, K.K., Dufore, C., Smiley, N., Jackson, C., Halley, R.B., 2007. Diurnal variation of oxygen and carbonate system parameters in Tampa Bay and Florida Bay. Mar. Chem. 104, 110–124. https://doi.org/10.1016/j.marchem.2006.12.008.

Biogeosciences, 21, 993–1016, 2024
https://doi.org/10.5194/bg-21-993-2024

Biogeosciences Open Access EGU

Atmospheric CO_2 exchanges measured by eddy covariance over a temperate salt marsh and influence of environmental controlling factors

Jérémy Mayen[1,2], Pierre Polsenaere[1], Éric Lamaud[3], Marie Arnaud[1,4], Pierre Kostyrka[1,5], Jean-Marc Bonnefond[3], Philippe Geairon[1], Julien Gernigon[6], Romain Chassagne[7], Thomas Lacoue-Labarthe[8], Aurore Regaudie de Gioux[5], and Philippe Souchu[2]

[1]IFREMER, Littoral, Laboratoire Environnement Ressources des Pertuis Charentais (LER/PC), BP 133, 17390 La Tremblade, France
[2]IFREMER, Littoral, Laboratoire Environnement Ressources Morbihan-Pays de Loire (LER/MPL), BP 21105, 44311 Nantes, France
[3]INRAE, Bordeaux Sciences Agro, ISPA, 33140 Villenave d'Ornon, France
[4]Institute of Ecology and Environmental Sciences Paris (iEES-Paris), Sorbonne University, 75005 Paris, France
[5]IFREMER, Dyneco, Pelagos, ZI de la Pointe du Diable – CS 10070, 29280 Plouzané, France
[6]LPO, Réserve Naturelle de Lilleau des Niges, 17880 Les Portes en Ré, France
[7]BRGM, 3 avenue Claude-Guillemin, BP 36009, 45060 Orléans, CEDEX 02, Orléans, France
[8]Littoral Environnement et Sociétés (LIENSs), UMR 7276, CNRS, La Rochelle Université, 2 Rue Olympe de Gouge, 17000 La Rochelle, France

Correspondence: Jérémy Mayen (jeremy.mayen@ifremer.fr)

Received: 17 July 2023 – Discussion started: 20 July 2023
Revised: 1 December 2023 – Accepted: 12 December 2023 – Published: 27 February 2024

Abstract. Within the coastal zone, salt marshes are atmospheric CO_2 sinks and represent an essential component of biological carbon (C) stored on earth due to a strong primary production. Significant amounts of C are processed within these tidal systems which requires a better understanding of the temporal CO_2 flux dynamics, the metabolic processes involved and the controlling factors. Within a temperate salt marsh (French Atlantic coast), continuous CO_2 fluxes measurements were performed by the atmospheric eddy covariance technique to assess the net ecosystem exchange (NEE) at diurnal, tidal and seasonal scales as well as the associated relevant biophysical drivers. To study marsh metabolic processes, measured NEE was partitioned into gross primary production (GPP) and ecosystem respiration (R_{eco}) during marsh emersion allowing to estimate NEE at the marsh–atmosphere interface ($NEE_{marsh} = GPP - R_{eco}$). During the year 2020, the net C balance from measured NEE was $-483\,g\,C\,m^{-2}\,yr^{-1}$ while GPP and R_{eco} absorbed and emitted 1019 and $533\,g\,C\,m^{-2}\,yr^{-1}$, respectively. The highest CO_2 uptake was recorded in spring during the growing season for halophyte plants in relationships with favourable environmental conditions for photosynthesis, whereas in summer, higher temperatures and lower humidity rates increased ecosystem respiration. At the diurnal scale, the salt marsh was a CO_2 sink during daytime, mainly driven by light, and a CO_2 source during night-time, mainly driven by temperature, irrespective of emersion or immersion periods. However, daytime immersion strongly affected NEE fluxes by reducing marsh CO_2 uptake up to 90 %. During night-time immersion, marsh CO_2 emissions could be completely suppressed, even causing a change in metabolic status from source to sink under certain situations, especially in winter when R_{eco} rates were lowest. At the annual scale, tidal immersion did not significantly affect the net C uptake of the studied salt marsh since similar annual balances of measured NEE (with tidal immersion) and estimated NEE_{marsh} (without tidal immersion) were recorded.

Published by Copernicus Publications on behalf of the European Geosciences Union.

1 Introduction

Salt marshes are intertidal coastal ecosystems dominated by salt-tolerant herbaceous plants located at the terrestrial–aquatic interface. Despite their low surface area at the global scale (54 650 km^2; Mcowen et al., 2017), salt marshes provide important ecosystem services such as an erosion protection (natural buffer zones), a water purification, a nursery for fisheries (Gu et al., 2018) and a high capacity for atmospheric CO_2 uptake and carbon (C) sequestration in their organic matter (OM) enriched sediments and soils (Mcleod et al., 2011; Alongi, 2020). In salt marshes, emersion at low tide and slow immersion at high tide favour this CO_2 fixation through photosynthesis of terrestrial and aquatic vegetations and also a strong benthic–pelagic coupling (Cai, 2011; Wang et al., 2016; Najjar et al., 2018). The high net primary production (NPP) rate of salt marshes on the Atlantic coast of the United States (1070 $g C m^{-2} yr^{-1}$; Wang et al., 2016) makes marshes one of the most productive ecosystems on earth (Duarte et al., 2005; Gedan et al., 2009). According to Artigas et al. (2015), approximately 22 % of C fixed through this marsh NPP is then buried in sediments as "blue C" thus allowing salt marshes to be a large biological C pool (Chmura et al., 2003; Mcleod et al., 2011). However, tidal immersion can generate strong lateral exports of organic and inorganic C to the coastal ocean (Wang et al., 2016), inducing in turn atmospheric CO_2 emissions from coastal ecosystems downstream (Wang and Cai, 2004; Jiang et al., 2008). Salt marshes represent a biogeochemically active interface area within the coastal zone but are also threatened by sea level rise and global warming (Gu et al., 2018) which could significantly alter their capacity to sink and store C (Campbell et al., 2022). Thus, atmospheric CO_2 exchanges need to be accurately measured and better understood, especially the influence of biotic and abiotic controlling factors, in order to be included in regional and global C budgets (Borges et al., 2005; Cai, 2011) and to predict future mash C sinks within the context of climate change.

In temperate salt marshes, actual and historical land and water management, plant species, tidal influence and environmental conditions have been shown to play an important role in the C cycle. Generally, strong seasonal variations in the net ecosystem CO_2 exchange (NEE) were recorded with a marsh CO_2 sink during the hottest and brightest months and a CO_2 source during the rest of the year (Schäfer et al., 2014; Artigas et al., 2015). At a smaller scale, in urban salt marshes (USA), the highest CO_2 uptake generally occurred at midday whereas the systems emitted CO_2 throughout the nighttime, illustrating the major role of net solar radiations in the marsh metabolic status (Schäfer et al., 2014, 2019). Tidal immersion over salt marshes can also strongly influence both daytime and night-time NEE fluxes, especially during spring tides (Forbrich and Giblin, 2015). For instance, negative correlations between NEE and tidal effects were computed in a temperate salt marsh (USA) with *Spartina alterniflora* and *Phragmites australis*, especially in summer and winter, with negative (sink) and positive (source) NEE fluxes during incoming and ebbing tides, respectively (Schäfer et al., 2014). Wang et al. (2006) showed a competitive advantage for the growth and productivity of *S. alterniflora* plants under a moderate level of salinity (15 ‰) and immersion conditions. These different eddy covariance (EC) studies highlight the complexity of the C cycle over salt marshes and the associated biophysical factors driving CO_2 fluxes that require more in situ and integrative NEE measurements within and between all compartments at the different temporal scales to better understand the biogeochemical functioning of these ecosystems under changing sea level conditions.

Within coastal wetlands, CO_2 fluxes at the sediment–atmosphere interface can be accurately assessed with static chambers by repeating measurements over different intertidal habitats (Xi et al., 2019; Wei et al., 2020a). Yet, a major limitation of this method is that it can hardly include the temporal and spatial CO_2 flux variability across different vegetations and habitats (Migné et al., 2004). In heterogeneous intertidal systems, the eddy covariance technique can be used to measure ecosystem-scale CO_2 fluxes (NEE) based on the covariance between fluctuations in the vertically velocity and air CO_2 concentration (Baldocchi et al., 1988; Aubinet et al., 2000; Baldocchi, 2003). This direct and non-invasive micrometeorological technique has been of growing interest over the coastal zone to obtain NEE time series through accurate, continuous and high-frequency CO_2 flux measurements (Schäfer et al., 2014; Artigas et al., 2015; Forbrich and Giblin, 2015). This method has been deployed over blue C systems such as mangroves (Rodda et al., 2016; Gnanamoorthy et al., 2020), seagrass meadows (Polsenaere et al., 2012; Van Dam et al., 2021) and salt marshes (Artigas et al., 2015; Forbrich et al., 2018; Schäfer et al., 2019) to assess their capacity of CO_2 uptake. In intertidal systems like salt marshes, the major advantage of the EC method is to measure NEE fluxes at the ecosystem scale, coming from all habitats inside the footprint, at various timescales from hours to years and at both the sediment–air and water–air interfaces (i.e. low and high tides, respectively) (Kathilankal et al., 2008; Wei et al., 2020b). Although many studies have used this method to assess tidal effects on NEE fluxes over salt marshes, only a limited number have looked at the loss of CO_2 uptake due to tidal effects. Moreover, NEE can be partitioned into marsh metabolic fluxes (gross primary production, GPP and ecosystem respiration, R_{eco}) during emersion periods through modelling approaches (Kowalski et al., 2003; Reichstein et al., 2005; Lasslop et al., 2010). However, use of the EC method requires significant qualitative and quantitative processing and data correction applied to each specific site since this method relies on the physical and theoretical backgrounds (Baldocchi et al., 1988; Burba, 2021) and is adapted (technically and scientifically) to the coastal systems.

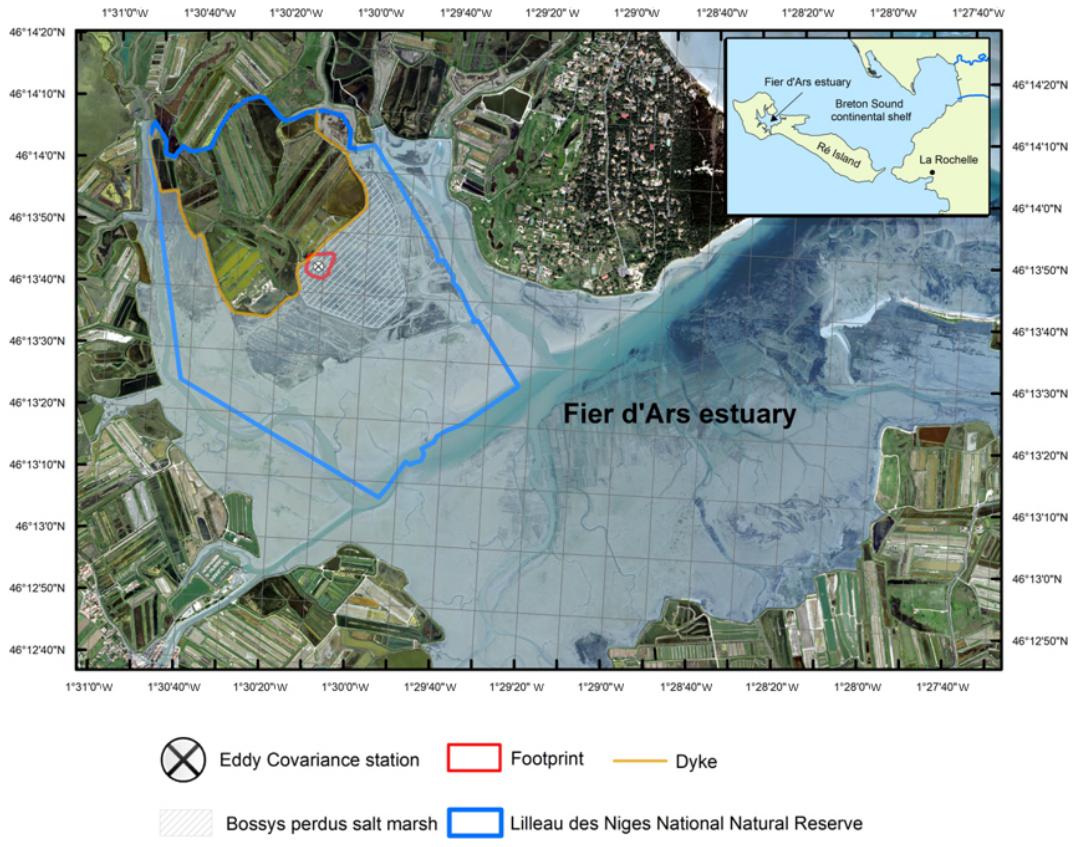

Figure 1. The studied Bossys perdus salt marsh located on the French Atlantic coast within the National Natural Reserve (blue line delimitation) on Ré Island. The salt marsh is connected to the Fier d'Ars tidal estuary (light blue). The dyke separates terrestrial and maritime marsh areas (orange line). The eddy covariance system and associated estimated footprint are indicated (black cross and red line; see Fig. 2). From geo-referenced IGN 2019 orthogonal images (Institut national de l'information géographique et forestière (IGN)).

Our study focused on the atmospheric CO_2 uptake capacity of a tidal salt marsh (old anthropogenic marsh) under the influence of biophysical factors and its potential role in global and regional C budgets. For this purpose, we deployed an atmospheric EC station to measure vertical CO_2 fluxes (NEE) during the year 2020 at the ecosystem scale on the Bossys perdus salt marsh on Ré Island connected to the French continental shelf of the Atlantic Ocean. Here, we aim to (a) describe NEE flux temporal series measured at different temporal scales (diurnal, tidal and seasonal scales) using the EC technique, (b) evaluate the relevant environmental factors that control atmospheric CO_2 exchanges (i.e. NEE) and (c) accurately qualify and quantify the effects of tides on the marsh CO_2 metabolism.

2 Materials and methods

2.1 Study site

The study was conducted at the Bossys perdus salt marsh situated along the French Atlantic coast on Ré Island (Fig. 1). It corresponds to a vegetated intertidal area of 52.5 ha that has been protected inside the National Natural Reserve (NNR) (Fig. 1). Between the 17th and most of the 20th century, the salt marsh experienced successive periods of intensive land use (salt harvesting and oyster farming) and returned to natural conditions before becoming a permanent part of the NNR in 1981 for the biodiversity protection without major restoration work (Julien Gernigon, personal communication, 2023). It is currently managed to restore its natural hydrodynamics while conserving the site's specific typology due to past human activities (channel networks, humps and dykes; Fig. 2). This salt marsh is linked to the Fier d'Ars tidal estuary that exchanges between 2.4 and 10.2 $\times 10^6$ m^3 of coastal waters with the Breton Sound continental shelf allowing a maximal tidal range of 5 m in the estuary (Bel Hassen, 2001). This communication allows (1) drainage of the intertidal zone of the estuary including mudflats (Mayen et al., 2023) and tidal salt marshes (Mayen et al., 2023) and (2) supply of coastal water to a large complex of artificial salt marshes (i.e. salt ponds) located upstream of the dyke (Fig. 1). The artificial marsh waters managed by the NNR for biodiversity protection (Mayen et al., 2023) are flushed back to the estuary downstream through the Bossys perdus channel (Fig. 1).

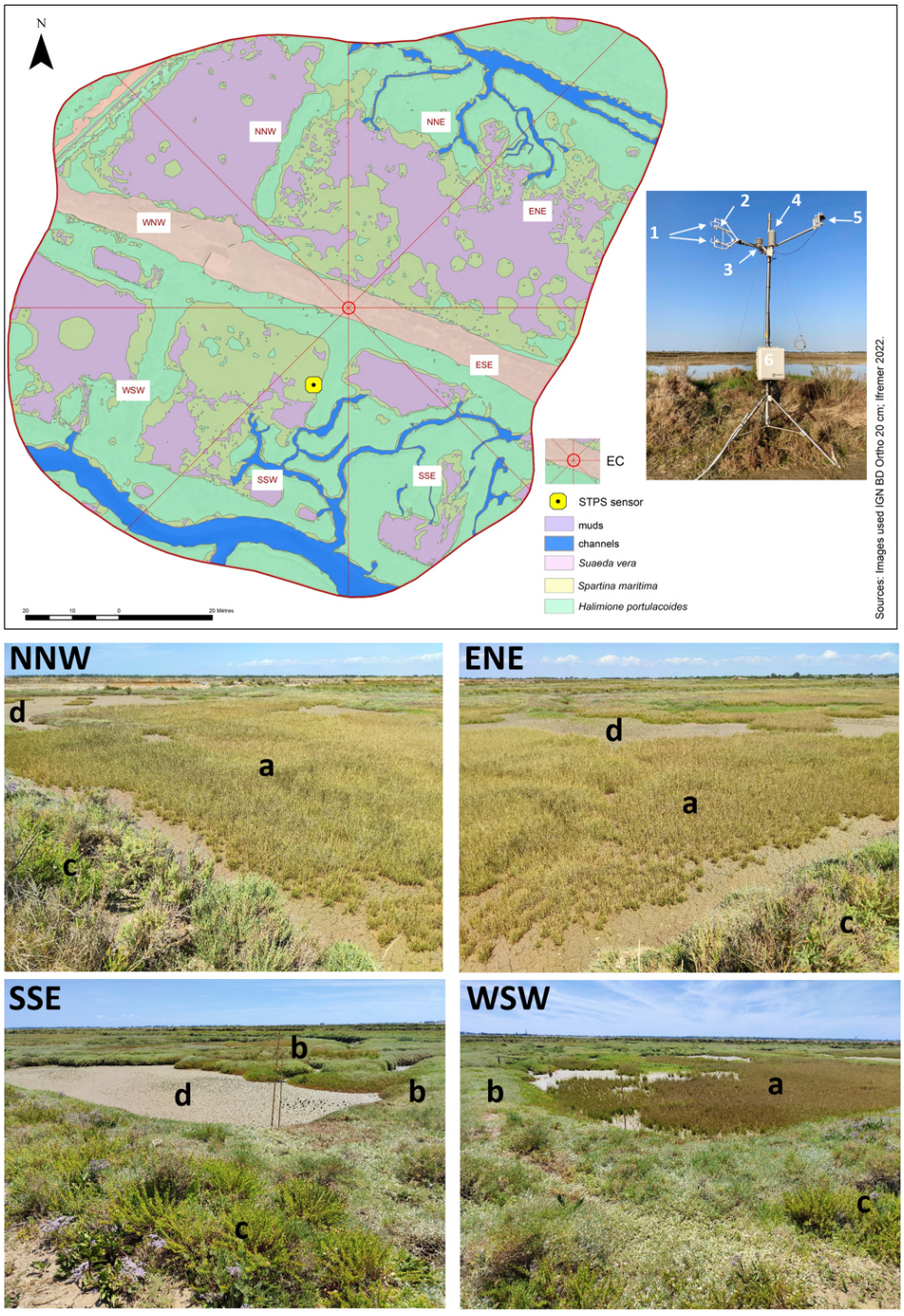

Figure 2. Location and set-up of the eddy covariance (EC) system within the Bossys perdus salt marsh and its associated footprint estimated from Kljun et al. (2015) and averaged over the year 2020 (70 % contour line, i.e. 13 042 m^2). Wind sectors (45°) and marsh habitats (see Table 1) are represented. The canopy height of the studied marsh is short and constant (from 0.15 m for *H. portulacoides* to 0.30 m for *S. maritima*). The STPS sensor (in yellow), measuring water heights (H_w) and temperatures (T_w), was located in the SSW sector. The EC system (Campbell Scientific) includes (1) the ultrasonic anemometer (CSAT3), (2) the open-path infrared gas analyser (EC150), (3) the temperature probe (100K6A1A thermistor), (4) the temperature/relative humidity sensor (HMP155A), (5) the silicon quantum sensor (SKP215) and (6) the central acquisition system (CR6) and the electronics module (EC100). A rainfall sensor (TE525MM; Rain Gauge, Texas Electronics) simultaneously measured the cumulative precipitation. From geo-referenced IGN 2019 orthogonal images. Photographs of four wind sectors within the studied footprint area (NNW, ENE, WSW and SSE) were taken from the EC system during an emersion period in summer 2021 when all the marsh habitats were emerged into the atmosphere: **(a)** *Spartina maritima*, **(b)** *Halimione portulacoides*, **(c)** *Suaeda vera* and **(d)** mudflat. © S.-C. Zech.

The Bossys perdus salt marsh, located upstream of the estuary (Mayen et al., 2023), is subjected to semi-diurnal tides from the Breton Sound continental shelf (Fig. 1) allowing the marsh immersion by two main channels differently in space, time and frequency according to the tidal periods (Fig. 2). At high tide, advected coastal waters can completely fill channels (Fig. S1b in the Supplement) and immerse the marsh through variable water heights depending on tidal amplitudes and meteorological conditions (Fig. S1c). In contrast, at low tide, the marsh vegetation at the benthic interface is emerged into the atmosphere without any coastal waters (Fig. S1a). During this time, Bossys perdus channels allow drainage of upstream artificial marsh waters to the estuary (Fig. 2). The marsh vegetation assemblage was mainly composed by three halophytic species as perennial plants (*Halimione portulacoides*, *Spartina maritima* and *Suaeda vera*; Fig. 2) that associated with different metabolic pathways (the C_3-type photosynthesis for *H. portulacoides* and *S. vera* and the C_4-type photosynthesis for *S. maritima*; Duarte et al., 2013, 2014). Whereas *H. portulacoides* and *S. vera* are evergreen plants throughout the year, the growing season for *S. maritima* was shorter (from spring) with a flowering period between August and October (plants persist only in the form of rhizomes in winter and fall; Julien Gernigon, personal communication, 2023).

2.2 Eddy covariance and micrometeorological measurements

The atmospheric eddy covariance technique allowed us to quantify the net CO_2 fluxes at the ecosystem–atmosphere interface through micrometeorological measurements of the vertical component of atmospheric turbulent eddies (Aubinet et al., 2000; Baldocchi, 2003; Burba, 2021). The averaged vertical flux of any gas (F, $\mu mol\,m^{-2}\,s^{-1}$) can be expressed as the covariance between the vertical wind speed (w, $m\,s^{-1}$), air density (ρ, $kg\,m^{-3}$) and the dry mole fraction (s) of the gas of interest as

$$F = \overline{\rho w s} \approx \overline{\rho}\,\overline{w's'}, \quad (1)$$

where the overbar represents the time average of the parameter (i.e. 10 min in this study due to strong fluctuations at the tidal scale; Polsenaere et al., 2012) and the prime indicates the instantaneous turbulent fluctuations in these parameters relative to their temporal average (Reynolds, 1883). The Reynold's decomposition was used to break the instantaneous term down into its mean and deviation (e.g. $w = \overline{w} + w'$) (Reynolds, 1883; Burba, 2021). This equation (Eq. 1) is obtained by assuming, on a flat and homogeneous surface, that (1) the variation in air density is negligible, (2) there is no divergence or convergence of large-scale vertical air motion and (3) atmospheric conditions are stable and stationary (Aubinet et al., 2012). A negative flux of atmospheric CO_2 is directed towards the ecosystem, and is therefore characterized as a sink, and vice versa for positive fluxes qualified as sources of CO_2 to the atmosphere.

An EC system was continuously deployed at the Bossys perdus salt marsh to measure the net ecosystem CO_2 exchange (NEE, $\mu mol\,m^{-2}\,s^{-1}$). The set of EC sensors (Fig. 2), at a height of 3.15 m, was composed of an open-path infrared gas analyser (model EC150; Campbell Scientific) to measure the CO_2 ($mg\,m^{-3}$) and H_2O ($g\,m^{-3}$) concentrations in the air as well as the atmospheric pressure (kPa) and an ultrasonic anemometer (model CSAT3; Campbell Scientific) to measure the three-dimensional components of wind speed (U, V and W; $m\,s^{-1}$) at a frequency of 20 Hz and averaged every 10 min (Fig. 2). The EC150 gas analyser also measured the air temperature using a thermistor probe (model 100K6A1A; BetaTherm). The EC100 electronics module (model EC100; Campbell Scientific) allowed us to synchronize high-frequency measurements and rapid communications between the CR6 datalogger (model CR6; Campbell Scientific) and EC devices including EC150 and CSAT3A (Fig. 2). The CR6 datalogger is a powerful core component for the data acquisition system. Additional meteorological data, such as relative humidity (RH, %), air temperature (T_a, °C) and photosynthetically active radiation (PAR, $\mu mol\,m^{-2}\,s^{-1}$), were recorded every 10 min simultaneously and at the same height as the EC sensors, by a temperature/relative humidity sensor (HMP155A; Campbell Scientific), with RAD14 natural ventilation shelter) and a silicon quantum sensor (SKP215; Skye Instruments), respectively (Fig. 2). The vapour pressure deficit (VPD, Pa) was calculated every 10 min from saturated vapour pressure (calculated from T_a) and from actual vapour pressure (calculated from RH). A rainfall sensor (TE525MM; Rain Gauge, Texas Electronics), located 10 m away and connected to the EC station, simultaneously measured the cumulative precipitation at a height of 1 m (rainfall, mm). All high-frequency EC data were recorded on an SD micro-card (2 Go; Campbell Scientific) that was replaced every 2 weeks, whereas meteorological data were recorded and stored in the central acquisition system (CR6). The EC system was connected to two rechargeable batteries (12 volts and $260\,A\,h^{-1}$; AGM) powered by a monocrystalline solar panel (24 V, 200Wp module with MPPT 100 V/30 A controller; Victron Energy). The EC sensors were checked and cleaned every 2 weeks and the EC150 was calibrated each season with a zero-air calibration of 0 ppm (Campbell Scientific) and a certificated CO_2 standard of 520 ppm (Gasdetect). Water height (H_w; ± 0.3 m) and water temperature (T_w; ± 0.1 °C) were also measured every 10 min along with EC data using a STPS probe (NKE Instrumentation) located 20 m away from the EC system (Fig. 2). The sensor was checked every two months at the laboratory to verify possible derivations in the measured parameters.

Table 1. Bossys perdus marsh habitat (percentages are in bold and associated surface area, in square metres, are in brackets) within each 45° wind sector in the corresponding footprint areas (Fig. 2) and the whole averaged footprint for the year 2020 (13 042 m^2, 70 % contour line).

Wind sectors		*Halimione portulacoides*	*Spartina maritima*	*Suaeda vera*	Muds	Channels
NNE	0–45	**48** (850)	**22** (390)	**1*** (9)	**22** (386)	**8** (150)
ENE	45–90	**31** (590)	**26** (492)	**1** (22)	**37** (704)	**4** (80)
ESE	90–135	**37** (335)	**21** (190)	**31** (288)	**9** (82)	**2** (22)
SSE	135–180	**60** (803)	**9** (124)	**0*** (4)	**21** (275)	**8** (113)
SSW	180–225	**48** (734)	**19** (283)	**0*** (2)	**8** (122)	**25** (388)
WSW	225–270	**33** (689)	**35** (745)	**0*** (6)	**25** (530)	**6** (132)
WNW	270–315	**30** (580)	**11** (216)	**29** (570)	**30** (588)	**0** (0)
NNW	315–360	**16** (249)	**26** (401)	**2** (31)	**56** (867)	**0** (0)
Total footprint (70 % contour line)		**37** (4830)	**22** (2841)	**7** (932)	**27** (3554)	**7** (885)

* Negligible surfaces on the total area of the sector.

2.3 Footprint estimation and immersion/emersion marsh heterogeneity

Footprints were estimated using the model of Kljun et al. (2015) applied to data from the year 2020 to obtain an annual averaged footprint from the constant measurement height ($Z_m = 3.15$ m), the constant displacement height ($d = 0.1$ m; estimated from 0.67 times the canopy height; LI-COR, EddyPro® 7 Software, LI-COR Environmental), mean wind velocities (u_mean, $m\,s^{-1}$), standard deviations of the lateral velocity fluctuations after rotation (sigma_v, $m\,s^{-1}$), the Obukhov length (L), friction velocities (u^*, $m\,s^{-1}$) and wind directions (°) obtained from the EC measurements and the processing software (EddyPro® v7.0.8; LI-COR) output. For verification, we performed the footprint estimations both with variable Z_m from water height measurements and with constant Z_m from data at emersion and we obtained the same footprint shapes and extends. For all calculations (i.e. habitat coverage, relationships with CO_2 fluxes, etc.), we used the 70 % footprint contour line that corresponds to an average footprint of 13 042 m^2 of the studied salt marsh area of interest (Fig. 2). A land-use map was also created (Fig. 2) from geo-referenced IGN BD orthogonal images with a resolution of 20 cm (2019) using ArcGIS 10.2 (ESRI). The spatial analysis tool of ArcGIS 10.2 was used to perform an unsupervised classification of the BD orthogonal images. We checked the resulting map by selecting 20 random locations within the footprint of the studied salt marsh and compared their land use on the ground and on the map.

In some situations, based on the tide (neap tides), due to meteorology influence (wind direction and atmospheric pressure) and the local altimetry heterogeneity, our one-location H_w measurements could not accurately account for the whole spatial emersion and immersion of the marsh in the EC footprint (Fig. 2). At incoming tide, when coastal waters begin to fill the channel and then overflow over the marsh (from 0.5 h in spring tides to 2.5 h in neap tides; data not shown), the SSW sector (Fig. 2) was first immersed and a non-zero H_w value was measured. However, although some marsh sectors were immersed at the same time, others were still emerged. Indeed, lowest marsh levels (56 % of the footprint area), mainly composed of mudflats and *S. maritima* (Fig. 2; Table 1), were quickly immersed from $H_w > 0$ m (south), whereas the whole marsh immersion (muds and plants) only occurred 0.75 h later from $H_w > 1.0$ m at high tide during spring tide. Thus, the highest marsh levels (44 % of the footprint area), mainly composed of *H. portulacoides* and *S. vera* (Fig. 2; Table 1), were still emerged for $0 < H_w < 1.0$ m. Conversely, at neap tide, this footprint immersion versus emersion marsh heterogeneity could still be present even at

high tide due to insufficient water levels. Although a digital field model for water heights could not be performed in 2020 to have a better spatial representation of the immersion/emersion footprint, all these important considerations were considered in our computations and analyses in this study.

2.4 EC data processing and quality control

Raw EC data measured at high-frequency were processed following Aubinet et al. (2000) with the EddyPro software. First, different correcting steps were applied to our raw data according to the procedures given by Vickers and Mahrt (1997) and Polsenaere et al. (2012) for intertidal systems: (1) unit conversion to check that the units for instantaneous data are appropriate and consistent to avoid any errors in the calculation and correction of CO_2 fluxes; (2) despiking to remove outliers in the instantaneous data from the anemometer and gas analyser due to electronic and physical noise and replaced the detected spikes with a linear interpolation of the neighbouring values; (3) amplitude resolution to identify situations in which the signal variance is too low with respect to the instrumental resolution; (4) double coordinate rotation to align the x axis of the anemometer to the current mean streamlines, nullifying the vertical and cross-wind components; (5) time delay removal by detecting discontinuities and time shifts in the signal acquisition from the anemometer and gas analyser; (6) detrending with removal of short-term linear trends to suppress the impact of low-frequency air movements; and (7) performing the Webb–Pearman–Leuning (WPL) correction to take into account the effects of temperature and water vapour fluctuations on the measured fluctuations in the CO_2 and H_2O densities (Burba, 2021). The turbulent fluctuations of CO_2 fluxes were calculated with EddyPro using the linear detrending method (Gash and Culf, 1996) which involves calculating deviations from around any linear trend evaluated (i.e. over the whole flux averaged period). High-frequency CO_2 fluxes were processed and averaged over intervals of 10 min (shorter than in terrestrial ecosystems) to detect fast NEE variations with the tide (Polsenaere et al., 2012; Van Dam et al., 2021). During the EC data processing by EddyPro, a correction for flux spectral losses in the low frequency range was performed according to Moncrieff et al. (2004).

A strict quality control was applied on EddyPro processed CO_2 flux data to remove bad data related to instrument malfunctions, processing and mathematical artefacts, ambient conditions that do not satisfy the requirements for the EC method, wind that is not from the footprint and heavy precipitation for the open-path IRGA (Burba, 2021). Processed data were screened using tests for steady state and turbulent conditions (Foken and Wichura, 1996; Foken et al., 2004; Göckede et al., 2004). In this study, we did not apply a ustar filter in our EC data processing because we measured only 11 % of night-time data corresponding to a ustar threshold below $0.1\,m\,s^{-1}$ and above which NEE does not increase anymore with ustar values (threshold close to values found in grassland; Gu et al., 2005). Contrary to terrestrial ecosystems (Gu et al., 2005), the low canopy height of the studied marsh strongly limited the CO_2 storage in the vegetation and favours the atmospheric CO_2 circulation. If the signal to noise ratio of the EC150 gas analyser was less than 0.7 and/or the percentage of high-frequency missing values over 10 min exceeded 10 % (i.e. data absent in the raw data file or removed through the quality screening procedures), no flux was calculated. This choice was the best compromise between removing poor-quality data and keeping as much of measured CO_2 flux data as possible (data and associated tests not shown). Then, we used the method of Papale et al. (2006) to detect and remove outliers in the 10 min flux data. The median and median absolute deviation (MAD) were calculated over a 2-week window separating daytime and night-time periods. Data above 5.2× MAD were removed. After all post-processing and quality controls, 18.3 % of the EC data were removed and gap-filled through a machine learning approach to obtain continuous flux data in 2020.

2.5 Flux gap filling and statistic tools

The random forest (RF) model was used to gap-fill our EC dataset. Random forest is a supervised machine learning technique proposed by Breiman (2001) that can model a non-linear relationship with no assumption about the underlying distribution of the data population. This method has been shown to be particularly suited to gap-fill EC data (Kim et al., 2020; Cui et al., 2021). Random forest builds multiple decision trees, each of which is based on a bootstrap aggregated data sample (i.e. bagging of the EC data) and a random subset of predictors (i.e. the selected environmental data; Table S1 in the Supplement). We build RF models with environmental predictors that have been identified in the literature to control CO_2 fluxes in salt marshes and which were available during the gaps and with measurements recorded between 2019 and 2020 (Table S1). Each random forest model was built from a trained bagging ensemble of 400 randomly generated decision trees (Kim et al., 2020) with the "randomForest" package in the R software (Liaw and Wiener, 2022). In this study, we used the RF2 model with PAR, air temperature, water height and relative humidity as environmental predictors because its performance indicators showed a high Pearson correlation coefficient ($R^2 = 0.88$) and low values of root mean square error (RMSE = 1.27) and model bias (0.0024) allowing us to correctly gap-fill a large EC data (Table S1). The calculated uncertainty of the RF2 model on the resulting annual C budget was 0.43 %. Each tree was trained from bagged samples including 70 % of the initial dataset. The remaining 30 % of the data were used to estimate the fit of each random forest model. The model used was then able to explain 88 % of the variability in the test data. Daytime data were better explained than night-time data (59 % vs. 38 %), with light being the main parameter of the model. However,

only 20 % of the night-time EC data were gap-filled with the random forest model. Using a partial dependence analysis and an ondelette analysis, we concluded that the relationships and temporal dynamics modelled allowed us to correctly fill the gaps in our dataset. However, extreme values of some predictors (i.e. PAR $> 1000\,\mu mol\,m^{-2}\,s^{-1}$) can reduce the random Forest model performance for estimation of EC data. This observation is common for random forest models, as they show poor results for extreme values. Other models, such as artificial neural networks, were also tested but showed poorer results (Table S1).

For all measured variables, the 10 min data did not follow a normal distribution (Shapiro–Wilk tests, $p < 0.05$). Non-parametric comparisons, such as the Mann–Whitney and Kruskal–Wallis tests, were carried out with a 0.05 level of significance. To assess the influence of meteorological and hydrological drivers on NEE fluxes at different temporal scales, we performed a pairwise Spearman's correlation analysis on the 10 min values and monthly mean values ("cor function" in R).

2.6 Temporal analysis of NEE fluxes and partitioning

During the year 2020, temporal variations in NEE fluxes were studied at the seasonal and diurnal/tidal scales. Seasons were defined based on calendar dates: the winter period from 1 January 2020 to 19 March 2020 and from 21 to 31 December 2020, the spring period from 20 March 2020 to 19 June 2020, the summer period from 20 June 2020 to 21 September 2020 and the fall period from 22 September 2020 to 20 December 2020. Daytime and night-time were separated into PAR > 10 and PAR $\leq 10\,\mu mol\,m^{-2}\,s^{-1}$, respectively. For the NEE flux analysis according to environmental drivers, NEE fluxes were grouped into five PAR groups ($0 <$ PAR ≤ 10, $10 <$ PAR ≤ 500, $500 <$ PAR ≤ 1000, $1000 <$ PAR ≤ 1500 and $1500 <$ PAR $\leq 2000\,\mu mol\,m^{-2}\,s^{-1}$) to reduce NEE fluctuations due to PAR variations. Water heights (H_w) measured at one location over the marsh (Fig. 2) relative to the mean sea level were used to distinguish emersion ($H_w = 0$ m at low tide) and immersion ($H_w > 0$ m at high tide) periods (see Sect. 2.3) and thus, the influence of tides on NEE fluxes.

To study marsh metabolism related to photosynthesis and respiration processes, measured NEE fluxes were partitioned into gross primary production (GPP) and ecosystem respiration (R_{eco}), respectively. During marsh emersion, NEE fluxes occur at the marsh–atmosphere interface involving only benthic metabolism (or marsh metabolism) resulting in $NEE = GPP - R_{eco}$. During marsh immersion, NEE fluxes are the result of benthic metabolism, planktonic metabolism and lateral C exchanges by tides thereby making it more difficult to study the marsh metabolism (Polsenaere et al., 2012). Negative NEE values indicated a marsh CO_2 uptake from the atmosphere and positive values indicated a marsh CO_2 source into the atmosphere. GPP was expressed in negative values and R_{eco} was expressed in positive values. In this study, NEE flux partitioning into marsh metabolic fluxes (NEE_{marsh}) was performed according to the following equation using the model of Kowalski et al. (2003):

$$NEE_{marsh} = GPP - R_{eco} = \frac{a_1 PAR}{a_2 + PAR} - R_{eco}, \quad (2)$$

where a_1 is the maximal photosynthetic CO_2 uptake at light saturation ($\mu mol\,CO_2\,m^{-2}\,s^{-1}$) and a_2 is the PAR at half of the maximal photosynthetic CO_2 uptake ($\mu mol\,photon\,m^{-2}\,s^{-1}$). The a_1/a_2 ratio corresponds to photosynthetic efficiency (Kowalski et al., 2003). R_{eco} was calculated as follows according to Wei et al. (2020b):

$$R_{eco} = R_0 \exp(bT_a), \quad (3)$$

where R_{eco} is the night-time ecosystem respiration ($\mu mol\,CO_2\,m^{-2}\,s^{-1}$), R_0 is the ecosystem respiration rate at 0 °C ($\mu mol\,CO_2\,m^{-2}\,s^{-1}$), T_a is the air temperature (°C) and b is a response coefficient of the temperature variation (Wei et al., 2020b).

For NEE flux partitioning, estimations of the GPP coefficients (a_1 and a_2; Eq. 2) and R_{eco} coefficients (R_0 and b; Eq. 3) were performed by the least squares method ("minpack.lm" package in R) at the monthly scale only during emersion periods where measured NEE fluxes corresponded to estimated NEE_{marsh} fluxes. First, for each month, R_0 and b were estimated during night-time emersion periods where $NEE = R_{eco}$ following Eq. (3) (Wei et al., 2020b). Then, a_1 and a_2 were estimated during daytime emersion periods using night-time respiration coefficients (R_0 and b) where $NEE = GPP - R_{eco}$ following Eqs. (2) and (3) (Kowalski et al., 2003). Finally, NEE_{marsh} (net marsh metabolic fluxes without tidal influence) were calculated from PAR and T_a values measured at a 10 min frequency throughout the year using the monthly coefficients calculated for the partitioning (Eq. 2). As our ecosystem had a low phenological variation (Table S2), we concluded that a monthly time step for the coefficient estimation was sufficient to answer our study objectives. During emersion periods, monthly net C balances (i.e. budgets) of measured NEE and estimated NEE_{marsh}, as well as the monthly mean fluxes, were very similar (Table S3), confirming the correct NEE flux partitioning calculations done in this study.

3 Results

3.1 Habitat covering of the footprint

Within the EC footprint, halophyte marsh vegetation (66 %) composed of *Halimione portulacoides*, *Spartina maritima* and *Suaeda vera* mainly dominated, whereas muds and channels only accounted for 27 and 7 %, respectively (Fig. 2). The area occupied by *S. vera*, crossing the EC footprint from WNW to ESE (Table 1), corresponded to the highest marsh

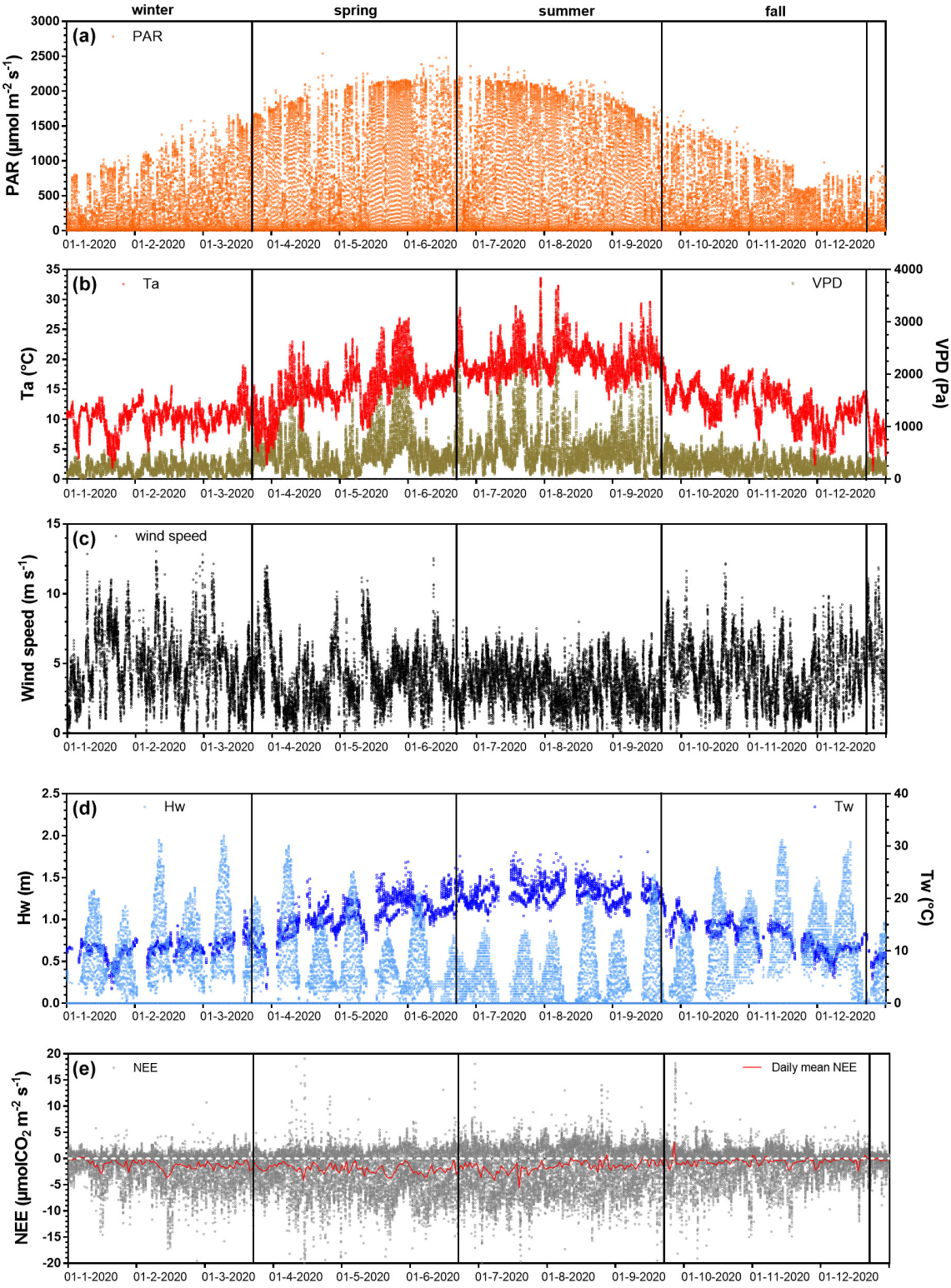

Figure 3. Net ecosystem exchanges and associated environmental parameters measured every 10 min throughout the year 2020. The measured environmental parameters include **(a)** the photosynthetically active radiation (PAR, µmol m^{-2} s^{-1}), **(b)** air temperature (T_a, °C), vapour pressure deficit (VPD, Pa), **(c)** wind speed ($m\,s^{-1}$), **(d)** water height (H_w, m), water temperature (T_w, °C) and **(e)** the net ecosystem exchanges (NEE, µmol CO_2 m^{-2} s^{-1}) computed from the 20 Hz atmospheric CO_2 and wind speed measurements with the EddyPro software. The red line in **(e)** is the moving average of NEE (daily mean). Seasons are delimited by vertical lines.

Table 2. Emersion and immersion periods (percentage in bold) at the studied salt marsh for four water height ranges of 0.5 m during the year 2020 and at the seasonal scale. The emersion and immersion durations in hours per day were calculated (shown in brackets).

	Emersion	Immersion			
	$H_w = 0$	$0 < H_w < 0.5$	$0.5 < H_w < 1$	$1 < H_w < 1.5$	$1.5 < H_w < 2$
Year 2020	**74.5** (17.9)	**12.4** (2.9)	**8.7** (2.1)	**3.6** (0.9)	**0.8** (0.2)
Winter	**76.3** (18.0)	**10.4** (2.5)	**8.6** (2.0)	**3.6** (0.9)	**1.1** (0.3)
Spring	**74.5** (18.0)	**13.7** (3.2)	**8.2** (2.0)	**3.0** (0.7)	**0.6** (0.1)
Summer	**75.1** (18.5)	**17.1** (4.2)	**5.9** (1.6)	**1.3** (0.3)	**0.0** (0.0)
Fall	**72.0** (17.0)	**8.5** (1.9)	**11.5** (2.7)	**6.4** (1.5)	**1.6** (0.4)

level that was partly immersed only during the highest tidal amplitudes (Fig. 2). *H. portulacoides* and *S. maritima* occupied mostly the NNE (70 %), SSE (69 %), WSW (68 %) and SSW (67 %) wind sectors. In contrast, mud habitats mostly covered the NNW sector, where the lowest vegetation cover was found (Fig. 2; Table 1). The highest channel area was found in the SSW sector (Fig. 2; Table 1).

3.2 Seasonal variations in environmental conditions and NEE fluxes

Throughout the year 2020, the full seasonal range in solar radiation was measured (Fig. 3a) with an increase in daytime PAR from winter (lowest light season) to summer (brightest season). A similar seasonal pattern was recorded for air temperatures (T_a) with values ranging from 1.5 °C in winter (coldest season) to 33.6 °C in summer (warmest season; Fig. 3b). On average, the winter and fall seasons were the wettest (RH > 82 %), associated with the lowest vapour pressure deficit (VPD) values, whereas spring and summer were the driest ones (RH < 75 %), associated with the highest VPD values (Fig. 3b). Indeed, the highest and lowest cumulative rainfalls were recorded in fall (342 mm) and summer (62 mm), respectively. The highest mean seasonal wind speed was measured in winter ($4.9 \pm 2.3\,m\,s^{-1}$) with maximal speeds up to $13\,m\,s^{-1}$ (Fig. 3c). Winds came mostly from the SSW–WSW sectors both in winter (55 %) and summer (41 %) and from the NNE–ENE sectors both in spring (51 %) and fall (31 %) (Fig. 2). Tidal activities reflected the typical hydrological conditions of the Atlantic coasts with a bi-monthly succession of spring tides and neap tides (Fig. 3d). Water heights (H_w) strongly varied according to tidal amplitudes with a maximal H_w of 1.4 m during neap tides and 2.0 m during spring tides (overall annual mean of 0.6 ± 0.4 m; Fig. 3d). Throughout the year, 25.5 % of the EC data were measured when the salt marsh was immersed through variable immersion durations and water heights (Table 2). On average, the daily immersion durations ranged between $5.7\,h\,d^{-1}$ in winter (23.7 % of the EC data) and $6.5\,h\,d^{-1}$ in fall (28 % of the EC data). In winter, the EC data during immersion were split into 19 % for $0 < H_w < 1$ m and 4.7 % for $1 < H_w < 2$ m, whereas in fall, these latter were split into 20 % for $0 < H_w < 1$ m and 8 % for $1 < H_w < 2$ m. In summer, the lowest marsh immersion was measured with no H_w value higher than 1.5 m (Table 2).

The annual mean NEE value was $-1.27 \pm 3.48\,\mu mol\,m^{-2}\,s^{-1}$ with strong temporal variabilities recorded over both long and short timescales (Fig. 3e). Significant NEE variations were highlighted between each season (Kruskal–Wallis test, $p < 0.001$) where, on average, the highest and lowest atmospheric CO_2 sinks were recorded in spring ($-1.93 \pm 3.84\,\mu mol\,m^{-2}\,s^{-1}$) and fall ($-0.59 \pm 2.83\,\mu mol\,m^{-2}\,s^{-1}$), respectively (Fig. 4). NEE flux partitioning gave an annual mean NEE_{marsh} value of $-1.28 \pm 3.16\,\mu mol\,m^{-2}\,s^{-1}$, ranging from $-2.00 \pm 3.49\,\mu mol\,m^{-2}\,s^{-1}$ in spring to $-0.53 \pm 2.51\,\mu mol\,m^{-2}\,s^{-1}$ in fall. On average, in winter and fall, the measured NEE values were more negative than the estimated NEE_{marsh} values, whereas in spring and summer, the opposite trend was recorded (Fig. 4). Contrary to NEE and NEE_{marsh}, the highest seasonal values of GPP and R_{eco} were estimated in summer, whereas the lowest seasonal values were estimated in winter (Fig. 4). The highest and lowest photosynthetic efficiencies (a_1/a_2 ratio) were found in winter (-2.08×10^{-2}) and summer (-1.36×10^{-2}), respectively.

3.3 Environmental parameter and NEE flux variations at diurnal and tidal scales

At each season, significant diurnal differences in NEE fluxes were highlighted (Mann–Whitney tests, $p < 0.05$)

Table 3. Diurnal/tidal variations (means ± SD in bold) of NEE fluxes (μmol CO_2 m^{-2} s^{-1}) during each season in 2020. The associated ranges (min/max) are indicated in brackets. Daytime and night-time periods were separated into PAR > 10 and PAR ≤ 10 μmol m^{-2} s^{-1}, respectively, whereas emersion and immersion periods were separated into $H_w = 0$ m and $H_w > 0$ m, respectively.

	Daytime emersion	Night-time emersion	Daytime immersion	Night-time immersion	Seasonal
Winter	**−3.15 ± 2.96** (−19.55/10.73)	**0.61 ± 0.86** (−4.80/5.40)	**−2.03 ± 2.30** (−16.06/6.49)	**−0.10 ± 0.99** (−5.31/3.34)	**−1.01 ± 2.61** (−19.55/10.73)
Spring	**−4.39 ± 3.76** (−25.67/19.09)	**1.25 ± 0.98** (−4.54/7.01)	**−2.59 ± 3.24** (−29.68/17.62)	**0.51 ± 1.22** (−4.60/6.04)	**−1.93 ± 3.84** (−29.68/19.09)
Summer	**−4.42 ± 3.88** (−23.71/18.07)	**2.11 ± 1.34** (−5.93/9.25)	**−2.22 ± 3.26** (−25.23/13.01)	**1.18 ± 1.44** (−4.86/9.36)	**−1.53 ± 4.19** (−25.23/18.07)
Fall	**−3.00 ± 3.32** (−21.54/17.74)	**1.12 ± 1.03** (−4.19/6.09)	**−1.53 ± 2.60** (−18.15/18.21)	**0.29 ± 1.07** (−3.97/5.50)	**−0.59 ± 2.83** (−21.54/18.21)

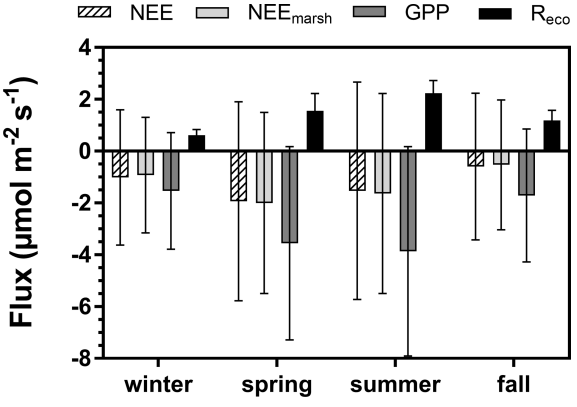

Figure 4. Seasonal variations (means ± SD) of the measured NEE, estimated NEE_{marsh}, estimated GPP and estimated R_{eco} (μmol CO_2 m^{-2} s^{-1}) recorded throughout the year 2020. NEE: net ecosystem exchange, NEE_{marsh}: net ecosystem exchange at the marsh–atmosphere interface without coastal water, GPP: gross primary production, R_{eco}: ecosystem respiration. The NEE fluxes were partitioned into GPP and R_{eco} according to Kowalski et al. (2003) and Wei et al. (2020b) (see Sect. 2.6).

with, on average, an atmospheric CO_2 sink during daytime and an atmospheric CO_2 source during night-time, irrespective of emersion or immersion periods (Table 3). For instance, in spring, NEE means were -3.93 ± 3.72 and 1.06 ± 1.09 μmol m^{-2} s^{-1} during daytime and night-time, respectively (Fig. 5b). Over all seasons, similar diurnal variations in measured NEE and estimated NEE_{marsh} were recorded with, on average, a rapid increase in CO_2 uptake during the morning up to the middle of the day (low T_a and VPD values) and then, a decrease in CO_2 uptake during the afternoon (high T_a and VPD values) to become a CO_2 source during night-time (Figs. 5 and S2). On average, during the afternoon, the GPP decreases and R_{eco} increases explained the measured decrease in CO_2 uptake (Fig. 5). For each season, the highest marsh CO_2 uptakes were measured during daytime emersion periods between 12:00 and 13:00 UT (maximal PAR levels), with the latter increasing from winter (-4.84 ± 2.87 μmol m^{-2} s^{-1}) to spring–summer (-6.94 ± 2.80 μmol m^{-2} s^{-1}; Fig. 5).

At each season, the tidal rhythm strongly disrupted NEE fluxes with, in general, no change in the marsh metabolism status (sink/source). During daytime, significantly lower CO_2 uptakes were recorded during immersion than during emersion (Mann–Whitney tests, $p < 0.05$) when marsh plants were mostly immersed in tidal waters, and during night-time, a similar tidal pattern was recorded for CO_2 emissions (Mann–Whitney tests, $p < 0.05$; Table 3). For instance, in spring, NEE means were -4.39 ± 3.76 and -2.59 ± 3.24 μmol m^{-2} s^{-1} during daytime emersion and daytime immersion, respectively, and were 1.25 ± 0.98 and 0.51 ± 1.22 μmol m^{-2} s^{-1} during night-time emersion and night-time immersion, respectively. In winter, during some night-time periods, weak CO_2 sinks were recorded both during emersion (-0.79 ± 0.84 μmol m^{-2} s^{-1}; 137 h over 71 d) and immersion (-0.82 ± 0.91 μmol m^{-2} s^{-1}; 143 h over 55 d associated with a mean H_w of 0.80 m; Fig. S2). The maximal CO_2 uptakes were −4.80 and −5.31 μmol m^{-2} s^{-1} during night-time emersion and night-time immersion, respectively (Table 3).

3.4 Influence of environmental drivers on temporal NEE variations

Throughout the year, NEE fluxes were significantly controlled by solar radiations and air temperatures at the multiple timescales studied, thereby favouring marsh CO_2 uptake. During daytime (PAR > 10 μmol m^{-2} s^{-1}), PAR and T_a displayed the strongest negative correlations with NEE at both the monthly scale (−0.87 and −0.65, respectively; $n = 12$, $p < 0.05$) and the 10 min scale (−0.77 and −0.21, respectively; $n = 27\,160$, $p < 0.05$). The highest and lowest correlations between NEE and PAR were recorded for

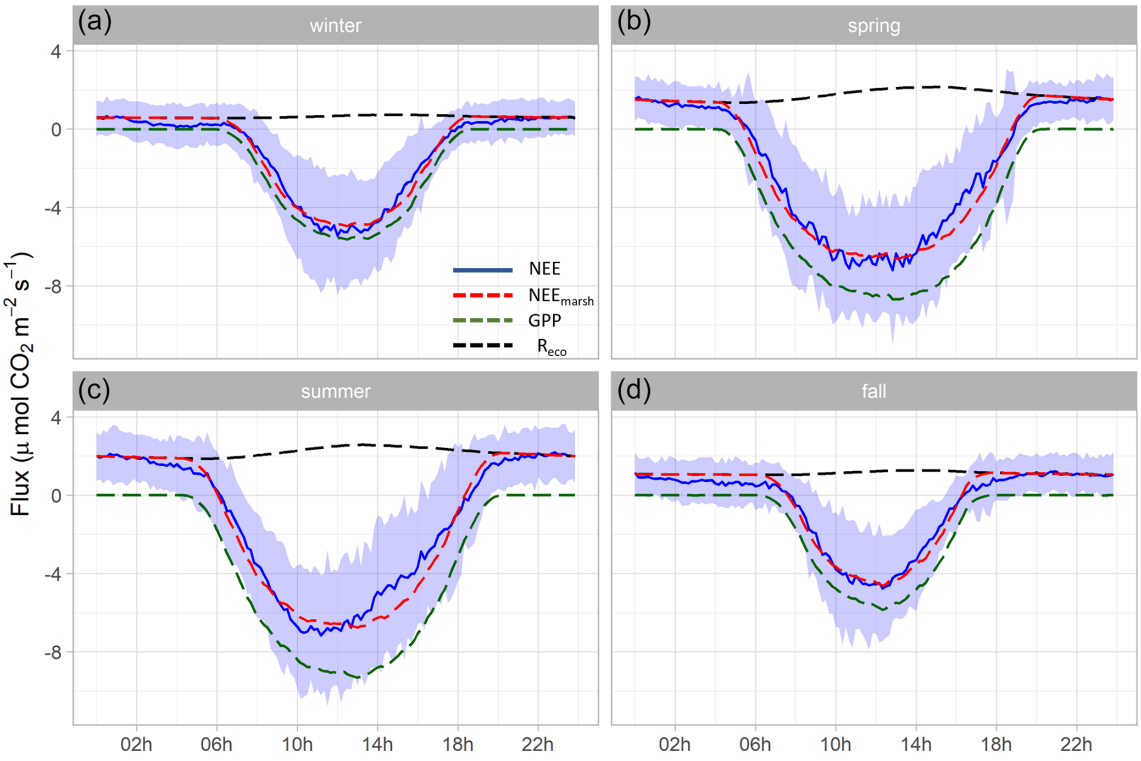

Figure 5. Hourly plots of the measured NEE, estimated NEE_{marsh}, estimated GPP and estimated R_{eco} diurnal variations obtained every 10 min in winter **(a)**, spring **(b)**, summer **(c)** and fall **(d)** for the year 2020. NEE averages are represented by solid blue lines and standard deviations are represented by blue areas. The NEE_{marsh}, GPP and R_{eco} averages are represented by dotted red, green and black lines, respectively. The measured NEE fluxes were partitioned into GPP and R_{eco} according to Kowalski et al. (2003) using monthly coefficients (see the "Materials and methods" section). Night-time periods correspond to $GPP = 0\,\mu mol\,m^{-2}\,s^{-1}$ and $NEE_{marsh} = R_{eco}$. All values are in $\mu mol\,CO_2\,m^{-2}\,s^{-1}$.

$10 < PAR \leq 500$ and for $1500 < PAR \leq 2000\,\mu mol\,m^{-2}\,s^{-1}$, respectively, confirming the rapid increase or decrease in CO_2 uptake for low daytime PAR values (Fig. 6a). During daytime, vapour pressure deficit (VPD) was negatively correlated with NEE (-0.31; $n = 27\,160$, $p < 0.05$) producing a large reduction in CO_2 uptake for all PAR levels and even led to a switch from sink to source of atmospheric CO_2 from VPD > 1200 Pa for low PAR levels ($PAR \leq 500\,\mu mol\,m^{-2}\,s^{-1}$; Fig. 6b). During night-time and daytime, air temperature (T_a) was positively (0.54; $n = 27\,190$, $p < 0.05$) and negatively (-0.21; $n = 25\,544$, $p < 0.05$) correlated with NEE, respectively. However, from $PAR > 500\,\mu mol\,m^{-2}\,s^{-1}$, high T_a values ($> 20\,°C$) decreased CO_2 uptake for all PAR levels (Fig. 6c). Water temperature (T_w) did not influence NEE during immersion (Fig. 6d). Indeed, for $PAR > 500\,\mu mol\,m^{-2}\,s^{-1}$ and $H_w > 0.5$ m, no significant relationship was found between NEE and T_w ($n = 1215$; $p = 0.26$). For low PAR levels ($PAR \leq 500\,\mu mol\,m^{-2}\,s^{-1}$), wind speeds quickly increased CO_2 uptake, whereas for high PAR levels ($PAR > 500\,\mu mol\,m^{-2}\,s^{-1}$), CO_2 uptake was increased only for wind speeds higher than $7\,m\,s^{-1}$ (Fig. 6e). For wind directions, a spatial heterogeneity of NEE was recorded according to wind sectors both during daytime and night-time (Fig. 6f). Within the footprint area composed of an assemblage of plants and muds (Fig. 2), the highest CO_2 uptakes were generally recorded from the southern sectors (high vegetation : mud ratios) whereas, the lowest CO_2 uptakes were generally recorded from the northern sectors (low vegetation : mud ratios; Fig. 7). For instance, our sectorial NEE analysis during daytime emersion showed that the SSE sector (vegetation : mud ratio of 2.4; Table 1) did uptake 32 % (winter), 25 % (spring) and 50 % (fall) times more atmospheric CO_2 than the NNW sector (vegetation : mud ratio of 0.8; Table 1). Moreover, in winter and fall, we highlighted that CO_2 uptake rates of *H. portulacoides* (C_3 species) were significantly higher than *S. maritima* (C_4 species) ones by comparing the SSE (60 % of *H. portulacoides* and 9 % of *S. maritima*) and WSW (33 % of *H. portulacoides* and 35 % of *S. maritima*) sectors during daytime emersion (Mann–Whitney tests, $p < 0.0001$). In contrast, in summer, no significant difference in NEE fluxes was recorded between these two sectors (Mann–Whitney test, $p = 0.06$; Fig. 7) and, more generally, between the different wind sectors (Fig. 7; Table 1). For all seasons, during night-time emersion, we recorded that southern sectors (ESE, SSE and SSW) emit-

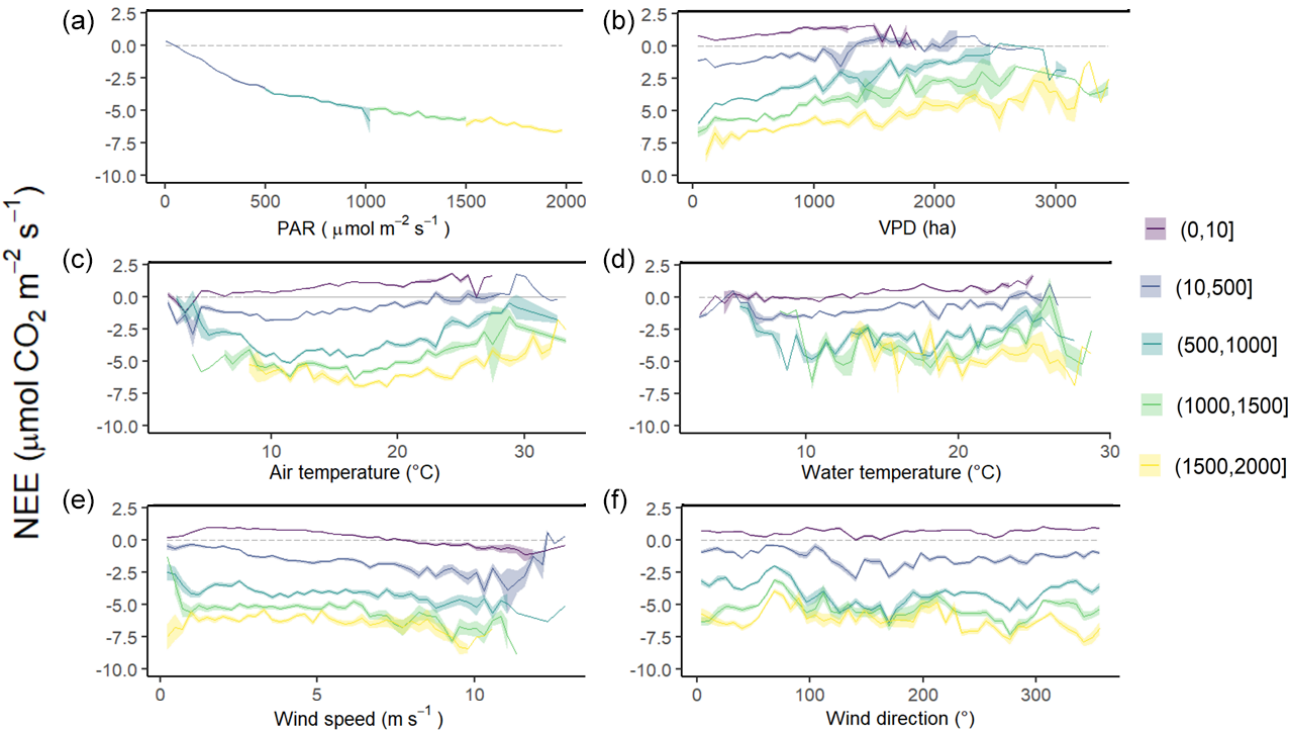

Figure 6. Diurnal variations of NEE fluxes (µmol CO_2 m^{-2} s^{-1}) measured every 10 min according to different variables within five PAR groups: 0–10 (night-time), 10–500, 500–1000, 1000–1500 and 1500–2000 µmol m^{-2} s^{-1}. Panel **(a)** shows PAR (µmol m^{-2} s^{-1}), **(b)** VPD (Pa), **(c)** air temperature (°C), **(d)** water temperature (°C), **(e)** wind speed (m s^{-1}) and **(f)** wind direction (°). NEE fluxes are averaged after separating each variable into five classes and the coloured area is the standard error at the mean.

ted higher atmospheric CO_2 than northern sectors (NNE and ENE), especially in winter and fall (Fig. 7; Table 1).

The tidal rhythm strongly influenced NEE fluxes during immersion depending on water heights (H_w) and PAR levels (Figs. 8 and S3). Throughout the year, NEE were positively correlated with H_w during the day but negatively correlated during the night (Fig. 8). More precisely, night-time immersion strongly reduced CO_2 emissions and even led to a switch from source to sink of atmospheric CO_2 from $H_w > 0.4$ m in winter (Fig. 8a), $H_w > 0.7$ m in spring (Fig. 8b), $H_w > 1.4$ m in summer (Fig. 8c) and $H_w > 1$ m in fall (Fig. 8d), on average. For low daytime PAR levels (PAR ≤ 500 µmol m^{-2} s^{-1}), immersion only slightly reduced CO_2 uptake (Fig. 8c). On the contrary, for higher daytime PAR levels (PAR > 500 µmol m^{-2} s^{-1}), immersion strongly reduced CO_2 uptake, especially from $H_w > 0.5$ m, to reach the lowest CO_2 sinks from $H_w > 1.0$ m, irrespective of the PAR levels (Fig. 8c).

3.5 Annual carbon budgets

Throughout the year, the annual NEE value was -483.6 g C m^{-2} yr^{-1}, associated with immersion duration of 6.1 h d^{-1}, on average. Simultaneously, estimated GPP and R_{eco} (marsh metabolic fluxes without tidal influence) absorbed and emitted 1019.4 and 533.2 g C m^{-2} yr^{-1}, respectively, resulting in an annual estimated NEE_{marsh} value similar to the measured NEE value (Fig. 9). At the seasonal scale, the highest CO_2 uptakes occurred in spring and summer, associated with the lowest marsh immersion levels, and the lowest CO_2 uptakes occurred in winter and fall, associated with the highest marsh immersion levels (Tables 2 and 4). In winter and fall, when the daytime immersion periods were the shortest, net C balances from measured NEE gave higher values than net C balances from estimated NEE_{marsh} (+7.9 and +6.2 g C m^{-2}, respectively; Table 4). Conversely, in spring and summer when the daytime immersion periods were the longest, the opposite pattern was observed between measured NEE values and estimated NEE_{marsh} values (-7.3 and -9.9 g C m^{-2}, respectively; Table 4).

4 Discussion

4.1 Marsh CO_2 uptake and influence of management practice

In the present EC study, the salt marsh absorbed 483 g C m^{-2} yr^{-1} from the atmosphere. This net C balance (i.e. budget) was lower than the values estimated for global tidal wetlands (1125 g C m^{-2} yr^{-1}; Bauer et al., 2013) and

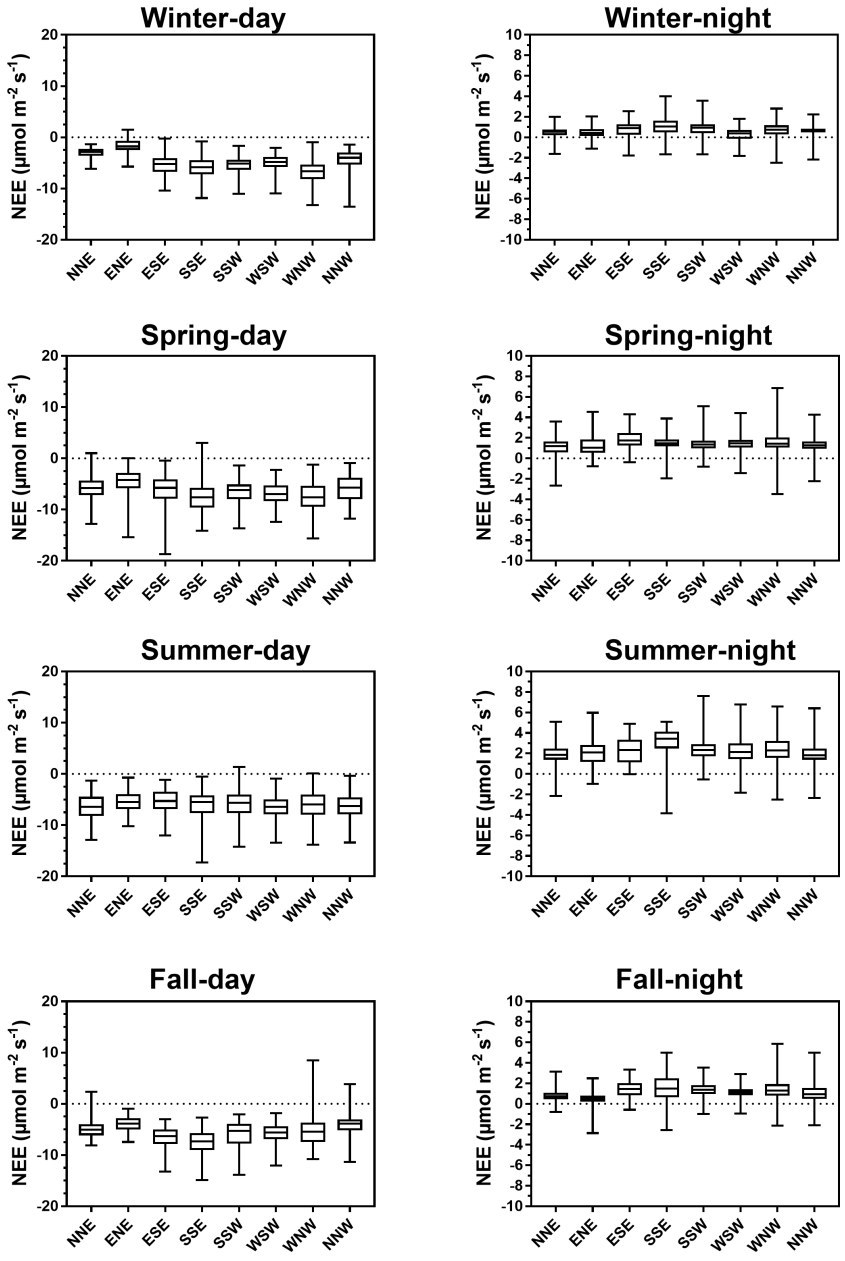

Figure 7. Spatial split of NEE fluxes (µmol CO_2 m^{-2} s^{-1}) within each 45° wind sector (Fig. 2) during emersion periods ($H_w = 0$ m) at the seasonal and diurnal scales. During daytime, the brightest emersion periods (PAR ≥ 500 µmol m^{-2} s^{-1}) were chosen to reduce NEE fluctuations due to PAR influence (see Fig. 6a).

for tidal marshes on the Atlantic coast of the United States (775 g C m^{-2} yr^{-1}; Wang et al., 2016) but similar to the C balance estimated by Alongi (2020) for global salt marshes (382 g C m^{-2} yr^{-1}).

Currently, an increasing number of EC measurements are being taken in salt marshes in order to obtain continuous NEE data series as well as to increase knowledge about the associated metabolic processes and fluxes for these tidal systems (Table 5) (Schäfer et al., 2014; Forbrich et al., 2018; Knox et al., 2018). These EC studies confirmed the estimates of CO_2 sinks in salt marshes (Wang et al., 2016; Alongi, 2020) but also revealed strong NEE flux heterogeneities according to climatic conditions and anthropogenic influences (Herbst et al., 2013; Schäfer et al., 2019). For instance, NEE measured in a natural salt marsh (*S. alterniflora*, *S. maritima* and *D. spicata*) showed a net C uptake from the atmosphere with high interannual variations in C balances (Table 5) mainly due to rainfall during the growing season for marsh plants (Forbrich et al., 2018). By comparison, in an urban tidal marsh, Schäfer et al. (2014) reported a higher interan-

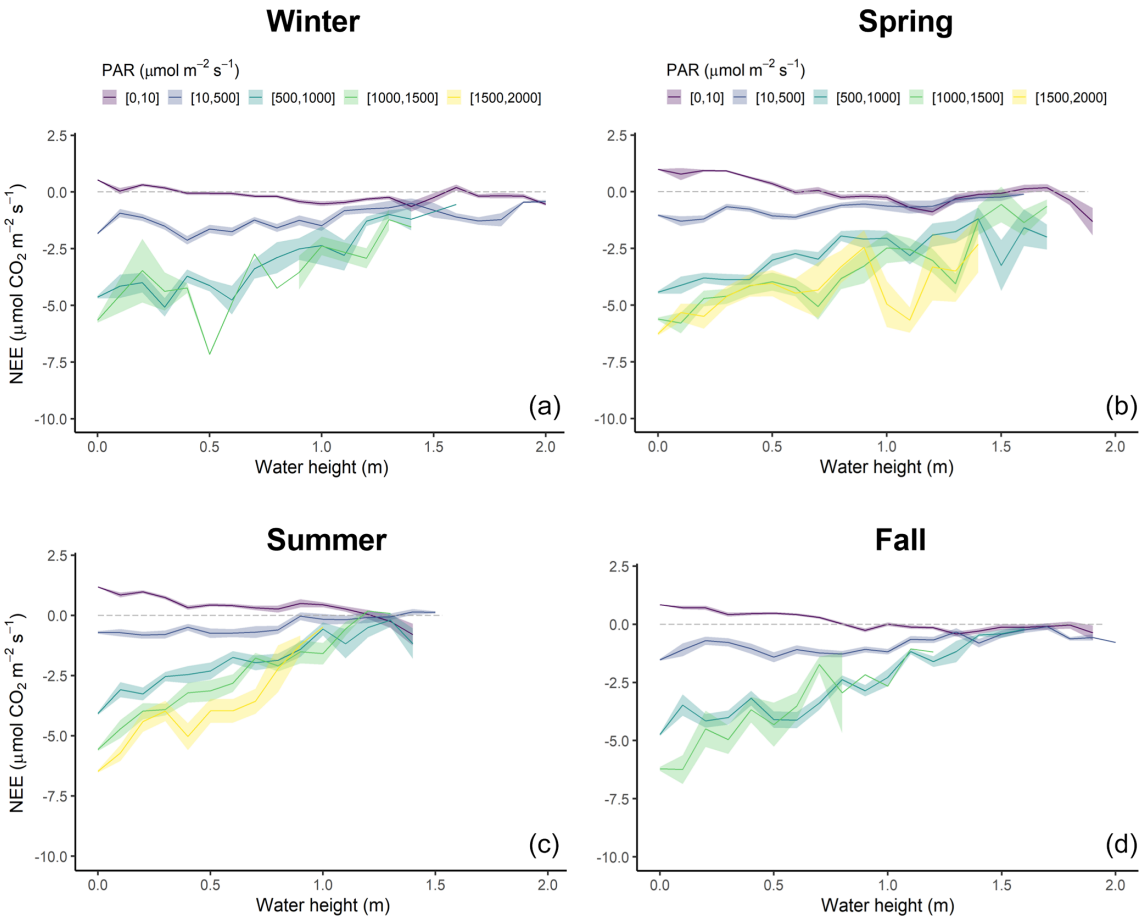

Figure 8. Diurnal variations of NEE fluxes (µmol CO_2 m^{-2} s^{-1}) measured every 10 min according to water height (H_w, m) within five PAR groups (see caption of Fig. 6) in winter **(a)**, spring **(b)**, summer **(c)** and fall **(d)**. NEE values were averaged every 0.1 m. The coloured areas represent the standard error of the mean.

Table 4. Net seasonal carbon balances for the measured NEE and estimated NEE_{marsh} values ($g C m^{-2}$). Corresponding seasonal percentages of marsh immersion and daytime marsh immersion are indicated. NEE corresponds to net vertical CO_2 exchanges measured by EC, whereas NEE_{marsh} corresponds to net vertical CO_2 exchanges estimated at the benthic interface without any tidal influence.

	Cumulative NEE ($g C m^{-2}$)	Cumulative NEE_{marsh} ($g C m^{-2}$)	$NEE - NEE_{marsh}$ ($g C m^{-2}$)	Immersion time (%)	Daytime immersion time (%)
Year 2020	483.6	485.9	−2.3	25.5	52.2
Winter	94.4	86.5	7.9	23.7	41.5
Spring	184.5	191.8	−7.3	25.5	63.4
Summer	149.3	159.2	−9.9	24.9	64.5
Fall	55.5	49.3	6.2	27.9	39.5

nual variability from 984 $g C m^{-2}$ in 2009 to −310 $g C m^{-2}$ in 2012 due to management practices and plant species (*P. australis* and *S. alterniflora* in 2009 and total elimination of *P. australis* in 2012; Table 5). In the same area, in another restored salt marsh in which the *P. australis* monoculture was replaced by a high diversity of emergent marsh plants (*S. patens*, *S. cynosuroides*, *S. alterniflora* and *D. spicata*), a net CO_2 uptake was recorded (Table 5) which once again confirms the importance of land management practices in marsh C balances (Artigas et al., 2015). In our studied salt marsh, the natural management for several decades has allowed for a return to the natural site hydrodynamics and the development of productive marsh halophytes, mainly composed of *H. portulacoides* and *S. maritima* (59 % of the footprint area). However, past human activities and water management practices for salt farming have shaped the marsh

Table 5. Comparison of the annual NEE budget ($g C m^{-2} yr^{-1}$) using EC measurements across the salt, brackish and freshwater marshes of the coastal zone.

Study site	Location	Annual NEE budget ($g C m^{-2} yr^{-1}$)	Reference
Tidal salt marsh[a]	Fier d'Ars tidal estuary, France	−483	This study
Tidal salt marsh[a]	Virginia, USA	−130[b]	Kathilankal et al. (2008)
Urban tidal marsh[a]	Hudson–Raritan estuary, New Jersey, USA	From +894 to −310	Schäfer et al. (2014)
Restored salt marsh[a]	Hudson–Raritan estuary, New Jersey, USA	−213	Artigas et al. (2015)
Tidal salt marsh	Plum Island Sound estuary, Massachusetts, USA	From −104 to −233 (−176 ± 32)[c]	Forbrich et al. (2018)
Tidal salt marsh	Duplin River salt marsh–estuary, Georgia, USA	From −139 to −309	Nahrawi (2019)
Urban tidal wetlands	Hudson–Raritan estuary, New Jersey, USA	−307[d]	Schäfer et al. (2019)
Brackish tidal marsh	San Francisco Bay, California, USA	−225	Knox et al. (2018)
Brackish marsh	Louisiana, USA	171	Krauss et al. (2016)
Para-dominated subtropical marsh	Taiwan	−376	Lee et al. (2015)
Reed-dominated marsh	Taiwan	−53	Lee et al. (2015)
Freshwater marsh	Louisiana, USA	−337	Krauss et al. (2016)
Freshwater wetland	Everglades National Park, Florida, USA	From −91 to +3 (−21 ± 17)[e]	Zhao et al. (2019)

[a] Managed and protected marshes. [b] NEE budget during the growing season (from May to October 2007). [c] Mean of annual NEE budgets over a 5-year period (from 2013 to 2017). [d] Annual NEE budget of three tidal marshes with different restoration histories. [e] Mean of annual NEE budgets over a 9-year period (from 2008 to 2016).

typology (channel network, humps and dykes), producing a time-delayed immersion of plants and muds between high and low marsh areas during spring tides. Thus, due to this emersion/immersion heterogeneity, mud and *S. maritima* were quickly immersed by coastal waters, whereas the whole immersion of marsh habitats only occurred during the highest tidal amplitudes favouring a higher atmospheric CO_2 uptake by *H. portulacoides* and *S. vera*. During the year 2020, our rewilded salt marsh took up more C from the atmosphere mainly due to strong plant photosynthesis than the other salt, brackish and freshwater marshes reported in the literature (Table 5). However, the net C balances calculated with the EC method are still too scarce to be able to take all temporal and spatial variabilities of salt marshes into account. Based on biomass production measurements in salt marshes, Sousa et al. (2010) estimated that the NPP of *H. portulacoides* was $505\,g C m^{-2} yr^{-1}$, whereas the NPP of *S. maritima* varied between 367 and $959\,g C m^{-2} yr^{-1}$ depending on the chemical–physical characteristics and marsh maturity. Thus, the net metabolism of these halophytic plants could play an important role in our net C balance but, according to "the marsh CO_2 pump" (Wang et al., 2016), a significant proportion of marsh NPP was respirated by heterotrophic processes and then (1) emitted as atmospheric CO_2 (38 ± 11 %) and (2) exported by tides as DIC (37 ± 15 %; Song et al., 2023).

Moreover, despite a lower benthic metabolism (photosynthesis and respiration) of muds than evergreen plants (Fig. 7), the microphytobenthos which can develop on mudflats (27 % of the footprint area) may also contribute to marsh production during daytime emersion, as highlighted in our studied marsh where static chamber measurements performed in March 2023 at midday showed a net CO_2 uptake to a non-vegetated mudflat (NEE mean

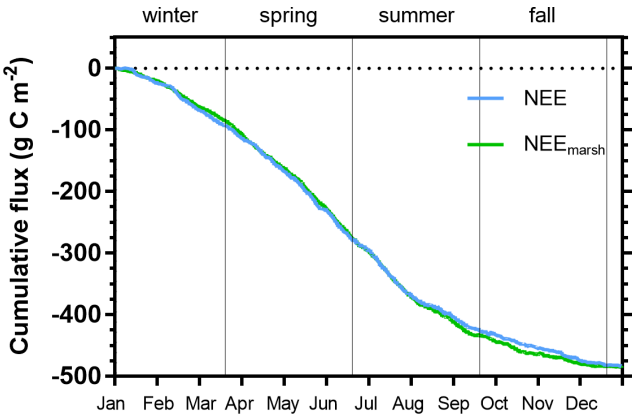

Figure 9. Cumulative carbon fluxes ($g C m^{-2}$) of the measured NEE (in blue) and estimated NEE_{marsh} (in green) throughout the year 2020. Vertical lines are used to delimit the four seasons. NEE fluxes correspond to net vertical CO_2 exchanges measured by EC, whereas NEE_{marsh} fluxes correspond to net vertical CO_2 exchanges estimated from NEE partitioning at the benthic interface only, without any tidal influence.

of $-2.92\,\mu mol\,m^{-2}\,s^{-1}$; unpublished results) and confirmed in an estuarine wetland in China (Xi et al., 2019). On an intertidal flat (France), EC measurements even showed a higher daily benthic metabolism with microphytobenthos ($1.72\,g C\,m^{-2}\,d^{-1}$; September/October 2007) than with *Zostera noltei* ($1.25\,g C\,m^{-2}\,d^{-1}$; July and September 2008), confirming the high biological productivity of mudflats (Polsenaere et al., 2012). However, due to the specific assemblage of our studied marsh (Fig. 2), it remains complex to accurately study these habitat effects (plants vs. microphytobenthos) on NEE fluxes at the marsh scale and draw more general conclusions. Thus, the microphytobenthos could play a significant role in the atmospheric CO_2 uptake of salt marshes but also, more generally, in the carbon cycle of the coastal ocean because the resuspension of the microphytobenthos primary production during tidal immersion induce a large export of organic carbon from muds to coastal waters (up to 60 % of the benthic primary production in a nearby tidal flat; Savelli et al., 2019). These fast-growing primary producers with high labile organic carbon could also be quickly degraded locally by microbial remineralization (Ruttenberg, 1992; De Brouwer and Stal, 2001; Morelle et al., 2022), contrary to evergreen plants contributing to long-term "blue carbon" burial in sediments (Mcleod et al., 2011).

4.2 Metabolism processes and controlling factors at multiple timescales

4.2.1 Seasonal scale

In a tidal salt marsh, the average monthly budgets from Forbrich et al. (2018) showed a net CO_2 sink during the growing season for marsh plants from June to September and a net CO_2 source to the atmosphere during the rest of the year, indicating a strong seasonal variability in marsh metabolic fluxes. In urban salt marshes, the growing season was longer switching from source to sink in May (Schäfer et al., 2014; Artigas et al., 2015) and even in April in a brackish marsh (Knox et al., 2018). In our studied marsh, the halophyte vegetation, mostly composed of evergreen species, was autotrophic throughout the year allowing a net C uptake from the atmosphere during both the growing and non-growing seasons (between $9\,g C\,m^{-2}$ in December and $73\,g C\,m^{-2}$ in July), whereas the senescence of smooth cordgrass plants in some salt marshes (*S. alterniflora* and *S. cynosuroides*, for instance) from October produced a marsh heterotrophy and a net C source to the atmosphere in winter and fall (Schäfer et al., 2014; Artigas et al. 2015; Forbrich et al., 2018). In our case, *S. maritima* is a perennial species with a relatively short growing period. Indeed, during winter and fall, the metabolism of this halophytic plant could have a significantly lower influence on marsh C uptake than *H. portulacoides* and *S. vera*. The spatial NEE analysis showed that, in summer during daytime emersion, CO_2 uptake rates of the northern sectors (high mudflats areas) were close to ones of the southern sectors (high plants areas) which suggests a low heterotrophic respiration in the mudflats during this period. The low R_{eco} rates related to plant and soil respiration processes resulted in lower atmospheric CO_2 emissions in the studied salt marsh than in urban salt marshes (Artigas et al., 2015) and brackish marshes (Knox et al., 2018), thus allowing a net CO_2 sink from winter to summer. Moreover, our low R_{eco} is also likely linked to the low OM decomposition observed at our site, notably due to recalcitrant OM (Arnaud et al., 2024). Furthermore, it is also important to better understand the direct and indirect effects of meteorological conditions and tidal immersion on photosynthesis and respiration processes and the associated marsh C balances (Knox et al., 2018).

Our study showed the predominant role of PAR and T_a on NEE variations in the salt marsh as has already been highlighted elsewhere by Wei et al. (2020b). Our correct NEE flux partitioning into GPP and R_{eco} during emersion indicated that plant photosynthesis was mainly driven by light, while ecosystem respiration was mainly driven by temperature. At the seasonal scale, the strongest CO_2 sinks were measured during warm and bright periods such as spring and summer, which were responsible for 70 % of the annual C uptake (Table 4). However, although the highest seasonal rate of GPP was measured in summer during the brightest months,

the simultaneously recorded high T_a values instead favoured ecosystem respiration producing a lower net CO_2 uptake in summer than in spring (Table 4). For instance, in two urban salt marshes, the T_a values above 30 °C reduced CO_2 uptake by increasing respiration and atmospheric CO_2 emissions (Schäfer et al., 2019). These two meteorological parameters controlled short- and long-term NEE variations, as confirmed in urban salt marshes where significant and strong pairwise correlations of NEE with net radiation and temperature were recorded on half hourly, daily and monthly averages (Schäfer et al., 2019).

At the studied salt marsh, we showed a significant influence of VPD and RH on daytime NEE variations favouring plant CO_2 uptake for the lowest VPD values (< 1000 Pa) and the highest RH values (> 80 %). The lack of a significant relationship between NEE and RH at night indicated that humidity influenced plant photosynthesis, by decreasing VPD and stomata opening, rather than their respiration. In a similar tidal salt marsh, Forbrich et al. (2018) showed a link between rainfall and C budgets on interannual variations in NEE, i.e. during the early growing season in spring, rainfall events produced a decrease in soil salinity and favoured CO_2 uptake through an increase in plant productivity. In a salt marsh in the Yellow River Delta, significant NEE increases and GPP decreases were recorded with high soil salinities during emersion using static chamber measurements (Wei et al., 2020a). High levels of soil salinity in salt marshes are a stressor for plants such as *Spartina* spp. and can lead to reduce biomass production by inhibiting nutrient and CO_2 uptake throughout stomatal closure (Morris, 1984; Hwang and Morris, 1994). Thus, in our studied marsh, we believe that the increase in dryness periods, especially in summer, with a decrease in rainfall events could profoundly modify plant productivity and marsh C uptake. This was confirmed by a significant reduction in the CO_2 sink at the studied salt marsh with low RH and high T_a values.

4.2.2 Diurnal and tidal scale influences

High-frequency EC measurements demonstrated that diurnal variations in NEE fluxes were driven by light, rather than air temperature (Xi et al., 2019; Wei et al., 2020b), with no significant time delay recorded between NEE and PAR variations (Fig. S2). At our studied site, the highest negative correlations between NEE and PAR were highlighted for low daytime PAR values, indicating that the increases in light during the morning strongly favoured CO_2 uptake mainly through plant photosynthesis up to the middle of the day. During the afternoon, the high T_a and VPD values (warm and dry periods) produced a reduction in photosynthetic rates through stomatal closure of the C_3 plants (Lasslop et al., 2010). This GPP decrease associated with a R_{eco} increase in afternoon reduced the net CO_2 uptake up to reach CO_2 emissions during night-time (Knox et al., 2018; Xi et al., 2019). In another tidal salt marsh, Kathilankal et al. (2008) confirmed the PAR importance on *Spartina* photosynthesis and diurnal NEE fluxes. In a restored salt marsh, EC measurements also showed that the time of day has a major influence on atmospheric CO_2 exchanges during the growing season, accounting for 49 % of NEE variability (Artigas et al., 2015). Moreover, in some cases, soil respiration can also be controlled by PAR or photosynthesis at the diurnal scale (Vargas et al., 2011; Jia et al., 2018; Mitra et al., 2019), once again highlighting the major role played by light in diurnal NEE variations (Kathilankal et al., 2008; Wei et al., 2020b). In winter, negative NEE fluxes were measured during some night-time emersion periods in the absence of any photosynthetic processes (18.5 % in January, 18.1 % in February and 10.7 % in March). These negative fluxes could have two main sources: (1) an inorganic CO_2 diffusion and dissolution processes in saline/alkaline soils over mudflats (Ma et al., 2013) and (2) an inflow of coastal waters undersaturated in CO_2 with respect to the atmosphere within the footprint area (in channel; Fig. 2) but not seen by the STPS probe due to our one-location water height measurement and immersion marsh heterogeneity (see Sect. 2.2). The negative values during night-time emersion could reduce the night-time random forest model performance for EC data gap-filling and produce an underestimation of respiration coefficients for NEE flux partitioning (particularly b) even causing a negative coefficient (February; Table S2).

At the daily scale, the intensity of atmospheric CO_2 exchanges and the metabolic status of the marsh (sink/source) were also significantly influenced by the tidal rhythm (Fig. 8). Tides produced a significant decrease in daytime CO_2 uptake with maximal reductions up to 90 % for the highest tidal amplitudes. In a *S. alterniflora* salt marsh, a mean reduction of 46 ± 26 % was measured during immersion, although large CO_2 amounts were still assimilated at a reduced rate (Kathilankal et al., 2008). In some cases, daytime NEE fluxes could be completely suppressed during immersion in salt marshes (Moffett et al., 2010; Forbrich and Giblin, 2015; Wei et al., 2020a) and brackish marshes (Knox et al., 2018). This drop in CO_2 uptake could be related to a physiological stress for plants under tidal immersion conditions resulting in a reduction in the effective photosynthetic leaf area and photosynthesis rates (Kathilankal et al., 2008; Moffett et al., 2010). Moreover, the physical barrier created by tidal waters could limit the CO_2 diffusion from waters to plants, thereby resulting in fewer CO_2 exchanges between the atmosphere and the benthic compartment (sediments and soil). Using chamber measurements at different tidal stages, Wei et al. (2020a) also highlighted the importance of water heights and marsh immersion levels in NEE variations and confirmed a significant GPP decrease during immersion. However, tidal effects on daytime NEE fluxes may be more variable depending on the immersion level of the marsh and the biogeochemistry state of the tidal waters. Indeed, during the brightest periods in winter and spring, the temporary increases in CO_2 uptake recorded during incoming tides could be related to

(1) an increase in the GPP of *H. portulacoides* and *S. vera* (highest marsh levels) favoured by VPD and T_a decreases due to tidal conditions and/or (2) tidal waters advected from the shelf that are undersaturated in CO_2 with respect to the atmosphere due to phytoplankton blooms (Mayen et al., 2024). Moreover, when the salt marsh was fully immersed at high tide during spring tides, NEE fluxes were mostly controlled by ecosystem respiration and/or inorganic processes (carbonate and physicochemical pumps) rather than by photosynthesis, as light was no longer a major controlling factor for CO_2 uptake in tidal waters.

During night-time, CO_2 emissions from the salt marsh were inhibited by tidal effects through a significant decrease in ecosystem respiration (Han et al., 2015; Knox et al., 2018; Wei et al., 2020a). The physical barrier formed by tidal waters limits the atmospheric CO_2 releases via respiration from plants and soils (Wei et al., 2020b). Moreover, saturation of surface soils in tidal waters during immersion could reduce oxygen availability in the soil and limit OM microbial decomposition and CO_2 emissions through aerobic respiration (Nyman and DeLaune, 1991; Miller et al., 2001; Jimenez et al., 2012; Han et al., 2015). In our case, night-time CO_2 exchanges were reduced up to 100 % (completely suppressed), sometimes even causing a change in metabolic status of atmospheric CO_2 from source to sink, especially in winter when the R_{eco} rates were the lowest. The presence of tidal waters advected from the shelf during the night, and CO_2 undersaturated with respect to the atmosphere due to previous phytoplankton production and/or $CaCO_2$ dissolution in the water column during the day (Gattuso et al., 1999; Polsenaere et al., 2012), could induce a sink which may lead to a net uptake of CO_2 at night (Fig. 8). The results of our study indicate that tidal NEE variations may be mainly related to the marsh immersion level, the PAR level and the time of the growing cycle of plants as reported in Nahrawi et al. (2020).

4.3 Salt marsh carbon budgets for future research perspectives

At the annual scale in 2020, the tidal rhythm did not significantly affect the net C balance of the studied salt marsh since similar annual measured NEE and estimated NEE_{marsh} values were recorded (Fig. 9). The loss of CO_2 uptake measured during daytime immersion due to a GPP decrease could be compensated by night-time immersion where CO_2 emissions and R_{eco} were inhibited. However, strong temporal variabilities were measured, especially between the growing and non-growing seasons. In winter and fall, the salt marsh did uptake more C from the atmosphere with the tidal influence (measured NEE) than without (estimated NEE_{marsh}), especially in December (+35.7 %), November (+19.7 %) and January (+15.4 %), associated with the highest photosynthetic efficiencies. An opposite trend was observed in spring and summer with a reduction in net C uptake under tidal influence, especially in August (−16.9 %) and September (−9.8 %). This significant difference in the seasonal C balances could be mainly related to the photoperiod of immersion periods. We demonstrated that daytime immersion decreased CO_2 uptake, whereas night-time immersion decreased CO_2 emissions up to a change in metabolic status for the highest immersion levels. Thus, during seasons where daytime immersion primarily occurs, such as spring and summer, the salt marsh did uptake less atmospheric CO_2 with tidal influence, whereas seasons that mostly have night-time immersion did uptake more atmospheric CO_2 with tidal influence (Table 4). However, this unpublished result was only possible provided that the salt marsh switched from a source to a sink of CO_2 during night-time immersion due to water undersaturation with respect to the atmosphere. In a salt marsh on Sapelo Island (USA), Nahrawi et al. (2020) highlighted tidal CO_2 flux reductions all year round by distinguishing neap tide and spring tide periods. Their results showed that the highest and lowest reductions in C uptake occurred in spring (−34 %) and summer (−13 %), respectively, with a similar but greater tidal influence on the C uptake values compared with our study.

To better constrain the tidal influence on the metabolism of the salt marsh, further investigations have been carried out in 2021 in parallel with our EC measurements, with the construction of a digital field model for water heights that can be used to spatially determine, over the whole EC footprint, the exact areas of immersion and emersion (especially for the low water levels) of the marsh in each sector at a 10 min step. Similarly, during marsh immersion, EC measurements do not directly capture CO_2 fluxes from benthic metabolism because of the physical barrier of the water and the lower CO_2 diffusion rates in water than in air. Consequently, at the same time as when the NEE measurements were taken, water pCO_2, inorganic and organic carbon concentrations associated with planktonic metabolism were determined each season through 24 h cycles to provide essential information on the contribution of planktonic communities and plants to CO_2 fluxes during immersion (Mayen et al., 2024). The lateral carbon export from salt marshes by tides plays a significant role in the coastal ocean carbon cycle (Guo et al., 2009; Wang et al., 2016). Plant respiration and microbial mineralization of marsh NPP could generate Dissolved Inorganic Carbon (DIC) in waters associated with a strong benthic–pelagic coupling. Thus, our 2021 measurements of the carbon parameters, planktonic metabolism (production and respiration) and other relevant biogeochemical variables over 24 h diurnal cycles, along with measurements of the soil compartment (root OM production vs. mineralization; Arnaud et al., 2024) carried out in the EC footprint, would allow for a more integrative calculation of the studied marsh carbon budget (Mayen et al., 2024). One advantage of the EC measurements is the aggregation of CO_2 fluxes from all compartments (waterbodies, soil, plants and atmosphere) in salt marshes. Yet, through this flux aggregation, we cannot mechanistically understand each marsh compartment, and there-

fore it can be challenging to predict CO_2 fluxes under multiple global changes. Therefore, future contributions should try to simultaneously quantify all these compartments, especially soil as it is where most of the carbon is stored in salt marshes (Arnaud et al., 2024). Ongoing atmospheric CO_2 exchange measurements are actually carried out since January 2023 up north over Aiguillon (intertidal) Bay in France where we precisely deployed an EC station at the edge between the tidal mud flat on the west side and salt marsh habitats on the east side of the footprint along with benthic chamber flux and water, sediment, soil carbon measurements and satellite analysis at each season to specially address questions on relative habitat (mudflat vs. salt marshes) influence on atmospheric CO_2 exchanges (Pierre Polsenaere, personal communication, 2023).

5 Conclusion

In this study, we used the micrometeorological eddy covariance technique to investigate the net ecosystem CO_2 exchanges (NEE) at different timescales and to determine the major biophysical drivers of a rewilded tidal salt marsh. During the year 2020, the net C uptake from the atmosphere ($-483\,\mathrm{g\,C\,m^{-2}\,yr^{-1}}$) was mainly related to a low OM decomposition rate coupled with an intense autotrophic metabolism of halophyte plants, especially during the growing season, driven by light, temperature and VPD. In summer, the brightest days increased the plant GPP and, simultaneously, high temperature and VPD values favoured R_{eco} resulting in a lower net CO_2 uptake in summer than in spring. At the daily scale, the tidal rhythm significantly influenced NEE fluxes according to the level of marsh immersion and PAR. During daytime, tides strongly limited atmospheric CO_2 uptake, up to 90 % reductions, whereas night-time immersion inhibited atmospheric CO_2 emissions through plant and soil respiration, sometimes even causing a change in metabolic status from source to sink. However, at the annual scale, NEE flux partitioning into NEE_{marsh} highlighted that the tidal rhythm did not significantly affect the net marsh C balance. Our continuous NEE measurements have made it possible to better understand the biogeochemical functioning of salt marshes over a wide range of environmental conditions and have provided essential information on NEE fluxes in marshes undergoing potential future changes such as global warming or sea level rise.

Data availability. All raw data can be provided by the corresponding authors upon request.

Supplement. The supplement related to this article is available online at: https://doi.org/10.5194/bg-21-993-2024-supplement.

Author contributions. TLL and PP facilitated the funding acquisition. PP, EL and JMB conceptualized and designed the study. JM and PP compiled and prepared the datasets. JM and PK performed statistical and time-series analyses. JM, PP, EL and PK investigated and analysed the data. PK and RC executed the random forest model. JM, PP, EL, PK, ARdG and PS confirmed the data. PP, EL, MA, JMB, PG, JG and RC provided resources. JM performed the graphics and wrote the manuscript draft. PP, EL, MA, PK, RC, ARdG and PS reviewed and edited the manuscript. PP, ARdG and PS supervised the PhD thesis of JM.

Competing interests. The contact author has declared that none of the authors has any competing interests.

Disclaimer. Publisher's note: Copernicus Publications remains neutral with regard to jurisdictional claims made in the text, published maps, institutional affiliations, or any other geographical representation in this paper. While Copernicus Publications makes every effort to include appropriate place names, the final responsibility lies with the authors.

Acknowledgements. Jérémy Mayen thanks Ifremer (the French research institute for exploitation of the sea) for financing his PhD thesis (2020–2023). We are grateful to our colleagues (Didier Garrigou, Jean-Michel Chabirand, Jean-Christophe Lemesle and Jonathan Deborde) who contributed to the fieldwork carried out during this study. We thank Susann-Catrin Zech for her contribution in the field (photographs) and trainees (Camille Pery, Maxime Coutantin and Maxime Paschal) for their contributions to data analysis. Our grateful acknowledgements also go to the two reviewers (Francisco Artigas and an anonymous referee) for their constructive comments and suggestions. The proofreading of the manuscript and the correcting of the English content were carried out by Sara Mullin (PhD; freelance translator). This work is a contribution to Jérémy Mayen's PhD thesis and the ANR-PAMPAS project.

Financial support. This research has been supported by the ANR-PAMPAS project (Agence Nationale de la Recherche "Evolution de l'identité patrimoniale des marais des Pertuis Charentais en réponse à l'aléa de submersion marine", ANR-18-CE32-0006).

Review statement. This paper was edited by Tyler Cyronak and reviewed by Francisco Artigas and one anonymous referee.

References

Alongi, D. M.: Carbon Balance in Salt Marsh and Mangrove Ecosystems: A Global Synthesis, J. Mar. Sci. Eng., 8, 767, https://doi.org/10.3390/jmse8100767, 2020.

Arnaud, M., Bakhos, M., Rumpel, C., Dignac, M. F., Norby, R. J., Bottinelli, N., Deborde. J., Geairon, P., Kostyrka, P., Gernigon, J.,

Lemesle, J. C., and Polsenaere, P.: Salt marsh litter quality and decomposition under sea-level rise scenarios: from leaves to fine absorptive roots, Commun. Earth Environ., submitted, January 2024.

Artigas, F., Shin, J. Y., Hobble, C., Marti-Donati, A., Schäfer, K. V. R., and Pechmann, I.: Long term carbon storage potential and CO_2 sink strength of a restored salt marsh in New Jersey, Agr. Forest Meteorol., 200, 313–321, https://doi.org/10.1016/j.agrformet.2014.09.012, 2015.

Aubinet, M., Grelle, A., Ibrom, A., Rannik, Ü., Moncrieff, J., Foken, T., Kowalski, A. S., Martin, P. H., Berbigier, P., Bernhofer, Ch., Clement, R., Elbers, J., Granier, A., Grünwald, T., Morgenstern, K., Pilegaard, K., Rebmann, C., Snijders, W., Valentini, R., and Vesala, T.: Estimates of the Annual Net Carbon and Water Exchange of Forests: The EUROFLUX Methodology, Adv. Ecol. Res., 30, 113–175, https://doi.org/10.1016/S0065-2504(08)60018-5, 2000.

Aubinet, M., Vesala, T., and Papale, D. (Eds.): Eddy Covariance: A Practical Guide to Measurement and Data Analysis, Springer Netherlands, Dordrecht, https://doi.org/10.1007/978-94-007-2351-1, 2012.

Baldocchi, D. D.: Assessing the eddy covariance technique for evaluating carbon dioxide exchange rates of ecosystems: past, present and future: CARBON BALANCE and EDDY COVARIANCE, Glob. Change Biol., 9, 479–492, https://doi.org/10.1046/j.1365-2486.2003.00629.x, 2003.

Baldocchi, D. D., Hincks, B. B., and Meyers, T. P.: Measuring Biosphere-Atmosphere Exchanges of Biologically Related Gases with Micrometeorological Methods, Ecology, 69, 1331–1340, https://doi.org/10.2307/1941631, 1988.

Bauer, J. E., Cai, W.-J., Raymond, P. A., Bianchi, T. S., Hopkinson, C. S., and Regnier, P. A. G.: The changing carbon cycle of the coastal ocean, Nature, 504, 61–70, https://doi.org/10.1038/nature12857, 2013.

Bel Hassen, M.: Spatial and Temporal Variability in Nutrients and Suspended Material Processing in the Fier d'Ars Bay (France), Estuar. Coast. Shelf S., 52, 457–469, https://doi.org/10.1006/ecss.2000.0754, 2001.

Borges, A. V., Delille, B., and Frankignoulle, M.: Budgeting sinks and sources of CO_2 in the coastal ocean: Diversity of ecosystems counts, Geophys. Res. Lett., 32, L14601, https://doi.org/10.1029/2005GL023053, 2005.

Breiman, L.: Random Forests, Mach. Learn., 45, 5–32. https://doi.org/10.1023/A:1010933404324, 2001.

Burba, G.: 9 – Atmospheric flux measurements, in: Advances in Spectroscopic Monitoring of the Atmosphere, edited by: Chen, W., Venables, D. S., and Sigrist, M. W., Elsevier, 443–520, https://doi.org/10.1016/B978-0-12-815014-6.00004-X, 2021.

Cai, W.-J.: Estuarine and Coastal Ocean Carbon Paradox: CO_2 Sinks or Sites of Terrestrial Carbon Incineration?, Annu. Rev. Mar. Sci., 3, 123–145, https://doi.org/10.1146/annurev-marine-120709-142723, 2011.

Campbell, A. D., Fatoyinbo, L., Goldberg, L., and Lagomasino, D.: Global hotspots of salt marsh change and carbon emissions, Nature, 612, 701–706, https://doi.org/10.1038/s41586-022-05355-z, 2022.

Chmura, G. L., Anisfeld, S. C., Cahoon, D. R., and Lynch, J. C.: Global carbon sequestration in tidal, saline wetland soils, Global Biogeochem. Cy., 17, 1111, https://doi.org/10.1029/2002GB001917, 2003.

Cui, X., Goff, T., Cui, S., Menefee, D., Wu, Q., Rajan, N., Nair, S., Phillips, N., and Walker, F.: Predicting carbon and water vapor fluxes using machine learning and novel feature ranking algorithms, Sci. Total Environ., 775, 145130, https://doi.org/10.1016/j.scitotenv.2021.145130, 2021.

De Brouwer, J. and Stal, L.: Short-term dynamics in microphytobenthos distribution and associated extracellular carbohydrates in surface sediments of an intertidal mudflat, Mar. Ecol. Prog. Ser., 218, 33–44, https://doi.org/10.3354/meps218033, 2001.

Duarte, B., Couto, T., Freitas, J., Valentim, J., Silva, H., Marques, J. C., Dias, J. M., and Caçador, I.: Abiotic modulation of Spartina maritima photobiology in different latitudinal populations, Estuar. Coast. Shelf S., 130, 127–137, https://doi.org/10.1016/j.ecss.2013.02.008, 2013.

Duarte, B., Santos, D., Silva, H., Marques, J. C., and Caçador, I.: Photochemical and biophysical feedbacks of C_3 and C_4 Mediterranean halophytes to atmospheric CO_2 enrichment confirmed by their stable isotope signatures, Plant Physiol. Bioch., 80, 10–22, https://doi.org/10.1016/j.plaphy.2014.03.016, 2014.

Duarte, C. M., Middelburg, J. J., and Caraco, N.: Major role of marine vegetation on the oceanic carbon cycle, Biogeosciences, 2, 1–8, https://doi.org/10.5194/bg-2-1-2005, 2005.

Foken, T., Göckede, M., Mauder, M., Mahrt, L., Amiro, B., and Munger, W.: Post-field data quality control, in: Handbook of micrometeorology, University of Bayreuth, 181–208, Springer, 2004.

Foken, Th. and Wichura, B.: Tools for quality assessment of surface-based flux measurements, Agr. Forest Meteorol., 78, 83–105, https://doi.org/10.1016/0168-1923(95)02248-1, 1996.

Forbrich, I. and Giblin, A. E.: Marsh–atmosphere CO_2 exchange in a New England salt marsh, J. Geophys. Res.-Biogeo., 120, 1825–1838, https://doi.org/10.1002/2015JG003044, 2015.

Forbrich, I., Giblin, A. E., and Hopkinson, C. S.: Constraining Marsh Carbon Budgets Using Long-Term C Burial and Contemporary Atmospheric CO_2 Fluxes, J. Geophys. Res.-Biogeo., 123, 867–878, https://doi.org/10.1002/2017JG004336, 2018.

Gash, J. H. C. and Culf, A. D.: Applying a linear detrend to eddy correlation data in realtime, Bound.-Lay. Meteorol., 79, 301–306, https://doi.org/10.1007/BF00119443, 1996.

Gattuso, J.-P., Frankignoulle, M., and Smith, S. V.: Measurement of community metabolism and significance in the coral reef CO_2 source-sink debate, P. Natl. Acad. Sci. USA, 96, 13017–13022, https://doi.org/10.1073/pnas.96.23.13017, 1999.

Gedan, K. B., Silliman, B. R., and Bertness, M. D.: Centuries of Human-Driven Change in Salt Marsh Ecosystems, Annu. Rev. Mar. Sci., 1, 117–141, https://doi.org/10.1146/annurev.marine.010908.163930, 2009.

Gnanamoorthy, P., Selvam, V., Deb Burman, P. K., Chakraborty, S., Karipot, A., Nagarajan, R., Ramasubramanian, R., Song, Q., Zhang, Y., and Grace, J.: Seasonal variations of net ecosystem (CO_2) exchange in the Indian tropical mangrove forest of Pichavaram, Estuar. Coast. Shelf S., 243, 106828, https://doi.org/10.1016/j.ecss.2020.106828, 2020.

Göckede, M., Rebmann, C., and Foken, T.: A combination of quality assessment tools for eddy covariance measurements with footprint modelling for the characterisation

of complex sites, Agr. Forest Meteorol., 127, 175–188, https://doi.org/10.1016/j.agrformet.2004.07.012, 2004.

Gu, J., Luo, M., Zhang, X., Christakos, G., Agusti, S., Duarte, C. M., and Wu, J.: Losses of salt marsh in China: Trends, threats and management, Estuar. Coast. Shelf S., 214, 98–109, https://doi.org/10.1016/j.ecss.2018.09.015, 2018.

Gu, L., Falge, E. M., Boden, T., Baldocchi, D. D., Black, T. A., Saleska, S. R., Suni, T., Verma, S. B., Vesala, T., Wofsy, S. C., and Xu, L.: Objective threshold determination for nighttime eddy flux filtering, Agr. Forest Meteorol., 128, 179–197, https://doi.org/10.1016/j.agrformet.2004.11.006, 2005.

Guo, H., Noormets, A., Zhao, B., Chen, J., Sun, G., Gu, Y., Li, B., and Chen, J.: Tidal effects on net ecosystem exchange of carbon in an estuarine wetland, Agr. Forest Meteorol., 149, 1820–1828, https://doi.org/10.1016/j.agrformet.2009.06.010, 2009.

Han, G., Chu, X., Xing, Q., Li, D., Yu, J., Luo, Y., Wang, G., Mao, P., and Rafique, R.: Effects of episodic flooding on the net ecosystem CO_2 exchange of a supratidal wetland in the Yellow River Delta, J. Geophys. Res.-Biogeo., 120, 1506–1520, https://doi.org/10.1002/2015JG002923, 2015.

Herbst, M., Friborg, T., Schelde, K., Jensen, R., Ringgaard, R., Vasquez, V., Thomsen, A. G., and Soegaard, H.: Climate and site management as driving factors for the atmospheric greenhouse gas exchange of a restored wetland, Biogeosciences, 10, 39–52, https://doi.org/10.5194/bg-10-39-2013, 2013.

Hwang, Y.-H. and Morris, J. T.: Whole-plant gas exchange responses of *Spartina alterniflora* (Poaceae) to a range of constant and transient salinities, Am. J. Bot., 81, 659–665, https://doi.org/10.1002/j.1537-2197.1994.tb15500.x, 1994.

Jia, X., Zha, T., Wang, S., Bourque, C. P.-A., Wang, B., Qin, S., and Zhang, Y.: Canopy photosynthesis modulates soil respiration in a temperate semi-arid shrubland at multiple timescales, Plant Soil, 432, 437–450, https://doi.org/10.1007/s11104-018-3818-z, 2018.

Jiang, L.-Q., Cai, W.-J., and Wang, Y.: A comparative study of carbon dioxide degassing in river- and marine-dominated estuaries, Limnol. Oceanogr., 53, 2603–2615, https://doi.org/10.4319/lo.2008.53.6.2603, 2008.

Jimenez, K. L., Starr, G., Staudhammer, C. L., Schedlbauer, J. L., Loescher, H. W., Malone, S. L., and Oberbauer, S. F.: Carbon dioxide exchange rates from short- and long-hydroperiod Everglades freshwater marsh: EVERGLADES MARSH CARBON DYNAMICS, J. Geophys. Res., 117, G04009, https://doi.org/10.1029/2012JG002117, 2012.

Kathilankal, J. C., Mozdzer, T. J., Fuentes, J. D., D'Odorico, P., McGlathery, K. J., and Zieman, J. C.: Tidal influences on carbon assimilation by a salt marsh, Environ. Res. Lett., 3, 044010, https://doi.org/10.1088/1748-9326/3/4/044010, 2008.

Kim, Y., Johnson, M. S., Knox, S. H., Black, T. A., Dalmagro, H. J., Kang, M., Kim, J., and Baldocchi, D.: Gap-filling approaches for eddy covariance methane fluxes: A comparison of three machine learning algorithms and a traditional method with principal component analysis, Glob. Change Biol., 26, 1499–1518, https://doi.org/10.1111/gcb.14845, 2020.

Kljun, N., Calanca, P., Rotach, M. W., and Schmid, H. P.: A simple two-dimensional parameterisation for Flux Footprint Prediction (FFP), Geosci. Model Dev., 8, 3695–3713, https://doi.org/10.5194/gmd-8-3695-2015, 2015.

Knox, S. H., Windham-Myers, L., Anderson, F., Sturtevant, C., and Bergamaschi, B.: Direct and Indirect Effects of Tides on Ecosystem-Scale CO_2 Exchange in a Brackish Tidal Marsh in Northern California, J. Geophys. Res.-Biogeo., 123, 787–806, https://doi.org/10.1002/2017JG004048, 2018.

Kowalski, S., Sartore, M., Burlett, R., Berbigier, P., and Loustau, D.: The annual carbon budget of a French pine forest (*Pinus pinaster*) following harvest: ANNUAL CARBON BUDGET OF A PINE FOREST AFTER HARVEST, Glob. Change Biol., 9, 1051–1065, https://doi.org/10.1046/j.1365-2486.2003.00627.x, 2003.

Krauss, K. W., Holm, G. O., Perez, B. C., McWhorter, D. E., Cormier, N., Moss, R. F., Johnson, D. J., Neubauer, S. C., and Raynie, R. C.: Component greenhouse gas fluxes and radiative balance from two deltaic marshes in Louisiana: Pairing chamber techniques and eddy covariance: Gas Fluxes From Louisiana Marshes, J. Geophys. Res.-Biogeo., 121, 1503–1521, https://doi.org/10.1002/2015JG003224, 2016.

Lasslop, G., Reichstein, M., Papale, D., Richardson, A. D., Arneth, A., Barr, A., Stoy, P., and Wohlfahrt, G.: Separation of net ecosystem exchange into assimilation and respiration using a light response curve approach: critical issues and global evaluation: SEPARATION OF NEE INTO GPP AND RECO, Glob. Change Biol., 16, 187–208, https://doi.org/10.1111/j.1365-2486.2009.02041.x, 2010.

Lee, S.-C., Fan, C.-J., Wu, Z.-Y., and Juang, J.-Y.: Investigating effect of environmental controls on dynamics of CO_2 budget in a subtropical estuarial marsh wetland ecosystem, Environ. Res. Lett., 10, 025005, https://doi.org/10.1088/1748-9326/10/2/025005, 2015.

Liaw, A. and Wiener, M.: Classification and Regression by randomForest, R news, 2, 18–22, 2022.

Ma, J., Wang, Z.-Y., Stevenson, B. A., Zheng, X.-J., and Li, Y.: An inorganic CO_2 diffusionand dissolution process explains negative CO_2 fluxes in saline/alkaline soils, Sci. Rep., 3, 2025, https://doi.org/10.1038/srep02025, 2013.

Mayen, J., Polsenaere, P., Regaudie De Gioux, A., Dupuy, C., Vagner, M., Lemesle, J.-C., Poitevin, B., and Souchu, P.: Influence of typology and management practices on water pCO_2 and atmospheric CO_2 fluxes over two temperate shelf–estuary–marsh water continuums, Regional Studies in Marine Science, 67, 103209, https://doi.org/10.1016/j.rsma.2023.103209, 2023.

Mayen, J., Polsenaere, P., Regaudie de Gioux, A., Deborde, J., Collin, K., Le Merrer, Y., Foucault, E., Ouisse, V., André, L., Lamaud, E., and Souchu, P.: Influence of aquatic metabolism on temporal marsh carbon dynamics and associated atmospheric CO_2 fluxes, in preparation, 2024.

Mcleod, E., Chmura, G. L., Bouillon, S., Salm, R., Björk, M., Duarte, C. M., Lovelock, C. E., Schlesinger, W. H., and Silliman, B. R.: A blueprint for blue carbon: toward an improved understanding of the role of vegetated coastal habitats in sequestering CO_2, Front. Ecol. Environ., 9, 552–560, https://doi.org/10.1890/110004, 2011.

Mcowen, C., Weatherdon, L., Bochove, J.-W., Sullivan, E., Blyth, S., Zockler, C., Stanwell-Smith, D., Kingston, N., Martin, C., Spalding, M., and Fletcher, S.: A global map of saltmarshes, Biodiversity Data Journal, 5, e11764, https://doi.org/10.3897/BDJ.5.e11764, 2017.

Migné, A., Spilmont, N., and Davoult, D.: In situ measurements of benthic primary production during emersion: seasonal variations and annual production in the Bay of Somme (eastern English Channel, France), Cont. Shelf Res., 24, 1437–1449, https://doi.org/10.1016/j.csr.2004.06.002, 2004.

Miller, W. D., Neubauer, S. C., and Anderson, I. C.: Effects of Sea Level Induced Disturbances on High Salt Marsh Metabolism, Estuaries, 24, 357, https://doi.org/10.2307/1353238, 2001.

Mitra, B., Miao, G., Minick, K., McNulty, S. G., Sun, G., Gavazzi, M., King, J. S., and Noormets, A.: Disentangling the Effects of Temperature, Moisture, and Substrate Availability on Soil CO_2 Efflux, J. Geophys. Res.-Biogeo., 124, 2060–2075, https://doi.org/10.1029/2019JG005148, 2019.

Moffett, K. B., Wolf, A., Berry, J. A., and Gorelick, S. M.: Salt marsh–atmosphere exchange of energy, water vapor, and carbon dioxide: Effects of tidal flooding and biophysical controls, Water Resour. Res., 46, 2009WR009041, https://doi.org/10.1029/2009WR009041, 2010.

Moncrieff, J., Clement, R., Finnigan, J., and Meyers, T.: Averaging, Detrending, and Filtering of Eddy Covariance Time Series, in: Handbook of Micrometeorology, Vol. 29, edited by: Lee, X., Massman, W., and Law, B., Kluwer Academic Publishers, Dordrecht, 7–31, https://doi.org/10.1007/1-4020-2265-4_2, 2004.

Morelle, J., Roose-Amsaleg, C., and Laverman, A. M.: Microphytobenthos as a source of labile organic matter for denitrifying microbes, Estuar. Coast. Shelf S., 275, 108006, https://doi.org/10.1016/j.ecss.2022.108006, 2022.

Morris, J. T.: Effects of oxygen and salinity on ammonium uptake by *Spartina alterniflora* Loisel. and *Spartina patens* (Aiton) Muhl., J. Exp. Mar. Biol. Ecol., 78, 87–98, https://doi.org/10.1016/0022-0981(84)90071-6, 1984.

Nahrawi, H.: Exchange of Carbon Dioxide between a Southeastern Salt Marsh and the Atmosphere, PhD thesis, The University of Georgia, 131 pp., 2019.

Nahrawi, H., Leclerc, M. Y., Pennings, S., Zhang, G., Singh, N., and Pahari, R.: Impact of tidal inundation on the net ecosystem exchange in daytime conditions in a salt marsh, Agr. Forest Meteorol., 294, 108133, https://doi.org/10.1016/j.agrformet.2020.108133, 2020.

Najjar, R. G., Herrmann, M., Alexander, R., Boyer, E. W., Burdige, D. J., Butman, D., Cai, W.-J., Canuel, E. A., Chen, R. F., Friedrichs, M. A. M., Feagin, R. A., Griffith, P. C., Hinson, A. L., Holmquist, J. R., Hu, X., Kemp, W. M., Kroeger, K. D., Mannino, A., McCallister, S. L., McGillis, W. R., Mulholland, M. R., Pilskaln, C. H., Salisbury, J., Signorini, S. R., St-Laurent, P., Tian, H., Tzortziou, M., Vlahos, P., Wang, Z. A., and Zimmerman, R. C.: Carbon Budget of Tidal Wetlands, Estuaries, and Shelf Waters of Eastern North America, Global Biogeochem. Cy., 32, 389–416, https://doi.org/10.1002/2017GB005790, 2018.

Nyman, J. A. and DeLaune, R. D.: CO_2 emission and soil Eh responses to different hydrological conditions in fresh, brackish, and saline marsh soils, Limnol. Oceanogr., 36, 1406–1414, https://doi.org/10.4319/lo.1991.36.7.1406, 1991.

Papale, D., Reichstein, M., Aubinet, M., Canfora, E., Bernhofer, C., Kutsch, W., Longdoz, B., Rambal, S., Valentini, R., Vesala, T., and Yakir, D.: Towards a standardized processing of Net Ecosystem Exchange measured with eddy covariance technique: algorithms and uncertainty estimation, Biogeosciences, 3, 571–583, https://doi.org/10.5194/bg-3-571-2006, 2006.

Polsenaere, P., Lamaud, E., Lafon, V., Bonnefond, J.-M., Bretel, P., Delille, B., Deborde, J., Loustau, D., and Abril, G.: Spatial and temporal CO_2 exchanges measured by Eddy Covariance over a temperate intertidal flat and their relationships to net ecosystem production, Biogeosciences, 9, 249–268, https://doi.org/10.5194/bg-9-249-2012, 2012.

Reichstein, M., Falge, E., Baldocchi, D., Papale, D., Aubinet, M., Berbigier, P., Bernhofer, C., Buchmann, N., Gilmanov, T., Granier, A., Grunwald, T., Havrankova, K., Ilvesniemi, H., Janous, D., Knohl, A., Laurila, T., Lohila, A., Loustau, D., Matteucci, G., Meyers, T., Miglietta, F., Ourcival, J.-M., Pumpanen, J., Rambal, S., Rotenberg, E., Sanz, M., Tenhunen, J., Seufert, G., Vaccari, F., Vesala, T., Yakir, D., and Valentini, R.: On the separation of net ecosystem exchange into assimilation and ecosystem respiration: review and improved algorithm, Glob. Change Biol., 11, 1424–1439, https://doi.org/10.1111/j.1365-2486.2005.001002.x, 2005.

Reynolds, O.: An Experimental Investigation of the Circumstances Which Determine Whether the Motion of Water Shall Be Direct or Sinuous, and of the Law of Resistance in Parallel Channels, Philos. T. R. Soc. Lond., 935–982, 1883.

Rodda, S., Thumaty, K., Jha, C., and Dadhwal, V.: Seasonal Variations of Carbon Dioxide, Water Vapor and Energy Fluxes in Tropical Indian Mangroves, Forests, 7, 35, https://doi.org/10.3390/f7020035, 2016.

Ruttenberg, K. C.: Development of a sequential extraction method for different forms of phosphorus in marine sediments, Limnol. Oceanogr., 37, 1460–1482, https://doi.org/10.4319/lo.1992.37.7.1460, 1992.

Savelli, R., Bertin, X., Orvain, F., Gernez, P., Dale, A., Coulombier, T., Pineau, P., Lachaussée, N., Polsenaere, P., Dupuy, C., and Le Fouest, V.: Impact of Chronic and Massive Resuspension Mechanisms on the Microphytobenthos Dynamics in a Temperate Intertidal Mudflat, J. Geophys. Res.-Biogeo., 124, 3752–3777, https://doi.org/10.1029/2019JG005369, 2019.

Schäfer, K. V. R., Tripathee, R., Artigas, F., Morin, T. H., and Bohrer, G.: Carbon dioxide fluxes of an urban tidal marsh in the Hudson-Raritan estuary: Carbon dioxide fluxes of an wetland, J. Geophys. Res.-Biogeo., 119, 2065–2081, https://doi.org/10.1002/2014JG002703, 2014.

Schäfer, K. V. R., Duman, T., Tomasicchio, K., Tripathee, R., and Sturtevant, C.: Carbon dioxide fluxes of temperate urban wetlands with different restoration history, Agr. Forest Meteorol., 275, 223–232, https://doi.org/10.1016/j.agrformet.2019.05.026, 2019.

Song, S., Wang, Z. A., Kroeger, K. D., Eagle, M., Chu, S. N., and Ge, J.: High-frequency variability of carbon dioxide fluxes in tidal water over a temperate salt marsh, Limnol. Oceanogr., 68, 2108–2125, https://doi.org/10.1002/lno.12409, 2023.

Sousa, A. I., Lillebø, A. I., Pardal, M. A., and Caçador, I.: Productivity and nutrient cycling in salt marshes: Contribution to ecosystem health, Estuar. Coast. Shelf S., 87, 640–646, https://doi.org/10.1016/j.ecss.2010.03.007, 2010.

Van Dam, B., Polsenaere, P., Barreras-Apodaca, A., Lopes, C., Sanchez-Mejia, Z., Tokoro, T., Kuwae, T., Loza, L. G., Rutgersson, A., Fourqurean, J., and Thomas, H.: Global Trends in Air-Water CO_2 Exchange Over Seagrass Meadows Revealed by Atmospheric Eddy Covariance, Global Biogeochem. Cy.,

35, e2020GB006848, https://doi.org/10.1029/2020GB006848, 2021.

Vargas, R., Baldocchi, D. D., Bahn, M., Hanson, P. J., Hosman, K. P., Kulmala, L., Pumpanen, J., and Yang, B.: On the multi-temporal correlation between photosynthesis and soil CO_2 efflux: reconciling lags and observations, New Phytol., 191, 1006–1017, https://doi.org/10.1111/j.1469-8137.2011.03771.x, 2011.

Vickers, D. and Mahrt, L.: Quality Control and Flux Sampling Problems for Tower and Aircraft Data, J. Atmos. Ocean. Techn., 14, 512–526, https://doi.org/10.1175/1520-0426(1997)014<0512:QCAFSP>2.0.CO2, 1997.

Wang, Q., Wang, C. H., Zhao, B., Ma, Z. J., Luo, Y. Q., Chen, J. K., and Li, B.: Effects of growing conditions on the growth of and interactions between salt marsh plants: implications for invasibility of habitats, Biol. Invasions, 8, 1547–1560, https://doi.org/10.1007/s10530-005-5846-x, 2006.

Wang, Z. A. and Cai, W.-J.: Carbon dioxide degassing and inorganic carbon export from a marsh-dominated estuary (the Duplin River): A marsh CO_2 pump, Limnol. Oceanogr., 49, 341–354, https://doi.org/10.4319/lo.2004.49.2.0341, 2004.

Wang, Z. A., Kroeger, K. D., Ganju, N. K., Gonneea, M. E., and Chu, S. N.: Intertidal salt marshes as an important source of inorganic carbon to the coastal ocean, Limnol. Oceanogr., 61, 1916–1931, https://doi.org/10.1002/lno.10347, 2016.

Wei, S., Han, G., Chu, X., Song, W., He, W., Xia, J., and Wu, H.: Effect of tidal flooding on ecosystem CO_2 and CH_4 fluxes in a salt marsh in the Yellow River Delta, Estuar. Coast. Shelf S., 232, 106512, https://doi.org/10.1016/j.ecss.2019.106512, 2020a.

Wei, S., Han, G., Jia, X., Song, W., Chu, X., He, W., Xia, J., and Wu, H.: Tidal effects on ecosystem CO_2 exchange at multiple timescales in a salt marsh in the Yellow River Delta, Estuar. Coast. Shelf S., 238, 106727, https://doi.org/10.1016/j.ecss.2020.106727, 2020b.

Xi, M., Zhang, X., Kong, F., Li, Y., Sui, X., and Wang, X.: CO_2 exchange under different vegetation covers in a coastal wetland of Jiaozhou Bay, China, Ecol. Eng., 137, 26–33, https://doi.org/10.1016/j.ecoleng.2018.12.025, 2019.

Zhao, J., Malone, S. L., Oberbauer, S. F., Olivas, P. C., Schedlbauer, J. L., Staudhammer, C. L., and Starr, G.: Intensified inundation shifts a freshwater wetland from a CO_2 sink to a source, Glob. Change Biol., 25, 3319–3333, https://doi.org/10.1111/gcb.14718, 2019.

COLLEGE VEGETAL
DOCTORAL ANIMAL, ALIMENT
PAYS DE LA LOIRE MER, ENVIRONNEMENT

Nantes Université

Titre : Échanges de CO_2 atmosphérique dans les marais Charentais : processus, dynamique et facteurs de contrôle associés

Mots clés : marais littoraux, pCO_2 de l'eau, flux de CO_2 atmosphérique, producteur primaire, métabolisme aquatique, variations temporelles.

Résumé : Les marais littoraux sont des écosystèmes productifs permettant la captation de CO_2 atmosphérique par une forte production primaire. Leur métabolisme entraine également une exportation latérale importante de carbone (C) organique et inorganique *via* le compartiment aquatique. Au regard de l'importance des marais dans le cycle du C, l'objectif général de la thèse a été de comprendre les processus biologiques et physico-chimiques contrôlant les flux de C aux interfaces terrestre-aquatique-atmosphérique des marais Charentais. Les mesures des pCO_2 de l'eau ont montré un fort contrôle de la typologie des écosystèmes côtiers sur la dynamique du C inorganique avec des variations spatiales significatives le long d'un continuum plateau continental – estuaire – marais. Dans les marais salés rétro-littoraux, les pratiques de gestion (naturelle ou anthropique) et les types de producteur (macroalgues ou herbiers) influencent le statut métabolique (source ou puits de C). Au sein d'un marais tidal, les échanges nets de CO_2 à l'échelle de l'écosystème (NEE) ont été mesurés pour quantifier le statut métabolique et évaluer l'influence des facteurs biotiques et abiotiques. Un fort puits de CO_2 atmosphérique a été mesuré par la photosynthèse des plantes émergées. Cependant, l'immersion a fortement influencé les flux métaboliques en diminuant la captation de CO2 le jour et les émissions de CO2 la nuit. Au sein d'une troisième partie, les formes organiques et inorganiques du C, les nutriments et le métabolisme planctonique ont été mesurés sur des cycles de 24-heures en simultané avec la NEE pour évaluer la contribution du métabolisme aquatique dans les flux horizontaux et verticaux de C des marais.

Title: Atmospheric CO_2 exchanges in the Charentais marshes: processes, dynamic and environmental controlling factors

Keywords: coastal marshes, water pCO_2, atmospheric CO_2 flux, primary producers, aquatic metabolism, temporal variations.

Abstract: Coastal marshes are shallow productive ecosystems allowing atmospheric CO_2 uptake through strong primary production of plants and algae. The metabolism of these dynamics systems also exports significant and variable amounts of organic and inorganic carbon (C) to coastal waters through the aquatic compartment. Due to the importance of marshes in the C cycle, the general objective of this PhD thesis was to measure and understand the biological, physical and chemical processes controlling C fluxes at the terrestrial – aquatic – atmospheric interfaces of the Charentais marshes. High-frequency measurements of water pCO_2 showed a strong control of the coastal ecosystem typology on inorganic C dynamics, with significant spatial variations along a continental shelf – estuary – marsh continuum. In artificial salt marshes, management practices (natural or anthropogenic) and the types of primary producer (macroalgae or seagrass) influence the metabolic status (source or sink of CO_2). Within a tidal salt marsh, net ecosystem CO_2 exchange (NEE) were measured to quantify the marsh metabolic fluxes and evaluate the relevant environmental factors that control NEE fluxes. The results showed a strong annual atmospheric CO_2 sink through the photosynthesis of emerged halophyte plants. However, tidal immersion significantly disrupted the marsh metabolic fluxes, reducing net CO_2 uptake during the day and net CO_2 emissions during the night. In the third part, organic and inorganic forms of C, nutrients and planktonic metabolism were measured over 24-h cycles simultaneously with the NEE fluxes to assess the contribution of aquatic metabolism to horizontal and vertical fluxes of C in marshes.